AN INFRARED STUDY OF THE MAGELLANIC CLOUDS

Piet Schwering

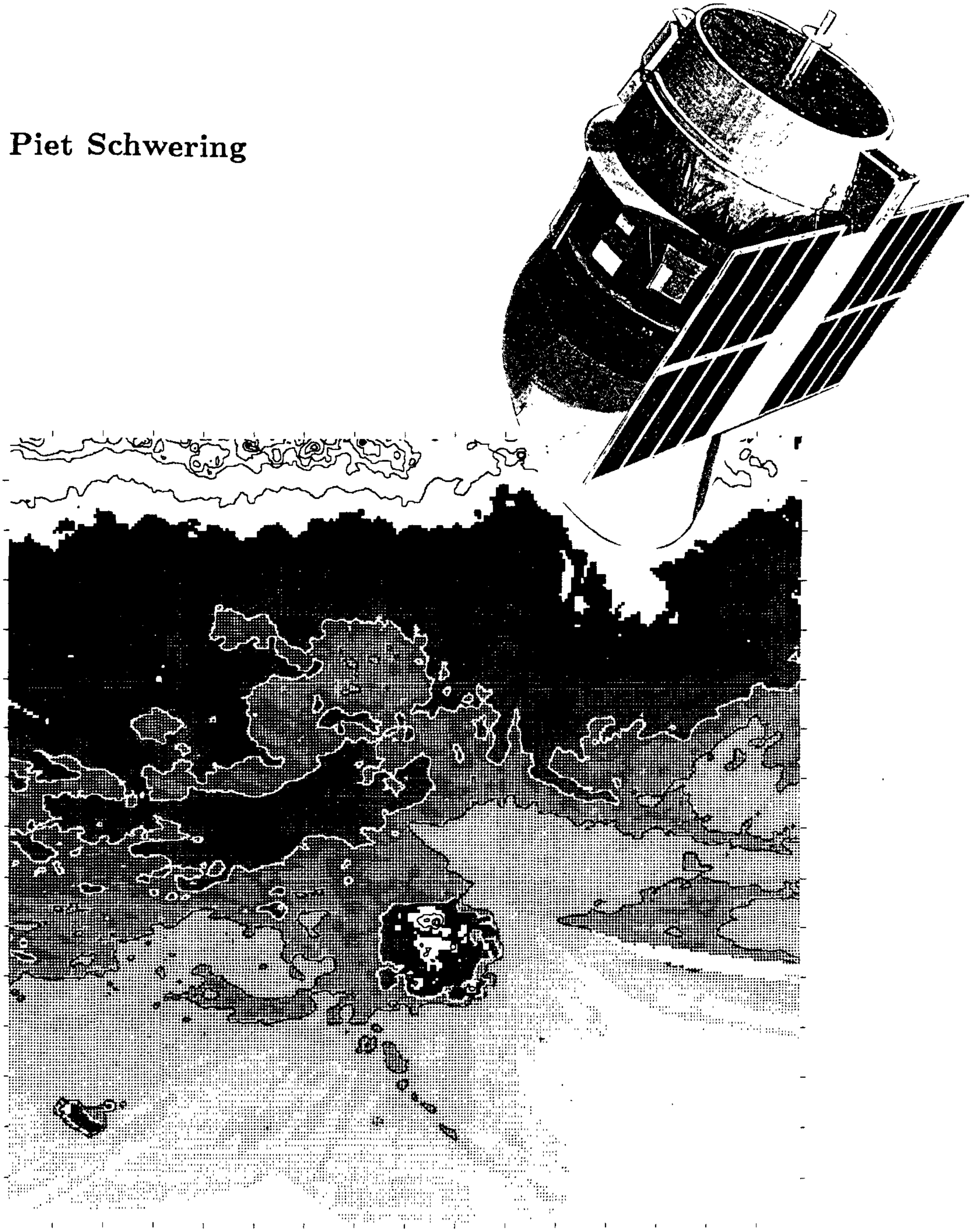

Promotiecommissie:

Promotor:	Prof. Dr. H.J. Habing
Co–promotor:	Dr. F.P. Israel
Referent:	Dr. J. Koornneef
Overige leden:	Prof. Dr. W.B. Burton Prof. Dr. A. Blaauw Prof. Dr. H. van de Laan Prof. Dr. G.K. Miley Prof. Ir. C. van Schooneveld Prof. Dr. W.J. Huiskamp

The Infrared Astronomical Satellite (IRAS) was developed and operated by the Netherlands Agency for Aerospace Programs (NIVR), the U.S. National Aeronautics and Space Administration (NASA) and the U.K. Science and Engineering Research Council (SERC).

Gracias a la Vida

Gracias a la vida que me ha dado tanto,
me dió dos luceros que cuando los abro
perfecto distingo lo negro del blanco,
en el alto cielo su fondo estrellado,
en las multitudes la mujer que yo amo.

Gracias a la vida que me ha dado tanto,
me dió el corazón que agita su marco
cuando miro el fruto del cerebro humano,
cuando miro el bueno tan lejos del malo,
cuando miro el fondo de tus ojos claros.

Violeta Parra

Mijn dank aan het leven

Mijn dank aan het leven dat me zo véél heeft gegeven,
het heeft me twee ogen gegeven zodat ik, wanneer ik ze open
perfekt het donkere van het lichte kan onderscheiden,
in de hoge hemel de besterde verte,
in de menigten de vrouw die ik liefheb.

Mijn dank aan het leven dat me zo véél heeft gegeven,
het heeft me mijn hart gegeven dat zo heftig klopt
als ik de vrucht bekijk van het menselijk brein,
als ik de goede mensen zo ver verwijderd zie van de slechte mensen,
als ik de diepte zie van jouw heldere ogen.

vertaald door Hannie van Loon

Contents

Chapter I Introduction

Chapter II Infrared Observations of the Small Magellanic Cloud

Chapter IV **Galactic infrared foreground emission in the direction of the Magellanic Clouds**

Chapter V **Overall infrared properties of the Magellanic Clouds**

Chapter VI Properties of dust in the Magellanic Clouds

Chapter VII Dust in the Magellanic Clouds

Appendix **On the interpretation of IRAS infrared observations**

The Antarctic Pole is not so starry as the Arctic. Many small stars clustered together are seen, which have the appearance of two clouds of mist. There is but little distance between them, and they are somewhat dim. In the midst of them are two large and not very luminous stars, which move only slightly. Those two stars are the Antarctic Pole.

Pigafetta (1520)

Chapter I

INTRODUCTION

1. The earliest observations of the Magellanic Clouds

Before the invention of the telescope only three galaxies had been seen with the naked eye, only one of which appeared in a catalogue. The Persian astronomer Al–Sûfi (903 – 986) recorded the Andromeda nebula for the first time in his star catalogue "Book of Fixed Stars" (964). The other two galaxies are the Magellanic Clouds, first described by Magellan's chronicler Pigafetta, after leaving the Estrecho de Magallanes in 1520. These two closer and therefore brighter galaxies were discovered later, since they are located in the southern hemisphere beyond the reach of traditional astronomers in Europe and Asia. However, according to Wilson (1899), Al–Sûfi possibly knew the Large Cloud, which he might have meant with an object called Al–Bakr ("white ox").

The Magellanic Clouds were known since the first voyages to the southern hemisphere. They were discovered by Portuguese seamen in the 15th century and named in honour of Fernão de Magalhães e Sousa, who undertook the first voyage around the world. They are mentioned from 1516 on, when the Italian navigator Andraes Corsali drew a map of the southern sky. The two objects, which look like clouds (Pigafetta *et al.*, 1962), were important to 16th century sailors for navigation purposes. Strangely enough the Magellanic Clouds do not appear in Messier's Catalogue of nebulae (1784), which indeed was biased to the northern hemisphere. Herschel claimed to have observed a connection between the Large Cloud and the Milky Way Galaxy on clear nights in 1838; *i.e.* an indication for interactions between these two galaxies. The New General Catalogue of Nebulae and Clusters of Stars and the Index Catalog (Dreyer, 1888, 1895, 1908) contain various objects in both Magellanic Clouds.

2. Modern observations

2.1. The Local Group of galaxies

In 1912, Leavitt discovered that the period and luminosity of pulsating Cepheid variable stars in the Small Magellanic Cloud were related, giving a key to measurements of stellar distances. Shapley calibrated the relation in 1917. Some years later Cepheids were found in the Andromeda nebula (from now on M31), revealing that spiral nebulae were indeed other galaxies at immense distances. In 1925 it became clear through the work of Hubble, that most of the nebulae are *"island universes"* outside our own Milky Way Galaxy. The Galaxy is a member of a small group of galaxies called the *"Local Group"*. Thirty (mostly small) members are now known within the Local Group. The two dominant galaxies are M31 and our Galaxy. They are surrounded by a number of smaller galaxies; the Magellanic Clouds are satellites of our Galaxy.

Tidal interactions between the Clouds and the Galaxy have played an important role in the evolution of the Clouds, and in forming the present structure. These interactions are indicated by distortions of the Small Cloud (Mathewson and Ford, 1984), the existence of the Magellanic Stream (a narrow band of neutral hydrogen) and the HI bridge between the Clouds. Lynden–Bell (1962) has suggested that many of the dwarf galaxies surrounding our Galaxy are tidal debris of an encounter between the Large Cloud and our Galaxy. At the moment, the Small Cloud seems to be breaking up into a Small Cloud–remnant and a Mini–Magellanic Cloud (Mathewson and Ford, 1984).

2.2. The Magellanic Clouds

Because of their position the Clouds can only be observed with southern hemisphere telescopes. Yet astronomers at all continents are studying the Galaxy's closest neighbours. The Large Magellanic Cloud (LMC) is located in the constellation Dorado and has an optical diameter of about 7° (Fig. 1). The Small Magellanic Cloud (SMC), with a diameter of 3°.5, is located in Tucana (Fig. 2). On deep plates they have diameters of 12° resp. 8°. The Magellanic Clouds are presumably gravitationally bound, 22° (25 kpc) apart. They are the nearest galaxies, more than ten times closer than M31, the closest spiral galaxy, and can be resolved into individual objects and nebulae. They are close enough that we can perform detailed investigations and henceforth use them as a link between the Milky Way and more distant galaxies.

The Clouds are regarded as blue irregular galaxies and have low luminosities (classes III – V). The LMC–Bar resembles the central bar of a barred spiral. Some evidence for the beginning of a spiral pattern at the ends of the Bar was found by de Vaucouleurs (1955); it was shown later that these arms are Galactic foreground material (Israel and Schwering, 1986). According to some authors (*e.g.* Schmidt–Kaler, 1977), the LMC's active filaments show spiral structure emerging from the 30 Doradus nebula. A thorough description of the morphological structure of Magellanic type galaxies is given by Feitzinger (1980).

Hodge and Wright (1967) presented an optical atlas of the LMC. The LMC is a true astronomical treasure–house. It contains objects as the Tarantula nebula (NGC 2070; better known as 30 Doradus), one of the largest known HII regions; the most luminous individual star known in the universe S–Doradus (the chief star of the cluster NGC 1910). Shapley has named ten major Constellations of active star formation in the LMC (van den

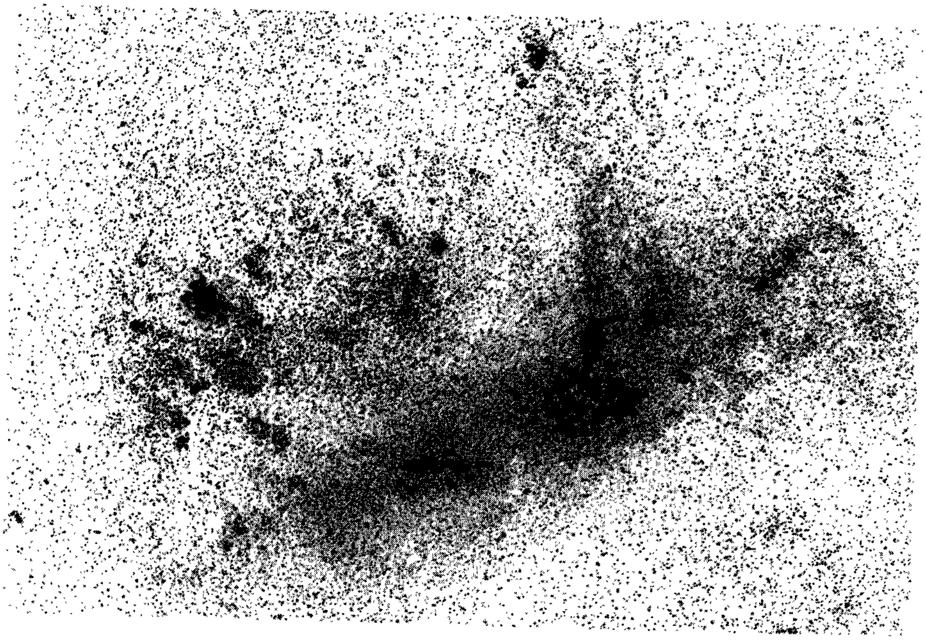

Figure 1. *The Large Magellanic Cloud.*
A black and white negative–print of a visual exposure obtained with the 61–cm Schmidt telescope of the Cerro Tololo Inter–American Observatory (CTIO). The figure shows the central region of about 6° x 4°. Clearly visible are the LMC–Bar, and the 30 Doradus complex at the left. The bright region at the top of the image is Constellation I, and the region between 30 Doradus and the Bar is Constellation II. Many Galactic forgeround stars are visible.

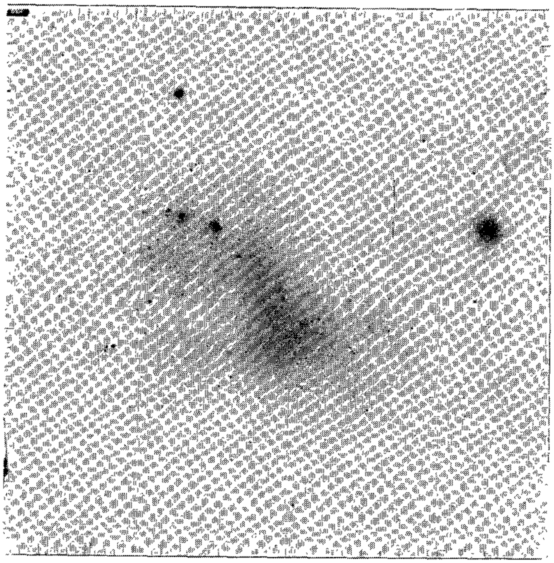

Figure 2. *The Small Magellanic Cloud.*
A negative–print of an ESO–SERC Sky plate. The total field is 6° x 6°. Many Galactic foreground stars are visible, as well as the Galactic globular cluster 47 Tuc at the right.

Bergh, 1981). Supernova SN 1987A in the LMC, became one of the most studied objects of 1987 (various ESO astonomers and ESO guest observers; see *Eso Messenger* **47**, 1987, pp 26 – 35).

Hodge and Wright (1977) presented an optical atlas of the SMC. The SMC, overshadowed by the larger LMC, contains few regions of bright nebulosity and the stellar population is less flamboyant. There are two main areas in the SMC; a Bar, and a Wing that was described by Shapley in 1940. The SMC HII region N 66, is referred to as a small copy of 30 Doradus in the LMC (Lequeux, 1987).

Without aiming for completeness, here follows a summary of the main Cloud surveys. Feast *et al.* (1960) listed the brightest stars in the Clouds, and found 50 stars in the SMC and 108 in the LMC. Azzopardi and Vigneau (1982) have enlarged the list of SMC stars to 524. The list of LMC stars was expanded by Sanduleak (1970) to 1272 with $m_{pg} < 14$. Fehrenbach and Duflot (1970, 1973 and 1981) observed 2990 stars in and towards the LMC. Various surveys were published for special types of stars and stellar products.

A total of 122 stellar associations are listed by Lucke and Hodge (1970) for the LMC and 70 by Hodge (1985) for the SMC. Up to now 601 star clusters have been identified in the SMC (Kron, 1956; Lindsay, 1958; Westerlund and Glaspey, 1971; Hodge and Wright, 1974; Brück, 1976; Hodge, 1986). A number of 1603 clusters were identified in the LMC (Shapley and Lindsay, 1963; Lyngå and Westerlund, 1963; Hodge and Sexton, 1966). Both globular and open clusters with various degrees of concentration have been found. The ages of these clusters range from 10^7 yr to 10^{10} yr and on average these clusters are more flattened than their Galactic or M31 counterparts (van den Bergh, 1984). The Clouds are surrounded by a number of young globular clusters.

2.3. Atomic, molecular and ionized gas

The first atomic hydrogen (HI) surveys of the Clouds were published by McGee and Milton (1966) on the LMC and Hindman (1967) on the SMC. Later surveys are by Rohlfs *et al.* (1984) and McGee and Newton (1981). All of them were obtained with the 64–m Parkes radio telescope (CSIRO) which has a resolution of 15$'$ at 1420 MHz. Although the LMC is larger than the SMC the HI masses are about the same for the two systems. Both galaxies contain a large fraction (10 % for the LMC and 30 % for the SMC) of the total dynamic mass in the form of HI. Neutral hydrogen observations also reveal the existence of a great gaseous envelope surrounding both Clouds (Mathewson and Ford, 1984).

An overview of radiocontinuum surveys of the Clouds can be found in Mills and Turtle (1984). Most of the high resolution surveys were obtained with the 64–m Parkes telescope; the latest being the 1400 MHz survey by Haynes *et al.* (1986). The Molonglo Observatory Synthesis Telescope (MOST) has yielded a high resolution ($< 1'$) map of the Clouds at 843 MHz (see Mills and Turtle, 1984). The radio observations show both thermal and non-thermal radio emission. The first component is related to individual HII regions, while the latter is related to the galactic disk.

The first detections of molecular carbon monoxide emission in the Clouds were by Huggins *et al.* (1975; CO 2.6–mm), Israel *et al.* (1982; CO 1.3–mm), and Israel *et al.* (1986). The first complete CO surveys of the Clouds was presented by Rubio *et al.* (1984) and Cohen *et al.* (1984), obtained with the Columbia Southern Millimeter–Wave telescope at CTIO, with a resolution of 8$'$. Final LMC CO maps are presented by Cohen *et al.* (1988).

A low CO abundance is indicated by all of these observations, which may imply molecular hydrogen underabundances. Presently, a large CO survey of the Clouds with the ESO–SEST telescope is underway; this survey has just started and will take years to complete (Israel, priv. comm.). In these galaxies the abundance of CO with respect to H_2 may be different from that in the Milky Way (Israel, 1985). The first molecular hydrogen observations of objects in the Clouds were obtained by Koornneef and Israel (1985) for N 81 in the SMC. Israel and Koornneef (1987) have observed the S1–line and Q–branch of H_2 in some 10 objects of both Clouds. A summary of observations of other molecules than CO and H_2 of the Clouds can be found in Israel (1984).

Henize (1956) published Hα photographs and a list of 221 nebulosities in the LMC and 90 in the SMC. Davies *et al.* (1976) obtained new photographs and listed 329 Hα nebulosities in the LMC and 167 in the SMC. Kennicutt and Hodge (1986) added Hα–fluxes for most of the HII–regions. From the Hα photographs Meaburn (1980) found numerous giant shells and 9 supergiant shells (with sizes of $\sim$ 1 kpc) in the LMC and 1 supergiant shell in the SMC.

2.4. Abundances and star formation

The Magellanic Clouds show low heavy element abundances. A summary of these abundances is given by Dufour (1984). In Cloud HII regions, O and Ne are deficient (relative to HII regions in the Solar Neighbourhood) by a factor of 2 in the LMC and 5 in the SMC. The deficiency of C and N is even larger, 4 and 16 times in the LMC and 30 times in the SMC. Hence, the metallicities in the SMC are more extremely underabundant than in the LMC.

With the use of balloons and spacecraft, ultraviolet studies have become available (Carruthers and Page, 1977; Koornneef, 1977; Vuillemin, 1988). These studies show strong radiation fields produced by hot OB–stars. The global star formation rate in the Magellanic Clouds (Lequeux, 1984) is higher per unit total mass in the Clouds than in the Galaxy (2.7 times in the LMC and 1.6 times in the SMC). Several bursts of star formation seem to have occurred in the LMC. Kennicutt and Hodge (1986) have estimated the total star formation in the Clouds at 0.14 $M_\odot$/yr in the LMC and 0.038 $M_\odot$/yr in the SMC. A number of protostars has been detected in both Clouds by Gatley *et al.* (1981), Gatley *et al.* (1982) and Jones *et al.* (1986).

Optical photometry shows that the Magellanic Clouds suffer little obscuration by dust. The dust content of the Clouds has been studied in different ways. A summary of dust observations is given by Israel (1984). Hodge (1972) listed 68 dark clouds in the LMC and Hodge (1974) listed 45 dark clouds in the SMC. These lists are not complete due to the fact that dark clouds are only seen on a stellar background. Dust is underabundant in the Clouds, resulting in gas–to–dust ratios 4 (LMC) and 17 times (SMC) higher than in the Galaxy (Koornneef, 1984).

Interstellar extinction curves of the Clouds are presented by Koornneef and Code (1981) for the LMC and by Lequeux *et al.* (1984) for the SMC. The general characteristics are that the 2200 Å bump is weaker in the LMC than in the Milky Way, and it is completely absent in the SMC. The far–ultraviolet rise is steeper in the LMC than in the Milky Way; and even steeper in the SMC.

3. Outline of this thesis

One of the principal motivations for studying the Magellanic Clouds is the high linear resolution that can be achieved. At distances of 53 kpc (LMC) and 63 kpc (SMC; Humphreys, 1984), details of order 10 times smaller than in the nearest spiral galaxy M31 and 50 times smaller than in comparable (dwarf) irregular galaxies can be seen.

In Fig. 3 the integrated flux densities of the Clouds over the whole spectral range are shown. The newest observations are the infrared data, obtained with the Infrared Astronomical Satellite (IRAS), which have the highest flux densities. These IRAS observations indicate the importance of filling in the infrared gap in the spectrum. This thesis deals with the infrared spectral range. Due to the fact that the atmosphere absorbs most energy at wavelengths between 20 and 1000 μm (Traub und Stier, 1976), far-infrared observations can only be obtained by balloon-borne telescopes or satellites.

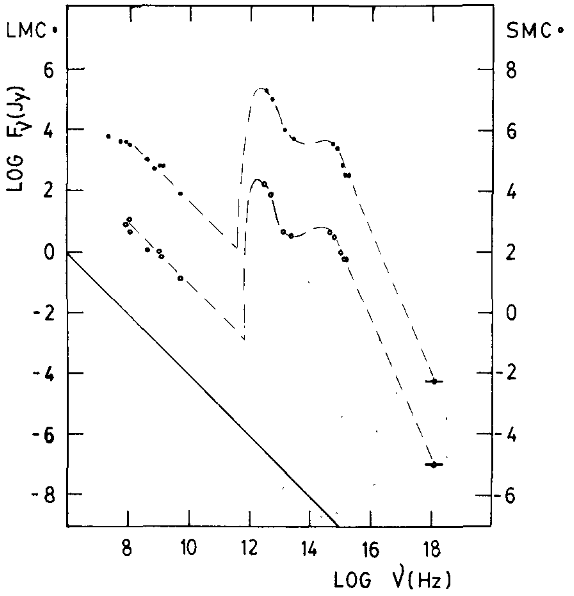

Figure 3. *Integrated flux densities f_ν of the Magellanic Clouds.*
The dashed curves are eye-bal fits to the data points. Note the offset between the left-hand (LMC) scale and right-hand (SMC) scale. The solid line represents the zero-level for the energy spectrum (νf_ν).

The next two chapters deal with the IRAS infrared observations that form the basis of this study. In Chapter II, the SMC observations are presented in the form of maps at 12, 25, 60 and 100 μm. From these maps a list of 219 discrete infrared sources is extracted. This source list is compared to known object lists (foreground stars, SMC stars, Hα nebulosities, clusters, supernova remnants, planetary nebula and dark clouds). In an Appendix to this chapter, a discussion of two fields at the SE and SW edge of the SMC are discussed. These areas contain 29 sources, which are also compared to other source lists.

Chapter III deals with IRAS infrared observations of the LMC. A similar presentation and discussion is given as for the SMC. A list of 1823 discrete sources is extracted, which are compared to other source lists. Seven fields at the North and West edges of the LMC are discussed in an Appendix to this chapter. These fields contain another 68 sources, which are also compared to other source lists.

In Chapter IV a discussion of the Galactic infrared foreground is presented. Especially towards the LMC, foreground filaments disturb the image of the Cloud. Observations are normally corrected for a constant Galactic foreground of $E_{B-V} = 0.07$ mag. The IRAS data suggest strong variations in the foreground (Israel and Schwering, 1986). The relation between the infrared foreground emission and the atomic hydrogen content is discussed; it is found to be non–linear. Temperature corrected infrared maps are produced, which are compared to the atomic hydrogen emission. An estimate for the foreground infrared emission is derived, based on the average observed gas–to–dust ratio. A more or less constant foreground of 0.08 mag towards the SMC is found. The foreground towards the LMC varies from 0.07 to 0.17 mag, with an average of 0.10 mag and minima in the directions of 30 Doradus and the Bar.

Chapter V deals with the large scale and global properties of the Magellanic Clouds. Integrated infrared flux densities are derived, infrared sizes, luminosities and temperatures. The infrared morphology is discussed, together with the temperature distribution. From the latter, the interstellar radiation field in the Clouds is estimated. At the outer edges of the Clouds we found radiation fields equal to the Solar Neighbourhood field and in HII regions the field is 10 – 20 times stronger. Comparisons of the infrared maps are presented with ultraviolet data, Hα maps and with radio continuum observations.

In Chapter VI a discussion is given of the dust properties in the Clouds. The mid–infrared (12 and 25 μm) emission is discussed in detail. Most probably very small grains are responsible for this emission. Dust masses are derived for the combined warm ($\sim$ 50 K) and cool (25 K) dust components. The mass present in a cold (15 K) dust component is estimated to be 30 – 100 % of the mass of cool dust. The mass of hot ($\sim$ 300 K) dust is 10^{-5} times that of cool dust. Dust column density maps are presented for both Clouds. From a comparison of the infrared maps with HI maps, similar non–linear relations are found as for the Galactic foreground in Chapter IV.

Chapter VII contains a further discussion of the global properties of the Clouds. It also contains a discussion of the global relation of the Clouds to (dwarf) irregular galaxies and the relation to Local Group galaxies. Relations between the Clouds global properties derived from the global infrared data, and data at $8'$ resolution, are established. An extensive discussion on the gas–to–dust ratios in the Magellanic Clouds is presented. This ratio is 3 times higher in the LMC compared to the Galaxy and 55 times in the SMC.

Finally, a summary of the quantities involved in IRAS observations is given in an Appendix. A review of the far-infrared radiative transfer theory is given. The Appendix contains tables and figures for colour corrections, dust temperature and mass calculations and bolometric corrections.

A summary of this thesis in English, Spanish and Dutch is given at the end. An atlas of the detailed IRAS infrared images of both Magellanic Clouds is presented by Schwering and Israel (1988).

Historical references

Jones, K.G.: 1968 – 1969, *Journal of the B.A.A.* **78**, 256, 360, 446

Jones, K.G.: 1969 – 1970, *Journal of the B.A.A.* **79**, 19, 105, 213, 268, 357, 450

Pigafetta, A., Transylvania, M. of, Corrêa, G.: 1962, *"Magellan's Voyage around the World"*, ed. C.E. Nowell, Nothwestern Univ. press., Evanston, 1962, p127

Richter, O.G.: 1984, *ESO Messenger* **35**, 17

Wilson, R.H.: 1899, *"Star Names and their Meanings"*, reprinted in 1963 as *"Star Names, their Lore and Meaning"*, Dover Publications

References

Azzopardi, M., Vigneau, J.: 1982, *Astron. Astrophys.* **50**, 291

van den Bergh, S.: 1981, *Astron. Astrophys. Suppl.* **46**, 79

van den Bergh, S.: 1984, in *"Structure and Evolution of the Magellanic Clouds"*, IAU Symp. 108, eds. S. van den Bergh, K.S. de Boer, Reidel Dordrecht, 1

Brück, M.T.: 1976, *Occ. Rep. R. Obs. Edinburgh* **1**

Carruthers, G.R., Page, T.: 1977, *Astrophys. J.* **211**, 728

Cohen, R., Montani, J., Rubio, M.: 1984, in *"Structure and Evolution of the Magellanic Clouds"*, IAU Symp. 108, eds. S. van den Bergh, K.S. de Boer, Reidel Dordrecht, 401

Cohen, R.S., Dame, T.M., Garay, G., Montani, J., Rubio, M., Thaddeus, P.: 1988 *Astrophys. J. Letters* in press.

Davies, R.D., Elliot, K.H., Meaburn, J.: 1976, *Mem. R. Aston. Soc.* **81**, 89

Dreyer, J.L.E.: 1888, *"New General Catalogue of Clusters of Stars"*, *Mem. R. Astron. Soc.* **44**, 1

Dreyer, J.L.E.: 1895, *"Index Catalogue"*, *Mem. R. Astron. Soc* **51**, 185

Dreyer, J.L.E.: 1908, *"Index Catalogue"*, *Mem. R. Astron. Soc.* **59**, 105

Dufour, R.J.: 1984, in *"Structure and Evolution of the Magellanic Clouds"*, IAU Symp. 108, eds. S. van den Bergh, K.S. de Boer, Reidel Dordrecht, 353

Feast, M.W., Thackeray, A.D., Wesselink, A.J.: 1960, *Mon. Not. R. Astron. Soc.* **121**, 337

Fehrenbach, C., Duflot, M.: 1970, *Astron. Astrophys. Special. Suppl.* **1**, 1

Fehrenbach, C., Duflot, M.: 1973, *Astron. Astrophys. Suppl.* **10**, 231

Fehrenbach, C., Duflot, M.: 1981, *Astron. Astrophys. Suppl.* **46**, 13

Feitzinger, J.V.: 1980, *Space Sci. Rev.* **27**, 35

Gatley, I., Becklin, E.E., Hyland, A.R., Jones, T.J.: 1981, *Mon. Not. R. Astron. Soc.* **197**, 17P

Gatley, I., Hyland, A.R., Jones, T.J.: 1982, *Mon. Not. R. Astron. Soc.* **200**, 521

Haynes, R.F., Caswell, J.L.: 1981, *Mon. Not. R. Astron. Soc.* **197**, 23P

Henize, K.G.: 1956, *Astrophys. J. Suppl.* **2**, 315

Hindman, J.V.: 1967, *Aust. J. Phys.* **20**, 147

Hodge, P.W., Sexton, J.A.: 1966, *Astron. J.* **71**, 363

Hodge, P.W., Wright, F.W.: 1967, *"The Large Magellanic Cloud"*, Smithsonian press, Washington D.C.

Hodge, P.W.: 1972, *Publ. Astron. Soc. Pac.* **84**, 365

Hodge, P.W., Wright, F.W.: 1974, *Astron. J.* **79**, 858

Hodge, P.W.: 1974, *Publ. Astron. Soc. Pac.* **86**, 263

Hodge, P.W., Wright, F.W.: 1977, *"The Small Magellanic Cloud"*, University of Washington press, Seattle and London

Hodge, P.W.: 1985, *Publ. Astron. Soc. Pac.* **97**, 530

Hodge, P.W.: 1986, *Publ. Astron. Soc. Pac.* **98**, 1113

Huggins, P.J., Gillespie, A.R., Philips, T.G.: 1975, *Mon. Not. R. Aston. Soc.* **193**, 69P

Humphreys, R.M.: 1984, in *"Structure and Evolution of the Magellanic Clouds"*, IAU Symp. 108, eds. S. van den Bergh, K.S. de Boer, Reidel Dordrecht, 145

Israel, F.P., de Graauw, Th., Lindholm, S., van der Stadt, H., de Vries, C.P.: 1982, *Astrophys. J.* **262**, 100

Israel, F.P.: 1984, in *"Structure and Evolution of the Magellanic Clouds"*, IAU Symp. 108, eds. S. van den Bergh, K.S. de Boer, Reidel Dordrecht, 319

Israel, F.P.: 1985, in *"New Aspects of Galaxy Photometry"*, Lecture Notes on Physics 32, ed. J.L. Nieto, Springer Verlag Berlin, 101

Israel, F.P., de Graauw, Th., van der Stadt, H., de Vries, C.P.: 1986 *Astrophys. J.* **303**, 186

Israel, F.P, Schwering, P.B.W.: 1986, in *"Light on Dark Matter"*, ed. F.P. Israel, Reidel Dordrecht, 383

Israel, F.P., Koornneef, J.: 1988, *Astron. Astrophys.* **190**, 21

Jones, T.J., Hyland, A.R., Straw, S., Harvey, P.M., Wilking, B.A., Joy, M. Gatley, I., Thomas, J.A.: 1986, *Mon. Not. R. Astron. Soc.* **219**, 603

Kennicutt, R.C., Hodge, P.W.: 1986, *Astrophys. J.* **306**, 130

Koornneef, J.: 1977, *Astron. Astrophys. Suppl.* **29**, 117

Koornneef, J., Code, A.D.: 1981, *Astrophys. J.* **247**, 860

Koornneef, J.: 1984, in *"Structure and Evolution of the Magellanic Clouds"*, IAU Symp. 108, eds. S. van den Bergh, K.S. de Boer, Reidel Dordrecht, 333

Koornneef, J., Israel, F.P.: 1985, *Astrophys. J.* **291**, 156

Kron, G.E.: 1956, *Publ. Astron. Soc. Pac.* **68**, 125

Lequeux, J.: 1984, in *"Structure and Evolution of the Magellanic Clouds"*, IAU Symp. 108, eds. S. van den Bergh, K.S. de Boer, Reidel Dordrecht, 67

Lequeux, J., Maurice, E., Prévot, L., Prévot–Burnichon, M.–L., Rocca–Volmerange, B.: 1984, in *"Structure and Evolution of the Magellanic Clouds"*, IAU Symp. 108, eds. S. van den Bergh, K.S. de Boer, Reidel Dordrecht, 405

Lequeux, J.: 1987, in *"Starbursts and Galaxy Evolution"*, eds. T.X. Thuan, T. Montmerle, J. Tran Thanh Van, Editiones Frontières, Gif–sur–Yvette, 59

Lindsay, E.M.: 1958, *Mon. Not. R. Astron. Soc.* **118**, 172

Lucke, P.B., Hodge, P.W.: 1970, *Astron. J.* **75**, 171

Lynden–Bell, D.: 1962, *Observatory* **102**, 202

Lyngå, G., Westerlund, B.W.: 1963, *Mon. Not. R. Astron. Soc.* **127**, 31

Mathewson, D.S., Ford, V.L.: 1984, in *"Structure and Evolution of the Magellanic Clouds"*, IAU Symp. 108, eds. S. van den Bergh, K.S. de Boer, Reidel Dordrecht, 125

McGee, R.X., Milton, J.A.: 1966, *Aust. J. Phys.* **19**, 343

McGee, R.X., Newton, L.M.: 1981, *Proc. Astron. Soc. Aust.* **4**, 189

Meaburn, J.: 1980, *Mon. Not. R. Astron. Soc.*, **192**, 365

Messier, C.: 1784, in *"Connaissance des Temps"*, Paris

Mills, B.Y., Turtle, A.J.: 1984, in *"Structure and Evolution of the Magellanic Clouds"*, IAU Symp. 108, eds. S. van den Bergh, K.S. de Boer, Reidel Dordrecht, 283

Rohlfs, K. Kreitschmann, J., Siegman, B.C., Feitzinger, J.V.: 1984, *Astron. Astrophys.* **137**, 343

Rubio, M., Cohen, R., Montani, J.: 1984, in *"Structure and Evolution of the Magellanic Clouds"*, IAU Symp. 108, eds. S. van den Bergh, K.S. de Boer, Reidel Dordrecht, 399

Sanduleak, N.: 1970, *Contr. Cello Tololo Inter-Am. Obs.*, **89**, 67

Schmidt–Kaler, Th.: 1977, *Astron. Astrophys.* **54**, 771

Schwering, P.B.W., Israel, F.P.: 1988, *"Atlas and Catalogue of IRAS far–infrared observations of the Magellanic Clouds"*, in preparation

Shapley, H., Lindsay, E.M.: 1963, *Irish Astron. J.* **6**, 74

Traub, W.A., Stier, M.T.: 1976, *Applied Optics* **15**, 364

de Vaucouleurs, G.: 1955, *Astron. J.* **60**, 126

Vuillemin, A.: 1988, *Astron. Astrophys. Suppl.* **72**, 249

Westerlund, B.E., Glaspey, J.: 1971, *Astron. Astrophys.* **10**, 1

Chapter II

INFRARED OBSERVATIONS OF THE SMALL MAGELLANIC CLOUD

Summary

Results of IRAS pointed observations in four infrared wavelength bands (12, 25, 60 and 100 μm) on the Small Magellanic Cloud are presented. Maps with orthogonal scan directions are shown and a source list containing 219 infrared sources is extracted from the data. Comparison with the IRAS Point Source Catalog (PSC) shows that only three entries in this catalogue are spurious. Thirty–three of the sources found (and listed in the PSC) are extended. We confirm all 13 entries in the IRAS Small Scale Structure Catalog (SSS) in the SMC. We found 72 new infrared sources, not included in either the PSC or in the SSS. Our SMC infrared source list is compared to other object lists. We identified 28 SAO stars, two blue globular clusters and seven planetary nebulae. We did not find any SMC–stars nor did we find a clear correlation with supernova remnants. In general there is a good correlation of infrared emission with the distribution of HII regions and dark clouds. Results of infrared maps of two additional fields at the SE and SW corners of the SMC are presented in an Appendix, together with a list of sources that were extracted from these maps.

1. Introduction

The Magellanic Clouds are the closest galaxies in the Local Group. In fact, with distances D = 53 kpc (LMC) and D = 63 kpc (SMC; Humphreys, 1984) they are the nearest (dwarf) irregular galaxies. As a result, with the same instrument linear resolutions on the Magellanic Clouds are of order 50 times better than those on comparable other blue dwarf irregulars, thus enabling terrestrial observers to conduct extensive studies on their detailed structure. Compared to the Solar Neighbourhood, both Magellanic Clouds are characterized by low dust and low heavy–element abundances (see *e.g.* the review by Israel, 1984). Relatively high present–day star formation rates, hence the presence of large numbers of luminous hot stars, nevertheless lead to significant infrared emission from warm dust. Only limited infrared information on the Clouds is available from ground based and airborne observations (see Table 1). All these observations were limited to the brightest a priori known objects and covered negligible fractions of the Cloud surfaces. A complete infrared survey of the Magellanic Clouds was first obtained by the Infrared Astronomical Satellite (IRAS). The IRAS mission (IRAS, 1985a) produced a list of point sources over the whole sky, including the Clouds, as well as a series of maps, both in the Survey mode and in pointing modes, and a catalogue of Small Scale Structure (SSS). However, the IRAS Point Source Catalog (PSC) entries for the Clouds in principle suffer from confusion. Potential effects of this on the PSC are artificial detections and missed real sources. Maps of the sky brightness as observed by IRAS in the $16^{\circ}\!.5$ extended emission images (Skyflux) and the Additional Observations (AO) program, give better information about (point and extended) sources in the Magellanic Clouds, because they represent two-dimensional images, while the PSC was obtained from one-dimensional detector datastreams. The advantage of the AOs over the 16°.5 Skyflux images is the higher resolution, better sampling, better pointing, higher sensitivity and less striping. Because of the position of the Clouds near the Ecliptic Pole many different scan angles occur which fill the present Skyflux maps with radial striping. Due to this striping and other background variations determination of good fluxes for both Magellanic Clouds from the Skyflux maps is very difficult, especially at 12 μm. Here we present full-resolution AO maps of the SMC and information on discrete sources extracted from these maps.

Table 1. *Other infrared observations of the Magellanic Clouds* [a,b].

Spectral range	Reference	Number of Objects SMC	LMC	Objects
Near-infrared photometry ($\lambda < 30$ μm):				
	Grasdalen and Joyce (1976)	6	0	N9,N13A,N25,N46, N64A,N81
	Price and Walker (1976) [c]	0	4	30 Dor,N159 (2 more)
	Gatley *et al.* (1981)	0	1	N159
	Gatley *et al.* (1982)	1	0	N76B
	Epchtein *et al.* (1984)	2	2	N160A,N105A
	Koornneef and Israel (1985)	1	0	N81
	Jones *et al.* (1986)	0	5	N10,N59A,N158C, N160,N159
	Israel *et al.* (1988)	9	16	Various sources
Near-infrared spectro-photometry ($\lambda < 5$ μm):				
	Koornneef and Israel (1985)	1	0	N81
	Israel and Koornneef (1988)	3	6	N81,N85,N88 (SMC); N7,N83B,N11A,N213A, 30 Dor,N159 (LMC)
Far-infrared photometry($\lambda > 30$ μm) [c]:				
	Werner *et al.* (1978)	0	4	30 Dor,N158, N160A,N159
	Jones *et al.* (1986)	0	4	N159,N160A,N59A,N158

Notes to Table 1:

a) *Near-infrared stellar surveys are excluded: Glass (1974), Allen and Glass (1976), Glass (1979), Feast et al. (1980), Catchpole and Feast (1981), Cohen et al. (1981), Feast and Whitelock (1984), Glass (1984), Welch and Madore (1984),* Russel and Hyland (1985).

b) *Near-infrared surveys of cluster stars and integrated cluster photometry are excluded: Mould and Aaronson (1980), Aaronson and Mould (1982), Mould and Aaronson (1982), Frogel and Cohen (1982), Persson et al. (1983).*

c) *The observations of Price and Walker (1976) were done with a rocket experiment; the far-infrared observations were obtained with NASA's Kuiper Airborne Observatory. The other observations in this table are all ground based.*

2. Observations and data reduction

The observations presented in this chapter were obtained with the IRAS satellite as part of the AO program carried out with the IRAS survey array. A full description of the instrument array, the survey and data processing can be found in the IRAS Explanatory Supplement (IRAS, 1985a). A description of the AO program and a list of all rasterscan AOs observed by the IRAS satellite of many different objects are given in *"A User's Guide to IRAS Pointed Observation Products"* (IRAS, 1986).

There is a variety of pointed observations on the SMC (see Israel and Schwering, 1986). Most of them (IRAS AO observation technique DPS) cover an area of $1\overset{\circ}{.}5$ x $0\overset{\circ}{.}5$, others (DSD) are useful only for small fields on selected objects. Deep Sky Mapping (DPM) observations are the only ones covering the entire SMC in a regular manner. Because these DPM observations are not limited by noise and the resolution cannot be improved by adding the other AO observations, it was decided not to combine observations obtained with different observing techniques. This also avoided possible problems in combining these different AOs, and in having inhomogeneous coverage of the SMC. The maps presented here are thus based on the DPM observations alone. The observations were made in the months of June, July and September 1983, and are summarized in Table 2.

In the DPM mode, a rasterscan of 6 or 7 legs of $166'$ length was made with a cross-scan step of $20'$, while scanning took place in the normal survey direction. Scanning each leg took about 43 seconds with a turnaround time of about 17 seconds, so that observing a single DPM field took about 8 minutes. The scan speed was $3\overset{\prime}{.}85$/sec, as for the survey. Compared to the survey the signal-to-noise ratio increased by a factor of about 1.4.

Deliberately two separate sets of DPM observations were made with almost orthogonal scanning directions: approximately EW and NS. This was possible because the SMC is close to the South Ecliptic Pole ($\beta_{SMC} = -65\,^{\circ}$), so that observations obtained three months apart yielded the required orthogonal scanning directions. Due to the rectangular form of the IRAS survey detectors (largest size in the cross-scan direction) the resolution is highest in the scan direction (timeresolution), so that these two sets of data supply us with maximum resolution in both directions. In June the SMC was scanned NS (average position angle of the scan direction 159°; observations set 1 NS in Table 2) in a double coverage, in July also NS (173°; set 2 NS) with a coverage of four. In September (three months later) the SMC was scanned EW (253°; set 3 EW) with double coverage. Because of the large size of the SMC compared to the area covered by a single DPM observation every coverage consists of four differently pointed observations. Another nine observations were made (two in June and seven in July), which were processed and later deleted for various reasons (see below).

The reduction was done in two stages. The first stage of data reduction took place at the IRAS Science Data Analysis System (SDAS). It contained the stim-flash calibration of the detector datastreams (see IRAS, 1985a) to the IRAS May 1984 standard. Dead detectors and the smaller edge-detectors were left out to obtain a consistent sampling for small sources. Detector offsets were eliminated to avoid detector striping in the maps (Kopan, 1984). Because each individual detector had its own gain characteristics and inconsistencies between different detectors in a single band remained, an unacceptably high striping level may result unless special care is taken. The method used reduced the stripes very effectively to a reasonably low level (but non-zero) by positionally aligning detector datastreams in–scan, histogramming the difference between each pair of adjacent detectors, identifying the mode of the histogram and subtracting the integrated mode for each detector datastream, while demanding the average subtraction over the whole DPM field to be zero. These datastreams were then combined with the pointing information and subsequently gridded to a spatial matrix of 3° (in–scan) x 2° (cross–scan) with pixels of $2'.0$ in the cross–scan direction and respectively $0'.25$, $0'.25$, $0'.50$ and $1'.0$ in the scan direction in the 12, 25, 60 and 100 μm bands by using standard software (Deep Sky Co-add Observation Processor DSCO; Kopan, 1982). Detector data were co–added to each grid cell whose centre falls within the detector size. This grid matrix represents the infrared surface brightness in the four IRAS wavelength bands. Only non–filtered intensity grids were produced so that flux information is preserved. We obtained 41 individual DPM grids on the SMC in this way (see Table 2).

The second stage of the processing, done at Leiden Observatory, consisted of combining individual DPM grids, and obtaining a qualitatively and quantitavely good final product. First, quality checks brought to light that one of the SMC DPM grids (number 5851 in Table 2) has degraded pointing reconstruction. To get an equal coverage of each area of the SMC, eight other grids were left out. The remaining 32 grids then were used to obtain three combined map sets (in four wavelength bands) of the whole SMC (each map covers an area of $4^{\circ}.3$ x $4^{\circ}.3$ with a grid spacing of $0'.25$ x $2'.0$; the two map sets that have their scan direction in constant Right Ascension are denoted by NS and the map set with scan direction in constant Declination by EW; Table 2 also shows which grid numbers were combined into each map set). These combined maps were made using standard SDAS software (Deep Sky Grid Adding Processor DSGAD; Kopan, 1982). This first converts all individual grids to the same reference map and then adds all grids together weighting global noise for minimum variance and matching overlapping areas of individual grids.

The SMC is positioned at high ecliptic latitude so that there is little variation in the Zodiacal light emission over the maps. Nevertheless, some Zodiacal emission is still present and can be clearly seen on the IRAS $16^{\circ}.5$ Skyflux images at levels of about 13 and 28 MJy/sr at 12 and 25 μm, and much less at 60 and 100 μm (about 5 MJy/sr). The galactic latitude of the SMC is -44° so that the Galactic foreground, is weak (8 MJy/sr at 100 μm, much less at other wavelengths). At the 60 and 100 μm wavelengths the Galactic foreground cirrus gives more severe problems than the Zodiacal foreground because the Galactic foreground dust is colder. These large scale, relatively smooth foregrounds were removed in a somewhat arbitrary fashion by fitting a plane to map areas considered to be free of SMC emission. Discrete non–SMC sources, such as foreground stars, were not removed from the maps. Our zero–level correction removes most of the foreground emission but assumes a planar foreground, which is only a first order approximation of the foreground. In Section 3 we decribe the uncertainties that are left in the map after the foreground removal.

To finally bring the IRAS AO (DPM) data to the current (IRAS November 1984 standard) calibration — the same calibration as the released primary IRAS products — we produced pixel–by–pixel scatterdiagrams of the DPM maps versus the Skyflux HCON-1 maps (the only one available at that time) at a resolution of $9'$. Because a pixel–to–pixel correlation was required here, the slope of the diagram yields the necessary correction factors to arrive at the November 1984 calibration; these factors have an estimated relative uncertainty of about 10 % and correspond well to those communicated to us by Kopan (priv. comm.) obtained in a different manner using many more AOs on NGC 6543 (IRAS Primary Photometric Reference, positioned near the North Ecliptic Pole). The error of 10 % gives a good estimate of the reliability of the IRAS data on any point in the map. The correction factors are in principle affected somewhat by positional and flux errors in both the Survey derived and AO DPM derived maps. We have empirically corrected for most of the positional errors by determining the (Skyflux HCON–1)/(DPM AO) intensity ratios with a beam large compared to position uncertainties and applying small shifts to minimize scatter in the pixel–to–pixel correlation. This method was very succesful on the LMC; on the SMC severe striping in the Skyflux data made this method more difficult to use at 12 and 25 μm, but the factors that we found did not differ much from those of Kopan, and therefore we used his factors in those wavelength bands.

Table 2. IRAS DPM Observations of the SMC.

(1)	(2)	(3)	(4)		(5)	(6)
IPAC[a] grid number	SOP-OBS[a]	Observation Id	Grid centre position[b] RA(1950) h m s	DEC(1950) ° ' "	Pos.Ang[c] (NESW) Deg	Map/Obs[d] set
11192	475-049	CG2023-01[e]	00 42 33	-74 00 47	255.7	3 EW
11123	473-045	CG2023-00	00 42 34	-74 00 54	254.7	3 EW
11152	474-024	CG2022-00	00 43 49	-72 32 25	254.6	3 EW
11440	484-010	CG2022-01	00 45 24	-72 29 19	258.8	3 EW
06006	339-012	CG1676-03	00 45 42	-73 58 49	184.3	2 NS
05694	321-007	CG1676-02	00 45 56	-73 57 29	175.1	2 NS
05699	321-018	CG1676-03	00 45 56	-73 57 31	175.2	----
05645	319-029	CG1676-00	00 45 56	-73 57 13	174.3	2 NS
05648	319-036	CG1676-01	00 45 56	-73 57 17	174.4	2 NS
05851	329-012	CG1750-00	00 46 55	-73 58 08	179.0	----
04915	293-010	CG1459-01	00 47 02	-73 56 16	161.1	1 NS
04870	290-030	CG1459-00	00 47 04	-73 56 03	159.9	----
05188	309-020	CG1459-01	00 47 05	-73 57 04	168.9	1 NS
05830	327-024	CG1675-02	00 47 47	-72 29 03	177.3	2 NS
05635	319-003	CG1675-02	00 47 48	-72 28 25	173.0	2 NS
05632	318-042	CG1675-01	00 47 48	-72 28 23	172.9	2 NS
05640	319-009	CG1675-03	00 47 48	-72 28 24	173.0	2 NS
05594	318-005	CG1675-00	00 47 48	-72 28 24	172.5	----
04820	288-036	CG1458-01	00 47 55	-72 27 00	158.3	1 NS
04755	287-016	CG1458-00	00 47 57	-72 26 52	157.5	1 NS
11218	476-028	CG2024-00	01 04 22	-72 30 11	250.2	3 EW
11257	478-004	CG2024-01	01 04 22	-72 30 07	250.9	3 EW
11129	473-052	CG2025-00	01 04 44	-73 59 03	249.0	3 EW
11211	476-022	CG2025-01	01 04 48	-73 58 57	250.2	3 EW
05907	333-028	CG1677-01	01 07 44	-72 26 25	175.6	----
05872	330-033	CG1751-00	01 07 49	-72 26 22	174.2	----
05875	331-006	CG1677-00	01 07 50	-72 26 39	174.3	2 NS
05560	317-025	CG1677-02	01 07 52	-72 26 13	167.5	2 NS
05587	317-054	CG1677-03	01 07 55	-72 26 07	167.8	----
05078	303-015	CG1460-01	01 07 57	-72 25 07	160.6	1 NS
04885	291-023	CG1460-01	01 07 58	-72 24 34	154.9	1 NS
04823	289-003	CG1460-00	01 07 59	-72 24 39	153.8	----
05245	311-006	CG1460-01	01 07 59	-72 25 15	164.3	----
05557	317-011	CG1677-01	01 08 00	-72 26 39	167.3	2 NS
05550	317-004	CG1677-00	01 08 00	-72 26 38	167.2	2 NS
05687	320-037	CG1678-02	01 08 57	-73 53 52	169.4	2 NS
05693	321-002	CG1678-03	01 08 57	-73 53 50	169.6	2 NS
05631	318-036	CG1678-00	01 08 58	-73 53 49	168.4	2 NS
05653	319-042	CG1678-01	01 08 58	-73 53 46	169.0	2 NS
04908	292-030	CG1461-01	01 09 05	-73 52 17	155.8	1 NS
04826	289-010	CG1461-00	01 09 08	-73 52 09	154.0	1 NS

Notes to Table 2:

a) For a description of names and abbreviations (Grid, SOP, OBS) we refer to IRAS (1985a) and IRAS (1986).

b) The field size of each observation is 3 degrees in the scan direction and 2 degrees in the cross-scan direction.

c) The scan direction is given by its position angle Pos.Ang (degrees NESW).

d) Map/Obs set 1 and 2 are scanned in the North-South direction, while Map/Obs set 3 is scanned East-West. The number of the set is identical to the number of the combined map in the text (see Section 2 and 3).
A dash in this column indicates that the grid was not used in the processing for various reasons.
In Figures 2, 3 and 4 we display all three Obs/Map sets.

e) Observation Id CG stands for Close Galaxies.

3. The maps of infrared radiation

Fig. 1 shows a 100 μm map of the SMC (and LMC) and their surroundings, constructed from Spline–I maps (van Albada *et al.*, 1985) by Braun, Walker and Deul at Leiden Observatory (taken from their collection of sky maps, see also Burton *et al.*, 1986). At the top the southern part of the Milky Way is visible (dust clouds associated with the Carina Arm at the top right, with peak intensities around 5000 MJy/sr). The LMC is just below the centre ($l = 280°, b = -33°$). The SMC ($l = 304°, b = -44°$) is seen at the bottom left, with a peak in the SW–Bar of only 42 MJy/sr. The diffuse SMC emission is at a level of 11 and the Galactic foreground of 8 MJy/sr. From the figure it is clear that the Galactic infrared foreground at the position of the SMC is not very complex and easy to remove.

Table 3. *Description of the SMC DPM–map characteristics.*

Characteristic (Unit)	Wavelength band			
	12 μm	25 μm	60 μm	100 μm
Effective frequency (10^{12} Hz)	25	12	5	3
Bandwidth (μm)	7.0	11.2	32.5	31.5
Bandwidth correction (10^{12} Hz) [a]	13.48	5.16	2.58	1.00
Zero–magnitude flux density f_ν (0.0 mag) (Jy)	28.3	6.73	1.19	0.43
Point Source Conversion factor (Jy / 10^{-8} Watt m^{-2} sr^{-1})	0.037	0.11	0.41	2.08
Positional accuracy ($''$)	15	15	15	15
Nominal detector size($'$x$'$)	0.75 x 4.5	0.75 x 4.7	1.5 x 4.8	3.0 x 5.0
Resolution ($'$x$'$) [b]	0.9 x 6.4	1.1 x 6.4	2.0 x 6.4	3.8 x 6.4
Absolute calibration (%)	10	10	10	10
Median noise (MJy/sr) [c]	0.096	0.097	0.12	0.20
(10^{-8} Watt m^{-2} sr^{-1})	1.3	0.5	0.3	0.2
Zero–level uncertainty (MJy/sr)	0.015	0.019	0.039	0.10
(10^{-8} Watt m^{-2} sr^{-1})	0.2	0.1	0.1	0.1
Stripe residuals (MJy/sr) [d]	0.052	0.058	0.12	0.30
(10^{-8} Watt m^{-2} sr^{-1})	0.7	0.3	0.3	0.3
Sensitivity (MJy/sr) [e]	0.3	0.3	0.4	0.6
(10^{-8} Watt m^{-2} sr^{-1})	4	2	1	0.5

Notes to Table 3:

a) Chester (priv. comm.).

b) The Gaussian resolution is given in arc–minutes (in–scan x cross–scan). One arcminute at the distance of the SMC (63 kpc) corresponds to 18 pc.

c) The value of the median noise is influenced somewhat by the extended emission of the SMC itself. The real detector noise is somewhat lower.

d) Higher stripe levels than the average level given in the table can occur.

e) The sensitivity indicates the intensity limits of Table 4. Note that the IRAS PSC sensitivity limits are 0.25, 0.25, 0.40, 1.00 Jy (see IRAS, 1985a).

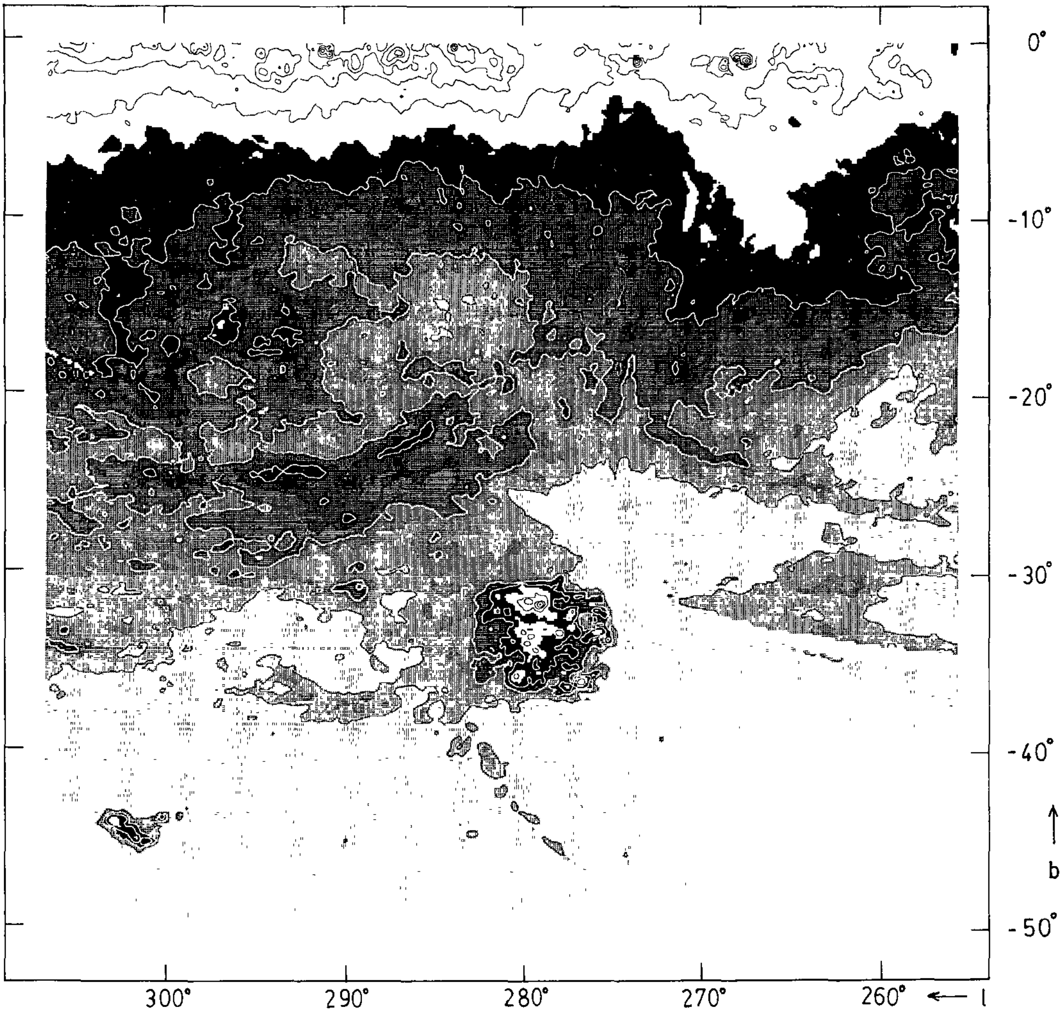

Figure 1. *IRAS Spline–I infrared map at 100 μm made at the Groningen Laboratory for Space research (van Albada et al., 1985; Braun, Walker and Deul, priv. comm.) showing an area of 50° x 50° around the Magellanic Clouds with a resolution of about 10′. Galactic 1950 coordinates are indicated. The infrared foreground can clearly be seen. Two extended infrared features (tidal arms) are in fact associated with HI at local Galactic velocities. Intensities between 4 and 35 Watt m^{-2} sr^{-1} are indicated by grey scales, with darker grey scales for higher intensities. Contours are at 11, 14, 21, 70, 175, 350, 700, 1750, 3500, 5250 x 10^{-8} Watt m^{-2} sr^{-1}.*

Fig. 2, 3 and 4 show the IRAS DPM–maps of the whole SMC field. In these figures we indicate the boundaries of the coverage of the IRAS DPM observations. The NS and EW scanned maps are shown because the resolution in the scan direction is higher than the the cross–scan resolution; thus, the two (NS and EW) sets are complementary in terms of resolution. There is less diffuse emission present in the 12 and 25 μm maps than in the other wavelength bands. In these maps the contrast between small, discrete sources and the diffuse more extended emission is much higher ($\sim$ 40) than at 60 or 100 μm ($\sim$ 10). The coverage of the SMC is not complete in the SE, where the HII–region N 90 is just outside of the map. Because HII region N 3 is just at the edge at the SW, good fluxes cannot be obtained for this source. Special Co–adds of IRAS Survey data have been done centered on these two objects and are presented in Appendix A.

Detailed maps in four fields on the SMC are presented in Schwering and Israel (1988) and are available in digital form at the Centre de Données Stellaires (Astronomical Data Centre CDS) in Strasbourg, France.

All maps shown in this chapter are given in in–band intensities $\int d\nu R_\nu I_\nu$ (Watt m^{-2} sr^{-1}), with R_ν the relative system response (see IRAS, 1985a; Table II.C.5 therein). To convert these values to specific intensities I_ν (Watt m^{-2} sr^{-1} Hz^{-1}) correction factors should be applied depending on the bandwidth (these factors are given in Table 3, assuming an intrinsic source spectrum $f_\nu \propto \nu^{-1}$, which is roughly correct for most dust clouds associated with HII regions: $T_d \approx 40$ K). For individual sources or positions, more accurate flux densities can be obtained by first determining the actual spectrum and then applying the relevant colour dependent correction (see IRAS 1985a and IRAS 1985b, Table VI.C.6 therein).

Figure 2. *Overall infrared maps of the Small Magellanic Cloud.*
Map set 1 (NS) of Table 2 is presented in equatorial coordinates for 1950. The maps are given in in–band intensities. All maps have sizes of 4°.3 x 4°.3. The coverage of the DPM–field is indicated by solid lines. Although not shown, the coverage differs somewhat in the four wavelength bands due to the location of detectors in IRAS's focal plane. See pages 20 – 21.
For the 12 μm band grey scales range from 9 to 33, with darker grey scales for higher intensities. Contours are at 5, 10, 15, 20, 50 x 10^{-8} Watt m^{-2} sr^{-1}.
For the 25 μm band grey scales range from 9 to 33, with darker grey scales for higher intensities. Contours are at 2, 4, 6, 8, 10, 30, 50, 100 x 10^{-8} Watt m^{-2} sr^{-1}.
For the 60 μm band grey scales range from 9 to 58, with darker grey scales for higher intensities. Contours are at 1, 2, 4, 6, 8, 10, 15, 20, 40, 80, 140, 200 x 10^{-8} Watt m^{-2} sr^{-1}.
For the 100 μm band grey scales range from 9 to 58, with darker grey scales for higher intensities. Contours are at 0.5, 1, 2, 4, 6, 8, 10, 15, 20, 40, 80 x 10^{-8} Watt m^{-2} sr^{-1}.

Figure 3. *Overall infrared maps of the Small Magellanic Cloud.*
Map set 2 (NS) of Table 2 is presented in an identical way as set 1 (NS) in Figure 2. The coverage of the DPM–field is indicated by solid lines. See pages 22 – 23.

Figure 4. *Overall infrared maps of the Small Magellanic Cloud.*
Map set 3 (EW) of Table 2 is presented in an identical way as set 1 (NS) in Figure 2. The coverage of the field by the DPM map is indicated by solid lines. See pages 24 – 25.

The estimated uncertainties in the DPM maps are given in Table 3. There are only minor differences in quality of the three different sets of maps. The noise (in MJy/sr) in the maps increases in the higher wavelength bands. Because the noise is based on map statistics, this is due to the increased extended emission of the SMC itself. The zero–level is also less well defined in those bands due to the extended emission. The sensitivity is based on reliable point sources that could be extracted from the maps. Just North of the SMC–Bar in map set 1, a bad detector scan makes that part of the map unusable, but as it falls completely outside the SMC it does not hamper the interpretation of the data.

4. The Infrared Source List in the SMC

4.1. The Source List

We searched the three sets of maps shown in Fig. 2, 3 and 4 for both resolved and unresolved discrete sources (Table 4) down to intensity levels of 5, 2, 1 and 0.5 x 10^{-8} Watt m^{-2} sr^{-1} at 12, 25, 60 and 100 μm (four times the median noise level). Intensity peaks, backgrounds and source sizes were estimated and used to obtain flux densities. The extended diffuse SMC infrared emission is also interpreted as background, whenever it was close to the source. A size estimate was obtained using the nominal gaussian resolutions in the different bands. All wavelength bands and all three different map sets were searched separately. In a single wavelength band flux densities are about equal in the three maps, especially in unconfused regions (deviation of about 15 %). The data were then merged. The IRAS PSC positions are quoted in Table 4 whenever an unambigious identification was made.

Table 4 contains the following information:

Column 1: Sequential number. We recommend the name LI–SMC for these sources (Leiden IRAS–SMC).

Column 2: The position of the source (1950). The Right Ascension is given in hours, minutes and seconds. If given in 0.1^s the position and error are that of the IRAS PSC entry given in Column 12, otherwise they are taken from the maps with an error of 12^s. The declination is given in degrees, arc–minutes and arc–seconds. If given in $1''$ the position and error are that of the IRAS PSC entry given in Column 12, otherwise they are taken from our maps and have an error of $1'$.

Column 3: 12 μm intensity peak and background level (in 10^{-8} Watt m^{-2} sr^{-1}). A dash indicates that the source is below the intensity level given in the text.

Column 4: The same as Column 3 for the 25 μm band.

Column 5: The same as Column 3 for the 60 μm band.

Column 6: The same as Column 3 for the 100 μm band.

Column 7: The size of the source in $\alpha(')$ x $\delta(')$. p denotes a source that cannot be discerned from a point source response. A semi–colon denotes an uncertain size. A dash indicates that no reliable size could be estimated because no FWHM could be determined.

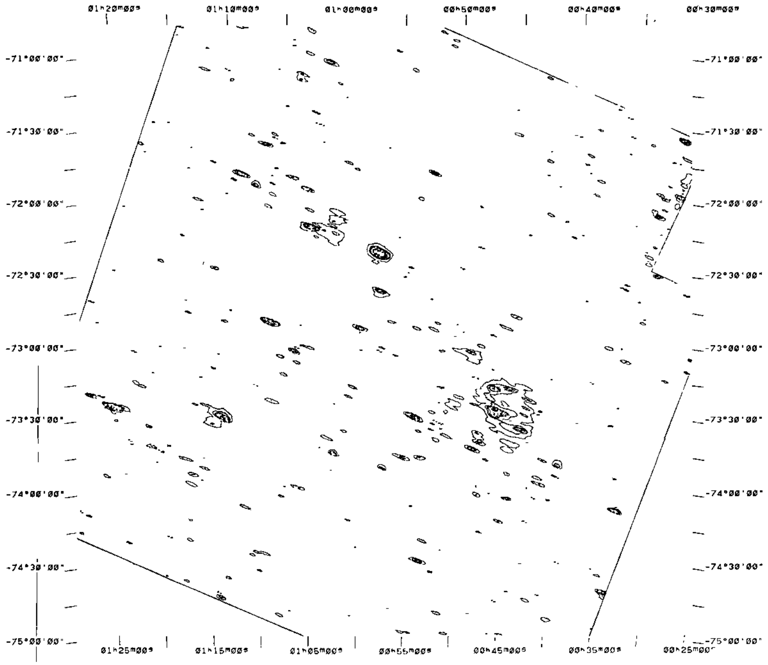

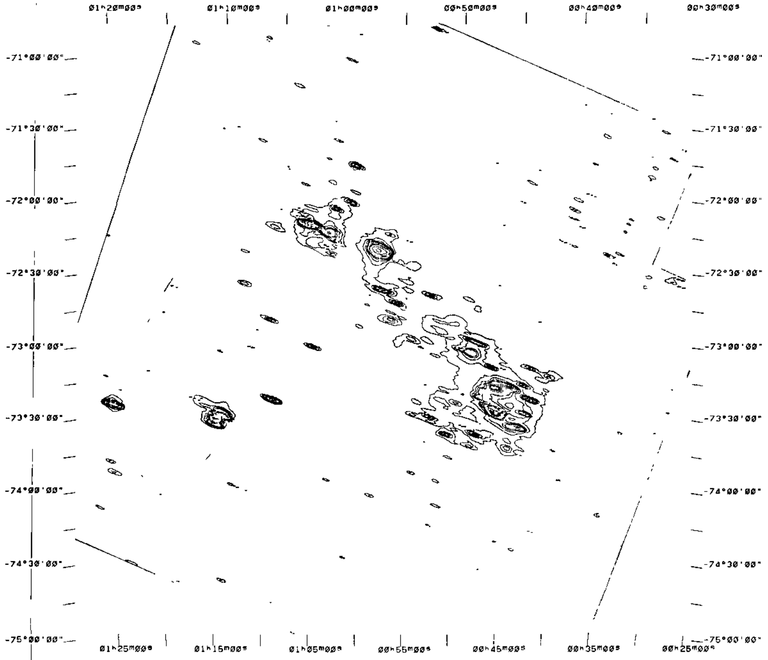

Fig. 2.1. SMC 12 μm DPM–map (set 1; NS).
Fig. 2.2. SMC 25 μm DPM–map (set 1; NS).

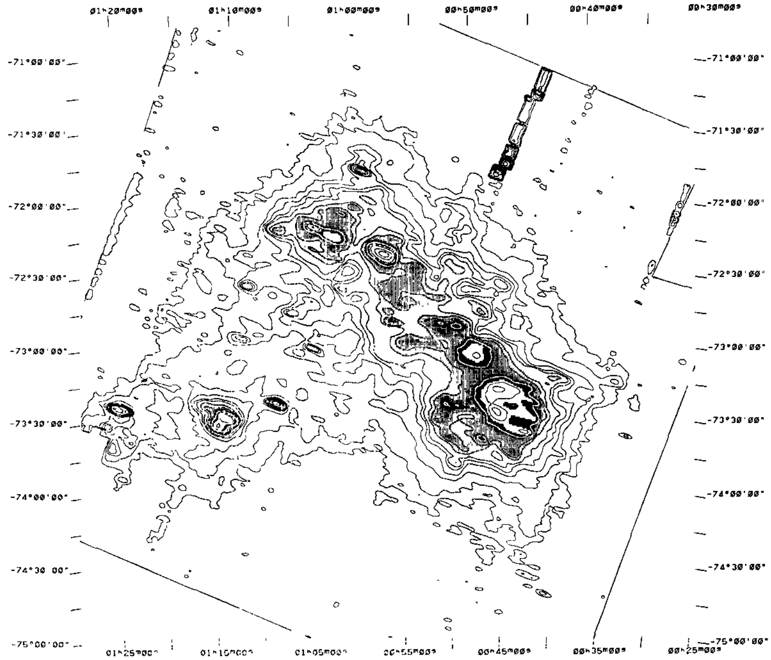

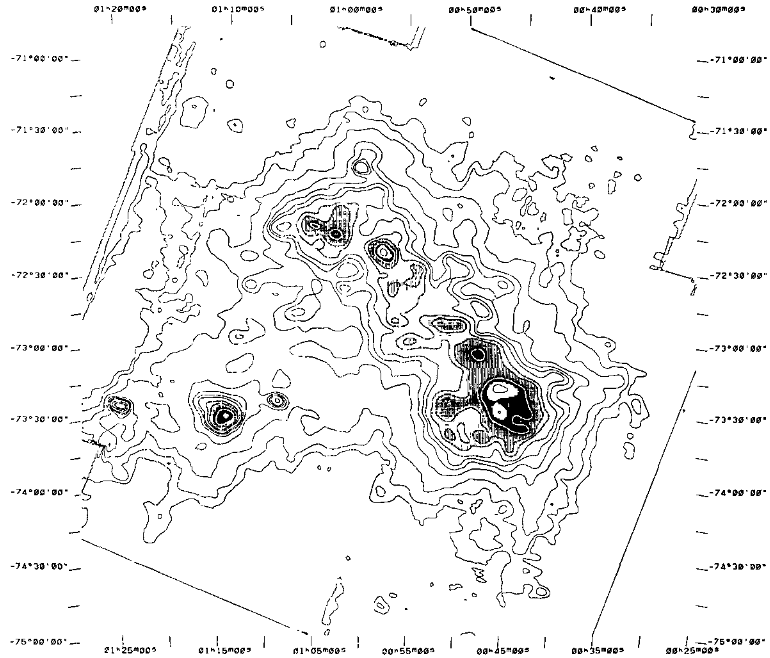

Fig. 2.3. SMC 60 μm DPM-map (set 1; NS).
Fig. 2.4. SMC 100 μm DPM-map (set 1; NS).

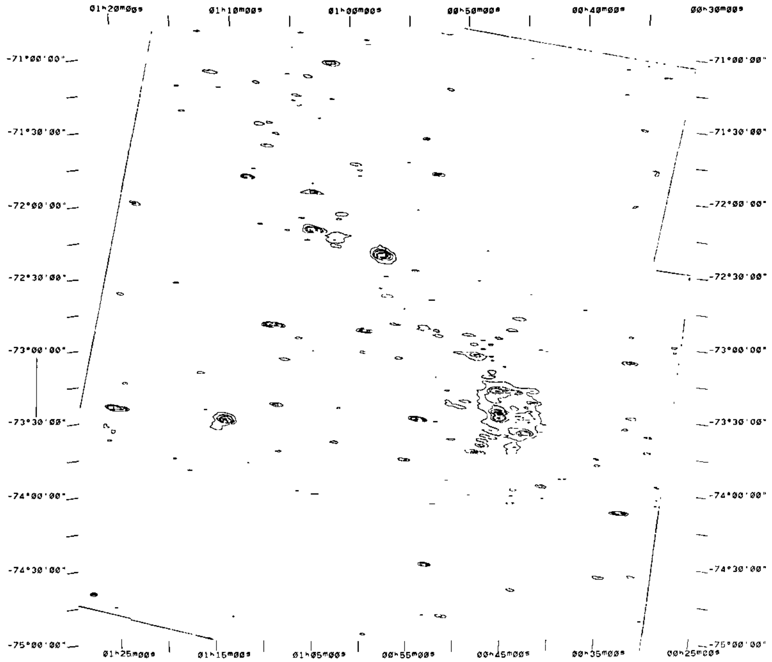

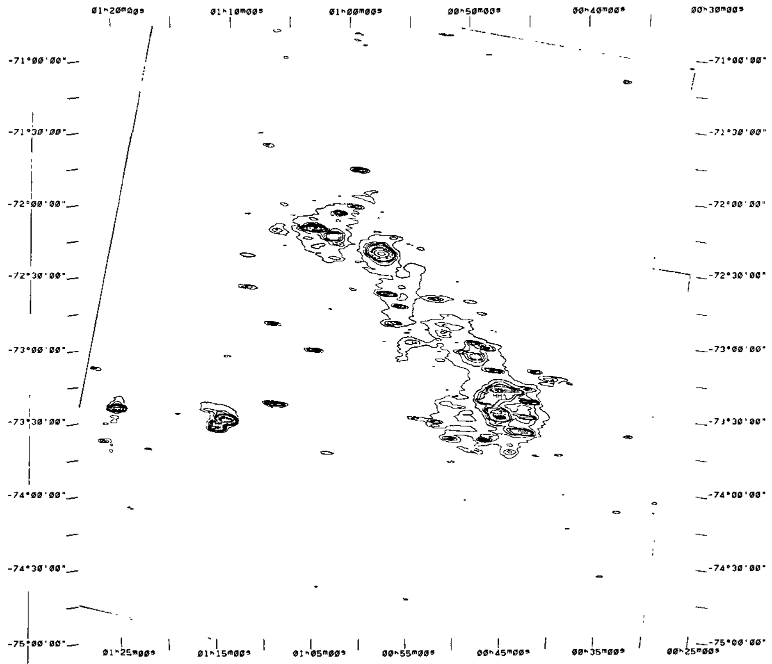

Fig. 3.1. SMC 12 μm DPM–map (set 2; NS).
Fig. 3.2. SMC 25 μm DPM–map (set 2; NS).

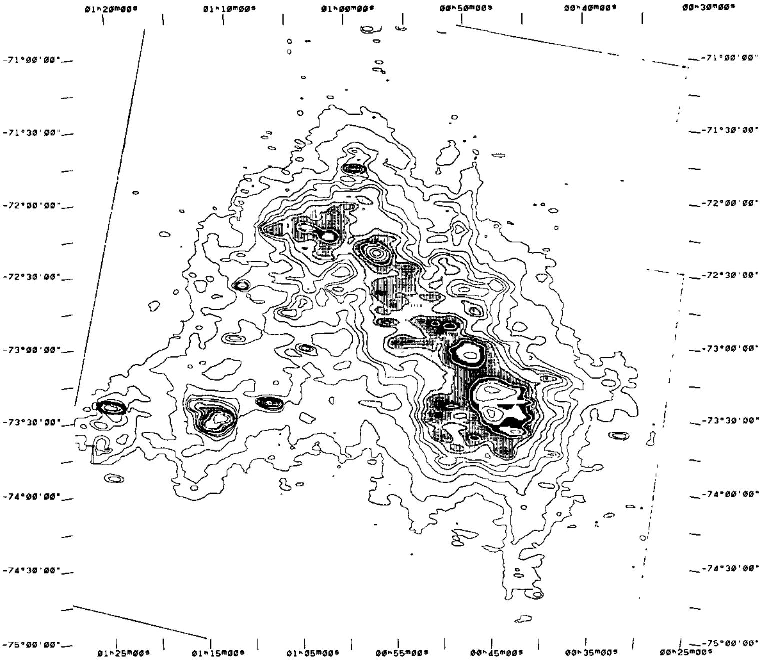

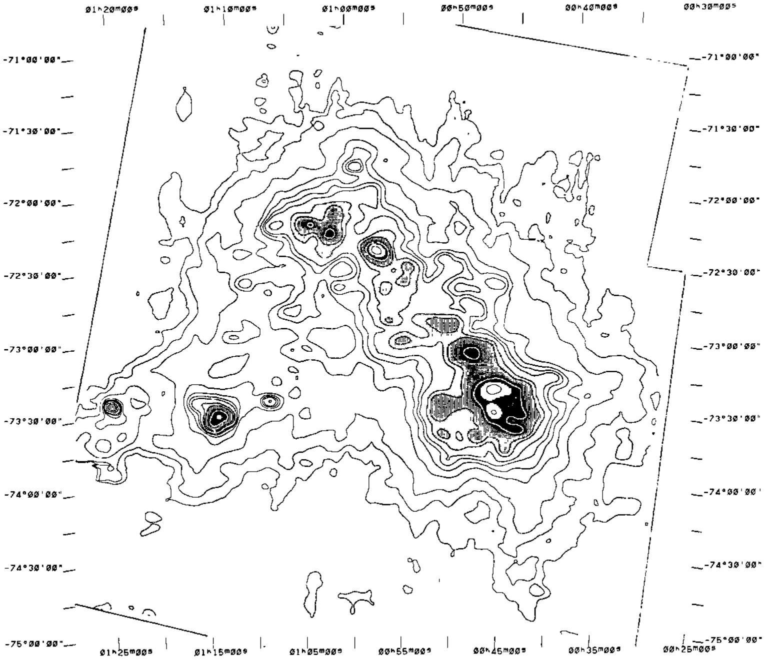

Fig. 3.3. SMC 60 μm DPM–map (set 2; NS).
Fig. 3.4. SMC 100 μm DPM–map (set 2; NS).

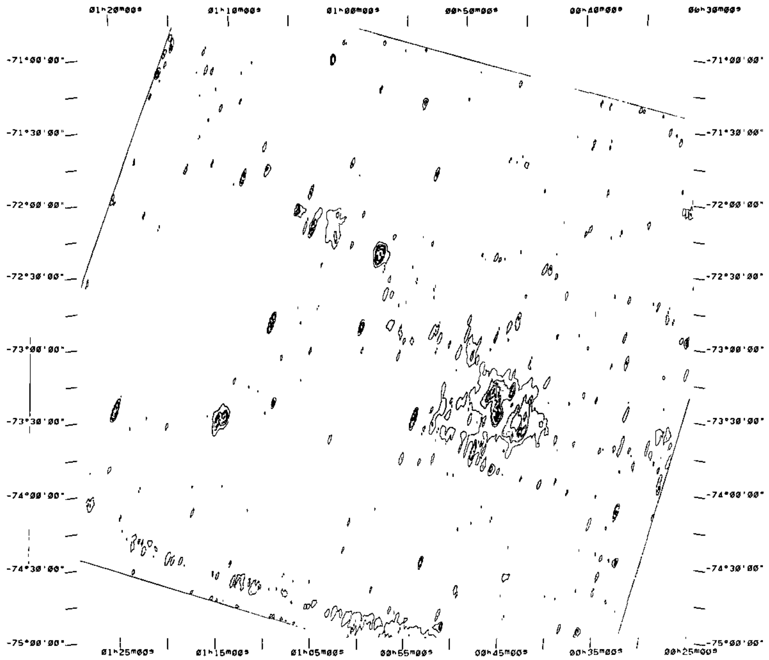

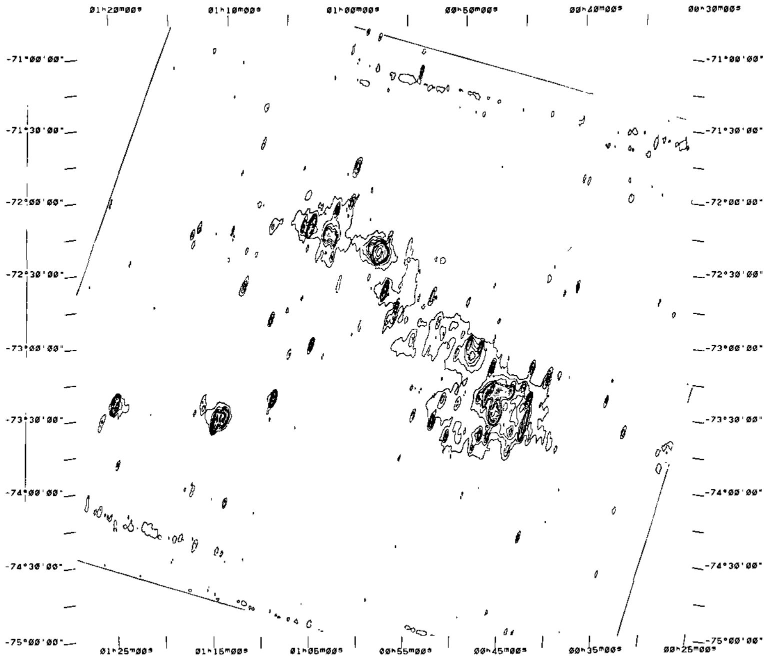

Fig. 4.1. SMC 12 μm DPM–map (set 3; EW).
Fig. 4.2. SMC 25 μm DPM–map (set 3; EW).

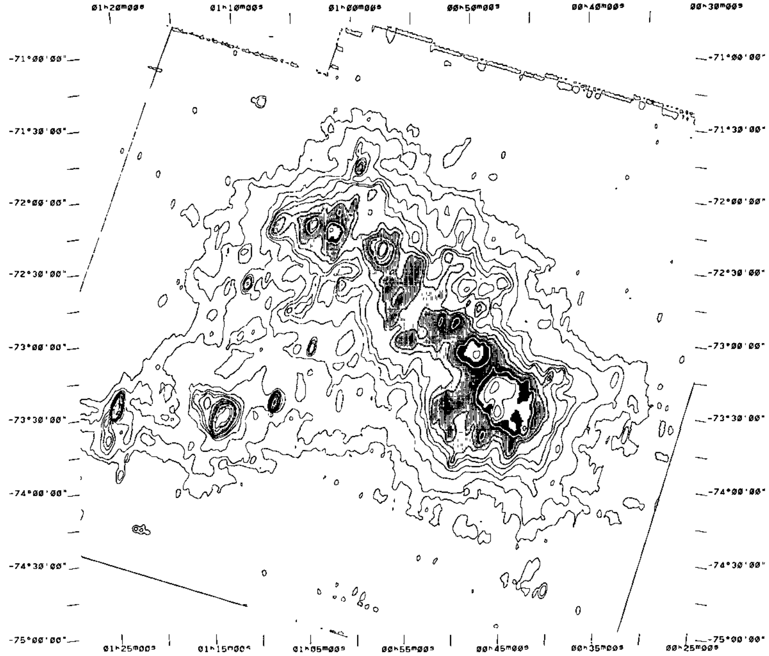

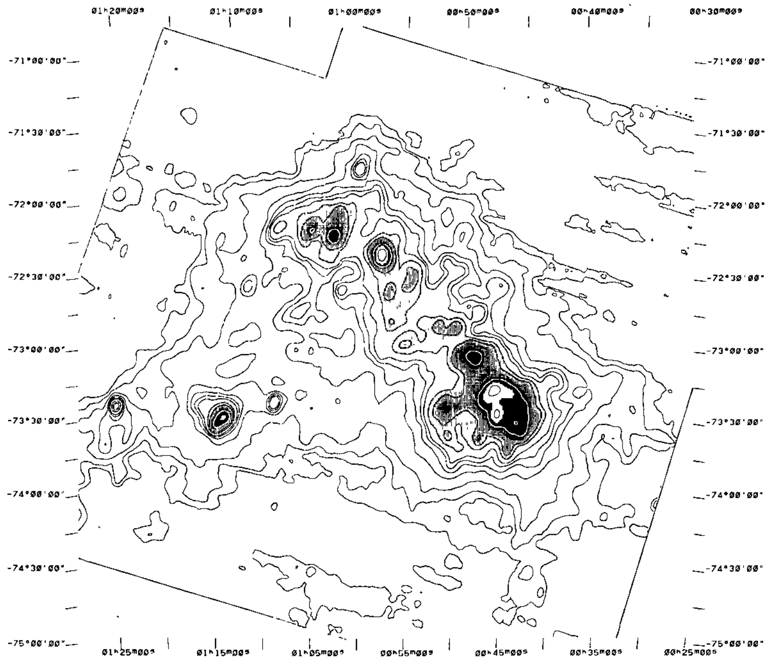

Fig. 4.3. SMC 60 μm DPM–map (set 3; EW).
Fig. 4.4. SMC 100 μm DPM–map (set 3; EW).

Column 8: Flux density of the source at 12 μm in Jy, assuming an intrinsic source spectrum $f_\nu \propto \nu^{-1}$ (the same as for the released IRAS products; IRAS, 1985a). C denotes confusion with either background or other discrete sources and a semi–colon indicates an uncertain flux density. Flux densities are calculated using the size of Column 7. When the size could not be measured the point source response was assumed. Table 3 gives Point Source Conversion Factors to convert (Peak–Background) Watt m^{-2} sr^{-1} to Jy. The error in flux densities is assumed to be about 10 %, but somewhat higher at the lower intensity levels.

Column 9: The same as Column 8 for the 25 μm band.

Column 10: The same as Column 8 for the 60 μm band.

Column 11: The same as Column 8 for the 100 μm band.

Column 12: If the source is present in the IRAS PSC (IRAS, 1985a) and/or in the IRAS SSS (IRAS, 1985b) the name in that catalogue is given. A semi–colon indicates that the associated PSC or SSS entry is at a large distance from the source. An asterisk indicates that the association has been made for more than one source in the list.

Column 13: The spectral type of the source. Spectrum type C is a typical cool dust spectrum (typical $T_d \approx 30$ K), peaking beyond 100 μm; colour correction factors are of order 1.00, 0.95, 0.99, 1.00. Type W is a warm dust spectrum (typical $T_d \approx 70$ K), peaking between 12 and 100 μm; colour correction factors are of order 1.03, 1.00, 1.00, 1.04. Type S is a stellar spectrum (typical blackbody of about 5000 K); colour correction factors are of order 1.43, 1.40, 1.32, 1.09. A semi–colon indicates that the infrared spectrum is uncertain. Actual flux densities can be calculated from the quoted ones by *dividing* the latter by these colour correction factors (see IRAS, 1985a).

Column 14: Comments information on identification in other catalogues.

Our source list contains 219 entries. In the area covered by the DPM fields 146 entries were found in the IRAS PSC, of which 138 could be identified unambigiously. Five PSC sources can be identified, but show some positional difference (about $1'.4$). The remaining three PSC sources could not be identified on the DPM maps: IRAS 00515–7227, 01062–7210, 01098–7225, almost certainly because of confusion problems. The last (100 and 60 μm) source has a (second and correct, 25 μm) IRAS PSC entry at $1'.5$ distance (01095–7225). We believe that these two PSC entries are in fact the same source. The other two sources have reliable PSC flux densities at 60 μm only. They are probably the result of confusion in the SMC Bar (see below). IRAS 00296–7404 (HII region N 3) peaks just inside one DPM map and is detected at 60 and 100 μm. We left it out of the source list, because the coverage of the source is not very good. In total 33 PSC sources are clearly extended, and 60 are confirmed to be a point source. The source types in our list and in the PSC agree very well. Frequently, our procedure yields flux determinations where the PSC only gives upper limits.

All 13 entries in the IRAS SSS and inside the DPM fields were detected. Two of them (IRAS X0110–724 and X0112–735) are associated with more than one of our sources. The associations for IRAS X0110–724, X0115–737 and for X0123–736 are farther than $3'$ away. Nine SSS sources have an association with an entry from the PSC; these must be sources

Table 4. Infrared Source List in the SMC.

(1)	(2)		(3)		(4)		(5)		(6)		(7)	(8)	(9)	(10)	(11)	(12)	(13)	(14)
umber	Position RA(1950) h m s	DEC(1950) ° ' "	12 µm Peak	Bg	25 µm Peak	Bg	60 µm Peak	Bg	100 µm Peak	Bg	Size arcmin	F 12µm Jy	F 25µm Jy	F 60µm Jy	F 100µm Jy	IRAS-Id	Spec-trum	Comments
					10^{-8} Watt $m^{-2}sr^{-1}$													
1	00 33 04.3	-73 25 06	-	-	-	-	1	-	1	-	4x9	-	-	1.9	5.7	00330-7325 X0032-734	C	
2	00 33 43.2	-73 37 49	2	-	4	-	2	-	1	0.5	p	0.07:	0.44	0.8	1.0	00337-7337	C	
3	00 33 47.8	-74 09 09	23	-	2	-	-	-	-	-	p	0.85	0.22	-	C	00337-7409	S	SAO 255684
4	00 34 04.0	-73 08 03	12	-	-	-	-	-	-	-	p	0.44	-	-	-	00340-7308	S	SAO 255686
5	00 35 04.2	-74 36 17	8	-	2	-	-	-	-	-	p	0.30	0.22	-	-	00350-7436	S	
6	00 35 10.5	-73 16 19	-	-	1	-	4	1	2	1	4x2	-	0.36:	2.5	3.0	00351-7316	C	
7	00 36 24	-74 14	3	-	-	-	-	-	-	-	-	0.11:	-	-	-		S	SAO 255689
8	00 36 44	-73 25	3	-	-	-	<3	-	-	-	-	0.11:	-	-	C		S	SAO 255690
9	00 37 46.8	-73 18 55	-	-	-	-	4	2	4	2	-	-	-	0.8	4.2	00377-7318	C	
10	00 38 55.4	-73 53 40	-	-	-	-	2	1	2	1	-	-	-	0.4	2.1	00389-7353	C	
11	00 39 33.5	-73 17 35	-	-	1	-	8	4	-	-	p	-	0.11:	1.7	C	00395-7317	W	
12	00 39 33.7	-74 03 45	-	-	2	-	1	-	-	-	-	-	0.22:	0.4:	C	00395-7403	W	
13	00 40 00	-73 58	5	-	-	-	<2	-	-	-	-	0.19	-	-	C		S	
14	00 40 16.3	-73 47 27	-	-	2	-	7	4	4	3	p	-	0.22	1.2	2.1	00402-7347	C	
15	00 40 20.7	-73 16 28	-	-	2	-	13	6	9	6	p	-	0.22	2.9	6.3	00403-7316	C	
16	00 40 25.8	-74 00 47	-	-	-	-	5	2	2	1	p:	-	-	1.2	2.1	00404-7400	C	
17	00 40 39.3	-74 45 25	-	-	-	-	3	-	1	0.3	p	-	-	1.2	1.5	00406-7445	C	
18	00 40 42	-73 31	-	-	-	-	11	6	10	5	-	-	-	2.1	10.0		C	
19	00 41 01.0	-73 39 45	3	-	-	-	-	-	-	-	-	0.11:	-	C	C	00410-7339	S	
20	00 41 10.0	-73 36 35	3	-	-	-	-	-	-	-	-	0.11:	-	C	C	00411-7336	S	
21	00 41 20.6	-73 16 38	3	-	6	-	18	6	12	5	px1	0.14:	0.80	5.3	15.0	00413-7316 X0040-732	C	
22	00 41 45.2	-74 00 29	12	-	-	-	-	-	-	-	p	0.44	-	C	C	00417-7400	S	
23	00 41 46.3	-73 18 34	3	-	2	-	14	11	-	-	p	0.11:	0.22	1.2	C	00417-7318	W	
24	00 42 51.1	-74 17 36	-	-	-	-	2	-	2	0.5	14x14	-	-	14.0	11.0	00428-7417	W	
25	00 42 59.9	-73 13 58	-	-	6	-	13	9	-	-	p	-	0.67	1.7	C	00429-7313	W	
26	00 43 03.7	-73 26 45	15	4	30	3	60	20	-	-	p	0.41	3.00	17.0	C	00430-7326	W	
27	00 43 13.8	-73 32 52	12	5	15	3	72	20	46	22	p	0.26	1.33	21.0	50.0	00432-7332	C	
28	00 43 30	-73 29	14	6	9	5	72	30	45	22	p	0.30	0.44	17.0	48.0:		C	
29	00 43 32.2	-73 39 10	22	5	21	4	88	20	48	22	p.	0.63	1.89	28.0	54.0	00435-7339	C	
30	00 43 37.1	-73 21 32	9	3	10	2	55	20	35	22	p:	0.22	0.89	14.0	27.0	00436-7321	C	
31	00 43 47.1	-73 34 33	9	6	6	4	-	-	-	-	-	0.11	0.22	C	C	00437-7334	W	
32	00 43 51	-73 39	17	6	6	4	-	-	-	-	p:	0.33	0.22	C	C		S	
33	00 44 32	-72 52	11	-	-	-	<3	-	<4	-	p:	0.41	-	-	-		S	
34	00 44 36	-74 08	9	-	-	-	<2	-	-	-	p	0.33:	-	-	C		S	
35	00 44 38.5	-73 39 02	13	5	12	4	65	30	42	22	1x2	0.60	1.60	19.0	46.0	00446-7339	C	
36	00 44 47.0	-73 22 29	20	6	21	5	100	50	60	40	p	0.52	1.78	21.0	42.0	00447-7322	C	
37	00 44 51	-73 44	9	3	4	2	25	20	-	-	-	0.22	0.22	2.1	C		W	
38	00 44 55.0	-73 47 35	7	-	8	1	36	12	23	10	1x2	0.51	1.40	13.0	30.0	00449-7347	C	
39	00 45 09	-73 39	13	4	6	3	-	-	-	-	2xp:	0.57	0.53	C	C		S:	
40	00 45 36	-72 57	8	-	-	-	<3	-	<4	-	p:	0.30	-	-	-		S	
41	00 45 38.1	-73 54 38	5	-	-	-	8	6	-	-	-	0.19:	-	0.8:	C	00456-7354	W	
42	00 46 00	-73 34	21	7	28	7	125	100	-	-	px1	0.64	2.79	11.0	C	X0045-735	W	
43	00 46 12	-73 24	15	10	15	11	125	100	70	60	p:	0.19	0.44	10.0	21.0		C	
44	00 46 15.6	-73 39 56	3	-	2	1	35	25	-	-	-	0.11:	0.11:	4.1	C	00462-7339	W	
45	00 46 17.3	-73 31 37	34	5	95	7	160	25	83	22	p	1.07	9.77	56.0	128.0	00462-7331	C	
46	00 46 21.7	-73 52 11	-	-	-	-	9	7	-	-	-	-	-	0.8	C	00463-7352	W	
47	00 46 23.8	-72 38 22	-	-	-	-	13	5	9	4	5x4	-	-	10.0	20.0	00463-7238	C	
48	00 46 34	-73 01	5	-	1	-	-	-	-	-	-	0.19	0.11:	C	C		S	
49	00 46 37.6	-73 22 10	23	5	33	8	155	30	93	22	p	0.67	2.78	52.0	149.0	00466-7322 X0046-733	C	
50	00 46 47.2	-73 14 30	5	-	11	2	36	25	27	25	p	0.19	1.00	4.5	4.2	00467-7314	W	
51	00 46 54	-73 26	14	5	20	8	100	50	63	45	p:	0.33	1.33	21.0	38.0	00472-7325:	C	
52	00 47 06	-73 43	3	-	7	2	20	15	-	-	p:	0.11:	0.56	2.1:	C	00469-7341:	W	
53	00 47 26.1	-73 50 07	3	-	1	-	9	8	-	-	-	0.11:	0.11:	0.4:	C	00474-7350	W	
54	00 47 26.9	-73 30 45	8	3	-	-	-	-	-	-	-	0.19:	C	C	C	00474-7330	S	
55	00 47 30	-73 27	5	-	12	5	55	30	-	-	p	0.19:	0.78	10.0	C	00477-7328:	W	
56	00 47 37	-73 45	12	-	-	-	-	-	-	-	p	0.44	-	C	C		S	SAO 255711
57	00 47 42.8	-73 43 04	5	-	12	2	50	16	25	12	p	0.19	1.11	14.0	27.0	00477-7343	C	
58	00 47 53.2	-73 05 08	5	-	13	2	50	30	-	-	p	0.19	1.22	8.3	C	00478-7305	W	
59	00 47 57	-73 19	5	-	3	2	36	30	-	-	-	0.19:	0.11:	2.5	C		W	
60	00 48 03	-72 25	5	-	-	-	<3	-	<3	-	-	0.19:	-	-	-		S	
61	00 48 22.1	-73 47 48	17	-	5	1	10	8	-	-	1xp	0.78	0.53	0.9:	C	00483-7347	W:	
62	00 48 23.9	-72 50 11	-	-	2	-	21	9	13	7	3x4	-	0.87:	12.0	19.0	00483-7250	C	
63	00 48 25	-73 09	5	-	10	7	88	25	43	18	3x4	0.83	1.31	61.0	80.0		C	
64	00 48 39.5	-72 37 39	3	-	-	-	10	6	6	4	p	0.11:	-	1.7	4.2	00486-7237	C	
65	00 48 45	-73 08	16	4	14	6	70	25	-	-	p	0.44	0.89	19.0	C	X0048-731	W	
66	00 48 57.5	-73 02 59	5	-	13	3	40	30	-	-	p	0.19:	1.11	4.1	C	00489-7302	W	
67	00 48 59.8	-72 35 48	-	-	-	-	11	9	7	4	2xp	-	-	1.0	6.8	00489-7235	C	
68	00 49 00.0	-73 36 26	-	-	3	2	24	18	16	14	1x1	-	0.15:	2.8	4.3	00489-7336	C	
69	00 49 00.3	-71 25 36	3	-	-	-	-	-	-	-	-	0.11:	-	-	-	00490-7125	S	SAO 255713
70	00 49 07.3	-73 40 54	3	-	4	2	22	17	16	15	p:	0.11:	0.22	2.1	2.1	00491-7340	W	
71	00 49 07.4	-72 46 43	-	-	2	-	15	11	10	8	1x2	-	0.40	2.2	4.6	00491-7246	C	
72	00 49 18	-73 27	5	-	4	2	-	-	-	-	-	0.19	0.22	C	C		W	
73	00 49 28.5	-73 47 29	3	-	2	-	20	15	16	12	p:	0.11:	0.22	2.1	8.4	00494-7347	C	
74	00 49 30	-73 00	5	-	3	1	-	-	-	-	p:	0.19	0.22:	C	C		W:	
75	00 49 35.7	-72 16 23	-	-	-	-	7	3	6	3	4x5	-	-	5.0	12.0	00495-7216	C	
76	00 49 54.5	-73 30 05	5	-	6	2	38	17	25	17	1x1	0.28	0.62	9.9	17.0	00499-7330	C	
77	00 50 03.0	-73 06 55	5	-	7	2	50	30	-	-	1xp	0.23	0.66	8.8	C	00500-7306	W	
78	00 50 09	-72 57	3	-	4	2	-	-	-	-	-	0.11:	0.22	C	C		W	
79	00 50 09.7	-72 22 14	-	-	-	-	8	4	4	3	-	-	-	1.7	2.1	00501-7222	C	
80	00 50 18.2	-72 20 02	-	-	-	-	6	3	6	3	-	-	-	1.2	6.3	00503-7220	C	
81	00 50 22	-72 35	-	-	-	-	17	9	14	6	4x4	-	-	8.8	28.0		C	
82	00 50 25.9	-73 53 09	-	-	2	-	15	6	10	6	2x2	-	0.50	5.6	9.8	00504-7353	C	
83	00 50 36	-72 57	-	-	4	2	44	15	25	10	5x4	-	1.18	37.0	59.0		C	
84	00 50 38.1	-72 07 39	-	-	-	-	4	2	4	2	10x3	-	-	3.8	11.0	00506-7207	C	
85	00 50 46.4	-72 45 56	-	-	1	-	12	9	10	8	-	-	0.11:	1.2	4.2	00507-7245	C	
86	00 50 54.7	-73 42 47	7	-	10	1	30	15	21	13	p	0.26	1.00	6.2	17.0	00509-7342	C	
87	00 51 15.2	-72 29 46	-	-	-	-	17	9	11	6	3x3	-	-	6.7	15.0	00512-7229	C	
88	00 51 18	-73 29	3	-	6	2	36	17	30	18	2xp	0.19:	0.71	9.7	27.0		C	
89	00 51 23	-73 23	5	-	-	-	-	-	-	-	p:	0.19	-	C	C		S	SAO 255715
90	00 51 24	-74 56	10	-	-	-	-	-	-	-	p	0.37	-	-	-	00515-7455:	S	SAO 255716

Table 4, continued (2).

(1)	(2)		(3)		(4)		(5)		(6)		(7)	(8)	(9)	(10)	(11)	(12)	(13)	(14)
Number	Position RA(1950)	DEC(1950)	12 µm Peak	Bg	25 µm Peak	Bg	60 µm Peak	Bg	100 µm Peak	Bg	Size	F 12µm	F 25µm	F 60µm	F 100µm	IRAS-Id	Spec-trum	Comments
	h m s	o ' "			10^{-8} Watt $m^{-2}sr^{-1}$						arcmin	Jy	Jy	Jy	Jy			
91	00 51 24	-73 01	-	-	6	2	-	-	-	-	p	-	0.44	C	C		W	
92	00 51 38.4	-72 59 12	5	-	5	2	36	20	23	20	p:	0.19:	0.33	6.6	6.3	00516-7259	W	
93	00 51 47.9	-72 40 19	-	-	1	-	17	10	10	7	3x5	-	0.51:	7.7	11.0:	00517-7240	C	
94	00 51 56.0	-72 55 35	5	-	6	2	42	20	24	12	2x3	0.57	1.22	16.0	32.0	00519-7255 X0051-729	C	
95	00 52 00	-73 10	-	-	2	-	17	10	-	-	-	-	0.22	2.9	C		W	
96	00 52 04	-72 59	5	-	-	-	-	-	-	-	-	0.19:	-	C	C		S	
97	00 52 06	-73 00	5	-	2	-	-	-	-	-	-	0.19	0.22:	C	C		W:	
98	00 52 12	-73 36	7	-	11	2	30	17	-	-	p	0.26	1.00	5.4	C	00524-7335: X0052-735	W	
99	00 52 17.7	-73 05 43	-	-	2	-	25	16	16	12	p:	-	0.22	3.7	8.4	00522-7305	C	
100	00 52 21	-73 38	3	-	4	-	-	-	-	-	p	0.11:	0.44	C	C		W	
101	00 52 25.2	-71 53 26	13	-	-	-	-	-	<1	-	p	0.48	-	-	-	00524-7153	S	
102	00 52 36.0	-72 45 15	5	-	6	-	22	15	14	10	4x1	0.58	1.86	5.2	11.0	00525-7245	C	
103	00 53 16.3	-72 44 11	-	-	2	-	18	15	-	-	-	-	0.22:	1.2	C	00532-7244	W	
104	00 53 21.4	-74 34 35	18	-	-	-	-	-	-	-	p	0.67	-	-	-	00533-7434	S	SAO 255721
105	00 53 31.0	-72 55 00	-	-	2	-	25	16	16	12	3x4	-	0.87:	8.6	13.0	00535-7255	C	
106	00 53 46	-72 58	5	-	-	-	-	-	-	-	-	0.19	-	C	C		S	
107	00 54 12.7	-73 34 43	31	-	5	-	-	-	-	-	p	1.15	0.56	C	C	00542-7334	S	
108	00 54 16.7	-72 21 00	-	-	-	-	10	7	8	6	4x3	-	-	2.9	6.4	00542-7220	C	
109	00 54 18	-72 37	3	-	2	-	31	20	-	-	p:	0.11:	0.22:	4.5	C		W	
110	00 54 28	-72 34	5	-	2	-	32	13	22	15	4x3	0.82	0.87	18.0	22.0		C	
111	00 54 28.6	-73 03 04	5	-	6	1	32	15	-	-	px1	0.23:	0.66	7.5	C	00544-7303	W	
112	00 54 32	-73 23	-	-	2	-	-	-	-	-	p:	-	0.22	C	C		W	
113	00 54 49	-72 39	-	-	3	1	27	17	21	15	p:	-	0.22	4.1	13.0		C	
114	00 55 00	-72 47	3	-	2	1	22	17	16	13	p:	0.11:	0.11	2.1	6.3		C	
115	00 55 00	-73 03	2	-	2	-	29	15	22	12	2x3	0.23:	0.61	10.0	27.0	X0055-730	C	
116	00 55 03	-72 56	-	-	2	-	-	-	-	-	-	-	0.22	C	C		W	
117	00 55 10	-73 04	3	-	2	-	27	15	23	12	5x1	0.41:	0.74	10.0	34.0		C	
118	00 55 18.6	-73 17 02	-	-	-	-	9	5	8	6	-	-	-	1.7	4.2	00553-7317	C	
119	00 55 24.8	-73 51 29	12	-	2	-	-	-	-	-	p	0.44	0.22	C	C	00554-7351	S	
120	00 55 30	-73 02	3	-	-	-	-	-	-	-	-	0.11:	-	C	C		S	
121	00 55 47.8	-72 48 41	5	-	10	1	34	17	18	15	p	0.19:	1.00	7.0	6.3	00557-7248	W	
122	00 55 57	-73 10	5	-	2	-	-	-	-	-	-	0.19	0.22	C	C		W	
123	00 56 00	-72 16	-	-	-	-	13	10	-	-	-	-	-	1.2:	C		W	
124	00 56 17.1	-72 55 23	5	-	8	1	35	13	21	13	p	0.19	0.78	9.1	17.0	00562-7255	C	
125	00 56 22.7	-72 20 22	3	-	5	2	21	12	16	10	p	0.11:	0.33	3.7	13.0	00563-7220	C	
126	00 56 34	-72 42	-	-	2	-	27	20	24	15	px2	-	0.35:	3.6	20.0		C	
127	00 56 40	-72 27	5	-	15	2	-	-	-	-	-	0.19:	1.44:	C	C		W	
128	00 56 41	-72 56	5	-	6	-	35	13	-	-	p	0.19	0.67	9.1	C		W	
129	00 56 45	-72 52	-	-	2	-	23	16	16	12	p:	-	0.22:	2.9	8.4		C	
130	00 56 59.9	-72 43 43	10	-	20	2	36	18	-	-	p	0.37:	2.00	7.4	C	00569-7243	W	
131	00 57 26.5	-72 26 36	43	-	120	2	260	20	93	10	3x3	5.99	43.50	200.0	242.0	00574-7226 X0057-724	C	
132	00 57 28.4	-73 09 12	-	-	-	-	12	9	-	-	-	-	-	1.2	C	00574-7309	W	
133	00 57 42	-72 31	5	-	6	2	-	-	-	-	-	0.19:	0.44:	C	C		W	
134	00 57 54	-72 03	-	-	1.5	-	13	6	10	5	3x3	-	0.55:	5.8	15.0		C	
135	00 58 06	-72 25	5	-	12	10	70	20	-	-	-	0.19:	0.22	21.0	C		W	
136	00 58 12	-71 47	-	-	1.5	-	7	3	7	5	px2	-	0.27:	2.0	4.5		C	
137	00 58 12	-72 24	-	-	12	4	60	15	-	-	p	-	0.89	19.0	C		W	
138	00 58 36	-72 05	-	-	2	-	17	10	13	9	2x3	-	0.61:	5.0	11.0		C	
139	00 59 06	-73 07	5	-	1	-	6	5	-	-	p:	0.19	0.11:	0.4	C		W	
140	00 59 10	-71 55	5	-	-	-	-	-	-	-	p:	0.19	-	C	C		S	
141	00 59 13.2	-72 58 17	18	-	1.5	-	-	-	-	-	p	0.67	0.17:	-	-	00592-7258	S	SAO 255729
142	00 59 18.4	-71 51 24	5	-	9	1	26	5	14	5	p	0.19	0.89	8.7	19.0	00593-7151	C	
143	00 59 25	-72 04	-	-	2	-	-	-	-	-	-	-	0.22	C	C		W	
144	00 59 27.9	-71 44 06	-	-	-	-	8	4	4	2	p	-	-	1.7	4.2	00594-7144	C	
145	00 59 51.8	-71 49 03	9	-	-	-	-	-	-	-	p	0.33	-	-	-	00598-7149	S	SAO 255730
146	00 59 52.2	-72 06 50	-	-	8	1	26	13	16	10	p	-	0.78	5.4	13.0	00598-7206	C	
147	00 59 56.1	-72 12 16	-	-	1.5	1	20	13	16	15	-	-	0.06	2.9	2.1	00599-7212	W	
148	01 00 04.8	-72 03 07	-	-	-	-	13	10	-	-	p:	-	-	1.2	C	01000-7203	W	
149	01 00 05.5	-71 55 32	-	-	1.5	-	7	4	6	5	p:	-	0.17:	1.2	2.1	01000-7155	C	
150	01 00 27	-74 17	5	-	-	-	-	-	-	-	-	0.19:	-	-	-		S	
151	01 01 00	-73 13	-	-	-	-	6	4	5	3	-	-	-	0.8	4.2		C	
152	01 01 09.3	-72 09 42	10	-	11	2	42	16	29	16	p	0.37	1.00	11.0	27.0	01011-7209	C	
153	01 01 12.8	-72 41 34	-	-	2	-	17	7	11	7	3x2	-	0.61:	7.2	11.0	01012-7241	C	
154	01 01 18	-72 14	5	-	5	2	30	20	-	-	p	0.19	0.33	4.1	C		W	
155	01 01 19	-72 18	11	4	10	3	-	-	-	-	p	0.26	0.78	C	C		W	
156	01 01 31.0	-72 22 16	10	-	8	2	-	-	-	-	p	0.37	0.67	C	C	01015-7222	W	
157	01 01 32.0	-72 56 42	-	-	-	-	7	5	6	5	-	-	-	1.2	2.1:	01015-7256	C	
158	01 01 32.8	-71 06 59	18	-	-	-	-	-	-	-	p	0.67	-	-	-	01015-7106	S	NGC 362
159	01 01 38	-73 30	5	-	-	-	4	2	3	2	-	0.19:	-	0.8	2.1		C	
160	01 01 41.9	-72 28 06	-	-	6	2	25	14	16	15	p	-	0.44	4.5	2.1	01016-7228	W	
161	01 01 42	-72 20	10	-	13	3	75	20	46	15	p:	0.37	1.11	23.0	65.0		C	
162	01 02 11.2	-72 19 19	5	-	17	3	85	20	-	-	p	0.19	1.55	27.0	C	01021-7219	W	
163	01 02 13.4	-72 24 53	-	-	4	1.5	26	17	18	15	p	-	0.28	3.7	6.3	01022-7224	C	
164	01 02 27.8	-73 43 47	5	-	-	-	-	-	-	-	-	0.19	-	-	-	01024-7343	S	
165	01 02 44.9	-72 07 39	3	-	2	-	18	15	16	14	-	0.11:	0.22:	1.2	4.2	01027-7207	C	
166	01 02 51.4	-73 10 15	-	-	1	-	5	3	5	3	-	-	0.11:	1.2	4.2	01028-7310	C	
167	01 03 30.1	-72 00 08	12	-	1.5	-	-	-	-	-	p	0.44	0.17:	C	C	01035-7200	S	SAO 255735
168	01 03 30.3	-72 15 28	37	-	100	2	128	20	43	15	p	1.37	10.90	45.0	59.0	01035-7215	C	
169	01 03 36.3	-72 40 39	-	-	-	-	9	5	7	5	p	-	-	1.7	4.2	01036-7240	C	
170	01 03 44	-72 25	-	-	2	-	20	15	13	12	p	-	0.22	2.1	2.1		W	
171	01 03 48.5	-71 12 03	10	-	-	-	-	-	-	-	p	0.37:	-	-	-	01038-7112	S	SAO 255738
172	01 03 50	-72 12	-	-	4	1.5	20	18	-	-	p	-	0.28	0.8	C		W	
173	01 03 56.9	-73 05 59	5	-	9	-	13	4	6	3	p	0.19	1.00	3.7	6.3	01039-7305	C	
174	01 03 59.2	-72 46 34	-	-	-	-	10	5	7	5	2x2	-	-	3.1	4.9	01039-7246	C	
175	01 04 06	-72 20	3	-	4	2	30	17	20	17	p	0.11:	0.22	5.4	6.3		C	
176	01 04 13.9	-72 15 51	5	-	12	2	35	15	-	-	p	0.19	1.11	8.3	C	01042-7215	W	
177	01 05 06	-73 24	-	-	-	-	5	2	4	3	-	-	-	1.2	2.1		C	
178	01 05 24	-72 51	-	-	-	-	11	5	9	5	2x2	-	-	3.7	9.8		C	
179	01 05 26.4	-73 07 22	5	-	2	-	7	3	6	3	p:	0.19:	0.22:	1.7	6.3	01054-7307	C	
180	01 05 45	-74 04	7	-	-	-	-	-	-	-	p	0.26:	-	-	-		S	

Table 4, continued (3).

(1) Number	(2) Position RA(1950) h m s	DEC(1950) o ' "	(3) 12 μm Peak	Bg	(4) 25 μm Peak	Bg	(5) 60 μm Peak	Bg	(6) 100 μm Peak	Bg	(7) Size arcmin	(8) F 12μm Jy	(9) F 25μm Jy	(10) F 60μm Jy	(11) F 100μm Jy	(12) IRAS-Id	(13) Spectrum	(14) Comments
					10^{-8} Watt $m^{-2}sr^{-1}$													
181	01 06 01.5	-72 50 21	-	-	1.5	-	11	5	8	7	p:	-	0.17:	2.5	2.1:	01060-7250	W	
182	01 06 41	-73 10	5	-	-	-	-	-	-	-	p:	0.19	-	C	C		S	NGC 419
183	01 06 46.1	-72 28 09	-	-	-	-	6	4	5	4	p:	-	-	0.8	2.1	01067-7228	C	
184	01 06 58.3	-72 15 46	-	-	5	1	26	6	18	6	3x3	-	1.48	17.0	35.0	01069-7215	C	
185	01 07 27.8	-71 40 06	11	-	4	-	-	-	-	-	p	0.41	0.44	-	-	01074-7140	W	
186	01 07 33.8	-72 54 39	70	-	7	-	4	3	-	-	p	2.59	0.78	0.4	C	01075-7254	S	
187	01 07 43.9	-73 27 40	12	-	23	-	46	2	16	3	p	0.44	2.55	18.0	27.0	01077-7327	C	
188	01 07 45.2	-72 45 35	-	-	-	-	5	3	-	-	-	-	-	0.8	-	01077-7245	W	
189	01 08 03.6	-72 37 25	-	-	-	-	6	3	4	3	2x2:	-	-	1.9	2.5	01080-7237	C	
190	01 09 18	-72 58	-	-	-	-	6	3	5	3	4x4	-	-	3.3	7.1		C	
191	01 09 27.6	-71 52 26	27	-	1.5	-	-	-	-	-	p	1.00	0.17:	-	-	01094-7152	S	
192	01 09 30	-73 21	-	-	-	-	4	2	5	3	-	-	-	0.8	4.2		C	
193	01 09 31.4	-72 25 33	-	-	3	-	7	3	5	3	p	-	0.33	1.7	4.2	01095-7225 X0110-724 *	C	
194	01 09 50.3	-72 38 47	-	-	6	-	13	3	7	3	1x1	-	0.93	4.7	8.7	01098-7238	C	
195	01 10 41.3	-73 00 12	-	-	-	-	8	3	6	3	2x2	-	-	3.1	7.4	01106-7300	C	
196	01 10 44	-74 11	5	-	-	-	-	-	-	-	p:	0.19:	-	-	-		S	SAO 255751
197	01 11 39.0	-72 26 36	-	-	-	-	4	2	2	1	p:	-	-	0.8	2.1	01116-7226 X0110-724 *	C	
198	01 12 10.9	-71 08 07	8	-	-	-	-	-	-	-	p	0.30	-	-	-	01121-7108	S	
199	01 12 29.2	-73 32 49	17	3	22	2	117	6	60	4	p	0.52	2.22	46.0	117.0	01124-7332 X0112-735 *	C	
200	01 12 41.2	-73 32 42	22	3	38	2	-	-	-	-	p:	0.70	4.00	C	C	01126-7332 X0112-735 *	W	
201	01 13 19.1	-73 33 42	10	2	20	2	-	-	-	-	p	0.30	2.00	C	C	01133-7333 X0112-735 *	W	
202	01 13 23.1	-73 36 33	11	2	22	2	83	6	48	6	p	0.33	2.22	32.0	88.0	01133-7336	C	
203	01 13 56.3	-72 34 44	-	-	-	-	2	1	2	1	-	-	-	0.4	2.1	01139-7234	C	
204	01 14 17.3	-73 27 38	5	-	4	1	21	6	14	9	p:	0.19:	0.33	6.2	10.0	01142-7327	C	
205	01 14 18.1	-73 26 04	-	-	4	-	-	-	-	-	p	-	0.44	C	C	01143-7326	W	
206	01 15 00	-73 45	-	-	-	-	4	2	3	2	-	-	-	0.8	2.1	X0115-737	C	
207	01 15 21.1	-73 24 14	-	-	-	-	8	6	-	-	p	-	-	0.8	C	01153-7324	W	
208	01 16 06	-73 59	7	-	1	-	-	-	-	-	p	0.26	0.11:	C	C		S	
209	01 16 28.7	-73 11 09	-	-	-	-	3	2	3	2	-	-	-	0.4	2.1	01164-7311	C	
210	01 19 36.8	-73 37 13	-	-	-	-	2	1	2	1	-	-	-	0.4	2.1	01196-7337	C	
211	01 20 00	-74 15	-	-	-	-	1	-	1	-	-	-	-	0.4:	2.1		C	
212	01 20 12	-73 20	-	-	-	-	2	1	2	1	-	-	-	0.4	2.1		C	
213	01 21 37.9	-74 50 50	-	-	-	-	1	-	<1	-	-	-	-	0.4:	-	01216-7450	W	
214	01 22 24.0	-73 38 54	-	-	-	-	5	2	4	2	1x2	-	-	1.6	4.6	01224-7338	C	
215	01 22 52.8	-73 24 45	42	2	150	2	120	2	24	3	1x1	2.21	22.90	55.0	46.0	01228-7324	W	
216	01 22 56.2	-73 29 43	2	-	1	-	7	4	6	5	-	0.07:	0.11:	1.2	2.1	01229-7329	C	
217	01 23 24.3	-73 53 31	-	-	2	-	2	-	1	-	p:	-	0.22:	0.8	2.1	01234-7353	C	
218	01 24 10.3	-73 40 01	-	-	-	-	8	2	6	3	p:	-	-	2.5	6.3	01241-7340 X0123-736	C	
219	01 24 12.7	-73 30 50	2	-	3	-	9	2	5	3	p:	0.07:	0.33:	2.9	4.2	01242-7330	C	

with unresolved and extended components. The extended structure of the SMC at 60 and 100 μm is complicated, and therefore sometimes does the SSS entry merely represent just one part of it. There are 72 new infrared sources in this source list, not included in the PSC nor in the SSS. The IRAS High Source Density Bin data (IRAS, 1985a) show that the condition of high source density exists at 100 μm over the whole SMC and at 60 μm in the SMC Bar. In these confused and high source density regions in the sky the IRAS PSC is constructed with the primary aim to be reliable, even when it means less complete. The majority of these new sources are point sources, and clearly show the incompleteness of the IRAS PSC in confused areas.

4.2. Positions

The positions of the sources in the maps were compared with sources in the IRAS PSC. There was a good correspondence, that allowed us to use PSC coordinates for an unambigious association. In the 12 μm map the correspondence with the known SAO star positions is very good (average deviation of 15″). We also compared the positions at a resolution of 9′ against the Skyflux HCON–1 maps. Compared to the Skyflux data there are small systematic position shifts of order of 1′ ($\frac{1}{2}$ Skyflux–pixel size), but because those shifts are not present when we compare the DPM maps with the PSC, this indicates that the positional accuracy in the DPM maps presented here is significantly better than that in the Skyflux maps. Ground based near–infrared observations at La Silla (Israel *et al.*, 1988) indicate an overall mean accuracy of 10″ for IRAS point sources (PSC) in the Magellanic Clouds.

4.3. Flux densities

We compared the flux densities from the DPM maps with those from the PSC (version 1.0, November 1984). This is a comparison of independent data obtained with the same instrument, but reduced in a different manner. At 12 and 25 μm we see a discrepancy at the low flux levels. The PSC fluxes are consistently higher below 0.4 Jy. The (known) flux overestimate in the PSC at low levels may be the explanation for this effect. At 12 μm the agreement is otherwise quite good, about the 10 % quoted in Section 2. For extended sources and for relatively low quality sources in our list or in the PSC we find higher fluxes than in the PSC. At the other wavelength bands the number of such sources increases. The agreement with the high–quality sources is nevertheless very good. In the 60 and 100 μm bands, most sources have higher fluxes than in the PSC. The determination of the background is very important for calculating fluxes in these bands. The PSC filter works in the scan direction, while we compare different two–dimensional maps. It is not known to us how the PSC point source filter has interpreted the extended background structure of the SMC. We estimated the background for each source individually, and we believe that this visual investigation of the maps gives better results in confused regions than automated programs. A comparison of the fluxes of our maps and the IRAS SSS shows that some have very good agreement, but several show a lower flux on the DPM maps.

5. Identification of Sources

5.1. Stars in the DPM fields

5.1.1. Comparison with SAO stars

We have compared the Smithsonian Astrophysical Observatory Star Catalog (1966, henceforth the SAO Catalog) with our source database. Here we searched deeper (to 10^{-8} Watt m^{-2} sr^{-1}) on averaged maps than in the infrared source list (Table 4) on the SAO positions. Detection of infrared emission on the known optical position depends on local noise and background (often 3 – 4 times less than the global noise given in Table 3). The area of the SMC covered by the DPM maps contains 45 SAO stars. We detect 28 of these (mainly at 12 μm) and we have possible detections of five (for positional accuracy, see Section 4.2). The remaining 12 stars are below the local map sensitivity limits. In Table 5 we give the relevant data. Columns 1, 2 and 3 are taken from the SAO Catalog (version 1984). Columns 4 and 5 give the colour–corrected 12 and 25 μm flux densities as measured from the DPM maps. The low flux densities are more affected by noise etc. and

Table 5. SAO (1966) stars in the field of the SMC.

(1) SAO number	(2) m_V mag	(3) Sp type	(4) $F^{a}_{12\mu m}$ Jy	(5) $F^{a}_{25\mu m}$ Jy	(6) $F_{25\mu m}/F_{12\mu m}$	(7) $m_V - m_{12}$ mag	(8) Infrared Id	(9) Detection quality[b]	(10) Remarks[c]
255682	9.2	K5	-	-	-	-		-	
255683	9.6	F5	0.03:	-	-	2.2		-	
255684	8.6	K5	0.59	0.16	0.27±0.07	4.4	3	+	Faint emission at 60 μm.
255686	8.6	K5	0.31	0.04	0.13±0.1	3.7	4	+	
255689	7.4	F2	0.08	-	-	1.0	7	0	
255690	6.9	A0	0.08	-	-	0.5	8	0	
255692	8.9	A3	0.03:	-	-	1.5		-	
255693	8.9	K5	0.09	0.04	0.44±0.4	2.7		+	
255694	8.5	F0	0.04:	-	-	1.4		-	
255695	9.4	G5	0.01:	-	-	0.8		-	In extended emission.
255698	7.7	F5	0.04:	-	-	0.6		-	
255699	8.5	F0	-	-	-	-		-	
255700	8.3	F5	-	-	-	-		-	
255707	9.5	F5	-	-	-	-		-	In extended emission.
255711	8.8	K0	0.31	-	-	3.9	56	+	In extended emission.
255713	7.1	F2	0.08	-	-	0.7	69	0	
255715	9.0	K0	0.13	-	-	3.2	89	+	In extended emission.
255716	7.8	G0	0.26	-	-	2.7	90	+	
255717	8.5	F8	-	-	-	-		-	
255721	6.8	G5	0.47	0.08	0.17±0.09	2.4	104	+	
255723	8.4	A5	0.04	-	-	1.3		0	
255725	9.1	F5	0.04	0.04	1.00±1.0	2.0		0	
255729	8.0	K0	0.47	0.12	0.26±0.08	3.6	141	+	Close to extended emission.
255730	7.6	K0	0.23	0.08	0.35±0.18	2.4	145	+	Close to extended emission.
255733	8.6	K0	0.08	-	-	2.0		0	In extended emission.
255735	7.5	K0	0.31	0.12	0.39±0.1	2.6	167	+	
255736	8.2	G0	0.08	0.04	0.50±0.5	1.8		0	
255738	7.9	K0	0.26	0.08:	0.31±0.1	2.8	171	+	
255743	8.6	F0	-	-	-	-		-	
255745	9.1	G5	0.10	-	-	3.0		+	
255746	8.0	G0	0.09	-	-	1.8		0	Close to extended emission.
255748	7.2	A0	0.04	-	-	0.1		0	
255751	7.5	F8	0.13	-	-	1.7	196	+	
255752	8.2	G5	0.21	0.04	0.19±0.2	2.9		+	2'W of 198.
255755	9.1	K2	-	-	-	-		-	2'E of N84.
255758	9.4	A0	-	-	-	-		-	
255759	8.6	K0	0.08	-	-	2.2		0	
255761	8.2	F5	-	-	-	-		-	
255763	10.0	G0	0.04	-	-	2.9		0	
255765	7.7	F0	0.04	-	-	0.6		0	
255766	9.0	G0							Not covered by IRAS DPM-map.
255767	8.4	K0	0 12	-	-	2.5		+	
255768	8.1	K0	0.08	-	-	1.7		0	
255769	8.8	F8	-	-	-	-		-	
255773	7.9	A2	-	-	-	-		-	
255774	8.2	A5							Not covered by IRAS DPM-map.
255778	8.6	F2	-	-	-	-		-	

Notes to Table 5:

a) The 12 and 25 μm flux densities in this table are colour-corrected (not in any of the other tables) by dividing the nominal flux densities by 1.43 and 1.40 (correction for a 5000 K black body; for stars with other temperatures these factors are about the same, see IRAS, 1985a).

b) Detection qualities at 12 μm are good (+), medium (0) or poor (-).

c) See Section 5.1.1 in the text.

therefore have higher uncertainties. Column 6 gives the ratio $f_{25\mu m}/f_{12\mu m}$ together with their uncertainties. If the spectrum of a star follows the Rayleigh–Jeans tail of the blackbody emission this ratio should be about 0.23. The ratio gives information about a possible 25 μm excess relative to 12 μm ($f_{25\mu m}/f_{12\mu m} > 0.23$). The uncertainties are rather high because of the faint 25 μm emission. Only one star (SAO 255735) may possibly have a 25 μm excess. Column 7 contains the $m_V - m_{12}$ colour, which informs us about a possible 12 μm excess (relative to the optical V band). We compared this column with the $V-[12]$ colours listed in Table 3 of Waters *et al.* (1987) for the range of spectral types (A0 – K5). The stars are scattered within a 1 magnitude band around the values of Waters *et al.* (1987). Most of them have somewhat higher $m_V - m_{12}$ values, but we do not find any star with a significant $m_V - m_{12}$ excess due to the large scatter. The error in $m_V - m_{12}$ is about 1.0 mag. On average these stars have an excess of 0.3 ± 0.2 mag. Column 8 gives the identification of the SAO star in the infrared source list of Table 4. Out of the full sample of SAO stars fourteen can be found in that table (with intensities larger than 3 x 10^{-8} Watt m^{-2} sr^{-1} at 12 μm). SAO 255752 is detected on the maps, but an optically weaker (non–SAO) star at about $2'$ East is brighter in the infrared (LI–SMC 198 in Table 4). Column 9 gives the quality of the detection of the star on the infrared maps, and Column 10 gives some remarks. Only SAO 255684 shows some possible 60 μm emission. All eight G–type stars and thirteen out of fifteen K–type stars were detected at 12 μm; four out of six A–type stars and eight out of sixteen F–type stars were detected. There is no clear correlation between detection and visible magnitude in the whole SAO sample. But A–stars have been detected up to $m_V \approx 8.4 \pm 0.5$, F–stars up to $m_V \approx 9.0 \pm 0.6$, G–stars up to 10.0 and K–stars up to 9.1 magnitudes. Emission at 25 μm is detected only from stars later than F5. All stars with 25 μm emission also have 12 μm emission. Most of these stars are probably Galactic foreground stars.

5.1.2. Comparison with Radcliffe SMC–stars

We also searched for emission from verified SMC stars (Feast *et al.*, 1960) and we detected emission in the direction of eight (out of 46). In the direction of another 18 we found possible weak emission. The Feast SMC stars are on average fainter than SAO stars by 3 or 4 magnitudes (the brightest being R 45 with $m_V = 10.13$). They are the brighest SMC members (see Azzopardi and Vigneau, 1982). One star, R 10 is within a beam size from SAO 255715, and the emission is caused by the SAO star. R 8 is weakly indicated in the maps. R 14 is close to the HII region N 66 and probably we see emission from N 66 at 12 μm rather than from the star. R 44 is associated with the HII region N 81 (HDE 7113), and we detect this HII region in the infrared. Four other stars (R 28, 29, 31, 32) are close to the Hα nebulosity N 76 so that their detection likewise is not quite certain. More details about the comparison are given in Table 6. We conclude that the emission found is due to positional coincidence with other objects, and is not from the SMC stars itself. For twelve Radcliffe stars we mention possible positional infrared identifications in Table 4, of which only three have an S–type infrared spectrum. We conclude that these associations are also due to positional coincidences.

Because these stars are the brighest SMC stars we did not continue to look for emission from the whole list of 524 objects of Azzopardi and Vigneau (1982). Using the definition of 12 μm magnitudes (see IRAS, 1985b; and Table 3) the IRAS sensitivity limit becomes $m_{12} \approx 6$ mag. Waters *et al.* (1987) give a relation between intrinsic $V-[12]$ colours and spectral type; for A–type stars $V-[12]$ is about 0 mag and for K–type stars about 2.5 mag. Therefore the weakest A–type stars detectable by IRAS are of a visible magnitude $m_V \approx 6$ mag and K–type stars have $m_V \approx 10$ mag. Because the brightest SMC stars have

$m_V \approx 10.1$ mag, only stars with an infrared excess can be detected at a distance of the SMC (63 kpc).

Table 6. Radcliffe stars (Feast et al., 1960) in the SMC.

(1) Radcliffe Id	(2) m_V[a] mag	(3) Sp type	(4) $F_{12\mu m}$ Jy	(5) Infrared[b] Id	(6) Detection quality	(7) Remarks[c]
1	12.0 V	F8Ia	0.2 :	13:	0	2'S of 13/ 2'W of 16.
2		B6Ie	0.1 :	19:	0	On edge of SW-Bar, 2'E of 19/ 3'S of 20.
3		A3:I:(e)	< 0.08:		-	
4		Be	-		-	In SW-Bar, on border of N19. 3'SE of 36.
5	11.0	B3I	0.2 :		-	In SW-Bar.
6	10.96	B6I	< 0.2 :		-	On edge of SW-Bar.
7	12.0 V	G0:I	< 0.2 :		-	2'N of 66/ 3'W of 74.
8	11.11	A0Ia:	0.2		-	On edge of SW-Bar.
9	10.98	B3Ia:	-		-	On edge of SW-Bar, 1'NE of R8.
10	10.91	A0Ia:	0.2	89:	-	0.3'SW of SAO 255715 (see Table 5).
11	10.75	B6Ia	-		-	In extended emission, on edge of N50.
12	12.2 V	F8Ia	-		-	
13		A3:Ia:(e)	< 0.08:		-	
14	11.61	Wp	0.2 :	135:	-	In N66, 2'NE of 131/1'W of 135/2'SW of 137.
15		(A-B)e	< 0.08:		-	
16		B	< 0.04:		-	
17	12.12	B0I	-		-	
18		B0.5I	-		-	Near edge of N66, 5'SE of 131.
19		A3Ia	-		-	3'NW of 142.
20	12.3 V	K5Ia:e	-		-	
21		A0Ia:	-		-	
22	12.27	A3I	-		-	
23		A1I	-		-	
24	12.50	A0:	0.2 :		-	Close to N76.
25		B1:	-		-	2'E of R23
26		F0Ia.	0.2 :		-	Edge of N76.
27	10.9	B^{9}Ia	< 0.08:		-	3'W of 160.
28		B0I	0.4	161	-	Border of N76, 1'W of R30.
29	12.74	K.	0.4	156	-	In N76, 1'W of R31.
30	13.2	Be	0.2 :	161	-	In N76, 1'E of R28.
31	12.3	O.f:	0.4	156	-	In N76, 1'E of R29.
32		B	0.2	162	-	In N76, 2'SW of R35.
33		B	< 0.08:	163	-	Edge of N76, 1'N of 163.
34	12.83	F0·I(e)	-		-	Non-SMC member (Azzopardi and Vigneau, 1982).
35		B1I:	0.2 :	162	-	Border of N76, 2'NE of R32.
36	11.26	B3I	< 0.08:		-	
37	11.20	B6I	< 0.08:		-	
38		Pec	-		-	
39		B2:I(e)	-		-	
40	10.73	B8Ie	< 0.08:		-	
41		Be	-		-	3.'SW of 187.
42	10.95	B2.5I	-		-	
43		A3I	-		-	
44[d]		Neb	0.4	187	-	Position of HDE 7113 (N81), 0.4'SE of 187.
45	10.13	A0Ia-0	-		-	4.'SW of 209/210.
46	V	G0	-		-	
47	11.56	FIe				Not covered by IRAS DPM-map.
48		e				Not covered by IRAS DPM-map.
49		(A-B)e				Not covered by IRAS DPM-map.
50	11.56	Pec				Not covered by IRAS DPM-map.

Notes to Table 6·

a) Magnitudes followed by a V indicate that the star is variable, the average of the maximum and minimum magnitudes are given in those cases.

b) Only associations 13, 19 and 89 from Table 4 have S-type infrared spectra, all others are associated to entries in Table 7 (HII regions). Infrared sources 156, 161, 162 and 187 have emission at other IRAS wavelength bands than 12 μm.

c) See Section 5.1.2 in the text.

d) According to Feast et al. (1960) R44 corresponds to N81/HDE 7113. We find that their Table 2 coordinates are 9'N of N81. Here we used the N81 (HII region) coordinates (Henize, 1956).

5.1.3. Comparison with Late Type Giants

A comparison with the list of Carbon and late M–type stars (Blanco *et al.*, 1980) gives one possible detection. LI–SMC 54 (in Table 4) is situated $1\overset{'}{.}5$ West of the position of B 13 in the SMC Bar. This star is one of the list of Blanco *et al.* from which Cohen *et al.* (1981) detected near–infrared emission. The list contains 83 stars in the Bar and 56 in the Wing. Confusion in the SMC Bar may have resulted in this association, but may also be the reason that no others were detected. Another infrared source, LI–SMC 140, is situated $1'$ NE of the position of an irregular variable star HV 11423 (Payne–Gaposchkin, 1966). Near–infrared emission from this star was detected by Glass (1979). The 12 μm flux density is about ten times higher than the 2.2 mag point of Glass shifted to the longer wavelengths via the Rayleigh–Jeans tail of a blackbody spectrum. If the association is correct the reason for this may be its (irregular) variability. HV 11423 is the brightest star in the K–band and is the most luminous M–type variable in the SMC (Glass, 1979).

5.1.4. Stars: Conclusion

In Table 4 there are 43 sources with an S–type infrared spectrum. Of these, fourteen are SAO stars. We looked at the other 29 objects on the photographic ESO–SRC Southern Sky Survey. Eightteen of them can be identified on those plates with stars (probably foreground; six fairly bright, twelve faint stars). Nine could not be identified because they are in the crowded SW–Bar. Most infrared spectra marked S in Table 4 (outside the Bar) have an optical identification, but often there is more than one star within a single beam so that these identifications are only tentative. We compared the list of infrared sources with an S–type spectrum with the list of SMC members of Azzopardi and Vigneau (1982). Six objects (infrared sources 19, 48, 96, 106, 107, 186) are within $2'$ from an SMC member in that list (respectively AZV 2*, 36, 148, 164, 170, 438*). These stars are A and B–type supergiants with $m_V \approx 13$ mag. They are situated in the crowded SMC Bar, and therefore may be misidentified due to confusion. If the association is correct they must have an infrared excess, otherwise they would have stayed invisible at 12 μm. Of the S–type infrared spectra there is one Galactic globular cluster NGC 362, and one SMC globular NGC 419 (Table 4; K 58 in Kron, 1956; L 85 in Lindsay, 1958) in our source list (see Section 5.3).

5.2. Hα nebulosities in the SMC

A good overall agreement between Hα emission regions and IRAS infrared emission was already noted by Schwering (1985). In Table 7 we present a more detailed comparison of the IRAS data with the Hα catalogues of Henize (1956) and of Davies *et al.* (1976, henceforth DEM). The DEM catalogue contains 167 entries ranging in size from $0'$ to $30'$. DEM entries 1 (N 3), 166 (N 90) and 167 are not covered by the IRAS DPM maps; they are discussed in Appendix A. About 70 % of all the bright Hα nebulosities have clear infrared counterparts, 15 % have possible counterparts and the remaining 15 % do not show any clear infrared emission. For the fainter nebulosities the statistics are 50 % detected in the infrared, and 25 % possible detections, while the remaining 25 % does not show any infrared emission. We conclude that there is a higher detection probability in the infrared for the brighter HII regions. We detected infrared emission from about 70 % of the compact Hα knots, while 60 % of the shells were detected.

Table 7. Infrared emission from H-alpha Emission Nebulae in the SMC (Davies et al., 1976; Henize, 1956).

(1) DEM Id	(2) Henize Id	(3) Intensity of H-alpha	(4) Infrared[a] Id	(5) Detection quality	(6) Remarks[b]
1	N 3	b			Not covered by IRAS DPM-map.
2		f	6	+	
3		b		0	On edge of IR extended emission.
4		b		0	On edge of weak IR extended emission.
5		vf	10	+	Offset 2'N. (Def: Offset=Pos(H-alpha)-Pos(IR)).
6		f+b	15	+	Offset 1'N.
7		b	16	+	
8		b		-	On edge of IR extended emission.
9	N 9	b	23	+	
10		f		+	Filament along edge of IR extended emission.
11	N10	b	26	+	Offset 1'N.
12		vf	24	0	Center H-alpha shell 3'NE.
13		f+b	26	+	IR 26 on N extension of H-alpha nebula; No IR peak on main body.
14		b	27	+	Offset 2'N.
15	N12 (part)	b	30	+	Offset 1'NW.
16	N13A,B	vb	29	+	
17		f+b	28	+	
18	N12B	b	30	0	Offset 2'N.
19		vf	31	+	IR coincides with southern part of nebula.
20	N12 (part)	b		0	On edge of IR 36.
21	N16	f+b	35	+	IR source on bright part of shell.
22		fb		+	Shell lining edge of IR 'hole'.
23	N12A	vb	36	+	
24		b		-	2'N of IR 35.
25	N17	b	38	+	
26		b		-	
27		fb		-	Near edge of IR 36.
28	N15	b		-	On edge of IR 29.
29		f	44,37	0	Delineating edge of extended IR emission, IR 44 coincides with E peak.
30		b		-	
31	N19	b		-	On edge of IR 49.
32		vb	43	0	IR follows nebular outline.
33		f	46	+	Nebulae on edge of IR emission.
34		fb		+	IR confused area. DEM 34, 35 and 36.
35		fb	42	+	IR peak 42 in between.
36		b		+	IR confused area: DEM 34, 35 and 36.
37	N22	b	45	+	IR peak 45 in between 37 and 38.
38	N25,N26	vb		+	IR peak 45 in between 37 and 38.
39		b		0	Coincides with IR 'hole'.
40	N27	b	49	+	
41		b		-	
42	N24	vb		-	On IR gradient (to IR 45 and 42).
43		b		-	On IR gradient (to IR 45).
44		f	52,56,57	+	IR peaks on East part of H-alpha nebulae.
45	N30	vb	51	+	Offset 3'NE.
46		f	48	+	IR on NW part of nebula.
47		f		-	On IR gradient (to IR 63).
48	N32	b	58	+	
49		f+b	54	+	Shell borders on IR extended emission.
50		b		-	On edge of extended emission.
51		vf	59	+	On extended emission.
52		b	68	+	Offset 2'W.
53		f	70	+	IR source in S of H-alpha nebula only.
54	N36,N41	vb	65	+	Shell coincides with extended IR source.
55	N37	vb	66	+	
56		b	62	+	
57	N35	b		0	On N edge of 62.
58		vf		-	On edge IR extended emission, in IR-hole.
59		fb	73	+	
60	N45	b	76	+	

Table 7, continued (2).

(1) DEM Id	(2) Henize Id	(3) Intensity of H-alpha	(4) Infrared Id	(5) Detection quality	(6) Remarks
61		b		0	On edge of IR extended emission.
62	N46	b	77	+	
63		fb	78	0	Edge of extended emission.
64		vf		0	Bright SE component coincides with IR peak.
65		fb		+	Extended IR emission peak of IR 81.
66		fb	75,79,80,87	+	IR complex at edge of extended emission.
67		fb	84	+	Center shell offset 2'W.
68	N50	b		0	On edge of IR 92,94 complex/pair.
69		fb		+	Weak IR emission.
70		fb		0	Edge of IR emission.
71	N48	b		0	On edge of IR 86.
72	N51	b	86	+	
73		fb		0	3'NE of IR 86.
74		vf	88,98	+	SE peak coincides with IR peak 98, N with 88.
75		vb		-	
76		fb	93	-	Offset 2'E.
77	N52A,B	b	94	+	
78		b		+	Weak IR emission.
79		vf		0	Edge of IR emission.
80		fb	105,106	+	Main source coincides with IR 'hole', bright part with IR 105.
81		f		-	Edge of IR extended emission.
82		b		0	On edge of IR 111.
83	N57	b		0	On edge of IR 110.
84		fb		0	On edge of IR 110.
85	N58	b	110	+	
86		fb	109	+	
87		f	114	0	
88		f	111	+	
89		vf	117	+	Follows extended IR emission, close to IR 111.
90		f		+	Shell follows edge of IR extended emission.
91	N59	b	119	+	Offset 1'N.
92		b		-	
93	N62	vb		+	Offset 3'SW of IR 124.
94	N63	vb	124	+	
95	N64A	vb	128	0	IR 128 in between DEM 94,95.
96		f		0	Edge of extended IR emission.
97		f		-	
98		fb		+	On IR gradient (to IR 131).
99		fb	133	+	On IR gradient (to IR 131).
100	N69	b		0	Extended IR emission.
101		f		-	
102		b		-	Edge of IR 131.
103	N66A,B,C,D	vb	131,135,137	+	IR 131 source covers only SW part of very large nebula. IR 135 and 137 are in centre of NE part.
104		vf		-	In extended emission.
105		f		-	On edge IR extended emission.
106	N69	b		+	Weak IR emission.
107		b	138	+	
108		f	136	+	Weak extended IR source.
109	N71	vb	142	+	
110		b	144	+	
111		fb	147	+	Offset 3'SW.
112	N72	b	146	+	Offset 2'SW.
113		fb	148	+	Offset 2'SW.
114		f		+	Nebular filament delineates edge of IR 'bay'.
115	N74	b		-	On edge of IR 152.
116	N75	b		-	
117a,b	N77B,A	b,vb	152	+	DEM 117b coincides with IR 152.
118		b	153	+	IR 153 lies on arc DEM 118.
119		b	156	+	1'W of IR 156.
120	N76B	vb	156	+	1'S of IR 156.

Table 7, continued (3).

(1) DEM Id	(2) Henize Id	(3) Intensity of H-alpha	(4) Infrared Id	(5) Detection quality	(6) Remarks
121		b		-	Edge of IR 152.
122		f		-	On edge IR extended emission.
123	N76A	vb	160,161, 162,163	+	Complex.
124		fb		0	Shell around H-alpha corresponds with IR emission.
125		f	169	+	Confused. H-alpha follows IR emission.
126	N78A,B	vb	168	+	Offset 2'S.
127	N78D	vb	168	+	Offset 1'E.
128		f	170	+	
129		fb	173	+	Offset 1'N.
130	N78C	vb		+	Weak IR peak.
131		b		0	Edge of weak IR peak.
132		fb		-	IR extended emission.
133		f	179	+	
134		fb	174,178,181	+	Complex.
135	N80	b	184	+	IR 184 lies on brighter E part.
136		f		-	Edge of extended IR emission.
137		fb	189	+	Offset 1'W.
138	N81	f+b	187	+	Offset 3'W.
139		vf	188	+	IR peak N of S-part; IR extended emission follows main source.
140		fb	190	+	Weak extended IR peak.
141		b	194	+	
142		b	193	+	3'SE of IR 193.
143		vf		0	Weak IR extended level.
144		fb	195	+	Shell at offset 2'W.
145		vf		+	Weak IR extended emission.
146		f+b		+	Weak IR peak.
147	N83A,C	vb		+	On extension of IR 199.
148	N83B	vb	199	+	
149	N84C	vb	200	+	
150	N84 (part)	b		0	Edge of IR 199, 200.
151	N84A	vb	201	+	Confused.
152	N84B,D	vb	202	+	Confused.
153		f		0	Weak extended IR emission.
154		fb	203	+	Offset 3'S.
155		b	204,205	+	
156		b		0	On extension of IR 204/205.
157		f		0	Filaments (follow it partially). IR 206 on S filament.
158		fb	207	+	Offset 1'S.
159		b		-	Edge of IR complex.
160		fb	214	+	IR between H-alpha peaks.
161	N88	vb	215	+	
162		f		0	Weak IR emission.
163		f	216,219	0	Confused.
164	N89	b	218	+	Shell around IR peak.
165		vf		-	On edge IR extended emission.
166	N90	vb			Not covered by IRAS DPM-map.
167		f			Not covered by IRAS DPM-map.

Notes to Table 7:
a) Associations 48, 54, 56, 106, 119 from Table 4 have S-type infrared spectra.
All other associated infrared sources have C-type or W-type infrared spectra.
b) See Section 5.2 in the text.

The whole SMC is covered by Hα nebulosities (see DEM, 1976), and also by 60 and 100 μm infrared radiation. From this comparison, we see that the discrete infrared sources correlate well with HII regions, and that HII regions are one of the main contributors to the infrared radiation in the SMC.

Table 8. Clusters in the SMC (Kron, 1956; Lindsay, 1958; Hodge and Wright, 1972), with infrared counterparts.

(1) Name[a]	(2) Other names	(3) F 12µm Jy	(4) F 25µm Jy	(5) F 60µm Jy	(6) F 100µm Jy	(7) Infrared[b] Id	(8) Detection quality	(9) Remarks[c]
K 12	L16, NGC176	0.07:	-	-	-		-	At edge, 3.7'SE of 1.
K 14	L18	-	0.4 :	2.5	3.0	6	-	0.6'SW of 6.
K 25	L35	0.1 :	-	-	-		-	At edge of SW Bar.
K 26	L37, NGC269	0.04:	0.2 :	-	-		-	At edge of SW Bar.
K 28	L43	0.06:	-	2.4:	12:		-	
K 31	L46	0.1 :	-	-	-		-	At edge of Bar.
K 33	L50, NGC306	0.06:	-	-	-		-	At edge of Bar.
K 35	L54, NGC330	0.15	0.04:	-	-		+	In Bar.
K 39	L60, NGC346	6	44	200	242	131	-	N66, 0.7'S of 131.
K 48	L71, NGC371	0.4	1.1	23	65	161	-	N76, 0.6'S of 161.
K 51	L75, NGC395	1.4	11	45	59	168	-	N78, 0.2'S of 168.
K 54	L79	0.07:	-	-	-		-	
K 57	L86	0.1 :	0.07	-	-		0	
K 58	L85, NGC419	0.2	0.1	C	C	182	+	1.4'N of 182.
K 64	L89, IC1660	0.04:	-	-	-		-	
K 65	L94, NGC456	0.5	2.2	46	117	199,200	-	0.7'NE of 199, 0.7'NW of 200.
K 66	L97, NGC460	0.3	2.0	C	C	201	-	0.6'SE of 201.
K 67	L99, NGC465	0.1 :	0.2 :	6:	31:		-	
L 41		0.2	0.2 :	C	C	74	0	1.4'N of 74; In Bar.
L 84		0.06:	1.5	17	35	184	-	0.8'NW of 184.
L101		2.2	23	55	46	215	-	1.1'E of 215.
L103		0.07:	0.33:	2.9	4.2	219	-	1.5'NW of 219.
L104		0.04:	0.22:	2.5	6.3	218	-	2.0'NE of 218.
HW16		<0.07	0.1 :	1.2	2.1	16	-	0.8'SW of 16.
HW25		0.06:	-	-	-		-	
HW36		-	-	0.1	0.6		0	
HW37		0.06:	0.6 :	6	15	134	-	1.7'NW of 134.
HW38		-	-	0.1:	0.6		0	
HW41		0.07:	-	-	-		0	
HW46		0.05:	-	-	-		0	
HW60		-	-	1.9	2.5	189	-	0.3'NW of 189.
HW72		<0.06	0.4	C	C	205	-	0.8'N of 205.
HW74		<0.06	0.2:	0.8	C	207	-	0.4'SE of 207.
HW75		0.1 :	-	-	-		0	
HW78		<0.06	-	0.4	2.1	212	-	0.5'SW of 212.
HW81		2.2	23	55	46	215	-	0.4'N of 215.
HW82		2:	20:	50:	40:	215:	-	1.9'SE of 215.

Notes to Table 8:
a) Only clusters which have possible infrared counterparts are given.
b) Only infrared associations 74, 134, 182 and 212 (in Table 4) were not previously included in Table 7 (HII regions). The other infrared associations have clusters and HII regions in a single beam, and thus are confused.
c) See Section 5.3 in the text.

5.3. Clusters in the SMC

We compared the list of star clusters of Kron (1956), Lindsay (1958) and of Hodge and Wright (1974) with our source list and the infrared maps. The clusters listed in Westerlund and Glaspey (1971) are not covered by the DPM maps. These four lists contain 220 clusters of sizes ranging from a few tenths of an arcminute to a few arcminutes. We searched deeper on the maps than in Table 4. In total we have 37 possible infrared detections of clusters, of which 20 have associations in Table 4. Sixteen of these infrared sources also have been associated to Table 7, showing the confusion with HII regions. Of these 37 possible detections, two are very reliable. They coincide with blue globular clusters; K 35 (= L 54 = NGC 330) and K 58 (= L 85 = NGC 419) are detected at 12 and 25 μm. These two are the brightest visual SMC globular clusters (van den Bergh, 1981). The remaining possible infrared associations have mainly 12 μm emission and are very weak. Some are also seen at 60 and 100 μm. Results of this comparison are given in Table 8.

We have also compared the globular clusters or compact groups from the list of 168 new clusters of Brück (1976; her types 1, 2 and 3). Only B 52 is such a cluster. All other new clusters are large loose groups, mainly blue or small blue clusters. There is an infrared source (LI–SMC 59) at about 1′ SE but there is some extended emission present as this position in the SMC–Bar. LI–SMC 59 is also associated to HII region DEM 51 (see Table 7), which shows the confusion in the Bar. Recently Hodge (1986) added 213 new clusters in the SMC which brings the total number of cataloged clusters to 601. These new clusters are very small and faint and we do not expect much infrared emission from them.

5.4. Supernova remnants in the SMC

We checked the list of six supernova remnants of Mathewson *et al.* (1983; their Table 2). All SNRs are smaller ($0\overset{\prime}{.}5 - 5'$) than the IRAS beam size at 100 μm. The first three remnants are situated in the crowded SW–Bar of the SMC. SNR 0045–73.4 coincides with extended emission between infrared sources LI–SMC 36 and 43 (see Table 4). SNR 0046–73.5 is located close to the edge of source 42, and SNR 0049–73.6 is situated in an infrared hole near sources 68 and 70. The last three are located in the NE part of the Bar. SNR 0101–72.4 can probably be associated with infrared source 160 (at $2\overset{\prime}{.}3$ South) at about 6′ from N 76. It is situated on infrared extended emission South of N 76. SNR 0102–72.3 is close to the East of N 76. There is some weak extended emission, but no clear correspondence with the remnant. SNR 0103–72.6 is situated $1\overset{\prime}{.}5$ North of the peak of LI–SMC 169. All these associations are already given in Table 7 of the Hα nebulosities. Table 9 summarizes this comparison.

Table 9. Known supernova remnants in the SMC (Mathewson et al., 1983).

(1) SNR Cat. number	(2) Infrared Id[a]	(3) SNR size arcsec	(4) Detection quality	(5) Remarks[b]
0045-73.4	3.2'W of 43 3.8'SE of 36	100x 70	-	In SW Bar, in extended emission between 36 and 43.
0046-73.5	3.1'SE of 42 4.6'N of 44 4.3'S of 45	120x 84	-	In SW Bar, close to edge of 42.
0049-73.6	2.9'SE of 68 3.0'NE of 70	110x 80	-	In SW Bar, in infrared hole.
0101-72.4	2.3'N of 160 2.7'W of 163 3.6'S of 156	98x 77	0	6'S of N76, on infrared extension. Probably 160.
0102-72.3	1.7'NE of 162 3.8'NE of 161	24x 24	-	In between N76 and N78.
0103-72.6	1.5'N of 169	292x187	0	On peak of 169.

Notes to Table 9:

a) All associations with Table 4 within 5' are given and all of them have C-type or W-type infrared spectra. All these associations have already been listed in Table 7 (HII regions).

b) See Section 5.4 in the text.

5.5. Planetary nebulae in the SMC

We compared the DPM infrared maps and the source list with the planetary nebulae identified by Sanduleak *et al.* (1978) and Sanduleak and Pesch (1981). Of their list of 34 nebulae numbers Sk 1, 2, 4, 20 and 29 are not covered by the IRAS DPM observations. The sizes of these nebulae are of order 1″. Many of the nebulae are situated in extended infrared emission in the Bar and in the Wing. Seven nebulae (Sk 5, 6, 11, 15, 17, 19, 27) have probably infrared counterparts, and we have possible detections of six. We give results of the comparison in Table 10. Again we searched deeper than in Table 4. Only four nebulae have associations in Table 4. Sk 9 (with infrared LI–SMC 29) is positioned within one beam size of Hα nebulosity N 13, therefore the association is not very reliable. Sk 19 is also close to an Hα structure, but is probably real. A few sources show up in all four wavelength bands.

Table 10. Planetary nebulae in the SMC (Sanduleak et al., 1978; Sanduleak and Pesch, 1981).

(1) Number	(2) F 12μm Jy	(3) F 25μm Jy	(4) F 60μm Jy	(5) F 100μm Jy	(6) Infrared Id[a]	(7) Detection quality	(8) Remarks[b,c]
1							Not covered by IRAS DPM-map.
2							Not covered by IRAS DPM-map.
3	-	-	0.2:	1		0	At end of extension of 1 (in Table 4).
4							Not covered by IRAS DPM-map.
5	-	0.1	0.1	C		+	In weak extended emission at edge of SW Bar.
6	0.06:	0.2:	0.4:	C	12	+	N 6, Ln 33, 0.5'N of 12. In weak extended emission of SW Bar.
7	-	-	-	-		-	At edge of SW Bar.
8	-	-	-	-		-	At edge of extended emission.
9	0.6	1.9	28	54	29	0	Ln 66, 1.1'S of 29. Peak in SW Bar.
10						-	At edge of SW Bar.
11	0.2	1.0	4.5	4.2	50	+	N29, Ln115, 0.3'N of 50. In SW Bar.
12	-	-	-	-		-	
13	-	-	-	-		-	At edge of SW Bar.
14	-	-	-	-		-	On edge of SW Bar.
15	<0.05	0.1	-	-		0	
16	-	-	-	-		-	In infrared-hole at 60 and 100 μm.
17	-	0.1	0.25	0.8		+	Weak infrared emission, far North from SMC Bar.
18	-	-	-	-		-	In SW Bar.
19	<0.05	0.44	C	C	91	+	Ln239, 0.2'SE of 91. In SW Bar.
20							Not covered by IRAS DPM-map.
21	-	-	-	-		-	In SW Bar.
22	-	-	-	-		-	Edge of Bar.
23	-	-	-	-		-	Ln343, at edge of SW Bar.
24	-	-	-	-		-	10'N of N66, in extended emission around N66.
25	-	-	-	-		-	Edge of Bar, 7'SW of 142.
26	<0.06	-	<0.1	-		0	In weak extended emission.
27	<0.06	0.1	0.4	1		+	In weak extended emission of N88.
28	<0.08	-	-	-		0	Near weak extended emission.
29							Ln 3. Not covered by IRAS DPM-map.
30	0.04:	-	-	-		0	At edge of Bar.
31	-	-	-	-		-	On infrared emission at edge of Bar.
32	-	-	-	-		-	At edge of SW Bar.
33	<0.05	-	-	-		-	0.7'E of 138 (H-alpha association).
34	-	-	-	-		-	

Notes to Table 10:

a) Association 29 (Table 4) with a C-type infrared spectrum was already associated to an HII region (see Table 7), the other three infrared associations have W-type infrared spectra.
Except for nebulae 9 and 19 the nebulae are not disturbed by other prominent visible objects in the beam.

b) References to nebulosities (N, see Henize, 1956) and emission-line objects (Ln, see Lindsay, 1961) are made.

c) See Section 5.5 in the text.

Nebula Sk 11 is very bright in the infrared. Extrapolating its flux densities using the ratio $f_{60\mu m}/f_{100\mu m}$ as a temperature measure ($T_d \approx 50$ K) and assuming a dust emissivity with a λ^{-1} wavelength dependence, we find $L_{IR} = 3.7 \times 10^4 L_\odot$. This is high for a planetary nebula. The luminosity of the star is usually 3 to 10 times higher than the infrared luminosity (Pottasch, 1986). Paczynski's (1971) evolution tracks for planetary nuclei give a stellar luminosity of $5 \times 10^4 L_\odot$ for the most luminous cases. For the Galactic planetary nebula NGC 6537 the IRAS PSC gives flux densities of 7.7, 58.3, 190 and 166 Jy at 12, 25, 60 and 100 μm. An extrapolation of these IRAS flux densities (with $T_d = 55$ K) gives $L_{IR} = 2300 L_\odot$ (16 times less). Pottasch (1986) finds for 16 Galactic planetary nebulae values for $L_{IR}/L_\odot$ of typically a few hundred. The extrapolation gives a good estimate of the infrared luminosity for a continuum spectrum. According to Pottasch (1986) line radiation can form a large fraction of the emission from average size nebulae in the IRAS survey bands and may even dominate the continuum in these bands, probably also at 60 and 100 μm (Leene and Pottasch, 1986). If that is the case the infrared luminosity is an overestimate. If we assume a distance of 2.4 kpc for NGC 6537 (Gathier, 1984), a nebula with the same infrared brightness as NGC 6537 would have flux densities of 0.01, 0.08, 0.3 and 0.2 Jy in the IRAS bands at the distance of the SMC. This is about equal to our detection limits. For most identifications other than the brightest (Sk 11) we actually find flux densities of this order (see Table 10). Four nebulae have their infrared emission peak at 25 or 60 μm, which is typical for planetary nebulae (see *e.g.* NGC 6537).

5.6. Dark clouds in the SMC

We compared the infrared data with the dark nebulae listed by Hodge (1974). In his paper about the LMC, Hodge (1972) discussed the uncertainties related to incompleteness of his list. These 45 dark clouds range in size from 1′ to 6′. In the comparison we used positions from his Plate–I after we discovered that six nebulae (21, 30, 37, 40, 41, 45) differ from the positions in his Table 1. Results are listed in Table 11. The infrared emission at 60 and 100 μm follows the nebulae in the SW–Bar very well. At the East side of the SW–Bar the infrared follows the dark clouds 29, 30, 32 and 33. All known dark nebulae are in the Bar and the Wing. Nineteen have an association in Table 4. Most clouds can be associated with an infrared feature but some (31, 39, 40, 43) are associated with an infrared minimum.

6. Conclusions

In the SMC DPM maps, 219 discrete sources were found; 143 of these are identified with sources in the IRAS Point Source Catalog (PSC). Sixteen sources correspond to sources in the IRAS Small Scale Structure Catalog (SSS). We found a total of 72 sources not listed in either of these catalogues. In many cases, we determine actual flux densities for sources while the PSC gives only upper limits. Most sources are associated with known HII regions and dark clouds in the SMC. At the positions of known objects in the SMC, we conducted deeper searches of the maps. The results are as follows.

Out of 45 SAO stars, we detected infrared emission from 28, and possibly five more. No cataloged stars in the SMC were identified with certainty, but 29 infrared, non–SAO

Table 11. Hodge (1974) dark clouds in the SMC.

(1)	(2)		(3)	(4)
Number[a]	Infrared[b] Id		Detection quality	Remarks[c]
1	30		+	1.8'S of 30; On infrared extension in SW Bar.
2	31		+	0.6' NW of 31; In SW Bar.
3	29		+	0.6'E of 29, 0.7'W of 32; In SW Bar.
4	35		+	1.1'W of 35; In SW Bar.
5			+	Infrared emission in SW Bar extended emission.
6			0	1.9'N of 35; On infrared gradient in SW Bar.
7	35		+	0.9'N of 35; In SW Bar.
8			0	On infrared gradient in SW Bar.
9	38		+	0.5'NE of 38; On infrared peak in SW Bar.
10	36		+	1.3'E of 36, Infrared extension towards peak 43; In SW Bar.
11	42		+	1.5'NW of 42; In SW Bar.
12	45		+	0.9'NW of 45; In SW Bar.
13	45		+	1.5'N of 45; In SW Bar.
14			+	1.7'E of 42; On infrared gradient to 42 and 45 in SW Bar.
15	44		0	1.0'E of 44. Weak infrared emission, on edge of SW Bar.
16			0	Weak infrared emission in Bar.
17			0	On infrared gradient to 51; In SW Bar.
18			+	1.1'SE of 58. Infrared extension near 63; In Bar.
19	63		+	1.3'NW of 63; In Bar.
20			+	Weak infrared extension on edge of SW Bar.
21			0	On infrared gradient SE of 62; In Bar. Pos:00h49m09s,-72°50'54".
22			0	On infrared gradient to 63 and 65 in Bar. 1.8'N of 65.
23			0	On infrared gradient to 63 and 65 in Bar. 2.7'NE of 65.
24	74	2	0	2.2'NW of 74; In extended emission of Bar.
25			0	On infrared extended emission around 63.
26	78	2	0	2.2'S of 78; On infrared gradient in Bar.
27			0	1.9'N of 78; On infrared gradient in Bar.
28	81		+	0.8'W of 81; At the edge of the Bar.
29			0	Near edge of infrared extended emission of SW Bar.
30	88		0	1.3'NE of 88. On edge of infrared extended emission of Bar. Pos:00h51m32s,-73°28'06".
31		4	-	Infrared minimum, in extended emission of Bar.
32			0	On edge of infrared extended emission; In SW Bar.
33			0	On edge of infrared extended emission; In SW Bar.
34		4	0	Near edge of 111, in extended emission of Bar.
35	108		+	1.1'S of 108; At the edge of the Bar.
36			0	On edge of extended emission of Bar.
37	130		+	1.0'SW of 130; In Bar. Pos:00h56m51s,-72°44'24".
38		2	-	7'S of N66, 3.6'SW of 133; In extended emission of Bar.
39		2	-	Infrared minimum in extended emission of Bar.
40		1	-	Infrared minimum in extended emission of Bar. Pos:00h58m57s,-72°16'12".
41			0	On extension to 153, edge of Bar. Pos:01h00m05s,-72°40'00"
42			0	Extension of extended emission in Wing.
43			-	On edge along 153, falls in infrared minimum at edge of Bar.
44			0	7'S of N76, extended emission; In between 156, 160, 163 in NW Bar.
45	200		+	Strong infrared emission peak of N83 of Wing; 1.0'E of 200, 1.8'E of 199, 1.9'NW of 201. Pos:01h12m55s,-73°32'56".

Notes to Table 11:

a) In the SW Bar region at 60 and 100 μm the infrared contours follow Hodge's dark clouds numbers 1, 2, 3, 4, 5, 6, 7, 8, 10, 11, 12, 13, 14, 17. An infrared extension is visible East of the SW Bar corresponding to clouds 29, 30, 32, 33.
All associations (with Table 4) in the SW Bar are suspect due to confusion.
Cloud numbers 21, 37, and 40 have somewhat bad positions, numbers 30, 41 and 45 have completely wrong positions in Hodge's Table 1 compared to Plate I (corrected 1950.0 equatorial coordinates are given).

b) All associations have W-type or C-type infrared spectra. Infrared sources 63, 74, 81, 108, 130 were previously included in Table 7 (HII regions).

c) See Section 5.6 in the text.

sources with stellar–type infrared spectra were found, most of which have possible optical counterparts. One Galactic globular cluster (NGC 362) and two SMC globular clusters (NGC 330 and NGC 419) were also detected. Thirty–five open clusters have possible infrared counterparts. No clear correlation between supernova remnants and infrared emission was found. Infrared emission is seen towards seven, and possibly six more, planetary nebulae (out of 29). However, the majority of these objects is confused with other infrared emitting objects.

Acknowledgements

We wish to thank the following people: The SDAS team that supported the first reduction stage and assisted PS during his stay at the Jet Propulsion Laboratory; E. Kopan, P. Alphenaar, A. Vos and D. Hogeweg for writing the necessary software; Drs. H. Habing, J. Emerson and T. de Jong for scheduling the observations; Drs. H. Habing, W. Rice, R. Walterbos, R. Braun, A. van Genderen and H. Caspers for discussions. PS is grateful for financial support from the Space Research Organisation in the Netherlands (SRON), a subsidiary of the Netherlands Organization for Scientific Research (NWO) during his stay at JPL. We also want to thank the Astronomical Data Center at the NASA Goddard Space Flight Center for providing the SAO Catalog (version 1984) and the library of the Royal Observatory of Edinburgh for a prompt sending of a copy of an Occasional Report.

Appendix A: Additions to the Infrared Source List

A.1. Introduction

This infrared survey at 12, 25, 60 and 100 μm covers the SMC with the exception of the outermost SE and SW parts, containing the HII regions DEM 1 (Davies *et al.*, 1976; N 3 in Henize, 1956), DEM 166 (N 90) and the Hα filaments of DEM 167 (see Section 5.2). The latter object corresponds to the only known supergiant shell in the SMC (Meaburn, 1980). To complement the maps obtained from the Additional Observations, we derived IRAS (Co–added) maps using Survey data to cover the missing regions. Because these maps are produced from a different database than the DPM derived maps described in this chapter, we decided to discuss these maps in an Appendix.

A.2. Observations and data reduction

The maps used in this Appendix are based on Co–added IRAS Survey data, specially produced at Leiden Observatory. We did not use the IRAS 16°.5 Skyflux images (IRAS, 1985a) because of their lower resolution (4′ to 6′). The Co–added Survey data give a resolution that is equal to the resolution of the Additional Observations (see Section 3). Input to the Co–add processor are the Boresight Pointing History File (BPHF) and Calibrated Reconstructed Detector Data (CRDD), calibrated to the May–1984 intermediate standard from the Leiden Observatory IRAS database.

First, we selected all IRAS Survey scans in an area of radius 1° centered on the supergiant shell DEM 167 (α_{1950} = $01^h28.0^m$, δ_{1950} = $-73°35'$), and DEM 1 (α_{1950} = $00^h29.6^m$, δ_{1950} = $-74°04'.3$). This was done by searching the Zodiacal Observation History File (ZOHF; IRAS, 1985a). In total 48 scans are covering the field of DEM 167 and 38 are covering the field of DEM 1; all these scans were used in the Survey Co–adds. The Zodiacal emission varies smoothly (see Skyflux's HCON–1, HCON–2 and HCON–3), and there is little variation in the infrared emission gradient with time at this high ecliptic latitude ($\beta = -65°$), allowing us to add all data from the three HCONs. Most scans have equal scan position angles to within 20°. The average scan position angle (NESW) in the field of DEM 167 is 107° and in the field of DEM 1 119°. In the first field there are 6 scans with very different scan angles (about 158°), while in the latter field only one scan has a clearly different scan position angle (42°). The search radius of 1° was chosen to obtain overlap between the DPM and Co–added maps so as to be able to compare the SMC extended emission and to compare discrete sources in the two independent map sets. The scan length selected from the CRDD is 32 seconds (at a scan rate of 3′.85/sec) enough to cover a 2° field.

The IRAS Survey scans were gridded onto a map of 2° x 2° centered on DEM 167, respectively DEM 1, by using the same software (DSCO, DSGAD) as described in Section 2. The scans were added in the order of increasing distance from the field centre in order to have as much overlap in the scan–maps as possible in all subsequent additions. This overlap is important in identifying a better median offset to adjust individual scan–maps to the same intensity level. Because of the inclusion of HCON–3 scans (SOP > 425; 30 % of all scans) the median noise dropped by a factor of 2 relative to individual scan–maps.

To bring the calibration to the November–1984 calibration of IRAS (IRAS, 1985a; final product), we applied multiplication factors of 0.97, 0.98, 0.93 and 0.74 in the 12, 25, 60 and 100 μm bands (Kopan, priv. comm.). These factors were checked against the behaviour of the eight IRAS calibration stars (see IRAS, 1985a), and NGC 6543 in a set of calibration Co–adds (Caspers, priv. comm.). As the low level infrared contours from the Co–added and the DPM maps connect very well, we did not attempt to further improve on the background correction.

A.3. The maps of infrared radiation

The 12 μm maps show some resulting stripes of $1'$ wide and $12'$ apart caused by the smaller edge detectors (see IRAS, 1985a). Special care was taken in the interpretation of positions affected by this artifact. These effects are not present in the other wavelength maps. Due to an error in the search for IRAS Survey scans, those covering only the outer edges were not accepted resulting in an increased noise at the NE and SW edges ($\sim 10'$) of the field centered on DEM 167, and noisy and not–covered NE and SW edges of the same size in the field centered on DEM 1. Further characteristics of the Co–added maps are given in Table A.1. These maps are presented in Schwering and Israel (1988).

Table A.1. *Description of the SMC Co–added map characteristics.*

Characteristic (Unit)	Wavelength band			
	12 μm	25 μm	60 μm	100 μm
Median noise (MJy/sr) [a]	0.04	0.04	0.03	0.05
(10^{-8} Watt m^{-2} sr^{-1})	0.6	0.2	0.09	0.05
Zero-level uncertainty (MJy/sr)	0.04	0.14	0.23	0.7
(10^{-8} Watt m^{-2} sr^{-1})	0.5	0.7	0.6	0.7
Stripe residuals (MJy/sr) [b]	0.04	0.06	0.07	0.2
(10^{-8} Watt m^{-2} sr^{-1})	0.5	0.3	0.2	0.2
Sensitivity (MJy/sr) [c]	0.3	0.3	0.4	0.6
(10^{-8} Watt m^{-2} sr^{-1})	4	2	1	0.5

Notes to Table A.1:

- *a) The value of the median noise is influenced somewhat by the extended emission of the SMC itself, but not so much as in Table 3.*
- *b) Higher stripe levels than the average level given in the table can occur.*
- *c) The sensitivity indicates the intensity limits of Table A.2.*

Comparing Table A.1 with Table 3 we note that the noise is about two times less at 12 and 25 μm and four times less at 60 and 100 μm compared to the AOs. This can be explained by the higher number of coverages (roughly ten for the Co–adds and about five for each AO set), but mainly by the lower amount of extended emission in the maps (especially at 60 and 100 μm). The zero–level is more uncertain (about five times), because no plane was fitted to the maps, but only an offset was subtracted. The stripe residuals are about the same.

In the 12 and 25 μm maps some Zodiacal foreground emission is present in the form of a background slope in the maps of both fields with higher levels at the NW (about $+10^{-8}$ Watt m^{-2} sr^{-1}) and lower at the SE edges (-10^{-8} Watt m^{-2} sr^{-1}). In the 60 and 100 μm maps variations in the fields are caused by the extended emission of the SMC itself. No variation due to the Galactic foreground cirrus can be seen in these maps.

A.4. Additions to the Infrared Source List in the SMC

We have searched these maps in the same way as the DPM–maps in Section 4. Note that we have only a single map of these two fields in contrast to the three independent DPM–maps. Table A.2 contains the additions to the source list of Table 4.

We checked all sources from the DPM–maps (Table 4) and all sources from the IRAS PSC (IRAS, 1985a) and the IRAS SSS (IRAS 1985b). The IRAS PSC and SSS are based on the same data that were used in preparing the Co–added maps in this Appendix. All IRAS PSC entries in these two fields were confirmed by us, and are included in our source list. For all IRAS SSS sources infrared counterparts were found on the maps. In total we found thirty additional infrared sources in these fields of which fifteen are related to the IRAS PSC and SSS catalogs. Thus fifteen new infrared sources were found.

Table A.2. Additions to the SMC Infrared Source List.

(1)	(2)		(3)		(4)		(5)		(6)		(7)	(8)	(9)	(10)	(11)	(12)	(13)	(14)
Number	Position RA(1950) h m s	DEC(1950) o ' "	12 µm Peak	Bg	25 µm Peak	Bg	60 µm Peak	Bg	100 µm Peak	Bg	Size arcmin	F 12µm Jy	F 25µm Jy	F 60µm Jy	F 100µm Jy	IRAS-Id	Spectrum	Comments
					10^{-8} Watt $m^{-2}sr^{-1}$													
220	00 14 58	-74 14	5	-	2	-	-	-	-	-	-	0.19:	0.22:	-	-		S:	SAO 255653
221	00 15 35.0	-73 56 10	5	-	-	-	-	-	-	-	p	0.19	-	-	-	00155-7356	S	
222	00 16 02.3	-73 25 51	-	-	2	-	3	-	0.5	-	p:	-	0.22	1.2	1.0	00160-7325	W	
223	00 16 21	-73 28	6	-	-	-	-	-	-	-	p	0.22	-	-	-		S	
224	00 16 21	-74 03	-	-	3	-	-	-	-	-	p:	-	0.33	-	-		W	
225	00 16 35.2	-74 18 54	14	-	3	-	-	-	-	-	p	0.52	0.33	-	-	00165-7418	S	
226	00 18 05.8	-73 37 30	-	-	-	-	1.5	-	-	-	p:	-	-	0.6	-	00180-7337	W	
227	00 18 49.3	-74 52 38	5	-	-	-	1.5	-	-	-	-	0.19:	-	0.6:	-	00188-7452	W:	
228	00 19 56.4	-74 26 10	-	-	4	-	12	-	3	-	p:	-	0.44	4.9	6.2	00199-7426	C	
229	00 21 53.8	-73 54 00	-	-	2	-	-	-	-	-	-	-	0.22	-	-	00218-7353	W	N 1, Sk 1
230	00 22 07	-74 34	-	-	-	-	-	-	0.5	-	-	-	-	-	1.0		C	
231	00 22 31	-74 21	-	-	-	-	-	-	0.5	-	-	-	-	-	1.0		C	
232	00 25 03	-74 35	-	-	-	-	-	-	0.7	-	-	-	-	-	1.5		C	
233	00 26 03.0	-73 15 18	6	-	20	-	16	-	1.5	-	p	0.22	2.20	6.6	3.1	00260-7315	W	
234	00 26 28.0	-74 37 47	-	-	-	-	1.5	-	0.5	-	p:	-	-	0.6	1.0	00264-7437	C	
235	00 26 37	-73 56	-	-	2	-	-	-	-	-	p	-	0.22	-	-		W	
236	00 27 20	-74 12	-	-	-	-	1.5	-	1	-	-	-	-	0.6	2.1		C	
237	00 27 40	-74 20	-	-	-	-	1	-	0.5	-	-	-	-	0.4	1.0		C	
238	00 28 05	-74 29	5	-	-	-	-	-	-	-	p	0.19	-	-	-		S	
239	00 29 37.0	-74 04 17	-	-	2	-	4	-	1.5	-	p	-	0.22	1.6	3.1	00296-7404	C	DEM 1, N 3
240	01 26 16	-73 31	5	-	-	-	2	-	1	-	p:	0.19	-	0.8	2.1		C	DEM 167
241	01 27 47	-73 30	-	-	-	-	1	-	1	-	-	-	-	0.4	2.1		C	DEM 167
242	01 28 23.1	-73 49 17	-	-	6	-	22	-	12	-	2xp	-	1.05	11.1	27.2	01283-7349 X0128-738	C	DEM 166
243	01 28 43	-74 10	-	-	-	-	-	-	0.5	-	-	-	-	-	1.0		C	
244	01 29 07.7	-73 25 38	6	-	2	-	-	-	-	-	p:	0.22	0.22	-	-	01291-7325	S:	SAO 255786
245	01 29 08	-73 28	-	-	-	-	-	-	0.5	-	-	-	-	-	1.0		C	DEM 167
246	01 31 19.7	-73 42 30	-	-	-	-	1	-	1.5	-	p:	-	-	0.4	3.1	01313-7342	C	DEM 167
247	01 33 06.0	-73 21 00	5	-	-	-	-	-	-	-	p:	0.19	-	-	C	01331-7321	S	
248	01 41 26	-73 33	-	-	-	-	-	-	0.5	-	-	-	-	-	1.0		C	
249	01 41 38.5	-73 43 12	-	-	-	-	-	-	0.5	-	p:	-	-	-	1.0	01416-7343	C	

A.5. Identification of Sources

In this Appendix we are primarily concerned with the identification of all sources that were not already present in the DPM–maps (*i.e.* the area with $\alpha > 01^h25^m$ or with $\alpha < 00^h31^m$). For the identification of known objects we searched deeper than the infrared source list of Table A.2. None of the known supernova remnants (Mathewson *et al.*, 1983) nor any of the known dark clouds (Hodge, 1974) in the SMC are present in these areas.

A.5.1. Stars in the fields

A.5.1.1. Comparison with SAO stars

In Table A.3 we list the seven stars from the SAO Catalog (1966) that are present in these areas in the Co–added fields and their colour–corrected 12 and 25 μm flux densities. None of these stars showed emission at 60 or 100 μm.

Table A.3. SAO (1966) stars in the additional SMC fields.

(1) SAO number	(2) m_V mag	(3) Sp type	(4) $F^a_{12\mu m}$ Jy	(5) $F^a_{25\mu m}$ Jy	(6) $F_{25\mu m}/F_{12\mu m}$	(7) $m_V - m_{12}$ mag	(8) Infrared Id	(9) Detection[b] quality	(10) Remarks[c]
255653	8.0	G5	0.13:	0.16:	1.2 ±1.0	2.2	220	0	On edge of Co-added map.
255665	8.8	G5	0.08	0.08:	1.0 ±1.0	2.4		0	
255675	9.2	A	-	-	-	-		-	
255786	8.3	K0	0.16	0.16	1.0 ±1.0	2.7	244	+	
255793	9.0	G5	-	-	-	-		-	
255805	9.3	--							Not covered by Co-added map.
255807	9.2	--							Not covered by Co-added map.

Notes to Table A.3:

a) The 12 and 25 μm flux densities in this table are colour-corrected (see Table 5).
b) Detection qualities at 12 μm are good (+), medium (0) or poor (-).
c) See Section A.5.1.1 in Appendix A.

A.5.1.2. Comparison with Radcliffe SMC–stars

Radcliffe stars (Feast *et al.*, 1960) R 47, 48, 49, which are positioned in the field of DEM 167, show no evidence for infrared radiation coming from these SMC stars. The other field does not contain Radcliffe stars that were not already discussed in Section 5.1.2.

A.5.2. Hα nebulosities in the SMC

The main reason for Co–adding the IRAS Survey data was the failure of the IRAS DPM maps to cover the outermost edges of the SMC, especially HII regions DEM 1 (Davies *et al.*, 1976; N 3 in Henize, 1956), DEM 166 (N 90) and 167. The ring of diffuse filaments DEM 167 forms the only SMC supergiant shell, discovered by Meaburn (1980). The bright HII regions DEM 1 (infrared LI–SMC 239) and DEM 166 (LI–SMC 242) are both detected in the infrared. N 1 of Henize corresponds to infrared source number 229. One field is centered on the supergiant Hα shell DEM 167, with a diameter of 32$'$. In the infrared shell–like filaments are visible at 25, 60 and especially at 100 μm with its centre at $1^h28.4^m, -73°38'$ and a diameter of 24$'$. The infrared emission follows the Hα quite well except in the North, where the infrared is about 8$'$ South of the Hα filaments. Infrared sources LI–SMC 240, 241, 245 and 246 are related to this supergiant shell.

A.5.3. Clusters in the SMC

The area of interest to this Appendix in the DEM 167 field, contains no clusters from the list of Kron (1956), four (L 105, 107, 109, 110) from the list of Lindsay (1958), one (WG 1) from Westerlund and Glaspey (1971) and one (HW 86) from Hodge and Wright (1974). Only cluster L 105 shows possible infrared radiation; it coincides with LI–SMC 242 in the infrared source list (see Table A.2). Confusion with the Hα nebulosity DEM 166 makes this identification uncertain; the infrared source is probably related to the HII region and not to the cluster. L 107 in positioned in extended emission of DEM 167.

The area of interest in the DEM 1 field, contains seven Kron clusters (K 1, 4, 5, 6, 8, 9, 10), eight Lindsay clusters (L 3, 4, 6, 7, 9, 12, 13, 15; the last seven are the same as the Kron clusters listed here) and three (HW 2, 3, 4) Hodge and Wright clusters. Of these only K 6 (= L 9) possibly shows weak infrared emission at 12 μm only (0.15 Jy).

A.5.4. Planetary nebulae in the SMC

The field of DEM 167 contains no planetary nebulae of the list of Sanduleak *et al.* (1978) and Sanduleak and Pesch (1981), that were not already discussed in Section 5.5. In the field of DEM 1 there are two planetary nebulae (Sk 1 and 29) which are in the area of interest. Sk 1 corresponds in position to our source with LI–SMC 229 (in Table A.2) and to the Hα object N 1. This source peaks at 25 μm with 0.2 Jy, and there is some possible weak 12 μm emission ($\sim$ 0.15 Jy). Sk 29 was not detected on the maps.

A.6. Conclusions

In this Appendix we discuss sources on the infrared maps at 12, 25, 60 and 100 μm of the outermost SE and SW corners of the Small Magellanic Cloud. We found 30 infrared sources, which brings the total of infrared sources in and around the SMC to 249. In the areas that were searched all IRAS Point Sources (PSC) were detected and all IRAS Small Scale Structure (SSS) entries have related infrared sources. Fifteen sources are new detections. We identified the infrared sources where possible. Three foreground SAO stars were detected in these fields; no Radcliffe SMC–stars yielded a detection. Hα nebulosities DEM 1, 166 and 167 (a supergiant shell) were all detected in the infrared. The cluster K 6 (L 9), and the planetary nebula Sk 1 (N 1) are possible detections.

References

Aaronson, M., Mould, J.: 1982, *Astrophys. J. Suppl.* **48**, 161

van Albada, G.D., Baud, B., de Pagter, P.J., Pol, W., Renes, J.J, Wesselius, P.R.: 1985, ROG Internal Report

Allen, D.A., Glass, I.S.: 1976, *Astrophys. J.* **210**, 666

Azzopardi, M., Vigneau, J.: 1982, *Astron. Astrophys.* **50**, 291

van den Bergh, S.: 1981, *Astron. Astrophys. Suppl.* **46**, 79

Blanco, V.M., McCarthy, M.F., Blanco, B.M.: 1980, *Astrophys. J.* **242**, 938

Burton, W.B., Deul, E.R., Walker, H.J., Jongeneelen, A.A.W.: 1986, in *"Light on Dark Matter"*, ed. F.P. Israel, Reidel Dordrecht, 357

Brück, M.T.: 1976, *Occ. Rep. R. Obs. Edinburgh* **1**

Catchpole, R.M., Feast, M.W.: 1981, *Mon. Not. R. Astron. Soc.* **197**, 385

Cohen, J.G., Frogel, J.A., Persson, S.E., Elias, J.H.: 1981, *Astrophys. J.* **249**, 481

Davies, R.D., Elliott, K.H., Meaburn, J.: 1976, *Mem. R. Astron. Soc.* **81**, 89

Epchtein, N., Braz, M.A., Sèvre, F.: 1984, *Astron. Astrophys.* **148**, 263

Feast, M.W., Thackeray, A.D., Wesselink, A.J.: 1960, *Mon. Not. R. Aston. Soc.* **121**, 337

Feast, M.W., Catchpole, R.M., Carter, B.S., Roberts, G.: 1980, *Mon. Not. R. Astron. Soc.* **193**, 377

Feast, M.W., Whitelock, P.A.: 1984, *Observatory* **104**, 193

Frogel, J.A., Cohen, J.C.: 1982, *Astrophys. J.* **253**, 580

Gathier, R: 1984, Ph.D. Thesis, University of Groningen

Gatley, I., Becklin, E.E., Hyland, A.R., Jones, J.J.: 1981, *Mon. Not. R. Astron. Soc.* **197**, 17P

Gatley, I., Hyland, A.R., Jones, J.J.: 1982, *Mon. Not. R. Astron. Soc.* **200**, 521

Glass, I.S.: 1974, *Mon. Not. R. Astron. Soc.* **168**, 249

Glass, I.S.: 1979, *Mon. Not. R. Astron. Soc.* **186**, 317

Glass, I.S.: 1984, *Mon. Not. R. Astron. Soc.* **209**, 759

Grasdalen, G.L., Joyce, R.R.: 1976, *Astron. Astrophys.* **50**, 297

Henize K.G.: 1956, *Astrophys. J. Suppl.* **2**, 315

Hodge, P.W., Wright, F.W.: 1974, *Astron. J.* **79**, 858

Hodge, P.W.: 1972, *Publ. Astron. Soc. Pac.* **84**, 365

Hodge, P.W.: 1974, *Publ. Astron. Soc. Pac.* **86**, 263

Hodge, P.W.: 1986, *Publ. Astron. Soc. Pac.* **98**, 1113

Humphreys R.M.: 1984, in *"Structure and Evolution od the Magellanic Clouds"*, IAU Symp. 108, eds. S. van den Bergh, K.S. de Boer, Reidel Dordrecht, 145

IRAS: 1985a, IRAS Catalogs and Atlases Explanatory Supplement, eds. C.A. Beichmann, G. Neugebauer, H.J. Habing, P.E. Clegg, T.J. Chester, JPL D–1855

IRAS: 1985b, IRAS Small Scale Structure Catalog, eds. G. Helou, D.W. Walker, JPL D–2988

IRAS: 1986, A guide to IRAS pointed observation products, eds. E.T. Young, G. Neugebauer, E.L. Kopan, R.D. Benson, T.P. Conrow, W.L. Rice, D.T. Gregorich, G.K. Miley, IPAC preprint PRE–008N

Israel F.P.: 1984, in *"Structure and Evolution of the Magellanic Clouds"*, IAU Symp. 108, eds. S. van den Bergh, K.S. de Boer, Reidel Dordrecht, 319

Israel, F.P., Koornneef, J.: 1988, *Astron. Astrophys.* **190**, 21

Israel, F.P., Koornneef, J., Schwering, P.B.W.: 1988, in preparation

Israel, F.P., Schwering, P.B.W.: 1986, in *"Light on Dark Matter"*, ed. F.P. Israel, Reidel Dordrecht, 383

Jones, T.J, Hyland, A.R., Straw, S., Harvey, P.M., Wilking, B.A., Joy, M., Gatley, I., Thomas, J.A.: 1986, *Mon. Not. R. Astron. Soc.* **219**, 603

Koornneef, J., Israel, F.P.: 1985, *Astrophys. J.* **291**, 156

Kopan, E.L.: 1982, IRAS/SDAS Subsystem Design Specification 623–75: Deep Sky Survey Subsystem Rev. A, Jet Propulsion Laboratory, California Institute of Technology, Pasadena California

Kopan, E.L.: 1984, Interoffice memorandum 84–SDAS–241, Jet Propulsion Laboratory, Pasadena California

Kron, G.E.: 1956, *Publ. Astron. Soc. Pac.* **68**, 125

Leene, A., Pottasch, S.R.: 1986, in *"Light on Dark Matter"*, ed. F.P. Israel, Reidel Dordrecht, 143

Lindsay, E.M.: 1958, *Mon. Not. R. Astron. Soc.* **118**, 172

Lindsay, E.M.: 1961, *Astron. J.* **66**, 169

Mathewson, D.S., Ford, V.L., Dopita, M.A., Tuohy, I.R., Long, K.S., Helfand, D.J.: 1983, *Astrophys. J. Suppl.* **51**, 345

Meaburn. J.: 1980, *Mon. Not. R. Astron. Soc.* **192**, 365

Mould, J., Aaronson, M.: 1980, *Astrophys. J.* **240**, 464

Mould, J., Aaronson, M.: 1982, *Astrophys. J.* **263**, 629

Paczynski, B.: 1971, *Acta Astronomica* **21**, 417

Payne–Gaposchkin, C.H., Gaposchkin, S.: 1966, *Smithsonian Contr. Astrophys.* **9**

Persson, S.E., Aaronson, M., Cohen, J.G., Frogel, J.A.: 1983, *Astrophys. J.* **266**, 105

Pottasch, S.R.: 1986, in *"Light on Dark Matter"*, ed. F.P. Israel, Reidel Dordrecht, 131

Price, S.D., Walker, R.G.: 1976, *"The AFGL Four Color Infrared Sky Survey: Catalog of Observations at 4.2, 11.0, 19.8 and 27.4 μm"*, AFGL–TR–76–0208, Hanscom Air Force Base, Massachusetts: Air Force Geophysics Laboratory

Russel, S.E., Hyland, A.R.:1985, *Proc. Astron. Soc. Aust.* **6**, 52

Sanduleak, S.N., MacDonnell, D.J., Davis Philip, A.G.: 1978, *Publ. Astron. Soc. Pac.* **90**, 621

Sanduleak, N., Pesch, P.: 1981, *Publ. Astron. Soc. Pac.* **93**, 431

Schwering, P.B.W.: 1985, in *"New Aspects of Galaxy Photometry"*, Lecture notes in Physics **32**, ed. J.L. Nieto, Springer Verlag Berlin, 115

Schwering, P.B.W., Israel, F.P.: 1988, *"Atlas and Catalogue of IRAS far–infrared observations of the Magellanic Clouds"*, in preparation

Smithsonian Astrophysical Observatory Star Catalog (4 vols.): 1966, Washington D.C., Smithsonian Institution (version 1984)

Waters, L.B.F.M., Cote, J., Aumann, H.H.: 1987, *Astron. Astrophys.* **172**, 225

Welch, D.L., Madore, B.F.: 1984, in *"Structure and Evolution of the Magellanic Clouds"*, IAU Symp. 108, eds. S van den Bergh, K.S. de Boer, Reidel, Dordrecht, 221

Westerlund, B.E., Glaspey, J.: 1971, *Astron. Astrophys.* **10**, 1

Werner, M.W., Becklin, E.E., Gatley, I., Ellis, M.J., Hyland, A.R., Robinson, G., Thomas, J.A.: 1978, *Mon. Not. R. Astron. Soc.* **184**, 365.

Chapter III

INFRARED OBSERVATIONS OF THE LARGE MAGELLANIC CLOUD

Summary

Results of IRAS pointed observations in four infrared wavelength bands (12, 25, 60 and 100 μm) on the Large Magellanic Cloud are presented. Maps are shown with orthogonal scan directions and a source list containing 1823 infrared sources is extracted from the data. Comparison with the IRAS Point Source Catalog (PSC) shows that twenty-eight entries in this catalogue are spurious. We confirm all 49 entries in the IRAS Small Scale Structure Catalog (SSS) in the LMC. We found 802 new infrared sources, not included in either the PSC or in the SSS. Our LMC infrared source list and the infrared maps are compared to other object lists. We identified 57 SAO stars, three LMC globular clusters and detected infrared emission from the direction of thirteen planetary nebulae. We detected infrared emission from four Radcliffe LMC-stars and five out of ten small size supernova remnants. In general there is a good correlation of infrared emission with the distribution of HII regions and dark clouds. A list of sources and comparison results from infrared maps of seven additional fields at the Northern and Western edges of the LMC are presented in an Appendix.

1. Introduction

The Magellanic Clouds are the closest galaxies in the Local Group (Humphreys, 1984). They are our first extragalactic beacon and hence are important for a variety of studies related to galactic structure and to global properties of much more distant galaxies. For this reason it is important to relate their detailed characteristics to their global properties.

A summary of infrared surveys on the Magellanic Clouds has been given by Schwering and Israel (1988a; Chapter II). These surveys are supplemented by data obtained from the IRAS satellite; however, the published official IRAS data (IRAS, 1985a) have two weaknesses: in confused areas such as the Magellanic Clouds the point source data are not completely reliable, and the 16°.5 extended emission infrared maps have a resolution of only 4′ − 6′.

In Chapter II we presented infrared maps and an infrared source list for the Small Magellanic Cloud (SMC). In this chapter we continue with the Large Magellanic Cloud (LMC). *Thus we present maps at the full IRAS resolution (ranging from 1′.1 at 12 μm to* 4′.3 at 100 μm) as well as a list of all sources identifiable in these maps. Some results of preliminary analysis were given by Schwering (1985, 1987).

2. Observations and data reduction

The observations presented in this chapter were obtained with the IRAS satellite as part of the AO program carried out with the IRAS survey array. A full description of the instrument array, the survey and data processing can be found in the IRAS Explanatory Supplement (IRAS, 1985a). A description of the AO program and a list of all rasterscan AOs observed by the IRAS satellite of many different objects are given in *"A User's Guide to IRAS Pointed Observation Products"* (IRAS, 1986).

There is a variety of pointed observations on the LMC (see Israel and Schwering, 1986), but Deep Sky Mapping (DPM) observations are the only ones covering the entire LMC in a regular manner and are therefore suited for a study of the whole LMC. The maps presented here are thus based on the DPM observations alone (see also Chapter II). The DPM observations were made in the months of June/July and September/October 1983, and are summarized in Table 1. For a description of the DPM observing mode see Chapter II.

As in the case of the LMC, two separate sets of DPM observations were made with almost orthogonal scanning directions: approximately EW and NS. This was possible because the LMC is close to the South Ecliptic Pole ($\beta_{LMC} = -86^{\circ}$), so that observations obtained three months apart yielded the required orthogonal scanning directions. Due to the rectangular form of the IRAS survey detectors (largest size in the cross–scan direction) the resolution is highest in the scan direction (time–resolution), so that these two sets of data supply us with maximum resolution in both directions. In June and July the LMC was scanned EW (average position angle of the scan direction 90°; observations set 1 EW in Table 1) in a double coverage. In September and October (three months later) the LMC was scanned NS (185°; set 2 NS) with double coverage. Because of the large size of the LMC compared to the area covered by a single DPM observation every LMC–coverage consists of sixteen differently pointed observations. Another observation was made in June/July and three more in September/October which were processed and later deleted for reasons of uniformity.

The reduction of the AOs was done in two stages and is explained in Chapter II. We obtained 68 individual DPM grids on the LMC (see Table 1). To get identical coverage of each area of the LMC, four grids were left out. The remaining 64 grids then were used to obtain two combined map sets (in four wavelength bands) of the whole LMC (each map covers an area of $8^{\circ}.5 \times 8^{\circ}.5$ with a grid spacing of $0'.50 \times 2'.0$; the two map sets that have their scan direction in constant Right Ascension are denoted by NS and the map set with scan direction in constant Declination by EW; Table 1 also shows which grid numbers were combined into each map set).

As the LMC is positioned near the South Ecliptic Pole there is little variation in the Zodiacal light emission over the maps. The galactic latitude of the LMC is -33°. At the 60 and 100 μm wavelengths the Galactic foreground cirrus creates more of a problem than the Zodiacal foreground, because it has a lower colour temperature. In Chapter II we have shown a 100 μm map of the Magellanic Clouds and their surroundings (Fig. 1 therein). From that figure it is clear that, even at this relatively high galactic latitude, the Galactic infrared foreground in the direction of the LMC is complex. As was discussed by Israel and Schwering (1986) and by McGee *et al.* (1986) prominent infrared filaments are associated with Galactic neutral hydrogen, leading to complications in the foreground removal. The large scale, relatively smooth foreground was removed by fitting a plane to map areas considered to be free of LMC emission. Our zero–level correction removes most of the foreground emission but assumes a planar shape, which is only a first order approximation to the actual foreground. Hence, some small–scale structure not belonging to the LMC and discrete non–LMC sources will be left. In Section 3 we decribe the uncertainties that are left in the map. The final calibration is explained further in Chapter II.

Table 1. IRAS DPM Observations of the LMC.

(1)	(2)	(3)	(4)		(5)	(6)
PAC[a] rid umber	SOP-OBS[a]	Observation Id	Grid centre position[b] RA(1950) h m s	DEC(1950) ° ' "	Pos.Ang[c] (NESW) Deg	Map/Obs[d] set
0657	462-024	CG2018-01[e]	04:56:38	-71:21:25	185.2	2 NS
0533	460-009	CG2018-00	04:56:44	-71:19:20	184.0	2 NS
4223	271-026	CG1454-00	04:57:06	-71:00:25	93.1	1 EW
4397	279-004	CG1454-01	04:57:12	-71:01:01	96.6	1 EW
0678	463-009	CG2034-00	04:58:26	-69:49:07	184.9	2 NS
0763	465-004	CG2034-01	04:58:28	-69:49:20	185.8	2 NS
4218	271-020	CG1450-00	04:58:54	-69:28:50	92.7	1 EW
4392	278-030	CG1450-01	04:58:59	-69:28:57	96.1	1 EW
1509	486-032	CG2030-01	05:00:33	-68:19:04	195.9	2 NS
1822	493-006	CG2080-00	05:00:35	-68:15:29	198.9	----
1343	481-003	CG2030-00	05:00:41	-68:19:01	193.0	2 NS
2191	501-056	CG2077-01	05:01:05	-66:50:39	203.1	2 NS
2153	501-007	CG2077-00	05:01:28	-66:45:20	202.5	2 NS
4104	266-035	CG1446-00	05:01:29	-67:58:12	89.9	1 EW
4403	279-011	CG1446-01	05:01:34	-67:58:18	95.7	1 EW
4410	279-018	CG1442-00	05:02:19	-66:30:04	95.6	1 EW
4445	281-003	CG1442-01	05:02:20	-66:30:17	96.4	1 EW
0753	464-025	CG2019-01	05:14:12	-71:15:07	182.0	2 NS
0665	462-031	CG2019-00	05:14:13	-71:13:00	181.0	2 NS
0758	464-036	CG2035-01	05:14:29	-69:57:22	181.9	2 NS
0672	463-003	CG2035-00	05:14:32	-69:55:17	181.0	2 NS
4498	282-042	CG1455-00	05:14:33	-71:04:27	94.5	1 EW
4875	291-004	CG1599-00	05:14:39	-71:04:45	98.4	1 EW
4413	279-022	CG1451-00	05:14:55	-69:36:35	92.7	1 EW
4455	281-023	CG1451-01	05:14:56	-69:36:36	93.7	1 EW
1391	483-009	CG2031-01	05:15:20	-68:27:21	190.5	2 NS
1341	480-037	CG2031-00	05:15:22	-68:27:21	189.5	2 NS
2124	499-049	CG2079-00	05:15:38	-68:16:39	198.8	----
4300	275-019	CG1447-00	05:16:03	-68:06:31	90.5	1 EW
4509	283-005	CG1447-01	05:16:07	-68:06:34	94.2	1 EW
1055	471-055	CG2027-01	05:17:01	-66:57:53	184.7	2 NS
0720	463-049	CG2027-00	05:17:09	-66:55:43	180.7	2 NS
4450	281-010	CG1443-00	05:17:23	-66:37:37	93.0	1 EW
4480	282-027	CG1443-01	05:17:25	-66:37:37	93.7	1 EW
1858	493-048	CG2075-00	05:31:30	-70:05:48	192.1	----
1897	494-014	CG2078-00	05:31:47	-66:59:42	192.2	2 NS
1908	494-025	CG2078-01	05:31:47	-66:59:50	192.2	2 NS
1499	486-011	CG2016-01	05:31:54	-70:00:13	188.3	2 NS
1449	484-032	CG2032-00	05:31:55	-68:26:10	187.6	2 NS
1381	482-031	CG2032-01	05:31:59	-68:26:08	186.6	2 NS

Table 1, continued (2).

(1)	(2)	(3)	(4)		(5)	(6)
IPAC grid number	SOP-OBS	Observation Id	Grid centre position RA(1950) h m s	DEC(1950) ° ' "	Pos.Ang (NESW) Deg	Map/Obs set
04569	283-062	CG1448-00	05:32:10	-68:08:43	91.0	1 EW
11285	479-003	CG2016-00	05:32:12	-69:54:12	184.7	2 NS
04487	282-034	CG1444-01	05:32:32	-66:38:54	90.3	1 EW
04452	281-016	CG1444-00	05:32:34	-66:39:10	89.6	1 EW
05073	303-002	CG1615-00	05:32:37	-68:09:37	99.9	1 EW
04553	283-047	CG1452-00	05:32:40	-69:37:14	90.7	1 EW
05579	317-044	CG1674-00	05:32:41	-68:10:49	107.0	----
04879	291-011	CG1598-00	05:32:44	-69:37:34	94.3	1 EW
04880	291-017	CG1600-00	05:33:18	-71:10:38	94.2	1 EW
10649	462-011	CG2020-01	05:33:29	-71:28:29	176.3	2 NS
04560	283-054	CG1456-00	05:33:31	-71:10:12	90.6	1 EW
10487	459-040	CG2020-00	05:33:34	-71:28:23	175.0	2 NS
11426	483-054	CG2029-01	05:47:22	-66:56:27	183.5	2 NS
04112	267-012	CG1445-00	05:47:32	-66:34:28	79.5	1 EW
04255	273-017	CG1445-01	05:47:33	-66:34:58	82.3	1 EW
11130	473-053	CG2029-00	05:47:40	-66:51:48	178.6	2 NS
04117	267-018	CG1449-00	05:48:16	-68:03:39	79.4	1 EW
04265	273-030	CG1449-01	05:48:17	-68:03:45	82.3	1 EW
12087	499-007	CG2076-00	05:48:23	-69:55:51	190.7	2 NS
12117	499-042	CG2076-01	05:48:25	-69:53:53	191.1	2 NS
10837	466-036	CG2033-01	05:48:32	-68:28:41	174.9	2 NS
10770	465-010	CG2033-00	05:48:36	-68:30:21	174.1	2 NS
04109	267-006	CG1453-00	05:48:54	-69:33:55	79.1	1 EW
04260	273-024	CG1453-01	05:48:57	-69:34:16	82.1	1 EW
04126	267-029	CG1457-00	05:50:36	-71:04:08	78.9	1 EW
04267	273-037	CG1457-01	05:50:36	-71:03:58	81.8	1 EW
10757	464-032	CG2021-00	05:50:40	-71:13:19	173.4	2 NS
10813	466-010	CG2021-01	05:51:06	-71:30:37	174.1	2 NS

Notes to Table 1:

a) For a description of names and abbreviations (Grid, SOP, OBS) we refer to IRAS (1985a) and IRAS (1986).

b) The field size of each observation is 3 degrees in the scan direction and 2 degrees in the cross-scan direction.

c) The scan direction is given by its position angle Pos.Ang (degrees NESW).

d) Map/Obs set 1 is scanned in the East-West direction, while Map/Obs set 2 is scanned North-South. The number of the set is identical to the number of the combined map in the text (see Sections 2 and 3).
A dash in this column indicates that the grid was not used in the processing for reasons of uniformity.
In Figures 1 and 2 we display both Obs/Map sets.

e) Observation Id CG stands for Close Galaxies.

3. The maps of infrared radiation

Fig. 1 and 2 show the IRAS DPM maps of the whole LMC field. In these figures we indicate the boundaries of the coverages of the IRAS DPM observations. These figures show detailed contour/grey scale representations of both DPM–maps at full IRAS resolution. We show both the NS and EW sets because the resolution in the scan direction is higher than the cross–scan resolution; thus, the two (NS and EW) sets are complementary in terms of resolution. There is less diffuse emission present in the 12 and 25 μm maps than in the other wavelength bands; this is similar to the situation in the SMC. In these maps the contrast between small, discrete sources and the diffuse more extended emission is much higher than at 60 or 100 μm. All maps shown in this chapter are given in in–band intensities (see also Chapter II).

Table 2. *Description of the LMC DPM–map characteristics.*

Characteristic (Unit)	Wavelength band			
	12 μm	25 μm	60 μm	100 μm
Effective frequency (10^{12} Hz)	25	12	5	3
Bandwidth (μm)	7.0	11.2	32.5	31.5
Bandwidth correction (10^{12} Hz) [a]	13.48	5.16	2.58	1.00
Zero–magnitude flux density				
f_ν (0 mag) (Jy)	28.3	6.73	1.19	0.43
Point Source Conversion factor				
(Jy / 10^{-8} Watt m^{-2} sr^{-1})	0.037	0.11	0.41	2.08
Positional accuracy (″)	15	15	15	15
Nominal detector size(′x′)	0.75 x 4.5	0.75 x 4.7	1.5 x 4.8	3.0 x 5.0
Resolution (′x′) [b]	1.1 x 6.9	1.1 x 6.9	2.1 x 6.9	4.3 x 6.9
Absolute calibration (%)	10	10	10	10
Median noise (MJy/sr) [c]	0.096	0.097	0.16	0.6
(10^{-8} Watt m^{-2} sr^{-1})	1.3	0.5	0.4	0.6
Zero–level uncertainty (MJy/sr)	0.015	0.097	0.39	1.0
(10^{-8} Watt m^{-2} sr^{-1})	0.2	0.5	1.0	1.0
Stripe residuals (MJy/sr) [d]	0.15	0.3	0.8	2.0
(10^{-8} Watt m^{-2} sr^{-1})	2.0	1.5	2.0	2.0
Sensitivity (MJy/sr) [e]	0.3	0.3	0.4	0.6
(10^{-8} Watt m^{-2} sr^{-1})	4	2	1	0.5

Notes to Table 2:

- *a)* *Chester (priv. comm.); assuming $f_\nu \propto \nu^{-1}$.*
- *b)* *The Gaussian resolution is given in arc–minutes (in–scan x cross–scan). One arcminute at the distance of the LMC (53 kpc) corresponds to 15 pc.*
- *c)* *The value of the median noise is influenced by the extended emission of the LMC itself, especially at 60 and 100 μm. The real detector noise is somewhat lower.*
- *d)* *Higher stripe levels than the average level given in the table can occur.*
- *e)* *The sensitivity indicates the intensity limits of Table 3. Note that the IRAS PSC sensitivity limits are 0.25, 0.25, 0.40, 1.00 Jy (see IRAS, 1985a).*

The estimated uncertainties in the DPM maps are given in Table 2. There are only minor differences in quality of the two different sets of maps. The median noise (in MJy/sr) in the maps increases in the 60 and 100 μm wavelength bands due to the increased extended emission of the LMC itself. The zero–level is also less well defined in those bands due to the complicated foreground emission. The sensitivity is based on reliable point sources that could be extracted from the maps and is roughly identical to the IRAS PSC sensitivity limit. The area of map set 1 (EW scanning), between the Greater 30 Doradus Region and the Bar, are influenced by a bad scan area (at the SE end of the Bar). This area has a relatively high degree of damage at 12 and 25 μm and has enhanced noise at 60 and 100 μm. Map set 1 also contains some radiation hits.

There are some differences in the data quality of these maps with the quality of the SMC map data. The higher median noise at 60 and especially at 100 μm in these maps is caused by the extended emission of the LMC. The zero–level is less accurate by a factor of ten at 60 and 100 μm due to the (uncertain) Galactic foreground; also at 25 μm there is a larger uncertainty. The stripe–uncertainty level is roughly five times higher than in the SMC. The infrared extended emission of the LMC, which fills a large fraction of the maps, makes the determination of these map uncertainties less reliable than for the maps of the SMC.

Maps in sixteen fields on the LMC are given by Schwering and Israel (1988b) and are available in digital form at the Centre Données Stellaires (Astonomical Data Centre CDS) in Strasbourg, France. Maps that represent the infrared emission from the Northern and Western–edges of the LMC have been analysed in Appendix A.

Figure 1. *Overall infrared maps of the Large Magellanic Cloud of map set 1 (EW) are given in equatorial coordinates for 1950. The maps are given in in–band intensities. All maps have sizes of* 8°0 x 8°0. *The coverage of the field by the DPM EW–scanned maps is indicated by solid lines. Although not shown, the coverage differs somewhat in the four wavelength bands due to the location of detectors in IRAS's focal plane. See pages 56 – 57.*
In the 12 μm map grey scales range from 9 to 33, with darker grey scales for higher intensities. Contours are at 5, 10, 20, 40, 100, 200, 500, 1000, 2000 x 10^{-8} Watt m^{-2} sr^{-1}. The overlap of neighbouring fields is roughly $7'$.
In the 25 μm map grey scales ranging from 9 to 33, with darker grey scales for higher intensities. Contours are at 2, 6, 10, 20, 40, 100, 200, 500, 1000, 2000 x 10^{-8} Watt m^{-2} sr^{-1}.
In the 60 μm map grey scales ranging from 9 to 58, with darker grey scales for higher intensities. Contours are at 2, 6, 10, 20, 40, 100, 200, 500, 1000, 2000, 3000, 4000, 5000, 6000 x 10^{-8} Watt m^{-2} sr^{-1}.
In the 100 μm map grey scales ranging from 9 to 58, with darker gre scales for higher intensities. Contours are at 2, 6, 10, 20, 40, 100, 200, 500, 1000, 2000 x 10^{-8} Watt m^{-2} sr^{-1}.

Figure 2. *Overall infrared maps of the Large Magellanic Cloud of map set 2 (NS). The maps are in an identical representation as Fig. 1. See page 58 – 59.*

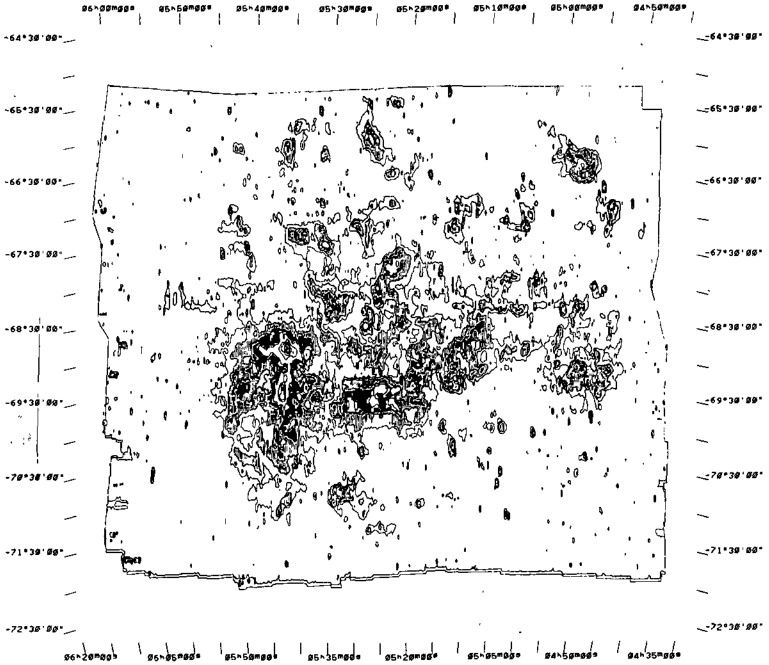

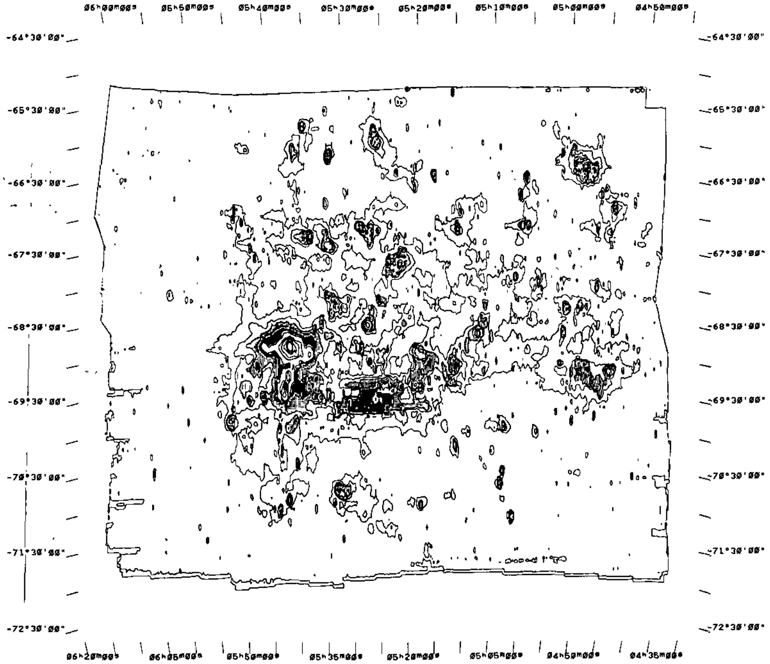

Fig. 1.1. LMC 12 μm DPM–map (set 1; EW).
Fig. 1.2. LMC 25 μm DPM–map (set 1; EW).

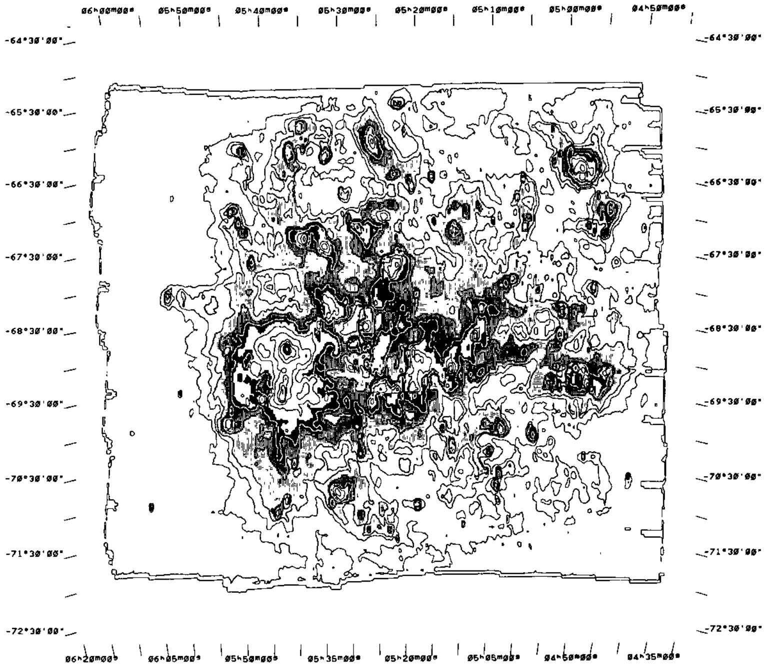

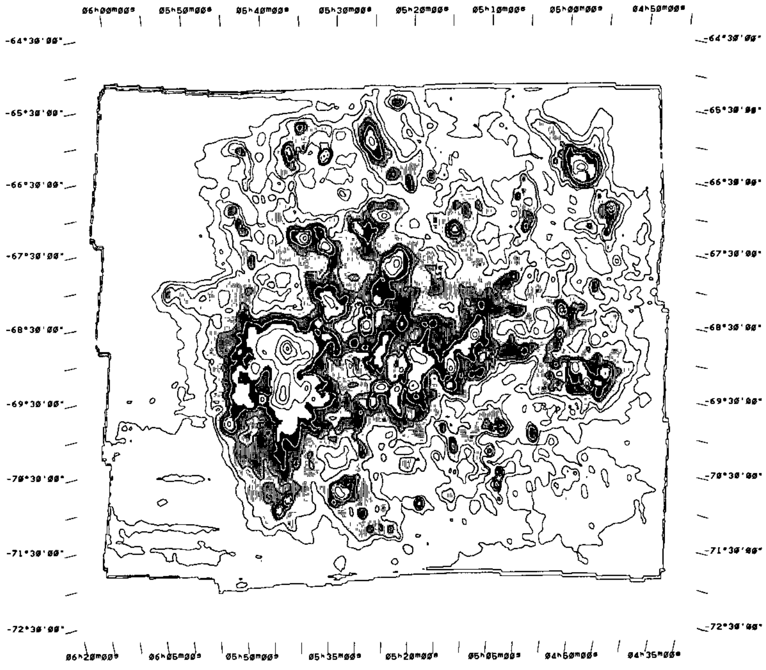

Fig. 1.3. ***LMC 60 μm DPM-map (set 1; EW).***
Fig. 1.4. ***LMC 100 μm DPM-map (set 1; EW).***

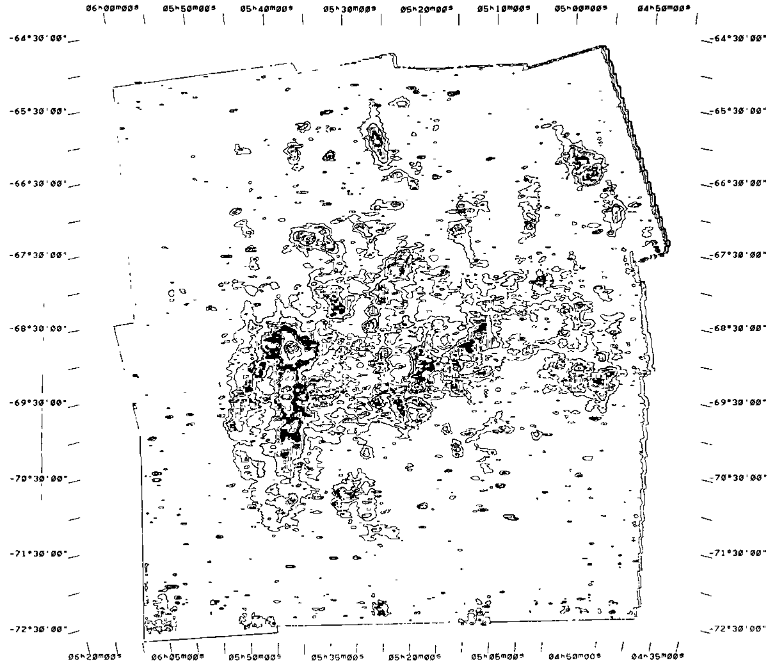

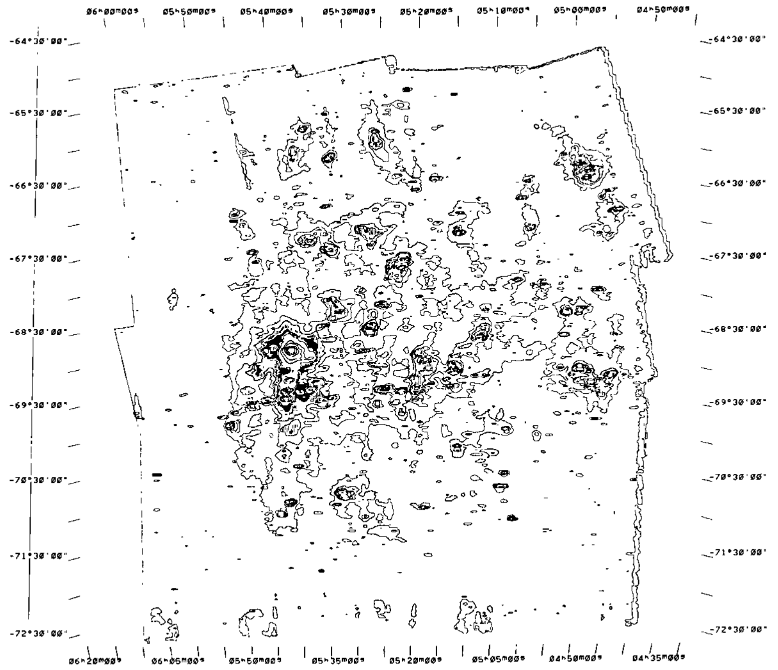

Fig. 2.1. LMC 12 μm DPM-map (set 2; NS).
Fig. 2.2. LMC 25 μm DPM-map (set 2; NS).

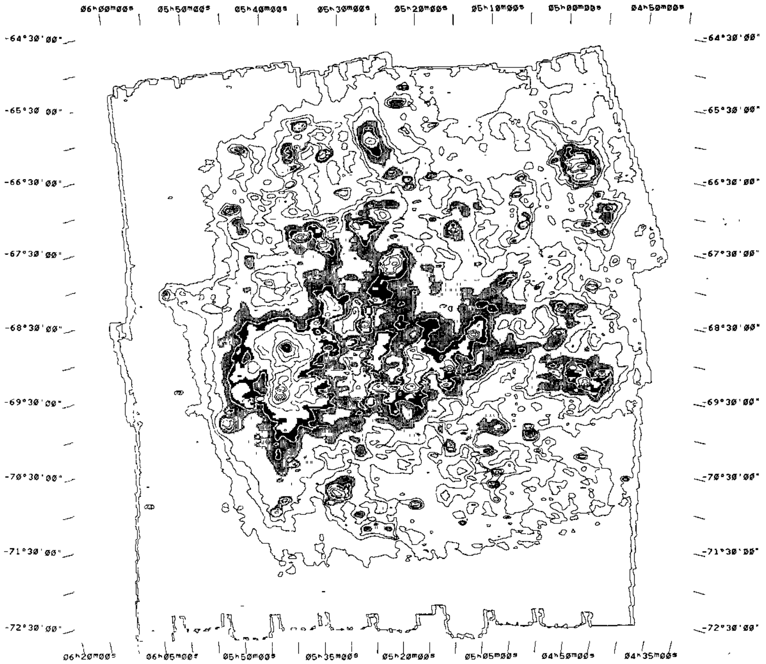

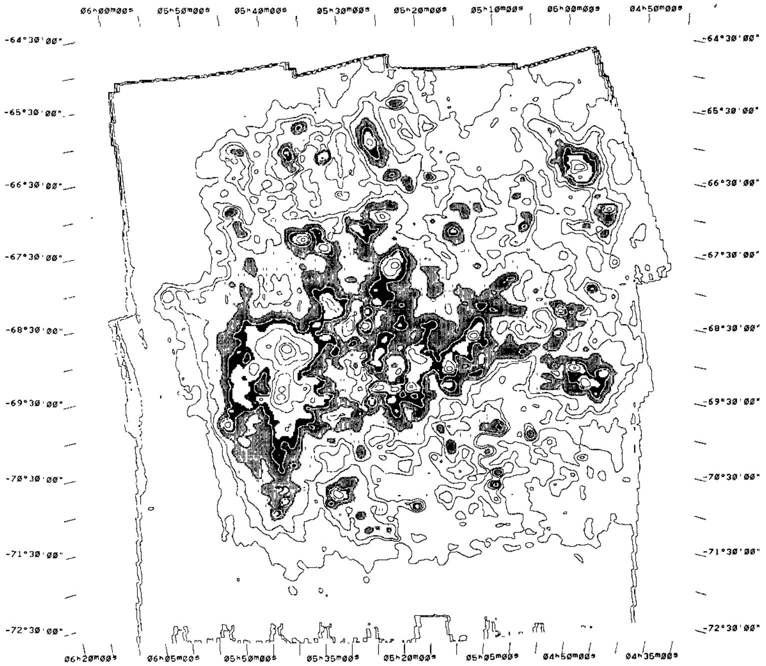

Fig. 2.3. ***LMC 60 μm DPM–map (set 2; NS).***
Fig. 2.4. ***LMC 100 μm DPM–map (set 2; NS).***

4. The Infrared Source List in the LMC

We searched the two sets of maps shown in Fig. a and 2 (and of Schwering and Israel, 1988b) for discrete sources down to intensity levels of 5, 2, 1 and 0.5 x 10^{-8} Watt m^{-2} sr^{-1} at 12, 25, 60 and 100 μm (respectively 4, 4, 3 and 1 times the median noise level in the maps). Intensity peaks, backgrounds and source sizes were estimated and used to obtain flux densities. The diffuse LMC infrared emission is also interpreted as background, whenever it was close to the source. A size estimate was obtained using the nominal gaussian resolutions in the different bands. All wavelength bands and both different map sets were searched separately. In a single wavelength band flux densities are about equal in the two maps, especially in unconfused regions (deviation of about 20 %). The data were then merged. The IRAS PSC positions are quoted whenever an unambigious identification was made. The source list is presented in Table 3. We recommend the use of the following names for sources in the list: LI-LMC (Leiden IRAS-LMC).

The LMC source list contains the same information as the SMC source list of Chapter II (Table 4 therein; see description). Our LMC source list contains 1823 entries. 1011 correspond to IRAS PSC sources, or can be identified with PSC sources with slight ($< 3'$) positional differences. Twenty-eight PSC sources could not be identified on the DPM maps. These spurious sources are listed in Table 4. The reason for most sources is confusion with close neighbours or with the extended emission. The source (spectral) types (as defined in Chapter II) in our list and in the PSC agree quite well. The source list contains 1095 (60 %) sources with a C-type spectrum (cool dust spectrum), 475 (26 %) sources with a W-type (warm dust spectrum) and 253 (14 %) with a S-type spectrum (stellar spectrum). Frequently, our procedure yields flux determinations where the PSC only gives upper limits, especially at 60 and 100 μm.

All 49 entries in the IRAS Small Scale Structure Catalog (IRAS SSS; IRAS, 1985b) that fall within the boundaries of the DPM fields were detected. Two of them (IRAS X0447-672 and X0509-685) are associated with more than one of our sources (both with one PSC and one non-PSC source). Forty-one SSS sources have an association with an entry from the PSC catalogue; these must be sources with unresolved and extended components. There are 802 new infrared sources in this source list, not included in the PSC nor in the SSS. The IRAS High Source Density Bin data (IRAS, 1985a) show high source densities at 100 μm in the whole LMC; at 60 and 100 μm over the face of the LMC; 25, 60 and 100 μm in the Bar and the 30 Doradus region; and at all four wavelength bands in the 30 Doradus region. In these confused and high source density regions in the sky the IRAS PSC is constructed with the primary aim to be reliable, even when it means less complete. The majority of these new sources are likely to be point sources, and clearly show the incompleteness of the IRAS PSC in confused areas. The positional uncertainties of these sources are about the same as the uncertainties described in Chapter II.

Table 3. Infrared Source List in the LMC.[a]

(1)	(2)		(3)		(4)		(5)		(6)		(7)	(8)	(9)	(10)	(11)	(12)	(13)	(14)
Number	Position RA(1950)	DEC(1950)	12 µm Peak	Bg	25 µm Peak	Bg	60 µm Peak	Bg	100 µm Peak	Bg	Size	F 12µm	F 25µm	F 60µm	F 100µm	IRAS-Id	Spectrum	Comments
	h m s	° ' "			10^{-8} Watt m^{-2}sr^{-1}						arcmin	Jy	Jy	Jy	Jy			
1	04 38 36	-70 53	13	-	-	-	-	-	-	-	p	0.48	-	-	-		S	
2	04 38 49.4	-70 42 47	3	-	3	-	1	0.5	1	0.5	p	0.11:	0.33	0.2:	1.0:	04388-7042	C	
3	04 40 24	-71 04	-	-	-	-	-	-	2	1	-	-	-	-	2.1:		C	
4	04 40 46.7	-70 00 54	22	-	6	-	-	-	-	-	p	0.81	0.67	-	-	04407-7000	S	
5	04 41 03.9	-69 13 00	-	-	-	-	1	-	1	-	-	-	-	0.4:	2.1:	04410-6912	C	
6	04 41 36	-71 28	6	-	-	-	-	-	-	-	p	0.22	-	-	-		S	
7	04 41 41.6	-68 42 08	5	-	-	-	-	-	-	-	-	0.19	-	-	-	04416-6842	S	SAO 249084
8	04 42 15	-70 50	-	-	-	-	1	-	4	3	-	-	-	0.4:	2.1		C	
9	04 42 59.0	-69 33 07	-	-	-	-	3	-	4	2	-	-	-	1.2	4.2	04429-6933	C	
10	04 43 00	-71 35	3	-	-	-	-	-	-	-	-	0.11:	-	-	-		S	SAO 256121
11	04 43 10	-70 43	-	-	-	-	4	-	5	3	-	-	-	1.7:	4.2		C	
12	04 43 26.9	-70 39 36	5	-	10	-	18	-	9	4	p	0.19:	1.11	7.5	10.4	04434-7039	C	
13	04 43 30	-70 58	-	-	-	-	-	-	4	3	-	-	-	-	2.1		C	
14	04 43 33	-71 01	4	-	-	-	-	-	-	-	p	0.15:	-	-	-		S	SAO 256122
15	04 43 56.4	-68 46 53	4	-	-	-	2	-	1	-	-	0.15:	-	0.8	2.1:	04439-6846	C	
16	04 44 31.0	-68 12 56	-	-	2	-	-	-	3	-	-	-	0.22:	-	6.2:	04445-6812	C	
17	04 44 33.6	-72 13 35	9	-	1	-	-	-	-	-	-	0.33	0.11:	-	-	04445-7213	S	SAO 256123
18	04 45 03.0	-70 48 24	7	-	1	-	-	-	-	-	p:	0.26	0.11:	-	-	04450-7048	S	
19	04 45 06	-68 29	5	-	-	-	-	-	-	-	-	0.19	-	-	-		S	SAO 249099
20	04 45 11	-68 07	5	-	-	-	-	-	-	-	-	0.19	-	-	-		S	SAO 249100
21	04 45 45	-69 53	2	-	-	-	1	-	2	1	-	0.07:	-	0.4:	2.1	04459-6955:	C	
22	04 46 10.8	-68 51 48	-	-	1	-	6	5	-	-	-	-	0.11:	0.4	C	04461-6851	W	
23	04 46 12.3	-68 23 01	-	-	-	-	4	2	2	-	-	-	-	0.8	4.2:	04462-6823	C	
24	04 46 40.8	-71 00 21	-	-	-	-	3	1	4	2	-	-	-	0.8	4.2	04466-7100	C	
25	04 46 46	-68 38	6	-	-	-	-	-	-	-	-	0.22	-	-	-		S	SAO 249109
26	04 47 00	-70 50	2	-	-	-	3	-	5	4	-	0.07:	-	1.2	2.1		C	
27	04 47 00	-71 22	-	-	-	-	1	-	2	1.5	-	-	-	0.4	1.0		C	
28	04 47 01.0	-67 12 17	5	-	3	-	10	4	9	5	p:	0.19	0.33	2.5	8.3	04470-6712 X0447-672*	C	
29	04 47 04.8	-71 09 08	-	-	-	-	3	1	4	2	-	-	-	0.8	4.2	04470-7109	C	
30	04 47 10	-71 12	5	-	-	-	-	-	-	-	-	0.19	-	-	-		S	SAO 256129
31	04 47 22.0	-68 29 43	8	-	2	-	-	-	-	-	p	0.30	0.22:	-	-	04473-6829	S	
32	04 47 25	-67 19	8	-	2	-	6	4	7	6	-	0.30	0.22	0.8	2.1:	X0447-672*	C	
33	04 47 30.5	-69 14 41	10	5	13	3	20	14	21	16	p	0.19	1.11	2.5	10.4	04475-6914	C	
34	04 47 50	-70 40	3	-	1	-	5	-	8	5	-	0.11:	0.11:	2.1	6.2	04481-7037:	C	
35	04 47 58	-69 48	5	-	1	-	4	2	3	2	-	0.19	0.11:	0.8:	2.1:		C	
36	04 48 00	-67 55	-	-	-	-	4	3	5	3	-	-	-	0.4	4.2		C	
37	04 48 08	-68 51	4	-	-	-	-	-	-	-	-	0.15:	-	-	-		S	SAO 249115
38	04 48 10.0	-68 24 01	-	-	-	-	4	2	5	3	-	-	-	0.8:	4.2:	04481-6824	C	
39	04 48 15	-68 55	4	2	1.5	-	13	10	13	11	-	0.07:	0.17	1.2	4.2		C	
40	04 48 30	-69 24	6	4	4	2	26	18	25	20	-	0.07:	0.22:	3.3	10.4		C	
41	04 48 30	-71 54	4	-	-	-	1	-	2	0.5	-	0.15:	-	0.4	3.1		C	
42	04 48 44.7	-70 24 06	2	-	1	-	2	-	5	4	-	0.07:	0.11:	0.8	2.1	04487-7024	C	
43	04 49 00	-70 30	2	-	1	-	3	-	5	4	-	0.07:	0.11:	1.2:	2.1:		C	
44	04 49 00	-71 11	-	-	-	-	2	1	4	3	-	-	-	0.4	2.1		C	
45	04 49 06.2	-69 26 02	12	7	7	5	30	25	-	-	-	0.19	0.22	2.1:	C	04491-6926	W	
46	04 49 07.7	-69 15 01	34	15	33	6	84	40	-	-	p	0.70	3.00	18.2	C	04491-6915	W	
47	04 49 09.2	-69 01 16	6	4	4	1.5	16	13	15	14	-	0.07:	0.28	1.2	2.1:	04491-6901	C	
48	04 49 14.5	-68 29 22	10	3	6	1.5	18	9	18	10	-	0.26	0.50	3.7	16.6	04492-6829	C	
49	04 49 15	-68 42	-	-	3	1.5	10	7	11	8	-	-	0.17	1.2	6.2		C	
50	04 49 17.1	-70 20 35	7	-	1	-	-	-	-	-	p:	0.26	0.11:	-	-	04492-7020	S	
51	04 49 20.3	-66 55 02	66	-	7	-	-	-	-	-	p	2.44	0.78	-	-	04493-6655	S	
52	04 49 30	-69 14	17	13	7	5	35	27	-	-	-	0.15	0.22	3.3:	C		W	
53	04 49 30.1	-68 35 29	8	4	3	1.5	12	8	13	10	-	0.15:	0.17	1.7	6.2	04495-6835	C	
54	04 49 33.2	-68 12 56	3	-	2	-	6	4	10	5	-	0.11	0.22	0.8	10.4	04495-6812	C	
55	04 49 35	-69 46	5	-	2	-	9	6	11	8	-	0.19	0.22	1.2	6.2		C	
56	04 49 37.5	-69 29 34	20	9	9	5	40	30	-	-	p:	0.41	0.44	4.1:	C	04496-6929	W	
57	04 49 38.4	-69 58 17	10	-	3	-	-	-	-	-	p	0.37	0.33	-	-	04496-6958	S	
58	04 49 40.5	-69 17 07	62	15	80	8	200	50	105	38	p	1.74	7.99	62.1	139.4	04496-6917	C	
59	04 49 47	-66 56	6	1	2	-	8	5	8	5	-	0.19	0.22	1.2	6.2		C	
60	04 49 50.3	-68 42 53	34	2	11	1	-	-	-	-	p	1.18	1.11	-	-	04498-6842	S	
61	04 49 52.2	-71 21 22	4	-	1	-	1	0.5	-	-	-	0.15:	0.11:	0.2	C	04498-7121	W	
62	04 49 53.0	-69 25 09	15	12	14	7	40	35	-	-	-	0.11:	0.78	2.1:	C	04498-6925	W	
63	04 49 55	-69 17	30	17	22	9	-	-	-	-	p	0.48	1.44	C	C		W	
64	04 50 14.9	-68 30 21	9	4	4	1	13	8	13	10	-	0.19	0.33	2.1	6.2	04502-6830	C	
65	04 50 15	-67 44	2	-	2	-	14	3	11	4	-	0.07:	0.22	4.6	14.6		C	
66	04 50 22.7	-69 45 32	10	3	2	-	9	7	-	-	-	0.26	0.22:	0.8:	-	04503-6945	W	
67	04 50 29.8	-69 34 47	25	10	15	7	74	38	61	38	-	0.56	0.89	14.9	47.8	04504-6934	C	
68	04 50 30	-66 51	2	-	1	-	9	5	9	6	-	0.07:	0.11:	1.7	6.2		C	
69	04 50 30	-69 17	19	11	7	5	45	35	50	40	-	0.30	0.22:	4.1:	20.8:		C	
70	04 50 30	-69 27	24	15	15	9	75	65	70	55	-	0.33	0.67	4.1	31.2		C	
71	04 50 30	-69 37	20	10	9	6	50	40	50	40	-	0.37	0.33	4.1	20.8		C	
72	04 50 30.0	-69 38 45	12	8	8	3	20	15	-	-	-	0.15:	0.56	2.1:	C	04505-6938	W	
73	04 50 30.7	-72 02 33	-	-	-	-	1	-	0.5	-	-	-	-	0.4:	1.0:	04505-7202	C	
74	04 50 31.1	-71 01 36	3	-	1	-	4	1	6	3	-	0.11:	0.11:	1.2	6.2	04505-7101	C	
75	04 50 31.2	-70 52 32	4	-	2	-	6	1	7	4	-	0.15:	0.22	2.1	6.2	04505-7052	C	
76	04 50 45	-70 22	2	-	1	-	2	-	2	1	-	0.07:	0.11:	0.8:	2.1:		C	
77	04 50 55.7	-69 22 32	36	16	17	8	-	-	-	-	p	0.74	1.00	C	C	04509-6922	W	
78	04 51 04.0	-69 54 49	135	-	14	-	2	-	-	-	p	4.99	1.55	0.8:	-	04510-6954	S	SAO 249123
79	04 51 14.7	-69 05 55	17	9	6	4	29	18	32	20	p	0.30	0.22	4.6	25.0	04512-6905	C	
80	04 51 16.7	-69 24 34	23	15	15	9	65	50	-	-	p	0.30	0.67	6.2:	C	04512-6924	W	
81	04 51 19.6	-70 27 07	10	-	5	-	17	-	10	3	p:	0.37:	0.56	7.0	14.6	04513-7027	C	
82	04 51 20	-67 01	11	5	7	4	20	12	-	-	-	0.22	0.33	3.3:	C		W	
83	04 51 20	-69 11	12	8	5	3	31	26	30	28	-	0.15	0.22:	2.1	4.2:		C	
84	04 51 22.0	-68 14 33	3	-	2	-	10	7	11	8	-	0.11:	0.22:	1.2	6.2	04513-6814	C	
85	04 51 22.3	-68 32 39	5	3	1.5	-	9	7	10	9	-	0.07:	0.17	0.8	2.1	04513-6832	C	
86	04 51 27.7	-69 31 36	15	6	35	6	83	50	-	-	p	0.33	3.22	13.7	C	04514-6931	W	
87	04 51 28.0	-68 09 00	11	-	3	1.5	-	-	-	-	p	0.41	0.17:	-	-	04514-6808	S	SAO 249125
88	04 51 30	-68 47	6	-	1	-	-	-	-	-	-	0.22	0.11:	-	-		S	
89	04 51 35.4	-67 10 14	17	8	8	3	-	-	-	-	p	0.33	0.56	C	C	04515-6710	W	
90	04 51 39.0	-69 19 12	15	10	6	4	35	30	37	33	-	0.19:	0.22	2.1:	8.3:	04516-6919	C	

Table 3, continued (2).

(1)	(2)		(3)		(4)		(5)		(6)		(7)	(8)	(9)	(10)	(11)	(12)	(13)	(14)
Number	Position RA(1950)	DEC(1950)	12 µm Peak	Bg	25 µm Peak	Bg	60 µm Peak	Bg	100 µm Peak	Bg	Size	F 12µm	F 25µm	F 60µm	F 100µm	IRAS-Id	Spectrum	Comments
	h m s	° ' "			10^{-8} Watt m^{-2} sr^{-1}						arcmin	Jy	Jy	Jy	Jy			
91	04 51 40	-67 26	4	-	2	-	9	7	10	8	-	0.15	0.22	0.8	4.2		C	
92	04 51 41.3	-69 02 49	24	7	9	2	17	14	-	-	p	0.63	0.78	1.2:	C	04516-6902 X0451-690	W	
93	04 51 41.5	-68 10 38	16	4	3	1.5	-	-	-	-	p	0.44	0.17:	-	-	04516-6810	S	SAO 249126
94	04 51 45	-67 07	17	8	7	4	35	20	35	25	-	0.33	0.33	6.2	20.8		C	
95	04 51 46.5	-65 51 32	-	-	-	-	3	-	-	-	-	-	-	1.2:	-	04517-6551	W	
96	04 51 50	-67 04	17	7	7	4	-	-	-	-	-	0.37	0.33	C	C		S	
97	04 51 50	-70 30	7	-	-	-	-	-	-	-	p:	0.26	-	-	-		S	
98	04 51 50.6	-67 34 15	6	-	2	-	10	4	10	6	-	0.22	0.22	2.5	8.3	04518-6734	C	
99	04 51 51.1	-68 52 23	10	-	2	-	-	-	-	-	p	0.37	0.22	-	-	04518-6852	S	
100	04 51 55	-67 15	13	6	2	1	-	-	-	-	-	0.26	0.11:	C	C		S	
101	04 52 00	-71 22	-	-	-	-	2	1	4.5	4	-	-	-	0.4	1.0		C	
102	04 52 04.8	-67 00 09	110	12	130	4	300	18	115	23	p	3.63	13.99	116.7	191.4	04520-6700	C	
103	04 52 09.5	-69 28 21	260	14	600	13	900	70	230	60	p	9.10	65.16	343.6	353.6	04521-6928	C	
104	04 52 11.0	-69 13 02	9	8	5	4	35	28	32	29	-	0.04:	0.11:	2.9	6.2:	04521-6913	C	
105	04 52 11.3	-69 45 29	7	4	3	1.5	15	9	16	12	-	0.11:	0.17	2.5	8.3	04521-6945	C	
106	04 52 11.7	-67 20 03	14	4	10	2	33	8	32	10	-	0.37	0.89	10.3:	45.8:	04521-6720	C	
107	04 52 17.9	-69 25 22	45	20	50	12	?20	70	-	-	-	0.93:	4.22:	62.1	C	04522-6925	W	
108	04 52 19.5	-70 43 23	14	-	4	-	9	3	12	7	p:	0.52	0.44	2.5	10.4	04523-7043	C	
109	04 52 20	-67 27	6	-	2	-	-	-	-	-	-	0.22	0.22:	-	-		C	
110	04 52 25	-68 27	6	-	2	-	0	7	10	8	-	0.22	0.22:	1.2	4.2		C	
111	04 52 25.9	-72 35 27	-	-	-	-	0.5	-	1.5	-	p:	-	-	0.2:	3.1:	04524-7235	C	
112	04 52 27.0	-67 21 43	9	4	9	2	33	8	-	-	-	0.19:	0.78	10.3:	C	04524-6721	W	
113	04 52 36.3	-69 51 47	5	-	2	-	10	7	11	7	-	0.19	0.22	1.2	8.3:	04526-6951	C	
114	04 52 41.4	-68 59 24	10	5	6	2	24	13	22	13	-	0.19	0.44	4.6	18.7	04526-6859	C	
115	04 52 42.8	-69 25 45	52	15	55	12	125	80	-	-	p	1.37	4.77	18.6:	C	04527-6925	W	
116	04 52 45	-67 02	12	6	4	2	29	22	-	-	p:	0.22	0.22	2.9	C		W	
117	04 52 45	-69 19	22	15	17	14	-	-	-	-	-	0.26	0.33	C	C		W	
118	04 52 50	-66 40	-	-	1	-	8	6	8	6	-	-	0.11:	0.8	4.2:		C	
119	04 53 00	-66 50	-	-	3	1	13	8	10	8	-	-	0.22:	2.1	4.2		C	
120	04 53 00	-68 12	9	4	4	2	-	-	-	-	-	0.19	0.22	C	C		W	
121	04 53 00.4	-69 16 43	73	17	58	12	125	65	84	65	p	2.07	5.11	24.8	39.5	04530-6916	C	
122	04 53 07.7	-68 08 41	30	3	39	1.5	94	8	39	10	p	1.00	4.16	35.6	60.3	04531-6808 X0453-681	C	
123	04 53 10	-67 10	10	-	6	1.5	28	12	-	-	-	0.37	0.50	6.6	C		W	
124	04 53 10	-68 50	4	-	2	-	13	9	12	9	-	0.15:	0.22:	1.7	6.2		C	
125	04 53 10	-69 32	14	9	6	4	-	-	-	-	-	0.19	0.22	C	C		W	
126	04 53 11.6	-69 35 46	9	6	6	4	30	20	30	25	-	0.11:	0.22	4.1:	10.4:	04531-6935	C	
127	04 53 12	-71 06	2	-	-	-	3	1	5	3	-	0.07:	-	0.8	4.2		C	
128	04 53 13.8	-70 51 02	4	-	2	-	7	5	8	6	-	0.15:	0.22	0.8	4.2:	04532-7051	C	
129	04 53 20	-68 09	9	-	4	2	12	10	-	-	-	0.33	0.22	0.8:	C		W	
130	04 53 25.2	-66 45 22	120	3	14	-	-	-	-	-	p	4.33	1.55	-	-	04534-6645	S	SAO 249138
131	04 53 29.7	-70 03 19	-	-	1	-	5	3	4	2	-	-	0.11:	0.8	4.2	04534-7003	C	
132	04 53 30	-66 58	7	1	5	2	28	15	19	14	-	0.22	0.33	5.4	10.4:		C	
133	04 53 30	-68 37	6	4	3	1.5	18	10	15	10	-	0.07	0.17	3.3	10.4		C	
134	04 53 30	-69 35	12	10	6	4	40	34	36	31	-	0.07	0.22	2.5	10.4		C	
135	04 53 30.5	-67 28 16	-	-	2	-	6	3	6	4	-	-	0.22	1.2	4.2:	04535-6728	C	
136	04 53 35.3	-66 16 31	5	-	3	-	5	4	-	-	p:	0.19	0.33	0.4:	-	04535-6616	W	
137	04 53 37.8	-67 04 04	9	4	4	2	26	12	24	16	-	0.19	0.22	5.8	16.6	04536-6704	C	
138	04 53 46.0	-69 22 36	18	12	20	10	-	-	-	-	-	0.22	1.11	C	C	04537-6922	W	
139	04 53 49.6	-70 40 30	5	-	2	-	9	5	9	6	-	0.19	0.22	1.7	6.2	04538-7040	C	
140	04 53 52.0	-69 52 39	5	-	2	-	12	7	13	9	-	0.19	0.22	2.1	8.3	04538-6952	C	
141	04 53 54.2	-68 21 11	9	4	2	-	-	-	-	-	p:	0.19	0.22	-	-	04539-6821	W	
142	04 53 55.1	-72 29 20	10	2	-	-	-	-	-	-	-	0.30:	-	-	-	04539-7229	S	SAO 256139
143	04 53 58	-69 03	9	6	3	1.5	-	-	-	-	-	0.11	0.17:	-	-		W	
144	04 54 00.8	-66 50 39	14	-	17	2	33	8	23	9	p:	0.52	1.66	10.3	29.1	04540-6650	C	
145	04 54 03.1	-67 21 05	4	-	20	1.5	27	8	15	9	-	0.15	2.05	7.9	12.5	04540-6721	C	
146	04 54 10	-66 57	4	-	2	-	15	10	-	-	-	0.15:	0.22:	2.1	C		W	
147	04 54 15	-67 22	23	3	5	2	-	-	-	-	p	0.74	0.33	-	-	04544-6722:	S	
148	04 54 17.0	-69 16 23	140	25	170	15	500	70	200	65	p	4.25	17.20	178.0	280.8	04542-6916	C	
149	04 54 19.4	-69 08 26	-	-	4	2	20	16	20	18	-	-	0.22:	1.7:	4.2:	04543-6908	C	
150	04 54 20	-70 54	5	-	1	-	7	6	9	8	-	0.19	0.11:	0.4:	2.1:		C	
151	04 54 20.8	-68 27 03	15	5	10	1.5	34	9	28	13	-	0.37	0.94	10.3	31.2	04543-6827	C	
152	04 54 22.5	-66 29 49	8	3	4	1	30	20	-	-	-	0.19	0.33	4.1	C	04543-6629	W	
153	04 54 24.6	-68 49 02	11	3	1.5	-	-	-	-	-	p:	0.30	0.17:	-	-	04544-6849	S	
154	04 54 25.2	-69 25 08	22	15	22	10	74	55	54	39	-	0.26	2.33	7.9	31.2	04544-6925	C	
155	04 54 30	-66 40	6	-	3	1	12	9	-	-	p:	0.22	0.22	1.2:	C		W	
156	04 54 30	-68 40	9	6	5	2	20	15	20	15	-	0.11	0.33	2.1	10.4		C	
157	04 54 30	-69 29	18	12	10	5	52	44	-	-	-	0.22	0.56	3.3:	C		W	
158	04 54 30.1	-69 46 33	4	-	1	-	9	7	10	8	-	0.15:	0.11:	0.8	4.2	04545-6946	C	
159	04 54 32.0	-70 00 44	12	-	8	-	5	3	6	4	p	0.44	0.89	0.8:	4.2:	04545-7000	C	
160	04 54 34.6	-66 44 35	-	-	1	-	9	7	10	8	-	-	0.11:	0.8	4.2:	04545-6644	C	
161	04 54 40	-65 56	-	-	2	-	9	7	-	-	-	-	0.22	0.8:	C		W	
162	04 54 40.6	-69 15 39	58	20	125	10	200	100	-	-	p	1.41	12.76	41.4:	C	04546-6915	W	
163	04 54 41.6	-65 58 00	5	-	2	-	10	6	9	4	-	0.19	0.22	1.7	10.4	04546-6558	C	
164	04 54 42.1	-69 34 23	19	9	9	6	37	30	34	28	p	0.37	0.33	2.9	12.5	04547-6934	C	SAO 249145:
165	04 54 43.8	-67 24 15	2	-	1	-	9	7	8	6	-	0.07:	0.11:	0.8:	4.2:	04547-6724	C	
166	04 54 45	-67 17	10	-	6	1.5	32	12	25	12	-	0.37	0.50	8.3	27.0		C	
167	04 54 50.2	-69 31 14	12	10	5	4	-	-	-	-	-	0.07:	0.11:	C	C	04548-6931	W	
168	04 54 55	-69 54	5	-	1	-	6	4	7	5	-	0.19	0.11:	0.8	4.2		C	
169	04 55 00	-65 48	-	-	-	-	4	-	4	-	10x10:	-	-	16.3	43.0		C	
170	04 55 00	-70 24	5	-	-	-	-	-	-	-	-	0.19	-	-	-		S	
171	04 55 00	-70 58	-	-	1	-	7	6	9	7	-	-	0.11:	0.4:	4.2		C	
172	04 55 00	-71 18	-	-	-	-	3	1	3	2	-	-	-	0.8	2.1		C	
173	04 55 05	-69 19	20	12	10	7	-	-	-	-	-	0.30	0.33	C	C		W	
174	04 55 10.0	-66 07 57	6	-	3	-	11	9	13	10	-	0.22	0.33	0.8	6.2	04551-6607	C	
175	04 55 10.1	-69 28 41	15	6	7	5	30	27	-	-	-	0.33:	0.22:	1.2:	C	04551-6928	W	
176	04 55 13.1	-66 05 58	4	-	3	-	11	9	-	-	-	0.15:	0.33	0.8	C	04552-6605	W	
177	04 55 13.6	-66 36 14	18	15	16	9	-	-	-	-	p:	0.11:	0.78	C	C	04552-6636	W	
178	04 55 15	-66 03	4	-	3	-	9	4	11	7	-	0.15	0.33	2.1	8.3:		C	
179	04 55 15	-66 24	18	12	9	7	55	35	-	-	-	0.22	0.22	8.3	C		W	
180	04 55 16.1	-65 36 17	4	-	2	-	3	2	1	-	-	0.15	0.22:	0.4	2.1	04552-6536	C	

Table 3, continued (3).

(1)	(2)		(3)		(4)		(5)		(6)		(7)	(8)	(9)	(10)	(11)	(12)	(13)	(14)
Number	Position RA(1950) h m s	DEC(1950) ° ' "	12 µm Peak	Bg	25 µm Peak	Bg	60 µm Peak	Bg	100 µm Peak	Bg	Size arcmin	F 12µm Jy	F 25µm Jy	F 60µm Jy	F 100µm Jy	IRAS-Id	Spec-trum	Comments
					10^{-8} Watt m^{-2} sr^{-1}													
181	04 55 18.4	-68 25 15	205	14	105	4	28	18	20	15	p	7.07	11.21	4.1	10.4:	04553-6825	W	
182	04 55 20	-69 25	17	9	6	4	-	-	-	-	-	0.30	0.22	C	C		S	
183	04 55 20.5	-69 33 53	23	5	10	4	28	23	-	-	p	0.67	0.67	2.1:	C	04553-6933	W	
184	04 55 21.5	-69 21 36	20	10	19	7	62	45	35	25	p:	0.37	1.33	7.0	20.8:	04553-6921	C	
185	04 55 25	-66 57	5	-	-	-	-	-	-	-	-	0.19	-	-	-		S	
186	04 55 25	-67 00	-	-	-	-	6	4	5	4	-	-	-	0.8	2.1:		C	
187	04 55 30	-68 28	20	10	9	3	-	-	-	-	-	0.37	0.67	C	C		W	
188	04 55 30	-72 27	-	-	-	-	1	-	1.5	-	10x10	-	-	3.8	16.0	04556-7225:	C	
189	04 55 30.4	-70 32 07	2	-	2	-	3	-	3	2	-	0.07:	0.22	1.2	2.1	04555-7032	C	
190	04 55 33.2	-66 32 23	45	12	30	13	125	50	85	55	p:	1.22	1.89	31.0	62.4	04555-6632	C	
191	04 55 33.3	-68 41 39	16	7	7	4	29	18	28	18	-	0.33	0.33	4.6	20.8	04555-6841	C	
192	04 55 35	-66 39	24	12	28	12	90	45	-	-	p	0.44	1.78	18.6	C	04557-6639:	W	
193	04 55 35	-69 11	11	7	4	2	20	18	28	23	p:	0.15	0.22	0.8	10.4		C	
194	04 55 35.3	-68 29 59	19	8	27	4	54	22	46	25	p:	0.41	2.55	13.2	43.7	04555-6829	C	
195	04 55 37.9	-66 30 24	35	16	22	14	100	60	-	-	p:	0.70	0.89	16.6:	C	04556-6630	W	
196	04 55 38	-70 53	2	-	2	-	10	7	11	8	-	0.07:	0.22	1.2	6.2	04557-7052:	C	
197	04 55 40	-68 37	15	6	4	3	-	-	-	-	-	0.33	0.11	C	C		S	
198	04 55 42.1	-67 53 25	7	-	2	-	-	-	-	-	p	0.26	0.22	-	-	04557-6753	S	
199	04 55 42.4	-69 20 41	16	10	8	4	20	16	-	-	-	0.22:	0.44	1.7:	C	04557-6920	W	
200	04 55 42.5	-69 52 01	11	-	4	-	4	3	5	4	p	0.41	0.44	0.4:	2.1:	04557-6952	C	
201	04 55 46.6	-65 57 21	-	-	1	-	7	4	6	4	-	-	0.11:	1.2:	4.2:	04557-6557	C	
202	04 55 50	-68 35	15	6	5	3	30	18	30	25	-	0.33	0.22	5.0	10.4		C	
203	04 55 57.3	-69 31 22	20	8	8	4	20	18	-	-	p	0.44	0.44	0.8:	C	04559-6931	W	
204	04 56 10	-68 49	3	2	4	2	19	14	16	14	-	0.04	0.22	2.1	4.2		C	
205	04 56 17.0	-66 41 40	15	10	20	15	-	-	-	-	-	0.19	0.56	C	C	04562-6641	W	
206	04 56 20	-66 20	19	9	7	4	50	40	-	-	-	0.37	0.33	4.1	C		W	
207	04 56 20	-69 38	9	4	3	1.5	-	-	-	-	-	0.19	0.17	C	C		S	
208	04 56 20.9	-67 19 29	6	-	3	-	13	8	12	8	-	0.22:	0.33	2.1	8.3:	04563-6719	C	
209	04 56 22.8	-71 25 37	-	-	-	-	3	1	2	1	-	-	-	0.8	2.1	04563-7125	C	
210	04 56 24.3	-66 29 48	60	20	125	30	-	-	-	-	-	1.48:	10.55:	C	C	04564-6629	W	
211	04 56 24.9	-70 56 48	-	-	-	-	2	-	-	-	-	-	-	0.8:	C	04564-7056	W	
212	04 56 25	-69 11	12	8	4	3	20	18	-	-	-	0.15	0.11	0 8:	C		W	
213	04 56 26.9	-69 35 47	9	5	4	2	22	19	21	18	-	0.15:	0.22	1.2	6.2	04564-6935	C	
214	04 56 35.4	-66 37 21	43	17	50	14	150	60	105	60	-	0.96	4.00	37.3	93.6	04565-6637	C	
215	04 56 40	-67 55	4	-	2	-	11	7	11	8	-	0.15	0.22	1.7	6.2		C	
216	04 56 40.0	-69 28 56	15	4	10	4	40	25	28	21	p	0.41	0.67	6.2	14.6	04566-6928	C	
217	04 56 41.2	-66 29 03	135	20	310	15	650	60	320	70	p	4.25	32.74	244.3	520.0	04566-6629	C	
218	04 56 43.5	-68 57 19	9	4	3	2	-	-	-	-	-	0.19	0.11	C	C	04567-6857	S	
219	04 56 48.1	-66 35 34	-	-	25	15	-	-	-	-	p:	-	1.11:	C	C	04568-6635	W	
220	04 56 50	-66 50	5	-	1	-	-	-	-	-	-	0.19	0.11:	-	-		S	
221	04 56 50	-70 19	5	-	1	-	9	3	9	2	-	0.19	0.11:	2.5	14.6		C	
222	04 57 00	-66 39	21	14	-	-	-	-	-	-	-	0.26	C	C	C		S	
223	04 57 01.1	-66 47 01	4	-	5	-	13	6	9	6	p	0.15	0.56	2.9	6.2:	04570-6647	C	
224	04 57 06	-71 14	-	-	-	-	3	1	4	1	p:	-	-	0.8	6.2		C	
225	04 57 08.5	-69 54 58	22	-	11	-	2	1	-	-	p	0.81	1.22	0.4:	-	04571-6954	W	
226	04 57 09.2	-66 27 45	60	33	75	30	-	-	-	-	-	1.00:	4.99:	C	C	04571-6627	W	
227	04 57 15	-68 08	2	-	1	-	10	7	10	8	-	0.07:	0.11:	1.2	4.2:		C	
228	04 57 20	-68 56	14	6	4	3	38	20	33	20	-	0.30	0.11:	7.5	27.0		C	
229	04 57 20.6	-66 23 52	35	25	15	10	-	-	-	-	-	0.37	0.56	C	C	04573-6623	W	
230	04 57 22.5	-69 16 13	22	7	12	3	59	24	47	22	p:	0.56	1.00	14.5	52.0	04573-6916 X0457-692	C	
231	04 57 23.2	-70 31 24	3	-	1	-	8	2	7	3	-	0.11:	0.11:	2.5	8.3	04573-7031	C	
232	04 57 23.3	-68 49 12	40	6	47	2	135	20	67	20	p	1.26	4.99	47.6	97.8	04573-6849 X0457-688	C	
233	04 57 23.8	-71 00 02	12	-	-	-	-	-	-	-	p	0.44	-	-	-	04573-7100	S	SAO 256146
234	04 57 25.4	-67 25 23	3	-	1	-	5	3	5	3	-	0.11:	0.11:	0.8	4.2:	04574-6725	C	
235	04 57 25.9	-68 29 36	80	4	120	4	305	20	135	25	p	2.81	12.88	118.0	228.8	04574-6829 X0457-685	C	
236	04 57 30	-68 22	4	-	3	2	17	10	15	10	-	0.15:	0.11	2.9	10.4		C	
237	04 57 30	-69 13	15	7	3	2	-	-	-	-	-	0.30	0.11:	C	C		S	
238	04 57 30	-71 04	-	-	1	-	5	2	4	2	-	-	0.11:	1.2	4.2		C	
239	04 57 30.4	-67 07 44	2	-	1	-	7	4	8	4	-	0.07:	0.11:	1.2	8.3	04575-6707	C	
240	04 57 32.9	-67 41 45	2	-	2	-	9	6	10	8	-	0.07:	0.22	1.2	4.2:	04575-6741	C	
241	04 57 35	-67 17	3	-	2	-	10	5	10	7	-	0.11:	0.22	2.1	6.2		C	
242	04 57 35	-69 35	8	3	6	3	33	22	25	20	p:	0.19	0.33	4.6	10.4		C	
243	04 57 36.1	-66 31 53	50	30	50	30	250	100	125	100	-	0.74:	2.22:	62.1	52.0	04576-6631	W	
244	04 57 36.2	-66 19 53	20	12	12	6	55	25	-	-	-	0.30	0.67	12.4	C	04576-6619	W	
245	04 57 37.9	-69 00 44	15	7	7	3	26	20	25	20	p:	0.30	0.44	2.5:	10.4:	04576-6900	C	
246	04 57 40	-68 27	17	6	11	3	52	20	-	-	-	0.41	0.89	13.2	C		W	
247	04 57 40	-69 52	4	-	-	-	3	1	2	1	-	0.15	-	0.8:	2.1:		C	
248	04 57 40.5	-66 33 19	85	20	130	17	270	80	-	-	p:	2.40	12.54	78.7	C	04576-6633	W	
249	04 57 56.3	-69 24 48	12	6	6	3	30	20	28	18	-	0.22	0.33	4.1	20.8	04579-6924	C	
250	04 57 59.2	-69 04 35	14	6	4	2	20	18	20	18	p	0.30	0.22	0.8:	4.2:	04579-6904	C	
251	04 58 00	-66 26	42	20	45	10	150	70	100	70	p:	0.81	3.88	33.1	62.4	04580-6626:	C	
252	04 58 04.4	-68 11 52	4	-	1.5	-	13	8	12	10	-	0.15:	0.17	2.1	4.2:	04580-6811	C	
253	04 58 08.7	-70 13 27	16	-	4	-	-	-	-	-	p	0.59	0.44	-	-	04581-7013	S	
254	04 58 08.8	-67 45 32	2	-	2	-	12	7	10	8	-	0.07:	0.22	2.1	4.2:	04581-6745	C	
255	04 58 10	-68 04	4	-	1	-	11	8	13	9	-	0.15	0.11:	1.2	8.3		C	
256	04 58 10	-69 09	9	5	3	2	19	17	-	-	-	0.15	0.11	0.8:	C		W	
257	04 58 20	-66 17	17	10	10	5	52	20	45	25	-	0.26	0.56	13.2	41.6		C	
258	04 58 20.5	-70 51 44	-	-	-	-	5	2	4	2	-	-	-	1.2	4.2	04583-7051	C	
259	04 58 25	-66 35	18	10	8	4	40	30	-	-	-	0.30	0.44	4.1	C		W	
260	04 58 25.5	-65 53 19	2	-	1	-	5	-	3	-	p	0.07:	0.11:	2.1	6.2	04584-6553	C	
261	04 58 27.8	-67 25 34	-	-	-	-	5	3	5	3	-	-	-	0.8:	4.2:	04584-6725	C	
262	04 58 29.5	-68 28 37	6	3	-	-	-	-	-	-	-	0.11:	C	C	C	04584-6828	S	
263	04 58 30	-68 57	7	-	4	2	24	16	22	20	-	0.26	0.22	3.3	4.2		C	
264	04 58 33.0	-67 35 24	-	-	-	-	7	5	6	4	-	-	-	0.8	4.2	04585-6735	C	
265	04 58 36.5	-70 27 28	6	-	3	-	12	5	10	4	-	0.22	0.33	2.9	12.5	04586-7027	C	
266	04 58 39.1	-66 14 17	18	8	12	4	-	-	-	-	-	0.37	0.89	C	C	04586-6614	W	
267	04 58 40	-69 36	5	-	4	2	25	20	20	17	-	0.19	0.22	2.1	6.2		C	
268	04 58 45	-66 20	23	14	9	6	40	20	55	35	p:	0.33	0.33:	8.3:	41.6:	04587-6618:	C	
269	04 58 45	-66 22	23	14	13	6	45	25	-	-	p:	0.33	0.78	8.3	C	04590-6621:	W	
270	04 58 45	-69 58	2	-	1	-	2	1	3	2	-	0.07:	0.11:	0.4	2.1:	04586-6955:	C	

Table 3, continued (4).

(1)	(2)		(3)		(4)		(5)		(6)		(7)	(8)	(9)	(10)	(11)	(12)	(13)	(14)
Number	Position RA(1950) h m s	DEC(1950) ° ' "	12 µm Peak	Bg	25 µm Peak	Bg	60 µm Peak	Bg	100 µm Peak	Bg	Size arcmin	F 12µm Jy	F 25µm Jy	F 60µm Jy	F 100µm Jy	IRAS-Id	Spec-trum	Comments
					10^{-8} Watt $m^{-2} sr^{-1}$													
271	04 58 46.2	-66 11 37	13	5	5	2	-	-	-	-	p:	0.30	0.33	C	C	04587-6611	W	
272	04 58 46.6	-69 11 59	12	6	5	3	30	20	28	19	-	0.22	0.22	4.1	18.7	04587-6911	C	
273	04 58 48.1	-68 11 39	8	-	3	-	-	-	-	-	p:	0.30	0.33	-	-	04588-6811	W	
274	04 58 52.8	-69 01 52	8	4	4	1.5	23	18	20	15	-	0.15	0.28	2.1	10.4:	04588-6901	C	
275	04 58 54.7	-68 25 07	7	3	5	1.5	20	12	16	12	-	0.15	0.39	3.3	8.3	04589-6825	C	
276	04 58 56.7	-65 47 38	2	-	4	-	-	-	-	-	p	0.07:	0.44	-	-	04589-6547	W	
277	04 58 59.7	-66 30 54	10	8	5	3	30	15	30	20	-	0.07:	0.22	6.2:	20.8:	04589-6630	C	
278	04 59 00	-66 40	4	-	2	-	16	8	15	8	-	0.15	0.22	3.3	14.6		C	
279	04 59 00	-70 35	-	-	-	-	3	-	2	-	-	-	-	1.2	4.2		C	
280	04 59 00	-71 46	-	-	-	-	2	-	2	-	-	-	-	0.8	4.2		C	
281	04 59 02.4	-69 21 48	9	5	5	2	-	-	-	-	-	0.15	0.33	C	C	04590-6921	W	
282	04 59 05.3	-68 29 37	4	-	-	-	-	-	-	-	-	0.15:	-	C	C	04590-6829	S	
283	04 59 15	-66 17	9	6	3	2	22	18	-	-	-	0.11	0.11	1.7	C		W	
284	04 59 15	-66 36	6	2	3	1	10	8	-	-	-	0.15	0.22:	0.8:	C		W	
285	04 59 19.9	-69 16 02	4	-	4	2	21	17	18	16	-	0.15:	0.22	1.7	4.2:	04593-6916	C	
286	04 59 26.4	-69 26 40	6	3	3	2	19	17	18	16	-	0.11:	0.11	0.8:	4.2:	04594-6926	C	
287	04 59 40.2	-67 48 17	5	-	3	-	12	7	10	7	p:	0.19	0.33	2.1	6.2	04596-6748	C	
288	04 59 43.8	-70 54 34	-	-	-	-	3	-	2	-	-	-	-	1.2	4.2:	04597-7054	C	
289	04 59 45	-66 12	9	4	4	2	17	11	22	14	-	0.19	0.22	2.5	16.6		C	
290	04 59 50	-66 21	14	5	17	2	33	13	25	15	p:	0.33	1.66	8.3	20.8		C	
291	04 59 52.5	-70 36 19	-	-	4	-	2	-	2	1	p	-	0.44	0.8	2.1:	04598-7036	C	
292	05 00 00	-68 04	3	-	2	-	12	7	12	10	-	0.11:	0.22	2.1	4.2		C	
293	05 00 02.0	-69 21 45	7	3	2	1	-	-	-	-	-	0.15	0.11	C	C	05000-6921	S	
294	05 00 03	-68 39	4	-	-	-	-	-	-	-	-	0.15:	-	-	-		S	SAO 249164
295	05 00 03.2	-70 13 22	18	5	10	2	56	4	35	4	p:	0.48	0.89	21.5	64.5	05000-7013	C	
296	05 00 07.9	-68 46 31	4	-	2	-	9	6	11	7	-	0.15	0.22:	1.2	8.3	05001-6846	C	
297	05 00 18.6	-67 12 21	12	-	4	-	5	3	4	3	p	0.44	0.44	0.8:	2.1:	05003-6712	C	
298	05 00 20	-66 28	8	4	5	2	14	10	-	-	-	0.15	0.33	1.7:	C		W	
299	05 00 20	-69 32	2	-	1.5	-	18	16	15	13	-	0.07:	0.17:	0.8	4.2		C	
300	05 00 20	-70 45	-	-	-	-	4	1	3	1	p:	-	-	1.2	4.2		C	
301	05 00 25	-68 29	11	4	1.5	-	16	10	13	10	-	0.26	0.17	2.5	6.2		C	
302	05 00 26.4	-70 07 49	5	-	4	-	17	7	10	6	p	0.19	0.44	4.1	8.3	05004-7007	C	
303	05 00 30	-70 32	6	-	-	-	-	-	-	-	-	0.22	-	-	-		S	
304	05 00 31.0	-69 36 11	3	-	2	-	15	11	12	9	-	0.11:	0.22	1.7	6.2:	05005-6936	C	
305	05 00 33.9	-65 59 02	2	-	2	-	9	4	-	-	-	0.07:	0.22	2.1	C	05005-6559	W	
306	05 00 40	-68 10	12	7	5	2	9	7	14	11	-	0.19	0.33	0.8	6.2		C	
307	05 00 45.2	-66 28 12	14	3	10	1	33	8	24	12	p	0.41	1.00	10.3	25.0	05007-6628	C	
308	05 00 49.9	-67 06 53	2	-	1	-	7	3	9	5	-	0.07:	0.11:	1.7	8.3	05008-6706	C	
309	05 00 50	-66 00	2	-	4	2	-	-	-	-	-	0.07:	0.22	-	-		W	
310	05 00 57.2	-66 16 58	7	-	2	-	-	-	-	-	p	0.26	0.22	-	-	05009-6616	S	
311	05 01 00	-71 28	-	-	-	-	2	-	3	1	10x10:	-	-	7.7	21.7		C	
312	05 01 01.7	-67 39 20	6	-	1.5	-	-	-	-	-	-	0.22	0.17:	-	-	05010-6739	S	
313	05 01 05	-66 03	8	4	4	2	17	12	20	14	-	0.15	0.22	2.1	12.5		C	
314	05 01 10	-69 02	10	5	4	2	23	17	26	18	-	0.19	0.22	2.5	16.6		C	
315	05 01 10.9	-68 15 01	9	4	11	1.5	30	12	22	15	p	0.19	1.05	7.5	14.6	05011-6815	C	
316	05 01 21.5	-65 58 20	6	2	4	1	22	12	15	12	-	0.15:	0.33	4.1	6.2:	05013-6558	C	
317	05 01 25	-70 21	-	-	-	-	5	3	2	1	-	-	-	0.8	2.1:		C	
318	05 01 30	-68 17	10	5	5	1.5	16	11	21	15	-	0.19	0.39	2.1	12.5		C	
319	05 01 30	-70 47	-	-	-	-	6	3	6	3	-	-	-	1.2	6.2		C	
320	05 01 32.1	-65 44 18	-	-	1	-	2	-	-	-	-	-	0.11:	0.8:	-	05015-6544	W	
321	05 01 39.1	-68 05 54	85	6	7	-	-	-	-	-	p	2.92	0.78	-	-	05016-6805	S	
322	05 01 40	-68 30	-	-	1.5	-	13	10	16	14	-	-	0.17:	1.2	4.2:		C	
323	05 01 40	-69 55	-	-	-	-	10	4	7	4	-	-	-	2.5	6.2		C	
324	05 01 41.4	-68 10 03	125	6	26	2	-	-	-	-	p	4.40	2.66	-	-	05016-6810	S	
325	05 01 50	-71 06	-	-	-	-	3	-	2	-	-	-	-	1.2	4.2		C	
326	05 01 54.0	-67 51 59	7	-	4	-	8	6	9	8	-	0.26	0.44	0.8	2.1:	05019-6751	C	
327	05 01 55	-69 34	5	-	1	-	-	-	-	-	-	0.19	0.11:	-	-		S	SAO 249172
328	05 02 00	-68 40	4	-	3	1.5	20	10	17	12	-	0.15	0.17	4.1	10.4		C	
329	05 02 00	-68 47	4	-	1.5	-	13	8	13	9	-	0.15	0.17	2.1	8.3		C	
330	05 02 00	-70 05	-	-	-	-	5	4	3	2	-	-	-	0.4	2.1:		C	
331	05 02 00	-70 33	-	-	-	-	2	-	3	2	-	-	-	0.8	2.1		C	
332	05 02 00.5	-69 03 22	22	11	6	3	23	20	-	-	p	0.41	0.33	1.2:	C	05020-6903	W	
333	05 02 10	-68 23	4	2	3	1.5	15	11	16	12	-	0.07	0.17	1.7	8.3	05023-6822:	C	
334	05 02 10.3	-66 44 02	-	-	-	-	4	2	4	2	-	-	-	0.8	4.2	05021-6644	C	
335	05 02 12	-71 26	3	-	2	-	-	-	-	-	-	0.11:	0.22:	-	-		W	
336	05 02 15	-67 55	3	-	1.5	-	10	8	11	9	-	0.11:	0.17:	0.8	4.2:		C	
337	05 02 15	-70 10	5	-	1	-	6	4	6	4	-	0.19	0.11:	0.8	4.2		C	
338	05 02 19.9	-69 12 21	-	-	3	1.5	18	14	-	-	-	-	0.17:	1.7	C	05023-6912	W	
339	05 02 20	-67 45	2	-	2	-	9	6	10	8	-	0.07:	0.22:	1.2	4.2:		C	
340	05 02 22.7	-69 37 55	3	-	1.5	-	12	7	10	6	-	0.11:	0.17	2.1	8.3	05023-6937	C	
341	05 02 27.1	-68 13 56	6	3	3	1	11	9	12	10	-	0.11:	0.22	0.8	4.2	05024-6813	C	
342	05 02 31.2	-69 06 24	24	11	10	5	54	32	50	31	1x1:	0.72	0.78	10.3	41.3	05025-6906 X0502-691	C	
343	05 02 33.9	-70 46 53	2	-	1.5	-	10	6	7	6	-	0.07:	0.17	1.7	2.1	05025-7046	C	
344	05 02 37.4	-68 09 39	13	4	7	1	9	7	9	8	p	0.33	0.67	0.8	2.1	05026-6809	C	
345	05 02 40	-67 04	6	-	2	-	10	7	13	9	-	0.22	0.22	1.2	8.3		C	
346	05 02 44.2	-71 24 15	22	-	80	-	13	1	3	2	p	0.81	8.88	5.0	2.1	05027-7124	W	
347	05 02 45.2	-69 09 00	19	10	7	4	40	33	-	-	p:	0.33	0.33	2.9:	C	05027-6908	W	
348	05 02 49.5	-68 31 08	8	3	5	2	24	13	20	15	p:	0.19	0.33	4.6	10.4:	05028-6831	C	
349	05 03 00	-66 56	4	-	3	1	12	8	12	10	-	0.15	0.22	1.7	4.2		C	
350	05 03 00	-71 37	-	-	-	-	2	-	2	-	-	-	-	0.8	4.2		C	
351	05 03 00.2	-65 56 50	6	-	3	-	15	9	18	12	-	0.22:	0.33	2.5	12.5	05030-6556	C	
352	05 03 06.3	-71 54 35	4	-	-	-	-	-	-	-	-	0.15	-	-	-	05031-7154	S	
353	05 03 10	-70 13	-	-	-	-	6	4	6	5	-	-	-	0.8	2.1:		C	
354	05 03 14.8	-67 38 08	3	-	2	-	9	7	9	8	-	0.11:	0.22	0.8	2.1:	05032-6738	C	
355	05 03 15	-65 53	6	-	2	1	-	-	-	-	-	0.22	0.11	-	-		S	
356	05 03 15	-67 16	14	6	5	2	25	16	28	20	-	0.30	0.33	3.7	16.6		C	
357	05 03 15.8	-70 19 18	-	-	-	-	5	3	5	3	p	-	-	0.8	4.2	05032-7019	C	
358	05 03 17.5	-70 41 20	2	-	-	-	10	7	9	6	-	0.07:	-	1.2	6.2	05032-7041	C	
359	05 03 21.0	-71 22 58	62	-	6	-	-	-	-	-	p	2.29	0.67	-	-	05033-7122	S	SAO 256154
360	05 03 25	-66 16	2	-	2	-	5	2	5	2	-	0.07:	0.22	1.2	6.2	X0503-662	C	

Table 3, continued (5).

(1)	(2)		(3)		(4)		(5)		(6)		(7)	(8)	(9)	(10)	(11)	(12)	(13)	(14)
Number	Position RA(1950) h m s	DEC(1950) ° ' "	12 μm Peak	Bg	25 μm Peak	Bg	60 μm Peak	Bg	100 μm Peak	Bg	Size arcmin	F 12μm Jy	F 25μm Jy	F 60μm Jy	F 100μm Jy	IRAS-Id	Spec-trum	Comments
					10^{-8} Watt $m^{-2}sr^{-1}$													
361	05 03 30	-67 50	2	-	1.5	-	12	10	13	11	-	0.07:	0.17	0.8	4.2		C	
362	05 03 30	-68 17	-	-	1	-	8	6	8	7	-	-	0.11:	0.8	2.1		C	
363	05 03 30.7	-65 43 54	2	-	1	-	4	2	6	2	-	0.07:	0.11:	0.8	8.3	05035-6543	C	
364	05 03 35	-67 15	13	7	4	3	23	18	23	20	-	0.22	0.11	2.1	6.2:		C	
365	05 03 35	-68 32	13	8	6	3	23	16	27	20	-	0.19:	0.33	2.9	14.6	05036-6832:	C	
366	05 03 36.9	-68 59 40	-	-	-	-	17	12	16	14	-	-	-	2.1	4.2:	05036-6859	C	
367	05 03 39.6	-66 49 00	9	3	7	1	12	9	14	10	p:	0.22	0.67	1.2	8.3	05036-6649	C	
368	05 03 40	-68 35	13	8	6	3	-	-	-	-	-	0.19	0.33	C	C		W	
369	05 03 40	-71 00	-	-	-	-	3	-	2	1	-	-	-	1.2	2.1		C	
370	05 03 45	-70 46	2	-	2	-	10	8	8	7	-	0.07:	0.22	0.8	2.1:		C	
371	05 03 51.6	-67 22 39	35	10	37	4	90	13	48	11	p	0.93	3.66	31.9	77.0	05038-6722 X0503-673	C	
372	05 03 52.5	-68 57 15	13	3	3	-	-	-	-	-	p	0.37	0.33	C	C	05038-6857	S	
373	05 03 54.3	-69 06 11	12	8	5	3	38	33	35	32	p	0.15	0.22	2.1	6.2:	05039-6906	C	
374	05 03 55.0	-70 02 06	4	-	5	-	4	2	4	3	p	0.15	0.56	0.8:	2.1:	05039-7002	C	
375	05 03 57.1	-67 24 37	22	12	15	4	-	-	-	-	p:	0.37	1.22	C	C	05039-6724	W	
376	05 04 00	-71 29	4	-	-	-	-	-	-	-	-	0.15	-	-	-		S	
377	05 04 05	-66 34	4	-	2	-	9	3	9	3	2xp:	0.26	0.35	3.1	13.6		C	
378	05 04 05.1	-68 02 14	6	3	3	1	15	12	16	14	-	0.11:	0.22	1.2	4.2:	05040-6802	C	
379	05 04 07	-66 31	5	-	-	-	-	-	-	-	-	0.19	-	-	-		S	
380	05 04 10	-68 37	15	7	6	3	29	20	30	28	-	0.30	0.33	3.7	4.2:		C	
381	05 04 13.0	-65 58 25	-	-	3	-	9	4	9	6	-	-	0.33	2.1	6.2	05042-6558	C	
382	05 04 13.7	-68 29 45	8	4	3	2	20	16	-	-	-	0.15:	0.11:	1.7	C	05042-6829	W	
383	05 04 15.9	-67 20 27	20	5	8	3	-	-	-	-	p	0.56	0.56	-	-	05042-6720	W	
384	05 04 16.6	-68 27 55	7	3	5	2	16	14	-	-	-	0.15:	0.33	0.8:	C	05042-6827	W	
385	05 04 16.8	-71 11 08	2	-	3	-	-	-	-	-	p	0.07:	0.33	C	C	05042-7111	W	
386	05 04 19.7	-67 15 09	12	9	6	4	22	15	20	15	-	0.11:	0.22	2.9	10.4:	05043-6715	C	
387	05 04 25	-67 09	9	6	2	1	15	10	17	15	-	0.11	0.11:	2.1	4.2		C	
388	05 04 30	-68 56	4	-	1.5	-	25	15	23	19	-	0.15:	0.17:	4.1	8.3		C	
389	05 04 30	-69 12	10	7	5	3	-	-	-	-	-	0.11	0.22:	C	C		W	
390	05 04 35	-69 03	9	5	5	3	34	30	32	30	-	0.15	0.22	1.7:	4.2:		C	
391	05 04 40	-68 08	12	7	5	3	-	-	-	-	-	0.19	0.22	C	C		W	
392	05 04 41.9	-65 43 45	-	-	-	-	4	2	5	3	-	-	-	0.8	4.2	05046-6543	C	
393	05 04 42.8	-67 54 00	4	-	3	1.5	19	13	19	13	-	0.15	0.17	2.5	12.5	05047-6753	C	
394	05 04 43.2	-66 44 22	16	2	26	2	47	7	23	9	p	0.52	2.66	16.6	29.1	05047-6644	C	
395	05 04 45.4	-71 10 53	2	-	5	-	16	2	11	3	p:	0.07:	0.56	5.8	16.6	05047-7110	C	
396	05 04 47.3	-66 42 02	10	1	6	1	13	7	-	-	p	0.33	0.56	2.5	C	05047-6642	W	
397	05 04 47.9	-66 53 28	11	4	7	1	21	8	17	12	1×1	0.39	0.93	6.1	10.9	05047-6653	C	
398	05 04 50	-70 14	14	10	9	5	30	26	-	-	p:	0.15	0.44	1.7:	C		W	
399	05 04 50	-70 50	20	3	23	4	65	10	35	10	p	0.63	2.11	22.8	52.0	05049-7047: X0504-708	C	
400	05 05 00	-68 33	13	8	5	2	33	24	34	31	-	0.19	0.33	3.7	6.2		C	
401	05 05 00	-69 08	15	9	7	4	42	38	40	36	-	0.22	0.33	1.7	8.3		C	
402	05 05 00	-69 49	-	-	1	-	6	4	7	6	-	-	0.11	0.8	2.1		C	
403	05 05 00	-71 28	4	-	-	-	4	2	4	2	-	0.15:	-	0.8	4.2		C	
404	05 05 04.5	-67 37 53	4	-	6	1.5	22	8	15	10	-	0.15:	0.50	5.8	10.4:	05050-6737	C	
405	05 05 08.0	-68 07 31	18	7	23	4	81	20	44	18	p	0.41	2.11	25.3	54.1	05051-6807 X0505-681	C	
406	05 05 09.0	-68 58 11	10	6	1	-	-	-	-	-	p:	0.15	0.11:	-	-	05051-6858	S	
407	05 05 10	-70 31	-	-	-	-	4	2	2	1	-	-	-	0.8	2.1		C	
408	05 05 10.1	-67 58 44	4	-	-	-	-	-	-	-	-	0.15:	-	-	-	05051-6758	S	
409	05 05 11.5	-70 58 30	42	-	109	3	161	9	48	7	p	1.55	11.77	62.9	85.3	05051-7058 X0505-709	C	
410	05 05 15	-66 57	3	-	5	-	16	10	-	-	-	0.11:	0.56:	2.5:	C		W	
411	05 05 15	-68 06	12	7	4	3	-	-	-	-	-	0.19	0.11	C	C		S	
412	05 05 17.4	-70 11 29	26	10	30	7	105	45	60	35	p	0.59	2.55	24.8	52.0	05052-7011 X0505-702	C	
413	05 05 19.1	-69 01 37	9	6	3	1.5	18	16	-	-	-	0.11	0.17	0.8:	-	05053-6901	W	
414	05 05 19.3	-66 59 03	22	6	70	1	87	10	33	12	p	0.59	7.66	31.9	43.7	05053-6659	C	
415	05 05 20	-69 21	4	-	3	1	11	8	11	9	-	0.15:	0.22	1.2	4.2		C	
416	05 05 27.0	-67 39 19	-	-	3	-	-	-	-	-	p:	-	0.33	-	-	05054-6739	W	
417	05 05 30	-70 09	9	8	4	3	30	26	34	30	-	0.04:	0.11	1.7	8.3		C	
418	05 05 30	-71 05	3	-	2	-	6	4	8	5	-	0.11:	0.22	0.8	6.2		C	
419	05 05 35	-68 11	13	7	6	4	44	35	37	33	-	0.22	0.22	3.7:	8.3:		C	
420	05 05 38.9	-69 52 38	-	-	1	-	9	7	8	6	-	-	0.11:	0.8	4.2	05056-6952	C	
421	05 05 45	-67 06	3	-	-	-	10	7	12	10	-	0.11:	-	1.2	4.2		C	
422	05 05 45	-68 32	11	7	3	2	30	25	23	21	-	0.15	0.11	2.1	4.2:		C	
423	05 05 46.4	-67 56 44	-	-	1.5	-	10	9	-	-	-	-	0.17:	0.4:	-	05057-6756	W	
424	05 05 48	-72 29	10	3	-	-	-	-	-	-	p	0.26	-	-	-		S	SAO 256158
425	05 05 53.8	-68 43 04	7	-	3	1.5	-	-	-	-	p	0.26	0.17:	-	-	05058-6843	S	
426	05 05 57.4	-66 46 38	-	-	2	-	9	6	9	7	-	-	0.22:	1.2	4.2:	05059-6646	C	
427	05 06 00	-69 14	12	4	4	3	30	28	26	24	-	0.30	0.11:	0.8	4.2		C	
428	05 06 00	-71 37	-	-	1	-	4	2	-	-	-	-	0.11:	0.8	-		W	
429	05 06 00.6	-68 14 57	8	5	9	4	44	25	-	-	-	0.11:	0.56	7.9	C	05060-6814	W	
430	05 06 05.1	-70 37 40	5	-	2	-	2	-	-	-	-	0.19	0.22	0.8	-	05060-7037	W	
431	05 06 09.9	-65 47 01	-	-	1	-	4	2	5	4	-	-	0.11:	0.8	2.1	05061-6547	C	
432	05 06 10	-66 47	5	-	2	-	9	6	9	7	-	0.19:	0.22	1.2	4.2:		C	
433	05 06 10	-67 24	-	-	-	-	10	7	11	9	-	-	-	1.2	4.2		C	
434	05 06 10.7	-68 41 38	-	-	-	-	18	12	16	15	-	-	-	2.5	2.1:	05061-6841	W	
435	05 06 15	-68 09	14	8	7	4	-	-	-	-	-	0.22	0.33	C	C		W	
436	05 06 20.6	-69 08 08	10	7	5	2	-	-	-	-	-	0.11:	0.33	-	-	05063-6908	W	
437	05 06 26.7	-65 26 26	8	-	1	-	-	-	-	-	p	0.30:	0.11:	-	-	05064-6526	S	SAO 249195
438	05 06 39.0	-69 03 12	2	-	4	3	23	19	20	18	-	0.07:	0.11:	1.7	4.2	05066-6903	C	
439	05 06 39.2	-70 02 46	5	3	-	-	17	14	-	-	-	0.07:	-	1.2	-	05066-7002	W	
440	05 06 39.3	-70 14 02	14	6	5	3	35	25	30	23	p	0.30	0.22:	4.1	14.6	05066-7014	C	
441	05 06 40	-65 39	-	-	-	-	5	2	5	2	-	-	-	1.2:	6.2		C	
442	05 06 40	-68 28	-	-	4	3	32	26	23	21	-	-	0.11	2.5	4.2:		C	
443	05 06 40	-68 36	17	8	6	3	40	30	35	30	-	0.33	0.33	4.1	10.4		C	
444	05 06 40	-69 41	6	-	1.5	-	-	-	-	-	-	0.22	0.17:	-	-		S	
445	05 06 40	-71 02	4	-	1	-	9	5	8	4	-	0.15	0.11:	1.7	8.3		C	
446	05 06 45	-69 35	4	-	1	-	5	3	4	3	-	0.15:	0.11:	0.8	2.1		C	
447	05 06 49.2	-68 13 15	14	7	9	4	42	24	35	23	p:	0.26	0.56	7.5	25.0	05068-6813	C	
448	05 06 51.8	-70 32 10	13	3	8	1.5	34	11	25	9	1×1:	0.55	1.00	10.8	34.8	05068-7032 X0506-705	C	
449	05 06 53.8	-67 10 19	-	-	-	-	8	6	8	7	-	-	-	0.8	2.1	05068-6710	C	
450	05 06 56.7	-70 47 46	4	-	2	-	14	8	11	9	-	0.15:	0.22:	2.5	4.2:	05069-7047	C	

Table 3, continued (6).

(1)	(2)		(3)		(4)		(5)		(6)		(7)	(8)	(9)	(10)	(11)	(12)	(13)	(14)
Number	Position RA(1950)	DEC(1950)	12 µm Peak	Bg	25 µm Peak	Bg	60 µm Peak	Bg	100 µm Peak	Bg	Size	F 12µm	F 25µm	F 60µm	F 100µm	IRAS-Id	Spectrum	Comments
	h m s	° ' "			10^{-8} Watt $m^{-2}sr^{-1}$						arcmin	Jy	Jy	Jy	Jy			
451	05 07 00	-69 17	10	6	5	3	32	26	-	-	-	0.15	0.22	2.5	C		W	
452	05 07 00.6	-69 21 58	8	4	3	2	20	16	21	18	-	0.15:	0.11:	1.7:	6.2:	05070-6921	C	
453	05 07 01.4	-65 34 20	-	-	-	-	3	2	6	3	-	-	-	0.4	6.2	05070-6534	C	
454	05 07 03.3	-67 57 41	4	-	1	-	9	6	10	7	-	0.15	0.11:	1.2	6.2	05070-6757	C	
455	05 07 03.3	-70 20 43	5	-	3	-	2	-	4	3	-	0.19	0.33	0.8	2.1:	05070-7020	C	
456	05 07 10	-66 53	-	-	-	-	10	7	8	6	-	-	-	1.2	4.2		C	
457	05 07 15	-68 26	10	6	6	3	34	26	29	25	-	0.15	0.33	3.3	8.3		C	
458	05 07 17.2	-68 44 59	2	-	3	2	23	20	-	-	-	0.07:	0.11:	1.2	-	05072-6844	W	
459	05 07 19.0	-68 50 31	7	4	2	1.5	23	20	17	13	-	0.11	0.06:	1.2:	8.3:	05073-6850	C	
460	05 07 20	-66 30	-	-	-	-	4	2	5	3	-	-	-	0.8	4.2		C	
461	05 07 20	-68 36	11	7	7	4	52	35	40	35	-	0.15	0.33	7.0	10.4:		C	
462	05 07 20	-69 56	-	-	1.5	-	10	8	12	10	-	-	0.17	0.8	4.2		C	
463	05 07 20.0	-67 52 43	6	-	4	-	6	4	-	-	p	0.22	0.44	0.8:	-	05073-6752	W	
464	05 07 27.9	-66 47 15	-	-	1	-	9	7	7	5	-	-	0.11:	0.8	4.2	05074-6647	C	
465	05 07 30	-69 06	14	6	5	3	33	28	32	30	-	0.30	0.22	2.1	4.2		C	
466	05 07 30	-69 12	9	6	5	3	24	22	22	21	-	0.11	0.22	0.8	2.1:		C	
467	05 07 35	-67 16	-	-	-	-	9	7	9	8	-	-	-	0.8	2.1		C	
468	05 07 40	-70 08	-	-	2	1	21	19	20	19	-	-	0.11:	0.8	2.1		C	
469	05 07 40.4	-70 47 04	8	4	3	-	18	12	17	12	-	0.15:	0.33	2.5	10.4	05076-7047	C	
470	05 07 44.2	-71 19 53	16	-	2	-	-	-	-	-	p	0.59	0.22:	-	-	05077-7119	S	SAO 256161
471	05 07 45	-70 12	-	-	-	-	24	22	24	22	-	-	-	0.8	4.2		C	
472	05 07 50	-68 33	14	10	6	3	47	39	-	-	-	0.15	0.33	3.3	C		W	
473	05 07 50	-68 36	12	8	7	5	59	36	40	35	-	0.15	0.22	9.5	10.4:		C	
474	05 07 50	-69 17	6	4	4	3	34	31	26	24	-	0.07:	0.11	1.2	4.2		C	
475	05 07 55	-68 51	-	-	3	1.5	27	24	20	18	-	-	0.17	1.2·	4.2		C	
476	05 08 00	-71 04	3	-	-	-	-	-	-	-	-	0.11:	-	-	-		S	
477	05 08 00	-71 36	-	-	-	-	4	2	4	2	-	-	-	0.8	4.2		C	
478	05 08 03.9	-68 59 56	21	10	7	4	42	30	38	35	p	0.41	0.33	5.0	6.2:	05080-6859	C	
479	05 08 05	-70 44	4	-	3	1	13	11	13	12	-	0.15:	0.22	0.8	2.1:		C	
480	05 08 11.2	-67 41 38	2	-	1	-	11	6	9	7	-	0.07:	0.11:	2.1	4.2	05081-6741	C	
481	05 08 11.9	-68 55 33	-	-	7	3	35	30	-	-	-	-	0.44	2.1:	C	05081-6855	W	
482	05 08 12	-68 29	11	7	4	3	39	30	30	28	-	0.15	0.11	3.7	4.2		C	
483	05 08 15.5	-68 44 21	6	4	4	3	35	30	-	-	-	0.07:	0.11	2.1:	C	05082-6844	W	
484	05 08 19.6	-70 55 43	3	-	1	-	9	7	-	-	-	0.11:	0.11:	0.8	C	05083-7055	W	
485	05 08 22	-66 52	2	-	2	-	9	7	6	5	-	0.07:	0.22:	0.8:	2.1		C	
486	05 08 30	-66 43	-	-	3	-	6	4	5	4	-	-	0.33	0.8:	2.1:		C	
487	05 08 30	-70 15	-	-	2	1	20	18	24	22	-	-	0.11:	0.8	4.2		C	
488	05 08 30	-70 32	3	-	2	1	13	11	12	11	-	0.11:	0.11	0.8	2.1		C	
489	05 08 30	-71 17	3	-	1	-	10	5	8	4	p	0.11:	0.11:	2.1	8.3	05079-7115:	C	
490	05 08 33.5	-70 09 38	2	-	2	1	20	18	-	-	-	0.07.	0.11:	0.8:	C	05085-7009	W	
491	05 08 34.2	-70 39 31	4	2	3	1.5	14	10	16	12	-	0.07:	0.17	1.7	8.3	05085-7039	C	
492	05 08 40	-68 23	7	4	4	2	31	21	28	24	-	0.11	0.22	4.1	8.3		C	
493	05 08 40	-68 57	16	13	7	6	-	-	-	-	-	0.11:	0.11:	C	C		C	
494	05 08 40	-69 03	19	14	9	6	49	41	47	42	-	0.19	0.33	3.3	10.4		C	
495	05 08 40	-69 25	23	12	8	5	45	38	40	35	-	0.41	0.33	2.9	10.4:		C	
496	05 08 44.4	-67 13 04	5	2	-	-	10	9	11	9	-	0.11:	-	0.4:	4.2	05087-6713	C	
497	05 08 50	-66 22	-	-	-	-	5	3	4	2	-	-	-	0.8	4.2		C	
498	05 08 50	-70 03	2	-	2	1	16	14	14	12	-	0.07:	0.11	0.8	4.2		C	
499	05 08 50	-70 35	4	-	2	1	13	10	13	12	-	0.15	0.11	1.2	2.1		C	
500	05 08 53	-67 14	6	-	1	-	-	-	-	-	-	0.22	0.11:	-	-		S	SAO 249201
501	05 08 54.8	-68 42 11	11	9	6	4	35	30	38	35	-	0.07:	0.22	2.1:	6.2:	05089-6842	C	
502	05 08 57.0	-69 28 28	25	18	14	9	65	42	67	43	p	0.26:	0.56	9.5	49.9	05089-6928	C	
503	05 08 58.5	-69 06 47	18	10	6	4	34	29	35	32	-	0.30	0.22	2.1	6.2:	05089-6906	C	
504	05 09 00	-71 21	5	-	2	-	6	2	7	5	p	0.19	0.22	1.7	4.2	05092-7121:	C	
505	05 09 02.2	-70 50 58	-	-	1	-	8	6	-	-	-	-	0.11:	0.8:	C	05090-7050	W	
506	05 09 05	-67 15	4	-	1.5	-	13	10	13	12	-	0.15	0.17	1.2	2.1		C	
507	05 09 10	-68 32	18	11	6	4	42	38	-	-	-	0.26	0.22	1.7:	C	X0509-685*	W	
508	05 09 10.3	-69 04 33	19	12	7	5	-	-	-	-	-	0.26	0.22	C	C	05091-6904	S	
509	05 09 15	-71 53	-	-	-	-	2	-	3	2	-	-	-	0.8	2.1		C	
510	05 09 16.1	-68 48 15	30	16	20	11	95	60	72	50	p	0.52	1.00	14.5	45.8	05092-6848	C	
511	05 09 24	-71 35	5	-	-	-	4	2	4	3	-	0.19	-	0.8:	2.1		C	
512	05 09 25	-70 10	5	-	1.5	-	-	-	-	-	-	0.19	0.17:	-	-		S	
513	05 09 25.7	-67 51 03	4	-	5	1	-	-	-	-	p	0.15:	0.44	-	-	05094-6751	W	
514	05 09 26.3	-68 33 53	20	11	23	3	68	30	52	34	p	0.33	2.22	15.7	37.4	05094-6833 X0509-685*	C	
515	05 09 30	-69 41	-	-	-	-	9	8	9	8	-	-	-	0.4	2.1		C	
516	05 09 30.3	-70 59 31	-	-	1	-	7	5	8	6	-	-	0.11:	0.8:	4.2:	05095-7059	C	
517	05 09 31.8	-65 25 35	4	-	2	-	-	-	-	-	-	0.15:	0.22:	-	-	05095-6525	W	
518	05 09 34.9	-68 51 44	30	18	17	14	100	85	80	70	p:	0.44	0.33	6.2	20.8:	05095-6851	C	
519	05 09 36	-71 07	-	-	1	-	8	3	8	5	-	-	0.11:	2.1	6.2		C	
520	05 09 38.6	-68 49 30	29	18	24	10	-	-	-	-	p:	0.41	1.55	C	C	05096-6849	W	
521	05 09 40	-69 21	14	9	6	4	23	21	-	-	-	0.19	0.22	0.8:	C		W	
522	05 09 45	-69 13	12	8	-	-	-	-	-	-	-	0.15:	-	-	-		S	SAO 249209
523	05 09 45	-70 22	8	-	3	1	20	17	23	19	-	0.30:	0.22:	1.2	8.3		C	
524	05 09 49.3	-68 42 23	23	14	14	5	58	36	47	38	p	0.33	1.00	9.1	18.7	05098-6842	C	
525	05 09 50	-67 58	7	3	2	-	22	14	22	15	-	0.15	0.22:	3.3	14.6		C	
526	05 09 50	-69 47	3	-	-	-	-	-	-	-	-	0.11:	-	-	-		S	SAO 249210
527	05 09 50	-70 55	5	-	2	1	10	8	12	9	-	0.19	0.11	0.8	6.2		C	
528	05 09 59.6	-67 40 19	5	-	4	-	6	4	7	5	p	0.19	0.44	0.8	4.2	05099-6740	C	
529	05 10 00	-68 46	20	15	10	7	-	-	-	-	-	0.19	0.33	C	C		W	
530	05 10 00	-69 28	21	15	9	7	-	-	-	-	-	0.22	0.22	-	-		W	
531	05 10 00.0	-68 50 04	27	18	14	8	-	-	-	-	p:	0.33	0.67:	C	C	05100-6850	W	
532	05 10 00.2	-66 29 03	21	-	2	-	-	-	-	-	p	0.78	0.22	-	-	05100-6629	S	SAO 249212
533	05 10 03.0	-68 12 10	-	-	-	-	18	13	17	14	-	-	-	2.1	6.2	05100-6812	C	
534	05 10 05	-68 57	220	27	490	20	830	70	280	65	p	7.14	52.17	314.6	447.2	05101-6855A:	C	
535	05 10 08.8	-69 05 58	12	9	5	4	40	35	-	-	-	0.11	0.11:	2.1:	C	05101-6905	W	
536	05 10 09.9	-69 17 38	25	14	9	7	55	35	45	35	-	0.41	0.22	8.3	20.8:	05101-6917	C	
537	05 10 22.0	-69 29 34	25	11	10	6	52	38	53	40	p:	0.52	0.44:	5.8	27.0	05103-6929	C	
538	05 10 22.0	-71 31 20	3	-	5	-	15	3	7	3	p	0.11:	0.56	5.0	8.3	05103-7131	C	
539	05 10 22.4	-69 59 25	5	-	1	-	9	8	8	7	-	0.19	0.11:	0.4:	2.1	05103-6959	C	
540	05 10 24	-71 39	-	-	-	-	4	2	4	3	-	-	-	0.8	2.1		C	

Table 3, continued (7).

(1) Number	(2) Position RA(1950)	DEC(1950)	(3) 12 μm Peak	Bg	(4) 25 μm Peak	Bg	(5) 60 μm Peak	Bg	(6) 100 μm Peak	Bg	(7) Size	(8) F 12μm	(9) F 25μm	(10) F 60μm	(11) F 100μm	(12) IRAS-Id	(13) Spectrum	(14) Comments
	h m s	° ' "			10^{-8} Watt $m^{-2} sr^{-1}$						arcmin	Jy	Jy	Jy	Jy			
541	05 10 25	-69 16	22	15	8	6	52	50	-	-	-	0.26	0.22	0.8:	C		W	
542	05 10 25	-69 25	13	8	6	3	25	17	30	28	p:	0.19	0.33	3.3	4.2:	05104-6923:	C	
543	05 10 30	-67 12	9	6	4	2	24	11	23	20	-	0.11	0.22	5.4	6.2		C	
544	05 10 32.4	-68 27 49	10	7	4	2	28	22	28	25	-	0.11	0.22:	2.5	6.2	05105-6827	C	
545	05 10 33.3	-67 58 28	-	-	2	1	17	15	16	15	-	-	0.11	0.8	2.1:	05105-6758	C	
546	05 10 35	-68 32	12	7	4	2	32	25	30	27	-	0.19	0.22	2.9	6.2		C	
547	05 10 38.2	-68 06 18	-	-	3	1	18	14	13	12	p:	-	0.22	1.7	2.1:	05106-6806	C	
548	05 10 38.5	-68 49 44	16	12	9	6	45	35	40	37	-	0.15	0.33	4.1	6.2:	05106-6849	C	
549	05 10 39.0	-66 36 51	-	-	1	-	6	4	5	3	-	-	0.11:	0.8	4.2	05106-6636	C	
550	05 10 39.3	-69 09 16	19	16	7	5	60	55	57	54	-	0.11:	0.22:	2.1:	6.2:	05106-6909	C	
551	05 10 44.2	-69 30 07	20	12	12	6	-	-	-	-	-	0.30:	0.67	C	C	05107-6930	W	
552	05 10 45.6	-69 53 43	8	-	2	-	11	9	9	8	p	0.30	0.22:	0.8	2.1	05107-6953	C	
553	05 10 46.1	-67 08 38	13	6	8	2	31	11	26	18	p	0.26	0.67	8.3	16.6	05107-6708	C	
554	05 10 50	-69 23	10	7	-	-	-	-	-	-	-	0.11:	-	-	-		S	SAO 249214
555	05 10 50	-70 35	5	-	1	-	7	5	7	6	-	0.19	0.11:	0.8	2.1		C	
556	05 10 52.3	-70 17 41	9	4	13	2	24	14	17	16	p	0.19	1.22	4.1	33.3:	05108-7017	C	
557	05 10 52.9	-68 39 34	17	8	5	3	28	20	-	-	p	0.33	0.22	3.3:	C	05108-6839	W	
558	05 10 54	-71 05	2	-	1	-	8	4	7	6	-	0.07:	0.11:	1.7	2.1		C	
559	05 10 55.3	-66 56 55	-	-	-	-	10	7	12	8	-	-	-	1.2	8.3	05109-6656	C	
560	05 10 55.9	-67 02 53	8	4	1.5	-	14	10	15	12	-	0.15:	0.17:	1.7	6.2:	05109-6702	C	
561	05 10 56.7	-65 57 35	-	-	-	-	3	-	2	1	p:	-	-	1.2	2.1:	05109-6557	C	
562	05 11 00	-68 21	9	6	4	2	22	20	24	22	-	0.11	0.22	0.8	4.2		C	
563	05 11 00	-70 25	4	-	3	1	17	15	24	22	-	0.15	0.22	0.8	4.2		C	
564	05 11 00.5	-67 11 25	6	4	4	1.5	-	-	-	-	-	0.07:	0.28	C	C	05110-6711	W	
565	05 11 01.4	-72 08 13	4	1	-	-	-	-	-	-	p	0.11	-	-	-	05110-7208	S	SAO 256166/5
566	05 11 05	-69 03	23	18	11	8	-	-	-	-	-	0.19	0.33	C	C		W	
567	05 11 05.5	-66 16 35	5	-	3	-	-	-	-	-	p	0.19	0.33	-	-	05110-6616	W	
568	05 11 10	-68 45	16	10	6	4	40	28	33	29	-	0.22	0.22	5.0	8.3	05112-6843:	C	
569	05 11 15	-69 41	9	2	1.5	-	-	-	-	-	p:	0.26	0.17:	-	-		S	
570	05 11 17.3	-67 55 49	16	5	5	2	15	12	16	15	p	0.41	0.33	1.2	2.1:	05112-6755	C	
571	05 11 18.4	-67 39 57	9	-	3	1.5	-	-	-	-	p	0.33	0.17	-	-	05113-6739	S	
572	05 11 20	-67 47	4	-	1.5	-	17	14	16	15	-	0.15	0.17:	1.2	2.1		C	
573	05 11 20	-68 57	22	15	13	9	-	-	-	-	-	0.26	0.44	C	C		W	
574	05 11 20	-70 08	-	-	1	-	14	11	12	10	-	-	0.11:	1.2	4.2		C	
575	05 11 20.1	-69 39 07	8	-	3	1	16	12	-	-	p:	0.30	0.22	1.7:	C	05113-6939	W	
576	05 11 24	-71 13	6	-	-	-	-	-	-	-	-	0.22	-	-	-		S	
577	05 11 30	-66 30	-	-	-	-	4	2	4	3	-	-	-	0.8:	2.1		C	
578	05 11 30	-66 56	5	-	1	-	-	-	-	-	-	0.19	0.11:	C	C		S	
579	05 11 30	-67 27	3	-	1.5	-	13	9	13	11	-	0.11:	0.17:	1.7	4.2		C	
580	05 11 30	-68 39	12	8	4	3	32	26	27	24	-	0.15	0.11	2.5	6.2		C	
581	05 11 38.4	-71 45 04	2	-	-	-	4	2	4	3	-	0.07:	-	0.8	2.1	05116-7145	C	
582	05 11 40	-69 12	30	18	13	8	80	70	75	70	-	0.44	0.56	4.1:	10.4:		C	
583	05 11 48	-71 07	-	-	1.5	-	8	5	8	6	-	-	0.17:	1.2	4.2		C	
584	05 11 48.4	-70 18 37	9	3	3	1	13	9	15	14	-	0.22	0.22	1.7:	2.1:	05118-7018	C	
585	05 11 49.7	-69 36 16	35	9	7	4	33	30	-	-	p	0.96	0.33	1.2	-	05118-6936	W	SAO 249217
586	05 11 50	-69 06	33	24	13	10	70	65	75	70	-	0.33	0.33	2.1:	10.4:		C	
587	05 11 50	-69 20	-	-	-	-	30	28	26	25	-	-	-	0.8	2.1		C	
588	05 11 51.7	-68 47 17	-	-	4	3	-	-	-	-	-	-	0.11:	-	-	05118-6847	W	
589	05 11 55.6	-68 52 28	8	6	4	3	36	30	27	24	-	0.07:	0.11:	2.5	6.2:	05119-6852	C	
590	05 12 00	-69 46	8	5	4	2	25	21	28	25	-	0.11:	0.22	1.7	6.2		C	
591	05 12 04.3	-69 31 19	22	14	10	6	47	33	42	37	p	0.30	0.44	5.8	10.4	05120-6931	C	
592	05 12 05.0	-67 17 46	6	4	4	2	24	16	25	18	-	0.07:	0.22	3.3	14.6:	05120-6717	C	
593	05 12 08.1	-70 42 18	2	-	1	-	10	8	10	9	-	0.07:	0.11:	0.8	2.1	05121-7042	C	
594	05 12 10	-67 15	13	6	6	2	-	-	-	-	p:	0.26	0.44	C	C		W	
595	05 12 10	-67 53	9	5	2	1	-	-	-	-	-	0.15	0.11:	-	-		S	
596	05 12 15	-66 04	-	-	-	-	2	-	2	1	p:	-	-	0.8	2.1		C	
597	05 12 15.4	-68 31 22	-	-	3	1.5	21	18	20	16	-	-	0.17	1.2	8.3:	05122-6831	C	
598	05 12 20	-68 35	10	6	3	1.5	28	23	22	20	-	0.15	0.17	2.1	4.2:		C	
599	05 12 29.5	-67 12 22	15	6	7	2	34	19	32	18	p:	0.33	0.56	6.2	29.1	05124-6712	C	
600	05 12 30	-69 23	15	10	6	4	50	45	-	-	-	0.19	0.22:	2.1:	C		W	
601	05 12 30	-69 43	16	10	5	3	31	29	35	33	-	0.22	0.22:	0.8:	4.2:		C	
602	05 12 30	-70 14	-	-	1	-	9	8	8	7	-	-	0.11:	0.4:	2.1		C	
603	05 12 32.4	-70 35 52	17	6	6	2	13	11	-	-	p	0.41	0.44	0.8:	C	05125-7035	W	
604	05 12 32.7	-68 02 59	-	-	1.5	-	14	10	12	10	-	-	0.17	1.7	4.2:	05125-6802	C	
605	05 12 33.4	-70 53 27	-	-	-	-	8	6	8	7	-	-	-	0.8:	2.1:	05125-7053	C	
606	05 12 36	-71 31	2	-	-	-	4	2	5	3	-	0.07:	-	0.8	4.2		C	
607	05 12 40	-68 22	3	-	3	1.5	19	17	19	17	-	0.11:	0.17	0.8	4.2		C	
608	05 12 40.0	-69 37 32	-	-	6	4	42	38	-	-	-	-	0.22	1.7	C	05126-6937	W	
609	05 12 42.0	-71 13 46	3	-	1	-	9	7	8	5	-	0.11:	0.11:	0.8	6.2	05127-7113	C	
610	05 12 45	-70 32	19	7	11	4	45	25	35	30	p:	0.44	0.78	8.3	10.4:	05127-7030: X0512-705	C	
611	05 12 45.8	-69 11 23	-	-	11	8	-	-	-	-	p:	-	0.33	C	C	05127-6911	W	
612	05 12 49.6	-67 23 08	13	6	5	2	-	-	-	-	p	0.26	0.33	-	-	05128-6723	W	
613	05 12 50	-67 38	8	5	3	1.5	22	19	23	21	-	0.11	0.17	1.2	4.2		C	
614	05 12 50	-69 07	32	20	11	8	58	54	65	60	-	0.44	0.33	1.7	10.4		C	
615	05 12 52.7	-69 19 27	19	13	-	-	-	-	-	-	-	0.22	-	-	-	05128-6919	S	
616	05 12 57	-71 12	9	1	3	-	12	6	13	5	-	0.30	0.33	2.5	16.6		C	
617	05 12 57.2	-68 13 55	7	4	2	1	15	12	16	13	-	0.11	0.11:	1.2	6.2	05129-6813	C	
618	05 13 00	-66 43	-	-	-	-	6	4	6	4	-	-	-	0.8	4.2		C	
619	05 13 00	-70 26	9	6	5	3	23	20	-	-	-	0.11:	0.22:	1.2	C		W	
620	05 13 00.2	-70 27 59	28	8	22	4	73	27	39	27	p	0.74	2.00	19.0	25.0	05130-7027	C	
621	05 13 02.6	-71 06 11	3	-	1.5	-	9	7	8	5	-	0.11:	0.17	0.8	6.2	05130-7106	C	
622	05 13 10	-70 36	11	5	5	3	14	12	-	-	-	0.22	0.22	0.8	C		W	
623	05 13 12.0	-69 41 08	21	14	9	7	-	-	-	-	-	0.26:	0.22:	C	C	05132-6941	S	
624	05 13 15	-67 41	-	-	-	-	20	15	20	18	-	-	-	2.1	4.2		C	
625	05 13 17.0	-66 54 28	-	-	-	-	10	7	10	8	-	-	-	1.2:	4.2:	05132-6654	C	
626	05 13 18	-71 28	-	-	-	-	4	2	4	3	-	-	-	0.8	2.1		C	
627	05 13 20	-69 11	19	15	11	9	70	62	-	-	-	0.15	0.22	3.3	C		W	
628	05 13 20.3	-69 48 21	-	-	-	-	19	16	17	14	-	-	-	1.2	6.2	05133-6948	C	
629	05 13 21.1	-69 31 53	15	10	8	6	46	41	40	37	-	0.19	0.22:	2.1:	6.2:	05133-6931	C	
630	05 13 21.1	-70 01 28	-	-	-	-	9	7	8	6	-	-	-	0.8	4.2	05133-7001	C	

Table 3, continued (8).

(1)	(2)		(3)		(4)		(5)		(6)		(7)	(8)	(9)	(10)	(11)	(12)	(13)	(14)
Number	Position RA(1950) h m s	DEC(1950) o ' "	12 µm Peak	Bg	25 µm Peak	Bg	60 µm Peak	Bg	100 µm Peak	Bg	Size arcmin	F 12µm Jy	F 25µm Jy	F 60µm Jy	F 100µm Jy	IRAS-Id	Spec-trum	Comments
					10^{-8} Watt $m^{-2}sr^{-1}$													
631	05 13 22.6	-69 37 07	20	14	9	6	60	50	50	45	-	0.22:	0.33:	4.1:	10.4:	05133-6937	C	
632	05 13 25.8	-67 31 57	18	7	9	4	45	28	-	-	p:	0.41	0.56	7.0	C	05134-6731	W	
633	05 13 30	-69 44	19	13	5	3	43	40	46	45	-	0.22	0.22	1.2	2.1:		C	
634	05 13 35	-69 39	33	20	17	13	70	65	-	-	-	0.48	0.44	2.1:	C		W	
635	05 13 40.2	-69 25 37	190	27	400	30	770	150	260	115	p	6.03	41.07	256.7	301.6	05136-6925	C	
636	05 13 43.8	-69 14 17	33	13	30	7	100	60	68	60	p	0.74	2.55	16.6	16.6:	05137-6914	C	
637	05 13 45	-69 01	-	-	3	2	31	28	27	26	-	-	0.11:	1.2	2.1		C	
638	05 13 45.4	-67 02 10	5	2	2	1	14	10	14	11	-	0.11:	0.11	1.7	6.2:	05137-6702	C	
639	05 13 47.3	-67 14 30	180	5	17	1.5	-	-	-	-	-	6.47	1.72	-	-	05137-6714	S	SAO 249225
640	05 13 50	-69 21	35	22	30	18	160	130	110	70	p:	0.48	1.33	12.4	83.2		C	
641	05 13 53.7	-67 10 26	17	7	7	2	36	26	28	17	-	0.37	0.56	4.1	22.9	05138-6710	C	
642	05 13 55.9	-67 30 39	50	14	90	5	175	28	76	22	p	1.33	9.43	60.9	112.3	05139-6730 X0513-674	C	
643	05 14 00	-67 24	11	6	6	2	20	16	-	-	-	0.19	0.44	1.7:	C		W	
644	05 14 00	-69 09	15	11	6	4	-	-	-	-	-	0.15	0.22:	-	-		W	
645	05 14 00	-70 00	-	-	-	-	10	8	-	-	-	-	-	0.8	-		W	
646	05 14 02.1	-67 26 12	18	7	18	3	59	27	-	-	p	0.41	1.66	13.2	C	05140-6726	W	
647	05 14 06	-71 11	4	-	4	-	10	6	10	5	p	0.15	0.44	1.7	10.4		C	
648	05 14 07.0	-69 38 57	40	20	32	13	135	65	85	50	px1	0.92	2.52	30.9	74.5	05141-6938	C	
649	05 14 07.3	-66 27 41	3	-	1	-	7	4	7	4	p:	0.11:	0.11:	1.2	6.2	05141-6627	C	
650	05 14 12	-71 42	-	-	-	-	3	2	4	2	-	-	-	0.4	4.2		C	
651	05 14 12	-71 48	-	-	1	-	4	2	4	2	-	-	0.11:	0.8	4.2		C	
652	05 14 15	-66 19	-	-	-	-	5	2	4	2	-	-	-	1.2	4.2		C	
653	05 14 15	-68 50	9	6	5	3	32	24	28	25	-	0.11	0.22	3.3	6.2		C	
654	05 14 15	-69 17	20	16	9	7	-	-	-	-	-	0.15	0.22	C	C		W	
655	05 14 15	-70 18	13	6	3	1	21	17	20	18	p	0.26	0.22	1.7	4.2:	05146-7018:	C	
656	05 14 20	-67 34	15	8	7	4	-	-	-	-	-	0.26	0.33	C	C		W	
657	05 14 30	-67 38	10	5	3	1.5	22	20	-	-	-	0.19	0.17	0.8:	C		W	
658	05 14 30	-70 47	-	-	-	-	7	6	8	7	-	-	-	0.4	2.1		C	
659	05 14 40	-69 13	16	11	6	5	48	44	45	40	-	0.19	0.11:	1.7:	10.4:		C	
660	05 14 40	-70 14	16	7	4	-	23	17	26	11	-	0.33	0.44	2.5	31.2	05145-7012:	C	
661	05 14 45	-68 25	-	-	3	1.5	18	15	16	14	-	-	0.17:	1.2	4.2		C	
662	05 14 48.5	-67 15 22	9	3	6	1	24	11	16	9	p	0.22	0.56	5.4	14.6	05148-6715	C	
663	05 14 53.4	-67 30 36	14	7	7	3	23	21	-	-	-	0.26	0.44	0.8:	C	05148-6730	W	
664	05 14 55.4	-72 05 57	6	-	1.5	-	-	-	-	-	p:	0.22:	0.17:	-	-	05149-7205	S	
665	05 14 58	-69 33	17	14	24	10	100	55	47	35	-	0.11:	1.55	18.6	25.0	05148-6933:	C	
666	05 15 00	-66 00	-	-	-	-	2	-	2	1	-	-	-	0.8	2.1:		C	
667	05 15 00	-66 29	-	-	-	-	7	3	6	4	-	-	-	1.7	4.2	X0514-664	C	
668	05 15 00	-69 28	20	15	10	8	80	65	60	50	-	0.19	0.22	6.2	20.8		C	
669	05 15 00	-69 30	20	15	10	8	80	70	-	-	-	0.19	0.22	4.1	C		W	
670	05 15 00	-71 33	4	-	-	-	-	-	-	-	-	0.15:	-	-	-		S	SAO 256169
671	05 15 03.5	-69 42 36	8	-	5	1	-	-	-	-	p	0.30	0.44	-	-	05150-6942	W	
672	05 15 06.6	-68 58 01	12	8	5	3	36	33	30	27	-	0.15	0.22	1.2	6.2:	05151-6858	C	
673	05 15 11.7	-69 05 13	11	8	4	3	30	27	30	28	-	0.11	0.11:	1.2	4.2:	05151-6905	C	
674	05 15 17.5	-67 59 34	2	-	1.5	-	13	8	12	9	p:	0.07:	0.17	2.1	6.2	05152-6759	C	
675	05 15 19.0	-66 22 24	-	-	1	-	5	3	4	2	-	-	0.11:	0.8	4.2:	05153-6622	C	
676	05 15 20	-71 06	-	-	-	-	5	2	5	2	p:	-	-	1.2	6.2		C	
677	05 15 24	-71 41	-	-	-	-	5	2	4	3	-	-	-	1.2	2.1		C	
678	05 15 24.2	-65 35 48	110	-	18	-	3	-	-	-	p	4.07	2.00	1.2:	-	05154-6535	S	
679	05 15 25.8	-69 22 02	15	11	8	6	-	-	-	-	-	0.15	0.22	C	C	05154-6922	W	
680	05 15 26.8	-67 34 44	3	-	2	1	16	12	16	14	-	0.11:	0.11:	1.7	4.2:	05154-6734	C	
681	05 15 30	-69 04	15	10	6	4	34	31	33	31	-	0.19	0.22	1.2	4.2		C	
682	05 15 31.3	-69 14 25	9	7	-	-	42	38	48	46	-	0.07:	-	1.7	4.2:	05155-6914	C	
683	05 15 31.6	-70 04 41	5	-	2	-	15	13	15	12	-	0.19	0.22:	0.8:	6.2	05155-7004	C	
684	05 15 33.9	-70 36 53	6	-	4	-	13	9	14	9	-	0.22	0.44	1.7	10.4	05155-7036 X0515-706	C	
685	05 15 34.4	-72 15 34	-	-	-	-	1	-	1	-	-	-	-	0.4:	2.1:	05155-7215	C	
686	05 15 36	-71 04	7	-	-	-	-	-	-	-	p	0.26	-	-	-		S	
687	05 15 37.6	-68 52 24	13	10	5	4	-	-	-	-	-	0.11	0.11:	-	-	05156-6852	S	
688	05 15 38.7	-69 55 30	3	-	1.5	-	15	13	13	12	-	0.11:	0.17:	0.8	2.1	05156-6955	C	
689	05 15 40	-68 17	9	6	3	1.5	22	17	20	19	-	0.11	0.17	2.1	2.1		C	
690	05 15 40	-69 01	13	10	6	4	35	32	32	30	-	0.11	0.22	1.2:	4.2:		C	
691	05 15 44.0	-66 45 01	5	-	2	-	10	4	12	5	p:	0.19	0.22	2.5	14.6	05157-6645	C	
692	05 15 49.3	-68 02 16	13	3	8	2	23	8	20	15	p	0.37	0.67	6.2	10.4	05158-6802	C	
693	05 15 49.5	-68 08 01	31	6	4	1.5	16	15	20	17	p	0.93	0.28	0.4:	6.2:	05158-6808	C	
694	05 15 50	-68 27	8	5	3	2	-	-	-	-	-	0.11	0.11	-	-		C	
695	05 15 50	-69 27	20	13	8	6	-	-	-	-	-	0.26	0.22:	C	C		S	
696	05 15 50	-70 31	5	-	1	-	-	-	-	-	-	0.19	0.11:	-	-		S	
697	05 15 55	-70 01	3	-	2	1	20	16	15	13	-	0.11	0.11:	1.7	4.2		C	
698	05 15 59.5	-70 37 39	5	-	2	-	9	7	-	-	-	0.19	0.22	0.8:	C	05159-7037	W	
699	05 16 00	-68 06	12	5	3	2	-	-	-	-	-	0.26	0.11:	-	-		S	
700	05 16 00	-68 11	9	6	3	2	-	-	-	-	-	0.11	0.11:	-	-		S	
701	05 16 00	-69 48	8	6	4	3	26	23	-	-	-	0.07	0.11	1.2	C		W	
702	05 16 00	-71 03	2	-	1	-	4	2	4	2	-	0.07:	0.11:	0.8	4.2		C	
703	05 16 00	-71 22	-	-	-	-	4	2	6	4	-	-	-	0.8	4.2		C	
704	05 16 05	-66 55	7	-	1	-	5	4	6	5	p:	0.26:	0.11:	0.4	2.1		C	
705	05 16 09.9	-66 12 10	-	-	-	-	3	-	4	2	-	-	-	1.2:	4.2	05161-6612	C	
706	05 16 10	-68 21	11	7	4	3	28	22	27	24	-	0.15	0.11	2.5	6.2		C	
707	05 16 10	-69 23	18	14	9	7	75	71	52	50	-	0.15	0.22	1.7:	4.2:		C	
708	05 16 10.9	-69 40 27	-	-	2	1	16	13	15	13	-	-	0.11:	1.2	4.2:	05161-6940	C	
709	05 16 30	-68 46	12	8	7	4	40	30	-	-	-	0.15	0.33	4.1:	C		W	
710	05 16 30	-68 49	13	8	7	5	50	40	45	38	-	0.19	0.22	4.1	14.6		C	
711	05 16 30	-69 20	20	16	12	9	-	-	-	-	-	0.15:	0.33:	C	C		W	
712	05 16 30	-69 48	11	7	4	2	38	32	33	30	-	0.15	0.22	2.5	6.2		C	
713	05 16 30	-69 50	11	6	4	3	-	-	-	-	-	0.19	0.11:	C	C		S	
714	05 16 33	-70 31	3	-	-	-	-	-	-	-	-	0.11:	-	-	-		S	SAO 256171
715	05 16 34.6	-71 50 47	3	-	2	-	8	3	5	2	-	0.11:	0.22	2.1	6.2	05165-7150	C	
716	05 16 35	-69 12	13	8	8	6	58	41	42	37	-	0.19	0.22	7.0	10.4	05164-6911:	C	
717	05 16 40	-68 14	9	5	4	2	25	18	25	23	-	0.15	0.22	2.9	4.2		C	
718	05 16 40	-68 18	10	7	4	2	-	-	-	-	-	0.11	0.22	C	C		W	
719	05 16 44.1	-68 25 17	14	6	4	2	20	18	23	18	p	0.30	0.22	0.8	10.4:	05167-6825	C	
720	05 16 44.9	-67 29 16	5	-	2	-	14	11	16	13	-	0.19	0.22:	1.2	6.2	05167-6729	C	

Table 3, continued (9).

(1)	(2)		(3)		(4)		(5)		(6)		(7)	(8)	(9)	(10)	(11)	(12)	(13)	(14)
Number	Position RA(1950)	DEC(1950)	12 μm Peak	Bg	25 μm Peak	Bg	60 μm Peak	Bg	100 μm Peak	Bg	Size	F 12μm	F 25μm	F 60μm	F 100μm	IRAS-Id	Spec-trum	Comments
	h m s	° ' "			10^{-8} Watt m^{-2} sr^{-1}						arcmin	Jy	Jy	Jy	Jy			
721	05 16 50	-68 03	12	6	4	2	23	19	23	22	p:	0.22	0.22	1.7:	2.1:		C	
722	05 16 50	-69 57	10	3	-	-	-	-	-	-	p:	0.26	-	-	-		S	
723	05 16 55.3	-67 22 55	15	3	10	1	33	10	23	11	p	0.44	1.00	9.5	25.0	05169-6722 X0516-674	C	
724	05 16 55.4	-68 52 57	13	10	6	4	46	43	-	-	-	0.11	0.22:	1.2:	C	05169-6852	W	
725	05 17 00.0	-69 30 40	12	7	-	-	-	-	-	-	-	0.19:	-	-	-	05169-6930	S	
726	05 17 01.1	-71 37 11	-	-	4	-	-	-	-	-	p	-	0.44	-	-	05170-7137	W	
727	05 17 02.6	-71 56 45	5	-	5	-	5	2	4	2	-	0.19	0.56	1.2	4.2	05170-7156	C	
728	05 17 03.4	-69 27 09	33	20	12	9	100	80	-	-	-	0.48	0.33:	8.3:	C	05170-6927	W	
729	05 17 06.2	-66 03 20	2	-	3	-	9	3	-	-	p:	0.07:	0.33	2.5	C	05171-6603	W	
730	05 17 10	-68 22	11	6	4	2	-	-	-	-	-	0.19:	0.22:	-	-		W	
731	05 17 10	-69 19	33	25	15	12	130	120	80	75	-	0.30:	0.33:	4.1:	10.4:		C	
732	05 17 11.8	-70 48 42	7	-	1.5	-	4	3	-	-	p	0.26	0.17	0.4:	-	05171-7048	W	
733	05 17 15	-68 04	-	-	-	-	26	18	25	22	-	-	-	3.3	6.2		C	
734	05 17 15	-68 56	14	10	6	5	45	40	-	-	-	0.15	0.11	2.1:	C		W	
735	05 17 20	-67 55	7	3	3	1.5	14	11	17	15	-	0.15	0.17	1.2	4.2		C	
736	05 17 20	-69 11	13	9	7	6	-	-	-	-	-	0.15	0.11	-	-		S	
737	05 17 20	-71 17	4	-	3	1	7	4	8	5	p:	0.15	0.22	1.2	6.2:		C	
738	05 17 27.4	-69 36 47	22	8	26	6	70	30	38	30	p	0.52	2.22	16.6	16.6:	05174-6936	C	
739	05 17 27.7	-66 34 01	2	-	-	-	6	4	8	6	p:	0.07:	-	0.8	4.2	05174-6634	C	
740	05 17 30	-69 42	11	7	7	5	-	-	-	-	-	0.15	0.22	C	C		W	
741	05 17 32.6	-66 45 53	18	-	52	-	85	5	34	5	1x2	1.33	10.39	43.3	67.0	05175-6645 X0517-667	C	
742	05 17 38.5	-69 22 43	38	28	17	15	-	-	-	-	-	0.37	0.22:	C	C	05176-6922	S	
743	05 17 38.5	-69 58 31	15	10	10	6	44	36	42	37	-	0.19:	0.44:	3.3:	10.4	05176-6958	C	
744	05 17 40	-67 37	-	-	1.5	-	12	8	11	9	-	-	0.17:	1.7	4.2		C	
745	05 17 40	-68 59	19	11	7	5	50	44	45	40	-	0.30	0.22	2.5	10.4		C	
746	05 17 40	-71 25	-	-	-	-	4	2	6	4	p:	-	-	0.8	4.2		C	
747	05 17 42.9	-68 23 40	8	3	7	2	20	15	17	15	-	0.19:	0.56	2.1:	4.2:	05177-6823	C	
748	05 17 45	-66 05	6	-	2	-	11	6	12	5	3x1:	0.56:	0.50	3.2	17.7		C	
749	05 17 45	-69 02	12	9	6	4	45	42	-	-	-	0.11	0.22	1.2:	C		W	
750	05 17 49.1	-68 38 40	7	-	2	1.5	-	-	-	-	p:	0.26	0.06:	-	-	05178-6838	S	SAO 249241
751	05 17 50	-68 52	12	8	6	5	-	-	-	-	-	0.15	0.11	C	C		S	
752	05 17 50	-70 01	14	9	4	3	38	36	-	-	-	0.19	0.11	0.8	C		W	
753	05 17 55	-67 57	-	-	3	1.5	16	14	-	-	-	-	0.17:	0.8	C	05179-6758:	W	
754	05 17 56.1	-69 29 42	24	14	13	9	95	70	72	67	-	0.37	0.44	10.3	10.4:	05179-6929	C	
755	05 17 57.8	-69 49 24	16	8	7	4	60	45	47	41	-	0.30	0.33	6.2	12.5	05179-6949	C	
756	05 17 59.3	-69 18 37	47	36	-	-	-	-	-	-	-	0.41	C	C	C	05179-6918	S	
757	05 18 00	-68 50	14	9	7	5	53	30	41	37	-	0.19	0.22	9.5	8.3		W	
758	05 18 00	-69 05	18	12	9	6	64	58	45	40	-	0.22	0.33	2.5	10.4		C	
759	05 18 00	-69 09	22	13	12	8	84	68	63	50	-	0.33	0.44	6.6	27.0		C	
760	05 18 04.2	-66 23 49	-	-	2	-	6	4	-	-	-	-	0.22	0.8	C	05180-6623	W	
761	05 18 05	-65 35	5	-	-	-	-	-	-	-	-	0.19	-	-	-		S	SAO 249242
762	05 18 08.9	-71 35 01	13	-	1	-	-	-	4	2	p	0.48	0.11:	-	4.2	05181-7135	C	SAO 256173
763	05 18 12.4	-72 44 56	10	3	-	-	-	-	-	-	p	0.26:	-	-	-	05182-7244	S	SAO 256174
764	05 18 13.3	-69 18 59	45	30	50	34	220	155	130	110	-	0.56	1.78	26.9	41.6	05182-6918	C	
765	05 18 13.8	-69 24 42	39	28	20	16	150	130	90	80	-	0.41	0.44	8.3	20.8:	05182-6924	C	
766	05 18 14.2	-71 18 00	27	3	23	1	85	5	44	5	2x2	2.23	5.46	49.4	95.8	05182-7117 X0518-713	C	
767	05 18 15	-69 48	11	7	7	6	60	58	-	-	-	0.15	0.11	0.8:	C		W	
768	05 18 15	-69 55	18	12	7	5	55	45	45	40	-	0.22	0.22	4.1	10.4	05181-6953:	C	
769	05 18 15	-70 19	5	3	3	2	23	17	19	16	-	0.07	0.11	2.5	6.2		C	
770	05 18 20	-69 33	22	15	9	6	-	-	-	-	-	0.26	0.33	-	-	05181-6932:	W	
771	05 18 24.6	-66 40 35	-	-	2	-	9	6	10	8	p:	-	0.22	1.2	4.2	05184-6640	C	
772	05 18 28.7	-69 35 42	26	10	11	6	70	60	-	-	p:	0.59	0.56	4.1:	C	05184-6935	W	
773	05 18 29.7	-70 40 43	-	-	-	-	10	8	10	9	-	-	-	0.8	2.1	05184-7040	C	
774	05 18 30	-65 58	4	-	1.5	-	7	5	9	6	-	0.15:	0.17:	0.8	6.2		C	
775	05 18 30	-67 36	6	-	1	-	-	-	-	-	-	0.22	0.11:	-	-		S	
776	05 18 32.3	-67 29 37	-	-	1	-	8	7	9	7	-	-	0.11:	0.4:	4.2:	05185-6729	C	
777	05 18 33.1	-68 06 29	9	4	5	1.5	16	14	15	14	-	0.19:	0.39	0.8	2.1:	05185-6806	C	
778	05 18 36.2	-68 56 58	8	5	4	3	27	24	23	21	-	0.11:	0.11:	1.2	4.2:	05186-6856	C	
779	05 18 40	-67 04	2	-	1	-	10	6	9	7	-	0.07:	0.11:	1.7	4.2		C	
780	05 18 41.1	-68 11 56	-	-	1.5	-	17	13	15	13	-	-	0.17:	1.7	4.2:	05186-6811	C	
781	05 18 43.6	-70 04 42	16	8	6	4	38	26	36	25	-	0.30:	0.22	5.0	22.9	05187-7004	C	
782	05 18 44.1	-70 33 32	5	-	7	-	7	6	7	6	-	0.19	0.78	0.4:	2.1:	05187-7033	C	
783	05 18 48.5	-67 07 48	2	-	2	-	11	8	9	8	-	0.07:	0.22	1.2	2.1:	05188-6707	C	
784	05 18 50	-69 10	18	13	11	8	90	85	72	68	-	0.19	0.33	2.1:	8.3:		C	
785	05 18 50.2	-69 43 01	48	28	35	20	210	150	100	60	p	0.74	1.66	24.8	83.2:	05188-6943	C	
786	05 18 55.2	-70 08 39	13	7	8	4	28	24	-	-	p	0.22	0.44	1.7	C	05189-7008	W	
787	05 19 00	-66 18	5	-	2	-	7	4	10	7	-	0.19	0.22:	1.2	6.2		C	
788	05 19 00	-66 31	5	-	2	-	10	6	12	8	-	0.19	0.22:	1.7	8.3		C	
789	05 19 00	-69 18	70	30	100	60	320	180	170	130	p	1.48	4.44	58.0	83.2	05192-6917:	C	
790	05 19 00	-69 54	17	13	8	6	53	50	45	42	-	0.15	0.22	1.2	6.2		C	
791	05 19 00	-71 30	3	-	-	-	-	-	-	-	p:	0.11:	-	-	-		S	
792	05 19 00.2	-69 28 11	39	23	20	14	140	100	85	70	p:	0.59	0.67	16.6:	31.2	05190-6928	C	
793	05 19 03.5	-67 48 23	10	2	3	1	-	-	-	-	p	0.30	0.22	-	-	05190-6748	S	
794	05 19 10	-69 37	-	-	16	12	-	-	-	-	-	-	0.44	C	C	05191-6936	W	
795	05 19 10	-70 09	13	9	7	4	20	18	20	18	-	0.15	0.33	0.8	4.2:	05193-7009:	C	
796	05 19 14.2	-68 33 49	4	-	2	1	20	17	20	16	-	0.15:	0.11:	1.2	8.3	05192-6833	C	
797	05 19 15	-67 59	9	4	4	3	20	18	20	18	-	0.19	0.11	0.8:	4.2:		C	
798	05 19 16.5	-68 24 22	13	6	14	3	52	23	33	24	p	0.26	1.22	12.0	18.7	05192-6824	C	
799	05 19 20	-70 22	4	-	2	1	18	15	15	14	-	0.15	0.11:	1.2	2.1		C	
800	05 19 23.6	-67 54 39	14	6	3	2	-	-	-	-	p	0.30	0.11:	-	-	05193-6754	S	
801	05 19 25	-67 44	5	-	3	1.5	15	11	16	14	-	0.19	0.17:	1.7	4.2		C	
802	05 19 30	-67 05	5	-	1	-	8	6	-	-	-	0.19	0.11:	0.8	-		W	
803	05 19 30	-67 15	2	-	1	-	10	8	9	8	-	0.07:	0.11:	0.8	2.1		C	
804	05 19 30	-69 41	110	30	130	30	500	200	220	100	p	2.96	11.10	124.2	249.6	05196-6941:	C	
805	05 19 30	-69 53	24	16	8	6	-	-	-	-	-	0.30	0.22	C	C		S	
806	05 19 30.3	-69 33 09	28	24	16	13	125	120	85	80	-	0.15:	0.33	2.1:	10.4	05195-6933	C	
807	05 19 30.7	-69 12 00	75	30	85	23	260	180	130	100	p	1.66	6.88	33.1	62.4:	05195-6911	C	
808	05 19 33.1	-69 21 47	20	13	12	9	90	80	80	75	p:	0.26	0.33:	4.1:	10.4:	05195-6921	C	
809	05 19 36	-71 18	5	-	2	-	8	4	8	6	-	0.19	0.22	1.7	4.2		C	
810	05 19 36.4	-69 23 21	27	13	14	9	-	-	-	-	-	0.52	0.56	C	C	05196-6923	W	

Table 3, continued (10).

(1)	(2)		(3)		(4)		(5)		(6)		(7)	(8)	(9)	(10)	(11)	(12)	(13)	(14)
Number	Position RA(1950) h m s	DEC(1950) o ' "	12 µm Peak	Bg	25 µm Peak	Bg 10⁻⁸ Watt m⁻² sr⁻¹	60 µm Peak	Bg	100 µm Peak	Bg	Size arcmin	F 12µm Jy	F 25µm Jy	F 60µm Jy	F 100µm Jy	IRAS-Id	Spec-trum	Comments
811	05 19 39.4	-69 15 28	52	29	40	22	165	140	140	100	p	0.85	2.00	10.3:	83.2:	05196-6915	C	
812	05 19 40	-67 57	11	7	4	3	-	-	-	-	-	0.15	0.11	C	C		S	
813	05 19 44.3	-69 50 20	25	12	23	7	76	48	50	40	-	0.48	1.78	11.6	20.8:	05197-6950	C	
814	05 19 47	-66 30	9	2	-	-	-	-	-	-	p:	0.26	-	-	-		S	SAO 249253
815	05 19 48	-71 49	-	-	1	-	2	-	3	2	-	-	0.11:	0.8	2.1		C	
816	05 19 48.4	-69 41 40	80	30	100	60	-	-	-	-	p	1.85	4.44	C	C	05198-6941	W	
817	05 19 51.7	-65 49 08	4	-	1	-	7	3	9	4	p:	0.15:	0.11:	1.7	10.4	05198-6549	C	
818	05 20 00	-66 37	2	-	2	-	13	8	17	9	-	0.07:	0.22	2.1	16.6		C	
819	05 20 09.9	-70 13 06	11	8	4	2	28	24	23	19	-	0.11:	0.22:	1.7	8.3	05201-7013	C	
820	05 20 10	-68 26	8	4	3	2	26	22	26	24	-	0.15	0.11:	1.7	4.2		C	
821	05 20 10	-68 50	11	9	6	4	42	35	32	30	-	0.07:	0.22:	2.9	4.2:		C	
822	05 20 12.2	-69 33 33	30	18	17	12	105	80	60	50	-	0.44	0.56	10.3	20.8:	05202-6933	C	
823	05 20 16.4	-66 55 49	13	3	25	2	73	7	32	13	p	0.37	2.55	27.3	39.5	05202-6655 X0520-668	C	
824	05 20 19.8	-71 16 48	3	-	2	-	8	3	10	5	p:	0.11:	0.22	2.1	10.4	05203-7116	C	
825	05 20 20	-69 13	17	8	8	5	60	50	-	-	-	0.33	0.33	4.1:	C	05205-6913:	W	
826	05 20 20	-70 48	5	-	2	-	13	11	15	12	-	0.19	0.22	0.8	6.2		C	
827	05 20 25.1	-68 33 15	8	6	4	3	32	28	35	32	-	0.07:	0.11:	1.7	6.2:	05204-6833	C	
828	05 20 27.4	-68 40 58	11	6	8	5	43	32	34	32	-	0.19	0.33	4.6	4.2:	05204-6840	W	
829	05 20 29.0	-69 04 02	4	2	5	3	29	25	25	22	-	0.07:	0.22:	1.7	6.2:	05204-6904	C	
830	05 20 30	-66 10	6	-	1	-	11	7	12	6	p:	0.22	0.11:	1.7	12.5		C	
831	05 20 33.4	-66 49 33	15	4	13	2	60	16	34	13	p	0.41	1.22	18.2	43.7	05205-6649	C	
832	05 20 40	-69 40	15	11	10	7	-	-	-	-	-	0.15	0.33	C	C		W	
833	05 20 42	-66 36	6	-	-	-	-	-	-	-	-	0.22	-	-	-		S	
834	05 20 45	-68 14	11	6	5	2	30	25	30	25	-	0.19	0.33	2.1	10.4		C	
835	05 20 45	-68 51	24	14	7	5	-	-	-	-	p:	0.37	0.22	C	C		S	
836	05 20 45	-69 58	8	6	5	2	-	-	-	-	-	0.07:	0.33	-	-	05207-6956:	W	
837	05 20 50	-67 13	-	-	1	-	13	10	10	9	-	-	0.11:	1.2	2.1		C	
838	05 20 50	-71 01	5	-	-	-	-	-	-	-	p:	0.19	-	-	-	05209-7101:	S	SAO 256178
839	05 20 52.3	-67 55 46	17	10	12	8	60	50	50	40	-	0.26	0.44	4.1	20.8:	05208-6755	C	
840	05 20 52.3	-68 06 45	13	10	6	4	50	45	45	42	-	0.11	0.22	2.1	6.2:	05208-6806	C	
841	05 21 00	-68 02	16	12	10	7	-	-	-	-	-	0.15	0.33:	C	C		W	
842	05 21 14.7	-68 30 48	8	6	4	3	33	29	37	32	-	0.07:	0.11:	1.7:	10.4	05212-6830	C	
843	05 21 15	-68 35	10	8	4	3	45	35	35	33	-	0.07:	0.11:	4.1	4.2:		C	
844	05 21 15	-70 19	-	-	2	1	19	16	20	18	-	-	0.11:	1.2	4.2		C	
845	05 21 15	-70 46	5	-	2	-	13	11	12	10	-	0.19	0.22	0.8	4.2		C	
846	05 21 19.7	-66 07 04	2	-	7	-	15	5	8	4	p	0.07:	0.78	4.1	8.3	05213-6607	C	
847	05 21 20	-68 51	26	12	12	8	68	40	60	45	-	0.52	0.44	11.6	31.2		C	
848	05 21 20	-69 36	16	8	8	4	69	50	39	30	-	0.30	0.44	7.9	18.7		C	
849	05 21 20	-70 07	20	15	7	6	-	-	-	-	-	0.19	0.11:	C	C		S	
850	05 21 21.4	-70 12 31	15	11	8	4	26	23	27	25	-	0.15	0.44	1.2:	4.2:	05213-7012	C	
851	05 21 24.3	-65 32 04	8	-	23	-	42	4	18	5	p	0.30:	2.55	15.7	27.0	05214-6532	C	
852	05 21 25	-65 56	5	-	2	-	9	3	8	5	1xp:	0.24	0.26	2.7	6.3		C	
853	05 21 25	-68 45	15	8	7	5	45	38	43	40	-	0.26	0.22	2.9	6.2		C	
854	05 21 25	-69 03	8	5	5	4	34	32	31	29	-	0.11:	0.11	0.8	4.2		C	
855	05 21 29.1	-67 49 45	18	7	28	4	50	35	50	45	p	0.41	2.66	6.2	10.4:	05214-6749	C	
856	05 21 30	-69 54	20	15	6	5	40	37	42	40	-	0.19:	0.11:	1.2	4.2:		C	
857	05 21 30	-70 10	16	11	6	4	32	29	32	30	-	0.19	0.22	1.2	4.2		C	
858	05 21 30	-71 17	4	-	-	-	-	-	-	-	-	0.15	-	-	-		S	
859	05 21 30.7	-67 08 00	3	-	2	1	13	10	13	12	-	0.11:	0.11:	1.2	2.1:	05215-6707	C	
860	05 21 36.7	-67 27 33	-	-	2	1	10	8	10	8	-	-	0.11	0.8	4.2	05216-6727	C	
861	05 21 37.4	-67 53 55	105	18	130	9	125	62	75	65	p	3.22	13.43	26.1	20.8:	05216-6753	W	
862	05 21 40	-66 45	4	-	4	1	-	-	-	-	-	0.15:	0.33	C	C		W	
863	05 21 40	-70 16	12	8	5	3	-	-	-	-	-	0.15	0.22	C	C		W	
864	05 21 40.7	-71 45 58	5	-	4	-	13	2	12	4	p	0.19	0.44	4.6	16.6	05216-7145	C	
865	05 21 45	-70 14	16	12	6	4	-	-	-	-	-	0.15	0.22:	C	C		W	
866	05 21 45.7	-70 01 54	40	25	17	10	72	50	64	55	p:	0.56	0.78	9.1	18.7	05217-7001	C	
867	05 21 48.3	-69 15 20	-	-	4	2	26	22	25	21	-	-	0.22:	1.7	8.3	05218-6915	C	
868	05 21 50	-68 41	13	7	6	4	35	31	-	-	-	0.22	0.22	1.7	C		W	
869	05 21 50	-69 33	8	4	2	1	-	-	-	-	-	0.15:	0.11:	-	-		S	
870	05 21 55.1	-67 44 02	10	6	4	2	17	14	23	17	-	0.15	0.22	1.2	12.5	05219-6744	C	
871	05 21 55.1	-72 08 27	8	-	1.5	-	-	-	-	-	p	0.30	0.17:	-	-	05219-7208	S	
872	05 21 59.3	-69 43 06	80	30	75	15	260	100	110	75	p	1.85	6.66	66.2	72.8	05219-6943	C	
873	05 22 00	-68 31	14	9	7	5	35	31	36	35	-	0.19	0.22	1.7	2.1		C	
874	05 22 00	-68 37	16	8	7	5	37	35	36	35	-	0.30	0.22	0.8:	2.1		C	
875	05 22 00	-71 19	2	-	-	-	6	4	8	6	-	0.07:	-	0.8	4.2		C	
876	05 22 03.5	-67 58 16	45	30	100	20	250	200	-	-	-	0.56:	8.88	20.7:	C	05220-6758	W	
877	05 22 08.4	-69 23 49	14	6	3	1.5	30	18	23	15	p	0.30	0.17:	5.0	16.6	05221-6923	C	
878	05 22 10.0	-65 46 06	22	2	8	2	27	5	35	3	2xp:	1.27	1.07	11.3	72.4	05221-6546 X0522-657	C	
879	05 22 10.5	-67 49 55	24	7	28	4	90	45	50	45	p	0.63	2.66	18.6	10.4:	05221-6749	W	
880	05 22 10.6	-68 00 32	140	33	340	50	770	175	290	140	p	3.96	32.19	246.3	312.0	05221-6800	C	
881	05 22 13.8	-69 58 28	36	25	10	8	48	45	52	50	p:	0.41	0.22	1.2	4.2:	05222-6958	C	
882	05 22 15	-66 45	9	4	3	1	23	16	-	-	-	0.19	0.22	2.9	C		W	
883	05 22 15	-69 12	-	-	5	4	31	28	25	23	-	-	0.11	1.2	4.2		C	
884	05 22 15	-70 51	-	-	-	-	9	8	8	7	-	-	-	0.4	2.1		C	
885	05 22 15.7	-67 37 42	10	2	8	2	24	12	20	15	p	0.30	0.67	5.0	10.4	05222-6737	C	
886	05 22 20	-70 13	15	12	4	3	25	23	-	-	-	0.11:	0.11:	0.8:	C		W	
887	05 22 23.7	-68 01 28	80	50	250	50	-	-	-	-	-	1.11:	22.20	C	C	05223-6801	W	
888	05 22 29.0	-68 07 18	50	30	70	14	170	80	-	-	-	0.74:	6.22:	37.3:	C	05224-6807	W	
889	05 22 30	-66 33	5	-	2	-	-	-	-	-	-	0.19	0.22:	C	C		W	
890	05 22 30	-70 09	15	12	7	6	-	-	-	-	-	0.11:	0.11:	C	C		W	
891	05 22 34.3	-68 42 34	8	6	5	4	33	28	28	25	-	0.07:	0.11	2.1	6.2	05225-6842	C	
892	05 22 35	-68 13	18	12	15	7	60	50	-	-	-	0.22	0.89	4.1	C		W	
893	05 22 40	-67 24	5	-	1	-	-	-	-	-	-	0.19	0.11:	-	-		S	SAO 249260
894	05 22 41 1	-67 58 22	60	30	50	9	330	160	150	125	p	1.11:	4.55	70.4	52.0:	05226-6758	W	
895	05 22 41.5	-65 44 35	15	3	8	2	27	5	-	-	1xp:	0.54	0.80	9.7	C	05226-6544	W	
896	05 22 45.3	-67 30 32	-	-	1.5	-	12	9	-	-	-	-	0.17	1.2	-	05227-6730	W	
897	05 22 46.0	-69 52 44	40	30	10	8	80	60	75	60	-	0.37:	0.22	8.3	31.2	05227-6952	C	
898	05 22 47.6	-67 10 09	12	9	7	4	38	14	34	18	p:	0.11	0.33	9.9	33.3	05227-6710	C	
899	05 22 49.1	-69 45 12	60	40	50	20	120	80	-	-	-	0.74	3.33	16.6:	C	05228-6945	W	
900	05 22 49.9	-66 43 51	24	5	20	2	63	20	44	14	p:	0.70	2.00	17.8	62.4	05228-6643 X0522-667	C	

Table 3, continued (11).

(1)	(2)		(3)		(4)		(5)		(6)		(7)	(8)	(9)	(10)	(11)	(12)	(13)	(14)
Number	Position RA(1950) h m s	DEC(1950) ° ' "	12 μm Peak	Bg	25 μm Peak	Bg	60 μm Peak	Bg	100 μm Peak	Bg	Size arcmin	F 12μm Jy	F 25μm Jy	F 60μm Jy	F 100μm Jy	IRAS-Id	Spectrum	Comments
					10^{-8} Watt $m^{-2} sr^{-1}$													
901	05 22 52.0	-68 25 05	18	12	9	6	44	35	48	42	-	0.22	0.33	3.7	12.5:	05228-6825	C	
902	05 22 52.4	-67 46 37	4	-	3	2	23	18	18	13	-	0.15	0.11:	2.1	10.4	05228-6746	C	
903	05 22 54.8	-69 31 23	-	-	-	-	17	14	13	12	-	-	-	1.2	2.1:	05229-6931	C	
904	05 22 55	-67 21	5	-	1	-	-	-	-	-	-	0.19	0.11:	-	-		S	
905	05 23 00	-67 39	4	-	1.5	-	18	14	15	14	-	0.15	0.17	1.7	2.1		C	
906	05 23 00	-68 51	14	7	7	4	40	37	36	34	-	0.26	0.33:	1.2:	4.2:		C	
907	05 23 00.2	-68 47 56	8	6	6	4	35	30	30	25	-	0.07:	0.22:	2.1	10.4:	05230-6847	C	
908	05 23 01.3	-68 58 19	15	9	7	4	-	-	-	-	-	0.22	0.33:	-	-	05230-6858	W	
909	05 23 02.2	-68 35 08	11	7	6	4	38	33	31	26	-	0.15	0.22	2.1	10.4	05230-6835	C	
910	05 23 02.3	-71 37 53	11	4	10	1	27	5	23	6	p	0.26	1.00	9.1	35.4	05230-7137 X0522-716	C	
911	05 23 03.2	-68 07 11	105	20	170	20	340	125	150	100	p	3.14	16.65	89.0	104.0	05230-6807	C	
912	05 23 07.7	-70 30 29	5	-	2	-	13	10	12	8	-	0.19:	0.22	1.2	8.3	05231-7030	C	
913	05 23 10	-66 48	9	5	4	2	-	-	-	-	-	0.15	0.22	C	C		W	
914	05 23 10	-67 10	17	7	6	3	-	-	-	-	-	0.37	0.33	C	C		S	
915	05 23 10	-69 13	7	4	6	4	34	30	-	-	-	0.11:	0.22	1.7	C		W	
916	05 23 10	-70 12	13	5	5	3	21	18	19	17	p:	0.30	0.22	1.2	4.2	05230-7011:	C	
917	05 23 12.4	-69 41 48	20	15	20	18	-	-	-	-	-	0.19:	0.22:	C	C	05232-6941	W	
918	05 23 13.8	-71 11 25	-	-	2	-	3	2	-	-	p:	-	0.22	0.4	-	05232-7111	W	
919	05 23 14.5	-66 26 20	11	3	8	1	27	10	22	15	p	0.30	0.78	7.0	14.6	05232-6626	C	
920	05 23 16.1	-71 42 23	6	1	3	1	15	8	18	7	-	0.19	0.22:	2.9	22.9	05232-7142	C	
921	05 23 17.5	-69 53 48	40	28	24	10	105	60	-	-	p:	0.44:	1.55	18.6	C	05232-6953	W	Damaged set 1
922	05 23 20	-66 47	15	5	6	2	30	14	-	-	p:	0.37	0.44	6.6	C		W	
923	05 23 20	-69 27	5	2	-	-	17	15	18	15	-	0.11:	-	0.8	6.2		C	
924	05 23 20	-71 23	3	-	2	-	9	5	9	7	p:	0.11	0.22:	1.7	4.2	05231-7120:	C	
925	05 23 23.7	-68 02 50	85	30	70	15	250	170	130	110	p	2.03	6.10	33.1	41.6	05233-6802	C	
926	05 23 25	-67 12	9	7	4	3	-	-	-	-	-	0.07	0.11	C	C		W	
927	05 23 25	-69 02	15	11	9	6	72	60	-	-	-	0.15	0.33	5.0:	C		W	
928	05 23 30	-68 35	11	7	4	3	40	38	34	33	-	0.15	0.11:	0.8:	2.1:		C	
929	05 23 30	-71 38	9	2	5	2	14	10	-	-	p	0.26:	0.33:	1.7:	C		W	
930	05 23 34.3	-70 04 17	-	-	-	-	26	23	24	21	-	-	-	1.2	6.2	05235-7004	C	Damaged set 1
931	05 23 35	-68 21	16	10	8	6	47	42	46	43	-	0.22	0.22	2.1	6.2		C	
932	05 23 35.7	-65 44 35	11	-	2	-	4	2	8	4	p	0.41	0.22	0.8:	8.3:	05235-6544	C	
933	05 23 37.0	-67 26 48	11	2	8	1	33	9	22	15	p	0.33	0.78	9.9	14.6	05236-6726	C	
934	05 23 38.1	-71 18 49	-	-	3	1	13	5	11	7	-	-	0.22:	3.3	8.3	05236-7118	C	
935	05 23 40	-69 58	17	9	6	4	38	36	-	-	p:	0.30	0.22	0.8:	C		W	Damaged set 1
936	05 23 42	-66 57	5	-	2	-	9	6	9	7	-	0.19	0.22:	1.2:	4.2:	05237-6655:	C	
937	05 23 42.8	-70 00 45	9	4	6	2	34	32	-	-	-	0.19:	0.44	0.8:	C	05237-7000	W	Damaged set 1
938	05 23 43.8	-67 55 15	12	8	20	5	60	50	-	-	-	0.15:	1.66	4.1:	C	05237-6755	W	
939	05 23 45	-68 50	8	4	4	3	30	24	-	-	-	0.15:	0.11:	2.5:	C		W	
940	05 23 50	-68 17	14	8	7	4	48	43	42	40	-	0.22	0.33	2.1	4.2		C	
941	05 23 50	-69 35	8	5	5	4	34	30	26	23	-	0.11:	0.11	1.7	6.2		C	Damaged set 1
942	05 23 50	-69 51	23	14	7	5	42	40	-	-	-	0.33	0.22:	0.8:	C		W	Damaged set 1
943	05 23 52.4	-68 02 42	46	25	64	22	150	75	100	80	p:	0.78	4.66	31.0	41.6:	05238-6802	C	
944	05 23 55	-69 13	22	14	12	8	83	77	-	-	-	0.30	0.44	2.5	C		W	
945	05 23 55	-69 27	8	4	4	3	32	30	25	23	-	0.15:	0.11:	0.8	4.2		C	
946	05 23 58.3	-67 59 54	26	13	44	15	100	55	-	-	p:	0.48	3.22	18.6	C	05239-6759	W	
947	05 24 00	-69 05	16	12	10	7	75	66	62	56	-	0.15	0.33	3.7	12.5		C	
948	05 24 00.8	-68 09 48	12	9	20	8	60	50	-	-	p	0.11:	1.33	4.1	C	05240-6809	W	
949	05 24 01.8	-68 44 40	9	4	4	2	34	19	23	17	p:	0.19	0.22	6.2:	12.5:	05240-6844	C	
950	05 24 05	-70 11	-	-	3	2	23	20	21	18	-	-	0.11:	1.2	6.2		C	Damaged set 1
951	05 24 06	-71 15	4	-	1.5	-	-	-	-	-	-	0.15	0.17:	C	C		W	
952	05 24 08	-66 26	12	6	5	3	40	25	30	20	p:	0.22	0.22:	6.2:	20.8:	05242-6623:	C	
953	05 24 08.7	-66 32 20	9	6	5	3	22	15	-	-	p:	0.11	0.22	2.9:	C	05241-6632	W	
954	05 24 10	-69 33	9	6	-	-	-	-	-	-	-	0.11:	-	-	-		S	SAO 249266
955	05 24 10	-69 42	45	35	34	14	160	130	-	-	-	0.37	2.22	12.4:	C		W	Damaged set 1
956	05 24 15	-67 29	12	5	7	3	47	20	35	24	p:	0.26	0.44	11.2	22.9		C	
957	05 24 16.1	-67 48 18	5	-	4	2	-	-	-	-	p	0.19	0.22	-	-	05242-6748	W	
958	05 24 20	-69 02	17	13	10	7	70	60	50	40	-	0.15	0.33	4.1:	20.8:		C	
959	05 24 20	-70 40	4	-	1	-	13	10	13	8	-	0.15	0.11:	1.2	10.4		C	
960	05 24 25.9	-71 22 40	5	1	3	1	20	8	19	8	p:	0.15	0.22	5.0	22.9	05244-7122	C	
961	05 24 26.9	-68 32 32	32	15	23	8	82	55	-	-	p	0.63	1.66	11.2	C	05244-6832	W	
962	05 24 30	-66 47	4	-	3	-	13	6	13	10	-	0.15	0.33:	2.9:	6.2:		C	
963	05 24 30	-70 31	5	-	2	-	12	8	13	8	-	0.19	0.22	1.7	10.4		C	
964	05 24 31.4	-67 12 03	11	4	5	2	32	19	27	22	-	0.26	0.33	5.4	10.4	05245-6712	C	
965	05 24 35	-69 13	24	15	11	9	94	81	75	55	-	0.33	0.22	5.4	41.6	05248-6915:	C	
966	05 24 39.0	-71 37 22	10	2	5	1	18	11	19	11	p	0.30:	0.44	2.9	16.6	05246-7137	C	
967	05 24 40	-68 14	14	9	7	5	43	34	40	35	-	0.19	0.22	3.7	10.4		C	
968	05 24 40	-69 23	24	16	14	9	90	75	70	60	-	0.30	0.56	6.2:	20.8:		C	
969	05 24 40	-69 32	11	7	6	4	43	40	32	30	-	0.15	0.22	1.2	4.2		C	
970	05 24 40	-70 19	-	-	2	-	11	9	8	7	-	-	0.22:	0.8	2.1:		C	
971	05 24 40.2	-70 03 49	38	5	5	2	-	-	-	-	p	1.22	0.33	-	-	05246-7003	S	Damaged set 1
972	05 24 40.7	-66 09 27	3	-	-	-	18	13	-	-	-	0.11:	-	2.1:	C	05246-6609	W	
973	05 24 40.9	-69 44 05	53	45	25	20	200	150	-	-	-	0.30	0.56:	20.7:	C	05246-6944	W	Damaged set 1
974	05 24 45	-68 26	17	14	7	5	48	44	-	-	-	0.11	0.22:	1.7:	C		W	
975	05 24 45	-69 03	16	12	6	4	-	-	-	-	-	0.15:	0.22:	C	C		W	
976	05 24 45.0	-69 41 30	65	37	50	25	-	-	-	-	p	1.04	2.77	C	C	05247-6941	W	Damaged set 1
977	05 24 49.9	-69 27 48	17	12	10	7	76	60	53	40	-	0.19	0.33	6.6	27.0	05248-6927	C	
978	05 24 50	-68 32	22	16	13	8	70	60	-	-	p:	0.22	0.56	4.1:	C		W	
979	05 24 50	-68 36	15	8	7	4	50	42	-	-	-	0.26	0.33	3.3:	C		W	
980	05 24 50	-68 52	13	5	-	-	-	-	-	-	-	0.30:	-	-	-		S	
981	05 24 50	-72 01	5	-	-	-	-	-	-	-	-	0.19	-	-	-		S	
982	05 24 50.6	-70 07 41	9	5	5	3	-	-	-	-	-	0.15	0.22	-	-	05248-7007	W	Damaged set 1
983	05 24 51.0	-66 29 14	18	6	10	4	53	20	50	20	p	0.44	0.67	13.7	62.4	05248-6629	C	
984	05 24 51.2	-69 15 02	24	14	10	7	90	70	70	60	-	0.37	0.33:	8.3:	20.8:	05248-6915	C	
985	05 24 54	-71 37	10	3	4	1	-	-	-	-	p:	0.26:	0.33:	C	C		W	
986	05 24 56.6	-69 56 28	17	4	8	5	40	30	-	-	-	0.48	0.33	4.1:	C	05249-6956	W	Damaged set 1
987	05 25 00	-69 18	24	12	9	7	-	-	-	-	-	0.44	0.22:	C	C	05249-6916:	S	
988	05 25 03.3	-71 34 34	9	2	5	1	21	9	18	12	p	0.26:	0.44	5.0	12.5	05250-7134	C	
989	05 25 05.9	-71 41 27	-	-	2	-	11	9	-	-	-	-	0.22	0.8	C	05250-7141	W	
990	05 25 09.7	-68 01 52	8	3	4	2	21	18	20	18	-	0.19	0.22:	1.2:	4.2:	05251-6801	C	

Table 3, continued (12).

(1)	(2)		(3)		(4)		(5)		(6)		(7)	(8)	(9)	(10)	(11)	(12)	(13)	(14)
Number	Position RA(1950) h m s	DEC(1950) o ' "	12 µm Peak	Bg	25 µm Peak	Bg	60 µm Peak	Bg	100 µm Peak	Bg	Size	F 12µm	F 25µm	F 60µm	F 100µm	IRAS-Id	Spec-trum	Comments
					10^{-8} Watt $m^{-2}sr^{-1}$						arcmin	Jy	Jy	Jy	Jy			
991	05 25 10	-68 19	18	14	8	6	48	44	-	-	-	0.15	0.22	1.7:	C		W	
992	05 25 10	-70 01	11	8	3	2	25	21	20	18	-	0.11	0.11:	1.7	4.2		C	
993	05 25 10.5	-69 53 01	14	10	-	-	-	-	-	-	-	0.15	-	C	C	05251-6953	S	Damaged set 1
994	05 25 11.9	-68 21 46	22	16	12	8	68	45	60	48	p:	0.22	0.44	9.5	25.0	05251-6821	C	
995	05 25 12	-71 37	9	4	3	2	-	-	-	-	p:	0.19	0.11	C	C		S	
996	05 25 12.3	-66 03 24	4	3	5	1	27	12	-	-	p:	0.04:	0.44	6.2	C	05252-6603	W	
997	05 25 18	-71 53	5	-	1	-	-	-	-	-	p	0.19	0.11:	-	-		S	
998	05 25 18.4	-69 08 16	12	8	-	-	-	-	-	-	-	0.15	C	C	C	05253-6908	S	
999	05 25 18.8	-68 30 53	48	18	52	8	147	52	87	47	p	1.11	4.88	39.3	83.2	05253-6830	C	
1000	05 25 20	-67 13	9	6	4	2	28	18	-	-	-	0.11	0.22	4.1	C		W	
1001	05 25 20	-70 10	-	-	-	-	20	18	17	16	-	-	-	0.8	2.1		C	Damaged set 1
1002	05 25 23.1	-66 18 57	40	15	25	9	-	-	-	-	-	0.93	1.78:	C	C	05253-6618	W	
1003	05 25 26.4	-67 32 13	16	6	18	7	75	40	47	35	p	0.37	1.22	14.5	25.0	05254-6732	C	
1004	05 25 30	-66 33	4	2	3	1	28	12	-	-	-	0.07	0.22	6.6	C		W	
1005	05 25 30	-69 14	17	11	12	8	82	75	-	-	-	0.22	0.44	2.9	C		W	
1006	05 25 30	-69 22	25	15	14	9	80	70	72	58	p:	0.37	0.56	4.1:	29.1	05253-6921:	C	
1007	05 25 30	-71 51	5	-	1.5	-	-	-	-	-	p:	0.19	0.17	-	-		S	
1008	05 25 32.3	-69 43 28	35	20	35	15	160	100	-	-	p:	0.56	2.22:	24.8	C	05255-6943	W	Damaged set 1
1009	05 25 34.7	-66 20 21	25	20	25	8	110	60	-	-	-	0.19:	1.89	20.7:	C	05255-6620	W	
1010	05 25 40	-66 15	42	20	20	12	-	-	-	-	p:	0.81	0.89	C	C	X0525-662	W	
1011	05 25 40	-66 59	-	-	-	-	6	4	6	4	-	-	-	0.8	4.2		C	
1012	05 25 40	-68 23	16	9	7	5	45	40	-	-	p:	0.26	0.22	2.1:	C		W	
1013	05 25 40	-69 50	14	8	6	3	25	21	-	-	p:	0.22	0.33	1.7	C		W	Damaged set 1
1014	05 25 42.1	-71 35 45	7	2	5	1	-	-	-	-	p:	0.19:	0.44	C	C	05257-7135	W	
1015	05 25 46.6	-66 17 36	75	10	135	8	240	20	130	20	p	2.40	14.10	91.1	228.8	05257-6617	C	
1016	05 25 47.9	-71 30 25	3	-	2	1	12	9	12	10	-	0.11:	0.11:	1.2	4.2	05257-7130	C	
1017	05 25 50	-67 13	13	5	9	3	43	22	34	21	p	0.30	0.67	8.7	27.0	05260-6711:	C	
1018	05 25 50.3	-69 28 57	17	8	11	5	60	30	35	25	p	0.33	0.67	12.4	20.8	05258-6928	C	
1019	05 25 52.9	-65 47 56	22	3	3	1	10	5	12	10	p	0.70	0.22:	2.1	4.2:	05258-6547 X0525-658	C	
1020	05 25 56.8	-66 11 54	36	15	18	8	78	40	60	50	-	0.78:	1.11	15.7	20.8:	05259-6611	C	
1021	05 25 58.1	-69 52 58	47	20	16	8	95	45	80	45	p	1.00	0.89	20.7	72.8	05259-6952	C	Damaged set 1
1022	05 25 59.5	-66 07 03	24	9	24	8	72	25	50	30	p:	0.56	1.78	19.5	41.6:	05259-6607	C	
1023	05 26 00	-68 42	13	9	8	5	60	50	-	-	-	0.15	0.33:	4.1:	C		W	
1024	05 26 00	-69 22	22	12	9	6	62	50	-	-	p	0.37	0.33	5.0	C		W	
1025	05 26 00	-69 55	33	28	13	8	80	70	-	-	-	0.19	0.56	4.1:	C		W	Damaged set 1
1026	05 26 00	-70 06	-	-	-	-	22	20	20	18	-	-	-	0.8	4.2:		C	Damaged set 1
1027	05 26 00	-70 19	3	-	2	-	12	10	9	7	-	0.11:	0.22:	0.8	4.2		C	
1028	05 26 00	-71 06	7	-	1	-	-	-	-	-	p	0 26	0.11:	-	-		S	
1029	05 26 02.2	-67 17 23	4	-	3	2	-	-	-	-	-	0.15:	0.11:	C	C	05260-6717	S	
1030	05 26 03.5	-68 57 54	12	6	5	3	50	35	50	27	-	0.22:	0.22:	6.2:	47.8:	05260-6857	C	
1031	05 26 05.1	-70 10 23	-	-	3	1.5	-	-	-	-	-	-	0.17	-	-	05260-7010	W	Damaged set 1
1032	05 26 06.8	-70 01 55	12	8	4	3	33	27	30	20	-	0.15	0.11:	2.5	20.8	05261-7001	C	Damaged set 1
1033	05 26 08.4	-66 14 34	30	15	15	8	80	60	-	-	-	0 56	0.78:	8.3:	C	05261-6614	W	
1034	05 26 08.9	-67 29 10	11	6	15	8	65	50	45	32	p:	0.19	0.78	6.2	27.0:	05261-6729	C	
1035	05 26 09.1	-66 22 46	16	5	6	2	60	50	-	-	-	0.41	0.44:	4.1:	C	05261-6622	W	
1036	05 26 10	-67 51	8	5	5	4	34	28	30	25	-	0.11:	0.11	2.5	10.4		C	
1037	05 26 11.1	-67 33 15	9	5	17	12	70	60	-	-	-	0.15:	0.56:	4.1:	C	05261-6733	W	
1038	05 26 11.5	-66 09 27	25	15	10	5	-	-	-	-	-	0.37:	0.56:	C	C	05261-6609	W	
1039	05 26 18.7	-68 00 30	2	-	1	-	20	16	-	-	-	0.07:	0.11:	1.7:	C	05263-6800	W	
1040	05 26 20	-68 42	19	8	13	8	72	55	60	45	-	0.41	0.56	7.0	31.2:	05266-6842:	C	
1041	05 26 20.4	-68 38 29	16	10	16	4	82	48	55	36	-	0.22	1.33	14.1	39.5	05263-6838	C	
1042	05 26 21	-65 58	9	5	3	1	15	10	20	15	-	0.15	0.22:	2.1	10.4		C	
1043	05 26 21.6	-67 39 59	14	8	16	7	73	45	45	35	-	0.22	1.00	11.6	20.8	05263-6739	C	
1044	05 26 22.8	-67 24 39	11	5	8	5	40	30	35	22	-	0.22	0.33	4.1:	27.0:	05263-6724	C	
1045	05 26 28.3	-67 33 20	13	7	23	10	80	60	55	45	-	0.22	1.44	8.3:	20.8:	05264-6733	C	
1046	05 26 30	-68 48	16	9	15	12	80	50	-	-	-	0.26:	0.33:	12.4:	C		W	
1047	05 26 30	-69 09	13	8	6	4	44	35	37	34	-	0.19	0.22	3.7	6.2:	05263-6905:	C	
1048	05 26 30	-70 39	2	-	1	-	13	11	11	9	-	0.07:	0.11:	0.8	4.2		C	
1049	05 26 33.8	-68 52 48	40	25	60	30	150	100	110	47	-	0.56:	3.33:	20.7:	131.0:	05265-6852	C	
1050	05 26 34.0	-68 10 47	8	3	4	2	19	15	21	16	-	0.19	0.22	1.7:	10.4:	05265-6810	C	
1051	05 26 35	-67 45	11	6	8	5	42	34	35	30	-	0.19	0.33	3.3	10.4:		C	
1052	05 26 36	-67 42	13	3	15	5	55	40	41	35	p	0.37	1.11	6.2	12.5	05266-6743:	C	
1053	05 26 38.2	-65 41 53	6	2	2	-	7	4	9	6	p:	0.15	0.22:	1.2	6.2:	05266-6541	C	
1054	05 26 40	-67 18	7	-	5	3	29	18	25	18	-	0.26:	0.22	4.6	14.6		C	
1055	05 26 40	-67 26	11	6	7	6	-	-	-	-	p:	0.19	0.11:	C	C		S	
1056	05 26 40	-67 36	14	8	11	8	90	65	60	55	-	0.22	0.33	10.3	10.4:		C	
1057	05 26 40	-69 24	10	4	9	6	-	-	-	-	-	0.22	0.33	C	C		W	
1058	05 26 40.5	-71 38 25	15	4	6	1	33	9	28	11	p	0.41	0.56	9.9	35.4	05266-7138	C	
1059	05 26 42.8	-69 13 17	13	4	7	5	-	-	-	-	p	0.33	0.22:	-	-	05267-6913	S	
1060	05 26 44.7	-69 41 08	-	-	-	-	11	8	10	8	-	-	-	1.2	4.2:	05267-6941	C	Damaged set 1
1061	05 26 45	-66 12	13	6	4	2	32	25	-	-	-	0.26	0.22	2.9:	C		W	
1062	05 26 45	-68 18	4	2	4	2	28	21	23	19	-	0.07:	0.22	2.9	8.3		C	
1063	05 26 45	-68 37	15	6	8	4	55	43	-	-	p:	0.33	0.44	5.0	C	05268-6836:	W	
1064	05 26 45	-68 56	15	6	15	8	82	35	45	30	-	0.33	0.78	19.5	31.2:		C	
1065	05 26 45	-69 22	12	4	15	8	60	30	42	30	p:	0.30	0.78	12.4	25.0	05268-6920:	C	
1066	05 26 50	-68 32	-	-	2	-	28	23	25	23	-	-	0.22:	2.1	4.2		C	
1067	05 26 50.5	-65 57 44	3	-	3	1.5	12	9	-	-	-	0.11:	0.17:	1.2:	C	05268-6557	W	
1068	05 26 50.5	-67 52 58	13	6	6	4	36	25	31	22	-	0.26	0.22	4.6	18.7	05268-6752	C	
1069	05 27 00	-66 07	9	5	3	1	23	9	20	10	-	0.15	0.22	5.8	20.8:		C	
1070	05 27 00	-68 59	10	6	5	3	20	18	-	-	p:	0.15	0.22	0.8:	C		W	
1071	05 27 00	-71 08	4	-	2	1	13	10	14	11	-	0.15:	0.11:	1.2	6.2	05273-7107:	C	
1072	05 27 00	-71 41	9	1	2	1	12	10	14	12	p:	0.30:	0.11:	0.8:	4.2:	X0526-716B	C	
1073	05 27 00.0	-66 52 10	3	-	2	-	10	4	7	3	p:	0.11:	0.22:	2.5	8.3	05269-6652	C	
1074	05 27 01.4	-68 27 56	4	2	5	2	28	25	24	20	p:	0.07:	0.33	1.2:	8.3	05270-6827	C	
1075	05 27 05	-72 31	5	-	-	-	-	-	-	-	-	0.19:	-	-	-		S	SAO 256187
1076	05 27 05.8	-68 51 36	112	25	250	30	460	73	110	47	p	3.22	24.42	160.2	131.0:	05270-6851	W	SAO 249279:
1077	05 27 06.6	-70 06 10	12	4	-	-	-	-	-	-	-	0.30	-	-	-	05271-7006	S	Damaged set 1
1078	05 27 11.6	-69 09 31	17	8	9	6	55	35	42	30	p:	0.33	0.33	8.3	25.0	05271-6909	C	
1079	05 27 15	-70 11	-	-	-	-	22	20	17	16	-	-	-	0.8	2.1		C	Damaged set 1
1080	05 27 15.4	-67 35 07	15	9	10	8	80	65	59	50	-	0.22	0.22:	6.2:	18.7:	05272-6735	C	

Table 3, continued (13).

(1)	(2)		(3)		(4)		(5)		(6)		(7)	(8)	(9)	(10)	(11)	(12)	(13)	(14)
Number	Position RA(1950) h m s	DEC(1950) o ' "	12 µm Peak	Bg	25 µm Peak	Bg	60 µm Peak	Bg	100 µm Peak	Bg	Size arcmin	F 12µm Jy	F 25µm Jy	F 60µm Jy	F 100µm Jy	IRAS-Id	Spectrum	Comments
					10^{-8} Watt $m^{-2} sr^{-1}$													
1081	05 27 16	-68 40	14	2	4	2	18	15	-	-	p	0.44	0.22	1.2:	-	05274-6841:	W	SAO 249281
1082	05 27 18.1	-66 24 52	9	1	4	-	-	-	-	-	p	0.30	0.44	-	-	05273-6624	W	
1083	05 27 20	-67 31	20	12	25	18	90	70	-	-	-	0.30	0.78:	8.3:	C	05272-6731:	W	
1084	05 27 30	-68 06	-	-	-	-	17	14	13	11	-	-	-	1.2	4.2:		C	
1085	05 27 36	-71 12	9	4	3	1	12	10	15	13	-	0.19	0.22	0.8:	4.2:		C	
1086	05 27 40.9	-71 25 31	10	4	4	1	32	9	30	13	p:	0.22	0.33	9.5:	35.4:	05276-7125	C	
1087	05 27 45	-70 33	12	9	5	3	28	20	27	24	-	0.11	0.22	3.3	6.2:		C	
1088	05 27 45	-70 59	4	2	3	1.5	15	13	16	14	-	0.07:	0.17:	0.8	4.2		C	
1089	05 27 45	-71 43	4	-	1.5	-	10	6	13	10	-	0.15:	0.17:	1.7	6.2		C	
1090	05 27 46.4	-67 29 31	36	16	65	18	200	100	90	60	p	0.74	5.22	41.4	62.4:	05277-6729	C	
1091	05 27 47.3	-70 24 24	-	-	-	-	19	16	17	15	-	-	-	1.2:	4.2:	05277-7024	C	
1092	05 27 48.2	-69 42 05	14	4	4	-	-	-	-	-	-	0.37	0.44	-	-	05278-6942	W	Damaged set 1
1093	05 27 50	-67 48	3	-	2	-	23	18	22	18	-	0.11:	0.22	2.1	8.3		C	
1094	05 27 50	-71 27	14	5	9	2	-	-	-	-	-	0.33	0.78	C	C	X0527-714	W	
1095	05 27 53	-68 07	8	5	-	-	-	-	-	-	-	0.11	-	-	-		S	SAO 249285
1096	05 27 53.0	-66 51 24	-	-	-	-	5	3	3	2	-	-	-	0.8	2.1:	05278-6651	C	
1097	05 27 55	-70 03	18	12	8	5	48	40	43	35	-	0.22	0.33	3.3	16.6		C	Damaged set 1
1098	05 27 58.1	-70 36 12	18	10	10	6	37	28	34	22	p:	0.30	0.44	3.7	25.0	05279-7036 X0527-706	C	
1099	05 28 00	-69 29	4	-	-	-	18	12	15	12	-	0.15:	-	2.5	6.2		C	
1100	05 28 00.3	-69 10 25	112	7	220	10	60	35	32	30	p	3.88	23.31	10.3	4.2	05280-6910	W	
1101	05 28 03.8	-70 39 10	10	6	4	3	16	12	-	-	-	0.15:	0.11	1.7:	C	05280-7039	W	
1102	05 28 05.9	-67 27 49	38	15	44	13	100	80	80	65	p	0.85	3.44	8.3:	31.2:	05280-6727	C	
1103	05 28 07.4	-69 15 45	13	5	4	2	-	-	-	-	p	0.30	0.22	-	-	05281-6915	S	
1104	05 28 09	-71 16	13	6	4	2	14	11	18	15	-	0.26	0.22	1.2	6.2		C	SAO 256193:
1105	05 28 10	-70 14	14	10	4	3	34	30	33	30	-	0.15:	0.11:	1.7:	6.2:		C	Damaged set 1
1106	05 28 10.0	-71 26 40	10	4	7	3	31	9	30	13	p	0.22	0.44	9.1:	35.4:	05281-7126	C	
1107	05 28 15	-67 02	5	-	1	-	4	3	4	3	p	0.19	0.11:	0.4:	2.1:		C	
1108	05 28 15	-70 27	10	7	-	-	20	18	20	18	-	0.11	-	0.8:	4.2		C	
1109	05 28 20	-68 13	6	3	5	3	28	15	25	18	-	0.11:	0.22	5.4	14.6		C	
1110	05 28 20	-69 04	14	9	9	5	70	40	-	-	-	0.19	0.44	12.4:	C		W	
1111	05 28 26.4	-69 23 39	14	8	6	3	35	20	27	15	p:	0.22	0.33	6.2	25.0	05284-6923	C	
1112	05 28 30	-67 43	3	-	1	-	22	16	16	14	-	0.11:	0.11:	2.5	4.2		C	
1113	05 28 30	-70 26	9	6	3	2	28	22	25	20	-	0.11	0.11	2.5	10.4		C	
1114	05 28 30	-70 48	3	-	1.5	-	14	11	15	13	-	0.11:	0.17	1.2	4.2		C	
1115	05 28 33.4	-69 55 36	22	9	7	4	34	25	33	20	p	0.48	0.33	3.7	27.0	05285-6955	C	Damaged set 1
1116	05 28 35	-67 30	9	5	5	3	-	-	-	-	-	0.15	0.22	C	C		W	
1117	05 28 35.2	-65 29 12	16	-	1.5	-	-	-	-	-	p	0.59:	0.17:	-	-	05285-6529	S	SAO 249286
1118	05 28 40	-69 06	-	-	12	9	75	50	58	30	-	-	0.33	10.3	58.2	X0528-690	C	
1119	05 28 40	-70 00	13	6	3	2	-	-	-	-	-	0.26	0.11:	-	-		S	Damaged set 1
1120	05 28 40	-70 05	12	9	4	3	36	30	34	30	-	0.11	0.11	2.5	8.3		C	Damaged set 1
1121	05 28 40	-70 14	15	10	4	3	40	30	33	30	-	0.19:	0.11	4.1	6.2:		C	Damaged set 1
1122	05 28 40	-70 54	10	6	3	2	18	14	17	15	-	0.15	0.11	1.7:	4.2:		C	
1123	05 28 40	-70 57	11	8	3	2	20	18	-	-	-	0.11	0.11:	0.8:	C		W	
1124	05 28 40	-71 23	8	5	2	1	12	10	20	15	p:	0.11	0.11	0.8:	10.4:		C	
1125	05 28 40.6	-68 09 32	10	5	5	3	-	-	-	-	-	0.19	0.22	-	-	05286-6809	W	
1126	05 28 42.1	-66 16 26	5	-	-	-	-	-	-	-	-	0.19	-	-	-	05287-6616	S	
1127	05 28 43.1	-69 10 59	45	15	23	10	-	-	-	-	p	1.11	1.44	C	C	05287-6910	W	
1128	05 28 50	-65 57	-	-	-	-	7	4	7	5	-	-	-	1.2	4.2		C	
1129	05 28 50	-68 27	9	5	8	3	37	20	30	24	-	0.15:	0.56	7.0	12.5:		C	
1130	05 28 58.9	-66 17 41	5	2	4	-	-	-	-	-	p	0.11	0.44	-	-	05289-6617	W	
1131	05 29 00	-67 20	8	4	5	3	22	16	-	-	-	0.15	0.22	2.5	C		W	
1132	05 29 00	-69 37	9	6	4	2	20	16	13	11	-	0.11:	0.22	1.7	4.2:		C	Damaged set 1
1133	05 29 00	-71 16	8	5	3	2	16	12	20	16	p:	0.11	0.11:	1.7:	8.3:		C	
1134	05 29 03.8	-67 56 25	-	-	-	-	16	14	13	11	-	-	-	0.8	4.2:	05290-6756	C	
1135	05 29 06.4	-66 43 31	8	-	1.5	-	-	-	-	-	p	0.30	0.17:	-	-	05291-6643	S	SAO 249293
1136	05 29 07	-67 23	9	5	5	3	28	14	23	14	-	0.15	0.22	5.8	18.7		C	
1137	05 29 08.1	-67 00 03	2	-	2	-	11	8	8	6	-	0.07:	0.22	1.2	4.2:	05291-6700	C	
1138	05 29 10	-66 51	-	-	1	-	4	2	2	1	-	-	0.11:	0.8:	2.1:		C	
1139	05 29 10	-69 04	12	8	9	5	-	-	-	-	-	0.15:	0.44	C	C		W	
1140	05 29 10	-70 34	2	-	-	-	11	9	11	10	-	0.07:	-	0.8	2.1:		C	
1141	05 29 15	-67 03	5	-	1	-	13	6	8	5	-	0.19:	0.11:	2.9	6.2	X0529-670	C	
1142	05 29 15	-70 07	22	15	4	3	-	-	-	-	p	0.26	0.11:	-	-		S	Damaged set 1
1143	05 29 15	-70 10	-	-	6	4	30	28	27	24	-	-	0.22	0.8	6.2		C	Damaged set 1
1144	05 29 15	-70 59	15	6	6	4	32	26	28	24	p:	0.33	0.22	2.5	8.3:		C	
1145	05 29 20	-69 09	13	9	8	6	-	-	-	-	-	0.15	0.22:	C	C		W	
1146	05 29 20	-69 45	15	8	-	-	-	-	-	-	-	0.26	-	-	-		S	Damaged set 1
1147	05 29 20	-70 16	10	7	-	-	-	-	-	-	-	0.11	-	-	-		S	Damaged set 1
1148	05 29 20	-70 23	12	7	-	-	26	22	20	18	p:	0.19	-	1.7	4.2		C	
1149	05 29 20.7	-67 15 44	11	-	3	-	-	-	-	-	p	0.41	0.33	-	-	05293-6715	S	
1150	05 29 21.4	-69 11 57	14	10	7	5	-	-	-	-	-	0.15:	0.22:	C	C	05293-6911	W	
1151	05 29 21.4	-70 13 08	-	-	-	-	32	28	25	20	-	-	-	1.7:	10.4	05293-7013	C	Damaged set 1
1152	05 29 22.3	-69 06 30	22	12	10	6	65	40	-	-	-	0.37:	0.44:	10.3	C	05293-6906	W	
1153	05 29 27.1	-71 04 44	25	5	10	3	-	-	-	-	p	0.74	0.78	C	C	05294-7104	W	
1154	05 29 27.8	-67 33 07	4	-	3	-	17	13	16	13	-	0.15:	0.33	1.7	6.2	05294-6733	C	
1155	05 29 30	-66 58	5	-	2	-	-	-	-	-	-	0.19	0.22	-	-		W	
1156	05 29 30	-71 14	10	5	4	2	27	15	30	20	p:	0.19	0.22	5.0	20.8:		C	
1157	05 29 31.6	-71 21 41	8	3	2.5	1	-	-	-	-	p	0.19	0.17	-	-	05295-7121	S	
1158	05 29 35	-70 43	2	-	1	-	12	9	10	8	-	0.07:	0.11:	1.2	4.2		C	
1159	05 29 42.9	-65 17 14	5	-	-	-	-	-	-	-	-	0.19:	-	-	-	05297-6517	S	
1160	05 29 45	-70 09	18	12	7	4	30	28	-	-	p:	0.22	0.33	0.8:	C		W	Damaged set 1
1161	05 29 47.3	-68 28 56	18	14	9	6	52	35	45	28	-	0.15:	0.33	7.0	35.4	05297-6828	C	
1162	05 29 50	-67 48	-	-	1	-	19	15	15	12	-	-	0.11:	1.7	6.2		C	
1163	05 29 50.4	-69 11 25	17	5	7	5	26	24	-	-	-	0.44	0.22:	0.8:	-	05298-6911	W	
1164	05 29 52.2	-69 57 27	31	8	15	3	30	27	-	-	p	0.85	1.33	1.2:	C	05298-6957	W	Damaged set 1
1165	05 29 53.3	-67 17 02	-	-	2	-	10	7	7	6	-	-	0.22:	1.2	2.1:	05298-6717	C	
1166	05 29 53.8	-68 42 38	11	7	6	4	40	30	-	-	-	0.15	0.22	4.1:	C	05298-6842	W	
1167	05 29 55	-68 32	22	13	13	7	60	40	45	40	-	0.33	0.67	8.3	10.4:		C	
1168	05 29 55	-69 51	13	8	6	3	39	30	18	16	-	0.19	0.33	3.7	4.2:		C	Damaged set 1
1169	05 29 57.1	-71 04 01	14	6	10	6	61	25	45	20	p:	0.30	0.44	14.9	52.0	05299-7104	C	
1170	05 29 59.9	-67 20 44	5	-	2	-	-	-	-	-	-	0.19	0.22	-	-	05299-6720	W	

Table 3, continued (14).

(1) Number	(2) Position RA(1950) h m s	DEC(1950) ° ' "	(3) 12 μm Peak	Bg	(4) 25 μm Peak	Bg	(5) 60 μm Peak	Bg	(6) 100 μm Peak	Bg	(7) Size arcmin	(8) F 12μm Jy	(9) F 25μm Jy	(10) F 60μm Jy	(11) F 100μm Jy	(12) IRAS-Id	(13) Spectrum	(14) Comments
					10^{-8} Watt $m^{-2}sr^{-1}$													
1171	05 30 00	-69 54	11	8	5	3	36	30	28	24	-	0.11	0.22	2.5	8.3		C	Damaged set 1
1172	05 30 01.4	-68 59 32	11	4	3	2	-	-	-	-	p:	0.26	0.11	-	-	05300-6859	S	
1173	05 30 04.6	-70 49 04	3	-	1	-	10	8	-	-	-	0.11:	0.11:	0.8:	C	05300-7049	W	
1174	05 30 05	-70 18	12	7	-	-	-	-	-	-	p:	0.19	-	-	-		S	Damaged set 1
1175	05 30 05.1	-70 14 53	8	4	-	-	32	27	24	21	-	0.15:	-	2.1	6.2:	05300-7014	C	Damaged set 1
1176	05 30 05.3	-66 59 46	4	-	4	1	20	6	13	4	p	0.15	0.33	5.8	18.7	05300-6659	C	
1177	05 30 05.6	-66 51 15	7	-	2	-	-	-	-	-	-	0.26:	0.22	-	-	05300-6651	S	
1178	05 30 10	-71 13	15	7	6	5	50	25	50	30	-	0.30	0.11:	10.3:	41.6:		C	
1179	05 30 12.2	-70 56 53	6	-	4	2	35	30	-	-	-	0.22:	0.22:	2.1	C	05302-7056	W	
1180	05 30 15	-70 08	18	12	5	3	32	28	30	24	-	0.22	0.22	1.7	12.5		C	Damaged set 1
1181	05 30 15.1	-69 34 14	-	-	4	3	26	20	15	13	-	-	0.11	2.5	4.2:	05302-6934	C	Damaged set 1
1182	05 30 15.7	-71 02 32	-	-	10	7	60	40	50	30	-	-	0.33	8.3:	41.6:	05302-7102	C	
1183	05 30 16.5	-71 05 33	22	8	12	6	50	30	50	40	p	0.52	0.67	8.3:	20.8:	05302-7105	C	
1184	05 30 20	-66 04	-	-	2	-	9	4	10	5	-	-	0.22:	2.1	10.4	05301-6602:	C	
1185	05 30 20	-68 38	19	14	13	10	70	45	-	-	-	0.19	0.33	10.3:	C		W	
1186	05 30 20.1	-66 55 04	6	-	2	-	-	-	-	-	-	0.22	0.22	-	-	05303-6655	W	
1187	05 30 23.6	-68 32 54	15	12	8	6	55	52	50	44	-	0.11:	0.22:	1.2:	12.5:	05303-6832	C	
1188	05 30 24.5	-70 00 23	13	5	-	-	-	-	-	-	p	0.30	-	-	-	05304-7000	S	Damaged set 1
1189	05 30 24.6	-71 36 30	7	-	1	-	10	5	13	9	-	0.26	0.11:	2.1	8.3	05304-7136	C	
1190	05 30 25.8	-67 22 23	13	-	4	2	-	-	-	-	p	0.48	0.22	-	-	05304-6722	S	
1191	05 30 28.2	-68 28 18	12	8	7	5	40	30	-	-	-	0.15:	0.22	4.1:	C	05304-6828	W	
1192	05 30 28.7	-69 24 56	3	-	5	3	27	20	18	15	-	0.11:	0.22	2.9	6.2	05304-6924	C	
1193	05 30 30	-67 40	4	2	3	1	21	15	16	11	-	0.07	0.22	2.5	10.4		C	
1194	05 30 30	-69 12	14	9	7	5	34	30	30	28	-	0.19	0.22	1.7	4.2		C	
1195	05 30 30	-69 44	-	-	5	3	29	22	21	18	-	-	0.22	2.9	6.2		C	
1196	05 30 35	-69 42	-	-	4	2	-	-	-	-	-	-	0.22	-	-		W	
1197	05 30 40	-66 45	3	-	2	-	-	-	-	-	-	0.11:	0.22	-	-		W	
1198	05 30 40.3	-70 32 52	8	-	3	-	-	-	-	-	p	0.30	0.33	-	-	05306-7032	W	
1199	05 30 42.4	-71 07 15	22	8	20	8	100	40	70	45	-	0.52	1.33	24.8	52.0	05307-7107	C	
1200	05 30 50	-71 31	4	-	2	-	10	8	14	13	3x3	0.57	0.73	1.6	2.9		C	
1201	05 30 55.6	-70 56 53	14	3	6	3	32	28	30	26	-	0.41:	0.33	1.7	8.3:	05309-7056	C	
1202	05 30 59.5	-68 08 53	4	-	3	2	-	-	-	-	-	0.15:	0.11:	C	C	05309-6808	S	
1203	05 31 00	-67 58	9	6	5	3	30	20	35	29	-	0.11	0.22	4.1	12.5:		C	
1204	05 31 00	-68 41	20	15	15	10	93	80	-	-	-	0.19:	0.56:	5.4:	C		W	
1205	05 31 00	-69 33	4	2	4	3	20	18	-	-	-	0.07:	0.11	0.8:	C		W	Damaged set 1
1206	05 31 00	-71 14	10	5	4	2	22	12	30	20	-	0.19	0.22	4.1	20.8:	05314-7115:	C	
1207	05 31 00.2	-67 22 18	8	2	8	2	20	11	15	9	p	0.22	0.67	3.7	12.5	05310-6722	C	
1208	05 31 02.6	-71 10 00	45	10	42	6	150	100	100	70	p	1.29	4.00	20.7	62.4:	05310-7110	C	
1209	05 31 03.1	-69 13 47	12	9	9	6	-	-	-	-	-	0.11:	0.33:	C	C	05310-6913	W	
1210	05 31 04.0	-68 14 05	8	3	4	2	30	26	28	22	p:	0.19	0.22	1.7	12.5	05310-6814	C	
1211	05 31 05	-68 45	12	8	7	5	-	-	-	-	-	0.15	0.22:	C	C		W	
1212	05 31 06.4	-69 18 02	11	5	5	4	-	-	-	-	-	0.22	0.11:	C	C	05311-6918	S	
1213	05 31 09.2	-68 36 38	44	20	50	13	140	90	110	75	p	0.89	4.11	20.7	72.8	05311-6836	C	
1214	05 31 09.3	-67 23 58	3	-	4	2	16	12	17	12	-	0.11:	0.22	1.7:	10.4:	05311-6723	C	
1215	05 31 10	-69 08	11	8	11	8	-	-	-	-	-	0.11	0.33	C	C		W	
1216	05 31 15	-67 52	12	6	6	4	42	35	35	30	-	0.22	0.22	2.9	10.4:		C	
1217	05 31 15	-69 46	12	7	5	3	-	-	-	-	p:	0.19	0.22:	-	-		W	
1218	05 31 16.4	-69 04 45	13	7	10	7	60	50	45	40	p:	0.22	0.33	4.1	10.4:	05312-6904	C	
1219	05 31 20	-67 46	9	6	6	4	30	25	-	-	-	0.11	0.22	2.1:	C		W	
1220	05 31 20	-69 36	-	-	-	-	27	23	21	19	-	-	-	1.7	4.2:		C	
1221	05 31 20	-70 12	-	-	4	2	28	24	24	22	-	-	0.22	1.7	4.2		C	
1222	05 31 21.9	-69 13 03	22	10	11	9	50	40	-	-	-	0.44	0.22:	4.1:	C	05313-6913	W	
1223	05 31 23.5	-69 20 51	15	5	7	5	32	27	24	21	p	0.37	0.22	2.1	6.2	05313-6920	C	
1224	05 31 25.3	-71 01 51	-	-	7	4	40	30	-	-	-	-	0.33	4.1:	C	05314-7101	W	
1225	05 31 26.6	-69 10 21	19	12	11	8	65	45	55	40	p:	0.26	0.33:	8.3	31.2	05314-6910	C	
1226	05 31 27	-66 08	5	-	2	-	13	5	14	6	-	0.19	0.22	3.3	16.6		C	
1227	05 31 30	-67 59	10	6	4	3	40	30	-	-	-	0.15	0.11:	4.1	C		W	
1228	05 31 30	-68 03	12	6	6	3	35	30	35	30	-	0.22	0.33	2.1	10.4:		C	
1229	05 31 30	-68 22	13	10	7	5	42	35	45	35	-	0.11	0.22	2.9	20.8:		C	
1230	05 31 30	-70 16	-	-	4	2	34	30	23	21	-	-	0.22	1.7	4.2		C	
1231	05 31 30	-71 10	76	10	70	6	225	40	125	30	p	2.44	7.10	76.6	197.6	05313-7109:	C	
1232	05 31 30.8	-71 45 07	4	-	7	-	4	2	5	4	p	0.15:	0.78	0.8	2.1:	05315-7145	C	
1233	05 31 33.6	-68 33 33	35	20	24	13	125	100	100	90	-	0.56	1.22	10.3:	20.8:	05315-6833	C	
1234	05 31 35.4	-66 31 52	9	-	2	-	-	-	-	-	p	0.33	0.22:	-	-	05315-6631	S	
1235	05 31 39.0	-66 16 02	-	-	2	-	10	4	9	6	-	-	0.22	2.5	6.2:	05316-6616	C	
1236	05 31 40	-67 01	-	-	1	-	5	3	4	2	-	-	0.11:	0.8	4.2:		C	
1237	05 31 40.9	-71 24 46	11	2	3.5	1.5	16	8	20	10	p	0.33	0.22	3.3	20.8	05316-7124	C	
1238	05 31 41.5	-66 04 53	14	3	5	1	-	-	-	-	p	0.41	0.44	-	-	05316-6604	W	
1239	05 31 45.3	-69 07 39	-	-	14	7	-	-	-	-	-	-	0.78	C	C	05317-6907	W	
1240	05 31 48.6	-69 56 22	-	-	6	4	44	30	32	25	-	-	0.22	5.8	14.6	05318-6956	C	Damaged set 1
1241	05 31 51	-66 43	3	-	1.5	-	-	-	-	-	-	0.11:	0.17:	-	-		W	
1242	05 31 51.7	-68 24 36	18	12	9	6	-	-	-	-	-	0.22:	0.33:	C	C	05318-6824	W	
1243	05 31 52.3	-72 47 56	12	-	-	-	-	-	-	-	p:	0.44:	-	-	-	05318-7247	S	
1244	05 31 54.4	-67 23 52	8	2	5	2	19	11	15	12	p:	0.22	0 33	3.3	6.2:	05319-6723	C	
1245	05 31 55	-68 06	12	6	4	3	32	26	30	28	-	0.22	0.11:	2.5:	4.2:		C	
1246	05 31 55	-71 04	18	8	11	7	-	-	-	-	-	0.37	0.44	C	C		W	
1247	05 31 55.9	-68 36 46	32	23	35	14	125	100	100	90	p:	0.33	2.33	10.3:	20.8:	05319-6836	C	
1248	05 32 00	-70 03	-	-	3	1.5	22	18	13	11	-	-	0.17	1.7	4.2:		C	Damaged set 1
1249	05 32 00.5	-68 32 03	48	30	26	17	155	105	115	100	p:	0.67	1.00	20.7	31.2:	05320-6832	C	
1250	05 32 01.6	-70 20 18	7	4	7	2	24	22	-	-	-	0.11	0.56	0.8:	-	05320-7020	W	
1251	05 32 01.8	-71 06 12	70	10	115	4	285	30	137	20	p	2.22	12.32	105.6	243.4	05320-7106	C	
1252	05 32 05	-69 49	12	9	4	3	60	50	45	40	p:	0.11:	0.11	4.1	10.4:		C	
1253	05 32 05.0	-66 26 08	25	4	32	1	60	12	60	10	-	0.78	3.44	19.9:	104.0:	05320-6626 X0532-664	C	
1254	05 32 07.8	-69 41 35	16	8	6	5	31	28	28	26	-	0.30	0.11	1.2	4.2:	05321-6941	C	
1255	05 32 09.0	-68 28 47	35	25	38	17	130	100	-	-	p	0.37	2.33	12.4	C	05321-6828	W	
1256	05 32 10	-66 23	5	-	2	-	12	10	-	-	-	0.19:	0.22:	0.8:	C		W	
1257	05 32 10	-69 00	14	10	9	6	-	-	-	-	-	0.15	0.33	C	C		W	
1258	05 32 10	-70 32	-	-	-	-	10	8	9	7	-	-	-	0.8	4.2:		C	
1259	05 32 10.8	-67 44 30	60	20	77	23	-	-	-	-	p	1.48	5.99	C	C	05321-6744	W	
1260	05 32 15	-71 24	5	3	2	-	12	10	-	-	-	0.07	0.22:	0.8:	C		W	

Table 3, continued (15).

(1)	(2)		(3)		(4)		(5)		(6)		(7)	(8)	(9)	(10)	(11)	(12)	(13)	(14)
Number	Position RA(1950) h m s	DEC(1950) ° ' "	12 μm Peak	Bg	25 μm Peak	Bg	60 μm Peak	Bg	100 μm Peak	Bg	Size arcmin	F 12μm Jy	F 25μm Jy	F 60μm Jy	F 100μm Jy	IRAS-Id	Spec-trum	Comments
					10^{-8} Watt m^{-2}sr^{-1}													
1261	05 32 15.2	-67 48 28	20	15	16	8	100	80	-	-	-	0.19	0.89:	8.3:	C	05322-6748	W	
1262	05 32 20	-66 05	-	-	-	-	12	7	12	8	-	-	-	2.1	8.3		C	
1263	05 32 20	-68 19	12	10	7	5	42	35	-	-	-	0.07	0.22	2.9:	C		W	
1264	05 32 20	-70 24	7	4	3	2	29	24	23	20	-	0.11:	0.11:	2.1	6.2		C	
1265	05 32 24.0	-69 24 07	-	-	-	-	28	25	-	-	-	-	-	1.2	-	05324-6924	W	
1266	05 32 25.5	-65 51 34	115	-	14	-	-	-	-	-	p	4.25	1.55	-	-	05324-6551	S	
1267	05 32 28.1	-68 12 32	-	-	5	3	30	27	28	24	-	-	0.22:	1.2	8.3	05324-6812	C	
1268	05 32 29.3	-66 19 17	2	-	1.5	-	11	6	10	8	-	0.07:	0.17	2.1	4.2	05324-6619	C	
1269	05 32 30	-69 39	10	7	6	5	43	40	30	28	-	0.11:	0.11:	1.2	4.2:		C	
1270	05 32 30	-69 49	15	10	7	5	70	60	48	40	-	0.19	0.22	4.1	16.6:		C	
1271	05 32 30	-69 56	12	9	6	4	52	48	37	35	-	0.11:	0.22	1.7	4.2		C	
1272	05 32 30	-71 18	18	6	4	2	20	10	25	18	p	0.44	0.22	4.1:	14.6:		C	
1273	05 32 30.0	-66 29 21	48	2	62	-	205	3	110	2	p	1.70	6.88	83.6	224.6	05325-6629	C	
1274	05 32 34.9	-67 43 41	78	30	105	25	350	75	180	45	p	1.78	8.88	113.8	280.8	05325-6743	C	
1275	05 32 35.2	-69 11 07	10	7	7	5	34	30	-	-	-	0.11:	0.22	1.7:	-	05325-6911	W	
1276	05 32 35.7	-71 06 17	16	10	20	6	100	40	-	-	-	0.22:	1.55	24.8:	C	05325-7106	W	
1277	05 32 37.0	-68 58 46	25	12	13	8	92	60	62	45	p	0.48	0.56	13.2	35.4:	05326-6858	C	
1278	05 32 38.5	-70 04 19	-	-	5	2	-	-	-	-	-	-	0.33	-	-	05326-7004 X0532-687	W	Damaged set 1
1279	05 32 39.4	-68 42 11	38	10	24	13	132	63	90	65	-	1.04	1.22	28.6	52.0	05326-6842	C	
1280	05 32 40	-67 10	14	-	6	2	-	-	-	-	-	0.52	0.44	-	-		S	
1281	05 32 45.1	-67 57 08	14	3	7	2	-	-	-	-	p	0.41	0.56	-	-	05327-6757	W	
1282	05 32 50	-67 32	24	15	14	10	80	50	60	40	-	0.33	0.44	12.4	41.6		C	
1283	05 32 51	-71 13	12	5	-	-	-	-	-	-	p:	0.26	-	C	C		S	
1284	05 32 52.5	-68 27 08	40	22	23	18	-	-	-	-	p:	0.67	0.56:	C	C	05328-6827	S	
1285	05 32 54.5	-71 15 18	30	4	17	2	62	10	48	13	p:	0.96	1.66	21.5	72.8	05329-7115	C	
1286	05 32 54.7	-67 08 54	23	-	18	1.5	3	2	-	-	p	0.85	1.83	0.4:	-	05329-6708	W	
1287	05 32 55.3	-69 40 26	10	8	6	4	42	36	33	30	-	0.07:	0.22	2.5:	6.2:	05329-6940	C	
1288	05 33 00	-67 36	12	9	9	6	70	54	-	-	-	0.11	0.33	6.6:	C		W	
1289	05 33 00	-67 38	15	10	10	7	70	60	45	40	-	0.19	0.33	4.1:	10.4:		C	
1290	05 33 00	-69 36	14	10	7	4	50	40	35	30	-	0.15	0.33	4.1	10.4:	05331-6935:	C	
1291	05 33 00	-70 13	11	7	5	3	37	30	32	25	-	0.15	0.22	2.9	14.6		C	
1292	05 33 00.9	-67 43 18	52	20	61	23	-	-	-	-	p	1.18	4.22	C	C	05330-6743	W	
1293	05 33 02.1	-68 26 03	43	18	53	18	167	90	100	70	p	0.93	3.88	31.9	62.4	05330-6826	C	
1294	05 33 08.3	-66 50 05	7	-	1	-	-	-	-	-	p	0.26	0.11:	-	-	05331-6650	S	
1295	05 33 14.8	-70 25 29	8	4	-	-	-	-	-	-	-	0.15:	-	-	-	05332-7025	S	
1296	05 33 15	-67 30	15	10	9	7	70	50	45	40	-	0.19	0.22	8.3:	10.4:		C	
1297	05 33 15	-70 11	11	7	-	-	-	-	-	-	-	0.15	-	-	-		S	
1298	05 33 19.9	-69 48 24	48	12	90	10	240	70	92	50	p	1.33	8.88	70.4	87.4	05333-6948	C	
1299	05 33 20	-69 06	13	10	9	6	55	50	48	45	-	0.11	0.33	2.1	6.2:		C	
1300	05 33 22	-69 00	23	12	16	9	110	65	70	45	p:	0.41	0.78	18.6	52.0	05334-6858:	C	
1301	05 33 26.7	-69 35 54	10	8	9	7	50	40	40	35	-	0.07:	0.22:	4.1:	10.4:	05334-6935	C	
1302	05 33 27	-71 53	5	-	1.5	-	2	1	3	2	-	0.19	0.17:	0.4	2.1		C	
1303	05 33 29.7	-66 04 19	6	2	3	-	18	6	16	10	p	0.15	0.33	5.0	12.5	05334-6604	C	
1304	05 33 29.8	-67 06 17	10	-	2	-	-	-	-	-	p	0.37	0.22	-	-	05334-6706	S	
1305	05 33 30	-67 28	12	7	9	6	60	45	-	-	-	0.19	0.33	6.2	C		W	
1306	05 33 30	-69 09	15	10	-	-	-	-	-	-	-	0.19:	-	-	-		S	
1307	05 33 34.0	-68 03 45	2	-	2	-	18	15	-	-	-	0.07:	0.22:	1.2	C	05335-6803	W	
1308	05 33 35	-69 24	10	7	7	5	45	40	-	-	-	0.11:	0.22	2.1:	C		W	
1309	05 33 35.9	-69 27 40	-	-	6	4	35	30	-	-	-	-	0.22	2.1	-	05335-6927	W	
1310	05 33 40	-67 54	3	-	-	-	17	14	15	13	-	0.11:	-	1.2	4.2:		C	
1311	05 33 40	-68 07	-	-	3	2	22	17	-	-	-	-	0.11:	2.1	C		W	
1312	05 33 40	-69 42	10	7	7	5	53	48	-	-	-	0.11:	0.22	2.1	C		W	
1313	05 33 40	-70 33	7	-	1	-	-	-	-	-	-	0.26	0.11:	-	-		S	
1314	05 33 42.2	-69 23 05	10	6	7	5	70	45	35	28	p:	0.15	0.22:	10.3:	14.6	05337-6923	C	
1315	05 33 45	-67 27	11	6	10	7	-	-	-	-	-	0.19	0.33	C	C	05338-6725:	W	
1316	05 33 45	-69 44	15	10	7	5	-	-	-	-	p	0.19	0.22	-	-		W	
1317	05 33 48.7	-66 17 29	-	-	1	-	-	-	-	-	-	-	0.11:	-	-	05338-6617	W	
1318	05 33 51.9	-68 22 21	23	12	9	6	53	38	52	37	p:	0.41	0.33	6.2	31.2	05338-6822	C	
1319	05 33 51.9	-71 59 42	19	-	2	-	-	-	-	-	p	0.70	0.22	-	-	05338-7159	S	
1320	05 33 52.7	-67 35 24	12	8	7	6	49	38	40	34	-	0.15	0.11:	4.6:	12.5:	05338-6735	C	
1321	05 33 52.8	-66 45 12	-	-	1	-	3	1	2	1	p:	-	0.11:	0.8	2.1:	05338-6645	C	
1322	05 33 55	-69 26	11	6	8	6	-	-	-	-	-	0.19	0.22	C	C		W	
1323	05 33 58.6	-68 47 52	48	10	70	8	220	65	93	42	p	1.41	6.88	64.2	106.1	05339-6847	C	
1324	05 33 58.9	-69 54 27	25	13	15	9	92	80	62	50	-	0.44	0.67	5.0	25.0:	05339-6954	C	
1325	05 33 59.2	-66 31 01	-	-	-	-	5	1	5	3	p:	-	-	1.7	4.2	05339-6631	C	
1326	05 34 00	-66 07	3	-	2	-	14	10	15	9	-	0.11:	0.22:	1.7	12.5		C	
1327	05 34 00	-68 39	12	7	6	3	34	30	-	-	p:	0.19	0.33	1.7:	C		W	
1328	05 34 00	-69 42	11	8	8	6	60	50	35	30	-	0.11:	0.22	4.1	10.4:		C	
1329	05 34 10	-68 18	11	8	6	4	38	33	-	-	-	0.11	0.22	2.1	C		W	
1330	05 34 15	-69 13	15	10	10	8	70	60	62	58	p:	0.19	0.22	4.1	8.3:		C	
1331	05 34 17.2	-67 27 17	8	4	9	5	40	30	-	-	p:	0.15	0.44	4.1:	C	05342-6727	W	
1332	05 34 20	-70 14	14	10	7	4	44	40	39	36	-	0.15	0.33	1.7	6.2		C	
1333	05 34 22.4	-68 27 30	11	6	5	4	30	25	35	25	-	0.19	0.11	2.1:	20.8:	05343-6827	C	
1334	05 34 30	-67 55	2	-	3	2	17	14	-	-	-	0.07:	0.11	1.2	C		W	
1335	05 34 30	-69 36	17	13	14	10	80	75	65	60	-	0.15:	0.44	2.1:	10.4:		C	
1336	05 34 35	-69 01	17	11	13	9	-	-	-	-	p:	0.22	0.44	C	C		W	
1337	05 34 36	-66 14	5	2	5	1.5	20	7	17	10	2xp	0.19:	0.62	6.7	15.9		C	
1338	05 34 36.2	-67 29 05	9	4	6	4	40	30	37	33	-	0.19	0.22:	4.1:	8.3:	05346-6729	C	
1339	05 34 40	-70 01	10	6	5	4	-	-	-	-	-	0.15:	0.11:	-	-		S	
1340	05 34 40	-70 20	-	-	4	3	25	22	24	22	-	-	0.11:	1.2	4.2		C	
1341	05 34 41.0	-69 49 13	215	15	220	30	170	120	80	70	-	7.40'	21.09	20.7	20.8:	05346-6949	W	
1342	05 34 45	-69 12	18	12	15	12	-	-	-	-	-	0.22	0.33	C	C		W	
1343	05 34 45	-71 05	7	-	1	-	10	8	13	10	p	0.26	0.11:	0.8	6.2		C	
1344	05 34 47.2	-68 37 04	6	2	7	3	29	17	20	16	p:	0.15	0.44	5.0	8.3	05347-6837	C	
1345	05 34 48.4	-70 24 48	16	3	4	1.5	-	-	-	-	-	0.48	0.28	-	-	05348-7024	S	
1346	05 34 52.3	-68 14 12	18	7	6	4	-	-	-	-	-	0.41	0.22	-	-	05348-6814	S	SAO 249316
1347	05 34 55.2	-70 42 40	3	-	2	-	13	11	11	9	p:	0.11:	0.22	0.8	4.2	05349-7042	C	
1348	05 35 00	-67 19	5	-	2	-	11	8	9	7	-	0.19	0.22	1.2	4.2		C	
1349	05 35 00	-68 08	11	6	6	4	27	20	34	20	-	0.19	0.22	2.9	29.1		C	
1350	05 35 00	-68 24	13	8	6	4	-	-	-	-	-	0.19	0.22	C	C		W	

Table 3, continued (16).

(1)	(2)		(3)		(4)		(5)		(6)		(7)	(8)	(9)	(10)	(11)	(12)	(13)	(14)
Number	Position RA(1950) h m s	DEC(1950) ° ' "	12 µm Peak	Bg	25 µm Peak	Bg	60 µm Peak	Bg	100 µm Peak	Bg	Size arcmin	F 12µm Jy	F 25µm Jy	F 60µm Jy	F 100µm Jy	IRAS-Id	Spec-trum	Comments
					10^{-8} Watt $m^{-2} sr^{-1}$													
1351	05 35 03	-66 21	7	2	4	1	20	5	19	10	1xp	0.24:	0.39	6.6:	19.1		C	
1352	05 35 03.5	-66 37 40	-	-	2	1	9	1	6	3	-	-	0.11	3.3	6.2	05350-6637	C	
1353	05 35 06.9	-69 43 48	17	12	17	15	-	-	-	-	-	0.19	0.22	C	-	05351-6943	W	
1354	05 35 10	-66 02	10	5	4	1.5	40	13	-	-	-	0.19	0.28	11.2	C	X0535-660	W	
1355	05 35 10	-68 00	4	-	3	1.5	19	14	18	17	-	0.15	0.17	2.1	2.1:		C	
1356	05 35 10	-68 16	12	7	6	4	32	25	35	25	-	0.19	0.22	2.9	20.8		C	
1357	05 35 10	-68 57	15	7	15	9	110	70	60	50	-	0.30	0.67	16.6	2.1:		W	
1358	05 35 10	-69 48	19	13	20	16	130	120	-	-	-	0.22	0.44	4.1:	C		W	
1359	05 35 12.8	-69 33 36	35	20	27	20	150	100	92	70	-	0.56	0.78	20.7	45.8	05352-6933	C	
1360	05 35 20	-67 05	5	-	1	-	-	-	-	-	-	0.19	0.11:	-	-		S	
1361	05 35 20	-69 06	43	30	33	28	140	120	110	100	-	0.48	0.56	8.3:	20.8:		C	
1362	05 35 20.2	-70 12 58	19	12	6	4	43	40	40	35	-	0.26	0.22:	1.2:	10.4:	05353-7012	C	
1363	05 35 21.0	-68 41 40	2	-	4	3	25	20	-	-	-	0.07:	0.11:	2.1:	C	05353-6841	W	
1364	05 35 25	-67 46	10	7	5	3	-	-	-	-	-	0.11	0.22	-	-		W	
1365	05 35 30	-69 25	10	8	10	8	64	58	40	35	-	0.07:	0.22	2.5	10.4:		C	
1366	05 35 30.0	-66 57 53	9	-	2	-	-	-	-	-	p	0.33	0.22	-	-	05354-6657	S	
1367	05 35 30.1	-67 36 34	150	22	330	12	700	60	240	55	p	4.74	35.30	265.0	384.8	05355-6736 X0535-676	C	
1368	05 35 35	-68 28	2	-	-	-	21	17	17	15	-	0.07:	-	1.7	4.2:		C	
1369	05 35 35	-68 58	17	13	21	15	100	80	-	-	-	0.15	0.67	8.3:	C		W	
1370	05 35 35.2	-69 15 55	-	-	52	40	-	-	-	-	-	-	1.33:	C	C	05355-6915	W	
1371	05 35 39.7	-69 54 40	-	-	9	8	-	-	-	-	-	-	0.11:	C	C	05356-6954	W	
1372	05 35 40	-67 01	-	-	1	-	6	4	5	3	-	-	0.11:	0.8	4.2		C	
1373	05 35 40	-69 51	26	20	27	20	160	140	110	80	p	0.22	0.78	8.3	62.4:		C	
1374	05 35 40	-70 05	12	8	7	5	50	40	-	-	-	0.15:	0.22	4.1:	C		W	
1375	05 35 40	-70 13	16	12	6	4	-	-	-	-	-	0.15	0.22	C	C		W	
1376	05 35 40.5	-66 04 03	22	5	33	1	93	13	54	12	2x1	1.25	6.39	43.3	97.2	05356-6604	C	
1377	05 35 50	-68 47	12	7	7	5	42	34	34	27	-	0.19	0.22	3.3	14.6		C	
1378	05 35 50	-70 01	19	11	7	6	-	-	-	-	p:	0.30	0.11:	-	-		S	
1379	05 35 55	-67 46	10	7	6	4	32	24	28	20	-	0.11	0.22	3.3	16.6		C	
1380	05 35 55.3	-71 10 01	29	1	2	-	-	-	-	-	p	1.04	0.22	-	-	05359-7110	S	SAO 256207
1381	05 36 00	-67 59	4	-	3	1	22	14	18	15	-	0.15	0.22	3.3	6.2:		C	
1382	05 36 00.8	-66 48 26	6	-	2	-	4	2	-	-	p	0.22	0.22	0.8:	-	05360-6648	W	
1383	05 36 02.2	-69 14 22	100	60	130	80	500	200	280	170	p:	1.48	5.55	124.2	228.8	05360-6914 X0535-692	C	
1384	05 36 05	-69 04	31	25	32	30	130	120	-	-	-	0.22	0.22	4.1:	C		W	
1385	05 36 06.1	-71 42 21	9	-	-	-	-	-	-	-	p	0.33	-	-	-	05361-7142	S	
1386	05 36 10	-66 37	7	-	10	8	22	10	-	-	-	0.26	0.22	5.0	C		W	
1387	05 36 10	-67 32	20	16	9	7	-	-	-	-	-	0.15	0.22:	C	C		W	
1388	05 36 10	-69 12	54	40	60	40	300	200	-	-	-	0.52	2.22	41.4:	C		W	
1389	05 36 10	-69 23	12	10	15	10	110	100	-	-	-	0.07:	0.56	4.1:	C		W	
1390	05 36 10	-70 03	22	18	11	8	-	-	-	-	-	0.15	0.33	C	C		W	
1391	05 36 10	-70 36	11	8	4	2	20	18	18	16	-	0.11	0.22	0.8	4.2:		C	
1392	05 36 12.3	-67 35 37	37	25	54	16	150	70	-	-	p	0.44	4.22	33.1	C	05362-6735	W	
1393	05 36 13.6	-69 26 44	-	-	10	8	75	65	-	-	-	-	0.22:	4.1	C	05362-6926	W	
1394	05 36 15	-71 22	7	1	5	-	8	5	10	7	p	0.22	0.56	1.2	6.2	05360-7121:	C	
1395	05 36 19.5	-66 19 09	45	2	6	2	-	-	-	-	p	1.59	0.44	-	-	05363-6619	S	SAO 249320
1396	05 36 20.8	-67 20 56	4	-	3	2	13	10	12	9	-	0.15	0.11:	1.2	6.2	05363-6720	C	
1397	05 36 21.0	-69 40 34	110	40	140	50	420	230	220	120	p	2.59	9.99	78.7	208.0	05363-6940	C	
1398	05 36 24	-66 16	-	-	-	-	18	10	17	12	1xp	-	-	3.5	10.6		C	
1399	05 36 27.8	-66 57 25	9	-	4	1	-	-	-	-	p	0.33	0.33	-	-	05364-6657	C	
1400	05 36 28.5	-66 01 27	5	-	1	-	14	10	12	10	-	0.19	0.11:	1.7	4.2:	05364-6601	C	
1401	05 36 30	-70 45	-	-	-	-	19	16	19	17	-	-	-	1.2	4.2:		C	
1402	05 36 32.1	-66 27 17	16	10	9	3	45	15	30	20	p:	0.22:	0.67	12.4:	20.8:	05365-6627	C	
1403	05 36 32.8	-69 34 05	44	28	40	27	160	90	95	70	-	0.59	1.44	29.0	52.0	05365-6934	C	
1404	05 36 35	-70 03	23	18	11	8	93	75	70	55	-	0.19	0.33	7.5	31.2		C	
1405	05 36 36.8	-70 50 43	-	-	2	1	8	6	17	14	-	-	0.11:	0.8:	6.2	05366-7050	C	
1406	05 36 38.0	-69 43 00	46	30	50	40	260	200	-	-	p:	0.59	1.11	24.8	C	05366-6942	W	
1407	05 36 42.8	-69 48 38	-	-	-	-	160	150	-	-	-	-	-	4.1:	C	05367-6948	W	
1408	05 36 43.6	-66 26 09	14	8	8	3	-	-	-	-	p:	0.22	0.56	C	C	05367-6626	W	
1409	05 36 45	-66 39	5	-	9	6	22	10	-	-	-	0.19	0.33	5.0	C		W	
1410	05 36 45	-67 15	3	-	2	-	14	10	11	9	-	0.11:	0.22:	1.7	4.2		C	
1411	05 36 45	-70 40	-	-	3	2	19	17	-	-	-	-	0.11:	0.8	C		W	
1412	05 36 47.9	-66 45 24	4	-	2	-	8	5	-	-	-	0.15:	0.22	1.2:	-	05367-6645	W	
1413	05 36 48.6	-69 24 43	37	10	25	18	-	-	-	-	p	1.00	0.78	C	C	05368-6924	S	
1414	05 36 50	-66 36	-	-	4	2	22	9	22	12	1xp	-	0.26	5.8	21.3		C	
1415	05 36 50	-67 07	5	-	4	1.5	20	10	14	9	-	0.19	0.28	4.1	10.4		C	
1416	05 36 50	-68 24	3	-	-	-	13	11	11	9	-	0.11:	-	0.8	4.2:		C	
1417	05 36 53.5	-69 20 12	33	22	46	33	210	180	120	100	p	0.41	1.66	12.4:	41.6:	05368-6920	C	
1418	05 36 55	-66 35	8	-	3	1	-	-	-	-	-	0.30	0.22	-	-		S	SAO 249322
1419	05 37 00	-66 32	9	3	6	2	26	17	-	-	-	0.22	0.44	3.7	C		W	
1420	05 37 00	-67 02	4	-	1.5	-	15	8	13	8	-	0.15	0.17:	2.9	10.4		C	
1421	05 37 00	-70 10	18	12	7	5	43	40	42	40	-	0.22	0.22	1.2	4.2:	05369-7011:	C	
1422	05 37 00.8	-66 23 44	23	8	22	4	80	12	68	15	p	0.56	2.00	28.2	110.2	05370-6623 X0536-664	C	
1423	05 37 02.5	-66 52 20	6	2	4	1	17	5	14	5	p:	0.15	0.33	5.0	18.7	05370-6652	C	
1424	05 37 04.5	-70 19 23	10	4	7	3	21	18	-	-	p	0.22	0.44	1.2	C	05370-7019	W	
1425	05 37 07.6	-69 31 27	11	9	24	12	60	55	-	-	p	0.07:	1.33	2.1:	C	05371-6931	W	
1426	05 37 08	-66 22	22	8	13	4	40	14	-	-	-	0.52	1.00	10.8	C		W	
1427	05 37 08.7	-70 45 15	12	5	-	-	-	-	-	-	p:	0.26	-	-	-	05371-7045	S	
1428	05 37 10	-67 34	20	14	10	7	57	28	55	35	-	0.22	0.33	12.0	41.6		C	
1429	05 37 10	-69 15	78	50	130	100	500	400	250	200	-	1.04	3.33	41.4	104.0	05373-6915:	C	
1430	05 37 13.7	-66 28 45	22	6	12	2	52	14	40	20	p	0.59	1.11	15.7:	41.6:	05372-6628	C	
1431	05 37 15.8	-68 16 03	7	2	5	1.5	13	8	12	8	p:	0.19	0.39	2.1	8.3	05372-6816	C	
1432	05 37 20	-70 49	-	-	2	1	15	13	16	15	-	-	0.11	0.8	2.1		C	
1433	05 37 30	-69 06	60	30	125	100	500	400	150	120	-	1.11:	2.77:	41.4:	62.4:		C	
1434	05 37 30	-69 50	55	40	34	27	-	-	-	-	-	0.56	0.78	C	C	05375-6949:	W	
1435	05 37 30.8	-70 02 21	29	20	13	10	90	80	-	-	-	0.33	0.33	4.1:	C	05375-7002	W	
1436	05 37 40	-69 47	62	35	36	25	250	200	170	140	p:	1.00	1.22	20.7	62.4		C	
1437	05 37 40	-69 58	25	20	13	10	110	100	85	75	-	0.19	0.33	4.1:	20.8	05373-6957:	C	
1438	05 37 40	-71 03	8	2	3	1	13	9	19	13	-	0.22	0.22	1.7	12.5		C	
1439	05 37 43.9	-67 28 21	9	5	4	2	25	16	20	12	-	0.15	0.22:	3.7:	16.6:	05377-6728	C	
1440	05 37 45	-67 09	7	-	2	-	16	11	13	11	-	0.26	0.22	2.1	4.2		C	

Table 3, continued (17).

(1)	(2)		(3)		(4)		(5)		(6)		(7)	(8)	(9)	(10)	(11)	(12)	(13)	(14)
Number	Position RA(1950) h m s	DEC(1950) o ' "	12 μm Peak	Bg	25 μm Peak 10^{-8} Watt $m^{-2}sr^{-1}$	Bg	60 μm Peak	Bg	100 μm Peak	Bg	Size arcmin	F 12μm Jy	F 25μm Jy	F 60μm Jy	F 100μm Jy	IRAS-Id	Spec-trum	Comments
1441	05 37 45	-69 40	33	26	32	25	160	150	-	-	p	0.26	0.78	4.1:	C		W	
1442	05 37 45.8	-66 46 43	3	-	2	-	8	6	8	6	-	0.11:	0.22	0.8:	4.2:	05377-6646	C	
1443	05 37 50	-68 38	8	4	5	3	-	-	-	-	-	0.15	0.22	C	C		W	
1444	05 37 58.9	-66 41 52	5	1	6	2	22	8	18	12	p	0.15	0.44	5.8	12.5	05379-6641	C	
1445	05 38 00	-66 13	-	-	-	-	9	5	9	7	-	-	-	1.7	4.2		C	
1446	05 38 00	-68 51	14	12	10	7	75	50	60	40	-	0.07	0.33	10.3:	41.6:		C	
1447	05 38 00	-69 22	32	26	43	35	220	200	-	-	-	0.22	0.89	8.3:	C		W	
1448	05 38 09.5	-69 12 47	200	120	450	250	1100	800	550	400	-	2.96	22.20	124.2:	312.0:	05381-6912	C	
1449	05 38 13.5	-67 01 59	-	-	2	1	9	7	9	8	-	-	0.11:	0.8:	2.1:	05382-6701	C	
1450	05 38 16.3	-68 36 21	5	2	4	2	20	15	16	11	-	0.11:	0.22:	2.1	10.4	05382-6836	C	
1451	05 38 17.7	-69 36 07	-	-	30	27	-	-	-	-	-	-	0.33	C	C	05382-6936	W	
1452	05 38 21	-71 03	10	3	2	1.5	12	9	20	15	-	0.26	0.06	1.2	10.4:		C	
1453	05 38 22.5	-67 55 45	6	-	2	-	18	13	15	13	-	0.22	0.22:	2.1	4.2:	05383-6755	C	
1454	05 38 24	-71 16	7	2	1.5	-	15	11	-	-	p	0.19	0.17	1.7	-		W	
1455	05 38 29.6	-67 46 32	5	-	3	2	14	11	14	12	-	0.19	0.11:	1.2	4.2:	05384-6746	C	
1456	05 38 30	-66 25	-	-	1.5	-	12	6	12	8	-	-	0.17:	2.5	8.3		C	
1457	05 38 30	-67 06	5	-	1.5	-	13	11	12	10	-	0.19	0.17:	0.8:	4.2:		C	
1458	05 38 30	-69 18	50	40	-	-	-	-	-	-	-	0.37:	C	C	C		S	
1459	05 38 30	-70 17	25	20	9	7	53	50	-	-	-	0.19	0.22	1.2	C		W	
1460	05 38 38.2	-69 55 59	26	20	14	12	110	100	97	93	-	0.22:	0.22	4.1:	8.3:	05386-6955	C	
1461	05 38 40	-69 33	50	38	40	30	-	-	-	-	-	0.44	1.11:	C	C		W	
1462	05 38 45	-70 10	54	40	15	10	83	75	90	75	-	0.52	0.56:	3.3	31.2	05386-7008:	C	
1463	05 38 45	-70 24	24	20	7	5	42	38	50	45	-	0.15	0.22	1.7	10.4		C	
1464	05 38 47.2	-70 03 58	-	-	10	8	80	75	-	-	-	-	0.22:	2.1:	C	05387-7003	W	
1465	05 38 48	-71 18	-	-	1	-	10	8	15	12	-	-	0.11:	0.8:	6.2		C	
1466	05 38 50	-70 28	20	16	6	4	35	30	35	30	-	0.15	0.22	2.1	10.4:	05389-7027:	C	
1467	05 38 55	-69 01	75	50	125	100	-	-	-	-	-	0.93:	2.77:	C	C		W	
1468	05 38 55.2	-68 44 28	12	10	7	4	50	40	-	-	-	0.07:	0.33:	4.1:	C	05389-6844	W	
1469	05 38 57.4	-69 08 02	2200	200	5000	750	7500	750	2200	700	-	74.00	471.75:	2794.5	3120.0	05389-6908	C	SAO 249329, 30 Doradus
1470	05 38 57.4	-69 22 08	77	20	60	40	-	-	-	-	p	2.11	2.22	C	C	05389-6922	W	
1471	05 38 57.6	-70 42 40	44	9	50	4	120	20	56	20	p	1.29	5.11	41.4	74.9	05389-7042 X0538-707	C	
1472	05 38 57.8	-68 54 59	30	25	30	28	-	-	-	-	-	0.19:	0.22:	C	C	05389-6854	W	
1473	05 38 58	-71 00	10	5	4	2	19	13	24	18	p:	0.19	0.22	2.5	12.5		C	
1474	05 39 00	-67 19	7	3	3	1.5	18	14	17	14	-	0.15	0.17	1.7	6.2		C	
1475	05 39 00	-70 20	28	24	9	7	-	-	-	-	-	0.15	0.22	C	C		W	
1476	05 39 04	-71 41	3	-	-	-	-	-	-	-	-	0.11:	-	-	-		S	SAO 256215
1477	05 39 09.7	-69 26 28	50	35	80	50	300	225	150	125	-	0.56	3.33	31.0	52.0:	05391-6926	C	
1478	05 39 15	-67 47	5	-	4	1.5	13	10	13	11	-	0.19	0.28:	1.2:	4.2:		C	
1479	05 39 15	-69 47	40	30	25	20	250	200	170	150	-	0.37	0.56	20.7:	41.6:		C	
1480	05 39 18	-66 34	2	-	1	-	10	7	10	8	-	0.07:	0.11:	1.2	4.2		C	
1481	05 39 20	-67 55	2	-	-	-	15	13	14	12	-	0.07:	-	0.8:	4.2:		C	
1482	05 39 20	-69 15	120	75	300	200	1000	800	500	400	-	1.66	11.10:	82.8:	208.0:		C	
1483	05 39 20	-69 30	80	60	-	-	-	-	-	-	p:	0.74	C	C	C		S	
1484	05 39 20	-70 35	14	11	4	3	20	18	31	29	-	0.11	0.11:	0.8:	4.2:		C	
1485	05 39 21.5	-69 36 16	60	50	-	-	-	-	-	-	-	0.37:	C	C	C	05393-6936	S	
1486	05 39 27.2	-70 15 14	40	33	15	12	-	-	-	-	-	0.26	0.33	C	C	05394-7015	W	
1487	05 39 30	-69 56	35	30	18	15	110	100	110	100	-	0.19:	0.33	4.1:	20.8:		C	
1488	05 39 33.1	-68 20 13	4	-	2	-	10	5	11	7	-	0.15:	0.22:	2.1	8.3	05395-6820	C	
1489	05 39 35.0	-71 03 31	-	-	3	2	15	12	-	-	-	-	0.11	1.2:	C	05395-7103	W	
1490	05 39 37.4	-69 31 56	205	85	405	125	1100	500	450	300	p	4.44	31.08	248.4	312.0	05396-6931	C	
1491	05 39 37.8	-71 08 04	8	4	3	2	17	12	23	18	-	0.15	0.11	2.1	10.4	05396-7108	C	
1492	05 39 40	-67 02	5	-	2	-	14	9	13	7	-	0.19	0.22:	2.1	12.5		C	
1493	05 39 40	-68 56	50	33	47	30	300	170	200	150	-	0.63	1.89	53.8	104.0:		C	
1494	05 39 50	-69 08	200	120	600	500	-	-	-	-	-	2.96	11.10:	C	C	05399-6906:	W	
1495	05 39 50	-69 19	50	40	54	40	300	250	-	-	-	0.37:	1.55	20.7:	C		W	
1496	05 39 51.6	-67 19 50	4	-	4	2	21	14	15	12	-	0.15:	0.22	2.9	6.2	05398-6719	C	
1497	05 40 02.2	-70 13 49	45	33	35	15	120	75	95	80	-	0.44	2.22	18.6	31.2	05400-7013	C	
1498	05 40 03	-66 40	-	-	-	-	6	4	6	4	-	-	-	0.8:	4.2		C	
1499	05 40 03	-66 48	-	-	-	-	9	5	8	4	1x1:	-	-	1.9	8.7		C	
1500	05 40 05.3	-70 01 31	36	30	15	12	84	75	-	-	-	0.22	0.33	3.7:	C	05400-7001	W	
1501	05 40 06.4	-69 47 37	320	200	600	400	1500	500	600	300	p:	4.44	22.20	414.0:	624.0:	05401-6947	C	
1502	05 40 06.4	-70 20 06	-	-	9	7	-	-	-	-	-	-	0.22	-	-	05401-7020	W	
1503	05 40 09.0	-69 40 13	530	125	1200	200	2100	500	720	350	p	14.98	111.00	662.4	769.6	05401-6940	C	
1504	05 40 10	-70 30	14	11	4	3	27	25	38	36	-	0.11:	0.11:	0.8:	4.2:		C	
1505	05 40 10	-71 10	12	6	4	2	-	-	-	-	-	0.22	0.22	C	C		C	
1506	05 40 13.2	-69 56 46	52	35	25	17	-	-	-	-	p:	0.63	0.89	C	C	05402-6956	W	
1507	05 40 15	-69 29	65	45	100	75	300	200	-	-	p:	0.74	2.77	41.4:	C	05402-6927:	W	
1508	05 40 17.9	-70 09 18	33	27	12	10	65	58	75	70	-	0.22	0.22:	2.9:	10.4:	05402-7009	C	
1509	05 40 18.9	-68 30 29	5	-	4	1.5	9	7	9	7	-	0.19:	0.28	0.8:	4.2:	05403-6830	C	
1510	05 40 20	-67 32	2	-	-	-	9	8	9	8	-	0.07:	-	0.4	2.1:		C	
1511	05 40 22.7	-70 46 41	16	12	-	-	28	25	35	32	-	0.15	-	1.2	6.2:	05403-7046	C	
1512	05 40 25.7	-67 38 33	4	-	3	1	13	10	13	9	-	0.15:	0.22:	1.2	8.3	05404-6738	C	
1513	05 40 28.1	-66 19 03	-	-	4	-	-	-	-	-	p	-	0.44	-	-	05404-6619	W	
1514	05 40 29.1	-69 33 15	-	-	80	70	240	200	-	-	-	-	1.11	16.6:	C	05404-6933	W	
1515	05 40 30	-68 39	10	6	3	2	-	-	-	-	p:	0.15	0.11:	C	C		S	
1516	05 40 30	-69 08	75	50	125	100	-	-	-	-	-	0.93	2.77:	C	C		W	
1517	05 40 30	-71 07	22	6	3	2	-	-	-	-	-	0.59	0.11	-	-		S	
1518	05 40 33.3	-69 46 10	310	200	700	400	1500	500	600	300	p	4.07	33.30	414.0:	624.0:	05405-6946	C	
1519	05 40 33.5	-69 00 54	30	25	35	30	-	-	-	-	-	0.19:	0.56	C	C	05405-6900	W	
1520	05 40 35.2	-69 35 47	70	60	80	70	-	-	-	-	-	0.37:	1.11:	C	C	05405-6935	W	
1521	05 40 36.3	-71 11 30	59	5	80	2	160	11	83	15	p	2.00	8.66	61.7	141.4	05406-7111 X0540-712	C	
1522	05 40 36.7	-69 24 14	48	25	32	25	-	-	-	-	p	0.85	0.78	C	C	05406-6924	S	
1523	05 40 40	-69 51	65	50	55	40	-	-	-	-	-	0.56	1.66	C	C		W	
1524	05 40 41.1	-66 08 19	-	-	2	-	5	3	9	4	-	-	0.22	0.8	10.4	05406-6608 X0540-661	C	
1525	05 40 45	-69 42	100	70	140	85	550	500	-	-	-	1.11:	6.10	20.7:	C	05409-6942:	W	
1526	05 40 45	-70 34	24	20	12	8	33	30	-	-	-	0.15	0.44	1.2:	C		W	
1527	05 40 46.7	-68 12 56	8	3	4	1.5	9	5	15	7	-	0.19	0.28	1.7:	16.6:	05407-6812 X0540-682	C	
1528	05 40 48	-66 13	5	-	1	-	5	4	6	4	-	0.19	0.11:	0.4:	4.2:		C	
1529	05 40 48	-71 28	4	-	3	1	12	8	17	9	3x3	0.57	0.73	3.4	23.3		C	
1530	05 40 52	-72 30	5	-	-	-	-	-	-	-	-	0.19:	-	-	-		S	SAO 256221

Table 3, continued (18).

(1)	(2)		(3)		(4)		(5)		(6)		(7)	(8)	(9)	(10)	(11)	(12)	(13)	(14)
Number	Position RA(1950) h m s	DEC(1950) ° ' "	12 µm Peak	Bg	25 µm Peak	Bg 10^{-8} Watt $m^{-2} sr^{-1}$	60 µm Peak	Bg	100 µm Peak	Bg	Size arcmin	F 12µm Jy	F 25µm Jy	F 60µm Jy	F 100µm Jy	IRAS-Id	Spec-trum	Comments
1531	05 40 53.0	-71 35 13	2	-	2	1	9	5	12	8	-	0.07:	0.11	1.7	8.3	05408-7135	C	
1532	05 40 54	-71 14	20	10	17	3	45	15	-	-	p	0.37	1.55	12.4:	C		W	
1533	05 40 57.5	-66 15 31	-	-	1	-	5	3	6	4	p:	-	0.11:	0.8:	4.2	05409-6615	C	
1534	05 40 59.4	-68 38 40	5	3	3	2	30	17	25	15	-	0.07:	0.11:	5.4:	20.8:	05409-6838	C	
1535	05 41 00	-68 54	33	25	20	15	-	-	-	-	-	0.30	0.56:	C	C		W	
1536	05 41 00	-70 40	17	13	6	5	33	30	42	40	-	0.15	0.11:	1.2	4.2:		C	
1537	05 41 01.3	-65 20 56	4	-	1	-	-	-	-	-	-	0.15:	0.11:	-	-	05410-6520	S	
1538	05 41 02.7	-67 26 52	3	-	-	-	10	7	9	7	-	0.11:	-	1.2	4.2	05410-6726	C	
1539	05 41 05.0	-69 27 06	30	20	25	20	120	100	-	-	p:	0.37	0.56	8.3:	C	05410-6927	W	
1540	05 41 05.1	-69 54 16	40	30	-	-	-	-	-	-	-	0.37	-	-	-	05410-6954	S	
1541	05 41 08.2	-70 12 04	36	30	18	13	70	50	70	60	-	0.22	0.56	8.3	20.8	05411-7012	C	
1542	05 41 10	-70 47	19	14	7	5	30	25	45	40	-	0.19	0.22	2.1	10.4:		C	
1543	05 41 10.4	-69 23 41	35	28	-	-	-	-	-	-	-	0.26	-	-	-	05411-6923	S	
1544	05 41 11.9	-70 03 34	23	18	11	8	73	60	65	55	-	0.19	0.33	5.4	20.8	05411-7003	C	
1545	05 41 15	-67 11	-	-	1.5	-	12	9	10	8	-	-	0.17	1.2	4.2		C	
1546	05 41 15	-67 55	-	-	1	-	15	11	14	11	-	-	0.11:	1.7	6.2		C	
1547	05 41 15	-68 58	33	25	25	20	210	170	150	125	-	0.30	0.56	16.6	52.0		C	
1548	05 41 15	-69 35	50	35	35	29	125	100	80	60	-	0.56	0.67	10.3:	41.6:	05413-6934:	C	
1549	05 41 15	-69 47	65	45	60	50	-	-	-	-	-	0.74	1.11	C	C		W	
1550	05 41 19.0	-70 29 34	18	14	15	7	48	35	-	-	p	0.15	0.89	5.4	C	05413-7029	W	
1551	05 41 21.6	-70 35 30	27	21	13	8	53	38	55	45	p	0.22	0.56	6.2	20.8	05413-7035	C	
1552	05 41 22.2	-69 38 37	30	20	35	30	-	-	-	-	-	0.37:	0.56:	C	C	05413-6938	W	
1553	05 41 22.9	-69 19 58	30	20	17	15	-	-	-	-	p	0.37	0.22:	C	C	05413-6919	S	
1554	05 41 23.4	-66 55 11	-	-	1	-	6	4	6	5	-	-	0.11:	0.8:	2.1:	05413-6655	C	
1555	05 41 28.2	-70 44 55	21	15	10	6	34	27	-	-	p	0.22	0.44	2.9	C	05414-7044	W	
1556	05 41 31.4	-72 04 26	24	-	2	-	-	-	-	-	p	0.89	0.22	-	-	05415-7204	S	
1557	05 41 32.5	-70 55 11	13	10	5	3	23	17	27	22	-	0.11	0.22	2.5	10.4	05415-7055	C	
1558	05 41 33.1	-68 47 38	36	12	11	7	-	-	-	-	p	0.89	0.44	-	-	05415-6847	S	SAO 249334
1559	05 41 34.3	-69 00 13	32	28	25	22	-	-	-	-	-	0.15:	0.33	C	C	05415-6900	W	
1560	05 41 36.0	-69 56 32	-	-	12	10	80	70	-	-	-	-	0.22	4.1:	C	05416-6956	W	
1561	05 41 39.6	-69 48 17	30	20	31	20	140	100	120	100	-	0.37	1.22	16.6:	41.6:	05416-6948	C	
1562	05 41 41.7	-70 25 02	30	21	12	7	47	32	50	40	p:	0.33	0.56	6.2	20.8	05416-7025	C	
1563	05 41 41.9	-68 46 11	11	9	7	5	55	40	40	35	-	0.07:	0.22:	6.2:	10.4:	05416-6846	C	
1564	05 41 45	-69 33	18	14	12	9	-	-	-	-	-	0.15	0.33	C	C		W	
1565	05 41 49	-67 26	5	-	-	-	-	-	-	-	-	0.19	-	-	-		S	SAO 249336
1566	05 41 50.2	-68 54 08	20	15	-	-	-	-	-	-	-	0.19:	C	C	C	05418-6854	S	
1567	05 41 58.8	-70 03 20	90	10	13	6	-	-	-	-	p	2.96	0.78	-	C	05419-7003	S	
1568	05 42 00	-67 02	5	-	2	-	13	6	14	7	-	0.19	0.22	2.9	14.6		C	
1569	05 42 00	-70 39	18	13	-	-	-	-	-	-	-	0.19	-	-	-		S	
1570	05 42 01.5	-69 43 33	22	12	18	15	-	-	-	-	-	0.37	0.33:	C	C	05420-6943	S	
1571	05 42 03.7	-71 18 45	17	8	10	4	35	15	-	-	p	0.33	0.67	8.3	C	05420-7118	W	
1572	05 42 06.9	-71 16 52	13	6	9	3.5	25	15	-	-	p:	0.26	0.61	4.1	C	05421-7116	W	
1573	05 42 15	-68 59	32	20	27	18	-	-	-	-	p:	0.44	1.00	C	C		W	
1574	05 42 16.4	-70 32 18	17	12	7	5	34	30	43	40	-	0.19	0.22:	1.7	6.2	05422-7032	C	
1575	05 42 20	-68 44	11	6	5	4	-	-	-	-	-	0.19	0.11:	-	-		S	SAO 249337
1576	05 42 21.6	-67 19 22	-	-	-	-	6	4	5	4	-	-	-	0.8	2.1:	05423-6719	C	
1577	05 42 21.8	-71 20 33	35	4	49	2	140	12	75	15	p	1.15	5.22	53.0	124.8	05423-7120 X0542-713	C	
1578	05 42 24	-71 13	10	6	3	2	15	12	25	20	-	0.15	0.11:	1.2	10.4		C	
1579	05 42 27.4	-68 13 25	7	2	4	1.5	7	6	5	4	p:	0.19:	0.28	0.4:	2.1:	05424-6813	C	
1580	05 42 30	-67 25	2	-	2	-	8	6	7	5	-	0.07:	0.22	0.8	4.2		C	
1581	05 42 30.4	-69 10 39	45	30	40	25	250	200	180	160	-	0.56	1.66	20.7	41.6:	05425-6910	C	
1582	05 42 32.1	-69 14 23	30	20	-	-	-	-	-	-	-	0.37	-	C	C	05425-6914	S	
1583	05 42 38.4	-69 29 10	14	9	6	4	34	31	34	32	p:	0.19	0.22	1.2	4.2:	05426-6929	C	
1584	05 42 40	-66 44	5	-	1	-	9	7	9	6	-	0.19:	0.11:	0.8	6.2:		C	
1585	05 42 41.4	-69 36 00	11	9	7	5	33	30	32	29	-	0.07:	0.22	1.2	6.2:	05426-6935	C	
1586	05 42 45	-69 08	60	40	42	35	250	200	170	150	-	0.74	0.78	20.7	41.6:		C	
1587	05 42 46	-67 10	4	-	-	-	-	-	-	-	-	0.15	-	-	-		S	SAO 249339
1588	05 42 46.1	-70 06 31	16	11	5	4	34	30	38	30	-	0.19	0.11:	1.7	16.6	05427-7006	C	
1589	05 42 54.3	-70 11 43	-	-	5	4	23	21	-	-	-	-	0.11:	0.8	C	05429-7011	W	
1590	05 42 59.5	-68 14 50	4	-	2	-	12	8	12	8	-	0.15:	0.22:	1.7	8.3	05429-6814	C	
1591	05 43 00	-66 27	3	-	1	-	9	6	12	10	-	0.11:	0.11:	1.2	4.2		C	
1592	05 43 00	-66 37	-	-	-	-	10	7	12	9	-	-	-	1.2	6.2		C	
1593	05 43 03.4	-69 13 01	28	20	15	11	110	90	90	80	-	0.30	0.44:	8.3:	20.8:	05430-6913	C	
1594	05 43 10	-69 06	55	35	54	35	250	200	150	140	-	0.74	2.11	20.7	20.8:		C	
1595	05 43 10	-70 24	13	9	3	1	22	21	31	30	-	0.15	0.22:	0.4:	2.1:		C	
1596	05 43 12.0	-67 42 26	2	-	3	2	9	8	10	9	-	0.07:	0.11:	0.4:	2.1:	05431-6742	C	
1597	05 43 12.6	-68 58 03	20	15	15	11	125	110	-	-	-	0.19:	0.44:	6.2:	C	05432-6858	W	
1598	05 43 13.7	-67 35 42	-	-	2	-	10	7	9	8	-	-	0.22:	1.2	2.1	05432-6735	C	
1599	05 43 14.6	-69 15 04	-	-	13	10	93	80	-	-	-	-	0.33:	5.4	C	05432-6915	W	
1600	05 43 16.3	-71 18 44	9	4	11	2	25	9	20	18	-	0.19	1.00	6.6	4.2:	05432-7118	W	
1601	05 43 16.6	-70 57 27	11	9	4	3	12	10	20	18	-	0.07:	0.11:	0.8:	4.2:	05432-7057	C	
1602	05 43 18.6	-67 28 56	4	-	2	-	9	7	-	-	-	0.15	0.22:	0.8:	C	05433-6728	W	
1603	05 43 20	-69 17	26	20	-	-	-	-	-	-	-	0.22:	C	C	C		S	
1604	05 43 20	-70 32	13	10	3	2	-	-	-	-	-	0.11	0.11:	-	-		S	
1605	05 43 20.2	-67 50 55	14	6	15	3	44	15	25	15	p	0.30	1.33	12.0	20.8	05433-6750 X0543-678	C	
1606	05 43 21	-66 48	6	-	2	-	11	7	13	8	-	0.22	0.22:	1.7:	10.4		C	
1607	05 43 21.3	-69 58 30	10	8	4	2	32	28	34	30	-	0.07:	0.22	1.7:	8.3:	05433-6958	C	
1608	05 43 25	-71 04	11	6	4	2	15	10	27	18	-	0.19	0.22	2.1	18.7		C	
1609	05 43 26.0	-69 46 26	55	20	45	10	200	60	120	60	p	1.29	3.88	58.0	124.8	05434-6946	C	
1610	05 43 27	-71 14	13	5	4	2	11	9	21	15	p	0.30	0.22	0.8	12.5:		C	
1611	05 43 30	-67 57	13	6	5	3	25	18	23	18	p	0.26	0.22	2.9	10.4		C	
1612	05 43 30	-70 11	11	8	4	3	22	20	28	26	-	0.11	0.11	0.8	4.2		C	
1613	05 43 31.3	-66 19 43	11	2	10	1	32	6	32	9	p:	0.33	1.00	10.8	47.8:	05435-6619 X0543-663	C	
1614	05 43 40	-66 22	9	2	6	2	25	12	-	-	p:	0.26:	0.44	5.4	C		W	
1615	05 43 41.0	-70 08 02	-	-	-	-	21	19	22	20	-	-	-	0.8	4.2:	05436-7008	C	
1616	05 43 43.5	-68 29 27	22	3	3	1.5	11	8	9	8	p	0 70	0.17	1.2:	2.1:	05437-6829	C	
1617	05 43 45	-71 13	10	6	2	1.5	-	-	-	-	-	0.15	0.06:	-	-		S	
1618	05 43 50	-68 06	10	-	3	2	13	11	14	13	p	0.37	0.11:	0.8:	2.1:	05439-6807:	C	SAO 249341
1619	05 43 50	-68 49	15	10	7	5	68	55	65	55	-	0.19	0.22	5.4	20.8		C	
1620	05 43 50	-69 41	12	9	7	5	40	35	37	35	-	0.11:	0.22	2.1	4.2:		C	

Table 3, continued (19).

(1)	(2)		(3)		(4)		(5)		(6)		(7)	(8)	(9)	(10)	(11)	(12)	(13)	(14)
Number	Position RA(1950) h m s	DEC(1950) o ' "	12 μm Peak	Bg	25 μm Peak	Bg	60 μm Peak	Bg	100 μm Peak	Bg	Size arcmin	F 12μm Jy	F 25μm Jy	F 60μm Jy	F 100μm Jy	IRAS-Id	Spectrum	Comments
					10^{-8} Watt m^{-2} sr^{-1}													
1621	05 43 52.0	-67 28 30	16	6	8	3	38	14	25	12	p	0.37	0.56	9.9	27.0:	05438-6728	C	
1622	05 43 52.0	-69 26 05	40	30	24	14	110	80	-	-	-	0.37:	1.11	12.4:	C	05438-6926	W	
1623	05 43 54.4	-67 43 10	225	4	43	2	11	9	-	-	-	8.18	4.55	0.8:	C	05439-6743	S	
1624	05 43 58.6	-65 55 11	5	-	2	-	1	-	1	-	p:	0.19	0.22	0.4:	2.1:	05439-6555	C	
1625	05 44 00	-71 31	2	-	1.5	-	6	3	12	8	-	0.07:	0.17:	1.2	8.3		C	
1626	05 44 00.9	-70 29 09	16	8	4	3	19	17	27	25	-	0.30	0.11:	0.8	4.2:	05440-7029	C	
1627	05 44 10	-68 17	10	6	4	2	22	15	24	18	-	0.15	0.22	2.9	12.5		C	
1628	05 44 10	-70 16	12	9	4	3	20	18	28	27	-	0.11:	0.11:	0.8:	2.1:		C	
1629	05 44 10.7	-69 16 52	40	25	26	20	150	100	-	-	p	0.56	0.67	20.7	C	05441-6916	W	
1630	05 44 11.7	-68 53 12	12	8	7	6	65	60	-	-	-	0.15:	0.11:	2.1:	C	05441-6853	W	
1631	05 44 12.7	-67 48 29	5	-	2	-	17	12	16	14	-	0.19:	0.22:	2.1	4.2:	05442-6748	C	
1632	05 44 13.2	-68 23 51	6	-	1	-	18	16	20	17	-	0.22:	0.11:	0.8	6.2:	05442-6823	C	
1633	05 44 17.6	-69 23 19	50	35	25	20	150	125	140	110	-	0.56	0.56	10.3:	62.4:	05442-6923	C	
1634	05 44 18	-66 18	14	4	4	2	15	10	20	15	1x1:	0.55	0.31:	2.4:	10.9		C	
1635	05 44 18	-66 22	9	3	5	2	-	-	-	-	-	0.22	0.33:	C	C		W	
1636	05 44 20	-70 18	11	9	4	3	23	20	28	27	-	0.07:	0.11	1.2	2.1:		C	
1637	05 44 27	-71 12	9	5	3	1.5	10	8	18	15	-	0.15	0.17	0.8:	6.2:		C	
1638	05 44 30	-67 26	11	7	5	3	32	18	25	20	p:	0.15	0.22	5.8	10.4:		C	
1639	05 44 30	-67 43	11	6	3	1.5	14	10	16	12	-	0.19	0.17	1.7	8.3		C	
1640	05 44 30	-69 01	13	10	8	5	80	70	65	55	-	0.11	0.33	4.1	20.8		C	
1641	05 44 30	-70 23	13	10	4	3	23	21	-	-	-	0.11	0.11	0.8	C		W	
1642	05 44 35	-68 49	18	13	8	5	-	-	-	-	-	0.19	0.33	C	C		W	
1643	05 44 35	-69 21	44	33	24	20	150	130	130	120	-	0.41	0.44	8.3:	20.8:		C	
1644	05 44 39.5	-65 45 19	33	-	3	-	1	-	-	-	p	1.22	0.33	0.4:	-	05446-6545	S	SAO 249346
1645	05 44 40	-69 39	14	10	9	7	54	50	-	-	-	0.15:	0.22	1.7	C		W	
1646	05 44 40.6	-69 45 25	24	14	10	7	-	-	-	-	p	0.37	0.33:	-	-	05446-6945	S	
1647	05 44 42.2	-68 33 10	9	5	3	2	27	20	27	22	-	0.15:	0.11:	2.9	10.4	05447-6833	C	
1648	05 44 45	-69 43	13	9	8	6	53	50	54	50	p	0.15	0.22	1.2	8.3		C	
1649	05 44 45	-70 07	-	-	-	-	18	16	21	19	-	-	-	0.8	4.2		C	
1650	05 44 46.3	-67 18 58	12	2	11	3	42	7	25	14	p	0.37	0.89	14.5	22.9:	05447-6718	C	
1651	05 44 49.9	-70 25 07	11	9	4	3	22	20	27	25	-	0.07:	0.11:	0.8	4.2:	05448-7025	C	
1652	05 44 50	-68 40	10	7	4	3	34	30	-	-	-	0.11	0.11:	1.7:	C		W	
1653	05 44 53.8	-66 41 09	3	-	1	-	8	3	10	4	-	0.11:	0.11:	2.1	12.5	05448-6641	C	
1654	05 44 58.1	-68 49 15	15	9	6	4	-	-	-	-	p:	0.22	0.22	C	C	05449-6849	C	
1655	05 45 00	-67 22	11	5	7	3	30	16	-	-	-	0.22	0.44	5.8	C		W	
1656	05 45 01.3	-69 29 59	20	15	11	9	67	57	65	55	-	0.19:	0.22	4.1:	20.8:	05450-6929	C	
1657	05 45 03.0	-70 39 12	20	14	6	4	20	15	-	-	-	0.22:	0.22:	2.1	C	05450-7039	W	
1658	05 45 10	-69 51	21	16	10	8	65	55	60	50	-	0.19	0.22	4.1	20.8:		C	
1659	05 45 10	-70 32	-	-	3	2	22	20	23	21	-	-	0.11:	0.8	4.2		C	
1660	05 45 10	-70 46	12	9	4	3	13	12	23	21	-	0.11	0.11	0.4:	4.2:		C	
1661	05 45 11.4	-66 29 23	-	-	-	-	4	3	5	4	-	-	-	0.4	2.1	05451-6629	C	
1662	05 45 14.2	-69 24 16	26	20	18	12	75	65	-	-	p	0.22	0.67	4.1:	C	05452-6924	W	
1663	05 45 15	-68 30	7	5	3	2	22	17	21	18	-	0.07:	0.11	2.1	6.2:		C	
1664	05 45 20	-67 38	2	-	2	1	12	10	13	11	-	0.07:	0.11:	0.8	4.2		C	
1665	05 45 20	-68 05	-	-	-	-	13	10	14	12	-	-	-	1.2	4.2:		C	
1666	05 45 21.6	-65 22 05	4	-	5	-	-	-	-	-	p	0.15:	0.56:	-	-	05453-6522	W	
1667	05 45 30	-67 08	13	1	7	2	31	9	-	-	p:	0.44	0.56	9.1	C		W	
1668	05 45 30	-68 12	5	3	2	1	15	13	16	15	-	0.07:	0.11:	0.8	2.1:		C	
1669	05 45 35	-69 37	30	18	14	10	80	65	70	65	-	0.44:	0.44	6.2	10.4		C	
1670	05 45 38.0	-72 34 07	-	-	-	-	2	-	1	-	-	-	-	0.8:	2.1:	05456-7234	C	
1671	05 45 44.2	-69 22 27	23	19	11	8	-	-	-	-	-	0.15:	0.33	C	C	05457-6922	W	
1672	05 45 45.8	-68 36 50	10	6	3	2	25	20	28	24	-	0.15	0.11	2.1	8.3	05457-6836	C	
1673	05 45 48.5	-67 10 49	16	1	18	1	56	9	37	6	p	0.56	1.89	19.5	64.5	05458-6710 X0545-671	C	
1674	05 45 53.1	-66 23 20	2	-	1	-	4	2	6	4	-	0.07:	0.11:	0.8	4.2	05458-6623	C	
1675	05 45 53.2	-69 47 37	32	17	50	10	150	70	86	70	p	0.56	4 44	33.1	33.3:	05458-6947	C	
1676	05 45 55	-70 39	16	11	4	3	17	14	26	23	-	0.19	0.11:	1.2:	6.2:		C	
1677	05 45 55.4	-69 51 28	23	16	12	8	60	50	-	-	p:	0.26	0.44	4.1:	C	05459-6951	W	
1678	05 45 57.0	-67 15 35	2	-	15	-	9	6	-	-	-	0.07:	1.66	1.2	C	05459-6715	W	
1679	05 46 00	-66 53	2	-	1	-	5	3	7	2	-	0.07:	0.11:	0.8	10.4	05458-6651:	C	
1680	05 46 00	-67 52	3	-	2	-	10	6	11	9	p:	0.11	0.22	1.7	4.2:		C	
1681	05 46 00	-69 32	20	15	9	7	-	-	-	-	p:	0.19	0.22:	C	C		W	
1682	05 46 00	-70 16	4	-	2	1	17	14	20	17	-	0.15:	0.11:	1.2	6.2		C	
1683	05 46 00.2	-69 57 40	9	7	2	-	27	24	-	-	-	0.07:	0.22:	1.2	C	05460-6957	W	
1684	05 46 06.3	-70 08 35	3	-	1	-	18	14	21	18	-	0.11:	0.11:	1.7	6.2	05461-7008	C	
1685	05 46 10	-69 07	15	10	8	5	60	50	60	40	-	0.19	0.33	4.1	41.6:		C	
1686	05 46 15	-67 44	4	-	-	-	-	-	-	-	-	0.15:	-	-	-		S	SAO 249353
1687	05 46 20	-68 10	4	-	2	-	11	8	18	15	p	0.15:	0.22:	1.2:	6.2		C	
1688	05 46 20	-68 26	-	-	2	-	17	13	17	14	-	-	0.22	1.7	6.2		C	
1689	05 46 20.3	-66 12 37	-	-	1	-	3	2	-	-	-	-	0.11:	0.4	-	05463-6612	W	
1690	05 46 27	-71 07	8	3	2	1	6	4	13	10	-	0.19	0.11:	0.8	6.2		C	
1691	05 46 28.2	-68 51 44	10	4	6	3	43	25	43	28	p:	0.22	0.33	7.5	31.2:	05464-6851	C	
1692	05 46 30	-69 40	30	17	9	7	85	65	-	-	-	0.48	0.22:	8.3	C		W	
1693	05 46 34.8	-69 17 14	12	8	7	4	64	45	-	-	-	0.15	0.33	7.9	C	05465-6917	W	
1694	05 46 40	-69 05	16	8	8	4	66	40	-	-	-	0.30	0.44	10.8	C		W	
1695	05 46 45	-70 31	-	-	-	-	15	13	23	22	-	-	-	0.8	2.1:		C	
1696	05 46 47.0	-69 35 45	29	19	18	10	93	66	80	65	p	0.37	0.89	11.2	31.2	05467-6935	C	
1697	05 46 50	-67 22	4	-	1	-	10	5	12	6	-	0.15:	0.11:	2.1	12.5		C	
1698	05 46 52.7	-67 10 15	-	-	2	-	8	5	-	-	-	-	0.22:	1.2:	C	05468-6710	W	
1699	05 47 00	-68 11	4	-	2	-	13	7	15	10	-	0.15	0.22:	2.5	10.4		C	
1700	05 47 00	-69 26	20	15	7	6	-	-	-	-	-	0.19	0.11:	C	C		S	
1701	05 47 00	-69 45	20	15	10	7	75	65	-	-	-	0.19:	0.33	4.1:	C		W	
1702	05 47 14	-71 16	8	2	1	-	-	-	-	-	-	0.22	0.11:	-	-		S	
1703	05 47 20	-70 15	9	6	2	1.5	-	-	-	-	-	0.11	0.06:	-	-		S	
1704	05 47 21.4	-70 08 01	-	-	3	2	23	18	30	17	-	-	0.11:	2.1	27.0	05473-7008	C	
1705	05 47 24	-71 05	6	2	1	-	-	-	-	-	-	0.15	0.11:	C	C		S	
1706	05 47 25	-69 09	14	7	6	4	43	30	42	30	-	0.26	0.22	5.4	25.0		C	
1707	05 47 25	-69 28	23	15	9	6	75	55	74	60	-	0.30	0.33	8.3	29.1		C	
1708	05 47 28.6	-68 42 20	1	-	2	-	14	10	16	12	-	0.04:	0.22:	1.7	8.3	05474-6842	C	
1709	05 47 30	-67 04	-	-	-	-	4	2	6	2	-	-	-	0.8	8.3		C	
1710	05 47 31.0	-67 46 29	75	-	8	-	-	-	-	-	p	2.77	0.89	-	-	05475-6746	S	

Table 3, continued (20).

(1)	(2)		(3)		(4)		(5)		(6)		(7)	(8)	(9)	(10)	(11)	(12)	(13)	(14)
Number	Position RA(1950) h m s	DEC(1950) ° ' "	12 µm Peak	Bg	25 µm Peak	Bg	60 µm Peak	Bg	100 µm Peak	Bg	Size arcmin	F 12µm Jy	F 25µm Jy	F 60µm Jy	F 100µm Jy	IRAS-Id	Spectrum	Comments
					10^{-8} Watt m^{-2} sr^{-1}													
1711	05 47 31.3	-67 52 29	3	-	1	-	5	2	7	4	-	0.11:	0.11:	1.2	6.2	05475-6752	C	
1712	05 47 31.5	-70 04 14	13	7	4	2	26	21	-	-	p	0.22	0.22:	2.1	C	05475-7004	W	
1713	05 47 31.5	-71 28 54	8	-	2	-	3	1	6	4	p	0.30	0.22	0.8	4.2:	05475-7128	C	
1714	05 47 32.5	-71 35 43	-	-	-	-	2	-	4	2	-	-	-	0.8:	4.2:	05475-7135	C	
1715	05 47 35.4	-67 43 01	-	-	-	-	6	2	7	3	-	-	-	1.7	8.3	05475-6743	C	
1716	05 47 38.7	-68 29 17	-	-	1	-	9	7	11	9	-	-	0.11:	0.8.	4.2:	05476-6829	C	
1717	05 47 40	-69 49	18	15	8	5	40	30	-	-	-	0.11	0.33	4.1:	C		W	
1718	05 47 40	-70 35	19	11	5	2	13	9	24	22	-	0.30	0.33	1.7	4.2		C	
1719	05 47 42.5	-70 40 50	11	7	4	2	10	7	19	17	-	0.15	0.22	1.2	4.2	05477-7040	C	
1720	05 47 50	-69 54	22	14	9	6	37	33	-	-	-	0.30	0.33	1.7	C		W	
1721	05 47 51.8	-70 45 14	14	7	6	2	8	7	17	12	p	0.26	0.44	0.4	10.4	05478-7045	C	
1722	05 48 00	-69 45	22	15	9	4	50	40	-	-	-	0.26	0.56	4.1	C		W	
1723	05 48 03.4	-68 39 50	8	-	2	-	9	7	13	10	p:	0.30	0.22	0.8:	6.2	05480-6839	C	
1724	05 48 08.4	-66 31 43	2	-	-	-	3	1	4	2	-	0.07:	-	0.8	4.2	05481-6631	C	
1725	05 48 14	-71 00	4	-	1	-	-	-	-	-	-	0.15	0.11:	-	-		S	SAO 256237
1726	05 48 15	-70 30	14	7	4	2	13	9	26	20	-	0.26	0.22	1.7	12.5		C	
1727	05 48 15.2	-68 56 19	2	-	2	1	23	20	25	20	-	0.07:	0.11:	1.2:	10.4	05482-6856	C	
1728	05 48 19	-66 39	6	-	1	-	-	-	-	-	-	0.22	0.11:	-	-		S	SAO 249361
1729	05 48 20	-69 13	10	7	3	2	30	15	30	20	-	0.11	0.11	6.2	20.8:		C	
1730	05 48 20	-70 16	10	6	2	1	16	14	23	18	-	0.15	0.11:	0.8:	10.4:		C	
1731	05 48 26.6	-69 45 53	38	8	7	4	-	-	-	-	p	1.11	0.33:	-	-	05484-6945	S	SAO 249363
1732	05 48 29.6	-71 01 28	-	-	1	-	4	2	7	4	-	-	0.11:	0.8	6.2	05484-7101	C	
1733	05 48 36.7	-69 53 53	25	8	18	4	62	25	58	45	p	0.63	1.55	15.3	27.0	05486-6953	C	
1734	05 48 40	-66 53	-	-	-	-	2	-	2	-	-	-	-	0.8	4.2		C	
1735	05 48 40	-68 16	-	-	-	-	9	6	11	9	-	-	-	1.2	4.2:		C	
1736	05 48 49.0	-72 43 04	25	4	-	-	-	-	-	-	p	0.78:	-	-	-	05488-7243	S	SAO 256239
1737	05 48 49.2	-68 50 58	2	-	3	-	16	9	20	15	-	0.07:	0.33:	2.9:	10.4	05488-6850	C	
1738	05 48 50	-68 10	6	-	1	-	-	-	-	-	-	0.22	0.11:	-	-		S	
1739	05 48 55	-68 58	8	3	3	2	20	12	28	18	-	0.19	0.11:	3.3	20.8		C	
1740	05 48 57.6	-70 02 29	20	12	30	8	-	-	-	-	p:	0.30	2.44	C	C	05489-7002	W	
1741	05 48 58.7	-70 09 44	26	12	12	5	35	20	-	-	p	0.52	0.78	6.2	C	05489-7009	W	
1742	05 49 00	-70 37	10	5	3	1	8	6	-	-	-	0.19	0.22	0.8	C		W	
1743	05 49 06.2	-70 06 24	33	12	30	10	-	-	-	-	p	0.78	2.22:	C	C	05491-7006 X0549-700	W	
1744	05 49 24.6	-70 04 14	36	10	51	6	165	24	120	20	p	0.96	4.99	58.4	208.0	05494-7004	C	
1745	05 49 34.3	-70 34 09	4	-	8	-	6	3	-	-	p	0.15	0.89	1.2	-	05495-7034	W	
1746	05 49 35.1	-68 59 11	-	-	2	1	16	13	-	-	-	-	0.11:	1.2:	C	05495-6859	W	
1747	05 49 50	-69 19	4	-	2	-	13	8	15	10	-	0.15:	0.22	2.1	10.4		C	
1748	05 49 55.5	-66 54 53	7	-	-	-	-	-	-	-	p	0.26	-	-	-	05499-6654	S	SAO 249368
1749	05 49 59.9	-70 10 49	-	-	-	-	18	10	-	-	-	-	-	3.3	C	05499-7010	W	
1750	05 50 00.8	-72 34 04	3	-	1	-	2	-	1	-	-	0.11:	0.11:	0.8:	2.1:	05500-7234	C	
1751	05 50 20	-68 17	2	-	2	-	8	6	13	9	-	0.07:	0.22	0.8:	8.3		C	
1752	05 50 24.1	-69 41 48	10	3	1	-	-	-	-	-	-	0.26:	0.11:	-	-	05504-6941	S	SAO 249372
1753	05 50 30	-68 27	6	-	2	-	15	9	17	12	-	0.22:	0.22	2.5	10.4		C	
1754	05 50 30	-68 47	-	-	-	-	8	6	13	10	-	-	-	0.8	6.2		C	
1755	05 50 30	-69 40	4	-	2	-	9	7	14	9	-	0.15:	0.22	0.8	10.4		C	
1756	05 50 36.1	-70 53 58	17	-	4	-	-	-	-	-	p	0.63	0.44	-	-	05506-7053	S	
1757	05 50 45.8	-67 51 08	4	-	2	-	-	-	-	-	-	0.15	0.22:	-	-	05507-6751	W	
1758	05 50 53.8	-71 46 43	3	-	-	-	-	-	-	-	-	0.11:	-	-	-	05508-7146	S	
1759	05 50 57.9	-69 56 53	13	-	7	-	7	4	10	8	p	0.48	0.78	1.2:	4.2:	05509-6956	C	
1760	05 51 01.5	-71 15 14	-	-	1	-	5	1	3	1.5	-	-	0.11:	1.7	3.1	05510-7115	C	
1761	05 51 02.5	-69 05 02	2	-	1	-	8	6	14	10	-	0.07:	0.11:	0.8	8.3	05510-6905	C	
1762	05 51 12.1	-69 28 53	3	-	1	-	9	6	10	8	-	0.11:	0.11:	1.2	4.2	05512-6928	C	
1763	05 51 30.1	-71 03 45	4	-	1	-	-	-	-	-	-	0.15	0.11:	-	C	05515-7103	S	
1764	05 51 38.3	-71 24 25	5	-	1	-	-	-	2	1	-	0.19	0.11:	-	2.1:	05516-7124	C	
1765	05 51 54	-71 07	4	-	-	-	-	-	-	-	-	0.15	-	-	-		S	
1766	05 52 15.3	-65 45 23	3	-	1	-	-	-	-	-	-	0.11:	0.11:	-	-	05522-6545	S	
1767	05 52 15.4	-69 56 42	-	-	-	-	5	2	6	3	-	-	-	1.2	6.2:	05522-6956	C	
1768	05 52 15.9	-71 20 10	5	-	2	-	-	-	-	-	-	0.19	0.22	-	-	05522-7120	W	
1769	05 52 29.2	-72 36 44	-	-	-	-	-	-	2	-	-	-	-	-	4.2:	05524-7236	C	
1770	05 52 38.8	-65 20 34	4	-	-	-	-	-	-	-	-	0.15:	-	-	-	05526-6520	S	
1771	05 53 10	-67 17	6	-	1	-	8	6	0.5	-	-	0.22	0.11:	0.8:	1.0:		C	
1772	05 53 15	-68 24	6	-	2	-	10	6	-	-	-	0.22:	0.22	1.7	C		W	
1773	05 53 40	-70 34	5	-	1	-	-	-	-	-	-	0.19	0.11:	-	-		S	
1774	05 53 42	-66 39	-	-	2	-	-	-	-	-	-	-	0.22	-	-		W	
1775	05 53 42	-71 37	12	-	-	-	-	-	-	-	p	0.44:	-	-	-		S	
1776	05 53 42.1	-66 53 14	-	-	4	-	4	-	1.5	-	p	-	0.44	1.7	3.1	05537-6653	C	
1777	05 53 44.5	-70 15 52	3	-	5	-	1	-	-	-	p	0.11:	0.56	0.4:	-	05537-7015	W	
1778	05 53 56	-68 14	5	-	1	-	11	5	16	9	-	0.19:	0.11:	2.5	14.6	05539-6811:	C	
1779	05 54 00.7	-68 21 42	6	-	2	-	10	6	14	10	-	0.22:	0.22	1.7	8.3	05540-6821	C	
1780	05 54 01.8	-65 33 37	8	-	3	1	-	-	-	-	p	0.30	0.22	-	-	05540-6533	S	
1781	05 54 12.2	-69 08 32	2	-	-	-	2	-	4	2	-	0.07:	-	0.8	4.2	05542-6908	C	
1782	05 54 17.4	-69 14 55	3	-	-	-	1	-	-	-	-	0.11:	-	0.4:	-	05542-6914	W	
1783	05 54 40.7	-69 49 59	-	-	-	-	3	-	3	1	-	-	-	1.2	4.2	05546-6949	C	
1784	05 54 43.2	-65 15 27	4	-	3	-	-	-	-	-	p	0.15:	0.33:	-	-	05547-6515	W	
1785	05 55 06.2	-65 28 39	-	-	4	2	-	-	-	-	p	-	0.22	-	-	05551-6528	W	
1786	05 55 12.4	-68 47 05	-	-	-	-	1	-	2	-	-	-	-	0.4:	4.2	05552-6847	C	
1787	05 55 25	-68 07	-	-	2	-	7	-	-	-	p:	-	0.22:	2.9	C		W	
1788	05 55 38.0	-67 34 31	5	-	-	-	-	-	-	-	p:	0.19	-	-	-	05556-6734	S	SAO 249396
1789	05 55 50.4	-68 03 15	12	-	1	-	-	-	-	-	p	0.44	0.11:	-	-	05558-6803	S	SAO 249398
1790	05 55 50.7	-70 00 24	20	-	6	-	-	-	-	-	p	0.74	0.67	-	-	05558-7000	S	
1791	05 56 04.7	-68 11 46	12	3	7	1	26	2	22	2	p:	0.33	0.67	9.9	41.6	05560-6811 X0556-682	C	
1792	05 56 10.1	-68 21 25	5	-	2	-	5	-	6	-	p:	0.19:	0.22:	2.1	12.5	05561-6821	C	
1793	05 56 10.7	-67 32 51	7	-	-	-	-	-	-	-	p	0.26	-	-	-	05561-6732	S	
1794	05 56 12.1	-69 33 58	6	-	5	-	10	-	5	1	p	0.22	0.56	4.1	8.3	05562-6933	C	
1795	05 56 49.6	-67 53 54	9	-	4	-	-	-	-	-	p	0.33	0.44	-	-	05568-6753	W	
1796	05 56 49.6	-70 25 03	-	-	-	-	2	-	1	-	-	-	-	0.8:	2.1:	05568-7025	C	
1797	05 56 51.3	-66 18 42	3	-	-	-	-	-	-	-	-	0.11:	-	-	-	05568-6618	S	SAO 249402
1798	05 56 51.6	-65 28 39	4	-	-	-	-	-	-	-	p	0.15:	-	-	-	05568-6528	S	
1799	05 57 07.3	-68 27 44	9	-	1	-	-	-	-	-	p	0.33	0.11:	-	-	05571-6827	S	
1800	05 57 12.5	-70 07 01	5	-	-	-	-	-	-	-	-	0.19	-	-	-	05572-7007	S	

Table 3, continued (21).

(1)	(2)		(3)		(4)		(5)		(6)		(7)	(8)	(9)	(10)	(11)	(12)	(13)	(14)
Number	Position RA(1950) h m s	DEC(1950) o ' "	12 µm Peak	Bg	25 µm Peak	Bg	60 µm Peak	Bg	100 µm Peak	Bg	Size arcmin	F 12µm Jy	F 25µm Jy	F 60µm Jy	F 100µm Jy	IRAS-Id	Spectrum	Comments
					10^{-8} Watt $m^{-2}sr^{-1}$													
1801	05 57 19.5	-69 51 26	-	-	-	-	1.5	-	1	-	-	-	-	0.6:	2.1:	05573-6951	C	
1802	05 58 30.9	-69 01 29	7	-	-	-	-	-	-	-	-	0.26:	-	-	-	05585-6901	S	
1803	05 58 52.1	-69 44 31	5	-	5	-	-	-	-	-	p	0.19	0.56	-	-	05588-6944	W	
1804	05 58 59.7	-69 51 29	22	-	1.5	-	-	-	-	-	p	0.81	0.17:	-	-	05589-6951	S	SAO 249408
1805	05 59 03	-71 20	6	1	-	-	-	-	-	-	-	0.19:	-	-	-		S	SAO 256257
1806	06 00 12.1	-66 20 05	-	-	-	-	1	-	0.7	-	-	-	-	0.4:	1.5	06002-6620A	C	
1807	06 01 08.9	-66 36 34	3	-	2	-	-	-	-	-	p:	0.11:	0.22:	-	-	06011-6636A	W	
1808	06 01 26.0	-66 28 59	-	-	-	-	1.5	-	0.7	-	p:	-	-	0.6:	1.5:	06014-6628	C	
1809	06 02 14.3	-70 06 41	20	-	2	-	-	-	-	-	p	0.74	0.22	-	-	06022-7006	S	
1810	06 02 17.1	-67 43 03	-	-	1	-	-	-	-	-	-	-	0.11:	-	-	06022-6743	W	
1811	06 02 25.4	-70 35 29	75	-	15	-	-	-	-	-	p	2.77:	1.66:	-	-	06024-7035	S	
1812	06 02 25.5	-66 45 54	4	-	-	-	-	-	-	-	-	0.15:	-	-	-	06024-6645A	S	
1813	06 02 35.3	-67 12 43	12	-	4	-	-	-	-	-	-	0.44:	0.44:	-	-	06025-6712	S	
1814	06 02 38.2	-72 08 44	40	3	3	-	-	-	-	-	p	1.37:	0.33:	-	-	06026-7208	S	SAO 256260
1815	06 02 40.4	-70 40 22	42	-	5	-	-	-	-	-	p	1.55	0.56	-	-	06026-7040	S	
1816	06 02 51	-71 03	4	-	-	-	-	-	-	-	-	0.15:	-	-	-		S	SAO 256261
1817	06 02 51.1	-67 22 15	18	-	3	-	-	-	-	-	-	0.67:	0.33:	-	-	06028-6722	S	
1818	06 03 07.4	-72 27 10	18	4	6	1	-	-	-	-	p	0.52:	0.56:	-	-	06031-7227	W	
1819	06 03 34.6	-71 02 58	-	-	6	-	12	-	3	1	p	-	0.67	5.0	4.2	06035-7102	W	
1820	06 04 13.0	-69 42 22	24	-	5	-	-	-	-	-	p	0.89:	0.56:	-	-	06042-6942	S	
1821	06 04 32.6	-67 22 54	12	-	3	-	-	-	-	-	-	0.44:	0.33:	-	-	06045-6722	S	
1822	06 04 47.0	-67 36 59	4	-	-	-	-	-	-	-	-	0.15:	-	-	-	06047-6736	S	
1823	06 06 55.7	-72 38 26	13	6	-	-	-	-	-	-	-	0.26:	-	-	-	06069-7238	S	

Note to Table 3:
a) The layout of this table is similar to Table 4 in Chapter II.

Table 4. Unconfirmed IRAS Point Sources (IRAS, 1985a).

(1)	(2)	(3)
IRAS PSC[a] name	Wavelength bands (µm)	Remarks
04525-6721	25,60	Confused by 04524-6721.
05090-6849	25	Confusion.
05100-6629	12,25	SAO 249212.
05150-6932	100	Confused by 05148-6933.
05163-7148	100	Confusion.
05174-6956	60	Confusion.
05214-6608	25	Confusion.
05228-6801	25	Confusion.
05244-6644	60	Confusion.
05254-6941	25	Confusion; damaged set 1.
05302-7102	25	Confusion.
05321-7110	12,25	Confusion.
05323-6933	60	Confusion.
05341-6917	60	Confusion.
05347-7147	60	Confusion.
05353-7026	12,25,100	
05360-7118	100	Confusion.
05372-6913	25	Confusion, 30 Doradus area.
05387-6927	12,25	Confusion.
05388-7153	60	Confusion.
05411-6952	25	Confusion.
05416-6906	12,60	Confusion.
05422-7003	60	Confusion.
05467-6712	60,100	Confusion.
05482-6927	60	Confusion.
05496-6933	100	Confusion.
05570-6722	25	
05585-7013	12	Only 0.26 Jy in IRAS PSC.

Note to Table 4:
a) Except for 05100-6629, 05353-7026, 05570-6722 and 05585-7013 all unconfirmed IRAS Point Sources are confused.

5. Identification of Sources

5.1. Stars in the DPM fields

5.1.1. Comparison with foreground stars

We have compared the Smithsonian Astrophysical Observatory Star Catalog (1966, henceforth the SAO Catalog) with our source database. For the comparisons we used maps obtained by averaging the two map sets with orthogonal scan directions, resulting in a somewhat higher signal–to–noise ratio and the special form of the point spread function makes point sources easier to recognize. On the SAO positions we have searched the maps deeper (to 10^{-8} Watt m^{-2} sr^{-1}) than for the infrared source list (Table 3). Detection of infrared emission on the known optical position depends on local noise and background (on these maps often three times less than the median noise given in Table 2).

The area of the LMC covered by the DPM maps contains 163 SAO stars. We detect 57 of these (with good detection quality at 12 μm) and we have possible detections of 43 (with medium or poor detection quality). The remaining 63 stars are below the local map sensitivity limits. In Table 5.A, similar to Table 5 in Chapter II, we give the results of the comparison. Nine stars show possible 60 or 100 μm emission, these are confused with HII regions. The detection statistics for the different stellar spectral types is given in Table 5.B. There is no clear correlation between detection and visible magnitude in the whole SAO sample. Except for G–type stars the visual detection limits are very similar to the ones found for the SMC foreground stars. These limits indicate that for the same infrared sensitivity later type stars are observed to lower visual magnitudes, as could be expected from their colours. Stars that have 25 μm emission also have 12 μm emission. Most of these SAO stars are probably Galactic foreground stars (but *e.g.* SAO 249329 corresponds to 30 Doradus).

Two infrared sources are associated to Variable Stars (Kukarkin *et al.*, 1969, 1970, 1971): LI–LMC 324 (RX Dor) and 1811 (RU Men, no LMC–member); three infrared sources related to Suspected Variable Stars (Kukarkin et al., 1981) are: LI–LMC 130 (01777; M0 star; also SAO 249138), 1748 (02693, B6; also SAO 249368), 1820 (02830, M3); infrared source LI–LMC 1077 is associated to Cool Carbon Star 363 (Stephenson, 1973). A search through the AFGL Catalog (Price and Walker, 1976) has given us another foreground star identification: HV 884 (Feast *et al.*, 1980) corresponds to the S–type infrared source LI–LMC 324.

5.1.2. Comparison with Radcliffe LMC–stars

We also searched for emission from verified LMC stars (Feast *et al.*, 1960) and we detected emission in the direction of several. The Feast LMC stars are on average fainter than SAO stars by 3 or 4 magnitudes (the brightest, with the exception of the 30 Doradus core, being R 76 with $m_V = 9.11$). Details are given in Table 6. In most cases there is confusion with HII regions.

Some Radcliffe stars show clear infrared emission: R 126, is the only star with a S–type infrared spectrum, may be showing emission from the star itself or more likely an infrared excess; two stars, R 66 and R 71 show emission from a warm dust shell (see Stahl *et al.*, 1983; Wolf and Zickgraf, 1986). The brightest LMC member, R 76 also shows 25 and

Table 5.A. SAO (1966) stars in the field of the LMC.

(1) SAO number	(2) m_V mag	(3) Sp type	(4) $F^a_{12\mu m}$ Jy	(5) $F^a_{25\mu m}$ Jy	(6) $F_{25\mu m}/F_{12\mu m}$	(7) $m_V - m_{12}$ mag	(8) Infrared Id[b]	(9) Detection quality[c]	(10) Remarks[d]
249074	8.0	K2							Not covered by IRAS DPM-map.
249084	8.2	K0	0.13	-	-	2.4	7	+	
249089	8.9	F8							Not covered by IRAS DPM-map.
249092	8.4	G0							Not covered by IRAS DPM-map.
249099	9.3	M0	0.13	-	-	3.5	19	+	
249100	8.1	F5	0.13	-	-	2.3	20	+	
249103	8.5	F5							Not covered by IRAS DPM-map.
249104	7.4	F0							Not covered by IRAS DPM-map.
249109	7.6	F8	0.16	-	-	2.0	25	+	
249115	9.2	F5	0.10:	-	-	3.1	37	0	
249120	7.8	A2	0.08:	-	-	1.4		0	
249123	7.8	M0	3.5	1.1	0.32±0.08	5.5	78	+	Faint 60 µm emission.
249125	6.8	G0	0.28	0.12	0.42±0.2	1.8	87	+	
249126	8.7	K5	0.31	0.12	0.38±0.2	3.8	93	+	
249134	8.1	A2	-	-	-	-		-	
249138	6.3	K5	3.0	1.1	0.36±0.08	3.9	130	+	
249143	9.0	K5	-	-	-	-		-	
249145	9.0	F5	0.26	0.24	0.91±0.4	3.9	164:	+	Infrared Id uncertain. Strong 60 and 100 µm. Close to DEM 23 (Table 7).
249147	9.2	Pec	-	-	-	-		-	
249153	8.6	G0	0.08:	-	-	2.2		0	
249154	7.3	A0	-	-	-	-		-	
249164	8.2	A2	0.10:	-	-	2.1	294	0	
249166	9.0	A0	0.08:	-	-	2.6		0	
249169	8.5	F8	-	-	-	-		-	
249171	8.6	F8	-	-	-	-		-	
249172	8.3	A3	0.12	0.04:	0.33±0.2	2.4	327	+	
249176	8.5	F2	-	-	-	-		-	
249184	8.9	G5	-	-	-	-		-	
249185	7.8	B9	-	-	-	-		-	
249192	8.2	G0	-	-	-	-		-	
249194	8.2	G5	0.08:	-	-	1.8		0	
249195	7.8	--	0.21:	0.08:	0.37±0.2	2.5	437	0	
249200	9.0	F2	0.05:	-	-	2.1		0	
249201	8.9	F8	0.16	0.08:	0.49±0.2	3.3	500	+	
249203	9.2	A2	-	-	-	-		-	
249204	8.7	G0							Not covered by IRAS DPM-map.
249209	8.5	A2	0.10:	-	-	2.4	522	0	
249210	8.9	F5	0.08:	-	-	2.5	526	0	
249211	8.8	--	-	-	-	-		-	
249212	7.8	K2	0.54	0.16	0.29±0.1	3.5	532	+	
249214	8.6	K0	0.08:	-	-	2 2	554	0	
249215	8.9	G0	0.10:	0.08:	0.79±0.6	2.8		0	
249217	7.6	K2	0.67	0.24	0.35±0.08	3.5	585	+	Also 60 µm emission present.
249218	7.1	F5	0.13	-	-	1.3	1866	+	Near edge of IRAS DPM-map; see Appendix A.
249221	8.5	B8	-	-	-	-		-	
249223	8.9	G5	-	-	-	-		-	
249224	8.6	F0	-	-	-	-		-	
249225	4.8	K0	4.5	1.2	0.27±0.05	2.8	639	+	Near DEM 107 (see Table 7).
249234	8.5	A3	0.10:	0.08:	0.79±0.6	2.4		0	
249237	8.9	A3	-	-	-	-		-	
249238	9.1	A2	0.10:	-	-	3.0		0	
249241	7.9	K0	0.18	0.04:	0.22±0.2	2.4	750	+	
249242	9.0	--	0.13	-	-	3.2	761	+	
249243	8.6	F5	-	-	-	-		-	
249246	9.6	G	-	-	-	-		-	
249248	9.5	G0	-	-	-	-		-	
249249	10.0	A0	-	-	-	-		-	
249252	9.1	A5	0.10:	-	-	3.0		0	
249253	8.4	K0	0.18	-	-	2.9	814	+	Near DEM 139 (see Table 7).
249255	7.6	F2	0.08:	-	-	1.2		0	

Table 5.A, continued (2).

(1) SAO number	(2) m_V mag	(3) Sp type	(4) $F_{12\mu m}$ Jy	(5) $F_{25\mu m}$ Jy	(6) $F_{25\mu m}/F_{12\mu m}$	(7) $m_V - m_{12}$ mag	(8) Infrared Id	(9) Detection quality	(10) Remarks
249260	8.8	G5	0.13	0:08:	0.60±0.4	3.0	893	+	
249263	9.4	F5	-	-	-	-		-	
249266	8.9	G0	0.08:	-	-	2.5	954	0	
249269	8.9	K0	-	-	-	-		-	
249271	9.0	A0	-	-	-	-		-	
249272	9.0	F5	-	-	-	-		-	
249273	8.6	G0	-	-	-	-		-	
249279	9.3	O	2.3	17.3	7.7 ±0.8	6.6	1076:	0	Also 60 and 100 µm emission; 1076 is probably related to DEM 199 (see Table 7).
249281	6.1	F0	0.31	0.16	0.51±0.2	1.2	1081	+	Also faint 60 µm emission.
249285	8.7	K0	0.08	-	-	2.3	1095	0	
249286	6.8	G0	0.41:	0.12:	0.29±0.15	2.2	1117	+	
249291	8.6	A2							Not covered by IRAS DPM-map.
249293	8.1	K0	0.21	0.12:	0.56±0.2	2.8	1135	+	
249294	8.4	A0	-	-	-	-		-	
249299	9.1	A2	0.13:	-	-	3.3		0	
249304	8.5	G0	0.08:	-	-	2.1		0	1.4'W of source 1241.
249310	9.1	K5	0.10	-	-	3.0		0	
249316	7.8	K0	0.28	0.16	0.56±0.2	2.8	1346	+	
249317	8.8	A3	0.08:	-	-	2.4		0	
249318	9.0	A0	-	-	-	-		-	
249320	8.4	MA	1.1	0.31	0.28±0.08	4.9	1395	+	
249321	9.2	F5							Not covered by IRAS DPM-map.
249322	6.4	A0	0.21	0.16	0.75±0.4	1.1	1418	+	0.3'S of 1418;0.8'NE of 1414.
249326	8.8	G5	-	-	-	-		-	
249328	8.7	G5	-	-	-	-		-	
249329	6.3	S3	52.	334.	6.4 ±0.7	7.0	1469:	0	30 Doradus centre; also 60 and 100 µm. 0.7'NE of 1469. DEM 263 (see Table 7).
249334	7.5	K5	0.62	0.31	0.51±0.2	3.4	1558	+	
249336	7.1	A0	0.13	-	-	1.3	1565	+	
249337	8.7	G5	0.13	0.08:	0.60±0.4	2.9	1575	+	
249339	7.7	F8	0.10	-	-	1.6	1587	+	
249340	8.8	G0	0.05:	-	-	1.9		-	
249341	7.6	K0	0.26	0.08	0.31±0.15	2.5	1618	+	Faint, probably unrelated 60 and 100 µm emission.
249342	9.2	--	-	-	-	-		-	
249343	9.3	F8	-	-	-	-		-	
249346	4.5	A5	0.85	0.24	0.28±0.08	0.7	1644	+	Faint 60 µm emission.
249353	8.1	A0	0.10:	-	-	2.0	1686	0	
249355	8.4	F8	0.03:	-	-	1.0		-	
249361	7.5	K0	0.16	0.08:	0.49±0.3	1.9	1728	+	
249362	7.6	K0							Not covered by IRAS DPM-map.
249363	9.1	M0	0.78	0.24:	0.30±0.08	5.2	1731	+	
249367	9.5	F2	-	-	-	-		-	
249368	5.1	B5	0.18	-	-	-0.4	1748	+	
249371	8.4	A0	-	-	-	-		-	
249372	8.8	K5	0.18	0.08	0.44±0.2	3.3	1752	+	
249373	8.0	A0	0.08:	-	-	1.6		0	
249375	9.2	K7	-	-	-	-		-	
249378	7.8	F2	0.05:	0.08:	1.6 ±1.5	0.9		0	
249380	9.2	F5	0.05:	-	-	2.3		0	
249389	9.1	G0	-	-	-	-		-	
249392	8.4	A0	-	-	-	-		-	
249396	9.0	K0	0.13	-	-	3.2	1788	+	
249398	7.5	K0	0.31	0.08	0.25±0.15	2.6	1789	+	
249400	8.7	G0	0.08:	-	-	2.3		0	
249402	8.3	K0	0.08:	0.04:	0.49±0.4	1.9	1797	0	
249403	8.1	F5	-	-	-	-		-	
249408	8.2	K5	0.57	0.12:	0.21±0.1	4.0	1804	+	
249411	9.2	A0	-	-	-	-		-	
249419	9.0	G0	-	-	-	-		-	
249435	7.3	A2							Not covered by IRAS DPM-map.
249436	9.1	A2	-	-	-	-		-	

Table 5.A, continued (3).

(1) SAO number	(2) m_V mag	(3) Sp type	(4) $F_{12\mu m}$ Jy	(5) $F_{25\mu m}$ Jy	(6) $F_{25\mu m}/F_{12\mu m}$	(7) $m_V - m_{12}$ mag	(8) Infrared Id	(9) Detection quality	(10) Remarks
249439	9.0	--	-	-	-	-		-	
249450	8.1	K5							Not covered by IRAS DPM-map.
249452	8.6	A2							Not covered by IRAS DPM-map.
249461	5.2	B9							Not covered by IRAS DPM-map.
256111	9.1	A0							Not covered by IRAS DPM-map.
256112	8.2	K2							Not covered by IRAS DPM-map.
256117	9.0	A0	-	-	-	-		-	
256121	8.7	F5	0.05:	-	-	1.8	10	-	
256122	5.7	B9	0.10	-	-	-0.4	14	+	
256123	8.5	K5	0.23	0.08:	0.33±0.15	3.3	17	0	Near edge of IRAS DPM-map.
256129	8.2	G5	0.10	-	-	2.1	30	+	
256130	8.4	F8	-	-	-	-		-	
256136	9.0	F8	0.05:	-	-	2.1		-	
256138	8.8	F5	-	-	-	-		-	
256139	6.2	F5	0.21	-	-	0.9	142	+	
256140	7.2	A0							Not covered by IRAS DPM-map.
256146	7.5	G5	0.31	-	-	2.6	233	+	
256149	7.7	F0	-	-	-	-		-	
256150	8.9	F8	-	-	-	-		-	
256154	5.3	K0	1.6	0.47	0.29±0.08	2.2	359	+	
256158	7.7	K0	0.18	-	-	2.2	424	+	
256161	7.5	K0	0.41	0.16	0.39±0.13	2.9	470	+	
256165	9.2	--	0.08	-	-	2.8	565:	0	4" W of SAO 256166.
256166	8.8	K0	0.08	-	-	2.4	565:	0	4" E of SAO 256165.
256169	8.2	K0	0.10	-	-	2.1	670	+	
256170	8.3	K0	0.06:	-	-	1.6		0	Near edge of IRAS DPM-map.
256171	8.4	A2	0.08:	-	-	2.0	714	0	
256173	7.8	K0	0.34	0.08:	0.23±0.1	3.0	762	+	Probably unrelated 100 µm emission.
256174	8.5	K5	0.18:	-	-	3.0	763	+	Near edge of IRAS DPM-map.
256178	8.4	G5	0.13	-	-	2.6	838	+	
256180	7.4	A3	-	-	-	-		-	
256181	7.6	A3	-	-	-	-		-	
256187	9.4	K0	0.13:	-	-	3.6	1075	+	
256191	8.2	K5							Not covered by IRAS DPM-map.
256193	8.9	F0	0.18	0.16	0.87±0.4	3.4	1104:	0	Infrared Id uncertain; also 60 and 100 µm emission.
256194	9.0	A	-	-	-	-		-	
256196	8.5	F5							Not covered by IRAS DPM-map.
256198	7.9	G5							Not covered by IRAS DPM-map.
256199	9.0	G5	-	-	-	-		-	
256200	8.5	A3							Not covered by IRAS DPM-map.
256205	8.7	A2	-	-	-	-		-	
256206	8.1	K0	0.08	-	-	1.7		0	
256207	7.7	K2	0.72	0.16	0.22±0.08	3.7	1380	+	
256212	8.6	F0	-	-	-	-		-	
256215	8.7	G0	0.08:	-	-	2.3	1476	0	
256219	9.2	A0	-	-	-	-		-	
256221	8.1	K2	0.13:	0.08	0.60±0.4	2.3	1530	+	
256223	8.4	G0	-	-	-	-		-	
256229	9.4	F8	-	-	-	-		-	
256232	8.4	G0	-	-	-	-		-	
256234	8.3	F5	-	-	-	-		-	Near edge of IRAS DPM-map.
256237	8.9	G0	0.10	-	-	2.8	1725	+	
256239	6.5	K0	0.54:	-	-	2.2	1736	+	Near edge of IRAS DPM-map.
256240	8.1	F5	-	-	-	-		-	
256244	9.4	G5	-	-	-	-		-	
256245	8.6	A2	0.05:	-	-	1.7		0	
256246	8.6	A5	-	-	-	-		-	
256250	8.7	A0	-	-	-	-		-	
256257	8.2	K0	0.13	-	-	2.4	1805	+	
256260	8.5	K5	0.96	0.24	0.25±0.08	4.8	1814	+	

Table 5.A, continued (4).

(1) SAO number	(2) m_V mag	(3) Sp type	(4) $F_{12\mu m}$ Jy	(5) $F_{25\mu m}$ Jy	(6) $F_{25\mu m}/F_{12\mu m}$	(7) $m_V - m_{12}$ mag	(8) Infrared Id	(9) Detection quality	(10) Remarks
256261	9.0	A2	0.26	-	-	3.9	1816	+	
256265	9.2	G5							Not covered by IRAS DPM-map.
256267	9.4	A0	-	-	-	-		-	
256269	8.8	K0							Not covered by IRAS DPM-map.
256272	9.0	A0	-	-	-	-		-	
256287	8.7	G5							Not covered by IRAS DPM-map.

Notes to Table 5.A:

a) The 12 and 25 µm flux densities in this table are colour-corrected (unlike those in any of the other tables) by dividing the nominal flux densities by 1.43 and 1.40 (correction for a 5000 K black body; for stars with other temperatures these factors are about the same; see IRAS, 1985a).
For possible 60 or 100 µm flux densities of these stars we refer to Table 3. Note that colour correction factors should be applied to the flux densities in that table (division factors of 1.32 and 1.09 resp.).

b) All associated infrared Id's have an S-type infrared spectrum, except for Id's 762 and 1104 with a C-type spectrum and Id's 585, 1076 and 1081 with a W-type spectrum. All associated infrared Id's are within 1' of the SAO star.
Three associations (164, 1076 and 1469) are also associated to HII regions (see Table 7); these are thus confused.

c) Detection qualities at 12 µm are good (+), medium (0) or poor (-).

d) See Section 5.1.1 in the text.

Table 5.B. Statistics of observed SAO spectral types.

(1) Spectral type[a]	(2) Number of observed stars	(3) Number of detected stars +	0	(4) Visual detection limit (mag.)	(5) Average $m_V - m_{12}$
O	1	0	1	9.3	6.6
B	4	2	0	6.7±0.5	-0.4±0.0
A	40	5	13	8.2±0.5	2.2±0.8
F	36	8	7	8.5±0.4	2.0±0.9
G	30	8	7	8.6±0.2	2.4±0.4
K	40	29	8	9.1±0.1	2.8±0.7
M	4	4	0	> 9.3	4.8±0.8

Note to Table 5 B:

a) One star of Peculiar type has not been detected.
Three out of six stars without a spectral classification in SAO (1966) have been detected.
The O-type star has a C-type infrared spectrum and shows strong 60 and 100 µm emission, showing cool dust emission.
The centre of 30 Doradus (SAO 249329) has an S3 type spectrum, with cool dust emission.

Table 6. Radcliffe stars (Feast et al., 1960) in the LMC.

(1)	(2)	(3)	(4)	(5)	(6)	(7)
Radcliffe Id[a]	m_V[b] mag	Sp type	$F_{12\mu m}$[c] Jy	Infrared Id[d]	Detection quality	Remarks[e]
51	11.28	B1.5Ia:	0.19	28:	-	0.7'N of 28, probably unrelated infrared Id.
52	10.49	B8I	-		-	Near edge of N79.
53	11.33	B0Ia:	0.07:	65:	-	Within N3. 1.1'SE of 65, probably unrelated infrared Id. See Table 7 (DEM 7).
54		Neb	9.10	103	0	Within N79 0.9'E of 103. See Tab.7 (DEM 10a).
55	10.69	B9Ieq	-		-	S69 in N79.
56	11.8	B2Ia	-		-	
57	10.73	B3I	0.22	132	0	Within N40.
58	11.0	B5I	-		-	
59	10.25	G5Ia	1.41	162	0	Within N83. 1.0'SW of 162. See Tab.7 (DEM 22).
60	V	F8:I	-	171:	-	m(pg)=13.8. 1.4'S of 171.
61	10.80	A0Ia	-		-	
62	9.65	B9Ie	-		-	S7 within N9. 0.6'NW of SAO 249147.
63	V	G2I	0.70	195:	-	m(pg)=13.0. Confused with HII region. 0.5'W of 195. See Table 7 (DEM 34).
64	10.8	WC6+O8:	-		-	Within N11.
65	11.89	B1Ia:	-		-	
66	10.64	Aeq	0.81	225	+	S73. 0.4'SW of 225; dust-shell emission.
67	11.4	Pec	-		-	S149 in N186.
68	10.95	B8I	-		-	
69	12.3 V	G2:I	-		-	
70	11.15	B3I	-		-	
71	10.91	B2.5Iep	0.81	346	+	S155. 0.2'NW of 346; dust-shell emission.
72	11.98	A0Ia	-		-	
73	10.62	B8Ia	-		-	
74	10.9	BIe	0.56	383	0	S17, outside N17. 1.5'N of 383. See Table 7 (DEM 59).
75	10.30	A0Ia	-		-	
76	9.11	A3:Ia-0(e)	-	423	+	S171 (visually brightest known LMC member). 0.5'SE of 423. See Table 7 (DEM 71). Only 25 and 60 µm emission.
77	13.0 V	F7I	-		-	
78	11.70	B0Ia	0.15	473/461:	-	Central star in N100. Confusion. 1.3'W of 473; 1.5'E of 461. See Table 7 (DEM 79).
79	12.01	B5I	0.33	531	0	Not in N103A. 0.7'NE of 531.
80	10.62	A0Ia-0	-		-	
81	10.43	B2.5Ieq	0.15	548	0	S86, not in nebulosity. 0.4'E of 548.
82	11.8	Pec	-		-	S89 in N113. In infrared extended emission.
83	V	F-G	-		-	m(pg)=13.1.
84	11.7	Pec	-		-	S91, not in nebulosity. In infrared extended emission.
85	10.87	B5Iae	0.56	764	-	Close to SAO 249242 = Id 761. In infrared extended emission. 0.5'NE of 764.
86		Cluster	-		-	Within N119. In infrared extended emission.
87	11.21	W+B1:I	-		-	Within N119. In infrared extended emission.
88	9.6 V	Aeq	-		-	S Dor = S96 within N119. In infrared extended emission.
89	11.3	B0I	1.85	816:	0	Within N120. Confused with HII region. 0.2'N of 816. See Table 7 (DEM 134).
90	12.0	WC6:	1.85	816:	0	9" South of R89. Confused with HII region. 0.2'N of 816. See Table 7 (DEM 134).
91	12.3 V	G0Ia	-		-	HD 269362 (K5).
92	9.74	F8Ia	-		-	
93	12.61	B0:	-		0	Within N43. Infrared extension at 12 and 25 µm.
94	10.03	B comp	-		0	Within N43. Close to R93 and R95.
95	12.72	B0I	-		0	Within N43. Close to R93 and R94.
96	12.29	B3I	-		-	
97	12.33	B0.5Ia:	-		-	Within N43.
98	10.54	A0Ia-0:	-		-	Near N43, within cluster NGC 1925.
99	11.5	Pec	-		-	S30 in N44.
100	11.56	B3I	-		-	Near N198.

Table 6, continued (2).

(1) Radcliffe Id	(2) m V mag	(3) Sp type	(4) F 12μm Jy	(5) Infrared Id	(6) Detection quality	(7) Remarks
101	11.61	B3Ia:	-		-	Near edge of N205B.
102		F8·Ip	-		-	m(pg)=14.9.
103	9.88	B3Ip	3.22	1076:	0	In N144 Close to SAO 249279 (with Id 1076). 0.7'SE of 1076. See Table 7 (DEM 199).
104	11.25	A0Ia:	-		-	
105	10.2 :	B8:I	1.11	1127:	0	In N135; V integrated from cluster. 0.8'W of 1127. See Table 7 (DEM 210).
106	12.5	A0I	-		-	
107	11.2	B6Ia	-		-	
108	12.9	Pec	-		-	S43.
109	12.0	B6I	-		-	
110	11.1	B9:Ieq	0.22	1218:	-	S116 in N135. 1.1'W of 1218. See Table 7 (DEM 232).
111	10.31	B9Ia-0:	0.07:	1205:	-	S117. 1.0'E of 1205. See Table 7 (DEM 224).
112	11.15	*B2Ia*	-		-	*In N206.*
113	11.7	O6e	2.22	1251:	0	Within N206A. Confused with HII region. 0.5'W of 1251. See Table 7 (DEM 221).
114	14.5	W	-		-	Within N57.
115	12.2	O5f	-		-	On border of N57, within N56.
116	10.55	B1.5Iaeq	-		-	S172, involved in N148C.
117	9.91	G0Ia	1.78	1274:	0	Within N57A. Confused with HII region. 0.3'S of 1274. See Table 7 (DEM 229).
118	9.87	A0Iae	-		-	
119	11.3	A0Ia-0	-		-	
120	10.89	B8Ia-0:	-		-	On border of N56.
121	10.49	B9Ia-0	-		-	On border of N56.
122	12.22	O6+Neb	-		-	Within N59A.
123	10.7	Pec	-		-	S124 in N149.
124	11.9	A0	-		-	Within N56.
125	11.80	B3I	-		-	Within N56.
126	10.9	Pec	1.00	1413	+	S127 in N135. 0.1'S of 1413. See Table 7 (DEM 261, 268).
127	11.4	Pec	0.07:	1425:	0	S128 in N135. 0.4'S of 1425. See Table 7 (DEM 248).
128	11.2	B1I	-	1425:	0	Close to R127. 0.5'SE of 1425. See Table 7 (DEM 248).
129	11.6	B0Ia:	-		-	Within N157; 30 Doradus outskirts.
130	11.8	B0:+W?	-		-	Within N157; 30 Doradus centre area; confused.
131	11.3	B9I	-	1469:	-	Within N157; 30 Doradus centre area; confused.
132		B-A	-	1469:	-	Within N157; 30 Doradus centre area; confused.
133		O8	-	1469:	-	Within N157; 30 Doradus centre area; confused.
134		WN7	-	1469:	-	Within N157; 30 Doradus centre area; confused.
135		WN7	-	1469:	-	Within N157, 30 Doradus centre area; confused.
136		O+WN	74.	1469	0	Central "star" in 30 Doradus, SAO 249329. See Table 7 (DEM 263).
137		B0.5Ia:	-	1469:	-	Within N157; 30 Doradus centre area; confused.
138		A0:I.	-	1469:	-	Within N157; 30 Doradus centre area; confused.
139		WN7:+O:	-	1469:	-	Within N157; 30 Doradus centre area; confused.
140		WN6	-	1469:	-	Within N157; 30 Doradus centre area; confused.
141		B0.5:	-	1469:	-	Within N157; 30 Doradus centre area; confused.
142		B	-	1469:	-	Within N157; 30 Doradus centre area; confused.
143		F7Ia	-	1469:	-	Within N157; 30 Doradus centre area; confused.
144	11.1	WN7	-	1469:	-	Within N157; 30 Doradus centre area; confused.
145	12.1	WN6-7	-	1469:	-	Within N157; 30 Doradus centre area; confused.
146	12.8	WN5	-		-	Within N157; 30 Doradus centre area; confused.
147		WN5+	-		-	Within N157; 30 Doradus centre area; confused.
148	11.98	B5I+Neb	-		-	Within N159.
149	12.26	Be+Neb	4.07	1518	-	Within N159. 0.5'NW of 1518. DEM 271 (Tab. 7).
150	9.96	G0Ia	1.11:	1525	-	Close to N160C. 0.3'NW of 1525.

Table 6, continued (3).

(1) Radcliffe Id	(2) m_V mag	(3) Sp type	(4) $F_{12\mu m}$ Jy	(5) Infrared Id	(6) Detection quality	(7) Remarks
151	11.4	A5Ia:	-		-	Within N157; 30 Doradus outskirts.
152	11.20	B2.5Ia	-		-	Within N135.
153	10.28	AIIa-O:	-		-	S143.
154	12.0	B1I	0.96	1744:	-	In N180B. Confused with HII region. 1.1'NE of 1744. See Table 7 (DEM 323).
155	11.62	B1.5Ia	-		-	
156	10.9	Cluster	-		-	
157	10.3	Cluster	0.41	216	0	0.8'NE of 216.
158	10.5	Cluster	-		-	

Notes to Table 6:

a) Radcliffe star numbers 1 to 50 are members of the SMC and are discussed in Chapter II.

b) Magnitudes followed by a V indicate that the star is variable, the average of the maximum and minimum magnitudes are given in those cases. If no visual magnitude is available in Feast et al. (1960) the average photographic magnitude m(pg) is given in column 7.

c) This table contains a 12 μm flux density only, for the 25, 60 and 100 μm flux densities we refer to Table 3.

d) Only association 1413 from Table 3 has an S-type infrared spectrum. Twenty infrared associations which have also been refered to Table 7 (HII regions) have been denoted in the remarks in column 7. Clearly these objects are confused.

e) See Section 5.1.2 in the text.

60 μm emission indicating dust shell emission (like Glass, 1984; no 12 μm emission was detected from this star). Nineteen other Radcliffe stars show some possible emission. Stars R 93, 94 and 95 are within 0.'5 of each other, and form an extension on the infrared maps at 12 and 25 μm to HII region N 43. R 94 is the brightest LMC member in JHKL (Glass, 1984) and was not detected by Glass at 10 μm.

Because these stars are the brighest LMC stars we did not continue to look for emission from other LMC-stars (see Section 5.1.3). Using the reasoning of Chapter II and looking at the detection limits for various spectral types of SAO stars (Section 5.1.1) LMC-stars, which have $m_V > 9.1$, can be detected at the distance of the LMC (53 kpc) only if they have an infrared excess.

5.1.3. Comparison with LMC Late Type Giants

A comparison of the infrared sources of Table 3 with the list of 288 Carbon and late M-type stars (Blanco *et al.*, 1980) gives three possible detections: LMC BW 9 (infrared source LI-LMC 465), BW 50 (LI-LMC 503) and O 86 (LI-LMC 992). These infrared sources have C-type infrared spectra and the associations are not completely certain.

Some other sources that show possible infrared emission are: HD 268743 (LI-LMC 243), the LMC-Cepheid HV 2294 (LI-LMC 432) and HD 34664 (LI-LMC 642). For the last one Glass (1984) detected 10 μm emission from circumstellar dust. However, these associations are not completely certain.

LI-LMC 1022 (C-type) is 1′ N of the 1979 Gamma Ray Burst GRB 03/05/79 (Apparao and Allen, 1982), which might possibly be a M-type star. Entries numbers LI-LMC 181 and 1341 (both W-type) correspond to the two luminous evolved LMC stars with thick dust shells found by Elias *et al.* (1986).

Table 7. Infrared emission from H-alpha Emission Nebulae in the LMC (Davies et al., 1976; Henize, 1956).

(1) DEM Id	(2) Henize Id	(3) Intensity of H-alpha	(4) Infrared Id	(5) Detection quality	(6) Remarks[a]
1		f		0	5'W of 40; extension on edge of infrared emission.
2	N 77D	b	46	+	Knot.
3	N 76	b	48	+	Knot 2'N of infrared source 48.
4	N 77E	b+f		+	Individual spots of DEM 4 on infrared peak 58.
4a	N 77C,B	b	69	+	
4b		b	58,63	+	DEM 4b is the brightest part of DEM 4 in the infrared.
4c	N 77A	fb		+	On infrared gradient to 58.
5		f		-	On infrared gradient to source 46 (see DEM 2).
6	N 79	b	55,56,62,67,70	0	Extended filaments on infrared emission.
7	N 3	f	65	+	IR source 65 on N-part, diffuse filaments follow infrared.
8a	N 4F	b	102	+	Irregular shell; both DEM 8a and 8b on infrared peak 102.
8b	N 4A	vb	102	+	Knot; both DEM 8a and 8b on infrared peak 102.
8c	N 4B	vb		0	Two knots on IR gradient 4'N of 102, inside IR emission.
9	N 79A,B	vf	110	+	
10	N 79A-E	vb		+	Nuclear structure and outer envelope.
10a		b	103	+	Knot DEM 10a is brightest DEM 10 spot in the infrared.
10b		b	107,111	+	Nuclear structure.
11	N 5	b	112	+	4'SE of infrared source 106.
12	N 4D,E	fb	132,146	+	Structure on infrared complex, adjacent to DEM 27.
13	N 8A	b+f	122,129	+	Envelope follows IR; bright nucleus on sources 122, 129.
14		f	114	+	2'NE of 114.
15a		vb	117	+	Around infrared peak 121; 117 on S-part.
15b		b	121	+	On infrared peak 121.
16		vf		-	6'SE of 124; on infrared filament.
17		vf		-	In infrared hole, between sources 108 and 128.
18		vf		-	In infrared hole, between sources 123 and 137.
19		vf	145,147	+	Infrared sources on SE part of shell-like structure.
20	N 7	vb	135	+	Knot.
21		f	139	+	Infrared source 139 corresponds to central blob of DEM 21.
22	N 83	b	148,162,173,193	+	
22a		vb	148	+	
22b	N 83A	vb	148	+	
22c	N 83B	vb	173	+	
22d		vb	193	+	Infrared source 193 in between filaments.
23	N 87	vb	164	+	Knot close to SAO 249145 (Id 164; see Table 5.A).
24	N 90	vb	199	+	Knot on infrared source 199 in infrared extended emission.
25	N185	b	131,159	+	Shell on edge of IR emission of sources 131 and 159.
26	N 80	f+b	151	+	Infrared source 151 coincides with bright knot on W-side.
27		vf	144,146,185,186	0	Diffuse filaments follow infrared emission. Extension of DEM 12. Bright infrared peak 144 at N-side of filament.
28		f	161,163	+	
29a	N 6	f		-	4'N of infrared source 144. In infrared extended emission.
29b		f		-	7'N of 144. In infrared extended emission.
30		f		-	Shell in infrared extended emission; towards source 166.
31	N 9	b	166	+	Blob structure follows IR; shell does not show up in IR.
32	N 84	b	194	+	Diffuse shell.
33	N 86	b	191	+	At W-side of irregular filamentary shell.
34	N10,N11A-L	vb	(see Remarks)	+	Follows infrared complex very well; related infrared sources: 177,179,190,192,195,205,206,210,214,217,219,222,226,229,243,248,259,278,284; also 244,277,283 on separate knots close to N11.
34a	N 11L	b		0	Shell and jet.
35	N 10 (part)	fb		0	5'E of 178. On edge of broad infrared peak consisting of sources 174, 176 and 178.
36	N 94A,B,C	fb	167,175,183,213,242,249	+	Irregular filaments on complex N11. IR peaks on brighter part.
37	N 93	fb	230	+	Two knots in faint nebulosity.
38	N 92A,B	b	232	+	Infrared source on nucleus of DEM 38.
39	N 91A,B	vb	235,246,262,275,282,301	+	Filaments follow IR emission. Source 235 on nucleus at W-side.
40		f	240	+	2'S of 240.

Table 7, continued (2).

(1) DEM Id	(2) Henize Id	(3) Intensity of H-alpha	(4) Infrared Id	(5) Detection quality	(6) Remarks
41	N 11E,K	vb	251	+	Knot with extension to NW.
42	N 12A	b	266	+	Shell
43		f	313	+	Extended loop follows IR emission; IR source 313 on S-part.
44		f	268	0	Diffuse nebula on infrared extended emission near N11.
45	N 16A	b+f		-	Shell 6'N of infrared source 292.
46	N 14	b	290	+	Diffuse shell 3'E of 290; at edge of N11 complex.
47		b		+	Shell 3'NE of 289; at edge of infrared peak.
48	N 13	f	305,309,316	+	Infrared sources on S-part of filaments.
49	N 15	f+b	307	+	Knot and envelope 3'E of 298.
50	N186C,D,E	b	295,317	+	Shell around IR peak 295; S-filaments on peak 317, along infrared edge.
51	N186B	vb	302	+	Knot.
52		f	315,318	+	
53		f		0	In between infrared peaks 330 and 337, on infrared filament.
54		f	340	+	2'E of 340.
55		f	300,319,343,358	+	Follows infrared emission. Infrared source 300 at W-edge.
56		f	334	+	IR source 334 on W-part of filaments; on edge of IR emission.
57		f	345	+	
58		f	348,365	+	In Bar; 4'N of infrared sources 348 and 365.
59	N 17A,B	b+f	371,375,383	+	Bright nucleus coincides with infrared source 371.
60		f	342	+	Diffuse nebula 4'SW on infrared gradient to 342.
61		vf	381	0	Infrared peak 381 on E-filaments.
62		f	373,389,390,401	+	Infrared peaks at edges of nebula structure.
63	N190	b+f	399	+	3'N of 399.
64a	N191B	b	409	0	Knot DEM 64a on infrared gradient, 3'NW of 409.
64b	N191A	b	409	+	Infrared source 409 coincides with knot DEM 64b.
65	N 21	b	404,416	+	Arc in Bar.
66	N 23A	b	405,411	+	Shell core and curved filaments in Bar.
67	N189	b	412	+	Near centre of DEM 68.
68		f	398,417,440	0	Diffuse filaments follow infrared structure.
69	N 20	b	414	+	
70		fb	419	+	Diffuse core and envelope in Bar.
71	in N 23	f	423	0	Circular ring in Bar.
72		fb	431	+	Sharp filaments 4'N of 431.
73	in N 23	f+b	429,435	+	*In Bar.*
74	in N 23	f+b	447	+	Core and diffuse envelope in Bar.
75		f	450,469,479,484	0	Faint arcs on IR complex; infrared is not followed very well.
76	*N100*	*fb*	442,457	*0*	*IR around filaments in Bar; central part in infrared hole.*
77		f		0	Diffuse arcs on edge of infrared extended emission.
78		f	454	+	In Bar.
79		f+b	461,473	+	Shell outline in Bar.
80		f	448,488,491,499	+	Filaments around 448 at W-side; on 488, 491, 499 at E-side.
81		*f*		-	*Arc 4'N of infrared source 489.*
82		f	504	0	3'S of 489; on infrared peak.
83		vf		-	4'SE of 476; at edge of extension in the infared.
84	N103B	b	475	0	Bright nucleus and shell in Bar, on IR gradient to source 510.
85	N103A	b	520	+	*Knot in Bar.*
86	N105A	vb	534	+	Bright core and outer filament in Bar.
87		f+b	573	+	Knot in Bar; on infrared gradient to peak 534.
88	N104A	f+b	514,546	+	In Bar; on infrared gradient to peak 514.
89		b	525	+	*Irregular shell, diffuse filaments.*
90		f	543	+	Shell on infrared peak.

Table 7, continued (3).

(1) DEM Id	(2) Henize Id	(3) Intensity of H-alpha	(4) Infrared Id	(5) Detection quality	(6) Remarks
91		vf	538	+	
92	N108	f		-	Diffuse shell in Bar; on edge of infrared source 551.
93	N 26	b	553	+	Knot.
94	N 27	b	564	+	Knot.
95		f		-	Knot in infrared extended emission of Bar.
96		f	586	+	Knot in Bar.
97		vf		-	Diffuse filaments on infrared gradient to 599 and 594.
98		f	592	-	Shell of diffuse filaments follows IR emission; 592 at W-side.
99		f		-	Shell in infrared minimum.
100	N193B,E,D	b	610	+	The three knots cannot be separated on the IRAS DPM-maps; near DEM 101.
101a	N193C	b	620	+	Knot. The components of DEM 101 cannot be separated on IRAS DPM-maps.
101b	N193A	b	620	+	Knot; DEM 101 is brighter than the close nebulae DEM 100,102.
102		f	619	+	Diffuse blob near DEM 101.
103		f		0	Diffuse nebula on infrared extension in Bar.
104	N113A-F	vb	635	+	In Bar.
105	N 30A	b	643,646	0	Shell outlines IR hole; IR sources 643 and 646 on the S-part.
106	N 30B,C,D	b	632,642	+	Cores and semicircular shell around infared peaks 632, 642.
107		b+f	641	+	Near SAO 249225 (infrared Id 639; see Table 5.A).
108	N113 (North)	b	640	+	Core and envelope in Bar; 7'N of DEM 104 (with source 635).
109	N112	b	636	+	Knot in Bar.
110		f		-	Irregular filaments outlining an infrared minimum in Bar. A knot (10'E of DEM 110) corresponds to source 591.
111		vf		0	Diffuse nebula on infrared extension to source 626.
112		vf		-	Diffuse filaments on gradient to infrared complex 642.
113	N114A	b	665,668, 669,695	+	Arc and irregular filaments follow infrared emission in Bar.
114	N115	b		-	Knot 6'N of 660; at edge of infrared emission.
115		vf		+	Diffuse patch corresponds to extension in infrared.
116	N 31	b+f	667	0	Core and envelope 3'SE in infrared extension of source 667.
117		vf		+	On infrared extension.
118	N 34A,B,C	f	691	+	Diffuse nebula.
119		f	677	+	Irregular filaments.
120		f		0	On edge of extension in Bar.
121	N 33	vb	723	+	Knot.
122		f	734	+	In Bar.
123		f+b	716,736, 745,749, 758,759	+	Filaments on infrared structure of sources in Bar.
124	N116	b		0	Knot at edge of infrared extension in Bar.
125	N 35	fb	748	+	Circular outline.
126		f	729,774	+	Extended loop around DEM 125 follows infrared.
127		f		0	Semicircular diffuse nebula follows extended IR emission.
128		f	757	+	Diffuse nebula in Bar; 2'N of 757.
129	N 36	b+f	753	+	Central knot corresponds to infrared source 753.
130		fb	742,754	+	Diffuse ring on infrared complex in Bar.
131	N195A,B	b	766	+	Nebula contains several neclei.
132a	N119 (part)	b	789	+	Shell on infrared complex in Bar.
132b	N119 (part)	b	807,811	+	In Bar. Apparently associated with DEM 132a.
133	N121	fb		-	In Bar, at edge of infrared emission complex.
134	N120A-D	b	804,816, 785,794	+	Diffuse partial shell on infrared peaks in Bar.
135		fb	817	+	IR source 817 at N-side; S-filaments follow edge of IR.
136	N 37	fb	823	+	
137		b		0	Arc and sharp filaments in infared emission.
137a		vb	851	+	Knot in DEM 137 on infrared emission peak 851.
138	N 38	b	831	+	Knot on SE-side of nebula. Nebula 3'N of IR source 831.
139		vf		0	Diffuse nebula follows infrared edge. Near SAO 249253 (Id 814; see Table 5.A).
140		fb	841	0	Shell-like filaments in infrared complex 880 (DEM 152).

Table 7, continued (4).

(1) DEM Id	(2) Henize Id	(3) Intensity of H-alpha	(4) Infrared Id	(5) Detection quality	(6) Remarks
141	N 41	b		0	On extension in infrared complex 880 (DEM 152).
142		b	878	+	Shell with sharp filaments on infrared emission peak.
143		f	847	+	Two knots (clusters?) 3'S of infrared source 847.
144		f		0	On extension in infrared complex 880 (DEM 152).
145	N127B	b	872	+	Knot in Bar; close to DEM 149; 2'W of IR source 872.
146	N197	vb	864	+	
147		f	866	0	In Bar; 4'N of 866.
148		f	866	0	In Bar; 4'E of infrared source 866.
149	N127A	b	872	+	Knot in Bar; in between DEM 145 and 153.
150	N 44J	vb	855	+	Knot.
151		fb	839	0	Filamentary loop in infrared complex 880 (DEM 152).
151a	N 44F	vb	861	+	
152	N 44B,C	vb	876,880, 887	+	Elliptical ring at centre of infrared complex 880.
153		fb	872	+	Knot close to DEM 149; in Bar 2'E of 872.
154		fb	830,846, 852	0	Arc and filaments resemble infrared emission.
155	N 43	fb	932	+	Filaments corresponds to IR source 932, surrounding 895.
155a		b	895	+	Diffuse circular region corresponds to IR source 895.
156	N 44I	vb	894	0	Knot 3'N of 894 (close to infrared complex 880, DEM 152).
157	N128	f	891	0	Diffuse nebula on infrared extension in extended emission.
158	N 44G,K	b	888	0	Close to IR complex 880 (DEM 152); source 888 in between two knots.
159		fb		0	Diffuse shell on IR complex 880 (DEM 152).
160	N 44D,H	vb	911,925	+	Several dense nuclei near infrared complex 880 (DEM 152).
161	N 45	fb	900	+	On infrared peak 900.
162	N 46	b	919	+	Knot.
163	N130	b	916	+	Knot.
164	N200	fb	858,934, 960	0	Shell on infrared extended emission.
165	N198	b	910,929, 966,985, 988	+	Filament around infrared sources 929 and 910.
166a	N 44L	b	925	+	Knot; DEM 166 cannot be separated; close to DEM 160.
166b	N 44E	b	925	+	Knot; DEM 166 cannot be separated; close to DEM 160.
167	N 44N	b	938,946	+	Irregular filamentary shell and knot on IR complex 880 (DEM 152).
168	N131	fb	921	0	Knot in Bar; 2'N of infrared source 921.
169	N 44M	b	943	+	Knot near infrared complex 880 (DEM 152).
170		f	948	+	4'SE of IR source 948; near IR complex 880 (DEM 152).
171	N132J,G	b		0	In Bar; on infrared gradient to 955.
172	N132A	fb	941	+	Diffuse arc in Bar.
173	N132B,C,E,I	fb	955	+	Four knots in Bar on IR peak 955; knots cannot be separated.
174	N138D,B	b	961	+	Diffuse shell.
175		fb	952	+	On infrared gradient to complex 1015 (DEM 189).
175a	N 48E	fb	983	+	Infrared source on S-part of elliptical shell.
176a	N137A	b		0	Knot on infrared extension related to DEM 177.
176b	N137	fb		0	Knot on infrared extension related to DEM 177.
177	N140	fb (see Remarks)		+	Extended filaments follow IR emission; related IR sources: 927,944,947,958,965,968,975,984,987,1005.
178		fb	977	+	2'S of infrared source 977.
179	N138C	b	978	+	Knot.
180	N138A	vb	999	+	Knot and arc.

Table 7, continued (5).

(1) DEM Id	(2) Henize Id	(3) Intensity of H-alpha	(4) Infrared Id	(5) Detection quality	(6) Remarks
181		fb	996	+	Loop of filaments on IR emission N of complex 1015 (DEM 189).
182		f	962,964, 1000,1073	+	Extended filaments around source 1073; peak in 962,964,1000.
183	N 48D	b		-	Knot on S-gradient to infrared complex 1015 (DEM 189).
184		f	1101	0	Infrared source at N-edge of shell; shell follows infrared.
185		vf	1042	0	Diffuse shell 3'W of 1042.
186	N132D,H	f		0	Knot in envelope on infrared gradient to 976.
187	N142	fb	1024	0	Infrared source 1024 on N-part of diffuse nebula.
188	N202	vb	1016	+	Knot on infrared source 1016.
189	N 48A,B,C	f+b	1015	+	Infrared complex 1015.
189a	N 48B	b	1002,1009	+	The S-side of DEM 189.
189b	N 48C	b	1010,1033	+	The N-side of DEM 189.
190	N 49	vb	1022,1038	+	Knots N of infrared complex 1015 (DEM 189).
191		fb	1020	+	N of infrared complex 1015 (DEM 189). 3'E of 1020.
192	N 51D	b	1003,1034, 1037,1045	0	Shell and bright filaments on IR complex 1090 (DEM 205).
193	N 50	fb	1017	+	Diffuse nebula.
194		f	989	+	
195		vf		0	Extended diffuse filaments on edge of IR complex 1015 (DEM 189).
196	N 51B,E	b	1043,1052	+	Near infrared complex 1090 (DEM 205).
197	N143	vb	1065	0	Infrared on W-side of core and envelope nebula.
198		fb	1047,1078	0	Irregular filaments on infrared structure.
199	N144A,B	vb	1049,1064, 1076	+	Shell of filaments DEM 199 on infrared peak. Near SAO 249279 (Id 1076; see Table 5.A).
200		f	1054	+	Infrared peak 1054 on S-blob of diffuse nebula; N-side of nebula is connected to DEM 182.
201	N 51A,C	vb	1080,1083, 1090	+	On S-side of irregular nebulosity; N-blob without IR.
202	N205C	b	1058,1094	+	Blob on N-side; filaments at S-side along IR. Close to DEM 206, 207.
203		fb	1023,1040, 1041,1063, 1066,1074 1129,1161	+	In general filamentary shell follows infrared emission.
204		b		-	Shell at edge of extended infrared emission.
205		b	1102,1090	+	Shell; infrared complex 1090.
206	N205A	fb	1086	+	Diffuse nebula on broad IR peak formed by 1086, 1094, 1106; close to DEM 202, 207.
207	N205A	fb	1106	+	Diffuse nebula on broad IR peak formed by 1086, 1094, 1106; close to DEM 202, 206.
208	N204	b	1098,1101, 1140,1158	+	IR peak 1098 on W-filaments; filamentary and diffuse shell follows infrared emission.
209		f+b	1099,1111	+	Diffuse and filamentary nebula follows infrared emission.
210		f+b	1100,1110, 1118,1127, 1139,1145, 1152	+	Scattered nebulosity on infrared emission.

Table 7, continued (6).

(1) DEM Id	(2) Henize Id	(3) Intensity of H-alpha	(4) Infrared Id	(5) Detection quality	(6) Remarks
211		vf	1093,1134, 1162	-	Centre of diffuse filaments on infrared source 1112.
212		vf	1131,1136, 1149,1165, 1170	0	Infrared peak 1136 at S-side of filament.
213		vf		-	In infrared minimum; 4'N of 1148.
214		f+b	1137,1141, 1176	+	Diffuse filaments follow infrared emission.
215		f	1168	+	Infrared source 1168 in centre of diffuse ring.
216		f+b	1180	0	Diffuse nebula on infrared emission; 3'E of 1180.
217		vf		0	Diffuse nebula follows IR extended emission at E-side; near 1193
218		fb	1166,1204, 1211	+	Diffuse filaments. On infrared extension near infrared complex 1249 (DEM 227).
219		f		+	Diffuse nebula on IR emission near complex 1274 (DEM 229).
220		f	1235	+	Blob on IR source 1235; filaments along edge of IR emission.
221	N206A,B	f+b	(see Remarks)	+	Nebular complex follows IR emission. Related IR sources: 1179,1182,1183,1199,1201,1206,1211,1224,1246,1251.
222a		f	1207	+	
222b		f	1214	+	
223		f		0	Semicircular arc on infrared filament.
224		f	1181,1192, 1205,1220, 1223,1265	0	Network of filaments follows infrared structure.
225		b	1244	+	Knot
226	N148I,G	b	1279	+	Filament with diffuse circle near IR complex 1249 (DEM 227).
227	N148A-F,H	b	(see Remarks)	+	Infrared complex 1249. Related IR sources: 1213,1233,1247,1249,1255,1284,1293. At E-side. Blob on IR source 1318; filaments on IR gradient.
228	N 55A	vb	1268,1273	+	Bright IR blob; complex nebular structure follows IR emission.
228a		vb	1253	+	Knot is extension at NW of infrared blob.
228b		vb	1256	+	Knot at N-side of infrared blob.
229	N 57A,D,E	vb	1219,1259, 1261,1274, 1292	+	Network of filaments; infrared complex 1274. IR peak on main nebula (also source 1261 on separate S-knot).
230		vf		-	Near infrared complex 1274 (DEM 229).
231	N 57C	b	1292	-	Diffuse ring on infrared gradient to complex 1274 (DEM 229).
232		b	(see Remarks)	+	Network of fine filaments follows IR structure. Related sources: 1209,1218,1222,1225,1257,1275,1277,1299, 1300,1336,1357.
233	N150	b	1323	+	Two knots in DEM 233.
234	N 57,N 58	f+b	1282,1288, 1296,1305, 1315,1320, 1331	0	Diffuse filaments on infrared emission.
235	N 62B	b	1303,1326	0	Arc of fine filaments on infrared peaks.
236		f		-	Diffuse nebula on extension in infrared emission.
237		vf		-	Diffuse nebula on edge of infrared complex 1376 (DEM 243).
238		f		-	Shell in infrared hole.
239	N 61 , N 62A (part)	f+b	1337,1351	+	Complex of filaments follows infrared emission.
240		b		-	Knot and envelope at edge on infrared peak.
241	N 59A,B,C	vb	1367,1392	+	Infrared peaks on nebular blobs.
242		b	1359	+	Knot on peak 1359. Filamentary structure follows IR emission.
243	N 63A	vb	1354,1376	+	Infrared complex 1376, infrared source 1354 on N-filament.
244	N 61 (part)	f	1352,1386	0	Diffuse filaments following extended infrared emission.
245		fb	1364,1379	+	Extended filaments; E-peak contains infrared filaments; W-side in infrared hole.
246	N154A,B	vb	1298,1341, 1353,1358, 1406	+	Complex in Greater Doradus Region.
247		f	1400	+	Diffuse loop follows IR emission; close to complex 1376 (DEM 243).
248		vb	1403,1425	0	Several knots on infrared gradient in Greater Doradus region.
249		vf	1411	0	Diffuse nebula.
250		fb		0	Diffuse shell on gradient to source 1367 (related to DEM 241).

Table 7, continued (7).

(1) DEM Id	(2) Henize Id	(3) Intensity of H-alpha	(4) Infrared Id	(5) Detection quality	(6) Remarks
251	N 64A,B	f	1402,1408	+	IR extension to source 1422 which follows diffuse DEM 251.
252	N 64C	vb	1422,1426	+	Infrared peaks on central blob of complex DEM 252.
253		vb		0	Knot on infrared gradient to DEM 252.
254		vf		-	Diffuse shell on IR complex 1422 (DEM 252); close to DEM 253.
255	N 65	fb	1409,1412	0	Elliptical shell on infrared sources; no clear resemblance.
256		f	1430	0	Shell on infrared gradient to conplex DEM 252.
257		vf	(see Remarks)	0	Diffuse filaments follow IR structure in general. Related infrared sources: 1348,1382,1396,1399,1410,1415,1420,1423, 1440,1454,1457,1492.
258	N 68	vb	1431	+	Knot.
259		f	1407	0	Diffuse circular patch 2'S of infrared source 1407. In Greater Doradus region.
260	N155	b	1436	+	Knot in Greater Doradus region.
261		vb	1413,1417, 1447,1470	+	Part of 30 Doradus nebulosity; directly S of DEM 263.
262		vb	1441	0	Part of 30 Doradus nebulosity; filament in infrared minimum.
263	N157A,B	vb	(see Remarks)	+	Centre of 30 Doradus nebulosity; related infrared sources: 1342,1361,1370,1383,1384,1388,1429,1433,1448,1458,1467, 1469,1472,1482,1493,1494.
264		f		-	Diffuse nebula on infrared gradient 4'N of source 1444.
265	N213	vb	1471	+	Nucleus and envelope.
266		f	1464	0	Diffuse nebula 3'E of 1464; on infrared extension in Dreater Doradus region.
267	N171A,B	f	1486	+	4'W of bright infrared peak 1497.
268		f	(see Remarks)	+	Filamentary structure on IR emission; related IR sources: 1368,1381,1413,1416,1443,1446,1450,1453,1468,1481,1527.
269	N158A,B,C	vb	1483,1490, 1507,1522	+	Complex structure; in Greater Doradus region.
270		vf	1524	0	Source 1524 at E-side; diffuse shell follows infrared at edge of emission.
271	N159A-K	vb	1501,1518	+	Several knots; in Greater Doradus region.
272	N159L	b		-	In Greater Doradus region; shell on IR gradient to 1501,1518.
273	N161	b	1519	+	In Greater Doradus region; knot near complex 1469 (DEM 263).
274	N214A,B	b	1505	+	Several knots; close to DEM 276, 278.
275	N172	vb	1506	+	Knot at S-edge of Greater Doradus region.
276	N214D	b	1521	+	*Diffuse arc 1'N of 1521; close to DEM 274, 278.*
277	N173	b		-	Knot at S-edge of Greater Doradus region.
278	N214E	b	1521	0	On infrared gradient to DEM 276; knot 1'S of 1521.
279		b	1523	0	Knot 2'S of 1523; in Greater Doradus region.
280	N176	vb	1541	+	Knot on IR peak 1541; at S-edge of Greater Doradus Region.
281	N175	b	1544	+	Diffuse ring at S-edge of Greater Doradus Region.
282		b	1560	0	Two knots at S-edge of Greater Doradus Region.
283	N160F	b	1549	+	Several diffuse knots on infrared gradient to DEM 271; in Greater Doradus Region.
284	N160A-E	vb	(see Remarks)	+	Part of 30 Doradus nebulosity; related infrared sources: 1503,1520,1525,1548,1552,1564,1570.
285		b	1561	+	Complex at S-edge of Greater Doradus Region.
286		f	1568	0	5'W of 1568; diffuse E- and S-filaments follow infrared.
287	N214 (part)	vf	1532	0	Diffuse nebula on infrared gradient to 1521.
288		f		-	Diffuse nebula close to IR peak 1521, on infrared emission.
289	N214G,F	b	1572	+	Two knots.
290	N216	b	1557	+	Knot.
291		f	1550	+	
292	N214H	f	1571	+	Ring of nebulosity.
293	N214C	vb	1577	+	Close to this complex two IR sources were associated with nebular emission: 1600 on a filament NE and 1529 on filaments SW of DEM 293.
294		f	1551	+	Diffuse nebula.
295	N177	f	1567	0	At S-edge of Greater Doradus Region.
296		f		0	Diffuse nebula at edge of infrared extended emission.
297		b	1573	+	Two arcs; in Greater Doradus Region.
298	N164	vb	1586,1594	+	Complex; in Greater Doradus Region.
299	N165	f+b	1597	+	Shell with second shell on NW; in Greater Doradus Region.
300	N163	vb	1609	+	*Core and envelope; at edge of Greater Doradus Region.*

Table 7, continued (8).

(1) DEM Id	(2) Henize Id	(3) Intensity of H-alpha	(4) Infrared Id	(5) Detection quality	(6) Remarks
301	N 70	b	1605	+	Shell with fine filaments.
302		vb	1613	+	Knot on infrared peak 1613.
303	N 71	vb	1602	+	Knot.
304	N 72	b+f	1629	+	Group of filaments; at E-edge of Greater Doradus Region.
305	N 73	f	1621	+	Knot.
306		fb	(see Remarks)	+	Irregular shell follows IR emission. Related IR sources: 1591,1614,1634,1635,1671,1674.
307	N167	b	1633	+	Diffuse shell on infrared gradient to source 1643.
308		f	1650,1655, 1697	+	Diffuse filaments follow infrared emission.
309	N 74A,B	b	1667,1673	+	Irregular filaments and shell in SE on infrared complex.
310		fb	(see Remarks)	+	Network of filaments (E of 30 Doradus) follows outline of IR; connected to Greater Doradus region. Related IR sources: 1658,1662,1671,1677,1685,1693,1694,1700,1706,1707,1729.
311	N168	vb	1675,1692	+	Diffuse shell on source 1675; source 1692 at N-tip of shell.
312	N169C	b		0	Diffuse nebula on IR extension in Greater Doradus region.
313	N169B	vb		0	Knot on infrared extension in Greater Doradus Region.
314	N169A	b	1696	+	Knot on infrared peak 1696.
315	N 74 (part)	f	1698	+	Shell on infrared extension.
316		fb		-	Two diffuse shells on IR gradient of Greater Doradus region.
317		vf		0	Diffuse nebula 4'S of 1704; on infrared extension.
318	N179C	b	1733	+	Knot on infrared source 1733. DEM 318-321 are not separable.
319	N179B	b	1733	+	Knot on infrared source 1733. DEM 318-321 are not separable.
320	N179A,D	vb	1733	+	Knot on infrared source 1733. DEM 318-321 are not separable.
321		f	1733	+	On infrared source 1733. DEM 318-321 are not separable.
322	N180C	vb	1740	+	Diffuse nebula near infrared complex 1744 (DEM 323).
323	N180A,B	vb	1743,1744	+	Circular filaments; infrared complex 1744.
324		f		-	Diffuse nebula on edge on infrared extended emission.
325		b		0	Diffuse shell N of DEM 323, on infrared gradient to 1744.
326	N180	fb	1741,1749	+	Shell surrounds DEM 323 and follows infrared outline around infrared complex 1744.
327		vf	1747	+	Diffuse nebula on edge of infrared extended emission.
328		vf	1753,1778	+	IR follows arc nebula. At E-end of arc: 1791 also in nebula.
329		f	1767	+	Galaxy?

Note to Table 7:
a) See Section 5.2 in the text.

5.1.4. Stars: Conclusion

Emission from stellar photospheres has been detected by us from foreground SAO stars. Some stars in the LMC have been detected which have infrared excesses due to dust shells. Probably no photospheric infrared emission from LMC–stars has been detected.

5.2. Hα nebulosities in the LMC

A good overall agreement between Hα emission regions and IRAS emission was already noted by Schwering (1985). In Table 7 we present a more detailed comparison of the IRAS data with the Hα catalogues of Henize (1956) and of Davies *et al.* (1976, henceforth DEM). The DEM catalogues contains 329 entries ranging in size from 0′ to 60′. All DEM entries are covered by the IRAS DPM maps. About 75 % of all the bright Hα nebulosities (very bright, bright or fairly bright) have clear infrared counterparts (good quality detections), 20 % have possible counterparts (medium quality) and the remaining 5 % do not show clear infrared emission (poor quality). For the fainter nebulosities (faint or very faint) the statistics are 50 % detected in the infrared, and 30 % possible detections, while the remaining 20 % does not show clear infrared emission. We conclude that there is a higher detection probability in the infrared for the brighter HII regions. We detected infrared emission from about 75 % of the compact Hα knots, while 60 % of the shells were detected. These statistics are very similar to the SMC Hα–statistics (see Chapter II).

The whole face of the LMC is covered by Hα nebulosities (see DEM, 1976), and also by 60 and 100 μm infrared radiation. From this comparison, we see that the discrete infrared sources correlate well with HII regions, and that HII regions are one of the main contributors to the infrared radiation in the LMC.

In the SMC we detected infrared emission from the supergiant shell SGS 1 (Meaburn, 1980; see Appendix A in Chapter II). On the infrared maps of the LMC there is evidence for infrared supergiant shells following the supergiant Hα shells of Meaburn. Shell SGS 1 (North of N 11) is visible at the edge of the maps, especially at 60 and 100 μm (see also Appendix A). Also clear infrared emission is found from SGS 4 and 5 (Appendix A). These three supergiant shells are relatively isolated from the bulk of the infrared extended emission of the LMC. Shell numbers 2 and 3 (surrounding 30 Doradus) are more complicated to be found, but there is evidence for infrared emission following their edges. Shells 6, 7, 8 and 9 are incomplete in Hα, but comparison with the infrared maps shows some evidence for counterparts. However, the complicated structure of the LMC's infrared emission could well give rise to spurious identifications of such incomplete structure. We conclude that shells 1, 2, 4 and 5 are clearly present in the infrared and that there is some evidence for possible infrared emission from the shells 3, 6, 7, 8 and 9.

5.3. Globular clusters in the LMC

We compared the list of globular clusters given by van den Bergh (1981) with our source list and the infrared maps. This is a limited set of the 1603 clusters from Shapley and Lindsay (1963), Lyngå and Westerlund (1963) and Hodge and Sexton (1966). The positional uncertainty of most of these clusters is more than 1$'$. Many of the clusters listed in these three catalogues are open clusters, embedded in HII regions. We searched deeper on the maps than in Table 3. In total we detected infrared emission from the direction of 41 clusters, of which 33 have associations in Table 3. Twenty–two of these infrared sources also are present in Table 7, indicating the confusion with HII regions. Of these 41 possible detections three have good detection qualities, showing emission at 12 and possibly 25 μm. These clusters are NGC 1978, 2002, 2100. NGC 1978 and 2100 are blue globular clusters (Hodge, 1984). Eleven clusters have medium detection quality, of which two belong to the brighter ones: NGC 1818 and 2004. Results of this comparison are given in Table 8.

5.4. Supernova remnants in the LMC

We checked the list of 25 supernova remnants of Mathewson *et al.* (1983; their Table 1). All SNRs are smaller ($0\overset{'}{.}1 <$ size $< 5'$) than the IRAS beam size at 100 μm. Table 9 summarizes the results. Five SNRs show good quality infrared emission: these are 0505–67.9, 0509–68.7, 0525–66.1, 0535–66.0 and 0538–69.1. There are eight SNRs which show

Table 8. Clusters in the LMC (Shapley and Lindsay, 1963; Lyngå and Westerlund, 1963; Hodge and Sexton, 1966) with infrared counterparts.

(1) Name[a]	(2) Other names	(3) F 12μm Jy	(4) F 25μm Jy	(5) F 60μm Jy	(6) F 100μm Jy	(7) Infrared[b] Id	(8) Detection quality	(9) Remarks[c]
NGC 1714	SL 64	3.63	13.99	116.7	191.4	102	-	0.3'S of 102. Infrared Id 102 is probably HII region DEM 8.
NGC 1727	SL 67	0.26	0.22	1.7:	C	107	-	0.7'E of 107. HII region DEM 10.
NGC 1732	SL 77	0.05:	-	-	-		0	
NGC 1743	SL 87	4.25	17.20	178.0	280.8	148	-	0.3'W of 148. HII region DEM 22.
NGC 1756	SL 94	0.30	0.33	C	C	173	-	1.4'W of 173. HII region DEM 22.
NGC 1767	SL120	0.41	0.67	6.2	14.6	216	-	0.9'NW of 216.
NGC 1805		0.11:	0.11:	-	-		0	
NGC 1818	SL201	0.08:	-	-	-		0	
NGC 1833	SL206	0.63	2.11	22.8	52.0	399	-	3.0'N of 399. HII region DEM 63.
NGC 1849	SL267	0.08:	-	-	-		0	
NGC 1852	SL264	0.15:	0.44	-	-	513	0	1.0'W of 513.
NGC 1856	SL271	0.15:	-	-	-	522	-	1.3'NW of 522. Infrared Id 522 is probably SAO 249209.
NGC 1858	SL274	7.14	52.17	314.6	447.2	534	-	1.1'SW of 534. Prob. HII region DEM 86.
NGC 1860	SL284	0.15	0.33	4.1	6.2:	548	-	0.1'W of 548. Located near HII region.
NGC 1869	SL326	0.41	1.66	13.2	C	646	-	1.3'W of 646. HII region DEM 105.
NGC 1870	SL317	0.15	0.22	3.3	C	627	0	0.7'S of 627.
NGC 1872	SL318	6.03	41.07	256.7	301.6	635	-	2.5'NW of 635. HII region DEM 104.
NGC 1873	SL324	0.19	0.44	1.7:	C	643	-	1.6'W of 643. HII region DEM 105.
NGC 1080		6.03	41.07	256.7	301.6	635	-	1.7'E of 635. HII region DEM 104.
NGC 1885	SL338	0.08:	0.11:	C	C		0	
NGC 1895		0.44	1.00	9.5	25.0	723	-	0.1'SW of 723. HII region DEM 121.
NGC 1903	SL356	0.37	0.22:	C	C	742	-	0.4'NW of 742. HII region DEM 130.
NGC 1916	SL361	0.59	0.67	16.6:	31.2	792	-	0.7'N of 792.
NGC 1918		2.96	11.10	124.2	249.6	804	-	0.5'SW of 804. HII region DEM 134.
NGC 1943	SL430	0.30	0.22	1.2	4.2	916	-	0.7'SW of 916. HII region DEM 163.
NGC 1978	SL501	0.19	-	-	-	1126	+	1.4'W of 1126.
NGC 1984	SL488	3.88	23.31	10.3	4.2	1100	0	0.1'E of 1100.
NGC 1994	SL499	1.11	1.44	C	C	1127	0	0.6'NW of 1127.
NGC 2001	SL507	0.11:	0.08:	-	-		0	
NGC 2002	SL517	0.22	0.22	-	-	1186	+	1.2'NW of 1186.
NGC 2004		0.08:	0.08:	-	-		0	
NGC 2009	SL534	0.26	0.33:	8.3	31.2	1225	-	1.2'SW of 1225. HII region DEM 232.
NGC 2058	SL614	0.22	0.22	1.2	4.2:	1421	-	1.3'E of 1421.In Greater Doradus Region.
NGC 2070	SL633	74.	472.:	2795.	3120.	1469	-	30 Doradus. 1.4'N of 1469. HII region DEM 263.
NGC 2098	SL667	0.05:	-	-	-		0	
NGC 2100	SL662	0.37	-	C	C	1562	+	0.8'W of 1582.
NGC 2118	SL717	0.26	0.22	5.4	25.0	1706	0	1.0'SE of 1706.In HII filaments DEM 310.
IC 2127		1.11:	22.20	C	C	887	-	0.5'NW of 887. HII region DEM 152.
IC 2128		2.03	6.10	33.1	41.6	925	-	2.6'S of 925. HII region DEM 160.
SL 562		0.44	0.22	4.1:	14.6:	1272	-	1.6'NE of 1272.
HS 314		1.11	1.44	C	C	1127	-	0.9'N of 1127. HII region DEM 210.

Notes to Table 8:

a) Only clusters which have possible infrared counterparts are given. These are taken from the selection of globular clusters of van den Bergh (1981).

b) Twenty infrared associations which were already refered to in Table 7 (HII regions) have been denoted in column 9, together with their HII region number. One association is probably a SAO star. Associations 522, 1126 and 1582 have S-type infrared spectra; all other associations have C- or W-type spectra.

c) See Section 5.3 in the text.

possible infrared emission (medium quality). Note that all five detected remnants have sizes less than about 1'; but not all the ten small (< 100″ diameter) SNRs were detected. Two of the detected ones (N 49 and N 63A) correspond to the SNRs recently found by Graham *et al.* (1987). Their two other detections are too confused to be identified unambigiously.

Table 9. Known supernova remnants in the LMC (Mathewson et al., 1983).

(1) SNR Cat. number	(2) Infrared Id[a]	(3) SNR size arcsec	(4) Detection quality	(5) Remarks[b]
0453-68.5	3.1'NE of 133	140x131	-	On extended infrared emission around peak.
0454-66.5	*2.0'E of 152*	*60x 53*	*0*	*N11L*
0455-68.7	2.8'SE of 191	217x183	-	N86; on extended infrared emission around peak. See Table 7 (DEM 33).
0500-70.2	1.7'NE of 295	116x116	0	N186D; on infrared gradient to 295 (other close infrared source 302). See Table 7 (DEM 50).
0505-67.9	0.3'NE of 423	83x 67	+	DEM 71, see Table 7 (other close infrared source 408).
0506-68.0	3.3'N of 435	53x 33	-	N23 (other close source 411). See Table 7 (DEM 73).
0509-68.7	1.0'N of 510	23x 18	+	N103B (other close infrared sources 520, 518, 529).
0509-67.5		25x 25	-	
0519-69.7	1.8'NE of 785	104x104	0	N120; in extended infrared emission (other close infrared sources 804, 816). See Table 7 (DEM 134).
0519-69.0	3.5'W of 829	28x 28	-	In extended infrared emission.
0520-69.4	4.7'N of 822	138x104	-	In extended infrared emission.
0525-66.0	2.0'NE of 996	110x110	0	N49B See Table 7 (DEM 181).
0525-69.6	2.5'N of 1008	120x100	0	N132D; in extended infrared emission, in LMC-Bar (other close infrared source 976).
0525-66.1	0.5'SW of 1022	68x 60	+	N49 (other close infrared sources 1038, 1020). See Table 7 (DEM 190).
0527-65.8		237x212	-	DEM 204
0532-71.0	3.7'NE of 1246	178x171	-	N206 (other close infrared sources 1251, 1276). See Table 7 (DEM 221).
0534-69.9	3.5'SE of 1324	116x108	-	(other close infrared source 1339).
0534-70.5		179x162	-	DEM 238
0535-66.0	0.2'NW of 1376	28x 20	+	N63A (other close infrared source 1354). See Table 7 (DEM 243).
0536-70.6	0.5'S of 1411	162x129	0	DEM 249, see Table 7; (other close infrared source 1401).
0538-69.1	0.9'N of 1448	28x 24	+	N157B; in extended infrared emission in 30 Doradus outskirts. See Table 7 (DEM 263).
0540-69.3	2.8'N of 1522	8x 8	0	In extended infrared emission in 30 Doradus outskirts. See Table 7 (DEM 269); (other close infrared sources 1543, 1495, 1553).
0543-68.9	2.4'SE of 1597	292x243	0	DEM 299, see Table 7; in infrared extended emission.
0547-69.7	2.7'NW of 1722	270x150	-	N135; on gradient in infrared extended emission (other close infrared source 701).
0548-70.4	3.6'NE of 1701	103x103	-	On gradient in infrared extended emission (other close infrared source 1726).

Notes to Table 9.

a) All associations with Table 3 within 5' are given as remarks, but only the closest one is given in column 2 Thirteen listed associations were already refered to in Table 7 (HII regions; see column 5). All associations, except 1522, have C- or W-type infrared spectra.

b) See Section 5.4 in the text.

5.5. Planetary nebulae in the LMC

We compared the DPM infrared maps and the source list with the planetary nebulae identified by Sanduleak *et al.* (1978) and Sanduleak (1984). Of their list of 128 nebulae numbers Sk 2, 3, 79, 81, 97 – 104A are not covered by the IRAS DPM observations. The sizes of these nebulae are of order 1″. Thirteen nebulae (Sk 1, 11, 28, 29, 31, 36, 51, 58, 62, 64, 75, 78, 85) have probably infrared counterparts, and we have possible detections of seventeen. We give results of the comparison in Table 10. Again we searched deeper than in Table 3. Thirty–two nebulae have close infrared associations in Table 3.

The contribution of line emission from planetary nebulae to the infrared emission in the IRAS bands can be very high (see Pottasch, 1986). Nebula Sk 64 is associated to a

Table 10. Planetary nebulae in the LMC (Sanduleak et al., 1978; Sanduleak, 1984).

(1) Number	(2) $F_{12\mu m}$ Jy	(3) $F_{25\mu m}$ Jy	(4) $F_{60\mu m}$ Jy	(5) $F_{100\mu m}$ Jy	(6) Infrared Id[a]	(7) Detection quality	(8) Remarks[b,c]
1	0.11:	0.33	0.2:	1.0:	2	+	N182, LM1-2, WS1, near edge of DPM-map; 1.3'NE of 2. *See also the maps in Appendix A.*
2							Not covered by IRAS DPM-map.
3							N1, LM1-3. Not covered by IRAS DPM-map.
4	-	-	-	-		-	
5	-	-	-	-		-	S1; near edge of IRAS DPM-map.
6	-	-	-	-		-	*N184, LM1-4, WS2; on edge of IRAS DPM-map.*
7	-	-	-	-		-	N77F, AL19?; in infrared extended emission.
8	0.15.	0.56	2.1:	C	72	0	N78, LM1-5; in infrared extended emission. 0.3'NE of 72.
9	-	-	-	-		-	In infrared extended emission.
10	-	-	-	-		-	In infrared hole.
11	0.33	0.56	C	C	89	+	0.7'N of 89.
12	-	-	-	-		-	In infrared extended emission.
13	0.22	-	-	-	303	0	LM1-9, WS4. 0.9'N of 303.
14	-	-	-	-		-	LM2-4
15	-	-	-	-		-	N186A, LM1-10, WS5
16	-	-	-	-		-	LM1-11
17	-	-	-	-		-	N96, LM1-12
18	-	-	-	-		-	L95
19	-	-	-	-		-	N188, LM1-13, WS6
20	-	-	-	-		-	LM2-5
21	-	0.11:	-	-		-	N97, LM1-16, WS7; close to LMC-Bar.
22	-	-	-	-		-	In infrared extended emission.
23	-	-	-	-		-	N24, LM1-17, WS8; close to LMC-Bar.
24	0.07.	0.11:	1.7	4.2	438:	0	In infrared extended emission. 1.0'SW of 438.
25	0.11:	0.33	-	-	436	0	L124, BE206; in infrared extended emission. 2.0'NE of 436.
26	0.11	0.22	0.8	2.1:	466:	0	N101, LM2-7; in infrared extended emission. 1.3'E of 466.
27	-	0.08:	-	-		-	
28	-	0.44	2.1:	C	481	+	In infrared extended emission of LMC-Bar. 0.4'SE of 481.
29	0.07:	0.11	2.1:	C	483	+	N102, LM1-19, WS9; in LMC-Bar. 0.6'NE of 483.
30	-	-	0.2:	-		-	LM2-8
31	0.15:	0.44	-	-	513	+	N25, LM2-9. 0.5'NW of 513.
32	-	-	-	-		-	N192, LM1-20, WS10
33	-	-	-	-		-	N104A, LM1-21, WS11, BE216. In LMC-Bar.
34	-	0.11:	-	-		-	N106, LM2-10; in LMC-Bar.
35	-	-	-	-		-	WS 12, LM1-22?
36	0.33	0.22	3.3:	C	557	+	N107, LM1-23, WS13. 0.4'SW of 557.
37	-	-	-	-		-	N28, LM1-24, WS14, in infrared extended emission.
38	-	-	-	-		-	N110, LM1-25, WS15
39	-	0.08:	-	-		-	LM2-11?; on infrared extension of LMC-Bar.
40	0.08:	-	-	-		-	WS16
41	-	-	-	-		-	LM1-26
42	-	-	-	-		-	In infrared extended emission.
43	0.15	0.11	-	-	736	-	*In extended emission.* 0.6'NW of 736. See Table 7 (OEM 123).
44	-	-	-	-		-	LM2-16; close to infrared emission peak.
45	-	-	-	-		-	LM1-27, WS17
46	-	-	-	-		-	In infrared extended emission, near LMC-Bar.
47	0.44	0.56	10.3	20.8:	822.	0	N122, LM1-28, WS18. 1.0'E of 822.
48	0.07:	0.33	-	-	836:	0	N123, LM1-29, WS19. In extended emission. 1.6'N of 836.
49	-	-	-	-		-	N196, LM1-30
50	-	0.17:	-	-		-	N39, LM1-31, WS20

Table 10, continued (2).

(1) Number	(2) F 12μm Jy	(3) F 25μm Jy	(4) F 60μm Jy	(5) F 100μm Jy	(6) Infrared Id	(7) Detection quality	(8) Remarks
51	0.15	0.44	1.2:	4.2:	850	+	N125, LM1-32. In extended emission;0.5'E of 850.
52	-	-	-	-		-	N124, LM1-33, WS21. In extended emission, close to Bar.
53	-	0.11:	-	-		-	N42, LM1-34, WS22
54	0.22	0.22	1.7	C	868	0	LM2-18, in extended emission, close to Bar. 0.7'SE of 868.
55	0.11	0.22:	1.7	4.2	924	0	N199, LM2-21. 60 and 100 μm emission probably confused. 0.7'N of 924.
56	-	-	-	-		-	N136, LM2-23, BE263. In extended emission. 1 8'SW of 947.
57	-	-	-	-		-	In infrared extended emission.
58	0.15	0.22	-	-	982	+	N133, LM1-36, WS23. In extended emission. 0.4'N of 982.
59	-	-	-	-		-	LM2-25
60	-	-	-	-		-	
61							N203, LM1-37, WS24. Not covered by IRAS DPM-map.
62	0.19:	0.44	C	C	1014	+	N201, LM1-38, WS25. 0.5'N of 1014.
63	0.08:	0.11:	C	C		-	N141, LM1-39, WS26. 1.7'W of 1030.
64	3.88	23.31	10.3	4.2	1100	+	N145, LM1-40. 0.8'S of 1100. DEM 210 (Table 7).
65	-	-	-	-		-	
66	-	0.11:	-	-		-	N52, LM1-42, WS27
67	0.15:	0.33	1.7	6.2	1154	-	N53, LM1-43. 2.1'S of 1154.
68	-	-	-	-		-	
69	0.41	0.33	-	-	1149	0	N54, LM2-27. 0.6'SE of 1149. DEM 212 (Table 7).
70	-	-	-	-		-	LM2-28; near edge of IRAS DPM-map.
71	-	-	-	-		-	N207, LM1-44, WS28
72	-	-	-	-		-	
73	-	0.11:	-	-		-	N208, LM1-45, WS29
74	-	-	-	-		-	N209, LM1-48, WS30
75	0.19	0.33	1.7:	C	1327	+	N151, LM1-47, WS31. 0.7'E of 1327.
76	0.07:	0.11	1.2	C	1334	0	N60, WS32. 1.8'W of 1334.
77	-	-	-	-		-	N152, LM2-35
78	0.22	0.44	C	C	1336	+	N153, LM1-49, WS33. 1.2'N of 1336. See Table 7 (DEM 232).
79							N210, LM1-50. Not covered by IRAS DPM-map.
80	-	-	-	-		-	LM2-37
81							N211, LM1-51, WS34. Not covered by IRAS DPM-map.
82	-	-	-	-		-	LM2-38
83	0.15	0.11:	1.2	6.2	1396	0	N66, LM1-52, WS35. 1.2'NE of 1396. See Table 7 (DEM 257).
84	-	-	-	-		-	N212, LM1-53, WS36
85	0.10:	0.44	-	-	1513	+	N69, LM1-54. 0.3'N of 1513.
86	-	-	-	-		-	LM2-41
87	-	-	-	-		-	N215, LM1-55, WS37; near edge of IRAS DPM-map.
88	0.11	0.11:	-	-	1604	0	LM2-42. 1.6'NW of 1604.
89	0.11	0.11	0.8	4.2	1589,1612	0	N178, LM1-56, WS38;1.2'W of 1612;2.1'NE of 1589.
90	-	-	-	-		-	LM2-43
91	-	-	-	-		-	LM1-57
92	0.30	0.33	5.4	25.0	1707	0	N170, LM1-58, WS39; 0.6'SE of 1707. DEM 310 (in Table 7). In infrared extended emission.
93	-	-	-	-		-	N181, LM1-59; at edge of extended emission.
94	-	-	-	-		-	S170, LM2-44
95	-	-	-	-		-	Near edge of IRAS DPM-map.
96	-	-	-	-		-	Near edge of IRAS DPM-map.
97							LM1-61, WS40. Not covered by IRAS DPM-map.
98							LM1-62, WS41. Not covered by IRAS DPM-map.
99							N221, LM1-63, WS42. Not covered by IRAS DPM-map.
100							LM1-65. Not covered by IRAS DPM-map.

Table 10, continued (3).

(1) Number	(2) F 12μm Jy	(3) F 25um Jy	(4) F 60μm Jy	(5) F 100μm Jy	(6) Infrared Id	(7) Detection quality	(8) Remarks
101							Not covered by IRAS DPM-map.
102							Not covered by IRAS DPM-map.
103							Or faint emission-line galaxy. Not covered by IRAS DPM-map.
104							LM1-1. Not covered by IRAS DPM-map.
104A							Savage et al. (1982).Not covered by IRAS DPM-map.
105	-	-	-	-		-	
106	-	-	-	-		-	In infrared extended emission of LMC-Bar.
107	-	-	-	-		-	LM2-6,in infrared extended emission;1.9'S of 451.
108	-	-	-	-		-	In infrared extended emission.
109	-	-	-	-		-	LM2-13, J5; in infrared extended emission.
110	-	-	-	-		-	On infrared extension in LMC-Bar. 1.6'SE of 597.
111	-	-	-	-		-	J15; in infrared extended emission.
112	-	-	-	-		-	J20; in infrared extended emission.
113	-	-	-	-		-	J26
114	0.19	0.11:	C	C	849	0	J31; in infrared extended emission;0.6'SE of 849.
115	-	-	-	-		-	J33; in infrared extended emission.
116	-	-	-	-		-	LM2-24, J38; in infrared extended emission. 1.8'W of 998.
117	-	-	-	-		-	
118	0.08:	-	C	C		-	J41
119	-	-	-	-		-	
120	0.19	-	-	-	1174:	0	1.1'S of 1174.
121	-	-	-	-		-	
122	-	-	-	-		-	1.6'E of 1335.
123	-	-	-	-		-	LM2-36
124	-	-	-	-		-	
125	-	-	-	-		-	
126	-	-	-	-		-	On edge of infrared extended emission.
127	-	-	-	-		-	Maybe faint 60 and 100 μm emission.

Notes to Table 10:

a) Six associations with Table 4 were already associated to HII regions (Table 8); for these notes are added in the remarks of column 8.

b) References (taken from Sanduleak et al., 1978; Sanduleak, 1984) are made to the following papers (column 8):
- AL : Andrews and Lindsay (1964).
- BE : Bohannan and Epps (1974).
- J : Jacoby (1980).
- L : Lindsay (1963).
- LM1: Lindsay and Mullan (1963; Table 1 therein).
- LM2: Lindsay and Mullan (1963, Table 2 therein).
- N : Nebulosities of Henize (1956).
- S : Emission-line stars of Henize (1956).
- WS : Westerlund and Smith (1964).

c) See Section 5.5 in the text.

very bright infrared object (LI-LMC 1100). Its flux density ratio $f_{12\mu m}/f_{25\mu m}$ and $f_{25\mu m}/f_{60\mu m}$ gives $T_c \approx 140$ K (using a λ^{-1} emissivity). The 60/100 μm ratio suggests $T_c \approx 95$ K; probably the 100 μm emission is partly due to more extended emission, hence lowering the temperature. Assuming that we are dealing with continuum emission only we can estimate the total amount of infrared radiation coming from this 140 K nebulae by extrapolating the spectrum over the whole infrared wavelength range (1 – 500 μm), this gives $L_{IR} \approx 9.3 \times 10^5$ $L_\odot$. For the brightest Galactic planetary nebula NGC 7027 (not observed by IRAS) Gathier (1984) adopts $L_{IR} \approx 1.6 \times 10^4$ $L_\odot$ (60 times lower). Another Galactic planetary nebula NGC 6537 the IRAS PSC gives flux densities of 7.7, 58.3, 190

Table 11. Hodge (1972) dark clouds in the LMC.

(1) Number[a]	(2) Infrared[b] Id	(3) Detection quality	(4) Remarks[c]
1		0	On infrared extension in Bar (2.7'E of 438; 2.9'NW of 465).
2	478	+	*0.4'E of 478. Infrared peak in LMC Bar.*
3	530	+	1.9'SW of 530. On infrared emission in Bar, peaking at 502.
4	541,536	+	1.4'W of 541; 1.8'N of 536. On infrared peak in Bar.
5		+	On infared gradient at 2 6'E of peak 582.
6	591	+	0 7'SE of 591. Infrared peak in Bar. See Table 7 (DEM 110).
7		–	Infrared minimum in Bar (2.8'N of 608).
8	601	+	1.6'NE of 601. On infrared gradient to 634.
9		+	On infrared gradient at 2.8'W of peak 635.
10	659	0	1.7'S of 659. On infrared extension in Bar.
11	660	+	0.7'SE of 660 In infrared peak, close to Bar. See Table 7 (note DEM 114).
12	728	0	1 6'SE of 728. At edge of infrared hole.
13	743	+	2 0'N of 743. On infrared extension in Bar.
14	768	+	*0.5'S of 768. On infrared extension in Bar.*
15		0	At edge of extension in Bar (2.5'N of 795; 2.7'NE of 786).
16	825	+	1 8'NW of 825. Close to infrared peak in Bar.
17		+	On infrared gradient of 816 in Bar.
18	854	+	1.5'W of 854. Infrared peak in Bar
19		+	On infrared gradient at 2.8'SE of 866.
20		+	(2.9'W of 897).
21		+	(4.4'NW of 897).
22	876	+	0.2'SE of 876. Infrared peak close to main peak of complex. DEM 152 (Table 7).
23	899	+	0.6'W of 899 Infrared peak in Bar
24		+	On infrared gradient in between peaks.
25	984,965	0	1.2'NW of 984; 1.4'S of 965. On infrared peak in Bar. See Table 7 (DEM 177).
26	1070	+	*2.0'NE of 1070. On infrared gradient to 1076.*
27		+	In between infrared peaks: 2.3'NW of 1080; 2.7'SW of 1083.
28		+	On infrared gradient at 3.4'SE of 1076.
29	1115	0	1.1'SE of 1115. At SE end of Bar.
30	1142	0	1.9'N of 1142. At SE end of Bar.
31	1171	0	1.8'SW of 1171. At SE end of Bar.
32		+	On infrared extension at SE end of Bar (2.7'SE of 1180).
33	1195	0	1.1'E of 1195. On infrared extension near Bar.
34		0	In infrared extended emission, near Greater Doradus region (3.3'W of 1218).
35	1222,1209	0	1.5'NW of 1222; 1 8'N of 1209. Infrared extension to 30 Doradus. See Table 7 (DEM 232).
36		0	Infrared emission at edge of 30 Doradus (2.6'SE of 1217; 2.7'NW of 1252).
37		0	*Infrared emission at edge of 30 Doradus (2.1'N of 1252; 2.5'NW of 1270).*
38		0	In infrared extended emission, near Greater Doradus region.
39		-	At edge of infrared extended emission, near Greater Doradus region.
40	1332	0	2.0'S of 1232.
41	1335	+	1 5'NE of 1335 At infrared edge of Greater Doradus region.
42		+	On extension to infrared peak 1323.
43		0	At edge of Greater Doradus region (2.4'NW of 1374).
44		+	In Greater Doradus region (2.6'SE of 1361).
45		+	On infrared extension in Greater Doradus region.
46		+	On infrared extension in Greater Doradus region (2.6'SW of 1433).
47		+	On infrared extension in Greater Doradus region (2.6'NW of 1436).
48	1435	+	1.4'W of 1435. On infrared extension in Greater Doradus region.
49		0	In Greater Doradus region.
50	1446	+	0.8'E of 1446. On infrared extension in Greater Doradus region. See Table 7 (DEM 268).
51	1467	+	1.4'W of 1467. On infrared extension in Greater Doradus region. See Table 7 (DEM 263).
52		+	In Greater Doradus region (2.8'SE of 1451).
53		+	Infrared peak in Greater Doradus region (2.6'N of 1486).
54	1487	0	1.7'NE of 1487. On infrared extension South of N159, in Greater Doradus region.
55		0	In infrared extended emission of Greater Doradus region (3.0'NE of 1483).
56		0	In 30 Doradus outskirts.
57	1525	+	0.7'S of 1525. Infrared peak in Greater Doradus region. See Table 7 (DEM 284).
58	1518	+	1.8'SE of 1518. Infrared peak in Greater Doradus region.See Table 7 (DEM 271).
59	1539	+	0 7'NE of 1539. In Greater Doradus region.
60		0	In 30 Doradus outskirts.

Table 11, continued (2).

(1) Number	(2) Infrared Id	(3) Detection quality	(4) Remarks
61	1553	+	1.7'SE of 1553. In Greater Doradus region.
62		+	On infrared extension in Greater Doradus region (2.6'W of 1588).
63	1586	+	1.4'N of 1586. Infrared peak in Greater Doradus region. See Table 7 (DEM 298).
64	1629	0	1.7'S of 1629. Infrared peak in Greater Doradus region. See Table 7 (DEM 304).
65		+	On infrared extension to 1643 (2.3'S of 1662).
66	1671	+	1.1'S of 1671. On infrared extension to 1643. See Table 7 (DEM 306).
67		+	On infrared extension to 1696 (2.9'NW of 1692).
68	1741	+	1.7'NW of 1741. On infrared gradient to 1743. See Table 7 (DEM 326).

Notes to Table 11:

a) The positions of the dark clouds have been taken from Hodge (1972; Table 1).

b) All associations, except 1142, have W-type or C-type infrared spectra. Eleven infrared associations were previously included in Table 7 of HII regions (see remarks in column 4).

c) See Section 5.6 in the text.

and 166 Jy at 12, 25, 60 and 100 μm. When we assume a distance of 2.4 kpc for NGC 6537 (Gathier, 1984), a nebula with the same infrared brightness as NGC 6537 would have flux densities of 0.02, 0.12, 0.4 and 0.3 Jy in the IRAS bands at the distance of the LMC. This is about equal to our detection limits. For most identifications other than the brightest (Sk 64) we actually find 25 μm flux densities of this order of magnitude (see Table 10). Sk 64 is about 200 times brighter at 12 and 25 μm and 20 times at 60 and 100 μm. There might be some confusion with NGC 1984 (see Table 8) but the spectrum is too hot for dust associated with an HII region ($T_c \approx 40$ K). The contribution of line emission coming from this planetary nebula could be very high which could give rise to high estimates of the total infrared emission. Ten of the probable planetary nebulae have their infrared emission peak at 25 or 60 μm, which is typical for planetary nebulae.

5.6. Dark clouds in the LMC

We compared the infrared data with the dark nebulae listed by Hodge (1972). Hodge discussed the uncertainties related to incompleteness of his list; see also the review by Israel (1984). These 68 dark clouds range in size from 1$'$ to 21$'$ x 8$'$ and they are mainly positioned in the Bar and the Greater Doradus area. In the comparison we used positions from his Table 1. Results are listed in Table 11. Thirty–five clouds have one or more association in Table 3. Most clouds can be associated with an infrared feature but clouds 7 and 12 are associated with an infrared minimum.

6. Conclusions

In the LMC DPM maps, 1823 discrete sources were found; 1011 of these are identified with sources in the IRAS Point Source Catalog (PSC) and forty–nine correspond to sources in the IRAS Small Scale Structure Catalog (SSS). We found a total of 802 sources not listed in either of these catalogues. In many cases, we determine actual flux densities for sources while the PSC gives only upper limits. Most sources are associated with known HII regions in the LMC. At the positions of known objects in the LMC, we conducted deeper searches of the maps. The results are as follows.

Out of 163 SAO stars, we detected infrared emission from 57, and possibly 43 more. No catalogued Radcliffe–stars in the LMC were identified with certainty, but 253 infrared sources with stellar–type infrared spectra were found. Three LMC globular clusters (NGC 1978, 2002 and 2100) were also detected. From five small size supernova remnants infrared emission was detected. Infrared emission is seen towards thirteen, and possibly seventeen more, planetary nebulae (out of 128). Of these nebulae, Sk 64 shows very strong infrared emission (about 100 times brighter than the brightest known Galactic planetary nebula).

Acknowledgements

I wish to thank the following people: The SDAS team that supported the first reduction stage and assisted PS during his stay at JPL; E. Kopan, P. Alphenaar, A. Vos and D. Hogeweg for writing the neccesary software; Drs. H. Habing, J. Emerson and T. de Jong for scheduling the observations; Drs. H. Habing, F. Israel, W. Rice, R. Walterbos and H. Caspers for discussions. I want to thank Mrs. H. Vesteege–Hensel for typing various tables and source lists. I am grateful for financial support from the Space Research Organisation in the Netherlands (SRON), a subsidiary of the Netherlands Organization for Scientific Research (NWO) during my stay at JPL. I also want to thank the Astronomical Data Center at the NASA Goddard Space Flight Center for providing the SAO Catalog (version 1984).

Appendix A: Additions to the Infrared Source List

A.1. Introduction

This infrared survey at 12, 25, 60 and 100 μm covers the entire LMC. Galactic foreground emission is coming in at the East and South edges of the LMC (see Fig. 1 in Chapter II). At the North and West edges however the DPM derived maps do not have much overlap with empty regions, and some prominent Hα features (Supergiant shells 1 and 5; Meaburn, 1980) are not entirely covered by the DPM maps. To complement the maps obtained from the Additional Observations, we derived IRAS maps using Survey data to cover these regions. Because these maps are produced from a different database than the DPM derived maps described in this chapter, we decided to add the analysis of these maps in an Appendix.

A.2. Observations and data reduction

The maps used in this Appendix are based on Co–added IRAS Survey data, produced at Leiden Observatory. We did not use the IRAS $16\overset{\circ}{.}5$ Skyflux images (IRAS, 1985a) because of their lower resolution ($4' - 6'$). The Co–added Survey data give a resolution that is equal to the resolution of the Additional Observations (see Section 3). A description of the method of Co–adding is given in Chapter II.

We chose seven connecting fields starting at the North–East corner of the LMC following the North edge to the North–West corner, and downwards following the West edge to the South–West corner of the LMC. The IRAS Survey scans that were found covering these regions; there are between 40 and 100 scans in each field (some scans were left out in order to select a certain scan angle). The LMC is positioned at the Ecliptic Pole and hence the Zodiacal emission does not vary (see Skyflux's HCON–1, HCON–2 and HCON–3), allowing us to add all data from the three HCONs. We allowed for overlap between the DPM and Co–added maps. The IRAS Survey scans were gridded onto $2\overset{\circ}{.}11 \times 2\overset{\circ}{.}11$ maps. As the low level infrared contours from the Co–added and the neighbouring DPM maps connect reasonably well, we did not attempt to further improve on the background correction.

A.3. The maps of infrared radiation

The maps of these seven fields are shown by Schwering and Israel (1988b). The outer edges of these fields show some increased noise and non–covered areas of $\sim 10'$. Other characteristics of the Co–added maps are given in Table A.1.

Comparing Table A.1 with Table 2 we note that the noise is about 2.5 times less at 12 and 25 μm and 5 – 8 times less at 60 and 100 μm compared to the AOs. This can be explained by the lower amount of extended emission in the maps (especially at 60 and 100 μm). The zero–level is more uncertain (about 5 times) at 12 and 25 μm, because no extra zero–level correction has been done on the maps; and similar at 60 and 100 μm. The stripe residuals are somewhat less ($\sim$ 3 – 10 times).

Table A.1. *Description of the LMC Co–added map characteristics.*

Characteristic (Unit) [a]	Wavelength band			
	12 μm	25 μm	60 μm	100 μm
Median noise (MJy/sr) [b]	0.040	0.037	0.035	0.07
(10^{-8} Watt m^{-2} sr^{-1})	0.54	0.19	0.091	0.07
Zero-level uncertainty (MJy/sr)	0.096	0.19	0.30	1.0
(10^{-8} Watt m^{-2} sr^{-1})	1.3	1.0	0.78	1.0
Stripe residuals (MJy/sr) [c]	0.045	0.12	0.078	0.2
(10^{-8} Watt m^{-2} sr^{-1})	0.6	0.6	0.2	0.2
Sensitivity (MJy/sr) [d]	0.3	0.3	0.4	0.6
(10^{-8} Watt m^{-2} sr^{-1})	4	2	1	0.5

Notes to Table A.1:

a) *Average values for the seven edge fields are given (30 % spread).*

b) *The value of the median noise is influenced somewhat by the extended emission of the LMC itself, but not so much as in Table 2. An improvement of a factor of 2 – 3 relative to the individual detector scans has been realized.*

c) *Higher stripe levels than the average level given in the table can occur.*

d) *The sensitivity indicates the intensity limits of Table A.2.*

In some Co–added maps we used a wide range of scan angles. The advantage is that we have more scans which reduces the noise level somewhat, and the point spread function (at 12 and 25 μm) has a particular shape which enables easier detection of point sources. The disadvantage of it is that the photometric accuracy drops due to the complicated point source shape (especially for extended emission at 12 and 25 μm). Three fields do not show this effect because the scan angles were carefully chosen to be roughly identical.

The maps presented in this Appendix give better information about the connection of the LMC with the infrared background in the emptier North and West regions.

A.4. Additions to the Infrared Source List in the LMC

We have searched these maps in the same way as we searched the DPM maps in Section 4. Note that we have only a single map of these fields in contrast to the two (orthogonally scanned) DPM–maps. Table A.2 contains the additions to the source list of Table 3.

We checked all sources from the edge of the DPM–maps (Table 3) and all sources from the IRAS PSC (IRAS, 1985a) and the IRAS SSS (IRAS 1985b). The IRAS PSC and

SSS are based on the same data that were used in preparing the Co–added maps in this Appendix. Most IRAS PSC entries in these seven fields were confirmed by us, and are included in our source list. Only IRAS 05309–6437 is not covered by the Co–added map; and IRAS 05114–6537 (a 25 μm only source) has not been detected. No IRAS SSS entries are in the newly covered areas. In total we found sixty–eight additional infrared sources in these seven fields of which fifty–two are related to the IRAS PSC catalogue. Thus sixteen new infrared sources were found, and the total number of infrared sources becomes 1891. Some DPM sources at the edge of those maps have been reconfirmed but adjusted in flux densities.

A.5. Identification of Sources

In this Appendix we are primarily concerned with the identification of all sources that were not already present in the DPM–fileds (*i.e.* the area in Co–added fields with $\alpha_{1950} < 04^h46^m$ or $\delta_{1950} > -65^\circ 20'$). For the identification of known objects we searched deeper than the infrared source list. None of the Radcliffe LMC–stars (Feast *et al.*, 1960), known supernova remnants (Mathewson *et al.*, 1983) nor any of the known dark clouds (Hodge, 1974) in the LMC are present in these areas.

A.5.1. Stars in the Co–added fields

In Table A.3 we list forty foreground stars from the SAO Catalog (1966) that are present in these areas in the seven Co–added fields and their colour–corrected 12 and 25 μm flux densities. Twelve of them show good quality 12 μm emission and five show medium quality emission.

Infrared LI–LMC 1842 corresponds to the non–LMC variable star RT Men (see Kukarkin *et al.*, 1969, 1970, 1971).

A.5.2. Hα nebulosities in the LMC

The Hα nebulosities of DEM (1976) and their related infrared emission are described in Section 5.2. The maps in this Appendix show additional information on the supergiant shells 1, 4 and 5 (Meaburn, 1980) at the Northern edge of the LMC.

A.5.3. Globular clusters in the LMC

The area of interest to this Appendix contains four clusters from the list of van den Bergh (1981): NGC 1644, 1651, 1652 and NGC 1831. Only NGC 1651 shows some possible 60 and 100 μm infrared emission and is positioned at $2\overset{\prime}{.}1$ NE of infrared source LI–LMC 1846.

A.5.4. Planetary nebulae in the LMC

The Co–added fields contain four planetary nebulae of the list of Sanduleak *et al.* (1978) and Sanduleak (1984): Sk 1, 2, 3 and 4. Additional data confirm the detection of Sk 1 (see Section 5.5; Table 10). Sk 2, 3 and 4 have not been detected on the Co–added infrared maps.

Table A.2. Additions to the LMC Infrared Source List.[a]

(1)	(2)		(3)		(4)		(5)		(6)		(7)	(8)	(9)	(10)	(11)	(12)	(13)	(14)
Number	Position RA(1950) h m s	DEC(1950) ° ' "	12 µm Peak	Bg	25 µm Peak	Bg	60 µm Peak	Bg	100 µm Peak	Bg	Size arcmin	F 12µm Jy	F 25µm Jy	F 60µm Jy	F 100µm Jy	IRAS-Id	Spec-trum	Comments
					10^{-8} Watt $m^{-2} sr^{-1}$													
1824	04 27 23.0	-71 00 38	46	-	6	-	-	-	-	-	p	1.70	0.67	-	-	04273-7100	S	
1825	04 28 41.9	-69 37 15	6	-	1.5	-	-	-	-	-	-	0.22	0.17	-	-	04286-6937	S	
1826	04 29 56.2	-68 51 07	-	-	-	-	-	-	0.5	-	-	-	-	-	1.0:	04299-6851	C	
1827	04 30 01.2	-69 04 42	-	-	-	-	1	-	0.5	-	-	-	-	0.4	1.0:	04300-6904	C	
1828	04 30 10	-67 59	5	-	-	-	-	-	-	-	-	0.19	-	-	-		S	SAO 249044
1829	04 31 35.2	-72 29 31	8	-	-	-	-	-	-	-	p	0.30	-	-	-	04315-7229	S	
1830	04 31 42.0	-71 09 48	-	-	-	-	1	-	-	-	-	-	-	0.4	-	04317-7109	W	
1831	04 32 16.6	-65 06 26	9	-	1	-	-	-	-	-	-	0.33	0.11:	-	-	04322-6506	S	SAO 249050
1832	04 32 29.5	-71 12 43	-	-	-	-	1.5	-	-	-	-	-	-	0.6	-	04324-7112	W	
1833	04 32 30	-65 21	4	-	-	-	-	-	-	-	-	0.15	-	-	-		S	SAO 249051
1834	04 32 42.2	-68 53 58	-	-	-	-	1	-	0.5	-	-	-	-	0.4	1.0	04327-6853	C	
1835	04 33 03.7	-67 25 09	12	-	1	-	-	-	-	-	-	0.44	0.11:	-	-	04330-6725	S	SAO 249055
1836	04 33 34.0	-71 37 06	-	-	-	-	1	-	-	-	-	-	-	0.4	-	04335-7137	W	
1837	04 34 25.0	-71 56 09	-	-	-	-	1	-	0.5	-	-	-	-	0.4	1.0	04344-7156	C	
1838	04 35 14.5	-66 43 59	-	-	-	-	1	-	-	-	-	-	-	0.4	-	04352-6643	W	
1839	04 35 31.3	-69 09 58	-	-	-	-	1	-	-	-	-	-	-	0.4	-	04355-6909	W	
1840	04 35 35.1	-70 08 03	22	-	2	-	-	-	-	-	p	0.81	0.22	-	-	04355-7008	S	
1841	04 37 00	-66 28	-	-	-	-	1	-	0.7	-	-	-	-	0.4	1.5		C	
1842	04 37 08.5	-70 24 38	10	-	1.5	-	-	-	-	-	-	0.37	0.17	-	-	04371-7024	S	
1843	04 37 14.4	-68 45 51	-	-	-	-	1	-	0.5	-	-	-	-	0.4:	1.0:	04372-6845	C	
1844	04 37 27.3	-68 31 10	5	-	1.5	-	-	-	-	-	-	0.19	0.17	-	-	04374-6831	S	
1845	04 37 31.2	-69 18 00	-	-	-	-	3	-	0.7	-	-	-	-	1.2	1.5	04375-6918	C	
1846	04 37 40	-66 16	-	-	-	-	1	-	0.7	-	-	-	-	0.4	1.5		C	
1847	04 38 15	-65 12	4	-	-	-	-	-	-	-	-	0.15	-	-	-		S	SAO 249071
1848	04 39 03.3	-69 33 01	21	-	2	-	-	-	-	-	p	0.78	0.22	-	-	04390-6933	S	SAO 249074
1849	04 39 05.4	-69 36 09	-	-	1.5	-	3	-	2	0.5	-	-	0.17:	1.2	3.1	04390-6936	C	
1850	04 39 09.6	-71 54 02	-	-	-	-	-	-	0.5	-	-	-	-	-	1.0	04391-7154	C	
1851	04 39 30	-65 46	5	-	-	-	-	-	-	-	-	0.19	-	-	-		S	SAO 249075
1852	04 40 54.2	-64 54 55	-	-	-	-	1.5	-	0.5	-	-	-	-	0.6	1.0	04409-6454	C	
1853	04 41 07.1	-69 38 47	-	-	-	-	1	-	2	1	-	-	-	0.4:	2.1:	04411-6938	C	
1854	04 41 31.1	-66 59 46	10	-	1	-	-	-	-	-	-	0.37	0.11:	-	-	04415-6659	S	
1855	04 42 18.3	-65 06 03	-	-	-	-	1.5	-	0.5	-	-	-	-	0.6	1.0:	04423-6506	C	
1856	04 42 40	-67 15	-	-	-	-	3	-	1.5	-	-	-	-	1.2	3.1		C	
1857	04 42 48.3	-65 53 49	-	-	-	-	1.5	-	1	-	-	-	-	0.6	2.1	04428-6553	C	
1858	04 43 05.9	-68 01 02	-	-	1	-	2	-	2	1	-	-	0.11:	0.8	2.1	04430-6801	C	
1859	04 43 45	-65 42	-	-	-	-	1.5	0.5	1.5	0.5	-	-	-	0.4	2.1		C	
1860	04 44 42.4	-68 22 03	-	-	-	-	-	-	4	3	-	-	-	-	2.1	04447-6822	C	
1861	04 45 20	-67 49	-	-	1	-	3	2	5	3	-	-	0.11:	0.4	4.2		C	
1862	04 45 40	-69 08	-	-	-	-	11	8	11	8	-	-	-	1.2	6.2		C	
1863	04 45 49.0	-66 22 50	-	-	4	-	4	-	-	-	-	-	0.44	1.7	-	04458-6622	W	
1864	04 45 50	-66 10	5	-	-	-	-	-	-	-	-	0.19	-	-	-		S	SAO 249104
1865	04 46 03.4	-66 48 06	-	-	2	-	2	-	3	2	-	-	0.22	0.8	2.1	04460-6648	C	
1866	04 48 30	-64 28	4	-	-	-	-	-	-	-	-	0.15:	-	-	-		S	SAO 249118
1867	04 49 21.3	-64 41 15	-	-	3	-	1	-	1	0.5	-	-	0.33	0.4	1.0	04493-6441	C	
1868	04 49 50	-71 48	-	-	-	-	1	-	2	1	-	-	-	0.4:	2.1		C	
1869	04 51 04.2	-70 35 23	-	-	-	-	1	-	2	1	-	-	-	0.4:	2.1	04510-7035	C	
1870	04 55 50	-64 40	4	-	-	-	-	-	-	-	-	0.15	-	-	-		S	SAO 249150
1871	04 57 33.0	-64 40 21	6	-	-	-	-	-	-	-	-	0.22	-	-	-	04575-6440	S	
1872	05 00 14.2	-64 27 47	24	-	1.5	-	-	-	-	-	p	0.89	0.17	-	-	05002-6427	S	SAO 249165
1873	05 02 57.0	-64 36 11	16	-	1	-	-	-	-	-	p	0.59	0.11	-	-	05029-6436	S	
1874	05 03 41.9	-65 04 45	130	-	13	-	0.5	-	-	-	p	4.81	1.44	0.2:	-	05036-6504	S	
1875	05 04 10.9	-64 33 24	-	-	-	-	1.5	-	0.4	-	-	-	-	0.6	0.8:	05041-6433	C	
1876	05 04 30	-64 37	5	-	-	-	-	-	-	-	-	0.19	-	-	-		S	SAO 249182
1877	05 06 47.9	-65 14 03	-	-	-	-	1	0.5	3	2	-	-	-	0.2:	2.1:	05067-6514	C	
1878	05 07 21.9	-64 46 30	-	-	-	-	1.5	-	0.7	-	-	-	-	0.6	1.5	05073-6446	C	
1879	05 11 50	-65 14	5	-	-	-	-	-	-	-	-	0.19	-	-	-		S	SAO 249218
1880	05 12 50.1	-64 55 03	4	-	2	-	-	-	-	-	-	0.15	0.22	-	-	05128-6455	W	
1881	05 12 58.2	-65 03 28	-	-	-	-	1	-	-	-	-	-	-	0.4	-	05129-6503	W	
1882	05 16 57.1	-65 00 36	-	-	1	-	5	-	2	-	-	-	0.11:	2.1	4.2	05169-6500	C	
1883	05 20 50.6	-64 59 30	9	-	2	-	-	-	-	-	-	0.33	0.22	-	-	05208-6459	S	
1884	05 30 53.4	-65 09 25	8	-	-	-	-	-	-	-	p	0.30	-	-	-	05308-6509	S	
1885	05 34 08.4	-65 09 24	-	-	-	-	2	-	1.1	0.4	p	-	-	0.8	1.5	05341-6509	C	
1886	05 35 36.8	-65 08 39	-	-	-	-	1.5	-	0.5	-	-	-	-	0.6	1.0	05356-6508	C	
1887	05 37 11.4	-65 05 49	-	-	-	-	1	-	0.3	-	-	-	-	0.4	0.6	05371-6505	C	
1888	05 39 03.8	-64 49 13	10	-	-	-	-	-	-	-	p	0.37	-	-	-	05390-6449	S	
1889	05 40 26.4	-64 58 47	6	-	-	-	-	-	-	-	-	0.22	-	-	-	05404-6458	S	
1890	05 47 12.7	-64 35 24	7	-	-	-	-	-	-	-	-	0.26	-	-	-	05472-6435	S	
1891	05 48 24.7	-65 10 54	12	-	-	-	-	-	-	-	p	0.44	-	-	-	05484-6510	S	SAO 249362

Note to Table A.2:

[a] The layout of this table is similar to Table 4 in Chapter II.

Table A.3. SAO (1966) stars in the additional LMC fields.

(1) SAO number	(2) m_V mag	(3) Sp type	(4) $F_{12\mu m}$ Jy	(5) $F_{25\mu m}$ Jy	(6) $F_{25\mu m}/F_{12\mu m}$	(7) $m_V - m_{12}$ mag	(8) Infrared Id	(9) Detection quality	(10) Remarks
249041	8.4	F0	-	-	-	-		-	
249043	9.2	G0	-	-	-	-		-	
249044	7.7	G0	0.13	-	-	1.9	1828	+	
249045	9.0	F8	-	-	-	-		-	
249048	8.5	K0	0.05:	-	-	1.7		0	
249050	8.7	K0	0.23	0.08:	0.34±0.15	3.5	1831	+	
249051	8.2	G0	0.10	-	-	2.1	1833	+	
249052	9.1	F8	-	-	-	-		-	
249055	8.7	K2	0.31	0.08:	0.25±0.10	3.8	1835	+	
249059	8.9	--	-	-	-	-		-	
249060	8.6	F5	-	-	-	-		-	
249061	8.7	F0	-	-	-	-		-	
249065	9.0	K0	0.08:	-	-	2.6		0	
249067	9.1	A0	-	-	-	-		-	
249069	8.7	F8	-	-	-	-		-	
249071	---	K0	0.10	-	-	-	1847	+	
249073	8.1	A0	-	-	-	-		-	
249074	8.0	K2	0.54	0.16	0.29±0.05	3.7	1848	+	
249075	8.4	K0	0.13	-	-	2.6	1851	+	
249079	9.0	G0	-	-	-	-		-	
249089	8.9	F8	-	-	-	-		-	
249091	8.9	F5	-	-	-	-		-	
249092	8.4	G0	-	-	-	-		-	
249103	8.5	F5	-	-	-	-		-	
249104	7.4	F0	0.13	-	-	1.6	1864	+	
249118	8.7	G5	0.10:	-	-	2.6	1866	0	
249150	8.6	G5	0.10	-	-	2.5	1870	+	
249165	7.4	K0	0.62	0.12	0.19±0.08	3.3	1872	+	
249174	8.7	F8	-	-	-	-		-	
249182	7.9	G5	0.13	-	-	2.1	1876	+	
249204	8.7	G0	-	-	-	-		-	
249222	8.8	G0	-	-	-	-		-	
249277	8.3	F8	-	-	-	-		-	
249291	8.6	A2	-	-	-	-		-	
249321	9.2	F5	0.08:	-	-	2.8		0	
249362	7.6	K0	0.31	-	-	2.7	1891	+	
256098	9.1	F5	0.08:	-	-	2.8		0	
256099	8.1	F5	-	-	-	-		-	
256102	8.3	F2	-	-	-	-		-	
256111	9.1	A0	-	-	-	-		-	

Notes to Table A.3:

a) The 12 and 25 μm flux densities in this table are colour-corrected (see Table 5.A).
b) Detection qualities at 12 μm are good (+), medium (0) or poor (-).
c) See Section A.5.1 in Appendix A.

A.6. Conclusions

Infrared emission in IRAS Co–added maps at 12, 25, 60 and 100 μm at the North and West edges of the Large Magellanic Cloud are analysed; the maps show supergiant shells 1, 4 and 5. In those maps we found 68 infrared sources, which brings the total of infrared sources in and around the LMC to 1891. In the areas that were searched all but one IRAS Point Sources (PSC) were detected; no IRAS Small Scale Structure (SSS) catalogue entries are available in these fields. Sixteen infrared sources are new detections. We identified the infrared sources where possible. Seventeen foreground SAO stars were detected in these fields, one variable star RT Men and possibly one globular cluster.

References

Andrews, A.D., Lindsay, E.M.: 1964, *Irish Astron. J.* **6**, 241

Apparao, K.M.V., Allen, D.: 1982, *Astron. Astrophys.* **107**, L5

van den Bergh, S.: 1981, *Astron. Astrophys. Suppl.* **46**, 79

Blanco, V.M., McCarthy, M.F., Blanco, B.M.: 1980, *Astrophys. J.* **242**, 938

Bohannan, B., Epps, H.W.: 1974, *Astron. Astrophys. Suppl.* **18**, 47

Davies, R.D., Elliott, K.H., Meaburn, J.: 1976, *Mem. R. Astron. Soc.* **81**, 89

Elias, J.H., Frogel, J.A., Schwering, P.B.W.: 1986, *Astrophys. J.* **302**, 675

Feast, M.W., Thackeray, A.D., Wesselink, A.J.: 1960, *Mon. Not. R. Aston. Soc.* **121**, 337

Feast, M.W., Catchpole, R.M., Carter, B.S., Roberts, G.: 1980, *Mon. Not. R. Astron. Soc.* **193**, 377

Gathier, R: 1984, Ph.D. Thesis, University of Groningen

Glass, I.S.: 1984, *Mon. Not. R. Astron. Soc.* **209**, 759

Graham, J.R., Evans, A., Albinson, J.S., Bode, M.F., Meikle, W.P.S.: 1987, *Atrophys. J.* **319**, 126

Henize K.G.: 1956, *Astrophys. J. Suppl.* **2**, 315

Hodge, P.W., Sexton, J.A.: 1966, *Astron. J.* **71**, 363

Hodge, P.W.: 1972, *Publ. Astron. Soc. Pac.* **84**, 365

Hodge, P.W.: 1984, in *"Structure and Evolution of the Magellanic Clouds"*, IAU Symp. 108, eds. S. van den Bergh, K.S. de Boer, Reidel Dordrecht, 7

Humphreys R.M.: 1984, in *"Structure and Evolution of the Magellanic Clouds"*, IAU Symp. 108, eds. S. van den Bergh, K.S. de Boer, Reidel Dordrecht, 145

IRAS: 1985a, IRAS Catalogs and Atlases Explanatory Supplement, eds. C.A. Beichmann, G. Neugebauer, H.J. Habing, P.E. Clegg, T.J. Chester, JPL D–1855

IRAS: 1985b, IRAS Small Scale Structure Catalog, eds. G. Helou, D.W. Walker, JPL D–2988

IRAS: 1986, A guide to IRAS pointed observation products, eds. E.T. Young, G. Neugebauer, E.L. Kopan, R.D. Benson, T.P. Conrow, W.L. Rice, D.T. Gregorich, G.K. Miley, IPAC preprint PRE–008N

Israel F.P.: 1984, in *"Structure and Evolution of the Magellanic Clouds"*, IAU Symp. 108, eds. S. van den Bergh, K.S. de Boer, Reidel Dordrecht, 319

Israel, F.P., Schwering, P.B.W.: 1986, in *"Light on Dark Matter"*, ed. F.P. Israel, Reidel Dordrecht, 383

Jacoby, G.H.: 1980, *Astrophys. J. Suppl.* **42**, 1

Kukarkin, B.V., Kholopov, P.N., Efremov, Yu.N., Kukarkina, N.P., Kurochkin, N.E., Medvedeva, G.I., Perova, N.B., Fedorovich, V.P., Frolov, M.S.: 1969, *"General Catalogue of Variable Stars, Volume I"*, Sternberg Institute, Moscow State University

Kukarkin, B.V., Kholopov, P.N., Efremov, Yu.N., Kukarkina, N.P., Kurochkin, N.E., Medvedeva, G.I., Perova, N.B., Fedorovich, V.P., Frolov, M.S.: 1970, *"General Catalogue of Variable Stars, Volume II"*, Sternberg Institute, Moscow State University

Kukarkin, B.V., Kholopov, P.N., Pskovsky, Y.P., Efremov, Yu.N., Kukarkina, N.P., Kurochkin, N.E., Medvedeva, G.I., Perova, N.B., Fedorovich, V.P., Frolov, M.S.: 1971, *"General Catalogue of Variable Stars, Volume III"*, Sternberg Institute, Moscow State University

Kukarkin, B.V., Kholopov, P.N., Artirukhina, N.M., Fedorich, V.P., Frolov, M.S., Goranskij, V.P., Gorynya, N.A., Karitskaya, E.A., Kireeva, N.N., Kukarkina, N.P., Kurochkin, N.E., Medvedevna, G.I., Perova, N.B., Ponomareva, J.A., Samus , N.N., Shugarov, S.Y.: 1981, *"New Catalog of Suspected Variable Stars"*, Moscow

Lindsay, E.M.: 1963, *Irish Astron. J.* **6**, 127

Lindsay, E.M., Mullan, D.J.: 1963, *Irish Astron. J.* **6**, 51

Lyngå, G., Westerlund, B.E.: 1963, *Mon. Not. R. Astron. Soc.* **127**, 31

Mathewson, D.S., Ford, V.L., Dopita, M.A., Tuohy, I.R., Long, K.S., Helfand, D.J.: 1983, *Astrophys. J. Suppl.* **51**, 345

Meaburn, J.: 1980, *Mon. Not. R. Astron. Soc.* **192**, 365

McGee, R.X., Haynes, R.F., Grognard, R.J.-M., Malin, D.: 1986, *Mon. Not. R. Astron. Soc.* **221**, 543

Pottasch, S.R.: 1986, in *"Light on Dark Matter"*, ed. F.P. Israel, Reidel Dordrecht, 131

Price, S.D., Walker, R.G.: 1976, *"The AFGL Four Color Infrared Sky Survey: Catalog of Observations at 4.2, 11.0, 19.8 and 27.4 μm"*, AFGL–TR–76–0208, Hanscom Air Force Base, Massachusetts: Air Force Geophysics Laboratory.

Sanduleak, S.N., MacDonnell, D.J., Davis Philip, A.G.: 1978, *Publ. Astron. Soc. Pac.* **90**, 621

Sanduleak, N.: 1984, in *"Structure and Evolution of the Magellanic Clouds"*, IAU Symp. 108, eds. S. van den Bergh, K.S. de Boer, Reidel Dordrecht, 231

Savage, A., Murdin, P.G., Clark, D.H.: 1982, *Observatory* **102**, 229

Schwering, P.B.W.: 1985, in *"New Aspects of Galaxy Photometry"*, Lecture notes in Physics 32, ed. J.L. Nieto, Springer Verlag Berlin, 115

Schwering, P.B.W.: 1987, in *"Starbursts and Galaxy Evolution"*, ed. T.X. Thuan, Th. Montmerle, J. Tran Thanh Van, Editiones Frontières, Gif Sur Yvette Cedex, 85

Schwering, P.B.W., Israel, F.P.: 1988a, *Astron. Astrophys.*, in press (Chapter II).

Schwering, P.B.W., Israel, F.P.: 1988b, *"Atlas and Catalogue of IRAS far–infrared observations of the Magellanic Clouds"*, in preparation

Shapley, H., Lindsay, E.M.: 1963, *Irish Astron. J.* **6**, 74

Smithsonian Astrophysical Observatory Star Catalog (4 vols.): 1966, Washington D.C., Smithsonian Institution (version 1984)

Stahl, O., Wolf, B., Zickgraf, F.-J., Bastian, U., de Groot, M.J.H., Leitherer, C.: 1983, *Astron. Astrophys.* **120**, 287

Stevenson, C.B.: 1973, *"A General Catalogue of Cool Carbon Stars"*, Publ. Warner Swasey Obs. 1, 4

Westerlund, B.E., Smith, L.E.: 1964, *Mon. Not. R. Astron. Soc.* **127**, 449

Wolf, B., Zickgraf, F.-J.: 1986, *Astron. Astrophys.* **164**, 435

Chapter IV

GALACTIC INFRARED FOREGROUND EMISSION IN THE DIRECTION OF THE MAGELLANIC CLOUDS

1. Introduction

For a reliable interpretation of measurements in the Magellanic Clouds, a good knowledge of the foreground material in our Galaxy (disk and halo) is essential in infrared, visual and ultraviolet wavelength regions. Until now, the line–of–sight towards the Magellanic Clouds has been assumed to contain Galactic gas and dust, mostly situated close to the Sun, with a uniform distribution over the face of the Clouds.

De Vaucouleurs (1955) has presented deep visual photographs of the Clouds on which a spur like feature is shown, that he suggests to be an optical tidal–spiral arm of the LMC. HI radio data (Cleary *et al.*, 1979; Colomb *et al.*, 1980) confirmed this narrow–arc feature, but showed it to have local velocities (+13 km/s) and thus to be foreground. Some years later, the Infrared Astronomical Satellite IRAS (Israel and Schwering, 1986; McGee *et al.*, 1986) also detected this feature in the infrared bands at 60 and 100 μm. Other infrared features related to foreground emission are a bridge (-4 to $+8$ km/s) between the LMC and Galactic cirrus emission (-20 to $+4$ km/s) and a thin filament (-4 to $+8$ km/s). Neither of these features are related to the LMC, and they show that the Galactic foreground is complex and non–uniform. This complexity was also shown by Johnson *et al.* (1982) who used high contrast prints to detect a region of faint filamentary Hα nebulosity in the Galactic foreground. Deep visual images of these filaments were presented recently by West *et al.* (1987). While the SMC is largely free from a complex foreground, it is clear that the LMC's foreground infrared emission and dust obscuration vary over much smaller scales than the size of the Cloud itself.

The mean Galactic foreground reddening in the directions of the LMC and SMC has been studied by McNamara and Feltz (1980; and references therein). Although E_{B-V} is small, there are large discrepancies between the various values derived (LMC: 0.04 - 0.08; SMC: 0.01 - 0.07 magnitude, based on stellar photometry or on the strength of the 2200 Å feature). McNamara and Feltz derive average E_{B-V} values of 0.034 ± 0.004 and 0.019 ± 0.004 mag for the LMC and SMC foreground respectively, assuming a constant value over the face of each Cloud. An areal search undertaken by them suggests that the foreground colour excess in the SW quadrant of the LMC is about 0.01 mag higher than in the NE quadrant. From the first available IRAS data on the Clouds Israel and Schwering (1986) concluded that the foreground extinction E_{B-V} towards the LMC varies between 0 and 0.15 mag but on the other hand the extinction towards the SMC is constant at about 0.02 mag. Note that the peak extinction value inside the LMC itself (at 30 Doradus) is about 0.4 mag (Isserstedt, 1975; Israel and Schwering, 1986) and the average Clouds' extinctions are about the same as that of the local Galactic foreground (Koornneef, 1984).

In this chapter we discuss the Clouds' infrared foreground and its relation to atomic hydrogen (HI). First we discuss the infrared and atomic hydrogen data in Section 2. Section

3 contains a derivation and discussion of the foreground infrared stellar contribution. The large scale foreground infrared cirrus component is derived in Section 4, which has been used to correct infrared maps of the Clouds. Thereafter we discuss the infrared–to–HI relation and compare it with those derived by other authors (Section 5). In Section 6 we derive an estimate for the distribution of the Galactic foreground colour excess in the direction of the Magellanic Clouds as well as the relation between infrared intensity and visual extinction, followed by its implications to visual and ultraviolet studies of the Clouds in Section 7. We summarize the conclusions in Section 8.

2. Data presentations and handling

2.1. Infrared data

Foreground features that we are interested in, extend over an area of 40°. In principle all IRAS large scale structure maps are useful in this study; these are the $16\overset{\circ}{.}5$ extended emission Skyflux images (IRAS, 1985), Spline–I (van Albada *et al.*, 1985) and the Zodiacal Observations History File data (ZOHF; see IRAS, 1985). The Skyflux maps have some disadvantages; they are relatively small and the LMC is located on four different plates that cannot be connected at 12 and 25 μm without elaborate (and not yet routine) procedures. Braun, Walker and Deul (priv. comm.) have combined the 6° x 6° Spline–I maps into 50° x 50° maps in Galactic coordinates (see *e.g.* Fig. 1 in Chapter II), but because Spline processing was done only for the IRAS 60 and 100 μm wavelength bands, we prefered to use the ZOHF data, which has all four IRAS bands at 12, 25, 60 and 100 μm.

Using the ZOHF data has several advantages. For his own use, Deul (1988) has combined the ZOHF scan–data into intensity maps in Galactic coordinates and subtracted his model of the Zodiacal Light (Deul and Wolstencroft, 1988). The residuals of Zodiacal emission in these maps, which are centered near the South Ecliptic Pole (at $l = 276°$, $b = -30°$), are small and negligible compared to residual stripes which are of the order of 0.5, 0.5, 0.2 and 0.1 MJy/sr at 12, 25, 60 and 100 μm respectively. These stripes are definitely of instrumental origin. The resolution of the original ZOHF maps is $30'$, which we have convolved to $48'$ (the HI resolution; see Section 2.2). This angular resolution corresponds to a linear resolution of < 1.4 pc for (local) distances (< 100 pc) and 770 pc at 55 kpc (the distance of the Clouds). The final maps, which are presented in Fig. 1, cover the area of $250° < l < 330°$ and $-60° < b < 0°$ with $15'$ pixel size. Note the radial striping pattern centered on the South Ecliptic Pole due to the scan direction of the IRAS satellite, and the Galactic plane at the top of the images. The features discussed in the Introduction are detected at 60 and 100 μm. The two filaments emerge from the lower left corner of the LMC (285°, −35°) in the (l, b) map, one extending downwards to the right and the other straight to the left. The bridge connecting the LMC with Galactic cirrus emission is located at (280°, −30°). These three features are below the striping level in the 12 and 25 μm bands; the grey scales are chosen to enhance the low intensity levels and show one of the filaments (going southwards). In all infrared maps presented in this chapter, the surface brightness is derived by deconvolving for the smearing by the IRAS frequency filters under the assumption of an intrinsic source spectrum $f_\nu \propto \nu^{-1}$.

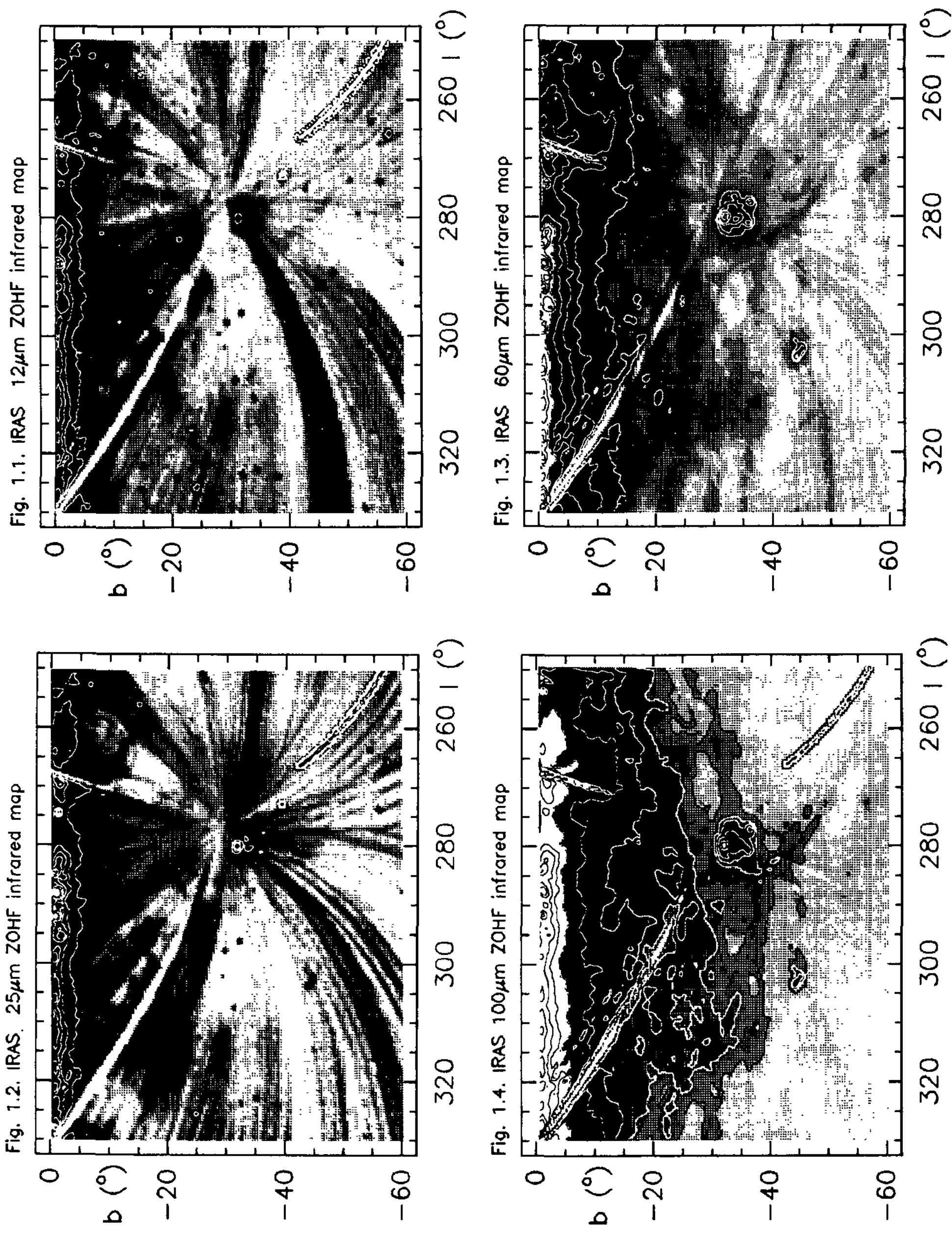
Fig. 1.1. IRAS 12μm ZOHF infrared map

Fig. 1.2. IRAS 25μm ZOHF infrared map

Fig. 1.3. IRAS 60μm ZOHF infrared map

Fig. 1.4. IRAS 100μm ZOHF infrared map

Figure 1. *Zody History File infrared maps at 12, 25, 60 and 100 μm with a resolution of 48′. The maps in this chapter are presented in Galactic 1950 coordinates. Note the LMC (280°, −33°) just right of the middle and the SMC (303°, −44°) at the lower left of the centre. Darker grey scales indicate higher intensities; they are chosen to enhance low level emission, ranging from 0 – 50 MJy/sr. Contours are at 2, 5, 10, 20, 50, 100, 200, 500, 1000 MJy/sr, similar in all four bands.*

2.2 Atomic hydrogen data

With the 18–m Parkes radiotelescope (CSIRO) Cleary *et al.* (1979) have observed HI from the Southern Hemisphere for $\delta < -30°$ (the area with $| b | < 10°$ was excluded), with a beam size of $48'$ (HPBW) and velocity sampling of 7 km/s. Drift scans were taken at constant declination, with 1° intervals in declination for $b \geq -25°$ (velocity range of $-148 < V_{LSR} < +300$ km/s) and 2° for $b < -25°$ ($-230 < V_{LSR} < +218$ km/s) and one beam width intervals in right ascension. Note that there is spatial undersampling and the individual profiles include contributions of both Clouds.

In order to resample the data to $15'$ pixels we have interpolated the original data by a Lagrangian interpolation of 4 x 4 surrounding pixels. We have integrated the profiles over the velocity range from −38 to +38 km/s. This range was chosen since the local foreground HI, in the direction of the Magellanic Clouds, has velocities ranging from about −30 to +20 km/s (see Colomb *et al.*, 1980). Furthermore we did not want to use a larger range than necessary as this will mean adding up uncorrelated signals, resulting in a higher noise level, and because the Magellanic Clouds start to contribute at V_{LSR} of about +88 km/s (SMC; McGee and Newton, 1981) and +190 km/s (LMC; Rohlfs *et al.*, 1984). We have derived atomic hydrogen column densities from

$$N_{HI}\ (10^{20}\ \mathrm{H-atoms\ cm^{-2}})\ =\ 0.0182/\eta_{mb} \int_{-\infty}^{+\infty} (T_A/\mathrm{K})\ (dv/\mathrm{km\ s^{-1}})$$

$$\approx\ 0.0182/\eta_{mb}\ (\Delta v/\mathrm{km\ s^{-1}}) \sum_{v=-38\mathrm{km/s}}^{+38\mathrm{km/s}} (T_A/\mathrm{K}) \qquad (1)$$

with antenna temperatures T_A(K) and a main beam efficiency $\eta_{mb} = 0.85$ for the Parkes 18–m telescope. We have implicitely assumed that the HI emission is optically thin. Optical depths larger than 1 occur at low (absolute) latitudes only (Strong *et al.*, 1982; in the Magellanic Cloud foreground region no evidence for this effect was found by McGee *et al.*, 1986). We have compared the final HI map with the qualitative map published by Colomb *et al.* (1980). These maps, which have the same velocity coverage and are constructed from the same data, agree well. We also compared this map with a map containing all available velocities (Deul, 1988) in the area surrounding the Clouds. This shows that our HI map contains 85 – 90 % of the total summed–velocity HI emission. Therefore we may expect an error of at most 15 % from underestimating the velocity range (note that uncorrelated signals might be added in the summed–velocity HI). The distribution of HI column densities is presented in Fig. 2.1. At the position of the Magellanic Clouds we see relatively weak HI compared to the HI at lower $| b |$.

In Fig. 2.2 we combine the infrared 100 μm map in contours with the HI column density grey scales map. Note the good correlation of infrared emitting dust with the atomic hydrogen gas of the Galactic foreground at these spatial scales, and the varying Galactic HI foreground towards the LMC. The HI towards the LMC 30 Doradus region and the LMC–Bar is about 30 % less than to other regions of the LMC. Just below the centre of the SMC we see a dense blob of HI which originates from HI structures following the drift scan with velocities of $-38 < V_{LSR} < -26$ km/s and with $+38 > V_{LSR} > +26$ km/s, velocities at which we find only noise in the individual scans. These velocities are too low for the SMC to be responsible for this blob. The blob does not appear on the original maps of Cleary *et al.* (1979). We conclude that it is probably the result of noise blow-up in the processing.

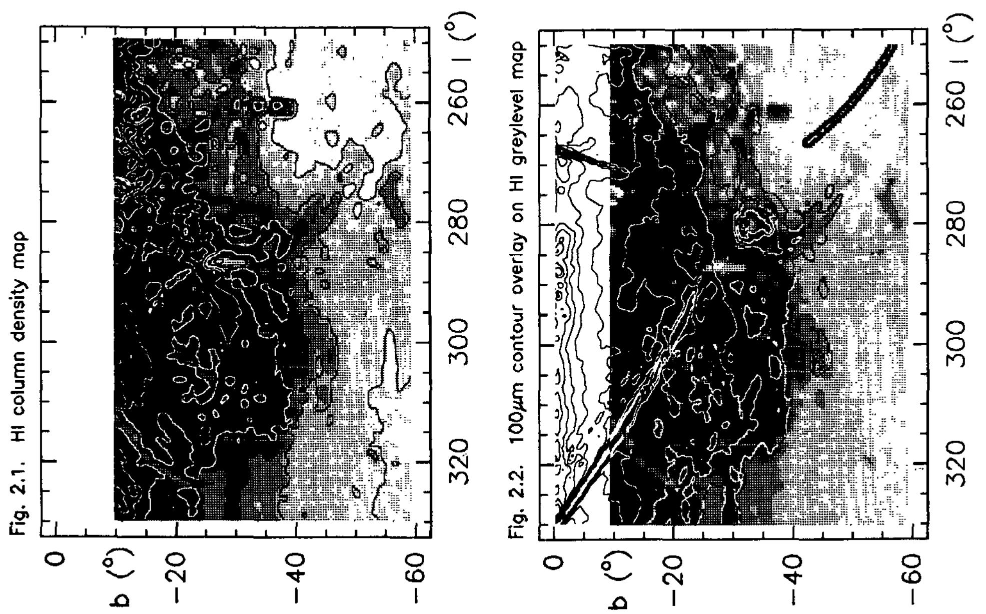
Fig. 2.1. HI column density map

Fig. 2.2. 100μm contour overlay on HI greylevel map

Figure 2. *Integrated 21–cm HI column density map with a resolution of 48′.*
Fig. 2.1. HI column density map. Grey scales enhance the low level intensities and range from 0 – 22, while contours are at 2, 4, 8, 12, 16, 20 x 10^{20} H–atoms cm^{-2}.
Fig. 2.2. Relation in overlay form between the infrared 100 μm contour map and the HI column density grey scales map. The infrared contours and neutral hydrogen grey scales are identical as in Fig. 1.4 and 2.1. Note the position of the Magellanic Clouds in the HI map.

3. The stellar infrared foreground

The Galactic infrared foreground can be separated into two categories: unresolved stellar sources (mainly at 12 and 25 μm) and a smooth foreground related to infrared cirrus (mainly at 60 and 100 μm). The latter will be discussed in Section 4; here we discuss the discrete component.

Due to their distance, stellar members of the Magellanic Clouds are only marginally detectable by IRAS (see Chapters II and III). We have therefore assumed that all sources of the Source Lists in Chapters II (LI–SMC) and III (LI–LMC) with a stellar infrared spectral type (*i.e.* strongest at 12 μm) are foreground stars. The stellar foreground infrared data are given in Table 1. Note that we do not include stars with "hot dust" in surrounding shells (OH/IR stars), of which only a few might be present in the foreground. From the number of sources with warm–dust spectra in the source lists and their flux densities we expect an error at 25 μm of no more than $\sim$ 2 Jy. Elias *et al.* (1986) have shown that the brightest warm–dust spectra in the point source lists are LMC–members. If any Galactic OH/IR stars were present they would have been much brighter than these LMC–stars.

The spectra of the integrated stellar flux densities approximately follow the Rayleigh–Jeans tail of the blackbody spectrum for the SMC; for the LMC the 25 μm flux density is too high by about 70 % as predicted from the 12 μm flux density (and follows roughly a 700 K blackbody). For 85 of the LMC foreground stars the 25 μm flux density is close to the detection limit; a possible overestimate of these low values may explain 25 % of the total 25 μm stellar foreground flux density. The twenty–five brightest stars with $f_{25\mu m} > 0.4$ Jy show an excess of about 28 % above the extrapolated 12 μm emission. For the brightest foreground stars, the IRAS Point Source Catalog (PSC; IRAS, 1985) gives flux densities at 12 μm which are about 1.2 times higher than in our LMC source list. Although the PSC 25 μm flux densities are similar to ours, they are still 30 % higher than predicted from the extrapolated 12 μm PSC flux densities. For both Clouds the average flux density per star ($f^b_{25\mu m}$) is very similar, but the total number of stars emitting at 25 μm is very different (for the SMC 30 % of the stars detected at 12 μm are detected at 25 μm, for the LMC this is 60 %). This shows that the difference in the number of stars must be the main reason for the larger 25 μm flux density in the LMC. Note that the colour correction that has to be applied cannot give an explanation for the high ratio $F_{25\mu m}/F_{12\mu m}$ as both bands must be corrected by the same amount (f_ν decreases by about 1.4 for a 3000 K blackbody).

The 12 μm stellar foreground surface brightness towards the LMC (area 8° x 8°) is two times larger than towards the SMC (4° x 4°) and at 25 μm about 4 times larger. For the SAO stars the ratio of the number of stars (186 in Chapter III and 47 in Chapter II) is just that expected for the difference in area only (indicating identical average surface densities of SAO stars). Note that the surface density of stars detected in the infrared for the LMC foreground is 1.5 times higher than for the SMC foreground. This difference might be explained by stochastical differences in the number of stars, but mainly the higher latitude of the LMC ($b = -33°$) compared to the SMC ($b = -44°$) will have influenced the result. The observed number of stars in the different latitude ranges are given by Mihalas and Binney (1981, Fig. 4.1 therein); for A–type stars it shows a ratio of 1.4 between $30° < | b | < 40°$ and $40° < | b | < 50°$, with a decrease for later types. Note that the Galactic foreground extinction towards the LMC is also a factor of 1.5 higher than towards the SMC ($\Delta E_{B-V} = 0.02$; see Sections 1 and 6). Its low value ($A_V < 0.5$ mag) implicates that no bright foreground stars will stay undetected.

The discrete foreground sources contain 3 % (LMC) respectively 10 % (SMC) of the total integrated flux densities of the Clouds at 12 μm (see Chapter V). Due to the difference in spectral shape between the Clouds' cool dust and Galactic foreground stars, this fraction falls to about 1 % at 25 μm and much less in the other bands. Hence, there is a negligible contribution of foreground stars to the 25, 60 and 100 μm flux densities of the Clouds, but the 12 μm emission of the Clouds must be corrected for the stellar foreground, the SMC more than the LMC.

Table 1. *Stellar infrared foreground emission* [a].

IRAS infrared band	LMC					SMC				
	N_*	F_ν (Jy)	f_ν^{max} (Jy)	f_ν^b (Jy)	f_ν^t (Jy)	N_*	F_ν (Jy)	f_ν^{max} (Jy)	f_ν^b (Jy)	f_ν^t (Jy)
12 μm	253	130.	8.2	0.51	0.51	43	17.	2.6	0.40	0.40
25 μm	154	51.	4.6	0.33	0.20	12	3.5	0.8	0.29	0.08
60 μm	4	3.2	1.2:	0.80:	0.01	1	0.4	0.4	0.40	0.01
100 μm	0	–	–	–	–	0	–	–	–	–

Note to Table 1:

a) *For each Cloud, and for each infrared band the first column N_* gives the total number of stellar objects. The various flux densities are given in columns 2 – 5: F_ν is the sum of the flux densities of all stars; f_ν^{max} is the maximum flux density that occurs in the sample of stars; f_ν^b is the average flux density normalized to the number of stars in the band; f_ν^t is the average flux density normalized to the total number of stars detected in the 12 μm band. Note that all flux densities assume an intrinsic spectrum $f_\nu \propto \nu^{-1}$.*

4. The cirrus infrared foreground

We determine the Galactic infrared cirrus foreground towards the Magellanic Clouds as follows. Because the 100 μm emission is optically thin, we have detected in the infrared all the dust in the line–of–sight, *i.e.* Galactic foreground dust and dust in the Magellanic Clouds, that can be regarded as main contributors to the emission between 8 and 120 μm ($I_\nu = \int_{Gal+Clouds} M_d\ \kappa_\nu\ B_\nu(T_d)\ dl$; note that the maps have already been corrected for the large scale Zodiacal emission). From the neutral hydrogen gas (which is assumed to be optically thin) we have selected only the velocity range in which the Clouds do not contribute, but we included all the Galactic HI ($N_{HI} = \int_{Gal} n_{HI}\ dl$). We furthermore assume a constant gas–to–dust ratio for the Galactic foreground and find the relation of gas and dust from comparing the HI with the infrared dust emission. The infrared foreground is then reconstructed by scaling the HI map taking into account the derived line–of–sight dust temperatures.

4.1. Atomic and molecular hydrogen column densities

The observed HI (see Section 2.2) originates from Galactic foreground material only, after applying the velocity cut–off at 38 km/s

$$N_{HI\ obs} = N_{HI\ Gal} \approx N_{H\ Gal}. \tag{2}$$

Because there is hardly any CO detected at high Galactic latitudes (Dame and Thaddeus, 1987; $I_{CO} < 5$ K km/s at $\mid b \mid > 5^\circ$ and $I_{CO} > 50$ K km/s for the Galactic plane) we expect little molecular hydrogen to be present; hence all the hydrogen gas is in atomic form and the approximation of Equation 2 holds. The same low CO emission is found at high latitudes in the third Galactic quadrant (May *et al.*, 1988). Note that some local high latitude molecular clouds are detected, but none are known in this part of the sky. In the absence of H_2 the HI gas–to–dust ratio should be constant over the whole area.

4.2. Infrared emission

First we study the relation of infrared emission with atomic hydrogen. The 12 and 25 μm infrared radiation at the latitudes of the Clouds, is possibly caused by very small grains (with radii 0.3 nm $< a <$ 10 nm) heated to high non–equilibrium temperatures (300 K $< T_{12-25\mu m} <$ 1500 K) by absorption of single high–energy (ultraviolet) photons (Puget *et al.*, 1985; Draine and Anderson, 1985; Cox *et al.*, 1986). The intensity of the 12 and 25 μm emission depends on the temperature distribution of these small grains, and this distribution is not necessarily related to the temperature distribution of the larger grains responsible for the 60 and 100 μm emission. As there is a close resemblance of the Galactic 12 and 100 μm (cirrus) maps, small grains are expected to be well mixed with the larger grains, and with HI. Hence we would expect a strong relation between $I_{12\mu m}$ and N_{HI}. However, the 1° pixel–to–pixel scatter diagrams (Fig. 3.1 and 3.2) do not show a strong relation. There is a large scatter which makes the shape of the relation of 12 and 25 μm with HI hard to determine. The range in infrared intensities is in these bands an order of magnitude smaller than for the 60 and 100 μm bands. Residual scan–stripes and Zodiacal emission in the maps, also contribute to the scatter. Correcting these bands for the 12 – 25 μm line–of–sight dust temperature (assuming equilibrium) gives only a marginally improved correlation. The cooler dust grains responsible for the 60 and 100 μm emission, are expected to be closely related to the HI distribution (Cox *et al.*, 1986) and therefore should show a good correlation. The scale height of HI and infrared are equal in our Galaxy (Burton and Deul, 1987). The 60 and 100 μm intensities have a much wider range in values and the map uncertainties are much smaller. We have determined the relations from the ${}^{10}\log I_\nu$ – ${}^{10}\log N_{HI}$ 1° pixel–to–pixel scatter diagrams, which are given in Fig. 3.3 and 3.4.

Fig. 3.1. Pixel-to-pixel scatterplot

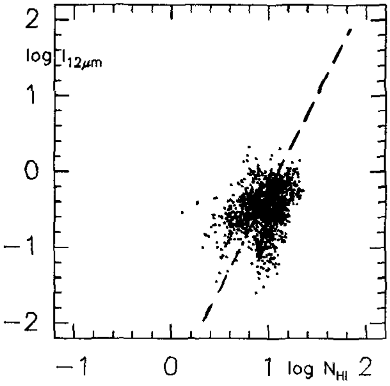

Fig. 3.2. Pixel-to-pixel scatterplot

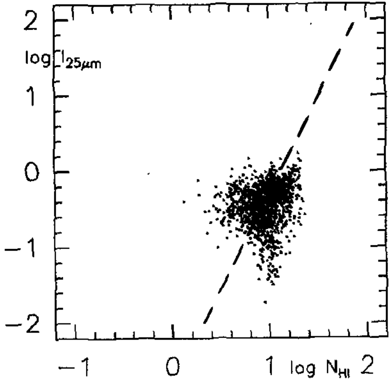

Fig. 3.3. Pixel-to-pixel scatterplot

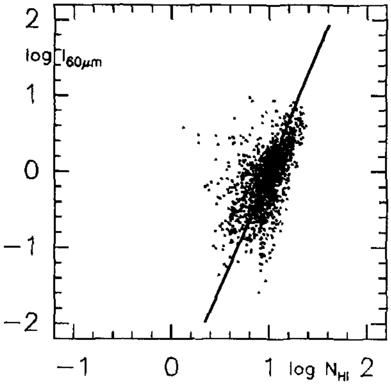

Fig. 3.4. Pixel-to-pixel scatterplot

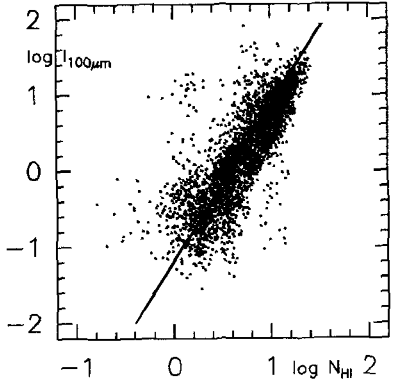

Figure 3. *Pixel-to-pixel scatter diagrams of the infrared emission at the four IRAS bands (in MJy/sr) with the HI column density (in 10^{20} H-atoms cm^{-2}; both ^{10}log). The solid or dashed lines correspond to the derived relations (see Table 2). Areas of 16 x 16 pixels (1 ° x 1 °) have been averaged before plotting.*

Fig. 3.1. 12 μm infrared map – HI column density.

Fig. 3.2. 25 μm infrared map – HI column density.

Fig. 3.3. 60 μm infrared map – HI column density.

Fig. 3.4. 100 μm infrared map – HI column density.

For the relation in Fig. 3.4 we have used all available pixels as the uncertainties in the 100 μm map are much less than in the other bands. Using the same area as before would lead to only the upper part of the diagram ($I_{100\mu m}$ > 1 MJy/sr) but would not influence the choice of the infrared–HI correlation.

We have fitted a power–law relation

$$I_{\nu\ Gal} = \alpha_\nu\ N_{HI\ Gal}^{\beta_\nu} \tag{3}$$

to the scatter plots; where α_ν and β_ν are determined from the figure's offset and slope. The empirical values, which have been derived for the HI range of (8 – 20) x 10^{20} H–atoms cm^{-2}, are summarized in Table 2. The 60 and 100 μm intensities correlate very well with HI and the diagrams indicate the expected non–linear relation between infrared and HI, which can only be understood when the grain temperature and the HI column densities are correlated. In Section 5.2 we will go into detail in the origin of these non–linearities.

Table 2. *Parameters describing the relation of infrared and dust with gas in the Galactic foreground for the specified HI ranges* [a].

Data	α_ν	β_ν	Comments
$I_{12\mu m}$	$0.0019\ ^{+0.003}_{-0.001}$	2.6 ± 2.0	From Fig. 3.1.
$I_{25\mu m}$	$0.0019\ ^{+0.003}_{-0.001}$	2.6 ± 2.0	Set equal to 12 μm relation; Fig. 3.2.
$I_{60\mu m}$	$0.00069^{+0.0007}_{-0.0004}$	3.4 ± 0.5	From Fig. 3.3; $N_{HI} = 10 - 20$.
$I_{100\mu m}$	$0.082\ ^{+0.06}_{-0.04}$	2.1 ± 0.2	From Fig. 3.4; $N_{HI} = 3 - 20$.
$I_{60\mu m}/I_{100\mu m}$	$0.24\ ^{+0.1}_{-0.05}$	—	$I_{60\mu m} - I_{100\mu m}$ scatter diagram.
T_d (K)	22^{+2}_{-2}	—	From Fig. 4.2.
$< N_d/N_{HI} >$	$0.0024\ ^{+0.0009}_{-0.0009}$	—	Linear fit to Fig. 4.4.
$< N_{HI}/N_d >$	420^{+250}_{-120}	—	Inversion of $< N_d/N_{HI} >$ above.

Note to Table 2:

a) *The coefficients α_ν and β_ν of Equation 3 are given for the relation of infrared intensity to HI column density of Fig. 3. The values for 12 and 25 μm contain large uncertainties due to the large scatter in Fig. 3, while the 60 and 100 μm relations are much more accurate. I_ν is expressed in MJy/sr and N_{HI} in 10^{20} H–atoms cm^{-2}. The ratio $I_{60\mu m}/I_{100\mu m}$ increases somewhat with increasing 100 μm intensities. Note the rather constant T_d and that the dust–to–gas (mass) ratio has been fitted in a linear way ($\beta_\nu \equiv 1$).*

4.3. Dust temperatures

As a result of the small optical depth of infrared radiation, dust column densities can be derived in each line–of–sight (see Appendix). In general two components, dust in the Galaxy and in the Clouds, are responsible for the infrared emission and hence the dust column densities consist of these two components

$$N_{d\ obs} = N_{d\ Gal} + N_{d\ Clouds}. \tag{4}$$

Fig. 4.1 shows the dust temperature map obtained from the 60 and 100 μm infrared maps. We have assumed a λ^{-n} wavelength dependence for the emissivity (with $n = 1.5$, see Appendix) and have applied intensity cut–offs at 0.2 MJy/sr to avoid noise blow–up. Due to the strong dependence of the infrared intensity on the temperature of large dust grains ($I_\nu \propto T_d^{4+n}$) a 15 % variation in temperature of 22 to 25 K (typical cirrus dust temperatures) will change the infrared emission by a factor of 2. Note that the lines–of–sight towards the LMC, the SMC and the Galactic plane are warmer than the Galactic Cloud–foreground. In general we see a correlation between infrared emission and dust temperature. The pixel–to–pixel relation of T_d with N_{HI} is given in Fig. 4.2. The mean foreground dust temperature is about 21 K around the LMC with a range in values of 17 – 28 K. The local Galactic foreground dust ($b \lesssim -10^\circ$) thus seems to be at a quite uniform temperature with little variation. Although we have applied an intensity cut–off, some low–level infrared emission areas influenced by striping yield unrealistically high temperatures above 30 K (*e.g.* at latitudes $b < -40^\circ$; the area with $250^\circ < l < 280^\circ$ and $-30^\circ < b < -25^\circ$). Note that these stripy areas follow the scan–pattern to the Ecliptic Pole. Uncertainties mainly in the 60 μm map give rise to these artificially high dust temperatures, indicating baseline problems at these positions. These two areas have been cut–out in the quantitative analysis (of *e.g.* Fig. 3).

4.4. Dust column densities

The use of $I_{100\mu m}$ as a measure for the dust content of objects is justified only if objects have single dust temperatures throughout. In general this is not the case and variations of $I_{100\mu m}$ with T_d will occur as described in Section 4.3. We calculated dust mass column densities M_d by correcting the 100 μm infrared map with the line–of–sight dust temperatures T_d and dividing by the mass absorption coefficient $\kappa_{100\mu m}$. The resulting map is shown in Fig. 4.3. These column densities are expressed in the number of hydrogen atoms that correspond in mass with the calculated dust column (*i.e.* $N_d \equiv M_d/m_{HI}$). They are relatively high in the Galactic plane, decreasing towards higher (negative) latitudes. In these "*temperature corrected infrared maps*", the LMC shows up only marginally as its dust is considerably warmer than the dust in the local Galactic foreground and its dust column densities apparently low. Note the reasonably good overall correlation between the 100 μm infrared emission and the dust column densities, which is a consequence of the rather uniform T_d distribution. The HI also correlates reasonably well with the dust column density map on these large scales. Fig. 4.4 shows the latter relation in a 1° pixel–to–pixel scatter diagram. Some points in this figure have high values for N_d (> 0.04) for relatively low values for N_{HI} of (5 – 11) x 10^{20} H–atoms cm^{-2}. These points, positioned at the upper left of the LMC, can be distinguished in Fig. 4.3 and have somewhat lower dust temperatures. These low temperatures are more influenced by noise and other uncertainties in the 60 or 100 μm maps and have more uncertain dust column densities.

4.5. Gas–to–dust ratio

Dust and gas are assumed to be well mixed in galaxies. Their ratio gives us information on the evolution of galaxies; low dust–to–gas ratios occur in relatively unevolved galaxies (like the Magellanic Clouds). From the area that can be considered free of Cloud infrared emission we now obtain the dimensionless mass–relation between temperature corrected Galactic foreground infrared emission N_d and atomic hydrogen emission N_{HI}, $< N_{HI}/N_d >$. From Fig. 4.4 we derive a value $< N_{HI}/N_d >= 420^{+250}_{-120}$ (see Table 2). According to our definition of N_d (Section 4.4), this is the gas–to–dust ratio by *mass*.

This ratio is determined from data with N_{HI} of (3 - 20) x 10^{20} H–atoms cm^{-2} and is 2 - 4 times higher than classical values for our Galaxy (100 - 200, Osterbrock, 1973; Hildebrand, 1983; Savage and Mathis, 1979). Using the same method, van Roermund (priv. comm.) derived a gas–to–dust ratio in the Scorpius region (near $b = 0°$) of 350±50; within our errorbars. The formal error in the derived value of $< N_{HI}/N_d >$ results from the scatter in the figure. Hence it is influenced by problems and artefacts in the infrared and HI data (see Section 2). The real uncertainty in $< N_{HI}/N_d >$ may be larger as potentially large systematic effects are introduced by uncertainties in dust particle properties (Draine and Anderson, 1985; Hildebrand, 1983). The effect is not easy to quantify but especially the absolute value of the mass absorption coefficient κ_ν is uncertain. According to Hildebrand (1983) this results in uncertainties which might well be a factor of 2.

The simplest explanation for the difference of the observed gas–to–dust ratio with classical values, is to allow for a spatial variation of the gas–to–dust ratio in the Galaxy. For example there are variations in this ratio for different galaxies (see *e.g.* Koornneef, 1984) and local variations in the Galaxy might also be present. In M31, Walterbos and Schwering (1987) have found a decreasing dust–to–gas ratio ($I_{cool\ dust}/N_{HI}$) for increasing radius (from 0 to 15 kpc) and a similar effect is suggested in our Galaxy by Burton and Deul (1987). Possible variations in the dust–to–gas ratio are indicated in Fig. 5, which shows maps of the ratios $I_{100\mu m}/N_{HI}$ and N_d/N_{HI} over the Galactic foreground. From Fig. 5.1 it is clear that there still is a correlation between $I_{100\mu m}/N_{HI}$ and $I_{100\mu m}$ (Fig. 1.4); in Fig. 5.2 we see that the correlation between N_d/N_{HI} and $I_{100\mu m}$ is less than this.

The general trend of higher dust–to–gas ratios near the Galactic plane may reflect a latitude dependence of this ratio. Dust, HI and CO all have higher densities near the plane and the observed gas–to–dust ratios indicate a possible relation of it with these forms of gases. Possible evolution effects, causing a higher gas–to–dust ratio at high latitudes, are unexpected; at these latitudes dust and gas are expected to be mixed in a similar way as near the Galactic plane (Mihalas and Binney, 1981; Burton and Deul, 1987).

Figure 4. *Foreground dust property maps derived from the infrared maps with a resolution of 48′, and their pixel–to–pixel relation with HI. See page 127.*

Fig. 4.1. Dust temperature map derived from the 60 and 100 μm maps assuming an emissivity with a $\lambda^{-1.5}$ wavelength dependence. An intensity cut–off has been applied at 0.2 MJy/sr. Grey scales enhance the low temperatures and range from 10 – 70 K, while contours are at 20, 30, 40, 50, 60, 70 K.

Fig. 4.2. Linear pixel–to–pixel scatter diagram of T_d (K) versus N_{HI} (10^{20} H–atoms cm^{-2}; each point represents the average of 16 pixels, i.e. 1° x 1°).

Fig. 4.3. Dust column density map derived from the 100 μm map and the dust temperature map of Fig. 4.1. Grey scales enhance the low dust columns and range from 0.0 – 0.2 while contours are at 0.001, 0.005, 0.01, 0.05, 0.1 x 10^{20} H–atoms cm^{-2}.

Fig. 4.4. Linear pixel–to–pixel scatter diagram of N_d versus N_{HI} (both in 10^{20} H–atoms cm^{-2}; each point represents the average of 16 pixels, i.e. 1° x 1°). The solid line corresponds to the derived relation of Table 2. The errorbars are drawn dashed.

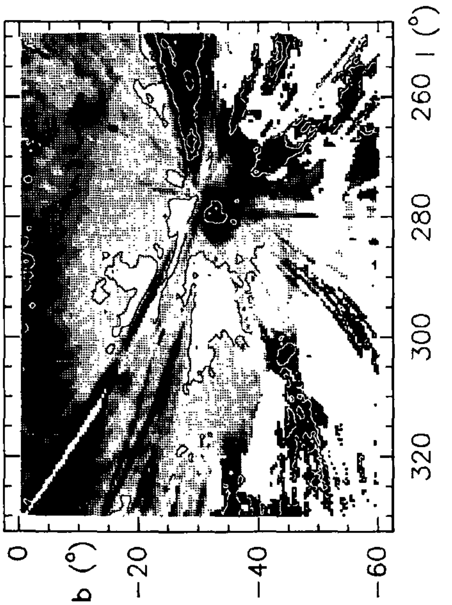

Fig. 4.1. Dust temperature map

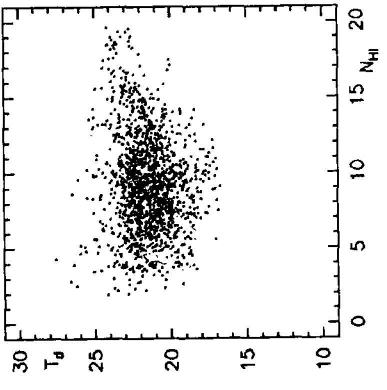

Fig. 4.2. Pixel-to-pixel scatterplot

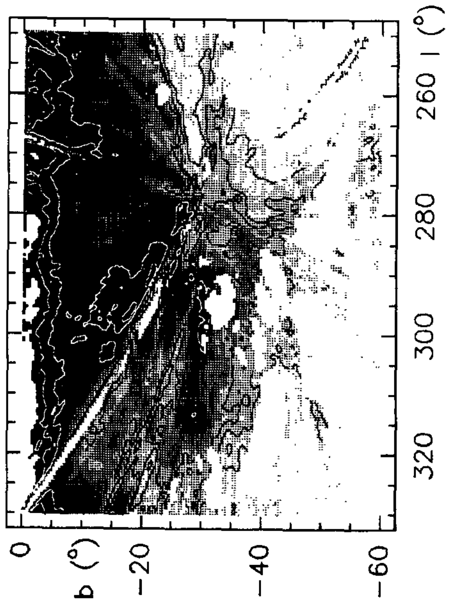

Fig. 4.3. Dust column density map

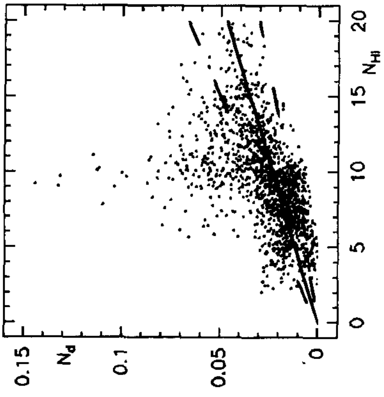

Fig. 4.4. Pixel-to-pixel scatterplot

We might have underestimated the HI column densities in two ways: HI optical depths of unity or not all HI in the lines–of–sight is observed. The optical depths of HI are not exactly known. If it is optically thick, its column density is underestimated and this can account for the observed increase of $I_{100\mu m}/N_{HI}$, close to the plane of the Galaxy ($| b |< 5°$). As variations occur even at high absolute latitudes optical depth effects cannot be important for the observed variations in the gas–to–dust ratio. The HI in the lines–of–sight might be underestimated by 15 %, roughly constant over the foreground. However, to correct the high gas–to–dust ratio an overestimate of the atomic hydrogen content is needed. It does therefore not seem possible to find an explanation for the high gas–to–dust ratio from systematic errors in the neutral hydrogen column densities.

The last possibility is an underestimate of the dust column densities. Draine and Lee (1984) have shown that for certain temperature ranges $< Q(a,T_d) > /a$ may depend on the dust temperature ($\propto T_d^2$ for $T_d < 50$ K; the exact relation depends on the type of grains); then $\kappa_\nu \equiv \frac{4}{3a\rho_d} < Q_\nu(a,T_d) >$ also depends on T_d. The derived line–of–sight temperatures are not influenced by this variation of κ_ν, but the dust column densities are.

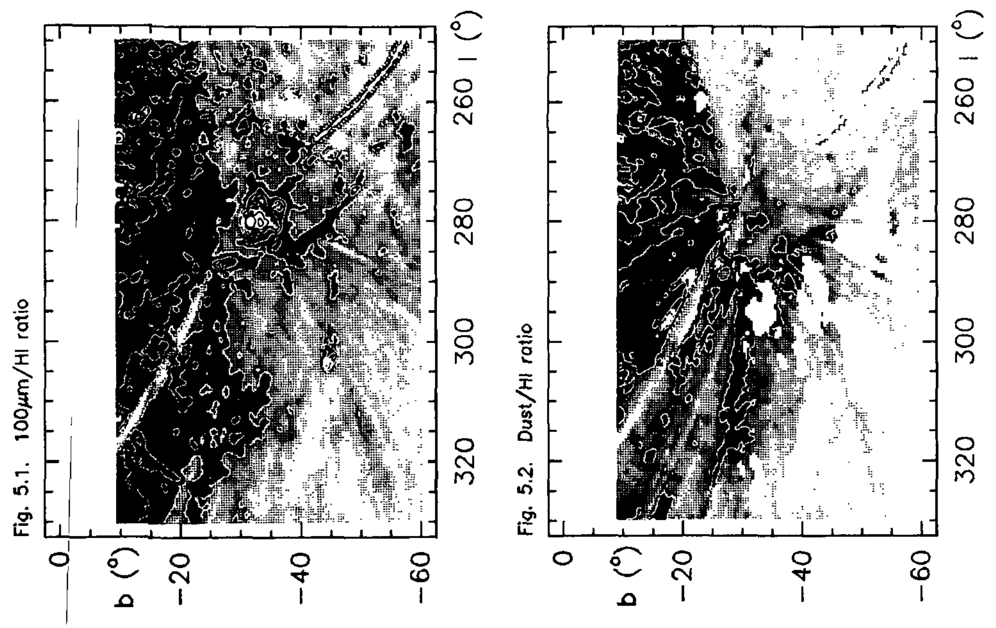

Figure 5. *Distribution of the ratio of infrared and dust with HI.*
Fig. 5.1. $I_{100\mu m}/N_{HI}$ *with grey scales enhancing the low ratios between 0 – 3, while contours are at 0.5, 1, 2, 5, 10 (MJy sr*$^{-1}$*) / (10*^{20} *H-atoms cm*$^{-2}$*).*
Fig. 5.2. N_d/N_{HI} *with grey scales enhancing the low ratios between 0 – 0.005, while contours are at 0.0025, 0.0075, 0.02.*

The effect of applying a correction for this effect is that dust masses of warm areas would decrease compared to masses in cool areas; and hence the dust–to–gas ratio, which is anti–correlated with T_d (see below), would show stronger gradients than without correction. By changing the absolute value of κ_ν we are able to explain the difference; an average value of 14 cm^2 g^{-1} (2.8 times lower than used) would be needed to obtain the classical gas–to–dust ratio from these observations.

The variations cannot be explained by assuming large amounts of cold dust (with $T_d = 15$ K, see Cox *et al.*, 1986); we need 2.8 times the amount of observed dust mass in order to obtain $< N_{HI}/N_d >= 150$. This dust radiates six times less in the infrared than 21 K dust and is therefore undetected by IRAS. There is only little CO detected at these high latitudes and therefore it is unlikely to expect large amounts of H_2 or associated dust. Note that the Galactic scale height of H_2 is less than that of HI (Burton and Deul, 1987). The distribution of the gas–to–dust ratio is opposite to what we expect when missing cold dust is needed to have a constant gas–to–dust ratio over the Galaxy (Fig. 5.2); to fix the gas–to–dust ratio we would need a H_2 distribution which is anti–correlated with HI. This is not expected, and is not observed in CO. Hence large amounts of dust associated with H_2 cannot be of importance for the variation in the gas–to–dust ratio found in this chapter.

The line–of–sight dust temperature can be overestimated if there is a contribution of very small grains to the 60 μm intensity (the contribution of these grains to the 100 μm intensity is negligible). To estimate the effect we now keep the 60 and 100 μm intensities fixed and define $< N_{HI}/N_d > \equiv 150$. The average dust temperature has to be dropped from 21 to 18 K, and we need 44 % of the original $I_{60\mu m}$ to come from these very small grains; this is a high percentage. A theoretical spectrum for the very small grains is derived from Draine and Anderson (1985). We took the difference of the spectra for $a_{min} = 3$ Å (modified grain size distribution) and the MRN–distribution for $a_{min} = 30$ Å; the Solar Neighbourhood radiation field was assumed in these calculations. The calculated relative very small grains spectrum is 1, 3, 4.5, 0 at 12, 25, 60 and 100 μm. The average observed spectrum for cool dust (with $T_d < 30$ K) is 1, 1, 3.6, 20 at 12, 25, 60 and 100 μm. We have fitted the 25 μm point and 42 % of the 60 μm emission might be coming from these very small grains. Hence just that needed for the difference in gas–to–dust ratio with classical observations. This effect can play a role only at low dust temperatures. At high T_d the warm dust component is dominating the 60 μm emission.

Due to the presence of multiple or continuous dust temperature components in the line–of–sight the dust temperature in each line–of–sight might also be overestimated. From Chapter VI we find that about 30 % in dust mass can be gained by doing a temperature decomposition in each line–of–sight.

In general the ratio N_d/N_{HI} decreases with increasing T_d. There is a steep rise near 22 K with a flat part of 0.0025 above 25 K; there is no clear minimum. This is an indication that for high line–of–sight dust temperatures the dust column density is underestimated. For low temperatures the dust–to–gas ratio rises to values larger than the classical Galactic one. Because we expect the small grain contribution to dominate at these lower temperatures this cannot give the explanation for the observed low dust–to–gas ratio; we expect the temperature overestimation to be the dominating factor resulting in an underestimated N_d.

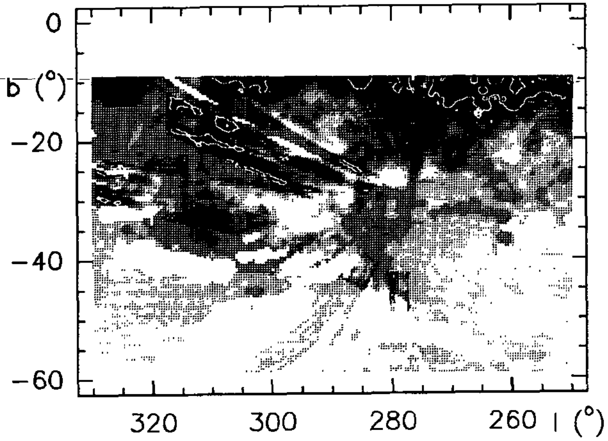

Fig. 6.1. Galactic foreground 60μm map

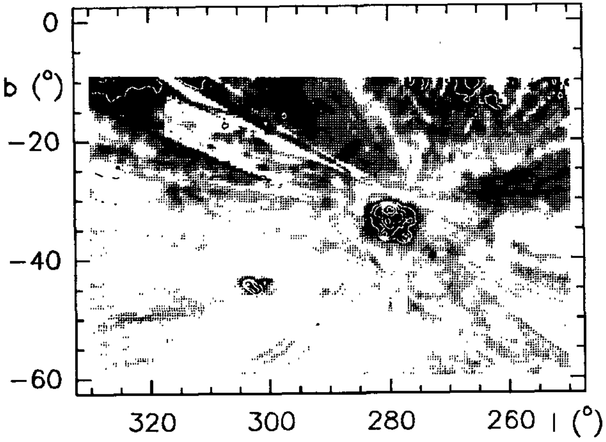

Fig. 6.2. Magellanic Clouds 60μm map

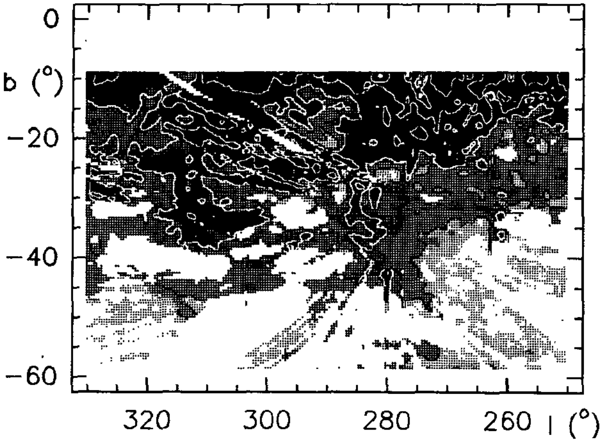

Fig. 6.4. Galactic foreground 100μm map

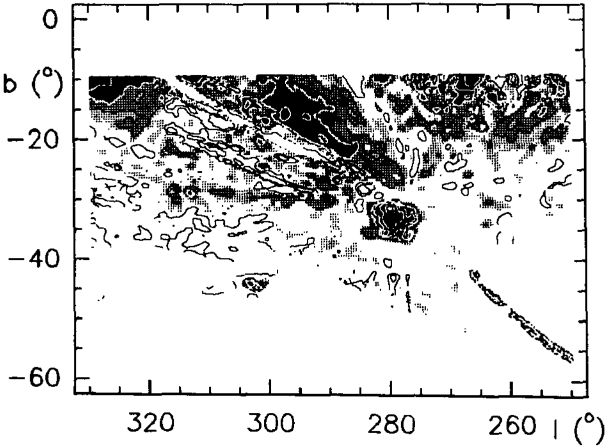

Fig. 6.5. Magellanic Clouds 100μm map

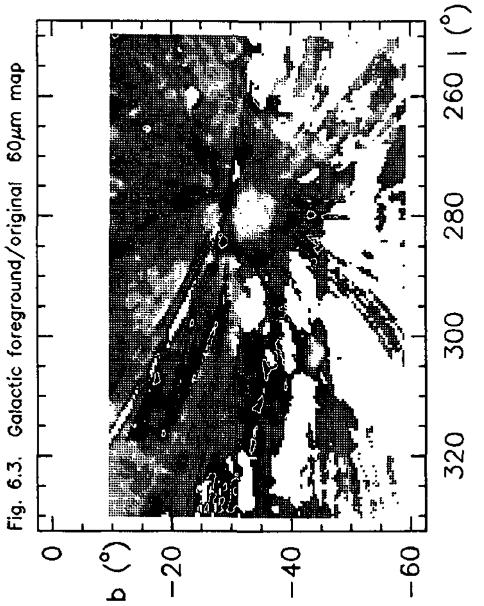

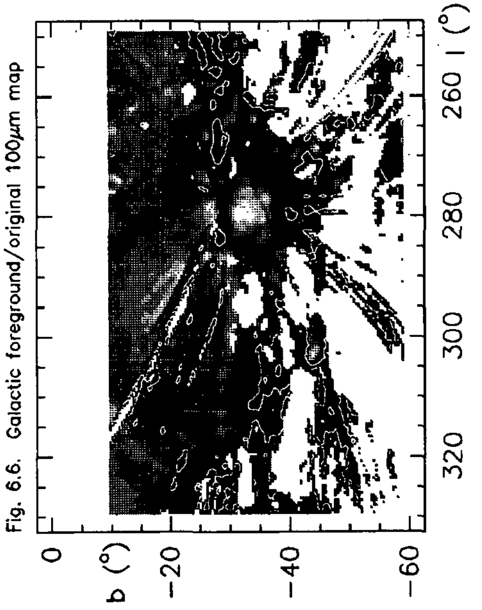

Figure 6. *Infrared maps of the Galactic foreground, Magellanic Clouds with the Galactic foreground emission subtracted, and the relative foreground contribution compared to the (total) observed infrared map of Fig. 1. See pages 130 – 131.*

Fig. 6.1. Galactic foreground 60 μm map. Contours and grey scales are as in Fig. 1.3.

Fig. 6.2. Magellanic Clouds 60 μm map. Contours and grey scales are as in Fig. 1.3; extra contours are at –5, –2 MJy/sr.

Fig. 6.3. Relative Galactic foreground 60 μm map. Grey scales are as in Fig. 1.3; extra contour levels are at 2, 5, 10.

Fig. 6.4. Galactic foreground 100 μm map. Contours and grey scales are as in Fig. 1.4.

Fig. 6.5. Magellanic Clouds 100 μm map. Contours and grey scales are as in Fig. 1.4; extra contours are at –5, –2 MJy/sr.

Fig. 6.6. Relative Galactic foreground 100 μm map. Grey scales are as in Fig. 1.3; extra contours are at 2, 5, 10.

Table 3. *Average foreground towards the Magellanic Clouds.*

Quantity (Unit)	LMC foreground	SMC foreground	Remarks
Literature values [a]:			
$A_V\ /E_{B-V}$	3.1		Savage and Mathis (1979).
$A_B\ /E_{B-V}$	4.1		
N_{HI}/E_{B-V} (H-atoms/cm^2 mag)	4.8 x 10^{21}		"
N_{HI+H_2}/E_{B-V} (")	5.8 x 10^{21}		" ; (Equation 6).
E_{B-V} (mag)	0.07 ± 0.04	0.04 ± 0.03	Koornneef (1984).
E_{B-V} (mag)	0.034 ± 0.004	0.019 ± 0.004	McNamara and Feltz (1980).
Atomic hydrogen content [b]:			
N_{HI} (10^{20} H-atoms/cm^2)	5.6 ± 2.0	4.3 ± 1.3	Cleary *et al.* (1979).
$< N_{HI}/N_{dust} >$ (mass)	420^{+250}_{-120}		Section 4.
Average infrared intensity [b]:			
$I_{12\mu m}$ (MJy/sr)	0.3 ± 0.1	0.6 ± 0.1	IR maps of Section 2.1.
$I_{25\mu m}$ (MJy/sr)	0.6 ± 0.1	0.3 ± 0.1	"
$I_{60\mu m}$ (MJy/sr)	0.5 ± 0.1	0.3 ± 0.1	IR maps Sec. 2.1 and 4.
$I_{100\mu m}$ (MJy/sr)	3.5 ± 0.6	1.2 ± 0.3	"
Dust properties [c]:			
T_d (K)	19 – 23	20 – 24	See Section 4.
N_d (10^{20} H-atoms/cm^2)	0.006 ± 0.003	0.003 ± 0.002	See Section 4.
N_{HI}/N_d (mass)	900 ± 600	1400 ± 1000	Local mass ratio; Sec. 4.
Integrated cirrus flux density [d]:			
$f_{12\mu m}$ (Jy)	3500 ± 600	300 ± 60	Extrapolated 100 μm.
$f_{25\mu m}$ (Jy)	3000 ± 500	260 ± 50	"; Section 4.
$f_{60\mu m}$ (Jy)	10000 ± 2000	1400 ± 400	
$f_{100\mu m}$ (Jy)	68000 ± 12000	5800 ± 1500	
Extinction [e]:			
E_{B-V} (mag)	0.07 – 0.17	0.07 – 0.09	See Section 6.
A_V (mag)	0.22 – 0.53	0.22 – 0.28	"
A_B (mag)	0.29 – 0.70	0.29 – 0.37	"
$E_{B-V}/I_{60\mu m}$ (mag /MJy sr)	0.20 ± 0.08	0.27 ± 0.09	"
$E_{B-V}/I_{100\mu m}$ (")	0.029 ± 0.015	0.06 ± 0.03	"
$A_V\ /I_{100\mu m}$ (")	0.09 ± 0.04	0.19 ± 0.06	"
$A_B\ /I_{100\mu m}$ (")	0.12 ± 0.05	0.25 ± 0.09	"

Notes to Table 3:

a) *The average internal colour excess for the Magellanic Clouds are* $E_{B-V} = 0.07 \pm 0.04$ *mag for the LMC and* 0.03 ± 0.03 *mag for the SMC (Koornneef, 1984).*

b) *The errors indicate the range of variation of the infrared intensity and the atomic hydrogen column density. The infrared foreground intensities, given here, do not contain a contribution* *from the Zodiacal emission. They were obtained by examining the areas surrounding the Clouds (figures of Section 2.1) and by HI–predicted foreground emission (Section 4). For the SMC $I_{12\mu m}$ is relatively high compared to $I_{25\mu m}$ due to residual scan–striping.*

c) *T_d has been calculated by fitting $\nu^{1.5}B_\nu(T_d)$ to the 60 and 100 μm data. The temperatures of the LMC line–of–sight dust ranges from 23 – 41 K and in the SMC from 24 – 35 K.*

d) *The average infrared foreground flux density was found from summing pixel areas of the LMC and SMC, and by fitting the foreground and also by using the predicted foreground; from $f_\nu = I_\nu\ \Omega$, where Ω is the solid angle of the Clouds (8° x 8° for the LMC and 4° x 4° for the SMC).*

The M31 cool dust spectrum was used to extrapolate the 100 μm point to the 12 and 25 μm points. The ratio $I_{60\mu m}/I_{100\mu m}$ of 0.18 – 0.19 suggests that this is a good value, however the correlation between infrared and HI at 12 and 25 μm wavelengths is very poor (the relative cool dust spectrum of M31, Walterbos and Schwering, 1987, is 0.051, 0.045, 0.15, 1.0 at 12, 25, 60 and 100 μm respectively). Note that the 12 and 25 μm foreground do not correspond well with this cool dust spectrum.

e) *Note that these relations are logarithmic relations as the magnitude is defined via the logarithmic scale.*

The variation in dust temperature in the Galactic foreground is not much (20 – 25 K) but is large enough to explain variations of about a factor of 2 in infrared intensity compared to the HI column density. Hence the use of a constant N_d/N_{HI} gives better results than the use of $I_{100\mu m}/N_{HI}$ as the variation for areas at $b = -30°$ compared to areas at $b = -10°$ is 1 – 2 for the first ratio and 2 – 3 for the latter ratio. It is important to note here that the absolute value of $< N_{HI}/N_d >$ and hence the difference with other literature values is *not* important for the calculation of the foreground infrared emission, predicted from the constant gas–to–dust ratio and neutral hydrogen column density with the derived dust temperatures; likewise it is not important for comparison with extragalactic gas–to–dust ratios calculated in the *same* way.

4.6. Predicted infrared foreground emission

We have constructed a map of the Galactic foreground infrared emission at 60 and 100 μm by converting the dust map (the atomic hydrogen map scaled by $< N_d/N_{HI} >$) with the Planck function B_ν at the derived line–of–sight dust temperatures T_d. The temperatures have been set equal to 21 K for the dust towards the Clouds and in the regions influenced by bad scans (see above). The value of 21 K gives the best connection with the area for which T_d could be derived. We have assumed a similar gas–to–dust ratio towards the Clouds as for the global Galactic foreground. Hence the predicted infrared intensity I_ν^{for} for the Galactic foreground becomes

$$I_\nu^{for} = (N_{HI}\ /\ < N_{HI}/N_d >)\ m_{HI}\ \kappa_\nu\ B_\nu(T_d). \qquad (5)$$

These foreground infrared maps are presented in Fig. 6.1 and 6.4 in a similar representation as Fig. 1. We see structure in the foreground emission on the same scales as the resolution (48′). Using a prediction based on this equation results in a consistent foreground at 60 and 100 μm for a constant gas–to–dust ratio in the Galaxy. The HI–predicted foreground has been compared with the original infrared maps at 60 and 100 μm. On average a linear relation, with slope unity, is seen in both bands. However, there is a considerable amount of scatter in the diagrams and some extreme data points are far off. Another way to obtain foreground emission is to use the relation between $I_{60\mu m}$ and $I_{100\mu m}$ with N_{HI} directly. In the latter case a variable gas–to–dust ratio has to be allowed. Local differences compared to the globally derived relations, make that the results of both methods are not very different and contain equal uncertainties.

We have subtracted the HI–predicted foreground infrared emission from the observed total infrared maps; these maps are shown in Fig. 6.2 and 6.5. Fig. 6.3 and 6.6 give the ratio of the predicted infrared foreground emission over the total observed infrared radiation at 60 and 100 μm. From Fig. 6.2 we see that the subtraction works fine at 60 μm, but it shows a foreground underestimation of 0.1 MJy/sr in the area towards the LMC (especially at $l = 275°$, $b = -40°$). This value is four times lower than the error estimate due to the AO–foreground adjustment on the LMC in Chapter III. At 100 μm the foreground surrounding the LMC is overestimated by roughly 1 MJy/sr (similar to Chapter III). The errors in the AO–foreground of the SMC (Chapter II) are much smaller than these values. The SMC DPM–field is much smaller and the SMC–foreground is not very complicated, therefore the infrared foreground can be handled better locally (Chapter II) instead of globally (as in this chapter). Note the differences of Fig. 6 with the original infrared maps of Fig. 1. For the 12 and 25 μm bands the lack of correlation of the intensity with the neutral hydrogen column density makes this foreground prediction unreliable. From Fig. 1 we see that the foregrounds in these bands are much weaker and less complex than in the 60 and 100 μm bands.

We have compared the application of the HI–predicted foreground removal with fitting the infrared foreground by a (2–dimensional) plane (see Chapters II and III). This results in small scale differences. The fit shows more foreground in the upper–left corner of Fig. 6 in both infrared bands. At 60 μm the planar fit underestimates the foreground in the LMC–South (in declination) and overestimates the foreground in the LMC–North. At 100 μm the foreground towards the whole LMC, except the Bar and the Greater 30 Doradus Region is underestimated; in these two regions the fit overestimates the HI–predicted foreground emission. On average the 60 μm fit is quite correct and predicts the same foreground (see Table 3). The fitted 100 μm foreground is (on average) 20 % lower than the HI–predicted foreground.

For the SMC, a comparison with the AO–maps shows that the foreground removal based on N_{HI}, is not an improvement. On the other hand, the HI–predicted infrared foreground towards the LMC is very realistic and is a good estimate for the true Galactic foreground in that region. It gives a better result in foreground subtraction than by removing a fitted plane. The foreground data is summarized in Table 3. The total foreground flux density at 60 μm is 10 – 20 % of the integrated Clouds flux density; at 100 μm it is even 30 – 40 %. The extrapolated values for 12 and 25 μm are also relatively high (30 – 70 %) but might be overestimated due to the fact that the infrared spectrum is not as cool as expected (note that these percentages do not include the Zodiacal emission). The higher percentages are for the SMC, which is fourteen times weaker at 60 and 100 μm than the LMC. The SMC foreground intensities reach 0.3 – 0.6 times the intensities of the LMC foreground.

5. The relation between Galactic infrared and atomic hydrogen emission

5.1. Comparison of Galactic infrared–atomic hydrogen relations

From the available foreground infrared and atomic hydrogen data we have derived the large scale ratio $I_{100\mu m}/N_{HI}$ in Section 4. Global values for this ratio have been derived from Table 3. Although there are reasons (see Section 4) that make $I_{100\mu m}/N_{HI}$ not the ideal ratio to study, several authors have done so and we therefore compare the Magellanic Cloud foreground ratios with the ratios derived by other authors. In Table 4 we have summarized the literature values together with our own ratios.

Table 4. *Galactic sudies of infrared–to–HI ratios.*

Region a)	$I_{100\mu m}/N_{HI}$ b)	$I_{60\mu m}/I_{100\mu m}$ b)	N_{HI} range b)	Authors
Global studies:				
ESO 025/487	0.64 ± 0.1	0.11 – 0.18	10	de Vries (1986) c).
$l = 125°, \mid b \mid < 10°$	0.64 ± 0.11	0.21	15 – 80	Terebey and Fich (1986).
$l = 225°, \mid b \mid < 10°$	0.42 ± 0.08	0.21	10 – 60	"
Forgeround filaments	0.74	0.10 – 0.20	2 – 7	McGee *et al.* (1986).
Cosecant law	0.85 ± 0.05	0.21	2 – 15	Boulanger and Perault (1988).
LMC foreground	0.63 ± 0.13	0.15	5.6	This chapter.
SMC foreground	0.28 ± 0.06	0.24	4.3	This chapter.
Global average	0.6 ± 0.2	0.10 – 0.22	2 – 80	
Discrete objects:				
$l = 90°, b = +67°$	1.4 ± 0.3	0.32	3.3	Boulanger *et al.* (1985).
Six HI clouds	1.0 – 2.2	0.19 – 0.25	2 – 20	Deul (1988).
Seven regions	0.5 – 2.4	0.18 – 0.30	2 – 15	Boulanger and Perault (1988).
Objects average	1.5 ± 0.5	0.18 – 0.32	2 – 20	

Notes to Table 4:

a) *For a better description of the studied regions we refer to the separate papers.*

b) $I_{100\mu m}/N_{HI}$ *is given in units of (MJy/sr)/(10^{20} H–atoms cm^{-2}),* $I_{60\mu m}/I_{100\mu m}$ *is the ratio of MJy/sr, and the HI range is given in 10^{20} H–atoms cm^{-2}.*

c) *The values of de Vries have been converted to a similar quantity from his relation* $A_B/I_{100\mu m} = (0.11 \pm 0.01)$ *mag / (MJy/sr) using* E_{B-V}/N_H *of Savage and Mathis (1979).*

Two different types of studies need to be separated. First of all there are global studies, using integrated HI and infrared over the full line–of–sight (de Vries, 1986; Terebey and Fich, 1986; McGee *et al.*, 1986; Boulanger and Perault, 1988; this chapter). Second, there are studies of discrete objects, in which case the relative contribution of the object is found by removing the foreground emission (Boulanger *et al.*, 1985; Deul, 1988; Boulanger and Perault, 1988). Table 4 shows good agreement between the listed global values. Note that the SMC foreground value is two times lower than the global average of 0.6 ± 0.2. The ratios derived for local areas are on average 2.5 times higher. Due to the correspondence of the global infrared–to–HI ratios we find these to be quite accurate. The variation in the ratios for the local estimates is much larger than for the global estimate, due to the larger spread in 60 – 100 μm colour temperatures.

Boulanger and Perault (1988) have shown that the longitude integrated data follows, on large scales, a cosecant–law with Galactic latitude. Using Parkes 64–m telescope HI data McGee *et al.* (1986) found the infrared–to–HI relation to be quite loose on scales of 15$'$; their average value of 0.74 corresponds well with our global average. Large scale variations are indicated in Fig. 5.1 where we find ratios of 0.2 – 2.0. These differences make it clear that extrapolations of $I_{100\mu m}/N_{HI}$ to other areas of the sky, as done *e.g.* by Boulanger *et al.* (1985), in general are wrong. If we assume a constant dust–to–gas ratio, $I_{100\mu m}/N_{HI}$ will be constant only if the dust temperature is constant. Hence from Fig. 4.1 we see that this is only the case on small scales (< 20°). Over the whole field a wide range of temperatures exist (17 – 28 K) and, due to the strong dependence of infrared intensity on dust temperature the ratio $I_{100\mu m}/N_{HI}$ will vary by about a factor of 4. Extrapolations can be done better with temperature corrected infrared data ("dust column densities").

5.2. Variations in the relation between infrared intensity and atomic hydrogen column density

We have found a large scale relation between 100 μm infrared intensity and HI column density that follows a power–law for atomic hydrogen column densities of (3 – 20) x 10^{20} H–atoms cm^{-2}. Terebey and Fich (1986) have found a linear relation for two outer Galaxy regions close to the Galactic plane. Burton and Deul (1987) found that $I_{100\mu m}$ is not related linearly with N_{HI}. They have used a large area containing low latitudes, extending 2.5 decades in N_{HI} and four decades in $I_{100\mu m}$. Similar correlations occur at higher latitudes. The flattening of their curve is explained by them by a non–negligible optical depth of HI. This effect is larger to the inner Galaxy ($270° < l < 90°$) and near the Galactic plane ($| b | < 5°$). The data of Terebey and Fich, near $b = 0°$, might also be influenced by non–negligible optical depths. The direction of the Magellanic Clouds is towards the inner Galaxy, but the longitude ($l \approx 300°$) and latitude ($b \approx -35°$) of the Clouds do not give us the impression that the optical depth plays an important role for these areas. Recently, de Geus (1988) has found a similar relation as us in the Ophiuchus region $I_{100\mu m} \propto N_{HI}^2$; however he also found $I_{60\mu m} \propto N_{HI}$.

Besides optical depth effects there are various posibilities for the non–linearity: spatial variations in the gas–to–dust ratio and dust temperature effects. Terebey and Fich (1986) discussed that some properties might vary with latitude b. Stochastical variations in dust–to–gas ratio, dust temperature, dust properties, molecular contents are to be expected in different regions. Systematic variations with latitude are also expected as the stellar density varies, resulting *e.g.* in variations in the radiation field. The molecular emission of the Galaxy is more concentrated towards the plane (Dame and Thaddeus, 1987; Burton and Deul, 1987) than the HI emission. Variations on large scale make it unlikely that the non-linear relation is due to the fact that N_{H_2} is correlated with N_{HI}. A primary possibility is a temperature effect, as the ratio $I_{60\mu m}/I_{100\mu m}$ varies somewhat over the whole range of infrared intensities. Terebey and Fich also mention the combination of different effects that "might conspire to give a linear relation".

Fig. 5.1 shows that variations occur in the infrared–to–HI ratios. At $b = -10°$ we see that $I_{100\mu m}/N_{HI}$ can vary from 0.7 - 1.5 in longitude only. This ratio is therefore not equal in all areas of the sky. Also note the variation of the dust temperature (hence $I_{60\mu m}/I_{100\mu m}$), especially close to the Galactic plane. Infrared cirrus areas in our Galaxy and in M31 have typical ratios of 0.2 (see Low *et al.*, 1984; Terebey and Fich, 1986; Walterbos and Schwering, 1987). No clear relation of $I_{100\mu m}/N_{HI}$ with temperature can be found from Table 4, nor in the paper by Boulanger and Perault, but the relation plays an important role for $I_{100\mu m}$ and therefore for $I_{100\mu m}/N_{HI}$.

The non-linearity of $I_{60\mu m}$ and $I_{100\mu m}$ can be accounted for completely by the differences in temperature. The dust temperature varies from 20 to 25 K in the range of HI values (3 - 20) x 10^{20} H–atoms cm^{-2}. At these infrared wavelengths this gives just the intensity increase that we observe. At lower HI column densities (hence lower b) the dust temperature does not vary. This is because there is no dust with temperatures below 20 K at these latitudes.

Because the infrared 60 and 100 μm intensities and the HI column densities are related each in a different non–linear way, the dust temperature should follow the HI. Evidence that temperature plays a role comes from the relation between N_{HI} and visual extinction. For higher HI column densities and associated dust, τ_{UV} increases, leading to relatively more photon trapping by dust and hence higher dust temperatures. If higher N_{HI} correspond to higher T_d the non–linearity is larger at 60 than at 100 μm. The different non–linear relations between infrared intensity and the HI column density are then the result of temperature effects present on these large scales. This is not very clear from comparing Fig. 4.1 with Fig. 2.1, nor is it easy to quantify from Fig. 4.2. What is needed to dissolve te exact relation between $I_{100\mu m}$ and N_{HI} is a systematic quantitative approach.

Figure 7. *Galactic foreground colour excess maps. See pages 138 - 139.*

Fig. 7.1. Galactic foreground E_{B-V}*. Darker grey scales indicate a higher* E_{B-V}*, grey scales are chosen to enhance low values. Contours are at 0.02, 0.04, 0.06, 0.08, 0.10, 0.14, 0.18, 0.22, 0.26, 0.30 mag.*

Fig. 7.2. Galactic foreground E_{B-V} *grey scales map overlayed on the infrared 100* μ*m contour map on the location of the LMC. Grey scale steps are at 0.04, 0.06, 0.08, 0.10, 0.12, 0.14, 0.16, 0.18, 0.20 mag.*

Fig. 7.3. Galactic foreground E_{B-V} *grey scales map overlayed on the infrared 100* μ*m contour map on the location of the SMC. Grey scale steps are at 0.05, 0.06, 0.07, 0.08, 0.09, 0.10, 0.11, 0.12 mag. Note that the blob at* $b = -45°$ *is due to noise blow–up.*

Fig. 7.1. Galactic foreground colour excess map

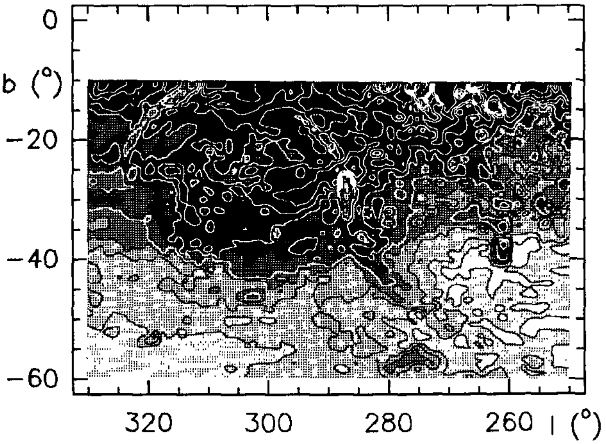

Fig. 7.2. LMC–foreground colour excess greyscale map
and 100μm contour map

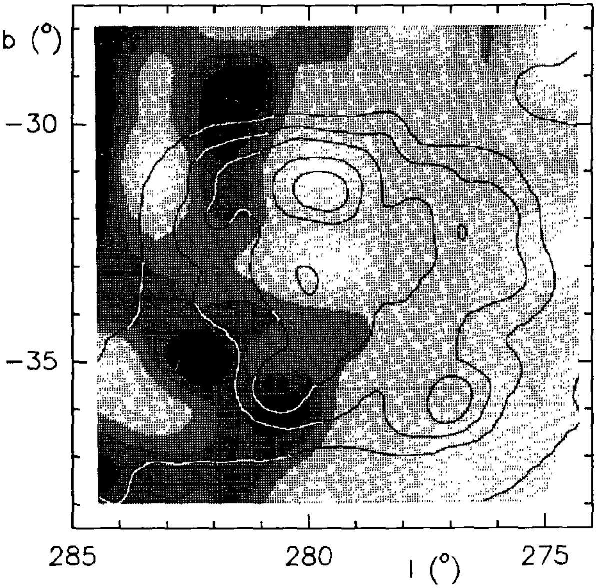

Fig. 7.3. SMC–foreground colour excess greyscale map and 100μm contour map

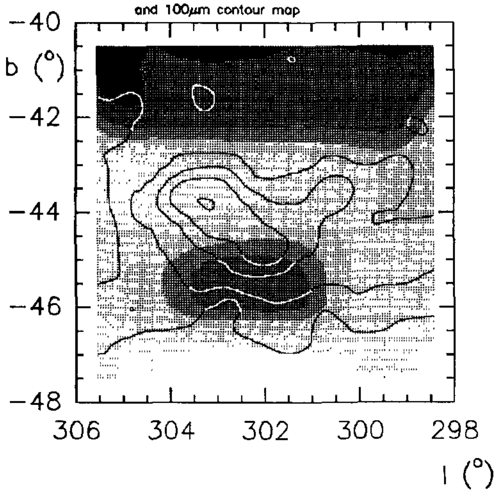

6. The Galactic foreground extinction

We have calculated the colour excess in the Galactic foreground towards the Magellanic Clouds from the total hydrogen gas content $N_H = N_{HI} + 2N_{H_2} \approx N_{HI}$ (assuming only HI to be present), following the relation of dust and gas as given by Bohlin *et al.* (1978) and Savage and Mathis (1979; and references therein)

$$N_H/E_{B-V} \;=\; 5.8 \text{ x } 10^{21} \text{ H} - \text{atoms cm}^{-2} \text{ mag}^{-1} \tag{6}$$

which was derived for the Solar Neighbourhood. Hence for the gas–to–dust mass–ratio derived in Section 4.5, the relation between E_{B-V} and M_d becomes

$$M_d/E_{B-V} \;=\; 2.3 \text{ x } 10^{-5} \text{ g cm}^{-2} \text{ mag}^{-1}. \tag{7}$$

Random errors in Equation 6 are estimated by Bohlin *et al.* (1978) at 6 %, while the unknown systematic errors in E_{B-V} probably dominate. Note the large scatter in Fig. 2 of Savage and Mathis, indicating large errors for individual points. The colour excess map was obtained from rewriting Equation 6 to E_{B-V} (mag) $=$ 0.017 N_{HI} (10^{20} H-atoms cm^{-2}). A_V and A_B can be deduced directly from the relations $A_V = 3.1\ E_{B-V}$ and $A_B = 4.1\ E_{B-V}$, A_V and A_B can be deduced directly. The so derived distribution of E_{B-V} is shown in Fig. 7, together with overlays of E_{B-V} with the 100 μm infrared radiation on the position of Magellanic Clouds. For the relatively smooth SMC foreground (neglecting the dense blob discussed in Section 2.2) we find values $E_{B-V} = 0.07 - 0.09$ mag, highest in the South (in declination; top in Fig. 7.3). The LMC foreground (on average $E_{B-V} = 0.10$ mag) shows significant variations, down to the resolution of 48'. E_{B-V} varies from 0.09 – 0.11 towards the North (in declination; right in Fig. 7.2), via smaller values of 0.07 – 0.09 towards Greater 30 Doradus Region and the LMC–Bar up to 0.13 – 0.17 mag towards the southern area. The average E_{B-V} approaches the higher literature values given in Section 1 (Azzopardi and Vigneau, 1977, for the SMC 0.044 ± 0.033 and Brunet, 1975 for the LMC 0.07 ± 0.01) and are somewhat higher but still within the errorbars of the values given by Koornneef (1984). The random errors are about 20 %, based on the uncertainties in the HI and the random error in Equation 6. A correction for the possible systematic error in the HI (15 % underestimate, see Section 2.2) will increase E_{B-V} by the same amount. In Section 7 the effects of a varying foreground are discussed for B and V data of the LMC.

The derivation of E_{B-V} from Galactic foreground stars (McNamara and Feltz, 1980) has the disadvantage that there are only a small number of these stars. They might not be far enough away to show all the Galactic foreground dust in the lines–of–sight towards the Clouds, in their spectra. The use of Magellanic Clouds stars (*e.g.* Isserstedt, 1975) gives rise to higher values of E_{B-V} and include all the foreground dust, but might be contaminated by Magellanic Cloud dust. The numbers that we obtain assume that the foreground dust is related well with atomic hydrogen and are unrelated to the Clouds and take into account all the foreground emission. On small scales a wide range of reddening values has been observed towards the LMC by Goudfrooij (priv. comm.).

Alternatively, we may take literature values of E_{B-V} to obtain the ratio N_H/E_{B-V}. We assume that the McNamara and Feltz (1980) value of E_{B-V} is correct and use it with the HI foreground data. Then we derive 16 x 10^{21} (H–atoms cm^{-2}/mag) for the LMC foreground and 23 x 10^{21} for the SMC foreground, 3 – 4 times higher than the Solar Neighbourhood value of Savage and Mathis (1979; see also Equation 6). For the dense cloud surrounding ρ Oph, Savage and Mathis (1979) have given a value of 15.4 x 10^{21} roughly equal to the LMC foreground value in this case. For the dust and gas in the LMC (Koornneef, 1984) N_{HI}/E_{B-V} equals 20 x 10^{21}. However the large area that we have studied does not have such dense concentrations and we should expect a value rather close to the typical Galactic ratio. From these numbers we conclude that it is not possible to find a reliable value for N_H/E_B from the known literature values for $E_{B-V} < 0.04$ mag and the HI data.

Due to the relation $A_\nu = 1.086\ \tau_\nu$ the colour excess E_{B-V} is proportional to N_d (Mihalas and Binney, 1981) and therefore to N_{HI}, as we assume a constant gas–to–dust ratio. A problem between the connection of the infrared dust emission and the dust absorption in the visual region (see Savage and Mathis, 1979) might be that the value of E_{B-V} is determined mainly by small dust grains ($a/\lambda < 10$) active as absorbers in B and V, while the larger dust grains do not contribute greatly to the colour excess; whereas the infrared emission (with $\lambda_{IR} \approx 100\ \lambda_B$) is mainly caused by these larger grains ($a/\lambda \approx 1$). If this is the case a larger scatter would be expected in the relation between N_{HI} and E_{B-V}. The good relation between these quantities shows that the grains are spatially related.

Infrared emission is emitted by dust, while dust also gives rise to extinction. To quantify the relation between infrared emission and E_{B-V}, we use Equations 3, 5 and 6 to derive the ratio $E_{B-V}/I_{100\mu m}$ (MJy/sr). This relation can be expressed in terms of the dust temperature T_d and the column density N_d, as

$$\begin{aligned} E_{B-V}/I_{100\mu m} &= (5.8 \text{ x } 10^{21}\ \alpha_{100\mu m}\ HI^{\beta_{100\mu m}})^{-1} \\ &= (5.8 \text{ x } 10^{21}\ (N_{HI}/ < N_{HI}/N_d >)\ m_{HI}\ \kappa_\nu\ B_\nu(T_d))^{-1}. \qquad (8) \end{aligned}$$

We find $E_{B-V}/I_{100\mu m} = 0.029 \pm 0.015$ (mag) / (MJy/sr) for the LMC foreground and 0.06 ± 0.03 for the SMC foreground. These values, together with A_V and A_B are given in Table 3. The errors are based on the possible variation in the foreground infrared and HI emission over the objects. The relation of $A_B/I_{100\mu m}$ for the LMC is very close to the relation derived by de Vries (1986). The SMC relation is clearly higher, which is the result of the relatively low infrared emission compared to HI.

7. Implications of the extinction by foreground dust on Magellanic Clouds studies

The Galactic foreground dust and infrared properties are used to study absorption influences on visual and ultraviolet data of the Magellanic Clouds. It has also been used to estimate the foreground infrared emission in the direction of the Magellanic Clouds (see Section 4). Comparisons between Galactic foreground and Cloud infrared and dust data will be dealt with in Chapter VI.

We have compared the LMC E_{B-V} data of Isserstedt (1975) and Isserstedt and Kohl (1984) with the foreground dust emission. The data of Isserstedt consist of LMC–stars with known colours that can be used to derive the colour excess. Isserstedt applied a constant foreground extinction correction of 0.07 mag. Our data show the LMC–Bar and the Greater 30 Doradus Region to be in relative weak HI foregrounds and therefore dust–free areas compared to the outer areas such as Shapley's Constellation III and the N 11 complex. The high values for E_{B-V} in 30 Doradus ($>$ 0.14 mag) must therefore be explained mainly by an internal LMC dust component and might be over–corrected for foreground dust by 0.03 mag. Note that we compare numbers in this section relative to the average foreground. The radiation from stars at the outer area, and especially in the southern part, of the LMC is more absorbed by Galactic foreground dust and should therefore still have a contribution of about 0.04 mag in E_{B-V} due to the varying foreground. There are a large number of stars visible in the outer area, with low colour excesses ($<$ 0.08 mag); a correction for the foreground would decrease E_{B-V} by a factor two. Obviously, we do not expect stars in the LMC to have $E_{B-V} <$ 0.04 mag. There are some reasons why they are observed. The number of stars used by Isserstedt and Kohl (1984) is lower in the South, where the foreground E_{B-V} is higher. The spectral type of the stars has to be known very accurately. This could result in systematic errors in E_{B-V}. A clear indication for this is the presence of stars with $E_{B-V} = -0.10$ in Isserstedt's (1985) diagram. According to Isserstedt, the large number of stars with reddening values less than 0.04 mag indicates that there are variations in the foreground on small spatial scales. Application of the varying foreground will result in an adjustment to the LMC dust–to–gas relation (E_{B-V}/N_H) of areas with non–average E_{B-V}; in the Greater 30 Doradus Region the ratio would become higher and in the South smaller.

Studies of the spatial distribution of the interstellar extinction curve of the LMC have been performed by Fitzpatrick (1985, 1986). From the data he obtains an "average" LMC extinction curve $A_{\lambda-V}/E_{B-V}$ which is more similar to the Galactic one (Savage and Mathis, 1979) than the 30 Doradus curve (Koornneef and Code, 1981). The latter curve, the "normal" LMC curve, has a weaker 2200 Å feature and rises steeper in the ultraviolet than the Galactic curve. Under the assumption that the foreground absorption and contribution to the colour excess do not vary, Fitzpatrick concludes that his new LMC curve is a better average than the 30 Doradus curve. This point has to be reconsidered due to the variation in the foreground. Depending on the assumed average extinction, the lower absorption towards the 30 Doradus region means that the foreground correction applied there is too high, while in the other areas the correction is too low. As a consequence, extinction curve differences between the 30 Doradus regions and other parts of the LMC are artificially enhanced, so that after a spatially dependent correction, the 30 Doradus and the LMC's "average" curve will in fact approach each other. As the lines–of–sight towards the reference stars have to be taken into account as well, this complicates the (small scales) interpretation of spatially varying absorption. We see that the directions towards a part of the LMC–Bar and the Greater 30 Doradus region are most suited to eliminate the influence of the Galactic foreground extinction.

The "normal" SMC extinction curve (Prévot *et al.*, 1984) is even more extreme. The 2200 Å feature is missing entirely and the ultraviolet rise is even steeper. Lequeux *et al.* (1984) have shown that three SMC stars, Sk 124, Sk 191 and especially Sk 143, have extinction curves which resemble the average Galactic one better. From our data we find no evidence for expecting a higher foreground contribution to any of these stars than to others with a "normal" SMC extinction curve.

8. Conclusions

The Galactic infrared and dust foreground towards the Magellanic Clouds has been discussed for the IRAS bands. The stellar foreground in the infrared is non–significant except at 12 μm, where it contributes 3 % of the total integrated flux density of the LMC and 10 % of the integrated flux density of the SMC.

The cirrus infrared foreground, which consists of large scale cool dust, is clearly non–planar and shows structure on all scales down to the resolution limit. A subtraction of the HI–predicted infrared foreground from maps of the LMC gives a better quantitative result than fitting a simple foreground plane. At 60 μm the cirrus foreground contains 10 – 20 % of the integrated flux densities of the Clouds over the same area. The percentage is 30 – 40 % for the 100 μm band. The higher percentages occur for the SMC which is fourteen times weaker than the LMC in the infrared. The foreground intensities towards the SMC are 0.3 – 0.6 times those for the LMC foreground.

The Galactic foreground infrared intensities $I_{60\mu m}$ and $I_{100\mu m}$ are well-correlated with N_{HI}, but the correlation is non-linear. At 60 and 100 μm the relation goes as a power-law with exponents of about 3.5 and 2.0 respectively. The global ratio $I_{100\mu m}/N_{HI}$ has an average value of 0.6 ± 0.2. In general the ratio is not constant and temperature effects are the main reason for the non-linearities.

We obtain a high average gas-to-dust ratio. The explanations for this high ratio are the uncertainties in the dust parameters and the underestimate of the dust column densities. This high gas-to-dust ratio does not influence the removal of the infrared foreground towards the Clouds.

We have showed that in the infrared, visual and ultraviolet wavelength regimes positionally dependent foreground extinction corrections have to be applied for the LMC. The E_{B-V} range of the foreground is 0.07 – 0.17 mag towards the LMC and 0.07 – 0.09 towards the SMC. These values are close to the highest values obtained from stellar photometry. Towards the LMC E_{B-V} probably varies on scales smaller than $48'$; especially towards 30 Doradus and the LMC-Bar where E_{B-V} is lower than average. The foreground is rather smooth towards the SMC. Observations of Isserstedt and Kohl (1984) and Fitzpatrick (1985, 1986) likewise contain supporting evidence for these variations in E_{B-V}.

References

van Albada, G.D., Baud, B., de Pagter, P.J., Pol, W., Renes, J.J., Wesselius, P.R.: 1985, ROG Internal Report

Azzopardi, M., Vigneau, J.: 1977, *Astron. Astrophys.* **56**, 15

Boulanger, F., Baud, B., van Albada, G.D.: 1985, *Astron. Astrophys.* **144**, L9

Boulanger, F., Perault, M.: 1988, *Astrophys. J.*, submitted

Bohlin, R.C., Savage, B.D., Drake, J.F.: 1978, *Astrophys. J.* **224**, 132

Brunet, J.P.: 1975, *Astron. Astrophys.* **43**, 345

Burton, W.B., Deul, E.R.: 1987, in *"The Galaxy"*, eds. G. Gilmore, R. Carswell, Reidel Dordrecht, 141

Cleary, M.N., Heiles, C., Haslam, C.G.T.: 1979, *Astron. Astrophys. Suppl.* **36**, 95

Colomb, F.R., Pöppel, W.G.L., Heiles, C.: 1980, *Astron. Astrophys. Suppl.* **40**, 47

Cox, P., Krügel, E., Mezger, P.G.: 1986, *Astron. Astrophys.* **155**, 380

Dame, T.M., Thaddeus, P.: 1987, *Astrophys. J.* **297**, 571

Deul, E.R.: 1988, Ph.D. Thesis, University of Leiden

Deul, E.R., Wolstencroft, R.D.: 1988, *Astron. Astrophys.* in press

Draine, B.T., Lee, H.M.: 1984, *Astrophys. J.* **285**, 89

Draine, B.T., Anderson, N.: 1985, *Astrophys. J.* **292**, 494

Elias, J.H., Frogel, J.F., Schwering, P.B.W.: 1986, *Astrophys. J.* **302**, 675

Fitzpatrick, E.L.: 1985, *Astrophys. J.* **299**, 219

Fitzpatrick, E.L.: 1986, *Astron. J.* **92**, 1068

de Geus, E.J.: 1988, Ph.D. Thesis, University of Leiden

Hildebrand, R.H.: 1983, *Quartly J. R. Astron. Soc.* **24**, 267

IRAS: 1985, IRAS Catalogs and Atlases Explanatory Supplement, eds. C.A. Beichmann, G. Neugebauer, H.J. Habing, P.E. Clegg, T.J. Chester, JPL D-1855

Israel, F.P., Schwering, P.B.W.: 1986, in *"Light on Dark Matter"*, ed. F.P. Israel, Reidel Dordrecht, 383

Isserstedt, J.: 1975, *Astron. Astrophys.* **41**, 175

Isserstedt, J., Kohl, W.: 1984, *Astron. Astrophys.* **139**, 115

Johnson, P.G., Meaburn, J., Osman, A.M.I.: 1982, *Mon. Not. R. Astron. Soc.* **198**, 985

Koornneef, J., Code, A.D.: 1981, *Astrophys. J.* **247**, 860

Koornneef, J.: 1984, in *"Structure and Evolution of the Magellanic Clouds"*, IAU Symp. 108, eds. S. van den Bergh, K.S. de Boer, Reidel Dordrecht, 333

Lequeux, J., Maurice, E., Prévot, L., Prévot–Burnichon, M.–L., Rocca–Volmerange, B.: 1984, in *"Structure and Evolution of the Magellanic Clouds"*, IAU Symp. 108, eds. S. van den Bergh, K.S. de Boer, Reidel Dordrecht, 405

Low, F.J., Beintema, D.A., Gautier, T.N., Gillett, F.C., Beichmann, C.A., Neugebauer, G., Young, E., Aumann, H.H., Boggess, N., Emerson, J.P., Habing, H.J., Hauser, M.G., Houck, J.R., Rowan–Robinson, M., Soifer, B.T., Walker, R.G., Wesselius, P.R.: 1984, *Astrophys. J. (Letters)* **278**, L19

May, J., Murphy, D.C., Thaddeus, P.: 1988, *Astron. Astrophys. Suppl.* submitted

McGee, R.X., Newton, L.M.: 1981, *Proc. Astron. Soc. Aust.* **4**, 189

McGee, R.X., Haynes, R.F., Grognard, R.J.–M., Malin, D.: 1986, *Mon. Not. R. Astron. Soc.* **221**, 543

McNamara, D.H., Feltz, K.A.: 1980, *Publ. Astron. Soc. Pac.* **92**, 587

Mihalas, D., Binney, J.: 1981, *"Galactic Astronomy"*, Freeman and Co., San Francisco, p182, p204

Osterbrock, D.E.: 1973, *"Astrophysiscs of Gaseous Nebulae"*, Freeman and Co., San Francisco, p181

Prévot, M.L., Lequeux, J., Maurice, E., Prévot, L., Rocca–Volmerange, B.: 1984, *Astron. Astrophys.* **132**, 389

Puget, J.L., Léger, A., Boulanger, F.: 1985, *Astron. Astrophys.* **142**, L19

Rohlfs, K., Kreitschmann, J., Siegman, B.C. and Feitzinger, J.V.: 1984, *Astron. Astrophys.* **137**, 343

Savage, B.D., Mathis, J.S.: 1979, *Ann. Rev. Astron. Astrophys.* **17**, 73

Schwering, P.B.W., Israel, F.P.: 1988, *Astron. Astrophys.* in press. (Chapter II)

Schwering, P.B.W.: 1988, *Astron. Astrophys.* submitted (Chapter III)

Strong, A.W., Riley, P.A., Osborne, J.L., Murray, J.D.: 1980, *Mon. Not. R. Astron. Soc.* **201**, 495

Terebey, S., Fich, M.: 1986, *Astrophys. J. (Letters)* **309**, L73

de Vaucouleurs, G.: 1955, *Astron. J.* **60**, 126

de Vries, C.P.: 1986, Ph.D. Thesis, University of Leiden, p163 – 164

Walterbos, R.A.M., Schwering, P.B.W.: 1987, *Astron. Astrophys.* **180**, 27

West, R.M., Pedersen, H., Madsen, C.: 1987, *ESO Messenger* **50**, 24

Chapter V

OVERALL INFRARED PROPERTIES OF THE MAGELLANIC CLOUDS

1. Introduction

Of all galaxies the Magellanic Clouds are the closest to the Milky Way galaxy. Because of their proximity they are ideal objects to study galactic structure in detail, while their large scale and integrated properties can also be determined. For most other galaxies only integrated data are available, especially in the infrared which has been surveyed only recently, by IRAS (IRAS, 1985a). Thus, a study of the global and integrated properties of the Magellanic Clouds as well as their detailed structure will provide reliable clues to the interpretation of infrared emission of more distant galaxies.

Detailed maps of the emission from the Magellanic Clouds as observed by IRAS are presented in Chapter II (SMC) and Chapter III (LMC). In this chapter we discuss the global and integrated infrared properties of the Magellanic Clouds. In Section 2 we describe the maps that are used. Section 3 contains a discussion of the integrated flux densities and spectra. The infrared size and the luminosity of each Cloud are also discussed. Section 4 contains a discussion of the global infrared morphology and the line–of–sight distribution of dust temperatures. A comparison of infrared emission with the Hα supergiant shells is presented and the strength of the interstellar radiation field is estimated. Section 5 contains a comparison of the infrared maps with ultraviolet, Hα and radiocontinuum data. Conclusions are given in Section 6.

2. Data presentation and data handling

The infrared observations used in this chapter were obtained with the Infrared Astronomical Satellite (IRAS) during its mission in 1983. For the derivation of the integrated properties we have used low resolution maps such as the $16\overset{\circ}{.}5$ extended emission "Skyflux" image plates (IRAS, 1985a), the "Spline–I" maps (van Albada *et al.*, 1985) and maps of the "Zodiacal Observations History File" (IRAS–ZOHF; see Chapter IV). For the SMC area a special 5° x 5° "IRAS Survey Co–add" was made, similar to the method as described in Chapter II (the LMC is too large for such an approach), and finally we used "IRAS Additional Observations" (AOs) of the DPM–type. Note that only the IRAS AO DPM–maps consist of independent observations and that all the other data are reprocessed versions of the IRAS Survey data (IRAS, 1985a). The AO data and their reduction have been fully described in Chapters II (SMC) and III (LMC). To compare IRAS data (with resolutions of $1'$ x $5'$ – $3'$ x $5'$) with those at other wavelengths and lower resolutions, it is necessary to convolve the IRAS data to lower resolutions. This is done by first applying a linear deconvolution with a theoretical beamprofile (calculated as described by Braun, 1985) using a spatial frequency taper truncated at the 1 % level. The highest gaussian resolution possible has a HPBW of $6\overset{\prime}{.}9$ in the cross–scan direction and $1\overset{\prime}{.}1, 1\overset{\prime}{.}1, 2\overset{\prime}{.}2$ and

4′.3 in the scan direction at 12, 25, 60 and 100 μm. At the distance of the Magellanic Clouds 1′ corresponds to 15 resp. 18 pc. At full resolution only the 30 Doradus peak is strong enough to produce dynamic range problems in the 25 μm map; it results in low level sidelobes. The low resolution data were obtained by convolution to resp. 8′ and 15′ gaussians (corresponding to a linear resolution of about 135 and 250 pc; the latter is identical to the IRAS in–scan resolution on M31; see Walterbos and Schwering, 1987). By averaging the two resp. three different scan–direction maps (see Chapters II and III) we increase the signal–to–noise ratio in the maps (at the SE end of the LMC–Bar, only the NS–scanned map was used due to an unacceptable stripe level in the EW–scanned map; see Chapter III). Especially for the SMC the convolution and map–averaging procedure gave a significant improvement in the 12 and 25 μm bands. We estimate that the relative photometric uncertainties in the maps are reduced from 10 % to about 5 %. The absolute photometric uncertainty does not change. The 8′ resolution maps are presented in Fig. 1 (8°.0 x 8°.0 around the LMC) and Fig. 2 (4°.8 x 4°.8 around the SMC).

3. Integrated infrared properties of the Magellanic Clouds

3.1. Flux densities and spectra

We have determined the integrated infrared flux densities as follows. For various representations of IRAS maps, pixel intensity values were summed in areas covered by the two Clouds, which were identical for all four infrared bands. Some of these maps have reduced, relative backgrounds (IRAS AO DPM–maps; Survey Co–add; ZOHF maps; see Chapter II and IRAS, 1985a), others have an absolute background level (IRAS Skyflux; Spline–I). A mean background contribution is then subtracted by extrapolation of the "background sum" to the "zero–area sum". This method is illustrated in Fig. 3 (LMC; ZOHF) and 4 (SMC; AO). After multiplying these sums by normalisation factors, by the pixel size and dividing the in–band fluxes so obtained by the bandwidth, integrated flux densities for these objects were obtained ($f_\nu = \int_{area} I_\nu d\Omega \approx \Delta\Omega_{pix} \sum_{pix} I_\nu$). This method gives us the integrated values of Table 1 for the LMC and Table 2 for the SMC. The errors presented in these tables are obtained from the flux density determination and do not incorporate the absolute photometric accuracy.

In order to remove the correct background, the area under consideration has to be larger than the Clouds. The method of background subtraction works well for a flat background. We have used a summing area that was primarily based on the optical size (de Vaucouleurs *et al.*, 1976), adjusted by inspection of the infrared maps and by the change in steepness of the slope in the sum–figures. For the LMC the derived flux densities assume a square box size of 8 °. For the SMC we find that a size of 2°.5 at 60 and 100 μm is sufficient. The integrated flux densities at 12 and 25 μm are more difficult to determine, because there is some structure present beyond the initial 2 ° x 2 ° size limit. With an area of 4 ° x 4 ° the whole wing is included, but a much larger spread in the determined integrated flux densities result ($f_{12\mu m} = 160 \pm 160$ Jy, $f_{25\mu m} = 420 \pm 100$ Jy; only a 10 % increase at 60 and 100 μm). In the LMC a size–increase from 6 ° to 8 ° gives a similar, but less pronounced trend. No accurate flux densities can be obtained from the IRAS Skyflux images at 12 and 25 μm.

Figure 1. *Infrared maps of the Large Magellanic Cloud at a resolution of* 8′. *Coordinates are for equinox 1950. All LMC maps in this chapter cover an area of* 8.0° x 8.0° *centered on* 05^h24^m *and* −69°00′. *See pages 148 – 149.*
In the 12 μm map grey scales are linear with a saw–tooth from 0.074 – 0.19 and from 0.26 – 0.56; darker grey scales indicate higher intensities. Contours are at 0.22, 0.37, 0.74, 1.1, 1.5, 3.0, 4.5, 5.9, 7.4, 15, 37, 51 MJy/sr.
In the 25 μm map grey scales are linear with a saw–tooth from 0.097 – 0.48 and from 0.68 – 1.5; darker grey scales indicate higher intensities. Contours are at 0.58, 0.97, 1.9, 2.9, 3.9, 7.8, 12, 16, 19, 39, 97, 190, 330 MJy/sr.
In the 60 μm map grey scales are linear with a saw–tooth from 0.6 – 1.0, from 1.4 – 2.9 and from 3.9 – 9.7; darker grey scales indicate higher intensities. Contours are at 3.9, 7.8, 12, 16, 25, 31, 39, 58, 78, 160, 270, 390, 580, 1200 MJy/sr.
In the 100 μm map grey scales are linear with a saw–tooth from 1.0 – 2.5, from 3.5 – 7.5 and from 10 – 25; darker grey scales indicate higher intensities. Contours are at 10, 20, 30, 40, 65, 80, 100, 150, 200, 400, 700, 1000, 1300 MJy/sr.

Figure 2. *Infrared maps of the Small Magellanic Cloud at a resolution of 8′. Coordinates are for equinox 1950. All SMC maps in this chapter cover an area of* 4.8° x 4.8° *centered on* 00^h58^m *and* −73°00′. *See pages 150 – 151.*
In the 12 μm map grey scales are linear with a saw–tooth from 0.074 – 0.19 and from 0.26 – 0.56; darker grey scales indicate higher intensities. Contours are at 0.22, 0.37, 0.74, 1.1, 1.3 MJy/sr.
In the 25 μm map grey scales are linear with a saw–tooth from 0.097 – 0.48 and from 0.68 – 1.5; darker grey scales indicate higher intensities. Contours are at 0.58, 0.97, 1.9, 2.9, 3.9, 5.8, 6.1 MJy/sr.
In the 60 μm map grey scales are linear with a saw–tooth from 0.19 – 0.97 from 1.4 – 2.9 and from 3.9 – 12; darker grey scales indicate higher intensities. Contours are at 1.2, 1.9, 3.9, 9.7, 16, 21, 27, 33, 39, 46 MJy/sr.
In the 100 μm map grey scales are linear with a saw–tooth from 0.5 – 2.5, from 3.5 – 7.5 and from 10 – 30; darker grey scales indicate higher intensities. Contours are at 3, 5, 10, 25, 40, 55, 70, 74 MJy/sr.

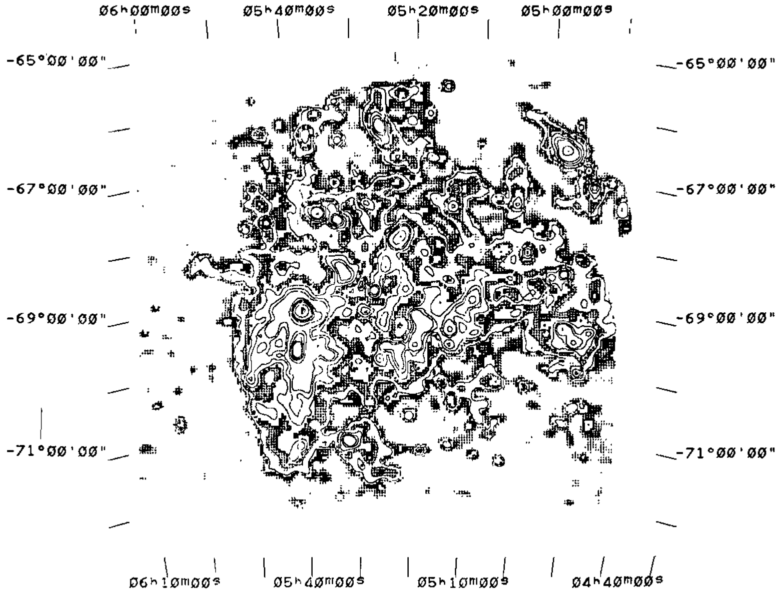

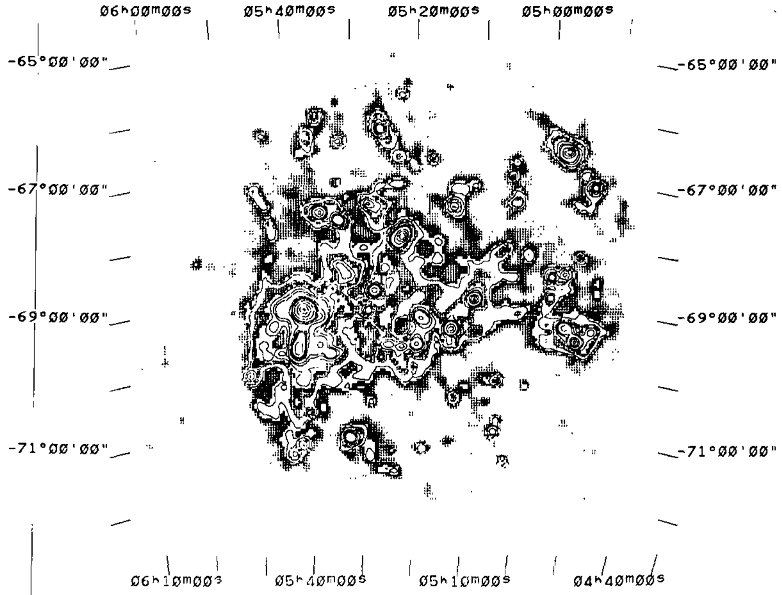

Fig. 1.1. LMC 12 μm AO DPM-map.
Fig. 1.2. LMC 25 μm AO DPM-map.

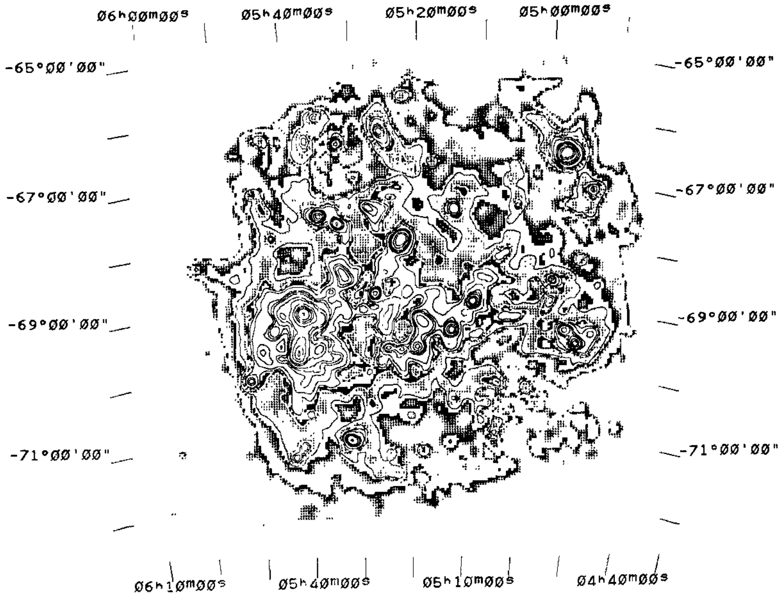

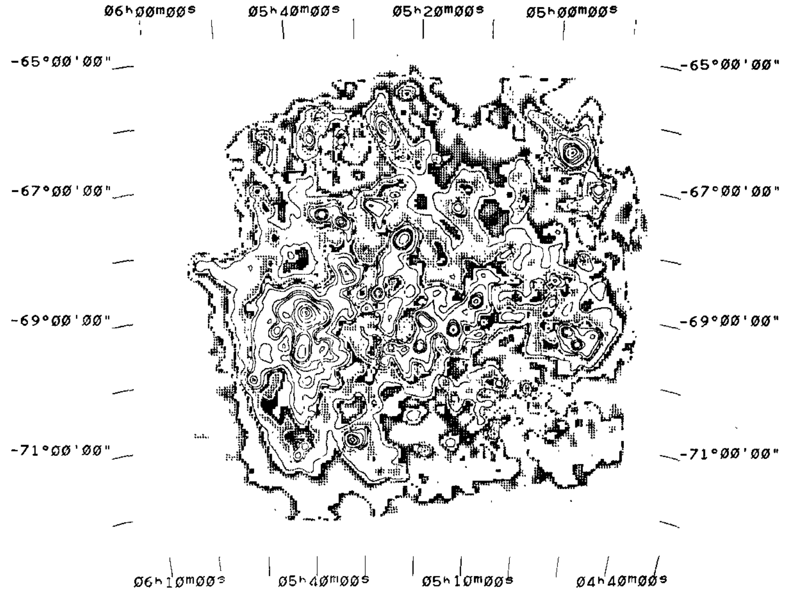

Fig. 1.3. LMC 60 μm AO DPM-map.
Fig. 1.4. LMC 100 μm AO DPM-map.

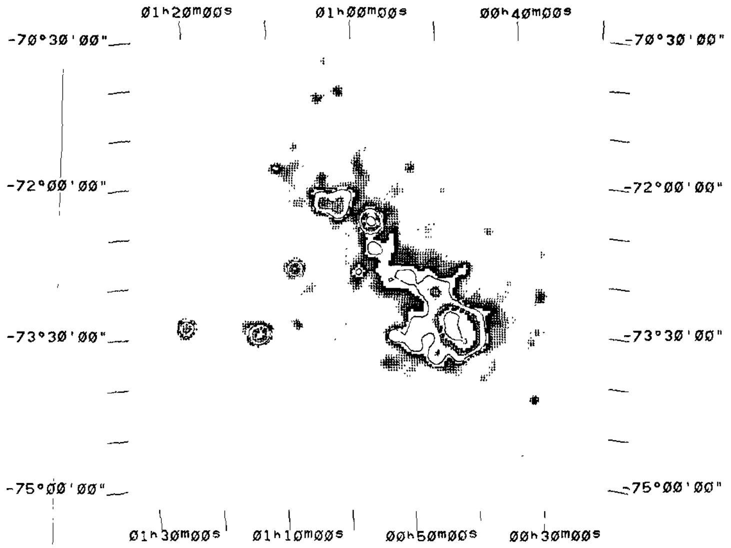

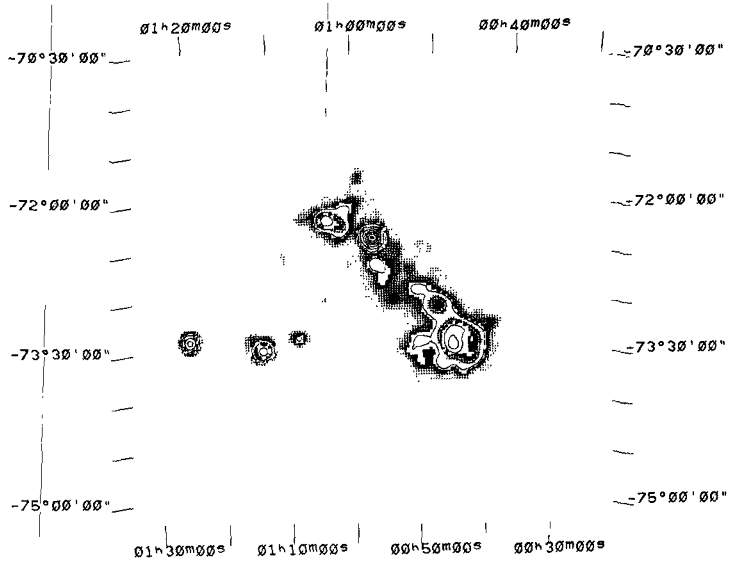

Fig. 2.1. SMC 12 μm AO DPM–map.
Fig. 2.2. SMC 25 μm AO DPM–map.

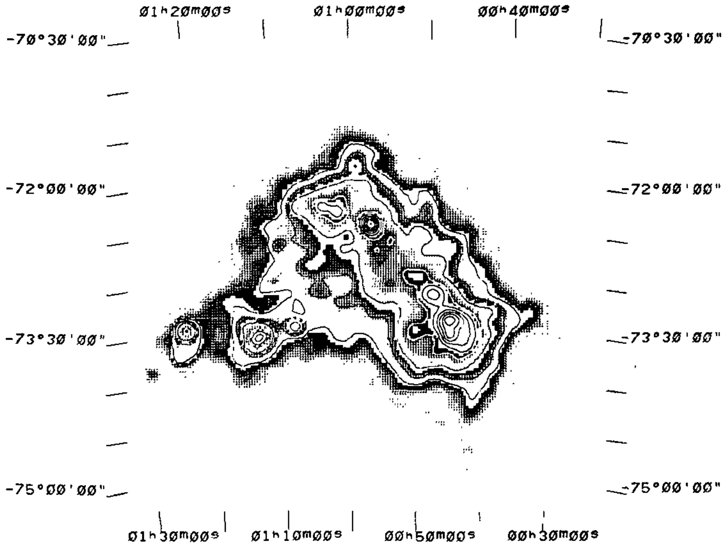

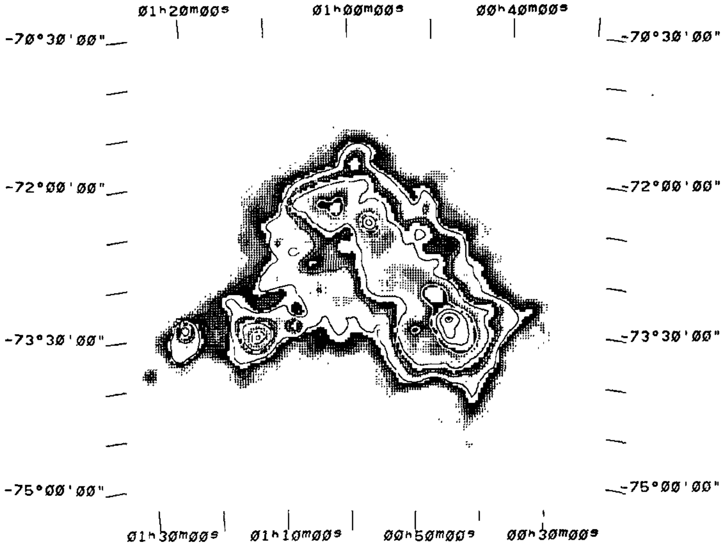

Fig. 2.3. SMC 60 μm AO DPM-map.
Fig. 2.4. SMC 100 μm AO DPM-map.

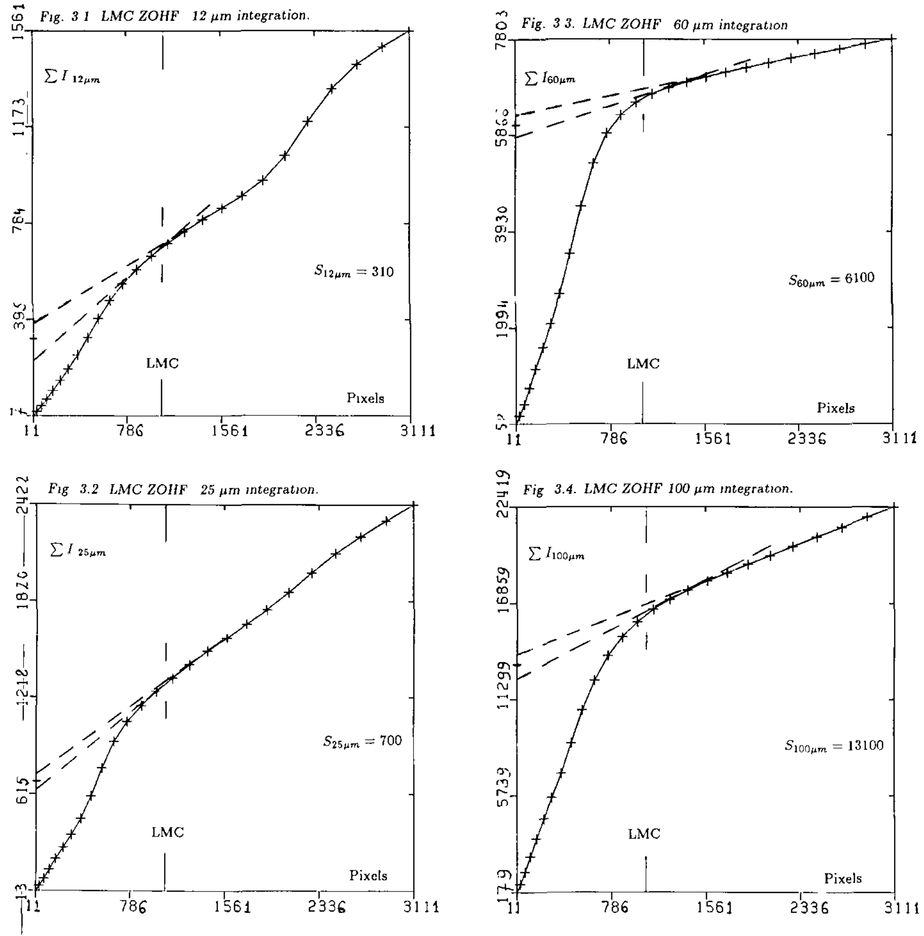

Figure 3. *LMC flux density integration using IRAS ZOHF data. The axes are the number of pixels in the integration, centered on the Cloud (with pixel size $\Delta\Omega = 15' \times 15'$), horizontally and the sum of the pixel intensities (MJy/sr) vertically. The size of the LMC is about 8° x 8°, which is indicated in the figures. The extrapolation of the background sum to the zero–area sum S_ν (MJy/sr) corrects for this background. The final flux density of the LMC is found from $(f_\nu/\text{Jy}) = 10^6\ (S_\nu/\text{MJy sr}^{-1})\ (\Delta\Omega/\text{sr})$.*

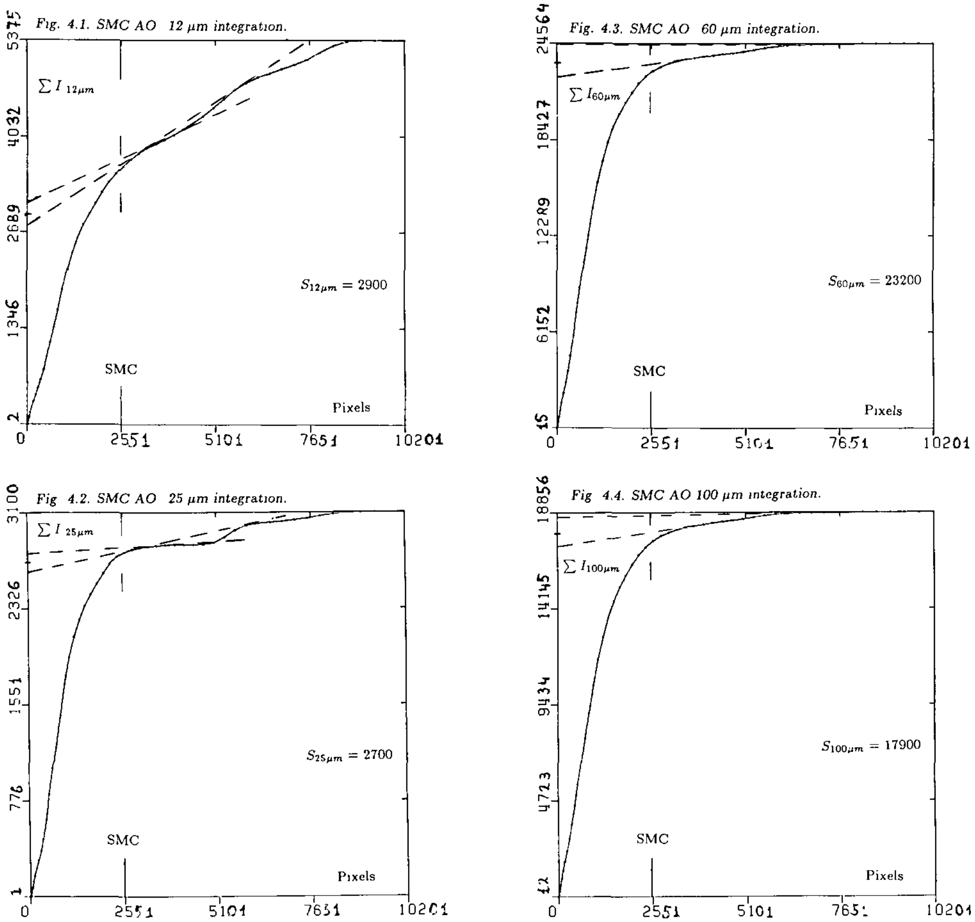
Fig. 4.1. SMC AO 12 µm integration.

Fig. 4.2. SMC AO 25 µm integration.

Fig. 4.3. SMC AO 60 µm integration.

Fig 4.4. SMC AO 100 µm integration.

Figure 4. *SMC flux density integration using IRAS AO data. The axes are the number of pixels in the integration, centered on the Cloud (with pixel size $\Delta\Omega = 3' \times 3'$), horizontally and the sum of the pixel intensities (10^{-8} Watt m^{-2} sr^{-1}) vertically. The size of the SMC is about 2°5 x 2°5, which is indicated in the figures. The extrapolation of the background sum to the zero–area sum S_ν (10^{-8} Watt m^{-2} sr^{-1}) corrects for this background. The final flux density of the LMC is found from $(f_\nu/Jy) = 10^{+18}\,(S_\nu/10^{-8}$ Watt m^{-2} $sr^{-1})\,(\Delta\Omega/sr)\,(\Delta\nu/Hz)^{-1}$.*

Table 1. *Comparison of observed integrated infrared flux densities of the LMC from various IRAS maps.*

Band	AO a) (Jy)	Skyflux b) (Jy)	Spline–I c) (Jy)	ZOHF d) (Jy)	Rice e) (Jy)	Infrared (MJy/sr)	background f) (MJy)
12 μm	4800	–	–	5950	2782	13	0.25
	±140			±750	–		
25 μm	10410	–	–	13300	7824	28	0.55
	±230			±1600	–		
60 μm	95700	95000	79000	116000	82917	9	0.18
	±2200	±10000	±8000	±5000	–		
100 μm	210400	219000	220000	249000	184687	9	0.18
	±5800	±16000	±18000	±16000	–		

Table 2. *Comparison of observed integrated infrared flux densities of the SMC from various IRAS maps.*

Band	AO a) (Jy)	Skyflux b) (Jy)	Spline–I c) (Jy)	Co–Add d) (Jy)	Rice e) (Jy)	Infrared (MJy/sr)	background f) (MJy)
12 μm	164	–	–	155	67	13	0.036
	±13			±25	–		
25 μm	401	–	–	303	270	29	0.080
	±18			±29	–		
60 μm	6860	6800	5600	7500	6688	8	0.022
	±230	±1000	±750	±280	–		
100 μm	13600	15100	13300	14700	15022	7	0.019
	±410	±2600	±2000	±900	–		

Notes to Tables 1 and 2:

First some general remarks: All flux densities assume an intrinsic source spectrum $f_\nu \propto \nu^{-1}$*; only a planar foreground removal has been done; i.e. detailed diffuse and stellar emission has not been subtracted. Note that* $1\ \mathrm{MJy/sr} = 305\ \mathrm{Jy}/(^\circ)^2 = 85\ \mathrm{mJy}/(')^2 = 24\ \mu\mathrm{Jy}/('')^2$.

- *a) The AO value was calculated by weighing the two independent full–resolution LMC maps, resp. the three SMC maps with the inverse of the determined error. Errors in the AO average are based on the flux determination, and not on the absolute photometry. The relative errors in the determination add up to 2 – 3 % for the LMC and 3 – 8 % for the SMC. Individual AO errors are 1.5 times higher than the LMC–average and 1.8 times higher than the SMC–average. Smoothed (8′ and 15′) AO's give about the same results as the average values in this table. The resolution of these maps is about* $0\overset{\prime}{.}8$ *x* $4\overset{\prime}{.}8$, $0\overset{\prime}{.}8$ *x* $4\overset{\prime}{.}8$, $1\overset{\prime}{.}5$ *x* $4\overset{\prime}{.}8$ *and 3′ x 5′ in the 12, 25, 60 and 100 μm bands.*
- *b) We have used only HCON–1 of Skyflux. The relative errors are considerably larger (7 – 17 %) than for AO maps. The 12 and 25 μm integrations in Skyflux were much hindered by a bad zero–level, and bad areas of field overlap. The 60 and 100 μm points are very similar to the AO determined values (1.0 – 1.1 times). The resolution of these data is 4′ – 6′.*
- *c) The calibration of the Groningen–IRAS Spline–I product (van Albada et al., 1985) was corrected with a factor of 0.7 (Deul, priv. comm.; see Walterbos and Schwering, 1987). We have used the 50° x 50° fields produced by Braun, Walker and Deul (priv. comm.) at Leiden Observatory. The Spline–I product only contains 60 and 100 μm data. For both galaxies the 60 μm point is about 0.82 of the AO average, while the 100 μm point is very similar (0.98 – 1.05). The relative errors in this determination are much larger than in the AO data (8 – 15 %). The resolution of these data is 10′.*
- *d) The Zodiacal Observations History File (ZOHF; IRAS, 1985a) were corrected for Zodiacal emission by Deul (see Deul and Wolstencroft, 1988). The LMC values are 1.2 – 1.3 times higher than the AO values. The SMC values are 1.4 times higher at 60 and 100 μm up to 2.1 – 3.6 at 12 μm. The relative error in the determination for the LMC is 4 – 13 %. The resolution of these data is 30′. The SMC ZOHF values are not given because they cannot be determined with enough accuracy. They give errors of 10 – 58 % and are 1.4 – 3.6 times higher than the AO values. Note the strong striping at 12 and 25 μm, especially at the position of the SMC (see Chapter IV). On the SMC we Co–added IRAS Survey data, which give the results as presented in this table. The relative errors are 4 – 16 %. The Co–add has a resolution similar as the AO data (see note a). The Co–added 25 μm point is 0.75 times lower than any other value; while the other bands correspond very well: 0.95 – 1.1 times the AO values.*
- *e) The numbers are from Rice et al. (1988a). Their 12 μm point is 0.4 – 0.6 times the AO, 25 μm is 0.7 – 0.8 times the AO and 60 and 100 μm are about equal (0.9 – 1.1).*
- *f) The average background intensity (produced by the Galactic foreground) was estimated from the Skyflux (HCON–1, –2 and –3) maps. At 12 and 25 μm they contain Zodiacal emission. Similar values are found at the South Ecliptic Pole for the Zodiacal emission by Deul and Wolstencroft (1988). At 60 μm the Skyflux maps contain both Zodiacal and Galactic diffuse emission and at 100 μm they contain only Galactic diffuse emission. The intensity values have been converted to absolute flux density levels by using a size of 8° x 8° on the LMC and 3° x 3° on the SMC. Note that these absolute values are 52 – 53 times higher than the LMC flux values at 12 and 25 μm and 0.9 – 1.9 times higher at 60 and 100 μm. For the SMC these ratios are 200 – 220 and 1.4 – 3.2.*

For comparison reasons, we have determined the 12 and 25 μm flux densities in another way. As the sizes of both Clouds are larger at 100 μm than at 12 and 25 μm we assume that the infrared radiation is coming only from the part of the Clouds for which $I_{100\mu m} > I_{cut-off}$. We have set a 100 μm cut–off limit in the AOs at various values ranging from 5.0 to 0.5 MJy/sr. If we sum the infrared data in these areas we obtain flux densities of 150 – 220 Jy at 12 μm and 370 – 440 Jy at 25 μm for the SMC. The values for the AO maps as given in Table 2, are found at a cut–off value of 2.7 MJy/sr in both bands. In the same way we obtain flux densities for the LMC at 12 μm of 4400 – 4800 Jy and at 25 μm of 9950 – 10300 Jy resp. The AO values in Table 1, are equal to a 100 μm intensity cut–off of 0.5 MJy/sr.

The values determined from the different map sets correspond very well for the LMC in all four bands. The two LMC and three SMC full resolution AOs are very similar and a good average is derived. The Spline–I 60 μm point is somewhat low but it may need recalibration (Walterbos and Schwering, 1987). The Skyflux 60 and 100 μm values are very similar, but since we have checked the AO calibration with the aid of the AO–Skyflux pixel–to–pixel scatter diagrams, they are not expected to be very different. The LMC values for the ZOHF are 1.2 – 1.3 times larger in all bands. This can be explained by the larger area that is covered by those maps, and is an indication for the presence of some structure in that larger area (which must be part of the LMC or Galactic foreground at 60 and 100 μm; at 12 and 25 μm some residual stripes are present in the ZOHF maps). For the SMC the situation is somewhat more complicated. For the 12 and 25 μm data the error may be larger due to a non–uniform background (partial Wing exclusion and possible extended emission). But the values are very similar and correspond well to the Co–added Survey data at full IRAS resolution of the SMC (less well at 25 μm). The SMC is not bright enough to produce a good estimate from the ZOHF data. The values obtained from these data are several times higher than the AO values due to the residual stripes that dominate at the position of the SMC. The low resolution 8$'$ and 15$'$ AO data confirm the observed higher resolution AO values.

The flux density values obtained by Rice *et al.* (1988a) are lower (0.4 – 0.8) than the AO values for both Clouds. The 60 and 100 μm flux densities are between 0.9 and 1.1 times the AO values. Although we do not know the details of Rice *et al.*'s determination, the discrepancies show the difficulties in determining total flux densities of such extended objects. A part of the differences might be explained by the fact that the Survey map flux densities in the 12 and 25 μm bands of the fainter sources are lower by as much as 50 % compared to the pointed AO observation measurements (see Rice *et al.*, 1988a). As many weak sources are present in these galaxies this can add up to a reasonable total flux density.

The difference between our AO derived integrated flux densities and the flux densities as derived by Rice *et al.* from IRAS Survey Co–adds might be the result of calibration differences (*i.e.* differences in the intensity scaling factor) or differences in the adopted background or both. Let us consider the first option: Rice's Co–add scaling is 0.4 – 0.8 at 12 and 25 μm compared to the AOs. We have checked the AO's LMC intensity levels with the Skyflux values and they resemble each other quite well in all four bands. For the SMC this was not possible at 12 and 25 μm (see Chapter II). Also the point sources that were compared with the IRAS Point Source Catalogue (IRAS PSC; IRAS 1985a) correspond quite well, especially stars at 12 μm, which indicates a good AO scaling. Due to the larger differences with the IRAS PSC entries in the 60 and 100 μm bands we would expect a larger error in those bands. Some bright LMC foreground SAO stars in the LI–LMC list are 20 % weaker at 12 μm than in the PSC (Chapter IV). We believe that this effect occurs only at the highest fluxes, but if it were more common it would explain a higher integrated flux density instead of a smaller one.

A more likely possibility is a difference in background between the AO maps and Rice *et al.*'s Co–added maps. Qualitatively, the differences in the 12 and 25 μm bands of our integrated flux densities with those of Rice *et al.* correlate with the background slope in Fig. 3 and 4. The determined background slopes of Fig. 4 (SMC) are caused by background levels of 0.019 at 12, 0.012 at 25 and 0.005 MJy/sr at 60 and 100 μm. Variations in the LMC–background slopes can explain only 10 % flux density variations. We tried to obtain Rice's 12 and 25 μm values from the AO map sets, but no unique background slope could be fitted to the various maps. The absolute infrared background level at the positions of the SMC and LMC, as determined from Skyflux images are given in Tables 1 and 2. The differences between the results obtained by Rice *et al.* and by us can be accounted for by background differences of 0.1 MJy/sr (LMC; 8 ° x 8 °) and 0.07 MJy/sr (SMC; 2 ° x 2 °); this is less than 1 % of the actual background emission. These suggested background differences are too high to be explained by the AO zero–level uncertainties as given in Chapters II and III. Those uncertainties predict 10 % flux errors in all bands for the LMC and 2 – 10 % for the SMC. Note that the 12 and 25 μm integrated flux densities for the Clouds are less than 1/50 of the absolute background for the LMC and about 1/200 of that for the SMC.

Flux densities derived for extended objects based on single AO data, or any other single–map infrared data, should be considered with great care. The agreement between the different map sets gives us confidence in the reliability of the here derived values. * Both the problems mentioned by Rice *et al.* for weak sources, and the extensive Zodiacal foreground are probably responsible for the difference in the flux densities at 12 and 25 μm derived by them and by us. The best estimate for the integrated infrared flux densities is obtained from the average of the AO and ZOHF values for the LMC and the average of the AO and Co–add values for the SMC, weighted by the inverse of the measured uncertainties. These values are given in Table 3, as *"Average observed flux densities"*.

In Table 3 we summarize the observed integrated infrared properties for the two Magellanic Clouds. We estimate the error in the absolute photometry to be 10 % (see Section 2). After the flat–background correction explained above, the observed flux densities were corrected for local variations (by stars and diffuse Galactic foreground; Chapter IV). The "Average observed" values of Table 3 were already corrected for a planar background. This is correct at 12, 25 and 60 μm; at 100 μm the SMC background is also planar, but the LMC background is increased by 20 % due to small scale structure especially at the southern side of the Cloud (Chapter IV). Colour–correction factors have been calculated from the "Average Observed" integrated spectrum using Table VI.C.6 of

---

* The values given earlier by Israel and Schwering (1986) were based on the same AO data, but corrected for stellar foreground emission and with a preliminary calibration (May–1984), and a less well corrected background; they are somewhat lower in all four bands (0.7 – 0.9 x).

Table 3. *Observed integrated infrared properties of the Magellanic Clouds.*

Property	Unit	LMC	SMC
General characteristics [a]:			
Distance D	kpc	53	63
Linear/angular scale	pc/′	15	18
Optical diameter	°	10.8	4.7
Absolute V–magnitude	mag	–18.5	–16.8
Average observed flux densities [b]:			
12 μm	Jy	4980 ± 500	161 ± 16
25 μm	Jy	10800 ± 1100	363 ± 36
60 μm	Jy	102000 ± 10000	7100 ± 710
100 μm	Jy	221000 ± 22000	13900 ± 1400
Galactic foreground flux densities [c]:		Stars / Diffuse	Stars / Diffuse
12 μm	Jy	130. / 3500	17. / 300
25 μm	Jy	51. / 3000	3.5 / 260
60 μm	Jy	3.2 / 10000	0.4 / 1400
100 μm	Jy	0.0 / 81000	0.0 / 5800
Clouds 100 μm flux density at other distances [d]:			
3 Mpc (M81 group)	Jy	68.	6.4
15 Mpc (Virgo cluster)	Jy	2.7	0.25
Limits for detection in the IRAS PSC [d]:			
12 μm ($f_\nu > 0.25$ Jy)	Mpc	7.5	1.6
25 μm ($f_\nu > 0.25$ Jy)	Mpc	11.	2.4
60 μm ($f_\nu > 0.40$ Jy)	Mpc	27.	8.4
100 μm ($f_\nu > 1.00$ Jy)	Mpc	25.	7.4
IRAS Colour correction factors [e]:			
12 μm	f^{true}/f^{quoted}	1.00	1.02
25 μm	f^{true}/f^{quoted}	1.05	1.07
60 μm	f^{true}/f^{quoted}	1.01	1.01
100 μm	f^{true}/f^{quoted}	1.00	1.00
Foreground and Colour corrected ("*Recommended*") flux densities [f]:			
12 μm	Jy	4850 ± 500	147 ± 16
25 μm	Jy	11300 ± 1100	385 ± 36
60 μm	Jy	103000 ± 10000	7170 ± 710
100 μm	Jy	208000 ± 22000	13900 ± 1400

Table 3, *continued.*

Property	Unit	LMC	SMC
Average infrared surface brightness [g]:			
12 μm	MJy/sr	0.17	0.028
25 μm	MJy/sr	0.40	0.073
60 μm	MJy/sr	3.7	1.4
100 μm	MJy/sr	7.4	2.6
Integrated flux density of discrete infrared sources [h]:			
12 μm	Jy / %	677 / 14	51 / 35
25 μm	Jy / %	2124 / 19	182 / 47
60 μm	Jy / %	14925 / 14	1421 / 20
100 μm	Jy / %	26252 / 13	2283 / 16

Notes to Table 3:

- a) *The distance is taken from Humphreys (1984), the optical diameter and the absolute visual magnitude are taken from de Vaucouleurs et al. (1976).*
- b) *The quoted IRAS flux densities assume a $f_\nu \propto \nu^{-1}$ intrinsic source spectrum. The LMC average is the AO and ZOHF value, weighted by the reciprocal uncertainties. The SMC average is the AO and Co–add value, weighted by the reciprocal uncertainties. The error is set equal to the 10 % photometric error.*
- c) *These Galactic foreground values are taken from Chapter IV and include an extra correction (of 20 %) for a non–planar foreground at 100 μm at the position of the LMC.*
- d) *The Clouds' flux densities at the distance of the M81–group and the Virgo cluster are given. Limits for detection of sources with the same infrared flux density as the Clouds are also given.*
- e) *These colour correction factors have been obtained from the average observed IRAS flux densities.*
- f) *These flux densities have been obtained by subtracting the total foreground stellar and diffuse contributions and multiplying the result by the colour correction factors; they are the true flux densities of the Magellanic Clouds.*
- g) *The average surface brightness is calculated from the flux densities and the surface area determined from the optical diameter as given in this table. The LMC values are 5.8 times higher than the SMC values at 12 and 25 μm and 2.7 times at 60 and 100 μm.*
- h) *The sum of all the discrete sources from Chapters II and III are given, together with the fraction of the total flux density.*

IRAS (1985b). To obtain the true flux density values these factors have been multiplied with the observed integrated flux densities. The final *"Recommended"* flux densities are listed in the table. Note that colour–correction factors depend on the resolution; here they are based on the integrated flux densities. Hence they are only good average values and are not necessarily correct for individual areas in the infrared maps.

Table 3 also contains the 100 μm flux densities the Clouds would have if they were at distances of 3 Mpc (in the M81 group) or 15 Mpc (in the Virgo cluster). The SMC would be below the IRAS PSC detection limit at the latter distance, even for IRAS Co-added Survey data (which have a detection limit which is 1.3 – 4 times better than the IRAS PSC, with the smallest increase at 100 μm; Caspers, priv. comm.). Furthermore we have calculated the detection limit of the Clouds for the IRAS PSC. Galaxies with the same infrared luminosity as the LMC are detectable at distances up to 27 Mpc, four times farther than those with the same luminosity as the SMC.

The integrated, foreground and colour corrected infrared spectra of both Clouds are shown in Fig. 5, together with the spectra of M31 (Walterbos and Schwering, 1987) and NGC 4449 (Hunter *et al.*, 1986); the two latter spectra are both scaled to the distance of the LMC. The LMC (with a diameter of 7.8 kpc) is, about 12 times more luminous in the infrared than the SMC (with a diameter of 2.6 kpc). A smaller difference is still present after we correct for the different sizes. The average surface brightness, given in Table 3, is 5.8 times higher in the LMC than in the SMC at 12 and 25 μm and 2.7 times at 60 and 100 μm. At 60 μm the LMC has the same infrared luminosity as the much larger Andromeda spiral galaxy M31 (60 kpc diameter). Note also that, for $\lambda > 12$ μm NGC 4449 (9.4 kpc diameter) is brighter than M31. NGC 4449 has a four times higher infrared luminosity than the LMC, and a 3 times higher surface brightness. At 25 and 60 μm M33 (not shown in Fig. 5; see Rice *et al.*, 1988b; with a diameter of 12 kpc) is also weaker than the LMC.

The integrated spectra of the LMC and SMC are very similar; the SMC spectrum is somewhat steeper between 60 and 25 μm. The spectra are characteristic of warm dust clouds associated with HII regions; they resemble the infrared spectrum of the active irregular galaxy NGC 4449 and are clearly warmer than most Local Group spiral galaxies. The peak in the Clouds' spectra is closer to 100 μm than in the spectra of M31 or diffuse Galactic emission (which have cool dust spectra $T_d \approx 25$ K peaking well beyond 100 μm); the dust in both Clouds has a high average temperature (33 K). The spectral difference at the 12 μm side of the spectrum shows that the 12 μm excess is less pronounced in the Clouds ($T_{12-25\mu m} \approx 240$ K) than in M31 and typical cirrus areas in our Galaxy, where $T_{12-25\mu m} \approx 320$ – 380 K (Walterbos and Schwering, 1987; and Boulanger *et al.*, 1985).

Using the Kuiper Airborne Observatory, Werner *et al.* (1978) observed a flux density of 2000 Jy for 30 Doradus at 200 μm, *i.e.* 40 % of their 100 μm flux density. Using the average temperature of 33 K and a $\lambda^{-1.5}$ dust emissivity we estimate the 200 μm integrated flux densities of the Clouds to be about 50 % of the 100 μm flux densities, hence 1 x 10^5 Jy for the LMC and 7 x 10^3 Jy for the SMC. This is valid if the 33 K component still dominates all the other components at 200 μm, hence if cold dust is not present in large amounts.

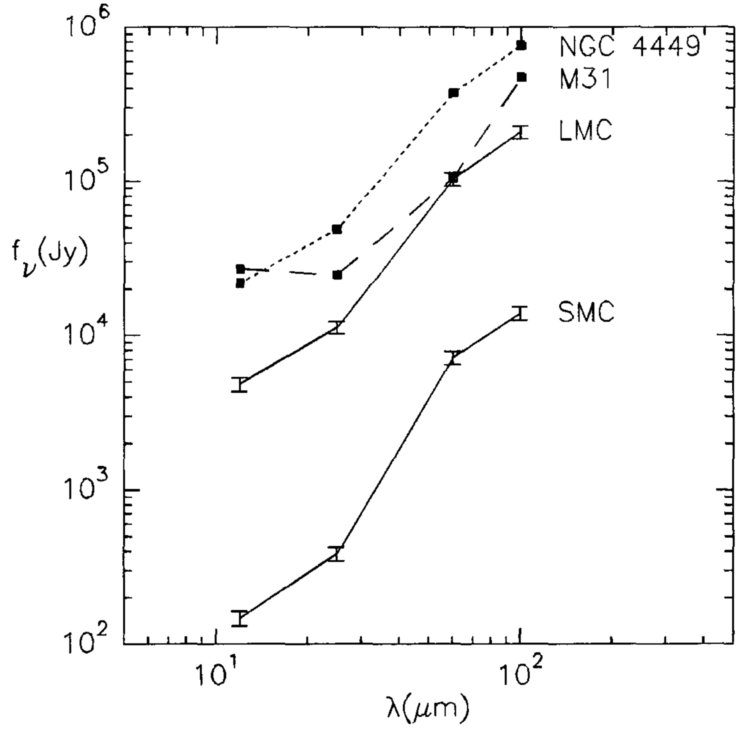

Figure 5. *Integrated infrared spectra of the Magellanic Clouds.*
The spectra of the LMC and the SMC are shown by solid lines. Note that the LMC is about 12 times more luminous than the SMC. The spectra of M31 (Walterbos and Schwering, 1987; dashed) and NGC 4449 (Hunter et al., 1986; dotted) are scaled to the distance of the LMC.

3.2. Infrared sizes

Rough estimates for the infrared size of the Magellanic Clouds were obtained from the summing method used to determine the integrated flux densities (see Section 3.1 and Fig. 3 and 4). The diameter derived from IRAS AO, Skyflux and Spline–I data for the LMC is 7° – 8° and for the SMC about 2° – 3° at 12 and 25 μm and 2°.5 – 4° at 60 and 100 μm. The LMC size obtained from the ZOHF data is 8° – 8°.6.

We now derive a more accurate value for the Clouds' sizes in the infrared. Similar to the definition of the size for galaxies in the optical (de Vaucouleurs *et al.*, 1976: 25

mag/('')^2, which corresponds to 0.019 MJy/sr in the blue) we may define the size by the area with intensity above a certain fixed in-band intensity level of 2.5 x 10^{-8} Watt m^{-2} sr^{-1}, which is about 2 – 5 times the effective noise in the maps. This level corresponds to 0.19, 0.48, 0.97 and 2.5 MJy/sr at the 12, 25, 60 and 100 μm bands (10 – 130 times higher than the visual B-limit of de Vaucouleurs). The values for the defined size are dependent on the sensitivity of the IRAS Survey instrument, its resolution and the surface brightness of the Clouds. The surface area of the Clouds with in-band intensities higher than the cut-off values equals an equivalent circular area a_{eq} with diameter d_{eq}; both are given in Table 4. Note that the equivalent diameter assumes a circular aperture for the source, while the equivalent area is independent of the shape of the object. The infrared size differs in the four wavelength bands and is largest in the 60 and 100 μm bands. The sizes are smallest at 25 μm. The 12 and 25 μm sizes are 0.4 – 0.8 times the 60 and 100 μm sizes. The equivalent diameter is smaller than the first estimates presented in this section; caused by the presence of areas below the intensity cut-off.

Similar sizes in all four bands are obtained by adopting different intensity cut-off levels for the individual bands, *e.g.* by lowering the intensity cut-off at 25 μm to 0.5 x 10^{-8} Watt m^{-2} sr^{-1} and to 1.3 x 10^{-8} Watt m^{-2} sr^{-1} at 12 μm, about equal to the noise levels in these bands. These cut-off values are unrealistically low, and the size may now be strongly influenced by the statistical properties of noise in the maps. We can also increase the 60 and 100 μm cut-off limits to about 10 x 10^{-8} Watt m^{-2} sr^{-1}, resulting in a similar size in all four infrared bands.

The Clouds' size in blue light (de Vaucouleurs *et al.*, 1976; Table 3) is roughly twice the infrared (60 and 100 μm) size. Deep visual photographic images of West *et al.* (1987) show a halo extending over 11° x 15° (*i.e.* a linear scale of 11 x 15 kpc). The infrared images show a size that corresponds to red isophotes of de Vaucouleurs (1957) of 0.06 MJy/sr for both Clouds, but for the SMC-Wing of about 0.03 MJy/sr. Also in red light much lower Cloud intensity levels are visible. The smaller infrared size is mainly the result of a higher sensitivity at visual wavelengths compared to infrared wavelengths.

3.3. Luminosities and luminosity ratios

The infrared luminosity of the Magellanic Clouds can be determined in different ways. In Table 4, we first give the infrared monochromatic luminosities L_ν for the 12, 25, 60 and 100 μm bands (these can also be called in-band luminosities, and are integrated over the IRAS bands); this is what has been measured by IRAS. As an estimate for the total infrared luminosity of the Clouds we give four values:

(1) the sum of the four monochromatic infrared luminosities: $L_{12+25+60+100\mu m}$;
(2) the total mid-infrared 'hot'-flux (8 – 30 μm) luminosity: L_{hot};
(3) the total far-infrared 'cool'-flux (42.5 – 122.5 μm) luminosity: L_{cool};
(4) the 'hot'-flux (2) and 'cool'-flux (3) components extrapolated from 1 – 500 μm and combined: $L_{hot'}$, $L_{cool'}$, L_{tot}.

Method (4) extrapolates the 60 – 100 μm spectra over the infrared from 1 – 500 μm using an emissivity $\epsilon_\nu \propto \nu^{1.5}$ and a 33 K grain temperature (based on $f_{60\mu m}/f_{100\mu m}$). We used a similar method as IRAS (1985c): a factor of 1.26 to fill in the 60 – 100 μm wavelength band gap and a factor of 1.35 to extrapolate beyond 100 μm follows from the observed dust temperature. This results in an integrated infrared 'cool-dust' luminosity $L_{cool'}$ for the LMC of 7.1 x 10^8 $L_\odot$ and for the SMC of 6.8 x 10^7 $L_\odot$. By extrapolating the 12 – 25 μm spectra (240 K) over the whole infrared 1 – 500 μm assuming a blackbody emission curve we found the 'hot–dust' luminosities $L_{hot'}$ to be 1.8 x 10^8 $L_\odot$ (20 % of the total integrated luminosity) for the LMC and 8.1 x 10^6 $L_\odot$ (11 % of the total) for the SMC. The two extrapolated luminosities sample different temperature regimes. The 240 K blackbody, discussed in Section 4.2, emits 10 times more in the 8 – 30 μm range than in the 42.5 – 122.5 μm wavelength range; while for the 44 K blackbody this ratio is 0.008. Because we have observed a ratio of "hot–flux"/"cool–flux" of only 0.1 – 0.3, *i.e.* very different from either two, we can add these integrated components yielding total infrared luminosities $L_{tot} \equiv L_{hot'} + L_{cool'}$ of 9 x 10^8 $L_\odot$ for the LMC and 8 x 10^7 $L_\odot$ for the SMC.

Table 4 also contains luminosities at other (Hα, Lyα, V, B, UV) wavelengths and ratios of L_{cool} with these data (Table 4 contains their definitions). The LMC value of L_{cool}/L_B is about 1.7 times higher than the SMC value, which in turn is about two times higher than the value for M31 (see Caspers, 1987). Thus, the importance of dust emission relative to stellar emission increases from M31 to the SMC, to the LMC; M33 is inbetween the two Clouds. This illustrates the relative increases in dust content. The ratio of $L_{cool}/L_{H\alpha}$ is much less than the other ratios due to the fact that Hα is line emission and fills only a small wavelength band (equivalent width W_λ = 35 Å). The ratio is 2.8 times higher for the LMC than for the SMC. From the Hα emission we have derived the equilibrium Lα emission for a HII region (10^4 K hydrogen gas).

We have calculated the stellar emission from two components. The spectral shapes of the visual data between 4400 and 6250 Å of de Vaucouleurs (1960) give both Clouds an average F5 (6700 K) spectrum. We compared the absolute magnitudes of the Clouds (V_{LMC} = –18.5 mag, V_{SMC} = –16.8 mag) with the F5 absolute magnitude (V_{F5} = 3.6 mag) and then integrated the F5 spectrum over all wavelengths. The magnitudes correspond to 6.9 x 10^8 F5–type stars for the LMC and 1.5 x 10^8 for the SMC. Each F5 dwarf has a luminosity of 2.5 $L_\odot$ (Mihalas and Binney, 1981, p114), and hence we obtain L_{F5} = 1.7 x 10^9 $L_\odot$ and 3.6 x 10^8 $L_\odot$ for the LMC and SMC resp. The ultraviolet 1690 Å data of Lequeux (1984) were used to determine the luminosity of hot stars. We assume a B0 spectrum (Mihalas and Binney, 1981) and derive a number of about 9000 of these stars in the LMC and about 2500 in the SMC. This results in a luminosity of L_{B0} = 5.8 x 10^9 $L_\odot$ for the LMC and 1.6 x 10^8 $L_\odot$ for the SMC (equal amounts of B0 main sequence stars and supergiants are assumed). The total stellar luminosity is the sum of the two components and is given in Table 4. The luminosities are correct within a factor of 2 due to extinction effects. We derive $L_{cool}/L_{stellar}$ = 0.23 and 0.10 for the LMC and SMC. In principle, all infrared radiation comes from stars; but 23 % of the stellar radiation of the LMC is re–emitted in the infrared and only 10 % in the SMC. This shows the relative weak conversion of starlight into infrared radiation by the SMC compared to the LMC, which can be caused by a low dust content.

The ratio of total infrared luminosity to gas mass for the LMC and SMC are 1.3 and 0.12 times the Solar Neighbourhood value of 1 $L_\odot/M_\odot$ (Boulanger and Perault, 1987). At 1690 Å, Lequeux (1984) has derived (extinction corrected) luminosity–to–mass ratios for the Clouds of 1.3 and 0.30. The LMC ratio corrsponds well to our value, but the SMC has a ratio 2.5 times higher than ours. This again shows the relative weakness of the SMC's infrared emission.

Table 4. *Derived integrated infrared properties of the Magellanic Clouds.*

Property	Unit	LMC	SMC
Equivalent infrared size/diameter a):			
($I_\nu \Delta\nu > 2.5 \times 10^{-8}$ Watt m^{-2} sr^{-1}):		a_{eq} / d_{eq}	a_{eq} / d_{eq}
12 μm ($I_\nu > 0.19$ MJy/sr)	$(^\circ)^2/^\circ$	20.7 / 5.1	1.1 / 1.2
25 μm ($I_\nu > 0.48$ MJy/sr)	$(^\circ)^2/^\circ$	10.8 / 3.7	0.7 / 0.9
60 μm ($I_\nu > 0.97$ MJy/sr)	$(^\circ)^2/^\circ$	31.2 / 6.3	4.4 / 2.4
100 μm ($I_\nu > 2.50$ MJy/sr)	$(^\circ)^2/^\circ$	34.0 / 6.6	4.2 / 2.3
Monochromatic infrared luminosities b):			
$L_{12\mu m}$	$L_\odot$	5.74×10^7	2.46×10^6
$L_{25\mu m}$	$L_\odot$	5.12×10^7	2.47×10^6
$L_{60\mu m}$	$L_\odot$	23.3×10^7	23.0×10^6
$L_{100\mu m}$	$L_\odot$	18.3×10^7	17.3×10^6
Sum of monochromatic luminosities b):			
$L_{12+25+60+100\mu m}$	$L_\odot$	52.5×10^7	45.2×10^6
Mid– and far–infrared fluxes b):			
'Hot–flux' (8 – 30 μm)	Watt m^{-2}	15.6×10^{-10}	5.00×10^{-11}
'Cool–flux' (42 – 122 μm)	Watt m^{-2}	59.7×10^{-10}	40.8×10^{-11}
Extrapolated mid– and far–infrared fluxes (1 – 500 μm) b):			
Extrapolated 'hot flux'	Watt m^{-2}	20.4×10^{-10}	6.55×10^{-11}
Extrapolated 'cool flux'	Watt m^{-2}	80.6×10^{-10}	55.1×10^{-11}
Mid–, far– and total–infrared luminosities b):			
L_{hot} (8 – 30 μm)	$L_\odot$	13.7×10^7	6.21×10^6
L_{cool} (42 – 122 μm)	$L_\odot$	52.4×10^7	50.6×10^6
$L_{hot'}$ (1 – 500 μm)	$L_\odot$	18.0×10^7	8.2×10^6
$L_{cool'}$ (1 – 500 μm)	$L_\odot$	70.7×10^7	68.3×10^6
L_{tot} (1 – 500 μm)	$L_\odot$	88.7×10^7	76.5×10^6
Luminosities at other wavelengths b):			
$L_{H\alpha}$	$L_\odot$	0.52×10^7	1.4×10^6
$L_{Ly\alpha}$	$L_\odot$	5.93×10^7	16.0×10^6
L_V	$L_\odot$	26.0×10^7	45.0×10^6
L_B	$L_\odot$	34.0×10^7	58.0×10^6
L_{UV}	$L_\odot$	31.0×10^7	32.0×10^6
L_{F5}	$L_\odot$	$174. \times 10^7$	$364. \times 10^6$
L_{B0}	$L_\odot$	$58. \times 10^7$	$160. \times 10^6$
$L_{stellar}$	$L_\odot$	$232. \times 10^7$	$524. \times 10^6$

Table 4. *continued.*

Property	Unit	LMC	SMC
Luminosity ratios $^{c)}$:			
$L_{cool}/L_{H\alpha}$	–	101.	36.
$L_{cool}/L_{Ly\alpha}$ (IRE)	–	8.8	3.2
L_{cool}/L_V	–	2.0	1.1
L_{cool}/L_B	–	1.5	0.87
L_{cool}/L_{UV}	–	1.7	1.6
$L_{cool}/L_{stellar}$	–	0.23	0.10
Luminosity–mass ratio $^{d)}$:			
L_{tot}/M_{gas}	$L_\odot/M_\odot$	1.3	0.12
Average temperatures for $\epsilon_\nu \propto \nu^n$ $^{e)}$:			
$T_{12-25\ \mu m}$ (n=0)	K	240 ± 10	230 ± 10
$T_{25-60\ \mu m}$ (n=0)	K	73 ± 3	63 ± 3
$T_{60-100 \mu m}$ (n=0)	K	45 ± 2	46 ± 2
$T_{60/\ 100 \mu m}$ (n=1)	K	36 ± 2	36 ± 2
$T_{60/\ 100 \mu m}$ (n=2)	K	30 ± 2	31 ± 2

Notes to Table 4:

a) *The equivalent diameter has been calculated as follows: The area a_{eq} of the two galaxies of all the pixels that have $I_\nu \Delta\nu > 2.5 \times 10^{-8}$ Watt m^{-2} sr^{-1} was selected and was transfered to a circular area with the same size. Both the area size (square degrees) as well as equivalent diameter d_{eq} are given. The chosen limit is about 2 times the noise at 12 μm and increases in the other bands to 4 – 5 times the noise at 100 μm. At the distance of the LMC 5° corresponds to 4.5 kpc; at the distance of the SMC 2° corresponds to 2.2 kpc.*

b) *The following luminosities have been calculated via $L = 4\pi D^2\ F$, using a distance D of 53 kpc for the LMC and 63 kpc for the SMC. We have used the true flux densities of Table 3. First of all the "monochromatic" luminosities for each IRAS band individually, for which we used $F \equiv \Delta\nu\ f_\nu$, and the sum of these four monochromatic luminosities (with $F \equiv \sum_{12+25+60+100 \mu m} \Delta\nu f_\nu$). To obtain luminosities with $F = \nu f_\nu$ the given monochromatic luminosities must be multiplied by 1.85, 2.32, 1.94 and 3.00 at 12, 25, 60 and 100 μm. The mid–infrared (8 – 30 μm) 'hot'–flux has been defined by us as $F_{hot} \equiv 1.26\ (13.48\ f_{12\mu m} + 5.16\ f_{25\mu m}) \times 10^{-14}$ Watt m^{-2} similar to the far–infrared (42.5 – 122.5 μm) 'cool'–flux (see IRAS 1985c: $F_{cool} \equiv 1.26\ (2.58\ f_{60\mu m} + 1.00\ f_{100\mu m}) \times 10^{-14}$ Watt m^{-2}). Both of these have been transformed to luminosities: L_{hot}, L_{cool}. The integrated 'hot–flux' has been defined by extrapolating the (8 – 30 μm) 'hot'–flux over the infrared range 1 – 500 μm using the appropriate 240 K colour temperature (multiplication by a factor 1.31): $L_{hot'}$. The integrated 'cool'–flux has been defined in the same way (33 K; multiplication by a factor of 1.35): $L_{cool'}$. L_{tot} is the sum of the luminosity of these two extrapolated components. The values of $L_{H\alpha}$, $L_{Ly\alpha}$, L_V, L_B and L_{UV} have been calculated in the same way (integrated over the observed band) from the following data: The Hα luminosities (λ = 6563 Å, $\Delta\lambda$ = 600 Å) were calculated from the uncorrected fluxes ($F \equiv \int f_\nu d\nu$) of Kennicutt and Hodge (1986). The luminosity of Lyα has been calculated from $L_{H\alpha}$ after applying a multiplication factor of $j_{Ly\alpha}/j_{H\alpha}$ = 11.4 (see Osterbrock, 1974; Table 4.1 therein) for a 10^4 K hydrogen gas. The* *ratio $L_{cool}/L_{Ly\alpha}$ is often refered to as the infrared excess IRE. The V (λ = 5500 Å, $\Delta\lambda$ = 0.087 Å) and B (λ = 4400 Å, $\Delta\lambda$ = 0.098 Å) magnitudes are from de Vaucouleurs (1960), they have been converted to luminosities using the recipe of Zombeck (1980). The ultraviolet (UV: λ = 1690 Å, $\Delta\lambda$ = 330 Å) is taken from Lequeux (1984). The F5 stellar luminosity has been calculated by comparing the V with the average Clouds' spectra (F5) and extrapolating the F5–spectrum in solar luminosity; the B0 luminosity from comparison of ultraviolet data. The stellar luminosity is the sum of these two components.*

c) *These ratios are calculated for the 'cool' dust luminosity. The ratios with L_{hot} are 3.8 times smaller for the LMC and 8.1 times for the SMC; the ratios with L_{tot} are 1.7 and 1.5 times larger resp.*

d) *The infrared luminosity–to–gas mass ratio has been obtained from the value of L_{tot} and the HI masses (5.4 and 4.8 x 10^8 $M_\odot$) corrected for He by multiplying with 1.3 (see Lequeux, 1984). The gas masses for both Clouds are very similar. The values L_{tot} /M_{tot} are 0.15 for the LMC and 0.05 for the SMC (with total dynamic masses of 6 and 1.5 x 10^9 $M_\odot$).*

e) *The average dust temperatures have been calculated assuming blackbody emission and $\epsilon_\lambda \propto \lambda^{-n}$. For $n = 0$ colour–temperatures are obtained (indicated by an index –), and for $n > 0$ dust temperatures are obtained by assuming an emissivity with the given value of n (indicated by an index /).*

Table 5. *Comparison with other galaxies.*

Galaxy	Distance (kpc)	Diameter (kpc)	Total infrared ($L_\odot$)	$\frac{LMC}{galaxy}$ (%)	$\frac{SMC}{galaxy}$ (%)	$\frac{12+25\mu m}{60+100\mu m}$ [a] (%)	Reference
LMC	53	7.8	8.9 x 10^8	100.	8.7	26	This chapter.
SMC	63	2.6	7.7 x 10^7	1160.	100.	12	This chapter.
MWG 1 [b]	—	50	1.5 x 10^{10}	6.	0.5	24	Cox *et al.* (1986).
MWG 2	—	50	8.6 x 10^9	10.	0.9	50	Cox and Mezger (1988).
M31	690	60	2.6 x 10^9	34.	3.0	70	Walterbos and Schwering (1987).
M33	660	12	1.1 x 10^9	81.	7.0	33	Rice *et al.* (1988).
NGC 4449 [c]	5400	9.4	5.8 x 10^9	15.	1.3	32	Hunter *et al.* (1986).

Notes to Table 5:

a) *The ratio $\frac{12+25\mu m}{60+100\mu m}$ is defined as: $\frac{\Delta\nu_{12\mu m}\ f_{12\mu m}+\Delta\nu_{25\mu m}\ f_{25\mu m}}{\Delta\nu_{60\mu m}\ f_{60\mu m}+\Delta\nu_{100\mu m}\ f_{100\mu m}}$.*

b) *For the Milky Way Galaxy, two references are used: MWG 1 is based on pre–IRAS data of Cox et al. (1986), and MWG 2 is based on post–IRAS data of Cox and Mezger (1988). The luminosity ratio $\frac{12+25\mu m}{60+100\mu m}$ calculated as (hot dust)/(warm + cold + very cold dust) of Cox et al. gives 15 %.*

c) *Note that the total infrared luminosity of NGC 4449 is 3 times higher than given by Hunter et al. as a result of the different definitions of the quantity.*

Infrared luminosities for other Local Group galaxies are given by Walterbos and Schwering (1987) on M31, Rice *et al.* (1988b) on M33 and by Cox *et al.* (1986) for the Milky Way galaxy. The active giant irregular galaxy NGC 4449, which is a reasonably well studied galaxy with similar infrared properties as the Clouds, has been described by Hunter *et al.* (1986). The values of the Magellanic Clouds and these other galaxies are listed in Table 5. The fact that the Clouds and the Galaxy have higher star formation rates per unit total mass than M31 and M33, indicates that the 'hot'–flux component is not related to star formation. Although the star formation rate of the SMC is smaller than that of the LMC, the 'hot'–flux component is also smaller. Hence there is not a perfect anti–correlation. The Clouds have lower 12 and 25 μm emission relative to 60 and 100 μm than the other galaxies.

4. Large scale infrared structure of the Magellanic Clouds

4.1. Infrared morphology

In this section we examine the large scale infrared structure of the Magellanic Clouds. The IRAS Additional Observation (AO) maps, centered on the Clouds and convolved to a resolution of $8'$ are shown in Fig. 1 and 2. Grey scales emphasize lower emission levels. In general the infrared maps resemble the optical image of the Magellanic Clouds. We see diffuse infrared emission in both Clouds, especially at 60 and 100 μm, that extends beyond obvious active star formation regions. This is less the case in the 12 and 25 μm bands, where the extended emission is less bright. There is a wide range in infrared intensity values in all four bands. For each Cloud, the infrared maps at different wavelengths are very similar in appearance: they show the same low level diffuse emission and similar peaks at the HII regions. This indicates that at a scale of $8'$ the mechanism responsible for the infrared radiation in each of the four IRAS bands has the same spatial distribution. Relatively small differences between the infrared wavelength maps result from different colour–temperatures (*e.g.* stars – $T \sim 3000$ K). The main infrared components in normal galaxies are dust associated with HII regions, heated to high temperatures (30 – 50 K) and dust heated by the interstellar radiation field to temperatures of 20 – 25 K, mixed with the neutral HI gas. In the Milky Way galaxy Cox *et al.* (1986) have estimated that roughly 50 % of the infrared radiation comes from either component. Recently a third component is introduced, Polycyclic Aromatic Hydrocarbons (PAHs; Puget *et al.*, 1985) to explain the relatively strong IRAS 12 and 25 μm emission; these grains are also well mixed with the HI distribution (see Chapter VI).

We have calculated the contribution to the integrated infrared flux densities from unresolved sources from the infrared source lists from Chapters II and III (see Table 3). The point sources were found on the full resolution AO maps which have a much higher resolution at the 12 and 25 μm bands and a somewhat higher resolution at 60 μm compared to 100 μm. At higher resolutions unresolved sources are more easily recognized (less confusion with other sources and with backgrounds), hence at 12 and 25 μm we expect a larger number of point sources. The significantly higher point source contribution at 25 μm, is an indication that this band is more dominated by point sources than the other bands. The explanation is most likely a minimum in the diffuse extended emission at 25 μm. At 60 and 100 μm the cool–dust component dominates and has a spectrum increasing with wavelength, while the hot–dust component related to the diffuse infrared emission has a spectrum decreasing with wavelength. For the LMC the relative point source component at 12 μm equals that of 60 and 100 μm; in the SMC it is a factor of 2 higher. The point source contribution in the SMC is higher than in the LMC, indicating that the infrared emission of the SMC is more dominated by point sources than that of the LMC. The ratio of the flux densities of the point sources in the LMC and of that in the SMC is constant (~ 12) in all four bands.

Table 6. *Infrared properties of some selected areas in the LMC* [a].

Property (Unit)	Bar	Shapley	Doradus	Region	LMC	30 Doradus
		Const.III	Greater	South	Rest	beam(8′)
Equivalent area Ω	1.22	2.11	1.78	0.85	11.5	0.00425
(10^{-3} sr / %)	7	12	10	5	66	—
$f_{12\mu m}$ [b] (Jy)	760	550	1560	250	1730	207
$f_{25\mu m}$ (Jy)	1290	1100	5800	260	2850	1360
$f_{60\mu m}$ (Jy)	15400	11600	43500	2790	29800	5050
$f_{100\mu m}$ (Jy)	31400	24600	72800	9260	69900	4850
$\sigma_{12\mu m}$ [c] (MJy/sr)	0.62	0.26	0.88	0.29	0.15	49.
$\sigma_{25\mu m}$ (MJy/sr)	1.1	0.52	3.3	0.31	0.25	320.
$\sigma_{60\mu m}$ (MJy/sr)	13.	5.5	24.	3.3	2.6	1190.
$\sigma_{100\mu m}$ (MJy/sr)	26.	12.	41.	11.	6.1	1140.
$T_{12-25\mu m}$ [d] (K)	265	245	190	335	265	160
$T_{25-60\mu m}$ (K)	67	71	76	70	70	92
$T_{60-100\mu m}$ (K)	45	44	50	35	42	73

Table 7. *Infrared properties of some selected areas in the SMC* [a].

Property (Unit)	NE–Bar	SW–Bar	Shapley Wing	N 66 beam(8′)
Equivalent area Ω	3.06	2.96	1.75	0.00425
(10^{-3} sr / %)	39	38	23	—
$f_{12\mu m}$ [b] (Jy)	41	82	24	3.4
$f_{25\mu m}$ (Jy)	136	183	68	25.5
$f_{60\mu m}$ (Jy)	2670	3810	690	168.
$f_{100\mu m}$ (Jy)	5160	7350	1390	210.
$\sigma_{12\mu m}$ [c] (MJy/sr)	0.013	0.027	0.014	0.80
$\sigma_{25\mu m}$ (MJy/sr)	0.044	0.062	0.039	6.0
$\sigma_{60\mu m}$ (MJy/sr)	0.87	1.3	0.39	40.
$\sigma_{100\mu m}$ (MJy/sr)	1.7	2.5	0.79	49.
$T_{12-25\mu m}$ [d] (K)	200	240	220	160
$T_{25-60\mu m}$ (K)	62	62	72	78
$T_{60-100\mu m}$ (K)	46	46	45	60

Notes to Table 6 and 7:

a) *The areas given in these tables are defined by masking the visual areas. The Greater Doradus Region contains some weak infrared emission at the East side. The LMC Rest–area is the total LMC minus the Bar, Constellation III, the Greater Doradus Region and the area South of the Doradus Region. 30 Doradus is a part of the Greater Doradus Region. N 66 is a part of the SMC NE–Bar.*

b) *The flux densities f_ν have been obtained by summing intensities in the defined areas and correcting for a planar background.*

c) *The surface brightness σ_ν is obtained by dividing the integrated flux density in each area by the equivalent area.*

d) *Colour temperatures ($T_{\nu 1-\nu 2}$ assuming ϵ_ν to be independent of frequency) have been derived from the integrated flux densities in the areas.*

For a discussion of the LMC and its young stellar constituent, in particular the 30 Doradus region we refer to Feitzinger (1980). The infrared emission follows the large–scale filaments of star formation as described in Feitzinger *et al.* (1988). The LMC 12 and 25 μm maps show some bright (stronger than 3 Jy) Galactic foreground stars (SAO 249123; SAO 249138; SAO 249225, RX–Dor, LI–LMC 324 and LI–LMC 1623). The 60 and 100 μm bands of the LMC show Galactic emission in the SW edge (which unfortionately has a spectrum similar to that of cool LMC dust). Prominent objects in the four LMC infrared maps are the Bar and the Greater 30 Doradus region. Another HII region that shows up clearly is N 11 in the NW corner. The area surrounding Constellation III is a weak infrared emitting area and therefore Constellation III itself can be distinghuised very well. At the LMC's South side a sharp edge can be seen East of the 30 Doradus region. Also in other wavelength regions (*e.g.* HI observations of Mathewson and Ford, 1984) sharp edges are seen there. Here no low level emission areas are present in any of the four wavelength bands. The integrated properties of some selected areas of the LMC are given in Table 6. The Greater 30 Doradus region contains about 30 – 40 % of the total emission, somewhat more at 25 μm (50 %), while it contains only 10 % of the total LMC surface area. The area called Rest in Table 6, which contains the 66 % of the LMC surface not already in the other areas, is less bright at 25, 60 and 100 μm and has a similar brightness as the Greater Doradus region at 12 μm. The surface brightness is highest for the Greater 30 Doradus region, it is about nine times brighter than Rest. The Bar region is four times, and the region Constellation III is two times brighter than the Rest region. The area South of the 30 Doradus region is 2 times brighter than Rest at 12 and 25 μm and equally at 60 and 100 μm as Rest. Thus the region South has an infrared spectrum that resembles the diffuse emission (and Galactic cirrus) spectrum. The spectrum of the Rest region resembles the integrated infrared spectrum of the LMC.

In the SMC infrared maps we distinguish the Bar and the Wing; at 60 and 100 μm Bar and Wing are connected by diffuse emission. In the SMC the Bar and its HII regions N 66, N 76 and N 78 show up prominently in the infrared. A foreground star (LI–SMC 186) is seen at 12 μm between the Bar and the Wing with 2.6 Jy (see also Section 4.2). The SW part of the Bar has a very long line–of–sight (Mathewson *et al.*, 1986; van Genderen, 1981) and the observed peak in the infrared emission is therefore not completely unexpected. It may be produced by the combined effect of the larger column of dust in this direction, and the wider spread in line–of–sight temperatures, resulting in a higher average T_d. The HII regions in the Shapley Wing of the SMC are also prominent infrared emitting objects (especially N 83/84). Integrated properties for some individual areas are given in Table 7. The SMC–Wing is clearly weaker than the Bar in the infrared. The surface brightness in the SW–Bar is about 1.5 times that in the NE–Bar (2 times higher at 12 μm). The surface brightness in the NE–Bar is identical to that in the Wing at 12 and 25 μm, but two times higher at 60 and 100 μm. In the average temperatures we see no clear differences between the three regions.

4.2. Line–of–sight temperature distribution of the dust

Using the spectral response of the photometric bands (IRAS Explanatory Supplement, IRAS 1985a; Table II.C.5 therein) we have calculated tables with theoretical in–band fluxes (Watt m^{-2} sr^{-1}), flux densities (MJy/sr) and in–band ratios for a fixed amount of dust of temperature T_d (K) at a fixed distance. To calculate theoretical in–band fluxes and ratios we have assumed equilibrium blackbody radiation from the dust grains and an emissivity $\epsilon_\nu \propto \nu^{1.5}$ (for a complete discussion see the Appendix). We call this temperature, dust temperature, because we have used an emissivity.

From the band ratios of 60 and 100 μm we calculate the average temperature T_d of the dust along the line–of–sight, yielding the distribution of T_d over the face of the Clouds (Fig. 6). Intensity cut–offs have been applied in both bands at about three times the noise level to avoid noise blow up.

We see significant temperature variations over the face of the Clouds. From Fig. 6 we see three main dust temperature regimes:

(1) a low level extended regime with a temperature of about 22 – 28 K. This regime, which is related to the diffuse emission, is present especially at the edges of the LMC, where no HII regions are found. This regime contains 20 % of the LMC area with 11 % of the total flux; its size is negligible for the SMC. Its origin is probably dust heated by the general interstellar radiation field. Its detection in the central parts of the Clouds is hampered by the presence of warmer dust in the lines–of–sight (regimes 2 and 3).

(2) an intermediate, extended regime of about 28 – 32 K around the warm HII regions. Basically this regime is associated with HII regions, but is much more extended; also the LMC and SMC bars show up. This regime contains 68 % of the LMC area with 52 % of the total flux and 45 % of the SMC area with 23 % of the flux. Note that this regime is more difficult to separate from regime 3 in much farther galaxies due to the lower spatial resolution (see *e.g.* Walterbos and Schwering, 1987). Its origin is, first of all, a mixture of warm (regime 3) and cool dust (regime 1) in the line–of–sight and dust heated by the average Cloud radiation fields.

(3) warm infrared sources associated with HII regions (32 – 45 K, like *e.g.* 30 Doradus in the LMC). This regime contains only discrete objects, with the exception of the Greater 30 Doradus region. This regime contains 12 % of the LMC area with 37 % of the total flux and 55 % of the SMC area with 77 % of the total flux. The emission comes from dust in and close to HII regions.

In the LMC area South of 30 Doradus we find, in order, the HII regions N 158, N 160 and N 159 (Henize, 1956). Here, the line–of–sight temperature remains above 35 K. In the LMC–Bar the temperature is about 30 – 35 K, peaking in HII regions to values above 35 K and in N 11 37 K. The high stellar density in the Bar is the origin for this higher temperature. Around Shapley's Constellation III the temperature is also higher than in the global component (31 K). This constellation shows only weak infrared intensities and is known to have many stellar associations (Lucke and Hodge, 1970).

The dust temperature in the SMC (Fig. 6.2) ranges from 28 to 43 K. The average temperature regime in the Bar of the SMC is about 32 – 34 K. The dust temperature peaks just above 37 K in the HII regions N 66, N 76 and N 78, and in the HII regions in the Shapley wing N 81, N 83 and N 84; the compact nebula N 88 is the hottest with a peak temperature above 43 K. Between the Bar and the Wing the temperature is lowest, about 28 – 30 K; this area resembles a Galactic cirrus area. In the main body of the SMC there is only a small area with diffuse emission. In the SMC–Bar the high stellar density produces a strong radiation field which in its turn heats up the dust grains in the Bar to higher temperatures.

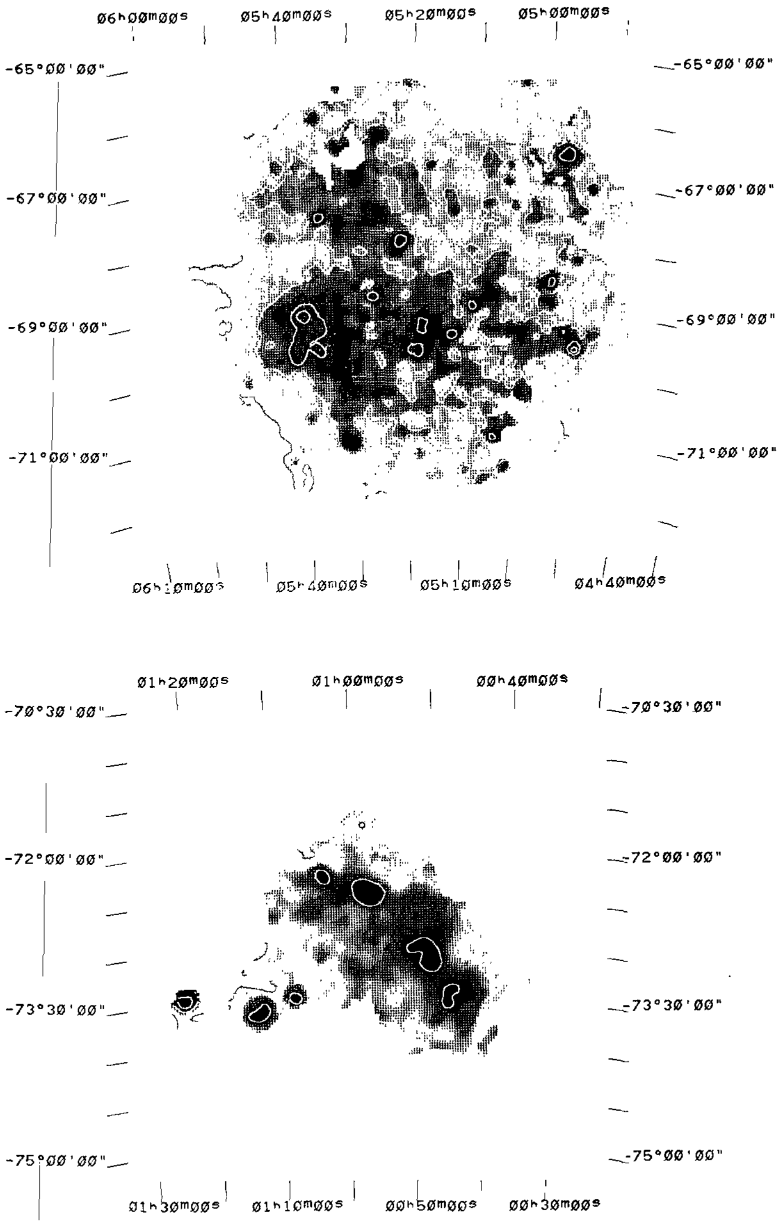

Figure 6. *Line–of–sight dust temperature distribution in the Magellanic Clouds deduced from the infrared maps at 60 and 100 μm at a resolution of 8′ and assuming a dust emissivity with a* $\lambda^{-1.5}$ *wavelength dependence. Intensity cut–offs at 2.5 x* 10^{-8} *Watt* m^{-2} sr^{-1} *have been applied to avoid noise blow–up.*

Fig. 6.1. Dust temperature map of the LMC. Darker grey scales indicate higher dust grain temperatures (22 – 43 K). Contours are at 25, 30, 35, 40 K.

Fig. 6.2. Dust temperature map of the SMC. Darker grey scales indicate higher dust grain temperatures (28 – 43 K). Contours are at 30, 35, 40 K.

Fig. 7.1 to 7.4 show the colour temperature distribution obtained from the 12 to 25 μm and from the 25 to 60 μm intensities for both Clouds. Colour temperatures are defined as the blackbody temperature that has the same intensity ratio between two frequencies as the observed ratio (because the emissivity is somewhat uncertain in this wavelength range we did not adopt an emissivity). The LMC maps have the following characteristics. The 12 – 25 μm colour temperature has a global hot component higher than 300 K; minima of 150 – 260 K occur in the HII regions like 30 Doradus and the maximum of about 350 K occurs in the area South of the Greater 30 Doradus region (this area is quite similar to Galactic cirrus). Three foreground stars, SAO 249225, LI-LMC 1623 and LI-LMC 324 (RX-Dor) peak at values of 800 K (lower than normal for stars due to beam dilution). For the 25 – 60 μm colour temperature we have a global component of 60 – 67 K over a large part of the LMC. HII regions peak at 70 – 90 K and in the region South of the Greater 30 Doradus region peaks are at 70 – 80 K. The maxima in these maps have a temperature of about 120 K and coincide with infrared sources LI-LMC 181 and 1100 (both W-type spectra, characteristic of hot dust shells; see Chapter III). Note that LI-LMC 181 was described by Elias *et al.* (1986) as a candidate OH/IR star. Their other candidate, LI-LMC 1341, also shows a peak in the 25 – 60 μm colour temperature map, just SW of N 160 in the Greater 30 Doradus region. A summary of line-of-sight temperatures is given in Table 8.

The characteristics of the SMC are as follows. In the 12 – 25 μm colour temperature map we see the SW-Bar (with a long line of sight and a high infrared intensity) with 150 – 200 K, maxima of about 200 – 280 K (at the edges some noise blow-up occurs due to the low-level 25 μm emission), while the HII regions again are coolests with 150 – 200 K. One foreground star, LI-SMC 186 shows up 800 K. The 25 – 60 μm colour temperature shows HII regions at 65 – 80 K and minima of about 58 – 66 K. Just North of the SW-Bar in the SMC at $\alpha = 00^h47^m$, $\delta = -73°07'$ we see a high dust temperature together with almost a minimum in the 25 – 60 μm colour temperature (at least much lower than normal HII regions). At this position the intensity drops very rapidly with decreasing wavelength. The SMC shows some 25 – 60 μm temperature peaks. A summary of characteristic line-of-sight temperatures is given in Table 9.

The Clouds average colour temperatures increase toward shorter wavelengths ($\partial T/\partial\lambda < 0$). This shows that the radiation at 12 and 25 μm is in excess over the cool dust emission (with $T_d \sim 33$ K) that is responsible for the infrared emission at 60 and 100 μm. For M31 Walterbos and Schwering (1987) found much more extreme values for the temperatures ($T_{60-100\mu m} = 24$ K, for $n = 1.5$; and $T_{12-25\mu m} = 380$ K) than we find for the Clouds. The diffuse emission areas in the Clouds have more similar temperature characteristics as M31.

Figure 7. *Line-of-sight colour temperature in the Magellanic Clouds deduced from the infrared maps at 12 and 25 μm and from the maps at 25 and 60 μm at a resolution of 8' (i.e. blackbody emission is assumed). In the LMC maps cut-offs have been applied at 1.5 x 10^{-8} Watt m^{-2} sr^{-1}, and in the SMC of 0.5 x 10^{-8} Watt m^{-2} sr^{-1}. See pages 174 – 175.*

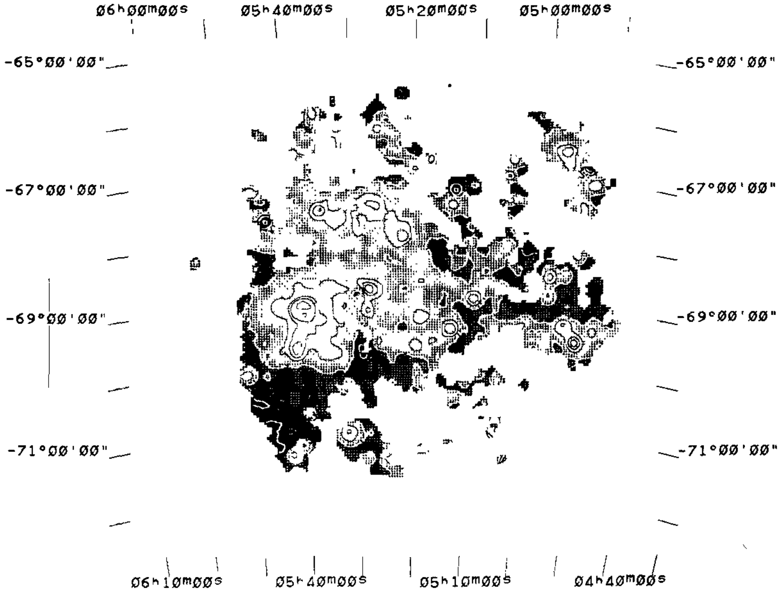

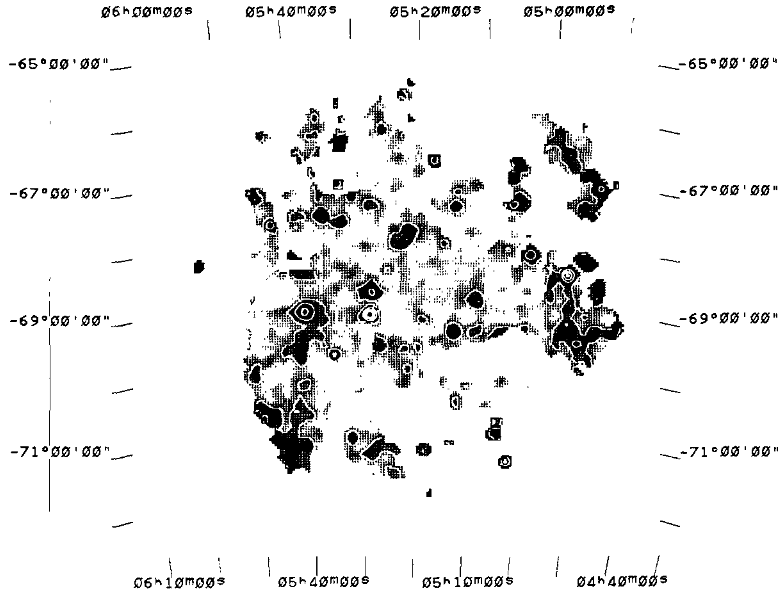

Fig. 7.1. LMC 12 – 25 μm colour temperature. Darker grey scales indicate higher colour temperatures (150 – 990 K). Contours are at 160, 180, 200, 240, 280, 320, 360, 400, 500, 600, 700, 800, 900 K.

Fig. 7.2. LMC 25 – 60 μm colour temperature. Darker grey scales indicate higher colour temperatures (58 – 170 K). Contours are at 60, 70, 80, 90, 100, 120, 140, 160 K.

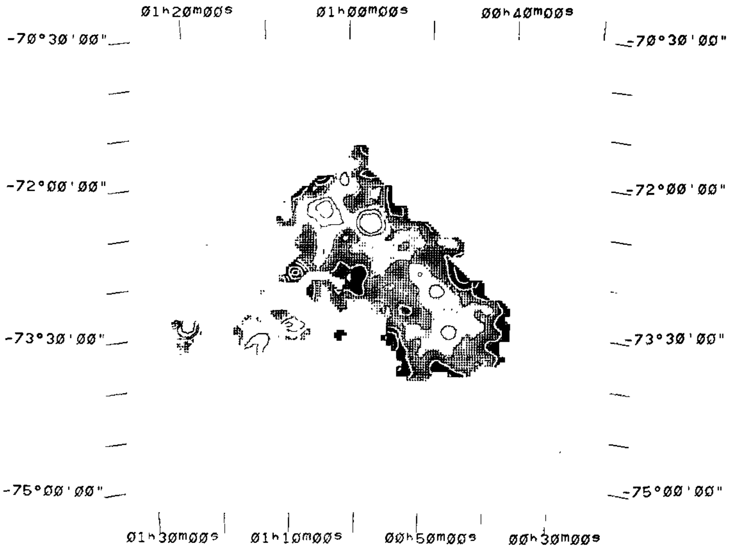

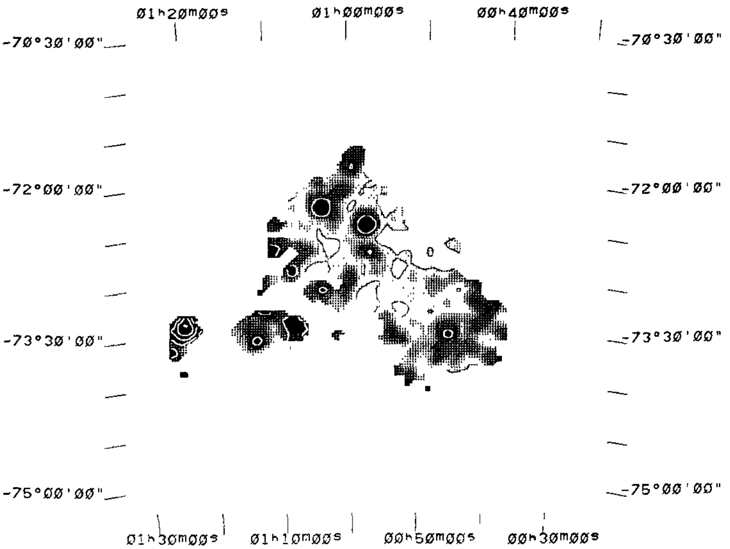

Fig. 7.3. SMC 12 – 25 μm colour temperature. Darker grey scales indicate higher colour temperatures (140 – 950 K). Contours are at 160, 180, 200, 240, 280, 320, 360, 400, 500, 600, 700, 800, 900 K.

Fig. 7.4. SMC 25 – 60 μm colour temperature. Darker grey scales indicate higher colour temperatures (55 – 110 K). Contours are at 60, 70, 80, 90, 100 K.

Table 8. *Dust temperatures for different areas in the LMC.* [a]

Object/Region Assumed emissivity	Area (%)	$T_{12-25\mu m}$ (K) ($\epsilon_\nu \propto \nu^0$)	$T_{25-60\mu m}$ (K) ($\epsilon_\nu \propto \nu^0$)	$T_{60-100\mu m}$ (K) ($\epsilon_\nu \propto \nu^{1.5}$)
HII regions	6	150 – 240	70 – 90	32 – 45
Intermediate component (around HII regions)	14	240 – 300	60 – 67	28 – 32
Diffuse emission	9	>300	70 – 80	22 – 28
LMC-Bar	14	240 – 280	67 – 74	30 – 35
LMC-Average	10	240 – 260	70 – 76	30 – 34

Table 9. *Dust temperatures for different areas in the SMC.* [a]

Object/Region Assumed emissivity	Area (%)	$T_{12-25\mu m}$ (K) ($\epsilon_\nu \propto \nu^0$)	$T_{25-60\mu m}$ (K) ($\epsilon_\nu \propto \nu^0$)	$T_{60-100\mu m}$ (K) ($\epsilon_\nu \propto \nu^{1.5}$)
HII regions	2	140 – 180	65 – 80	34 – 43
Intermediate component (around HII regions)	7	170 – 200	55 – 65	31 – 34
Diffuse emission	2	–	–	28 – 31
SMC-Bar	5	170 – 200	55 – 65	32 – 34
SMC-Average	8	220 – 240	60 – 66	31 – 35

Note to Tables 8 and 9:

a) The area that is characteristic for each component is given; hence the sum is less than 100 %.

Comparing the temperature distribution $T_{60-100\mu m}$ (Fig. 6) with the infrared intensity $I_{60\mu m}$ distribution (Fig. 1) we see that on scales of 135 pc ($8'$ resolution) the temperature distribution correlates well with the infrared intensity (an exception is Constellation III with a higher T_d and a relatively low infrared intensity). For thermal infrared emission we expect the intensity to go with a high power of the temperature ($I_\nu \propto T^{4+n}$) so that a correlation is to be expected. The effect is particularly visible in pixel-to-pixel scatter diagrams (see Fig. 8). At high values of $I_{100\mu m}$ the slope $I_{100\mu m}/I_{60\mu m}$ decreases, showing that higher intensities are related to higher temperatures. At $I_{100\mu m} = 20 - 30$ MJy/sr, the LMC diagram shows a clear change in slope. A large fraction of the infrared radiation has high dust temperatures and is related to the intermediate and warm temperature components.

At higher intensities (*i.e.* in and near HII regions) the 25/60 μm ratio map correlates well with infrared intensity. Discrepancies appear at lower intensity values (along the edges of the SMC–Bar; South of 30 Doradus in the LMC). In fact, at lower intensities there appears to be an anti-correlation between the 25 – 60 μm colour temperature and intensity. The 12 – 25 μm colour temperature distributions anti-correlate with infrared intensity at all intensity levels. This effect (already noticed on much larger scales in M31 by Walterbos and Schwering, 1987; in the Galaxy by Boulanger *et al.*, 1985; Boulanger *et al.*, 1988) is seen in the SMC maps and is more clearly present in the LMC maps. Therefore, we expect an anti-correlation of $I_{12\mu m}/I_{25\mu m}$ and $I_{60\mu m}/I_{100\mu m}$; hence also between $T_{12-25\mu m}$ and $T_{60-100\mu m}$. This expectation is confirmed by Fig. 9, which shows three types of colour-colour pixel-to-pixel scatter diagrams of the band ratios, in the same way as Helou (1986) did for integrated flux densities of a large sample of unresolved galaxies. Cut-offs in intensity were applied at 3 – 5 times the noise level to reduce noise blow-up effects. We find a similar relation as Helou, somewhat below his curve marked H. The importance of this diagram is that it connects the infrared structure of the Clouds to the integrated properties of the galaxies studied by Helou. The SMC diagram shows a lesser amount of cool 60 and 100 μm emission.

For HII regions the ratio $I_{25\mu m}/I_{60\mu m}$ correlates with $I_{60\mu m}/I_{100\mu m}$; for diffuse emission regions it correlates with $I_{12\mu m}/I_{25\mu m}$. We have already seen that the two ratios $I_{12\mu m}/I_{25\mu m}$ and $I_{60\mu m}/I_{100\mu m}$ anti-correlate. Thus in areas with low $I_{25\mu m}/I_{60\mu m}$ we do not expect to find typical diffuse areas nor HII regions, but merely the intermediate temperature regime (2). For the California Nebula, Boulanger *et al.* (1988) showed the colour temperatures as a function of the distance from the star. From their profiles we see the same effect: if $f_{25\mu m}/f_{60\mu m}$ is low neither $f_{12\mu m}/f_{25\mu m}$ nor $f_{60\mu m}/f_{100\mu m}$ are high. For the diffuse regions, the fact that $T_{60-100\mu m}$ correlates with $T_{12-25\mu m}$ suggests the possibility that very small grains (Puget *et al.*, 1985) contribute to the emission at 60 μm. In Chapter VI we find that 17 % (LMC) and 8 % (SMC) of the integrated 60 μm emission can come from small grains.

With a beam size of $8'$ we observe an overall correlation between infrared intensity I_ν and dust temperature T_d. On smaller scales a breakdown of this correlation might be possible. Indeed Werner *et al.* (1978) observed the 30 Doradus region at wavelengths of 30, 50, 100 and 200 μm with a smaller beam size ($1' = 15$ pc). They find that the temperature peak is anti-correlated with infrared intensity. Their resolution is about 8 times better than what we use here and the correlation that we found therefore seems to

Fig. 8.1. LMC $I_{12\mu m}$ – $I_{25\mu m}$.

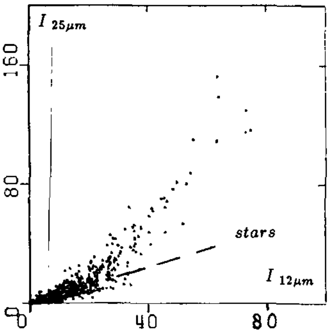

Fig. 8.2. LMC $I_{25\mu m}$ – $I_{60\mu m}$.

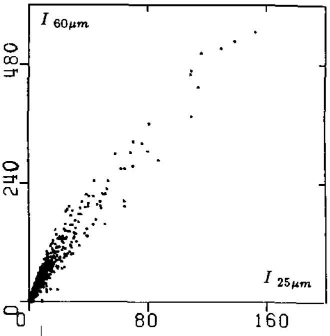

Fig. 8.3. LMC $I_{60\mu m}$ – $I_{100\mu m}$.

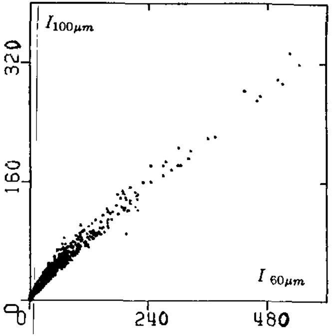

Fig. 8.4. SMC $I_{12\mu m}$ – $I_{25\mu m}$.

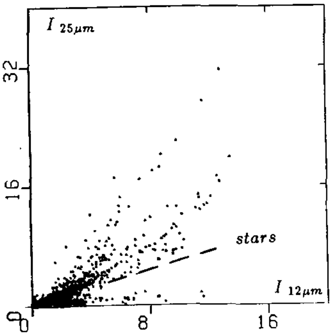

Fig. 8.5. SMC $I_{25\mu m}$ – $I_{60\mu m}$.

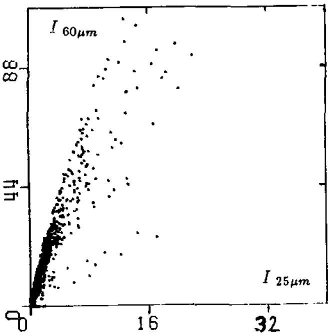

Fig. 8.6. SMC $I_{60\mu m}$ – $I_{100\mu m}$.

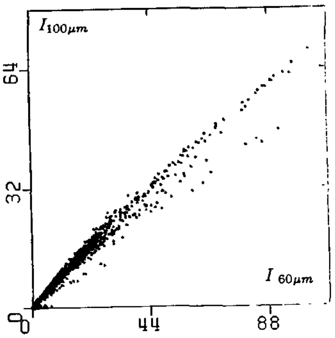

Figure 8. *Pixel–to–pixel scatter diagrams of adjacent IRAS bands for the Magellanic Clouds. For the LMC diagrams, pixels of 6′ were used; for the SMC diagrams, pixels of 3′ were used. Intensity units are in 10^{-8} Watt m^{-2} sr^{-1}.*

Fig. 9.1. LMC I_{60}/I_{100} - I_{12}/I_{25}.

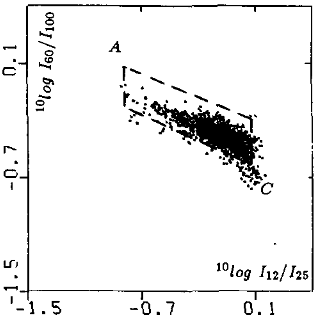

Fig. 9.2. LMC I_{60}/I_{100} - I_{25}/I_{60}.

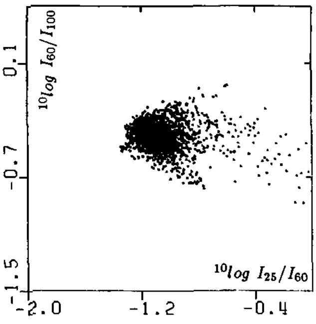

Fig. 9.3. LMC I_{25}/I_{60} - I_{12}/I_{25}.

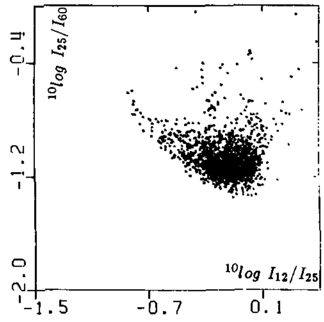

Fig. 9.4. SMC I_{60}/I_{100} - I_{12}/I_{25}.

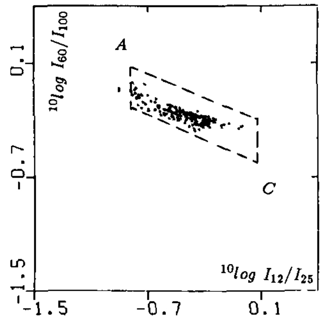

Fig. 9.5. SMC I_{60}/I_{100} - I_{25}/I_{60}.

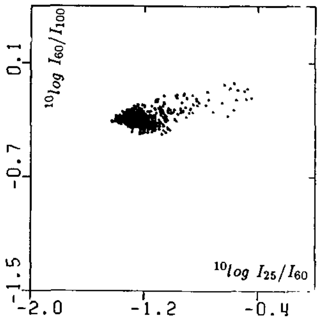

Fig. 9.6. SMC I_{25}/I_{60} - I_{12}/I_{25}.

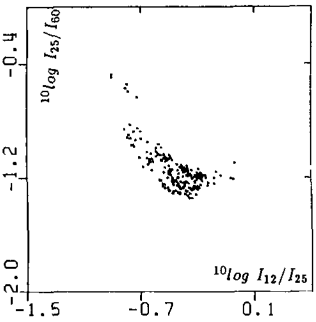

Figure 9. *Colour–colour diagram showing the relation between the intensity band ratios in the Magellanic Clouds; pixel-to-pixel values of $^{10}log\ (I_{\nu_1}/Jy\ sr^{-1})/(I_{\nu_2}/Jy\ sr^{-1})$ are shown. The resolution is 8′ and the pixel size is 3′ x 3′. The Cirrus (diffuse emission) point and the Active (HII region) point are indicated by C and A. The dashed box gives the position of integrated galaxy data (Helou, 1986).*

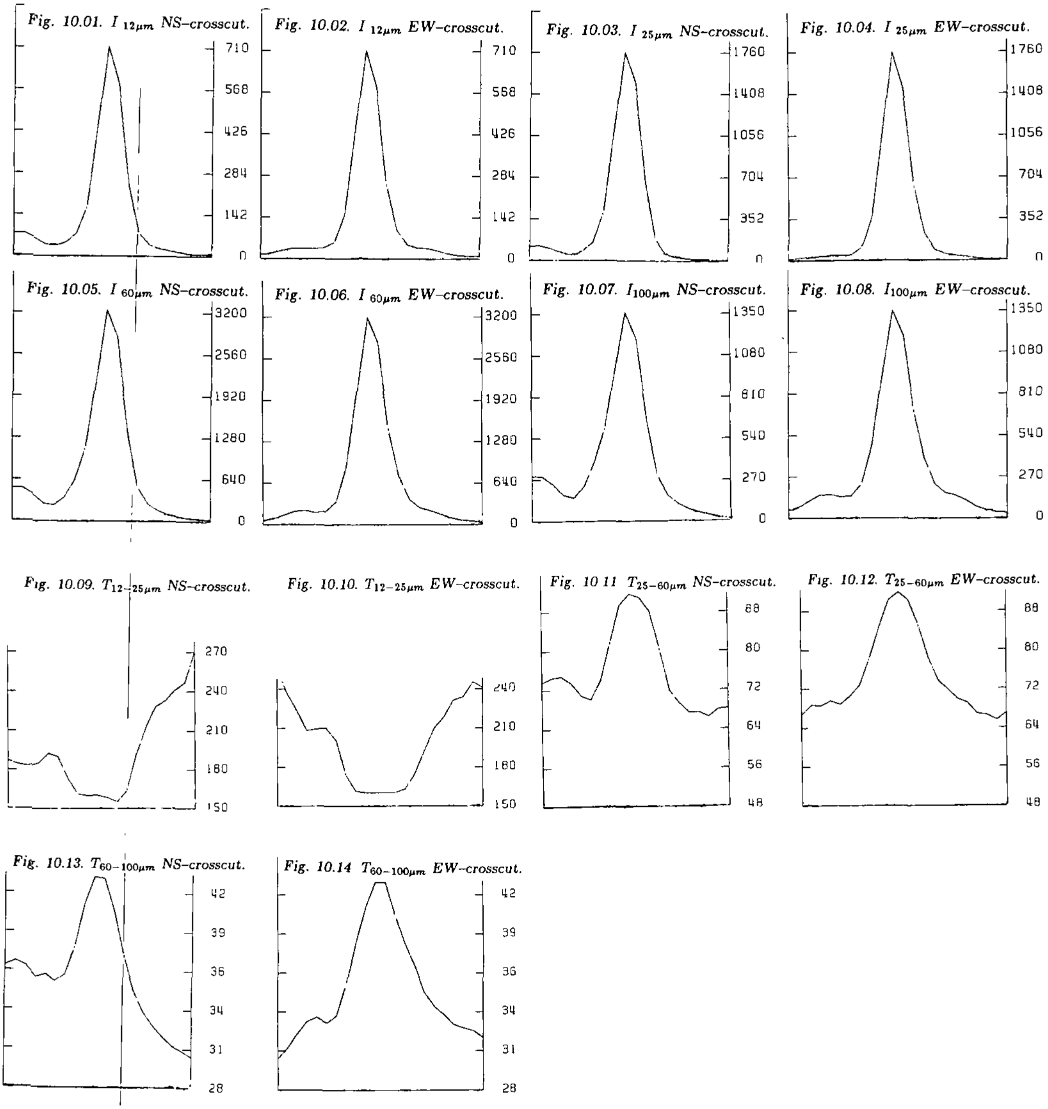

Fig. 10.01. $I_{12\mu m}$ *NS-crosscut.*

Fig. 10.02. $I_{12\mu m}$ *EW-crosscut.*

Fig. 10.03. $I_{25\mu m}$ *NS-crosscut.*

Fig. 10.04. $I_{25\mu m}$ *EW-crosscut.*

Fig. 10.05. $I_{60\mu m}$ *NS-crosscut.*

Fig. 10.06. $I_{60\mu m}$ *EW-crosscut.*

Fig. 10.07. $I_{100\mu m}$ *NS-crosscut.*

Fig. 10.08. $I_{100\mu m}$ *EW-crosscut.*

Fig. 10.09. $T_{12-25\mu m}$ *NS-crosscut.*

Fig. 10.10. $T_{12-25\mu m}$ *EW-crosscut.*

Fig. 10 11 $T_{25-60\mu m}$ *NS-crosscut.*

Fig. 10.12. $T_{25-60\mu m}$ *EW-crosscut.*

Fig. 10.13. $T_{60-100\mu m}$ *NS-crosscut.*

Fig. 10.14 $T_{60-100\mu m}$ *EW-crosscut.*

Figure 10. *30 Doradus cross cuts NS and EW in intensity and in temperature. Notice that the temperature values are much smoother than the intensity fall off. Units are in* 10^{-8} *Watt* m^{-2} sr^{-1} *for the intensity maps and in K for the temperature maps. In the EW diagrams E is left; in the NS diagrams S is left. The shown field size in all diagrams is 1°.*

be good at large scales but is an oversimplification at small scales of 15 pc. Jones *et al.* (1986), using NASA's KAO at 50 and 100 μm with 40$''$ (= 10 pc) resolution, observed a mild peaking of temperature (45 K) in N 158 and N 159 on the peak infrared intensities, and this effect showed up even more strongly in the compact HII region N 160A. The HII regions observed by Jones *et al.* are much smaller than 30 Doradus and are not resolved by them. This confirms the above conclusion.

Fig. 10 contains NS and EW crosscuts through the 30 Doradus area. The intensity maps show sharp peaks at 30 Doradus, but the temperature peaks are much broader. This illustrates the much smoother distribution of the dust and colour temperatures compared to the distribution of the infrared emission in this region. It also shows the anti–correlation of the 12 – 25 μm colour temperature with the infrared emission. Note the differences in the NS and EW crosscuts. The NS cuts pass through the active region (with N 158 and N 160 South of 30 Doradus), while the EW cuts only show the 30 Doradus peak.

4.3. Comparison of infrared radiation with Hα /HI supergiant shells

The SMC and LMC supergiant shells (SGS) described by Meaburn (1980) show up in the infrared data (see also Chapters II and III). The clearest example of these shells, LMC–SGS 4, is also detected in HI (Rohlfs *et al.*, 1984), and was already noted by Westerlund and Mathewson (1966). In the infrared we clearly detect SMC–SGS 1, and LMC–SGS 1, 2, 4 and 5. All these shells show enhanced infrared emission on top of diffuse infrared emission. The supershells have sizes in the order of 600 – 1400 pc and are not spherical. Their circumferences are places of recent star formation; LMC–SGS 4 contains many HII regions (Davies *et al.*, 1976), OB associations (Lucke and Hodge, 1970) and giant (< 300 pc) shells (Meaburn, 1980). Not all shells are clearly detectable in the infrared; two others are possibly detected, LMC–SGS 3 and 6, and LMC–SGS 9 shows only infrared emission at the East edge. LMC–SGS 7 and 8 are within the complex infrared background of the LMC are cannot be distinguished.

In Fig. 11 we show maps of the relation of the 100 μm infrared intensity, the line–of–sight temperature distribution and dust column density distribution (Chapter VI) of the LMC in grey scales overlayed with the outline–contours of the supergiant shells (Meaburn, 1980). Note the correspondence between the infrared and column density of dust with the supergiant shells, especially LMC–SGS 4. Note the global agreement of dust temperature with the shells. The temperature near the edges of LMC–SGS 4 is clearly higher than in the cool interstellar medium. However, there is no clear tendency for the dust temperature to follow the perimeter exactly; the temperature is higher in a much larger area, inside and outside the shell. Although LMC–SGS 4 is a very bright shell in the infrared, we are not able to recognize it on the basis of the line–of–sight temperature map. This suggests that the higher infrared emission at the perimeter, compared to the inside region, is mainly a dust mass effect. Similar, but less clear, correlations as for LMC–SGS 4 are found for the other shells.

4.4. The density of the Interstellar radiation field

We estimate the density of the interstellar radiation field in the Magellanic Clouds from the line–of–sight dust temperatures T_d. The energy absorbed each second by a single dust grain, $W_a = \int_0^\infty 4\pi J_\nu \sigma_\nu d\nu$, in equilibrium equals the emitted energy per second at

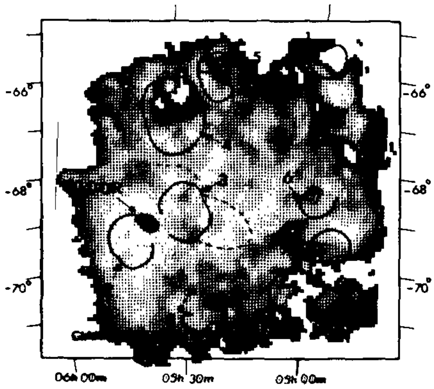

Fig. 11.1. $I_{100\mu m}$ *and SGS outlines.*

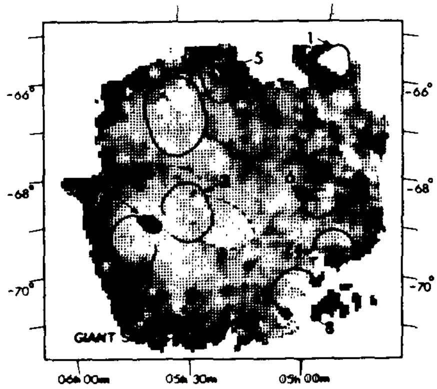

Fig. 11.2. T_d *and SGS outlines.*

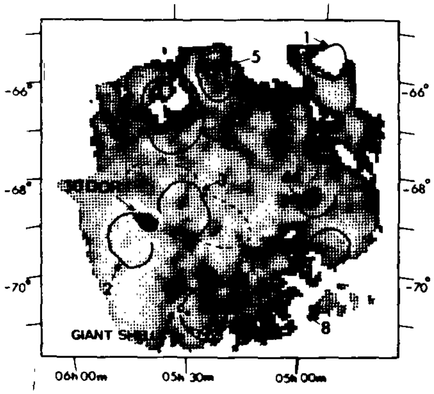

Fig. 11.3. M_d *and SGS outlines.*

Figure 11. *The relation between the LMC's 8′ infrared map, the line–of–sight dust temperature map and the dust column density map (all in grey scales) with the supergiant Hα shells (SGS contours) of Meaburn (1980). Lighter grey scales indicate higher levels.*

the observed dust temperature, $W_e = \int_0^\infty 4\pi B_\nu(T_d)\sigma_\nu d\nu$. We have used the absorption cross-section σ_ν as given by Cox *et al.* (1986). The average interstellar radiation field we use is a scaled version of the Solar Neighbourhood field: $J_\nu = \chi\ J_{\odot;\ \nu}$ as given by Mathis *et al.* (1983). We calculated an equilibrium temperature for this field of 16 K. From calculations with other absorption cross sections and radiation fields (de Vries, 1986) equilibrium temperatures of 15 ± 5 K are found. Note that the equilibrium temperature of dust in the diffuse interstellar medium is about 25 K (*e.g.* Boulanger and Perault, 1987). From this we obtain the factor χ, the ratio of the Clouds local interstellar radiation field and the average Galactic interstellar radiation field. From the temperature maps shown in Fig. 5 we see that the average radiation field in the Clouds must be much stronger than the Solar Neighbourhood field. In view of the large difference between the observed Solar Neighbourhood field and the measured dust temperatures, we normalize the field at a level of 25 K; hence a 10 times higher level. The coolest dust observed in the SMC has temperatures of 27 K, and in the LMC of 22 K; hence those radiation fields will have $\chi \approx 1$.

Fig. 12 shows the spatial distribution of the radiation fields (qualitatively these are similar to the dust temperature maps). At the outer edges we find, after the re-normalisation, the lowest values $\chi \approx 1$; peaks occur of $\chi \approx 10$ in average HII regions, up to 20 in the brightest HII regions as 30 Doradus in the LMC and N 66 and N 88 in the SMC. For the Galaxy van der Kruit (1986) estimates the total disk surface brightness 5 times higher than the local value of 20 $L_{\odot,B}/\mathrm{pc}^2$. The integrated Clouds temperatures of 33 K leads to a average value of $\chi \approx 7$. Hence, the total Galactic value is quite similar to the total Clouds value. Note that we have derived the absorbed part of the ultraviolet radiation field. Due to the influence of the line-of-sight on the dust temperatures the radiation fields may be higher than the average fields in the line-of-sight.

5. Comparison of infrared emission with data at other wavelengths

Ultraviolet radiation from OB stars is the most important heating agent for dust. Radiation in the visible also contributes, but much less. Calculations of the absorption of photons in the interstellar radiation field show that more than 95 % of the energy comes from photons with 900 Å $< \lambda <$ 3000 Å. In this section we compare the observed infrared data with three tracers of the OB stellar distribution: (1) the observed ultraviolet radiation gives us this distribution directly; (2) Hα emission is due to ionisation by OB stars; (3) thermal radio continuum of the ionized medium around OB stars. The last two give indirectly positions of the OB stars. The comparisons of infrared data with ultraviolet and Hα emission is influenced by sensitivity and extinction.

5.1. Comparison of infrared with ultraviolet radiation from the LMC

If we neglect scattering effects, the measured ultraviolet radiation is that part of the ultraviolet radiation emitted by the stellar population of the LMC that is not absorbed by interstellar dust. In the Galaxy infrared radiation is mainly caused by dust embedded in extended low density HII regions and by dust heated by the general interstellar radiation field (Mezger *et al.*, 1982; Cox *et al.*, 1986; Cox and Mezger, 1988). Hence the absorbed ultraviolet radiation is, together with absorbed visual radiation, directly related to the

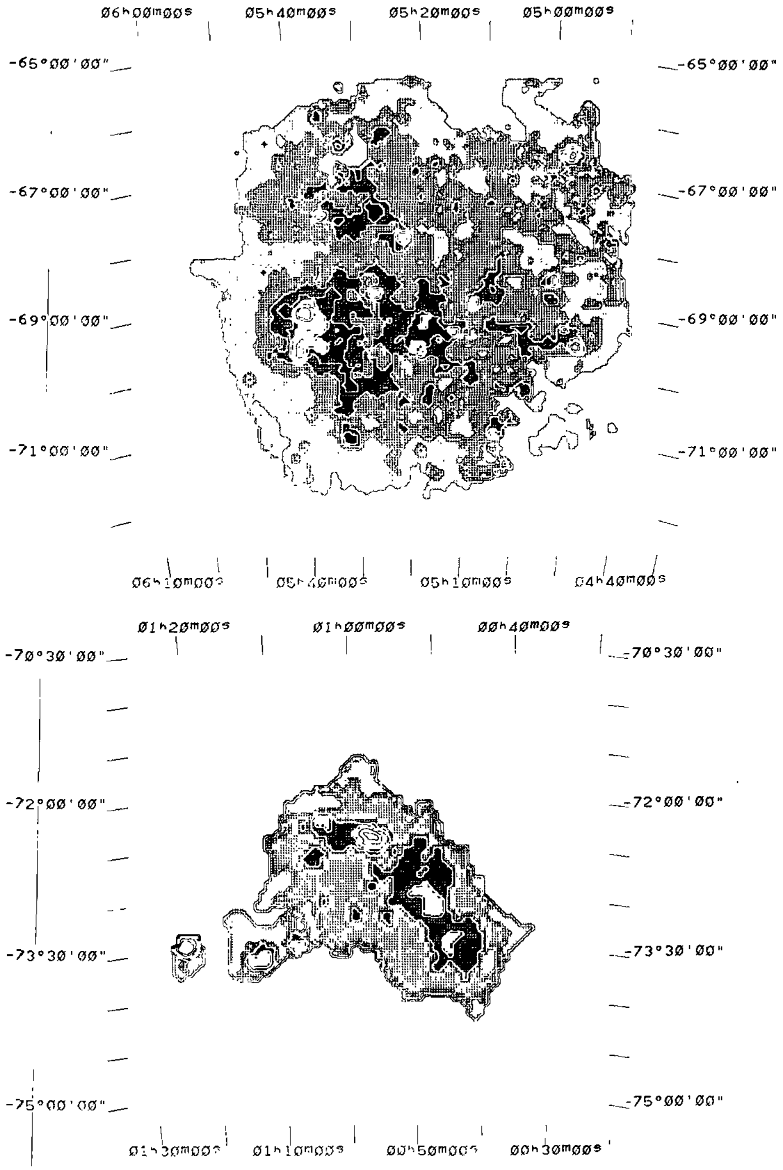

Figure 12. *Radiation fields in the Magellanic Clouds, expressed in terms of the average interstellar radiation field (after re-normalisation to $T_d = 25$ K). Grey scales range from 0 – 10, contour levels are at 1, 3, 5, 7, 9, 15, 20. The resolution is 8'.*

Fig. 12.1. Radiation field density in the LMC.

Fig. 12.2. Radiation field density in the SMC.

infrared emission that IRAS measured. In general $E(UV)_{abs} + E(UV)_{obs} = E(UV)_{emitted}$. On large scales we may assume that dust densities are constant, and that the heating agents (OB stars) are distributed homogeneously. In that case, the absorbed fraction of the ultraviolet radiation field is derived from the observed infrared emission, and the remainder is observed directly. The amount of infrared emission in the Clouds is available from the foregoing. Also, ultraviolet data on the Clouds are available from spacecrafts and balloon platforms. Thus, we can in principle determine the total emitted ultraviolet radiation field strength in the Clouds. In Section 4.4 we discussed the radiation field of the absorbed ultraviolet component.

Vangioni–Flam *et al.* (1980) published integrated ultraviolet flux densities at 1690, 2200 and 3100 Å from low resolution 1° x 3° data previously published by Maucherat–Joubert *et al.* (1980). Studies of ultraviolet observations covering a large part of the LMC with spatial resolution of $3' - 5'$ were made by Carruthers and Page (1977), Page and Carruthers (1981), with the Apollo 16 Far–ultraviolet camera/spectrograph on the moon (1050 - 1600 Å and 1200 - 1600 Å). A recently published study by Vuillemin (1988) shows a Skylab 2600 Å LMC map with a angular resolution of $4' - 5'$. These ultraviolet studies show us the concentrations of hot OB stars. Detailed ultraviolet data were obtained by Koornneef (1977) in the Greater 30 Doradus region with the Astronomical Netherlands Satellite ANS.

For a comparison of infrared with ultraviolet the observations of Vuillemin (1988) are very well suited; they cover only the SE–half of the LMC. In Fig. 13 we show an overlay of the infrared 60 μm intensity map and the line–of–sight dust temperatures, as grey scales, with the ultraviolet iso–contours of Vuillemin (1988). There is a global correspondence of the infrared and ultraviolet maps. The ultraviolet maps show the Greater 30 Doradus region and the LMC–Bar surrounded by some extended emission; N 11 and Constellation III are also strong UV emitters. Weak extended emission is visible on the published UV maps, but does not cover the extend of the infrared emission. On smaller scales there are differences, as might be expected from variations in dust density. Dust concentrations are expected to be associated with young star forming regions, which also represent concentrations of ultraviolet producing OB stars. The brightest UV point in the LMC is not the 30 Doradus HII region, but association 41 (Lucke and Hodge, 1970; in HII region N 119) in the LMC–Bar. In the infrared the 30 Doradus peak is much brighter than any other point in the LMC, 10 - 30 times brighter than N 119. Extinction measurements of Caplan and Deharveng (1983) show larger dust contents in the 30 Doradus region than in the area of N 119 in the Bar. This can explain the difference in relative observed ultraviolet radiation in these two regions.

The line–of–sight dust temperature map (Fig. 13.2) correlates better with the ultraviolet map than the infrared intensities (Fig. 13.1). Because the radiation field derived in Section 4.4 is directly related to dust temperatures, the relation between ultraviolet radiation and the radiation field needed to produce the infrared emission are also well correlated. The lowest UV–contour 0 (at 1.52 x 10^{-14} erg cm^{-2} s^{-1} Å^{-1}) of Vuillemin (1988) corresponds to a UV intensity of 0.040 MJy/sr and is enclosed by the dust temperature level of 31 K ($\chi \approx 4$ in Section 4.4). The 3 times higher UV–contour labeled 2 entirely fits in temperatures above 34 K ($\chi \approx 8$); the 5 times higher UV–contour labeled 4 above 36 K ($\chi \approx 11$). Some ultraviolet emission peaks do not correlate at these

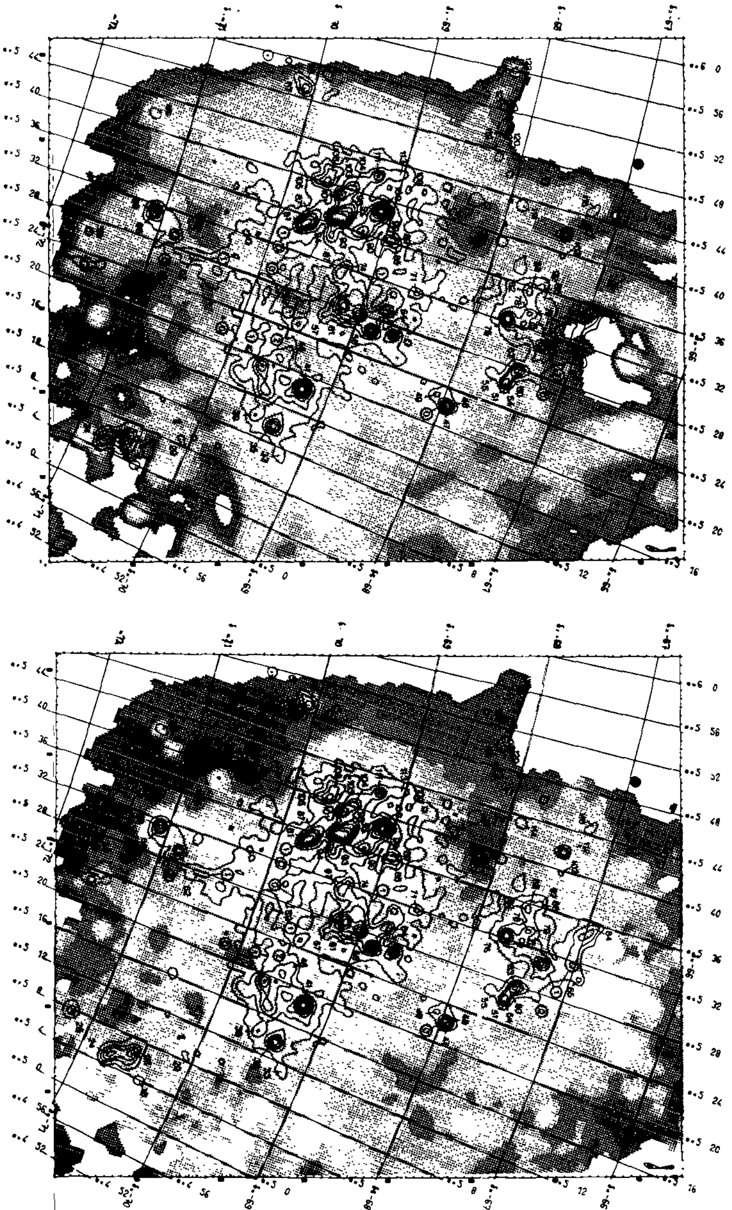

Figure 13. *The relation between the LMC's infrared emission and line-of-sight dust temperature distribution as grey scales with 8′ resolution, and the ultraviolet iso-contours (Vuillemin, 1988). Lighter grey scales represent higher intensities or temperatures. The labels of the contours are explained in Vuillemin (1988).*

Fig. 13.1. $I_{60\mu m}$ and *UV isocontours.*

Fig. 13.2. T_d and *UV isocontours.*

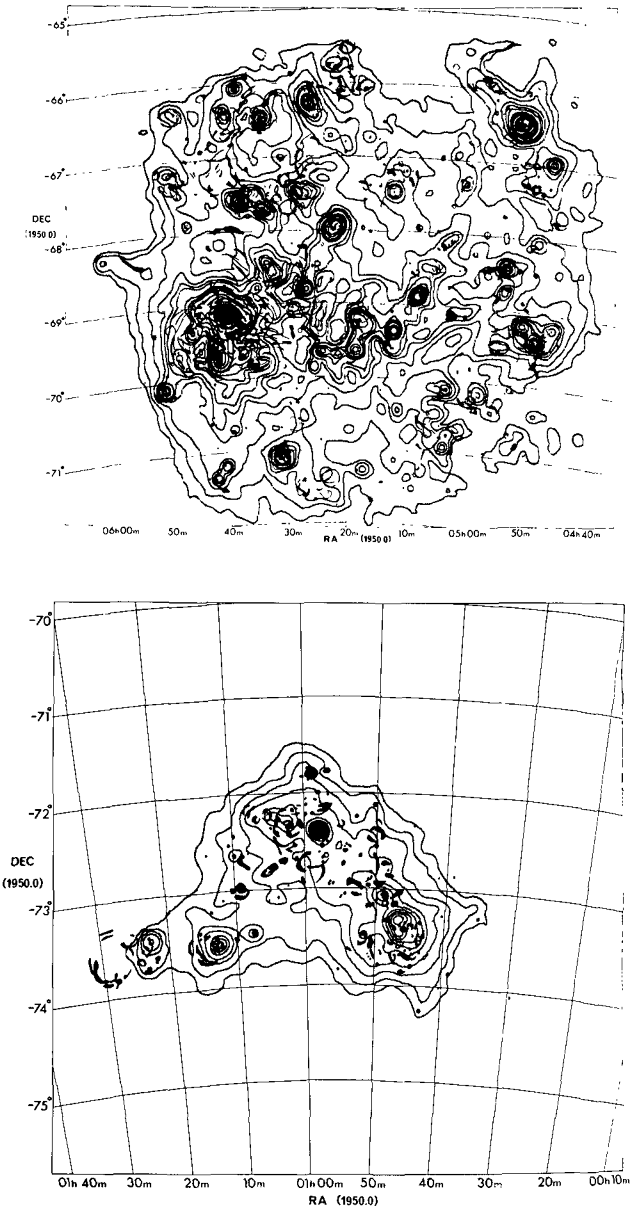

Figure 14. *The relation between the 8′ infrared 60 μm contour maps and the Hα nebulosities (dark areas) obtained by Davies et al. (1976).*
Fig. 14.1. The LMC.
Fig. 14.2. The SMC.
Note the incomplete infrared coverage of SMC–SGS 1 in the SE.

higher levels. Nine clear UV peaks fit well in the temperature maps, while on the other hand Lucke and Hodge association numbers 57, 61 (both in the Bar), 76, 63 (both in Constellation III) and 69 do not fit. From this comparison we conclude that there is good global correlation of infrared emission and especially dust temperature and its heating field with ultraviolet emission. OB stars are the most important heating agents.

We now look at the ultraviolet radiation field. We used the integrated 1690 Å data of Vangioni-Flam *et al.* (1980) and compared it to the Solar Neighbourhood (1 kpc^2). We corrected the integrated Clouds' data for the sizes and obtained for the LMC a similar field as for the Solar Neighbourhood. For the SMC the average field is 3 times stronger. After UV extinction correction, Vangioni-Flam *et al.* (1980) derived intrinsic fields of 4 (LMC) resp. 5 (SMC) times stronger than the Solar Neighbourhood. From the emitted ultraviolet and infrared, we need intrinsic fields of 8 times (LMC) and 10 times (SMC) the Solar Neighbourhood field. These numbers are 2 times higher, and suggest that corrections based on $A_\lambda = k_\lambda E_{B-V}$ underestimate the intrinsic ultraviolet emission. The uncertainties in the derivations of of the intrinsic field are possibly of the same order.

5.2. Comparison of infrared radiation with Hα emission

HII regions are formed around hot O- and B-type stars, and have much more intense radiation fields than the average interstellar medium. We therefore expect an indirect relation between Hα emission and infrared emission. Integrated Hα luminosities of the Clouds are given in Table 4. A detailed correlation of infrared sources with HII regions is given in Chapters II and III. We now compare the overall infrared maps with Hα maps.

From Hα plates presented by Davies *et al.* (1976) and Kennicutt and Hodge (1986) we see that there is less diffuse Hα emission than infrared emission. In Fig. 14 we present overlay images of the Hα nebulosities (Davies *et al.*, 1976) and the 60 μm infrared radiation from the Clouds. We see that the infrared emission correlates very well qualitatively with the Hα emission, especially at higher intensities. There is also a good correlation of the Hα maps with the dust temperature map (compare Fig. 6 and Fig. 14).

The total infrared luminosity for Magellanic Clouds HII regions covers a wide range. The 30 Doradus peak is over 10 times more luminous than other, more representative regions. Although the presence of HII regions is indicated by strong infrared emission, the strength of the infrared emission is possibly not a good characterisation for HII regions.

5.3. Comparison of infrared with radio continuum radiation

Radio continuum radiation is produced by two mechanisms. The first one is thermal free-free emission and has a weak frequency dependence. It is associated with the young stellar population. The second mechanism is non-thermal radiation with a stronger frequency dependence and associated with the old stellar population (Sancisi and van der Kruit, 1981; Hummel, 1981) or with the young stellar population (Lequeux, 1971; Klein, 1982; Kennicutt, 1983). Galaxies show a combined spectrum of thermal radio continuum (relatively stronger in the HII regions) and non-thermal emission (relatively stronger in the extended disk). Several of these studies comment on a good large scale correlation between both thermal and non-thermal radio continuum emission.

In Fig. 15 we present overlays of the 60 μm infrared contour maps with the 21-cm radio continuum grey scales maps of Haynes *et al.* (1986). In the radio continuum maps

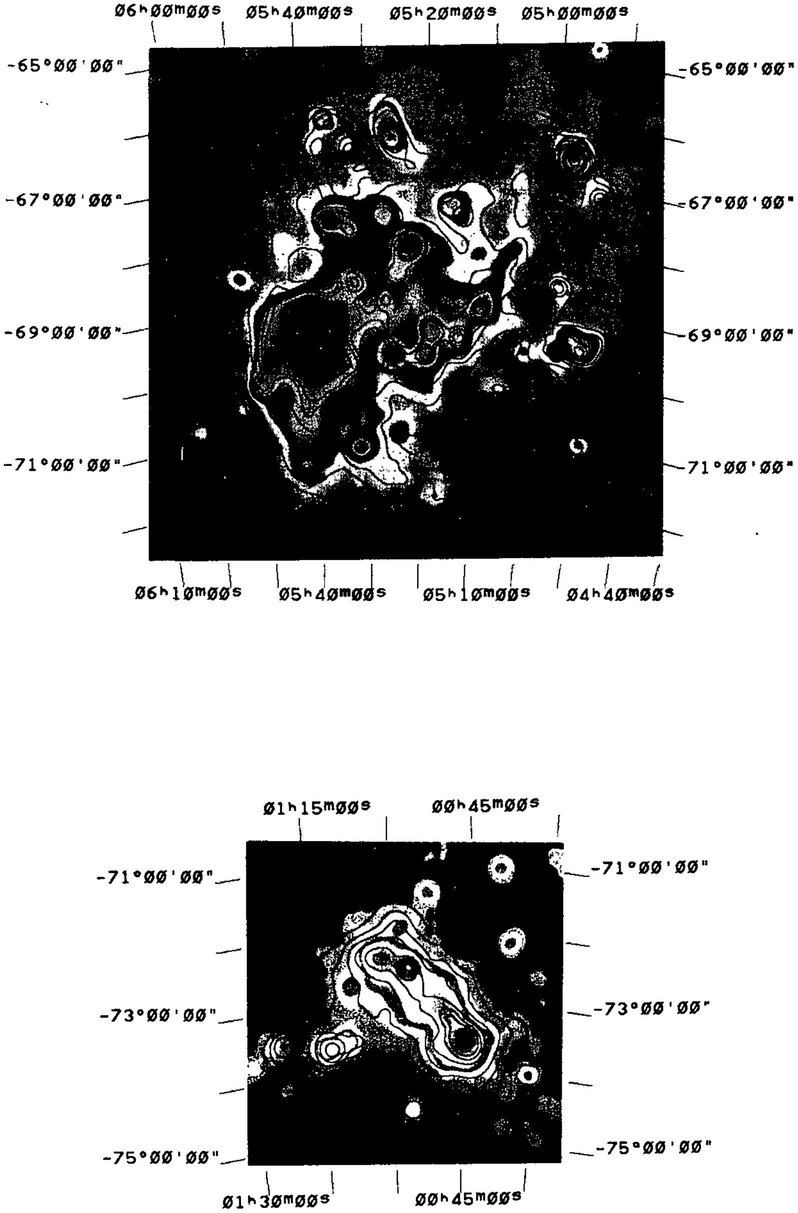

Figure 15. *The relation between the infrared 60 μm contour maps at 15' and similar resolution radio continuum grey scales maps of Haynes et al. (1986). The higher radio intensities are lighter, via a saw–tooth.*
Fig. 15.1. The LMC.
Fig. 15.2. The SMC.

some background sources are present. The SMC infrared maps show a similar size as the non–thermal 21–cm radio continuum disk. The infrared LMC emission area is somewhat smaller than the 21–cm 0.1 Jy/beam contour. On the IRAS Skyflux maps the 100 μm emission covers the same area as the radio continuum in the North; but near the South end, Galactic infrared foreground filaments are projected on top of the LMC.

The IRAS infrared maps follow the radio continuum maps very well (see also Feitzinger *et al.*, 1988); qualitatively these two maps correlate better with each other than the infrared correlates with the Hα or ultraviolet data. The dust temperature also corresponds well with the radio continuum peaks. The influence of the lower sensitivity and the extinction on the ultraviolet and Hα data are the main reasons for the correlation differences with infrared emission compared to the radiocontinuum maps.

In the SMC there is a bright radio source in the Wing, just East of N 83 (number 21, at $01^h09^m18^s, -73°30'00''$; in the list of Haynes *et al.*, 1986) which does not show up in the infrared. This may indicate that this radio source is a background galaxy.

6. Conclusions

We have presented low resolution (8′) infrared maps of the Large and Small Magellanic Clouds (LMC and SMC) at 12, 25, 60 and 100 μm. We have derived integrated infrared flux densities (Table 3). These integrated flux densities are sensitive to the background determination. Galaxies with similar infrared luminosities as the LMC are detectable up to distances of 27 Mpc; galaxies as the SMC up to about 8 Mpc.

The spectrum of the LMC is much like that of the SMC and of the irregular galaxy NGC 4449 (which is 4 times brighter); they represent warm dust spectra of 33 K. The nearby spiral galaxies M31 and M33 have cooler infrared spectra, and show higher mid–infrared (12 and 25 μm) excesses. The SMC shows a very small mid–infrared excess (15 %), while the LMC shows the same excess as NGC 4449 and M33, but a lower $f_{12\mu m}/f_{25\mu m}$ ratio than M33. The infrared sizes are resp. $6\overset{\circ}{.}6$ and $2\overset{\circ}{.}4$, which is a factor of two smaller than the cloud size for deep visual images. The infrared luminosities for the LMC are 12 times higher than for the SMC, representing a factor of 6 in 12 and 25 μm surface brightness and 3 in 60 and 100 μm surface brightness. The extrapolated total infrared luminosity of the LMC is 9 x 10^8 $L_\odot$ and that of the SMC is 8 x 10^7 $L_\odot$. For the LMC 23 % of the stellar emission is re–emitted in the infrared, for the SMC this is 10 %. The luminosity–to–mass ratios are 1.3 and 0.12 $L_\odot/M_\odot$ for LMC and SMC, as compared to 1 $L_\odot/M_\odot$ for the Solar Neighbourhood.

The four infrared maps follow the optical emission of the Clouds; they are very similar. The 25 μm band shows a much higher percentage of point source contribution to the total infrared flux density, than the other three bands, in effect reflecting the minimum at 25 μm of the extended emission. The total flux density of unresolved sources in the LMC is 12 times higher than in the SMC, proportional to the ratio of the integrated flux densities. The Greater 30 Doradus region contains about 40 % of the total infrared emission of the LMC. The amount of low level extended emission in the SMC is relatively small. The line–of–sight dust temperature in the Clouds correlates well with the line–of–sight infrared intensities. Although the maps of T_d have steep gradients, there are in general three temperature regimes (HII–region warm–dust; diffuse cool–dust; intermediate). The

$T_{60-100\mu m}$ temperatures are 22 – 28 K for the diffuse component, 28 – 32 K for the intermediate and 32 – 45 K for the HII region component in both galaxies. The temperature derived from the ratio of 12 and 25 μm, $T_{12-25\mu m}$, is anti-correlated with infrared intensity and with $T_{60-100\mu m}$, while $T_{25-60\mu m}$ correlates with $T_{60-100\mu m}$ for hot areas (and anti-correlates with $T_{12-25\mu m}$) and anti-correlates with $T_{60-100\mu m}$ for cool areas (and correlates with $T_{12-25\mu m}$).

The dust temperature decreases with increasing wavelength ($\partial T/\partial\lambda < 0$). This shows that there is excess infrared emission at 12 and 25 μm compared to the 'cool'-dust component responsible for the 60 and 100 μm emission (see Chapter VI). We found infrared emission related to a number of Hα supershells. The energy density of the interstellar radiation field in diffuse emission areas of the Clouds is about equal to the average Galactic interstellar radiation field (Mathis *et al.*, 1983). In the HII regions a difference is found of a factor of 10 – 20. From the infrared emission we derive 7 times stronger (absorbed) radiation fields in the Clouds than the local Galactic field, and about similar to the total Galactic field. Taking into account the emitted ultraviolet radiation, the total fields become 8 (LMC) and 10 (SMC) times stronger then the Solar Neighbourhood field.

The infrared radiation correlates well with other tracers of OB star distribution (ultraviolet radiation, Hα nebulosities and radio continuum). The ultraviolet radiation strength is well correlated with dust temperatures. The Hα and radio continuum distribution, both related to HII regions and a global component, have the same distribution over the face of each Cloud as the infrared intensity. The correlation between infrared and radio continuum is better than between any of the other data, largely reflecting sensitivity and extinction effects.

References

van Albada, G.D., Baud, B., de Pagter, P.J., Pol, W., Renes, J.J., Wesselius, P.R.: 1985, ROG Internal Report

van den Bergh, S.: 1981, *Astron. Astrophys. Suppl.* **46**, 79

Boulanger, F., Baud, B., van Albada, G.D.: 1985, *Astron. Astrophys.* **144**, L9

Boulanger, F., Perault, M: 1988, *Astrophys. J.* submitted

Boulanger, F., Beichman, C.A., Désert, F.X., Helou, G., Perault, M., Ryter, C.: 1988, *Astrophys. J.* in press

Braun, R.: 1985, Ph.D. Thesis, University of Leiden, p35

Caplan, J., Deharveng, L.: 1983, *ESO messenger* **32**, 3

Carruthers, G.R., Page, T.: 1977, *Astrophys. J.* **211**, 728

Caspers, H.C.M.: 1987, in *"Starbursts and Galaxy Evolution"*, eds. T.X. Thuan, T. Montmerle, J. Tran Thanh Van, Editiones Frontères, Gif-sur-Yvette, 173

Chini, R., Kreysa, E., Mezger, P.G., Gemünd, H.-P.: 1984, *Astron. Astrophys.* **137**, 117

Cox P., Krügel, E., Mezger, P.G.: 1986, *Astron. Astrophys.* **155**, 380

Cox, P., Mezger, P.G.: 1988, in *"Comets to Cosmology"*, Lecture Notes on Physics **297**, ed. A. Lawrence, Springer Verlag Berlin, 97

Davies, R.D., Elliot, K.H., Meaburn, J.: 1976, *Mem. R. Astron. Soc.* **81**, 89

Deul, E.R., Wolstencroft, R.D.: 1988, Astron. *Astrophys.* in press

Elias, J.H., Frogel, J.A., Schwering, P.B.W.: 1986, *Astrophys. J.* **302**, 675

Feitzinger, J.V., Haynes, R.F., Klein, U., Wielebinski, R., Perschke, M.: 1978, *Vistas in Astronomy* in press.

Feitzinger, J.V.: 1980, *Space Sci. Rev.* **27**, 35

van Genderen, A.M.: 1981, *Astron. Astrophys.* **101**, 289

Haynes, R.F., Klein, U., Wielebinski, R., Murray, J.D.: 1986, *Astron. Astrophys.* **159**, 22

Helou, G.: 1986, *Astrophys. J. (Letters)* **311**, L33

Henize, K.G.: 1956, *Astrophys. J. Suppl.* **2**, 315

Hummel, E.: 1981, *Astron. Astrophys.* **93**, 93

Humpreys, R.M.: 1984, in *"Structure and Evolution of the Magellanic Clouds"*, IAU Symp. 108, eds. S. van den Bergh, K.S. de Boer, Reidel Dordrecht, 145

Hunter, D.A., Gillett, F.C., Gallagher III, J.S., Rice, W.L., Low, F.J.: 1986, *Astrophys. J.* **303**, 171

IRAS: 1985a, IRAS Catalogs and Atlases Explanatory Supplement, eds. C.A. Beichmann, G. Neugebauer, H.J. Habing, P.E. Clegg, T.J. Chester, JPL D–1855

IRAS: 1985b, IRAS Small Scale Structure Catalog, eds. G. Helou, D.W. Walker, JPL D–2988

IRAS: 1985c, Cataloged Galaxies and Quasars observed in the IRAS survey, eds. C.J. Lonsdale, G. Helou, J.C. Good, W. Rice, JPL D–1932

Israel, F.P., Schwering, P.B.W.: 1986, in *"Light on Dark Matter"*, ed. F.P. Israel, Reidel Dordrecht, 383

Jones, T.J., Hyland, A.R., Straw, S., Harvey, P.M., Wilking, B.A., Joy, M., Gatley, I., Thomas, J.A.: 1986, *Mon. Not. R. Astron. Soc.* **219**, 603

Kennicutt Jr., R.C.: 1983, *Astron. Astrophys.* **120**, 219

Kennicutt Jr., R.C., Hodge, P.W.: 1986, *Astrophys. J.* **306**, 130

Klein, U.: 1982, *Astron. Astrophys.* **116**, 175

Koornneef, J.: 1977, *Astron. Astrophys. Suppl.* **29**, 117

van der Kruit, P.C.: 1986, *Astron. Astrophys.* **157**, 230

Lequeux, J.: 1971, *Astron. Astrophys.* **15**, 42

Lequeux, J.: 1984, in *"Structure and Evolution of the Magellanic Clouds"*, IAU Symp. 108, eds. S. van den Bergh, K.S. de Boer, Reidel Dordrecht, 67

Lucke, P.B., Hodge, P.W.: 1970, *Astron. J.* **75**, 171

Mathewson, D.S., Ford, V.L.: 1984, in *"Structure and Evolution of the Magellanic Clouds"*, IAU Symp. 108, eds. S. van den Bergh, K.S. de Boer, Reidel Dordrecht, 125

Mathewson, D.S., Ford, V.L., Visvanathan, N.: 1986, *Astrophys. J.* **301**, 664

Mathis, J.,S., Mezger, P.G., Panagis, N.: 1983, *Astron. Astrophys.* **128**, 212

Maucherat–Joubert, M., Lequeux, J., Rocca–Volmerange, B.: 1980, *Astron. Astrophys.* **86**, 299

Meaburn J.: 1980, *Mon. Not. R. Astron. Soc.* **192**, 365

Mezger, P.G., Mathis, J.S., Panagia, N.: 1982, *Astron. Astrophys.* **105**, 372

Mezger, P.G.: 1985, in *"Birth and Infancy of Stars"*, eds. R. Lucas, A. Omont, R. Stora, North–Holland, Amsterdam, 31

Mihalas, D., Binney, J.: 1981, *"Galactic Astronomy"*, Freeman and Co., San Francisco, p114

Osterbrock, D.E.: 1974, *"Astrophysics of Gaseous Nebulae"*, Freeman and Company, San Francisco, p65

Page, T., Carruthers, G.R.: 1981, *Astrophys. J.* **248**, 906

Puget, J.–L., Léger, A., Boulanger, F.: 1985, *Astron. Astrophys.* **142**, L19

Rice, W., Lonsdale, C.J., Soifer, B.T., Neugebauer, G., Kopan, E.L., Lloyd, L.A., de Jong, T., Habing, H.J.: 1988a, *"A Catalog of IRAS Observations of Large Optical Galaxies"*, IPAC preprint No. 0032

Rice, W., Boulanger, F., Viallefond, F., Soifer, B.T., Freedman, W.L.: 1988b, in preparation

Rohlfs, K., Kreitschmann, J., Siegman, B.C. and Feitzinger, J.V.: 1984, *Astron. Astrophys.* **137**, 343

Sancisi, R., van der Kruit, P.C.: 1981, in *"Origin of Cosmic Rays"*, IAU symp. 94, eds. G. Setti, G. Spada, A.W. Wolfendale, Reidel Dordrecht, 209

Schwering, P.B.W.: 1987, in *"Starbursts and Galaxy Evolution"*, eds. T.X. Thuan, T. Montmerle, J. Tran Thanh Van, Editiones Frontières, Gif-sur-Yvette, 85

Schwering, P.B.W., Israel, F.P.: 1988b, *"Catalogue of far-infrared observations of the Magellanic Clouds"*, Sterrewacht Leiden

Vangioni-Flam, E., Lequeux, J., Maucherat-Joubert, M., Rocca-Volmerange, B.: 1980, *Astron. Astrophys.* **90**, 73

de Vaucouleurs, G.: 1957, *Astron. J.* **62**, 69

de Vaucouleurs, G.: 1960, *Astrophys. J.* **131**, 574

de Vaucouleurs, G., de Vaucouleurs, A., Corwin, H.G.: 1976, *"Second Reference Catalogue of Bright Galaxies"*, Texas University Press

de Vries, C.P.: 1986, Ph.D. Thesis, University of Leiden

Vuillemin, A.: 1988, *Astron. Astrophys. Suppl.* **72**, 249

Walterbos, R.A.M., Schwering, P.B.W.: 1987, *Astron. Astrophys.* **180**, 27

Werner, M.W., Becklin, E.E., Gatley, I., Ellis, M.J., Hyland, A.R., Robinson, G., Thomas, J.A.: 1978, *Mon. Not. R. Astron. Soc.* **184**, 365

West, R.M., Pedersen, H., Marsden, C.: 1987, *ESO Messenger* **50**, 24

Westerlund, B.E., Mathewson, D.S.: 1966, *Mon. Not. R. Astron. Soc.* **131**, 371

Wood, P.R., Bessell, M.S., Whiteoak, J.B.: 1986, *Astrophys. J. (Letters)* **306**, L81

Zombeck, M.V.: 1980, *"High Energy Astrophysics Handbook"*, SAO Report 386

Chapter VI

PROPERTIES OF DUST IN THE MAGELLANIC CLOUDS

1. Introduction and data presentation

Estimates of the amount of dust in the Magellanic Clouds have been based mainly on three methods, which are all subject to some controversy: reddening of individual Cloud stars (photometry and spectroscopy); surface extinction values (galaxy counts) and mapping of individual dust clouds by tracing their silhouet against the stellar background (for an overview see Israel, 1984). IRAS has now made it possible to observe thermal dust emission at mid- and far-infrared wavelengths; because this emission is optically thin all dust is observed.

We examine first the nature of the mid-infrared emission (*i.e.* 12 and 25 μm; Section 2). The nature of the 60 and 100 μm emission of galaxies is relatively clear: dust heated by hot O- and B-type stars in extended low density HII regions or by the general interstellar radiation field (Mezger *et al.*, 1982; Cox *et al.*, 1986). However, extrapolation of the 100 and 60 μm measurements towards shorter wavelengths does not explain the observed mid-infrared emission; this may indicate that a different population of dust particles produces the 12 and 25 μm emission. In Section 3 we estimate the total mass of dust in the Clouds, together with the distribution of dust over the face of the Clouds. In Section 4 we investigate the relation of infrared emission and dust to atomic hydrogen.

The IRAS data contain information in four infrared wavelength bands at 12, 25, 60 and 100 μm. The infrared maps used are the Additional Observation (AO) maps described in Section 2 of Chapter V. The mid-infrared distribution of Section 2 and the dust column density distribution of Section 3, have been estimated using the 8$'$ resolution infrared maps (corresponding to a linear resolution of 135 pc at the distance of the Clouds). For HI, we used maps of Rohlfs *et al.* (1984) on the LMC and those of McGee and Newton (1981) on the SMC. These HI observations were obtained with the 64-m Parkes (CSIRO) radiotelescope, with a resolution of 15$'$. For the comparison we therefore convolved the infrared data to the HI resolution.

2. Nature of dust emitting at mid-infrared wavelengths

Infrared emission at 12 and 25 μm is remarkably strong. The mid-infrared emission of the Galaxy and its nature are discussed by Cox *et al.* (1986), revised by Cox and Mezger (1988). Similar strong mid-infrared intensities are seen in the nearest spiral galaxies M31 (Walterbos and Schwering, 1987) and M33 (Rice *et al.*, 1988a). The favoured explanation for the mid-infrared emission in these galaxies is the presence of very small grains (VSG; see Draine and Anderson, 1985) with radii a of 0.4 nm $< a <$ 1.5 nm, $\sim$ 100 times smaller than "normal" large dust grains. The latter have sizes ranging from 5 nm to 1 μm; the size distribution depends on whether those grains have graphite or silicate cores — see

Appendix —; $< a > \approx 0.1$ μm. The VSG are transiently heated by single (ultraviolet) photon absorption to high non–equilibrium temperatures of 300 – 1000 K (Sellgren, 1984; Puget *et al.*, 1985), and they emit infrared radiation while cooling down. A collection of VSG will thus have a distribution of temperatures with a small fraction of hot particles.

2.1. The Clouds' integrated mid–infrared excess emission

In Table 1 we summarize the infrared spectra of the Magellanic Clouds, and those of three colour temperatures T_c (which is defined as the temperature of the blackbody that fits two adjacent spectral bands). For reference we add the Clouds' stellar spectrum. A single temperature component cannot explain the full infrared spectrum from 12 to 100 μm. The 60 – 100 μm emission is dominated by cool dust with $T_c \approx 44$ K. The colour temperature increases for the 25 – 60 μm intensity ratios to 63 – 73 K, and is highest (230 – 250 K) for the 12 – 25 μm ratio.

The 60 – 100 μm emission of the Clouds can easily be explained by "normal" interstellar dust, even though it is warmer than dust in cool Galactic regions. The higher temperature is the consequence of on average stronger radiation fields than present in the Galaxy (for a quantitative analysis see Chapter V). The average 25 – 60 μm colour temperature of 68 K is comparable to that of other galaxies. Extrapolation of the 100 and 60 μm flux densities via a modified blackbody spectrum ($\nu^{1.5} B_\nu(T_d)$) to 25 μm, predicts 3 % of the observed 25 μm emission. An extrapolation of the 60 and 25 μm emission via a (modified) blackbody to 12 μm, predicts much less than 1 % of the observed emission. The strength of the mid–infrared flux densities of the Clouds relative to the 60 and 100 μm emission, shows that most of the 25 μm emission and nearly all 12 μm emission is unlikely to be produced by the "normal" grains that give rise to the cool dust emission. We call the mid–infrared emission that cannot be explained by the extrapolation of the cool dust emission, the *mid–infrared excess.*

Here we roughly estimate what fraction of 12 and 25 μm emission could be due to integrated starlight. We extrapolate the integrated visual magnitudes of de Vaucouleurs (1960) at 4400 Å (B), 5500 Å (V) and 6250 Å using a 6700 K blackbody for both Clouds (corresponding to the spectrum of an F5 star, peaking at 7600 Å). As we neglect extinction effects the intrinsic average spectrum may be of somewhat earlier type. We predict only 77 Jy at 12 μm in the LMC and 10 Jy in the SMC; *i.e.* 2 resp. 7 % of the observed $f_{12\mu m}$. The observed spectral shape of the mid–infrared emission excludes a large contribution of starlight at 25 μm. Additional arguments follow from the distribution of the 12 μm emission: the distribution of infrared emission does not follow the general stellar distribution (compare for instance the optical–stellar bar with the infrared–dust bar in the LMC; see Chapter V), but rather that of the younger population (embedded HII regions). Hence we conclude that direct starlight does not contribute significantly to the integrated mid–infrared flux density (see also Section 2.2).

We have compared the integrated infrared spectra of the Clouds to those of the galaxy M31 (Fig. 5 in Chapter V). The Clouds' spectra do not show a minimum at 25 μm, as in the Galaxy (in high latitude dust clouds; see Boulanger *et al.*, 1985), M31 (Walterbos and Schwering, 1987) and M33 (Rice *et al.*, 1988a).

Table 1. *Integrated flux densities of various temperature components compared to the Clouds, normalized to $f_{60\mu m}$.*

T_c *(K)*	Based on	$f_{12\mu m}$	$f_{25\mu m}$	$f_{60\mu m}$	$f_{100\mu m}$
SMC	*IRAS Observations*	0.02	0.06	1.0	2.0
LMC	*IRAS Observations*	0.05	0.11	1.0	2.2
240 K [a]	12 – 25 μm	1.5	2.4	1.0	0.5
68 K	25 – 60 μm	3×10^{-4}	0.1	1.0	1.0
44 K	60 –100 μm	4×10^{-8}	0.007	1.0	2.0
6700 K [b]	0.44 – 0.625 μm	23.2	5.6	1.0	0.4

Notes to Table 1:

a) Colour temperatures based on adjacent bands.

b) The 6700 K component is based on the B, V and 6250 Å steller data of de Vaucouleurs (1960; F5 spectrum).

Table 2. *IRAS integrated infrared band ratios of some galaxies.* [a]

Object	$\frac{L_{IR-tot}}{L_\odot}$	$\frac{f_{12\mu m}}{f_{100\mu m}}$	$\frac{f_{12\mu m}}{f_{25\mu m}}$	$\frac{f_{25\mu m}}{f_{60\mu m}}$	$\frac{f_{60\mu m}}{f_{100\mu m}}$	Reference
LMC	8.9×10^{8}	0.023	0.43	0.11	0.50	*Chapter V.*
SMC	7.7×10^{7}	0.011	0.38	0.05	0.52	*Chapter V.*
MWG 1 [b]	1.5×10^{10}	0.027	0.96	0.07	0.43	*Cox et al. (1986).*
MWG 2	8.6×10^{9}	0.034	0.51	0.28	0.24	*Cox and Mezger (1988).*
M31	2.6×10^{9}	0.062	1.17	0.25	0.21	Walterbos and Schwering (1987).
M33	1.1×10^{9}	0.034	1.02	0.10	0.34	*Rice et al. (1988a).*
NGC 4449	5.8×10^{9}	0.029	0.45	0.13	0.49	*Hunter et al. (1986).*

Notes to Table 2:

a) The flux densities assume $f_\nu \propto \nu^{-1}$.

b) For the Milky Way Galaxy, pre–IRAS MWG 1 data of Cox et al. (1986; Fig. 1 therein) and post–IRAS MWG 2 data of Cox and Mezger (1988; Fig. 2 therein) are given. Note the discrepancies between the pre– and post–IRAS ratios for the Galaxy. Both are obtained from data of the inner Galaxy (R < 8 kpc). For MWG 2, the total infrared luminosity is obtained for $\lambda > 25$ μm.

Thus the Magellanic Clouds appear to show a mid-infrared excess which is, however, considerably smaller than that of the Local Group spiral galaxies and that of the Solar Neighbourhood. In Table 2 we give the total infrared luminosity and the IRAS flux density ratios for the Clouds, the Local Group spiral galaxies and the giant irregular galaxy NGC 4449. The ratios of the LMC are identical to those of NGC 4449. The SMC has the lowest $f_{12\mu m}/f_{100\mu m}$, and hence the smallest global mid-infrared excess. From the table we see that the ratio $f_{12\mu m}/f_{25\mu m}$ is a stronger indicator for cirrus mid-infrared emission than the ratio $f_{12\mu m}/f_{100\mu m}$ (used by *e.g.* Boulanger *et al.*, 1985). The irregular galaxies, the LMC, the SMC and NGC 4449 which have relatively high star formation rates per unit mass (see *e.g.* Lequeux, 1984), have a considerably lower $f_{12\mu m}/f_{25\mu m}$ and higher $f_{60\mu m}/f_{100\mu m}$. The least active galaxy of this sample, M31 (Walterbos and Schwering, 1987), has the highest $f_{12\mu m}/f_{25\mu m}$ and lowest $f_{60\mu m}/f_{100\mu m}$. Two sets of data are given for the Milky Way: pre-IRAS and post-IRAS data, which have remarkable differences (Table 2).

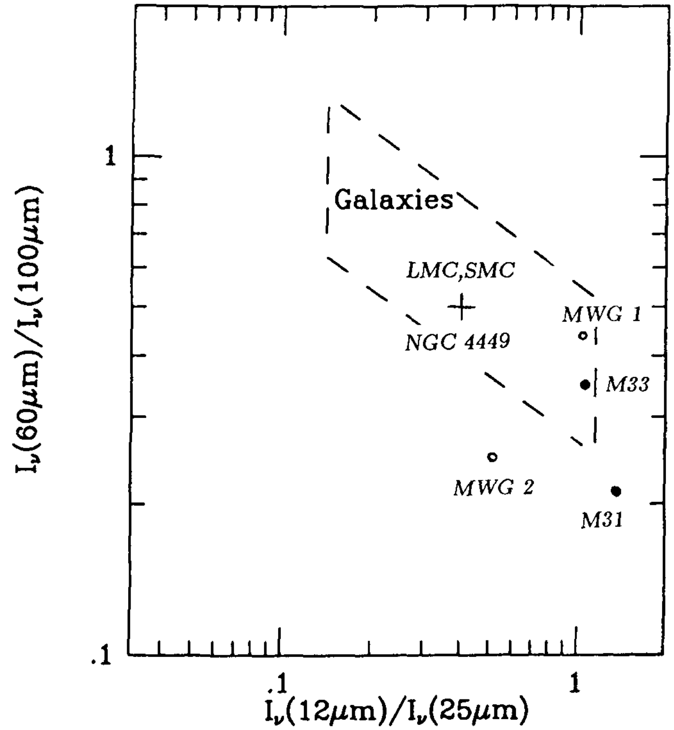

Figure 1. *Colour-colour diagram of integrated galaxy data of Table 2. The plus sign represents the LMC, the SMC and NGC 4449. The large Local Group spiral galaxies (dots, open circles) are at the lower right. The dashed lines outline parts of the diagram occupied by galaxies (Helou, 1986). Note the two very different locations for the Milky Way, based on pre-IRAS (MWG 1) and post-IRAS (MWG 2) data.*

Helou (1986) has showed that the ratio f_{12}/f_{25} is anti–correlated with the ratio f_{60}/f_{100} for integrated flux densities of galaxies. The six galaxies of Table 2 fit this picture; Fig. 1 presents these galaxies in Helou's colour–colour diagram. The three irregular galaxies occupy the same positions in the galaxy–area. The spiral galaxies are to the right of the diagram, indicating relatively cooler dust emission together with a high $f_{12\mu m}/f_{25\mu m}$. Note the very different position of the Milky Way galaxy, after the post–IRAS revision. The average dust temperature in the Clouds is higher than in the Local Group spiral galaxies. A reduction in T_d for the Clouds would move them downward in the diagram, outside the galaxy–area. The positions of these galaxies in the diagram shows that it is difficult to reduce one of the two colours by a large factor while keeping the other constant.

2.2. The contribution of star–like objects to the mid–infrared excess emission

The nature of the mid–infrared (12 – 25 μm) excess emission is discussed in terms of the available IRAS spectral and spatial data on the Magellanic Clouds. We follow Cox *et al.* (1986) in discussing the options for the mid–infrared excess emission, and recall that the extrapolated mid–infrared luminosities of the Clouds are 1.8 x 10^8 $L_\odot$ for the LMC and 8.1 x 10^6 $L_\odot$ for the SMC (see Chapter V). We also note that the IRAS 12 and 25 μm infrared maps resemble the 60 and 100 μm maps. The latter certainly represent the distribution of warm and cool dust. We therefore expect the heating agents of the 12 and 25 μm emission to be spatially related to the 60 and 100 μm dust distribution.

2.2.1. Cool stellar photospheres; *i.e.* cool K– and M–giants (3000 – 4000 K)

First we estimate the percentage of the infrared emission that can be accounted for by cool giant stars. Dust grains are formed in the outer envelope of late type giants and are blown into the interstellar medium by stellar winds or supernova explosions. These stars, with temperatures of 3000 – 4000 K, have their maxima of the Planck curve B_ν at 1.2 – 1.7 μm.

We estimate the number of K– and M–type (super)giants by $N_{K,M} = \Psi_{O,B}\ \tau_{K,M}/M_{O,B}$; here $\Psi_{O,B}$ is the O– and B–type star formation rate, $\tau_{K,M}$ is the lifetime of the K– and M–type stars and $M_{O,B}$ the mass of O– and B– type stars. The star formation rate for stars with $M > 10\ M_\odot$, is taken from Kennicutt and Hodge (1986); the values are 0.022 and 0.006 $M_\odot$/yr for the LMC and SMC. The K– and M–type giant lifetime, of order 3 x 10^6 yr, is estimated from Mihalas and Binney (1981) for stars with masses of 9 and 15 $M_\odot$; their total number then is 5.5 x 10^3 for the LMC and 1.5 x 10^3 for the SMC. As the luminosity of these stars is 10^4 $L_\odot$, the total luminosity L_{tot}, integrated over all frequencies is 5.5 x 10^7 and 1.5 x 10^7 $L_\odot$. In the infrared bands we estimate a luminosity from these stars of $L_{IRAS,\ \nu} = (\pi B_\nu(T)\ \Delta\nu_{IRAS,\nu})/(\sigma T^4)\ L_{tot}$. The highest fractions $L_{IRAS,\nu}/L_{tot}$ are found for the 3000 K stars: 0.43 % at 12 μm and 0.042 % at 25 μm. This implies monochromatic 12 μm luminosities of 2.4 x 10^5 $L_\odot$ for the LMC and 6.5 x 10^4 $L_\odot$ for the SMC; respectively 0.4 and 3 % of the observed values. The contribution of stars in the 25 μm band is 10 times less than that in the 12 μm band. The image of the LMC–Bar in the mid–infrared (dust bar) is not identical to the optical (stellar) bar, in the SMC the stellar and dust bars coincide well. We conclude that photospheres of cool giant stars do not contribute significantly to the observed mid–infrared emission of the LMC and at best a little to that of the SMC.

2.2.2. Dust shells surrounding main sequence stars

Dust in shells surrounding main sequence stars can attain temperatures high enough to emit at mid–infrared wavelengths. The most luminous of these stars may, as a result of their higher ultraviolet and optical radiation, have a larger volume of hot dust around them. Although the number of early type hot stars is smaller than the number of late type cool stars, their contribution to mid–infrared emission is higher due to the larger luminosities. The contribution of dwarf stars is of no importance, even though there are many more of these stars. Typical peaks in f_ν occur at wavelengths between 10 and 60 μm; the spectra of observed emission is indeed similar to that of such shells. In the Galaxy (Cox *et al.*, 1986) and M31 (Walterbos and Schwering, 1987), there are not enough of these embedded main sequence stars to be of importance. For the Galaxy, de Muizon and Rouan (1985) showed that their luminosity is roughly two orders of magnitude too low. We find that for the Magellanic Clouds the same applies.

In the LMC we have detected infrared — 12 and 25 μm — emission from shells around Radcliffe LMC–stars R 66 and R 71; these stars are A– and B–type supergiants and they are among the brightest LMC–stars in the infrared, about 1 Jy at 12 μm. They belong to the brightest visual stars (Feast *et al.*, 1960). The A–type supergiant star R 76 is an example of an LMC star with emission at 25 and 60 μm from a dust shell. To estimate an upper limit for the total 12 μm flux density of all Radcliffe–like stars, we sum the fluxes densities with positive detection quality (see Chapters II and III) and add detection limits for the rest of the stars. We find that only 30 Jy can be explained. Hence, we would need 160 of these Radcliffe samples to explain the LMC 12 μm emission, too many to attribute to incompleteness of the bright star sample.

The Radcliffe sample of brightest SMC stars, contains 50 stars with infrared flux densities below the detection limit. Hence their (detection limit) sum is below 15 Jy; this is 10 % of the 12 μm flux density but can be a large upper limit. Thus, we would need at least 10 times more of these stars; again this seems unlikely.

We conclude that there are not enough main sequence stars with dust shells in the Clouds to explain the mid–infrared excess emission. At best a small fraction of the mid–infrared excess might come from the brightest stars. The distribution of infrared emission supports this statement.

2.2.3. Late–type stars with thick dust shells (OH/IR stars and Miras)

The masses of late–type–stars with dust shells range from $\sim 1 - 8\ M_\odot$. They are related to both young and evolved stellar populations (Habing, 1988). In the Galaxy, Cox *et al.* (1986) have estimated about half of the mid–infrared emission to come from these objects.

The first detection of an OH/IR star in the LMC is by Wood *et al.* (1986). Some objects in the source lists of Chapters II and III show weak infrared emission, with a spectrum typical of OH/IR stars. The brightest of these objects are distinguished relatively easily in the 25 – 60 μm colour temperature maps as isolated peaks. Their 12 – 25 μm ratio is low. At 60 and 100 μm the OH/IR stars are too weak compared to the cool dust infrared emission to account for a large fraction (even if all 25 μm emission comes from these objects only 10 % of the 60 μm infrared emission can be accounted for).

We have estimated the number of OH/IR stars in the Clouds as follows. In the Milky Way Cox *et al.* (1986) have estimated this number to be 6 x 10^4 with an average luminosity of 2 x 10^4 $L_\odot$. Recently Habing (1988) has estimated the average luminosity of these stars to be less: about 4 x 10^3 $L_\odot$. Using the Galactic stellar density $N_{OH/IR}/N_{tot}$, the number of OH/IR stars in the Clouds will be about 550 resp. 70. Using the density of Wolf–Rayet stars in the Solar Neighbourhood and the Clouds (Conti, 1987) and a density of 30 OH/IR stars kpc^{-3} (van der Veen, priv. comm.) in the Solar Neighbourhood we derive $N_{OH/IR}/N_{WR} \approx 6.7$. If we assume the same ratio to apply in the Clouds, we find similar numbers as above. We thus find total OH/IR star luminosities for the Clouds of 2.2 x 10^6 and 2.8 x 10^5 $L_\odot$; resp. 1 and 3 % of the mid–infrared emission; if we take a luminosity of 2 x 10^4 $L_\odot$, as Cox *et al.*, these percentages would be 5 times higher, but still inadequate.

Mira type variable stars can also contribute to mid–infrared emission. Their number is possibly 10 times larger than the number of OH/IR stars, but their luminosity is 3 times less at 12 μm and 10 times less at 25 μm (van der Veen, priv. comm.). Then their integrated luminosities would be 3 and 9 % for the LMC and SMC resp. at 12 μm and 1 and 3 % at 25 μm. The observed spectral shape of the Clouds is very different from that of Mira stars; therefore to explain the mid–infrared emission by Mira stars would lead to problems for the 25 μm flux density. We conclude that neither OH/IR stars, nor Mira type stars are responsible for the bulk of the mid–infrared excess emission.

2.2.4. Proto stellar objects or young stars still embedded in dust

We have attempted to quantify the contribution from these objects, by calculating the expected infrared luminosity for an Initial Mass Function $\phi(m)$ (IMF; Miller and Scalo, 1978) at the present Star Formation Rate $\Psi(t)$ (SFR). The emitted infrared luminosity is given by

$$L_{IR} = \frac{\int_{m_{low}}^{m_{up}} dm\ \phi(m) \int_{t_0}^{t_f} dt\ \Psi(t)\ f_{IR/*}(m,t)\ L_*(m,t)}{\int_{m_{low}}^{m_{up}} dm\ m\ \phi(m)}$$

$$\approx \frac{\sum_m(\phi(m)\ L_*(m,t)\ t_*}{\sum_m m\ \phi(m)}\ \Psi(t_0)\ f_{IR/*}(m,t). \tag{1}$$

We have used the power–law approximation of the Miller–Scalo IMF (Mezger, 1985) with $m_{low} = 0.1\ M_\odot$ and $m_{up} = 60\ M_\odot$. The IMF in the Galaxy is similar to the IMF in the LMC (Scalo, 1987); we assume the same for the SMC IMF. The evolutionary pre–main sequence tracks in the Hertzprung–Russel diagram, luminosities $L_*(m,t)$ and time scales t_*, were taken from Mihalas and Binney (1981), for stars from 0.5 to 50 $M_\odot$. The major contribution to the infrared luminosity comes from stars with $M \approx 10\ M_\odot$ (for a 10 $M_\odot$ star $L_*(m) = 2$ x 10^3 $L_\odot$, $t_* = 3.8$ x 10^5 yr). The luminosity has been weighed towards the main–sequence at the end of the tracks as the life–time is larger. The total star formation rates have been taken from Kennicutt and Hodge (1986) and are 0.14 and 0.038 $M_\odot$/yr for the LMC and SMC resp. For the fraction of the emission of these objects in the infrared, we used $f_{IR,*}(m,t) = 0.5$: early in their evolution the shell is optically thick at 12 μm and most emission will be emitted at longer infrared wavelengths; while close to the main sequence, the shell breaks up and visible light can travel through.

For proto stellar objects or young stars embedded in dust, the adopted numerical values result in luminosities of 8 x 10^6 and 2 x 10^6 $L_\odot$ which are 4 and 25 % of the measured total mid–infrared luminosities. For the LMC only a small fraction of the mid–infrared emission can be explained in this way. For the SMC on the other hand, these objects can produce a reasonably large fraction of the mid–infrared emission.

A few proto stellar objects have been found in the LMC (K2 and P2 in N 159; Gatley *et al.*, 1981; Jones *et al.*, 1986) and SMC (K2 in N 76B; Gatley *et al.*, 1982). The protostars in N 159 have an infrared luminosity of ~ 2 x 10^4 $L_\odot$; this is only 4 % of the infrared luminosity of the nebula N 159 in which they are embedded (10^6 $L_\odot$; see Werner *et al.*, 1978). The protostar in N 76B in the SMC has a luminosity of ~ 4 x 10^3 $L_\odot$. From the infrared maps we find an infrared luminosity for the nebula N 76B of about 4 x 10^5 $L_\odot$. Hence, only 1 % of the emission of the nebula is produced by the protostar. These objects were found in an active HII regions where we expect most protostars to occur. Although possibly some protostars were not detected in the regions, the total number of these objects remains small, and hence their luminosity at most only a few percent of the total observed mid–infrared luminosity. The fact that the relative 12 μm excess anti–correlates with the HII regions (Section 2.3.2) indicates that young stars are not the main cause of the excess emission. The number of observed proto stars in the SMC shows that the calculated contribution of 25 % is probably an overestimate.

Table 3. *Maximum stellar contribution to mid–infrared emission from the Clouds.* [a)]

Nature	*L M C (%)*		*S M C (%)*	
	$L_{12\mu m}$	$L_{25\mu m}$	$L_{12\mu m}$	$L_{25\mu m}$
Clouds' luminosity (10^6 $L_\odot$)	57	51	2.5	2.5
Late type giants: K–, M–stars	0.4	0.05	3	0.3
Main sequence stars with dust shells	0.6	0.6	10	10
OH/IR stars	1	1	3	3
Mira stars	3	1	9	3
Proto stars	4	4	25	25
Total stellar contribution (upper limit)	9	7	50	41

Note to Table 3:

a) *The spectrum of the dust shells around main sequence stars and of the protostars has been assumed to be similar to that of the Clouds.*

2.3. The nature of the mid–infrared excess emission

2.3.1. Very small grains mixed with large grains in infrared cirrus

The possible contributions to the mid–infrared emission of all components described above are summarized in Table 3. Together they can account for at most about 10 % (LMC) and 50 % (SMC) of the emission. For the SMC this number is much higher than for the LMC, because we assume Galactic properties in our estimations while the mid–infrared excess of the SMC is rather small, even compared to the LMC. We now consider the hypothesis that, at least, the remaining 90 and 50 % of the mid–infrared emission is caused by non–equilibrium emission of very small grains. Although alternatives for very small grains are not excluded, we will from now on adopt the hypothesis of Puget *et al.* (1985).

These grains can then be understood as being large (50 atom) molecules: Polycyclic Aromatic Hydrocarbons (PAHs). Their heat content $C_V(T)$ is small due to their small size; hence absorption of single ultraviolet photons $h\nu$ increase their initial temperature T_i to T_f, by a large amount ($h\nu = \int_{T_i}^{T_f} C_V(T)\ dT$). Such grains, especially the smallest, can be destroyed easily by single ultraviolet photons if $T_f > T_{subl}$ (with T_{subl} the sublimation temperature of $\gtrsim 1000$ K). The cooling process of the excited grain happens fast compared to the time–scale for new photon encounters; they are not in equilibrium. The observed infrared radiation is the temperature–weighted emission of the ensemble of these small grains.

Small grains can be produced in different ways: photoelectric disruption of large grains may occur in strong radiation fields, and shocks in the interstellar medium modify the grain size distribution. Strong radiation fields influence the minimum grain radius a by sublimation of the smallest grains. This radius is not very sensitive to radiation fields of stars later than type A, or the general interstellar radiation field ($a_{min} = 0.4 - 0.5$ nm; Puget *et al.*, 1985). For earlier type stars there is a large increase in a_{min} to about 1.0 nm in the radiation field of an O5–star at a distance of 1 pc.

In our Galaxy these very small grains (PAHs) are supposedly well mixed with the larger grains on 100 pc scales (Cox *et al.*, 1986); it explains the observed similarity between 12 and 25 μm emission with 60 and 100 μm emission. In various Galactic cirrus areas their presence has been suggested. De Vries (1986) and Boulanger *et al.* (1985) have studied high latitude dust clouds; the strength of their mid–infrared emission is most easily explained by the PAHs. A new study by Boulanger *et al.* (1988) also shows strong evidence for these grains. Beichmann *et al.* (1988) found a correlation between 100 μm intensity and ^{13}CO in the dark cloud Barnard 5, but an anti–correlation between 12 μm and CO line emission This is interpreted as due to the presence of a thin shell of PAHs.

From pre–IRAS observations of the Milky Way galaxy, Cox *et al.* (1986) calculated that the mid–infrared emission is produced equally by the OH/IR stars and small grains. In other nearby galaxies (M31; Walterbos and Schwering (1987), M33; Rice *et al.* (1988a)) only these grains are necessary to explain the mid–infrared emission.

The integrated mid–infrared excess emission of the Clouds is less than that in the nearby spiral galaxies ($f_{12\mu m}/f_{25\mu m}$ in Table 2). If very small grains are responsible for the excess in the Local Group spiral galaxies, this excess is comparatively small in the Clouds and small grains should easily be capable of producing the observed excess. Also, the flux density ratios of the Clouds obey the $f_{12\mu m}/f_{25\mu m}$ – $f_{60\mu m}/f_{100\mu m}$ relation in the diagram of Helou (1986); see Fig. 1: the mid–infrared excess is indeed what we expect for galaxies with the observed $f_{60\mu m}/f_{100\mu m}$.

From Draine and Anderson (1985), we derive the relative spectrum of very small grains (with radii 0.3 nm $< a <$ 3.0 nm) to be 1, 3, 4.5 and 0 in the 12, 25, 60 and 100 μm bands (see Appendix). The integrated Clouds flux densities are taken from Chapter V. We have fitted the 12 and 25 μm integrated emission from the Clouds, neglecting other possible contributors, with the small grain spectrum. The fit is very accurate at 25 μm and within 10 – 20 % of the observed flux density at 12 μm. Small grains contribute 17 % of the 60 μm flux density in the LMC and 8 % in the SMC. Comparing the result on M31 (Walterbos and Schwering, 1987), very small grains in the Clouds do not give a large contribution to the 60 μm flux densities. The main reason for this is the higher Clouds' average T_d of the "normal" grains. We conclude that the mid–infrared emission of the Clouds can be well explained by very small grains.

2.3.2. The distribution of the mid–infrared excess emission

After global estimates for the very small grain contribution to the mid–infrared emission, we now look at the distribution and positional differences in the mid–infrared excess of the Clouds. Table 6 of Chapter V already shows that the area South of the 30 Doradus region, with on average $f_{12\mu m}/f_{25\mu m} = 0.96$ and $f_{60\mu m}/f_{100\mu m} = 0.3$, closely resembles typical Galactic cirrus areas. On the other hand, the 30 Doradus region shows infrared flux density ratios similar to that of Galactic HII regions.

Indications of spatial variations of the mid–infrared excess over the face of the Clouds come from the IRAS maps at 12 and 25 μm (Chapter V; Fig. 2 and 3). At no position in these maps a single temperature component, based on the 60 and 100 μm data, can explain the observed 12 or 25 μm emission. A region of special interest is the area South of the nebula N 159 (Henize, 1956) in the LMC; its 12 – 25 μm colour temperature ($f_{12\mu m}/f_{25\mu m}$) is higher compared to any other area and the 12 μm intensity from this region is relatively high. (Chapter V; Table 6). We find a typical Galactic cirrus infrared spectrum in this region with $T_{12-25} = 335$ K; HII region complexes have typically $T_{12-25} = 160$ K.

To quantify the mid–infrared excess emission we modelled pixel–by–pixel the expected 12 and 25 μm maps by extrapolating the longer wavelength data (taking $\epsilon_\nu \propto \nu^n$, $n = 1.5$). For the 12 μm model we used the 60 – 100 μm maps (with $n = 1.5$) and also the 25 – 60 μm maps (with $n = 0$); for the 25 μm model we have only the 60 and 100 μm data. The model is defined by

$$I_\nu^{mod} \equiv I_{\nu_1} \frac{B_\nu(T_{\nu_1-\nu_2})}{B_{\nu_1}(T_{\nu_1-\nu_2})} (\frac{\nu}{\nu_1})^n. \tag{2}$$

As explained in the previous section, only small fractions of the mid–infrared emission can be accounted for by extrapolated far–infrared emission, and $(I_\nu - I_\nu^{mod})$ maps are very similar to infrared maps in Chapter V. For this reason we show in Fig. 2 and 3 the *relative excess emission maps* at 12 and 25 μm, defined by

$$R_\nu \equiv \frac{I_\nu - I_\nu^{mod}}{I_\nu^{mod}}. \tag{3}$$

This (relative) excess emission shows an anti–correlation with the infrared brightness distribution at all wavelengths. It also anti–correlates with T_d (from 60 and 100 μm), but it correlates with the 12 – 25 μm colour temperature. Very systematically, HII regions show the lowest excess emission, both in the 12 and 25 μm extrapolation.

This is a very important result. In HII regions, dust particles are on average much closer to the heating stars than in the main body of the Clouds. One would thus expect HII regions to have a more significant hot component, and thus a larger mid–infrared excess than other parts of the Clouds, contrary to what is observed !

The fact that the mid–infrared excess is associated with the diffuse medium rather then the HII regions is a powerful indicator that (a) the mid–infrared excess is caused by VSGs in the diffuse medium and (b) that these VSGs are largely absent in or near HII regions. The depletion of VSG emission in HII regions is even stronger than suggested by Fig. 2 and 3, because as noted above, in HII regions there will also be a mid–infrared excess contribution by normal dust heated to higher temperatures which is absent or weak outside HII regions. With respect to this, note that in the 1′ KAO beam 30 Doradus (Werner *et al.*, 1978) shows indeed enhanced emission at 30 μm correlated with 50 – 100 μm temperatures.

In the extrapolations, we have assumed that the dust emissivity in HII regions is constant with wavelength, and that a single temperature applies. More realistically, the emissivity may change with wavelength and instead of a single temperature throughout, temperature gradients apply.

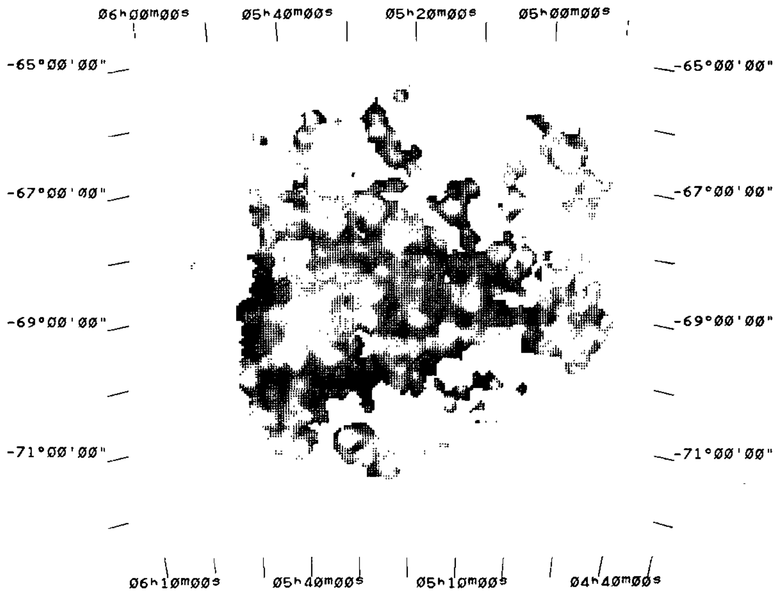

Figure 2. *LMC mid–infrared excess emission (8′ resolution). In all maps, of 8° x 8° size, darker grey scales indicate higher map values. The relative infrared excess emission at frequency* ν *is defined as* $R_\nu \equiv (I_\nu - I_\nu^{mod})/I_\nu^{mod}$. *See also pages 206 – 207.*

Fig. 2.1. LMC $R_{12\mu m}$ *map, with model 25 – 60* μ*m emission.*

Grey scale range: 200 – 1500.

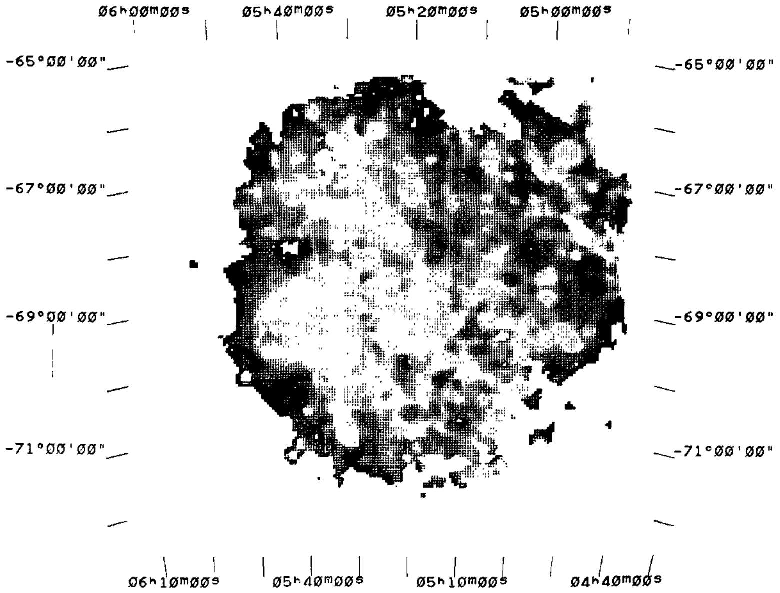

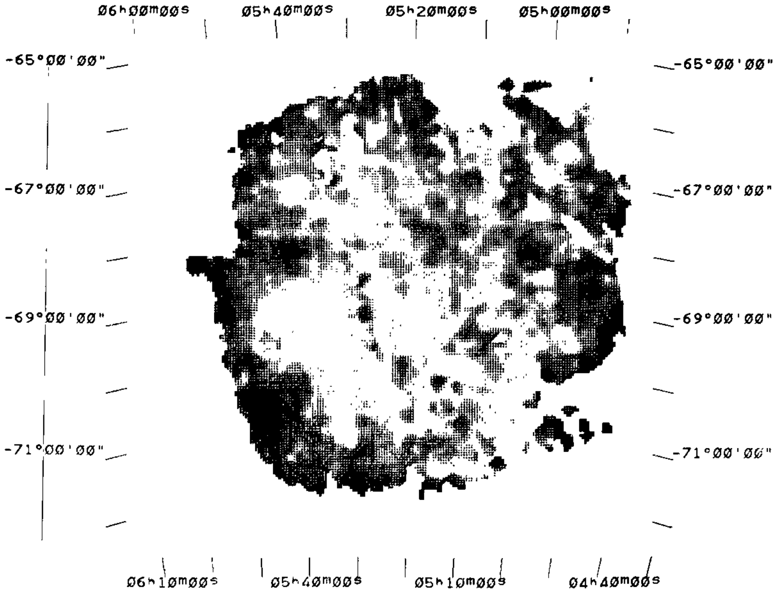

Fig. 2.2. LMC $R_{12\mu m}$ map, with model 60 – 100 μm emission. Grey scale range: 1 x 10^{8} – 5 x 10^{10}.

Fig. 2.3. LMC $R_{25\mu m}$ map, with model 60 – 100 μm emission. Grey scale range: 30 – 400.

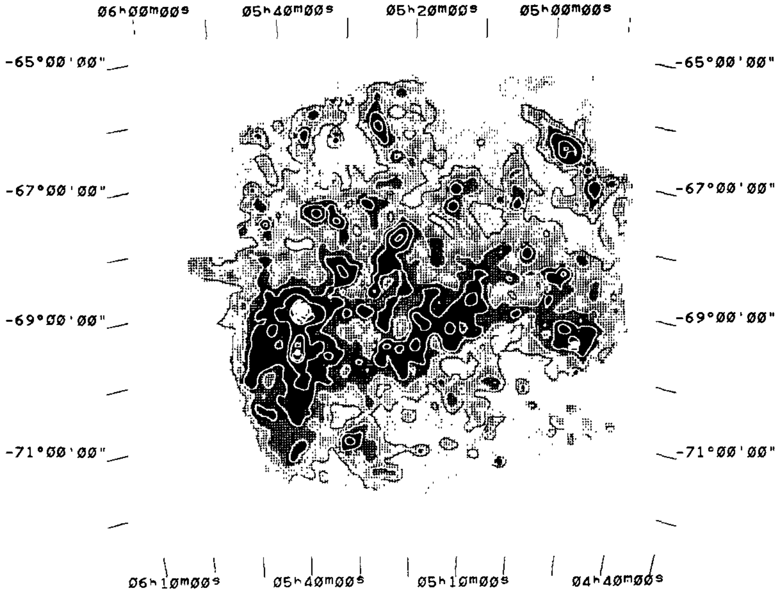

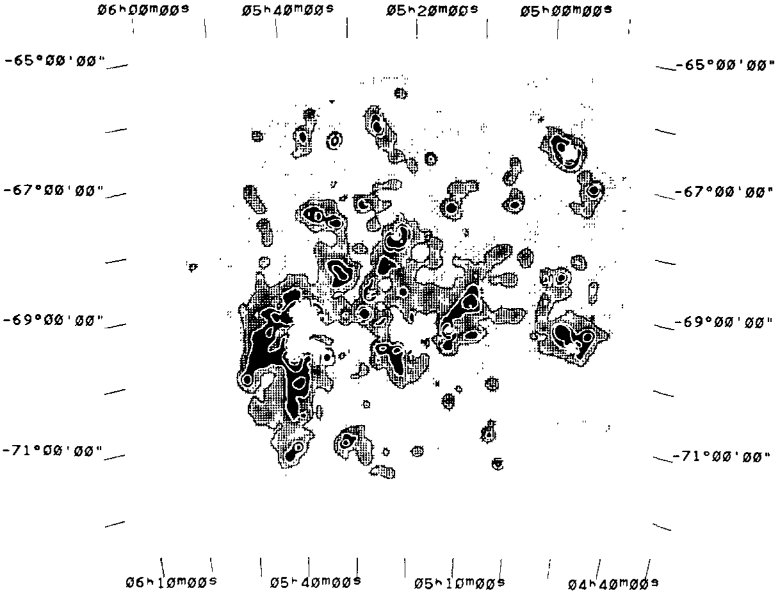

Fig. 2.4. LMC 12 μm cirrus intensity map.
Grey scales: 0 – 9.6 MJy/sr; contours are at 0.15, 0.37, 0.74, 1.9, 3.7, 5.6, 7.4 MJy/sr.
Fig. 2.5. LMC 25 μm cirrus intensity map.
Grey scales: 0 – 7.8 MJy/sr; contours are at 0.39, 0.97, 1.9, 4.8 MJy/sr.

We have attempted to empirically compensate for these effects in the following manner. We determine the mean infrared spectrum of the brightest HII regions in both LMC and SMC. We assume that cirrus emission is negligible in these lines–of–sight. We then determine, from $\nu^{1.5}B_\nu(T_d)$, the average dust temperature T_d (HII), and then reduce the effect of (both) emissivity law changes and temperature gradients to an apparent change in emissivity by fitting the observed 12 and 25 μm points to $\nu^n B_\nu(T_d(HII))$. Thus, for 60 μm $< \lambda <$ 100 μm, $n \equiv 1.5$, while for 12 and 25 μm higher values for n are found. These values obviously have no direct physical meaning; they merely serve as convenient parameters to describe the observed HII region infrared spectrum. Numerical values are given in Tables 4 and 5. We now assume these values for n to hold for *all* normal grains in the Clouds, and use it to extrapolate the "normal grain emission' maps at 60 μm and 100 μm to 12 μm and 25 μm. The difference between the observed maps and these extrapolated maps are the maps of the VSG (cirrus) emission at 12 μm and 25 μm (Fig. 2.4, 2.5, 3.4 and 3.5). Strictly speaking, these maps are lower limits to the cirrus emission outside the HII regions since large grain temperature gradients are probably less important in the diffuse medium than in HII region environments. As the extrapolation to 25 μm is over a smaller wavelength range than the 12 μm, the 25 μm cirrus maps are more reliable than the 12 μm maps. At 25 μm, about 25 % of the Clouds integrated emission appears due to cirrus, at 12 μm about 90 % (Tables 4 and 5).

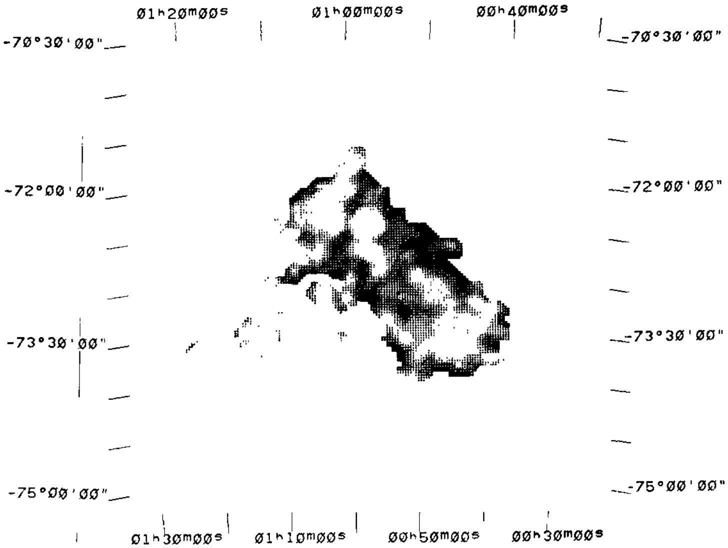

Figure 3. *SMC mid–infrared excess emission (8′ resolution). In all maps, of 4°.8 x 4°.8 size, darker grey scales indicate higher map values. Note the spatial scale difference between the LMC maps and the SMC maps in this chapter. The relative infrared excess emission at frequency ν is defined as $R_\nu \equiv (I_\nu - I_\nu^{mod})/I_\nu^{mod}$. See also pages 209 – 210.*
Fig. 3.1. SMC $R_{12\mu m}$ map, with model 25 – 60 μm emission.
Grey scale range: 250 – 2200.

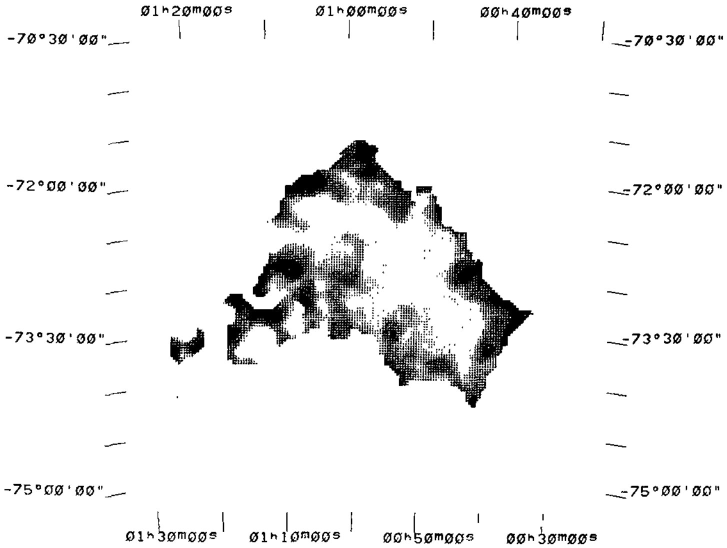

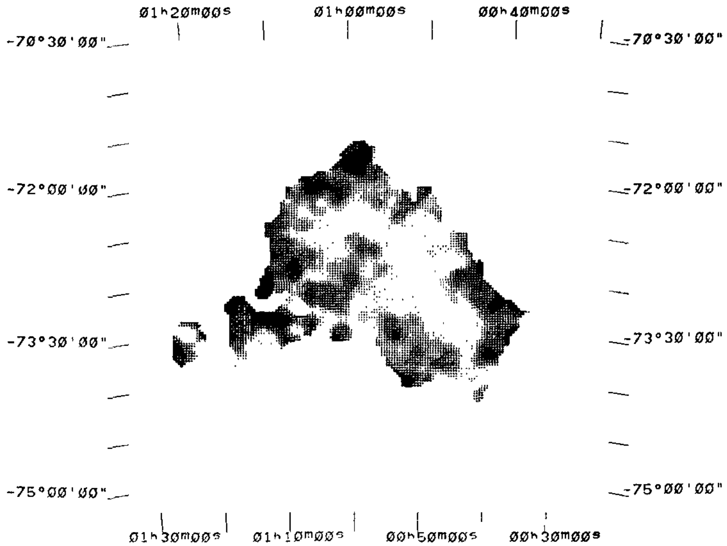

Fig. 3.2. SMC $R_{12\mu m}$ map, with model 60 – 100 μm emission. Grey scale range: 1 x 10^7 – 1 x 10^9.

Fig. 3.3. SMC $R_{25\mu m}$ map, with model 60 – 100 μm emission. Grey scale range: 10 – 80.

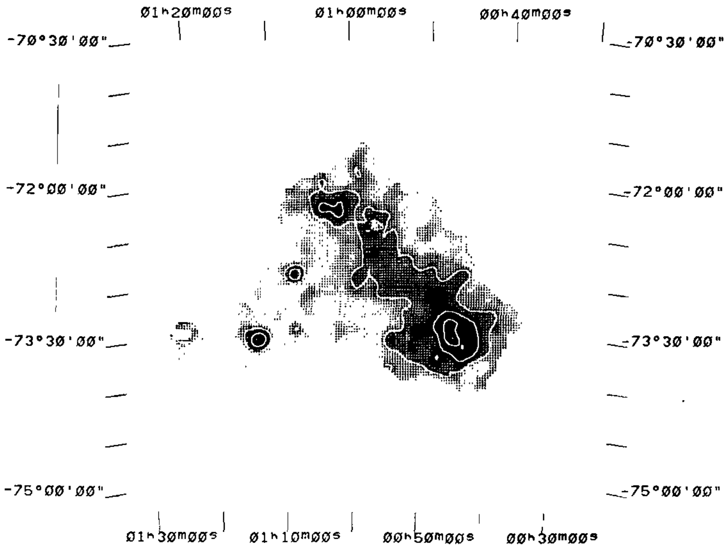

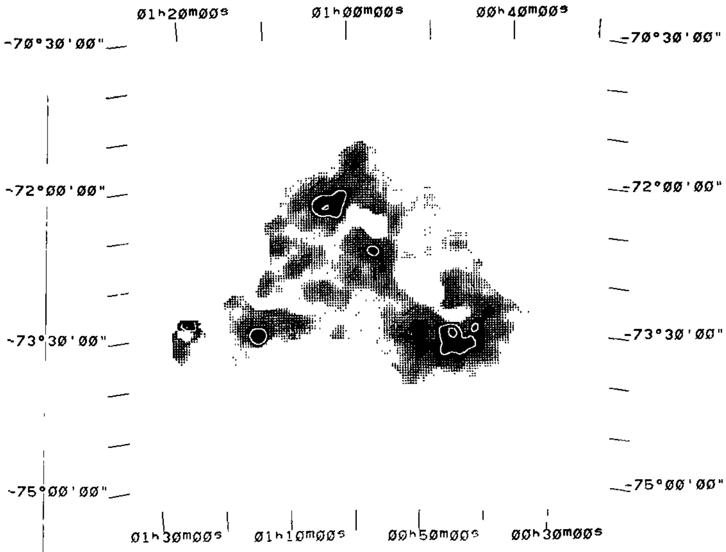

Fig. 3.4. SMC 12 μm cirrus intensity map.
Grey scales: 0 – 0.97 MJy/sr; contours are at 0.15, 0.37, 0.74 MJy/sr.
Fig. 3.5. SMC 25 μm cirrus intensity map.
Grey scales: 0 – 1.2 MJy/sr; contours are at 0.39, 0.97 MJy/sr.

Table 4. *Mid-infrared cirrus in the LMC.*

Quantity	12 μm	25 μm	60 μm	100 μm
$\nu/\nu_{100\mu m}$	8.33	4.00	1.67	1.0
$f_{\nu,\,HII}$ [a]	0.021	0.075	0.58	1.00
T_d/K [b]	35	35	35	35
$B_\nu(T_d)$ [a]	$1.30\ 10^{-9}$	$3.64\ 10^{-4}$	0.29	1.00
n [c]	15.4	5.3	1.5	—
$< n >$ [d]	7.8	3.8	1.5	—
f_ν/Jy [e]	4850	11300	103000	208000
f_{cirrus}/f_{tot}	0.78	0.20	—	—
f_{HII}/f_{tot}	0.22	0.80	—	—

Table 5. *Mid-infrared cirrus in the SMC.*

Quantity	12 μm	25 μm	60 μm	100 μm
$\nu/\nu_{100\mu m}$	8.33	4.00	1.67	1.0
$f_{\nu,\,HII}$ [a]	0.014	0.045	0.58	1.00
T_d/K [b]	35	35	35	35
$B_\nu(T_d)$ [a]	$1.30\ 10^{-9}$	$3.64\ 10^{-4}$	0.29	1.00
n [c]	15.5	4.7	1.5	—
$< n >$ [d]	7.6	3.5	1.5	—
f_ν/Jy [e]	147	385	7170	13900
f_{cirrus}/f_{tot}	0.95	0.28	—	—
f_{HII}/f_{tot}	0.05	0.72	—	—

Notes to Tables 4 and 5:

a) The HII region infrared spectrum $f_{\nu,HII}$ has been determined by adding fluxes at positions with $I_{100\mu m} > 40$ MJy/sr. It and the Planck blackbody function $B_\nu(T_d)$ are given relative to the 100 μm values.

b) T_d has been derived assuming $f_\nu \propto \nu^{1.5} B_\nu(T_d)$ at 60 and 100 μm.

c) n_i is the average emissivity exponent between bands i and j, and is derived from $f_i/f_j = (\nu_i/\nu_j)^n (B_i(T_d)/B_j(T_d))$, with i and j adjacent bands.

d) $< n >$ gives the average value of n for $j \equiv 100\ \mu m$; hence the average emissivity exponent between band i and the 100 μm band.

e) The integrated flux densities are taken from Chapter V. The mid-infrared cirrus and HII contributions are normalized to the integrated fluxes.

2.3.3. Conclusion: mid-infrared emission in the Magellanic Clouds

The anti-correlation of the relative 12 μm excess with the dust temperature, as shown in Fig. 2 and 3, is possibly caused by the destructive nature of the strong radiation field near hot stars, on these small grains (see Section 2.3.1). Close to HII regions PAHs are hit by photons with energies higher than the sublimation energy of the grains, resulting in a destruction of the smallest grains. Recently Boulanger *et al.* (1988) found that in the California Nebula, the 12 μm intensity profile peaks farther away from the star ξ Per than the 100 μm intensity profile. This difference is interpreted as a result of the destruction of PAHs close to the star. For a radiation field 50 times stronger than the Solar Neighbourhood field they calculated that 80 % of the PAHs are destroyed. Thus we expect the mid-infrared excess to be smallest where the ultraviolet radiation field is strongest in the Clouds. In Chapter V we showed that the radiation fields in Magellanic Cloud HII regions are possibly even stronger than 50 times the Solar Neighbourhood field; in Fig.

4.1 we show the relation between ultraviolet emission (Vuillemin, 1988) and the 25 μm cirrus map. Note the generally strong anti–correlation. Fig. 4.2 shows the relation of the ultraviolet emission to $T_{12-25\mu m}$; again an anti–correlation is seen. Hence, our conclusion that Cloud HII regions are largely, if not entirely void of these PAHs is clearly supported: the derived distribution of cirrus emission is what is to be expected from PAHs.

We conclude that the most probable nature of the mid–infrared excess emission in the Magellanic Clouds are the very small grains (PAHs). We also find that these VSGs are present in significant quantities mainly in the diffuse interstellar medium. More specifically, HII regions and their immediate environments appear to be largely free of VSGs which is probably due to radiative destruction of these small particles. The best estimates for the distribution of VSGs is shown in Fig. 2.5 (LMC) and 3.5 (SMC).

3. Amount of emitting dust in the Magellanic Clouds

Dust grains absorb starlight, thereby heating up and emitting in the infrared. Thus, infrared radiation is re–emitted starlight. For this mechanism, theoretical in–band fluxes have been calculated for a range of dust temperatures and are presented in the Appendix. It is assumed that only one type of dust radiates at 60 and 100 μm, that it is located at a fixed distance D from us (53 kpc for the LMC and 63 kpc for the SMC; Humphreys, 1984) and that it is optically thin at these wavelengths. The equations used to obtain dust masses M and dust (mass) column densities M_d are

$$M = \frac{f_\nu \; D^2}{\kappa_\nu \; B_\nu(T_d)} \tag{4}$$

and

$$M_d = \frac{I_\nu \; D^2 \; \Delta\Omega}{\kappa_\nu \; B_\nu(T_d)}, \tag{5}$$

where $\Delta\Omega$ is the solid angle of the area corresponding to 1 cm^2 at the distance D. The equation to calculate the dust mass is essentially the one given by Hildebrand (1983), although we use a somewhat different dust emissivity (see the Appendix for a discussion). This assumed absorptivity, κ_ν (cm^2/gram) $=$ 40 $(\lambda/100\ \mu\mathrm{m})^{-1.5}$, results in somewhat lower ($\sim$ 0.9) temperatures and dust masses.

3.1. Dust mass estimated from global emission

Straightforward use of the integrated 60 and 100 μm infrared flux densities yields a total dust mass of 1.4 x 10^5 $M_\odot$ for the LMC and 1.2 x 10^4 $M_\odot$ for the SMC, at an average (60 – 100 μm) T_d of 33 K (see Chapter V). These values are lower limits as they do not take into account actual spatial variations in temperature (in the line–of–sight or in the sky plane). Because of the strong dependence of thermal dust emission on temperature ($I_\nu \propto M_d \; \kappa_\nu \; B_\nu(T_d) \propto M_d \; T_d^{4+n}$), mass estimates of dust with a range of temperatures are biased towards the hottest dust in the beam. For this reason, the assumption of a

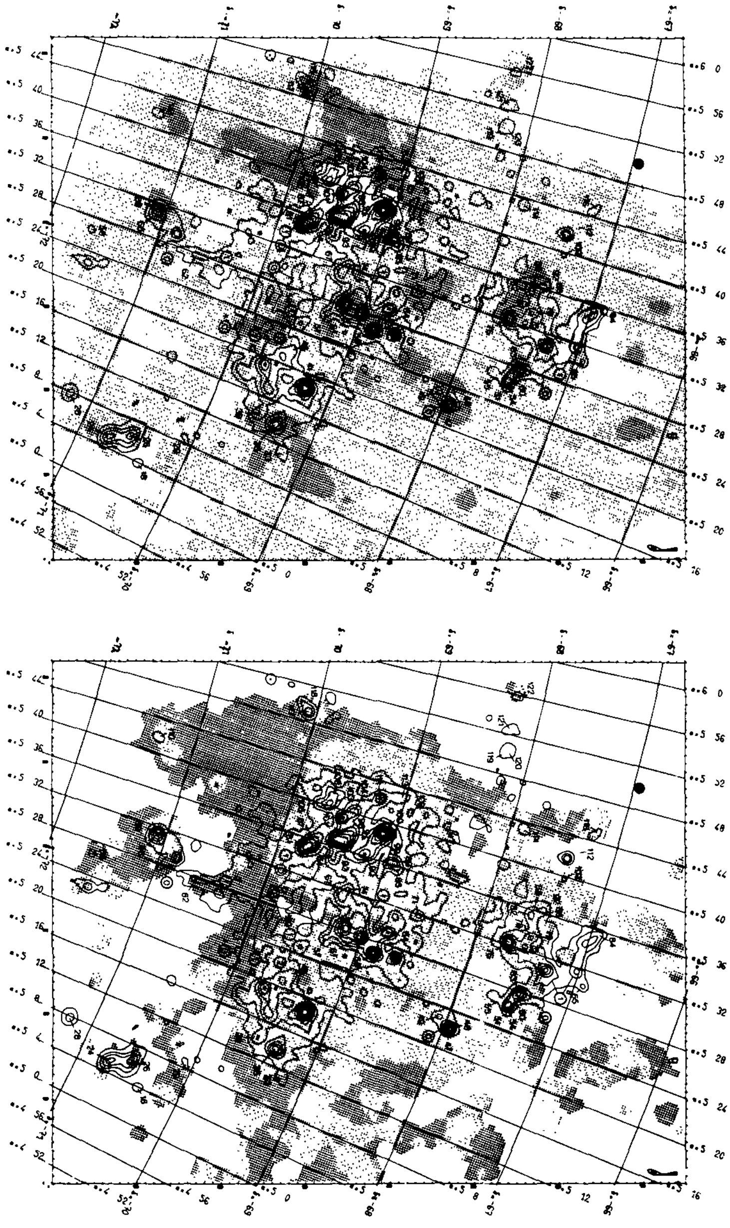

Figure 4. *Overlays showing the relation between mid-infared excess emission (grey scales) and ultraviolet radiation (contours) in the LMC. Darker grey scales represent more intense excess emission. The contours are taken from Viullemin (1988; added labels are described in that paper). Note the different orientation of these maps with respect to the other maps in this chapter.*

Fig. 4.1. LMC 25 μm cirrus intensity map (grey scales as in Fig. 2.5) and ultraviolet emission (contours).

Fig. 4.2. LMC $T_{12-25\mu m}$ map (V.7.1, grey scales as in Fig. V.7.1) and ultraviolet emission (contours).

single temperature derived from emission ratios tends to underestimate the cool and total amounts of dust mass present.

In Section 2.3.1 we calculated that 17 % of the 60 μm flux densities of the LMC and 8 % of that of the SMC are produced by very small grains. Correcting the 60 μm intensities for small grains contributions, T_d drops to 31 and 32 K respectively, resulting in an increase in dust mass of about 34 and 15 % respectively.

The mass of the hot dust component (with $T_d \gtrsim 200$ K) is calculated from the integrated 12 and 25 μm flux densities using Equation 4. We derived masses of 2 $M_\odot$ for the LMC and 0.1 $M_\odot$ for the SMC, negligible compared to the mass of the cool and warm dust component.

3.2. Dust mass estimated from line–of–sight temperature distribution

The above estimate, derived from global properties can be improved by taking into account the structure of the Clouds as revealed by the IRAS maps. First, we consider the effect of varying temperature across the Clouds, *i.e.* the temperature distribution over the sky plane. We still assume that in each line–of–sight dust is adequately represented by the single line–of–sight temperature derived from the 60 to 100 μm emission ratio. Maps of the line–of–sight temperature can then be combined with *e.g.* 100 μm (or 60 μm) intensity maps to yield dust column density maps. Integration of these column density maps over the face of the Clouds then yields the total dust mass. The mass so derived will be higher than the mass derived from the global emission because dust at temperatures lower than the emissivity–weighted global mean is now more adequately represented: dust with lower T_d has a much smaller emissivity; therefore, its column density and mass has to be higher to produce the same intensity as hotter dust. Spatial resolution is also a factor of importance. With finite sensitivity, convolution to lower resolution increases the detectability of low–surface brightness regions. If, as is the case at the edges of the LMC, such regions also have relatively low dust temperatures, they may contribute significantly to the local mass without being an important contributor to the total infrared intensity. It turns out that this effect is not very important for the SMC. Obviously, further degradation of the spatial resolution leads to diminishing returns as relatively cool regions become progressively more blended with hotter regions. The limit, of course, is the reduction of the object to a point source, where we have reduced the observations to the case discussed in Section 3.1.

Use of the line–of–sight temperature distribution in the Clouds raises the lower limit to the dust mass of the LMC to 2.0 x 10^5 $M_\odot$ (increase of 45 %) and 1.2 x 10^4 $M_\odot$ for the SMC (no increase). If the contribution of PAHs to the 60 μm emission is taken into account the masses are resp. 24 and 15 % higher. They are still lower limits, because we have still ignored possible variations in dust temperature in the line–of–sight.

If the clouds are relatively flat and seen face-on, line–of–sight depths are small. If these depths are of order 150 pc or less, we expect only small temperature gradients in the line–of–sight, and the estimate would be essentially correct. If line–of–sight depths are much larger than this, cool dust may be present in significant amounts, and we would have underestimated the total mass possibly by a large factor. To estimate the potential range of dust masses, we assume (unrealistically) that all observed infrared emission originates in the coolest dust component. In this way, we can derive an upper limit to the total amount of dust as a function of the assumed cold dust temperature. The results of this calculation are given in Table 6. Since the Magellanic Clouds are characterized by stronger radiation fields than the Solar Neighbourhood (Chapter V) and by lower dust abundances (Koornneef, 1984), we do not expect dust in the Clouds to be colder than dust in the Solar Neighbourhood. If most of the dust were at 15 K, the upper limit to the mass is two orders of magnitude higher than the lower limit we have just derived. More realistically, for 20 K, the range between lower and upper mass limits is only an order of magnitude. Thus, our first attempts yield a mass estimate that — barring systematic errors in the Chicago assumptions (Hildebrand, 1983) — is correct to within an order of magnitude.

Table 6. *Integrated dust mass from 100 μm flux densities assuming fixed and variable dust temperatures.*

T_d (K)	M_d, LMC ($M_\odot$)	M_d, SMC ($M_\odot$)
Fixed T_d:		
15 K	2.5×10^7	3.2×10^6
20 K	2.4×10^6	2.1×10^5
25 K	5.8×10^5	5.1×10^4
30 K	2.2×10^5	1.9×10^4
35 K	1.1×10^5	9.3×10^3
40 K	6.2×10^4	5.4×10^3
45 K	4.0×10^4	3.5×10^3
50 K	2.9×10^4	2.5×10^3
Variable T_d:		
Line–of–sight T_d	2.0×10^5	1.2×10^4
Decomposition of T_d	6.2×10^5	1.6×10^4

3.3. Dust mass estimated from decomposition of line–of–sight temperatures

In order to further improve our mass estimate, we have decomposed the emission from each line–of–sight into emission from dust at different temperatures. The procedure is as follows. We start with the lowest observed line–of–sight temperature T_0 (at the Cloud edges) covering at least a few per cent of the total Cloud surface area. The surface brightness corresponding to this temperature is then extrapolated over the full face of the Clouds, and subtracted from the observed maps. With a suitable temperature step ΔT, this procedure is then repeated on the remaining map, but now extrapolating over the surface area with line–of–sight temperatures larger than T_1; yielding a map of dust emitting at temperature $T_1 = T_0 + \Delta T$, and a new set of intensity maps now only containing dust at temperatures $T > T_1$. The procedure is then repeated untill the highest observed temperature is reached, so that we have decomposed the observed maps into a set of intensity maps at different, but constant temperatures. The sum of the intensity maps reproduces the observed total intensity maps, and the constant temperature maps can be converted into column density maps. Summing these constant temperature colum density maps yields the total column density map, and summing that map yields the total mass.

In effect, the method redistributes observed infrared intensities to temperatures lower than the line–of–sight temperature while keeping the total intensity constant and equal to the observed intensity. This procedure then yields a "best" estimate for the total mass, because it neither assumes that all dust radiates at the line–of–sight temperature (*i.e.* close to the maximum temperature in that line–of–sight), nor that all dust radiates at the lowest temperature seen anywhere in the Clouds. The results are listed in Table 7, as a function of temperature step ΔT used in the decomposition. Obviously, the result becomes more accurate with smaller steps. For the LMC, the mass derived in this way converges at 6.2 x 10^5 $M_\odot$, and for the SMC at 1.6 x 10^4 $M_\odot$.

Table 7. *Total dust masses for line–of–sight temperature decomposition.*

ΔT *(K)*	$M_{LMC}/M_\odot$	$M_{SMC}/M_\odot$	M_{MWs}/M_{los} [a]
T–range	*22 - 43*	*27 - 43*	*23 - 29*
30 [b]	*2.0 x* 10^5	*1.2 x* 10^4	*1.00*
15	*2.0 x* 10^5	*1.3 x* 10^4	*1.00*
10	*2.4 x* 10^5	*1.5 x* 10^4	*1.00*
5	*4.2 x* 10^5	*1.5 x* 10^4	*1.00*
2.5	*5.6 x* 10^5	*1.5 x* 10^4	*1.07*
1	*5.7 x* 10^5	*1.6 x* 10^4	*1.24*
0.5	*6.2 x* 10^5	*1.6 x* 10^4	*1.27*

Notes to Table 7:

a) The Galactic foreground data of Chapter IV has been used to give the relative increase in the integrated dust mass. The foreground column density is normalized to 1386 x 10^{20} *H–atoms* cm^{-2}*. The foreground data has been convolved to 35° resolution, the same linear resolution as the infrared data on the LMC.*

b) The value for ΔT = 30 *K corresponds to the mass calculation from the line–of–sight temperatures.*

There are two basic assumptions underlying this estimate. The first is that in each line–of–sight, dust is present at all temperatures between the lowest temperature seen in the Clouds and the emissivity–weighted line–of–sight temperature. As mentioned before, this is probably not true if the Clouds have only small line–of–sight depths. In that case, the above values are overestimates. The second assumption is that the lowest observed temperature in the Clouds is indeed the lowest dust temperature present. Although we have confidence in this assumption, we must point out that colder dust could be present, in which case the above values are underestimates (see Section 3.4). From this, and the preceeding section, we conclude that realistic estimates for the mass of cool ($T_d \approx 25$ K) dust present in the Magellanic Clouds are between 2 and 6 x 10^5 $M_\odot$ for the LMC and between 1.2 and 1.6 x 10^4 $M_\odot$ for the SMC. A possible contribution by cold (15 K) dust is discussed in Section 3.4.

In the LMC, about 50 % of the total surface area emits at line–of–sight temperatures < 30 K. Our decomposition leads to the situation that in fact 90 % of all LMC dust emits at $T_d < 30$ K, contributing 60 % of the observed 100 μm intensity. Average temperatures as opposed to emissivity–weighted temperatures are 26 K for the LMC and 31 K for the SMC. The small mass range for the SMC reflects the fact that it contains only a small area with line–of–sight temperatures < 30 K. Extrapolation of the LMC decomposition on SMC dust shows that dust with temperatures between 22 and 27 K has a mass of (0 – 2) x 10^4 $M_\odot$. For comparison purposes a similar decomposition has been applied on the Galactic foreground of Chapter IV. The foreground maps were first convolved to a resolution of 35° (*i.e.* identical linear resolution as on the LMC). The temperatures then range from 23 to 29 K, showing a similar lowest dust temperature as in the LMC. We find an increase in dust column densities for the foreground emission of 27 %.

3.4. The cold dust mass

The mass of cold ($T_d < 20$ K) dust is a potential problem. Because $I_\nu \propto M_d\ \kappa_\nu\ T_d^{4+n}$, large masses of cold dust will not contribute commensurably to intensity and hence, will go unnoticed with the presence of a reasonable amount of cool (~ 25 K) or warm (~ 50 K) dust (*cf.* Table 6). In the preceeding sections we have assumed that cold dust is present in insignificant amounts. In this section we will take a closer look at this assumption.

Chini *et al.* (1984) observed continuum emission from several spiral galaxies at 1–mm. We have combined their data with integrated IRAS flux densities (Rice *et al.*, 1988b). From the 60 and 100 μm IRAS data we calculated dust temperatures T_d and masses M_{T_d}, and predicted 1–mm flux densities. Comparison of predicted with observed flux densities then gives the ratio M_{15K}/M_{T_d}. For the six spiral galaxies we find $M_{15K} \approx M_{T_d}$ (with the exception of the peculiar galaxy NGC 4736). Due to the Clouds lower metallicities (Dufour, 1984) and higher star formation activity (Lequeux, 1984), we expect more cold dust in these large spiral galaxies than in the Magellanic Clouds. This comparison therefore sets the upper limit of cold dust in the Magellanic Clouds equal to the dust mass based on integrated flux densities (Section 3.1): 1.4 x 10^5 $M_\odot$ for the LMC and 1.2 x 10^4 $M_\odot$ for the SMC.

According to Cox *et al.* (1986) dust associated with quiescent molecular clouds in our Galaxy has a temperature of about 15 K, so that B_ν peaks at infrared wavelengths of 340 μm. The total molecular gas content of the Galaxy equals the atomic gas content. The total molecular hydrogen content of the Clouds is estimated by Cohen *et al.* (1988) and Rubio *et al.* (1988) to be about 1/3 of the atomic hydrogen content, *i.e.* 1.8 x 10^8 $M_\odot$ for the LMC and 1.6 x 10^8 $M_\odot$ for the SMC. According to Cox *et al.* (1986), in the Galaxy both HI and H_2 clouds have the same gas–to–dust ratio. If we adopt the same for the Clouds, we find from the global estimates of cool dust that $M_c = 5$ x 10^4 $M_\odot$ for the LMC and 5 x 10^3 $M_\odot$ for the SMC. Thus, realistic estimates for a cold (15 K) dust component are (1.0 ± 0.5) x 10^5 $M_\odot$ for the LMC, and (0.8 ± 0.4) x 10^4 $M_\odot$ for the SMC.

3.5. The total dust mass of the Magellanic Clouds

In Table 8 we summarize the dust masses of the Clouds for the different temperature components (also gas masses and the total dynamic mass are given). For the LMC we derive a total dust mass of $M_{LMC} = (5.5 \pm 2) \times 10^5\ M_\odot$ and for the SMC we find $M_{SMC} = (2.4^{+2.2}_{-0.2}) \times 10^4\ M_\odot$. The correction for a contribution of PAHs at 60 μm has been applied. The large relative error in the SMC value results from the unknown dust component with temperatures between 23 and 27 K.

Table 8. *Masses in the Magellanic Clouds (in $M_\odot$).*

Property		*LMC*	*SMC*	*Reference*
Dust masses:				
Warm + cool	M_{w+c}	4.1×10^5	1.4×10^4	*Section 3.3.*
Correction far PAHs		0.4×10^5	0.2×10^4	*Section 3.1.*
Cold	M_c	1.0×10^5	0.8×10^4	*Section 3.4.*
Total	M_d	5.5×10^5	2.4×10^4	*Section 3.5.*
Gas masses:				
HI	M_{HI}	5.4×10^8	4.8×10^8	*McGee and Milton (1966),* *Hindman (1967).*
H_2	M_{H_2}	1.8×10^8	1.6×10^8	*Cohen et al. (1988),* *Rubio et al. (1988).*
He	M_{He}	1.6×10^7	1.4×10^7	*Lequeux (1984).*
Total	M_{gas}	8.8×10^8	7.8×10^8	
Dynamic mass:				
Total	M_{dyn}	6.0×10^9	1.5×10^9	*McGee and Milton (1966),* *Hindman (1967).*

3.6. The distribution of the warm and cool dust

The dust column density maps of the Magellanic Clouds are shown in Fig. 5. As mentioned in Section 3.1, derived line–of–sight temperatures may overestimate the average line–of–sight temperature and dust column densities may therefore be underestimated. This effect may be progressively more important in the higher temperature regions (*e.g.* the Greater 30 Doradus Region).

In general there is good agreement between the infrared maps (see Chapter V; Fig. 1 and 2) and the dust column density maps. High dust column densities appear on peaks in the dust temperature maps (Fig. 5 in Chapter V). This suggests that overcorrection

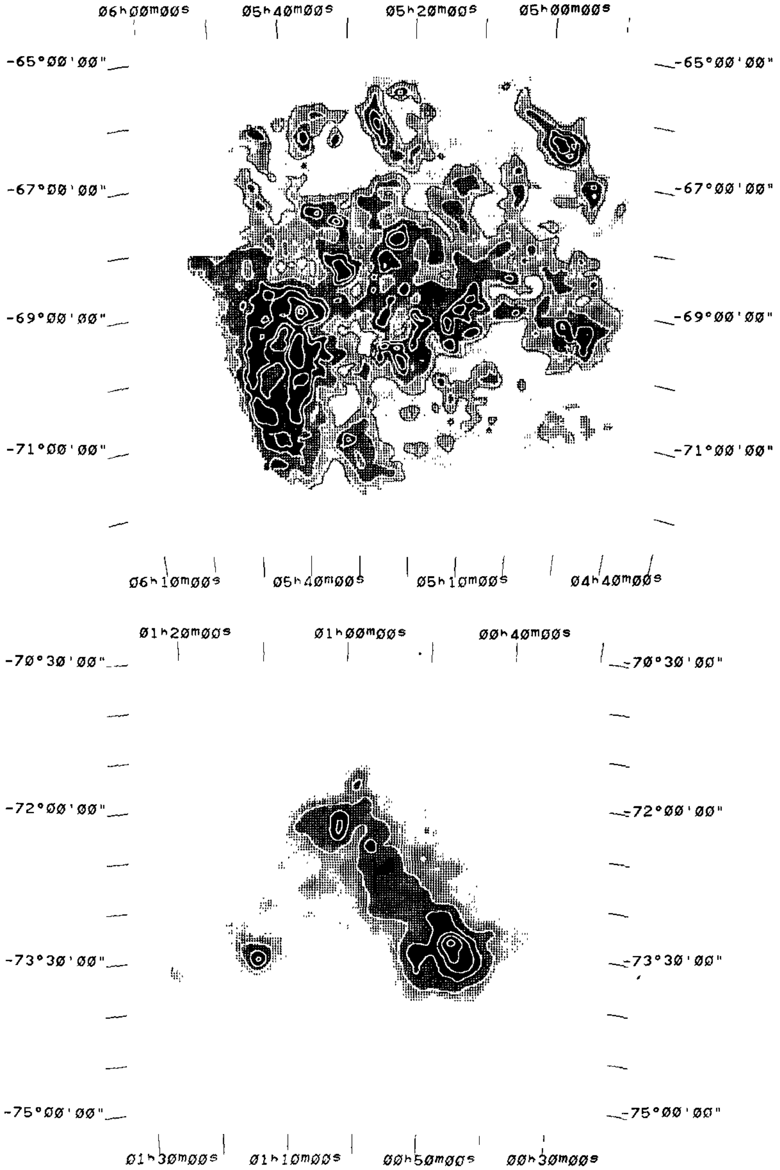

Figure 5. *Dust column density maps (M_d) of the Magellanic Clouds, based on line-of-sight infrared data, at a resolution of 8'.*

Fig. 5.1. The LMC. Grey scales range from 1 – 300 x 10^6 $M_\odot$/sr. Darker grey scales correspond to higher dust column densities. Contours are at 10, 20, 40, 60, 100, 200, 275 x 10^6 $M_\odot$/sr. At the distance of the LMC (53 kpc) a column density of 10^6 $M_\odot$/sr corresponds to a mass of 3.17 x 10^{16} H-atoms cm^{-2}.

Fig. 5.2. The SMC. Grey scales range from 1.4 – 54 x 10^6 $M_\odot$/sr. Darker grey scales correspond to higher dust column densities. Contours are at 10, 20, 30, 40, 50 x 10^6 $M_\odot$/sr. At the distance of the SMC (63 kpc) a column density of 10^6 $M_\odot$/sr corresponds to a mass of 4.48 x 10^{16} H-atoms cm^{-2}.

Fig. 6.1. LMC $T_d - I_{100\mu m}$.

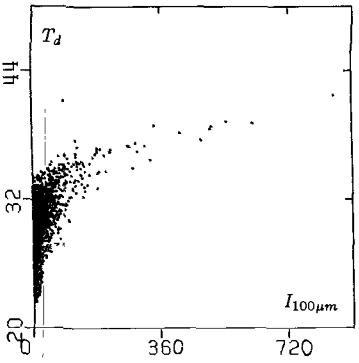

Fig. 6.2. LMC $M_d - I_{100\mu m}$.

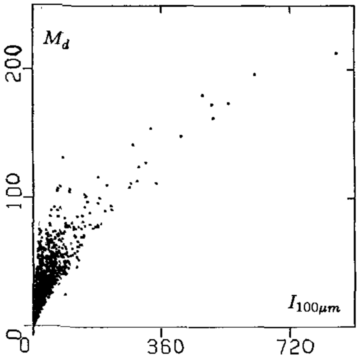

Fig. 6.3. LMC $M_d - T_d$.

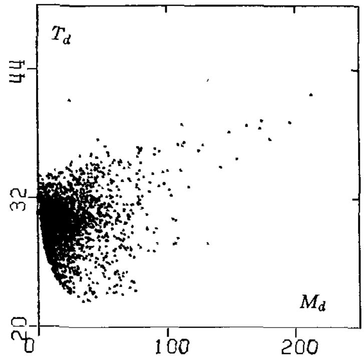

Fig. 7.1. SMC $T_d - I_{100\mu m}$.

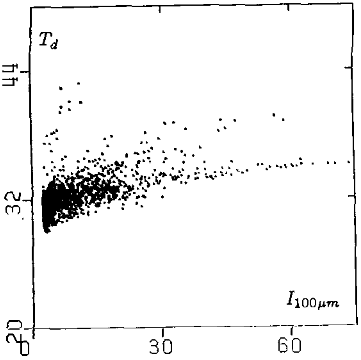

Fig. 7.2. SMC $M_d - I_{100\mu m}$.

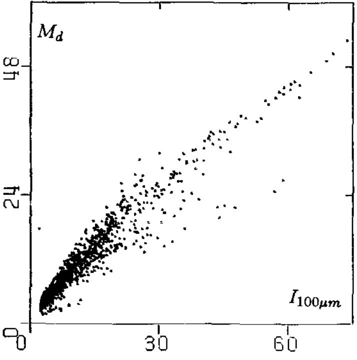

Fig. 7.3. SMC $M_d - T_d$.

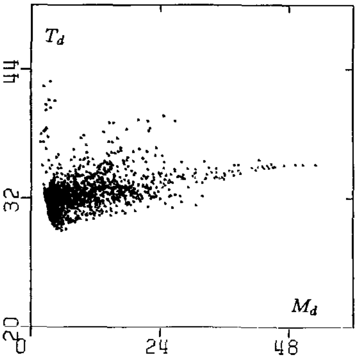

Figure 6. *LMC 6′ pixel-to-pixel scatter diagrams of the dust column density M_d (10^6 $M_\odot$/sr), dust temperature T_d (K) and 100 μm intensity $I_{100\mu m}$ (MJy/sr).*

Figure 7. *SMC 3′ pixel-to-pixel scatter diagrams of the dust column density M_d (10^6 $M_\odot$/sr), dust temperature T_d (K) and 100 μm intensity $I_{100\mu m}$ (MJy/sr).*

for temperature is relatively small in regions with high dust temperature. The relation between M_d and $I_{100\mu m}$, between M_d and T_d and between $I_{100\mu m}$ and T_d are given in pixel-to-pixel scatter diagrams in Fig. 6 and 7 for both Clouds. The dust column densities are uncorrelated with temperature. The continuously changing slope in Fig. 6.2 and 7.2 shows the temperature effect in the intensity maps.

In the LMC, derived dust column densities peak in the 30 Doradus region at 250 x 10^6 $M_\odot$/sr. This area looks point-like on the map, indicating a relatively compact dust concentration. The diffuse LMC dust component varies between (3 – 8) x 10^6, while about half the face of the LMC reaches above 10 x 10^6 $M_\odot$/sr. The Bar has an enhanced column density (20 – 70) x 10^6 while some HII regions have even higher densities of dust (N 11, N 140, N 210: (20 – 90) x 10^6 $M_\odot$/sr). In the LMC, a large dust mass concentration is located in the Greater Doradus Region. This area is about 1.5 x 1 kpc in size and it coincides with the well known star formation region, containing the HII regions 30 Doradus, N 160, N 158 and N 159. In a large area of this complex densities are above 20 x 10^6 $M_\odot$/sr. Due to the higher temperature of the dust grains, dust column densities could be underestimated somewhat more in the Greater 30 Doradus Region than in other regions, increasing the contrast. In Table 9 we give integrated line–of–sight dust masses for the LMC areas defined in Chapter V; atomic hydrogen and cirrus contents are also given, as well as local gas–to–dust ratios (based on line–of–sight data). Note the large amount of dust and gas in the Greater Doradus Region. The relative mid–infrared excess emission is much less in the Greater Doradus Region than in the other regions (see Section 2.3.2).

Table 9. *Dust and gas in some selected areas in the LMC* [a].

Property (Unit)		*Bar*	*Shapley*	*Doradus Region*		*LMC*
			Const. III	*Greater*	*South*	*Rest*
Equivalent area Ω		1.22	2.11	1.78	0.85	11.5
(10^{-3} *sr / %*)		7	12	10	5	66
M_d (10^4 $M_\odot$)		2.8	2.4	5.5	1.9	7.1
T_d (*K*)		33	32	36	27	31
$f_{12\mu m,cirrus}/f_{12\mu m,area}$	(%)	100	97	53	97	81
$f_{12\mu m,cirrus}/f_{12\mu m,tot}$	(%)	16	11	17	5	29
$f_{25\mu m,cirrus}/f_{25\mu m,area}$	(%)	26	31	6	43	40
$f_{25\mu m,cirrus}/f_{25\mu m,tot}$	(%)	3	3	3	1	10
σ_d (10^7 $M_\odot/sr$)		2.3	1.1	3.1	2.2	0.6
M_{HI} (10^7 $M_\odot$)		3.5	4.0	7.5	3.9	14.0
M_{HI}/M_d (—)		1250	1670	1360	2050	1970

In contrast to the LMC, there is no large dust concentration visible in the column density map of the SMC. There are 5 clear peaks in the SMC dust distribution: two in the SW–Bar, a main one at $\sim$ 55 x 10^6 $M_\odot$/sr and one just East of it at $\sim$ 25 x 10^6 $M_\odot$/sr; in the NE–Bar N 76 shows a peak ($\sim$ 33 x 10^6 $M_\odot$/sr), while the complex N 83/84 dominates the dust content of the Wing ($\sim$ 32 x 10^6 $M_\odot$/sr). Although high in infrared intensity, N 66 in the NE–Bar is not a strong peak in the dust column density map ($\sim$ 25 x 10^6 $M_\odot$/sr). The increased infrared in this region is therefore mainly a temperature effect. The entire SMC–Bar shows densities of (12 – 18) x 10^6 $M_\odot$/sr while the extended component is (2 – 10) x 10^6 $M_\odot$/sr surrounding the Bar and connecting it to the SMC–Wing. In Table 10 we give integrated dust masses for the same areas as defined in Chapter V. We see that the NE–Bar and SW–Bar have identical dust properties, but that the dust and cirrus properties in the Shapley Wing are different; the Wing shows a much higher gas–to–dust ratio (based on line–of–sight data) than the Bar region and the cirrus emission at 12 μm is much smaller.

Table 10. *Dust and gas in some selected areas in the SMC* [a].

Property (Unit)		*NE–Bar*	*SW–Bar*	*Shapley Wing*
Equivalent Area Ω		*3.06*	*2.96*	*1.75*
(10^{-3} *sr / %*)		*39*	*38*	*23*
M_d (10^3 $M_\odot$)		*4.8*	*6.4*	*1.0*
T_d (*K*)		*34*	*34*	*33*
$f_{12\mu m,cirrus}/f_{12\mu m,area}$	(%)	*100*	*99*	*37*
$f_{12\mu m,cirrus}/f_{12\mu m,tot}$	(%)	*34*	*55*	*6*
$f_{25\mu m,cirrus}/f_{25\mu m,area}$	(%)	*31*	*27*	*23*
$f_{25\mu m,cirrus}/f_{25\mu m,tot}$	(%)	*11*	*13*	*4*
σ_d (10^6 $M_\odot/sr$)		*1.6*	*2.2*	*0.6*
M_{HI} (10^7 $M_\odot$)		*13.7*	*17.5*	*8.8*
M_{HI}/M_d (-)		*28500*	*27300*	*91700*

Note to Tables 9 and 10:

a) The total flux density in each area related to cirrus at 12 and 25 μm has been calculated relative to the total Clouds' flux densities and relative to the flux densities in the specific areas.
Dust masses are calculated from line–of–sight data.

4. Comparison of infrared radiation and dust with atomic hydrogen

4.1. Infrared and atomic hydrogen emission

We compared the infrared maps with HI observations of Rohlfs *et al.* (1984) on the LMC and of McGee and Newton (1981) on the SMC. HI column densities are higher in the SMC than in the LMC. Integration of the HI data shows that the SMC map contains 90 % and, due to the limited field size, the LMC map only 60 % of the integrated HI mass of Hindman (1967) and McGee and Milton (1966); this does not influence our discussion. Large scale HI maps of Mathewson and Ford (1984), have a highest contour enclosing both Clouds at 3 x 10^{20} H–atoms cm^{-2}. The HI column density, corresponding to the infrared sizes of Chapter V are about 25 x 10^{20} for the SMC and 10 x 10^{20} H–atoms cm^{-2} for the LMC, well above the map noise level. Fig. 8.1 and 8.3 give overlays of the infrared 100 μm intensity of the Clouds with HI column densities. Note the good qualitative correlation between the infrared and the HI emission on these large (15′) scales.

The LMC HI and infrared emission peak in the 30 Doradus region, but the HI peak is much more extended. The LMC–Bar is not as pronounced in HI as it is at 100 μm; in the infrared maps it is seen mainly due to the emission from individual HII regions. SMC areas with weak extended HI emission are not prominent at 100 μm. Note some remarkable differences between 100 μm emission and HI data. In the SMC the HII region N 66 is a bright peak at 100 μm but it does not show up in the HI map, as in fact it did not in the dust column density map either. In the LMC, HII region N 55 has a similar high infrared–to–HI ratio, but here there is a clear dust column density peak. Possibly, gas is completely blown away, or most of the gas is in molecular form. New ESO–SEST CO observations show the presence of a compact CO cloud in this region (Israel, priv. comm.).

Figure 8. *Relation between infrared maps and HI maps (at 15′ resolution). See pages 224 – 225.*

Fig. 8.1 overlays LMC $I_{100\mu m}$ *with* N_{HI}. N_{HI} *grey scales range from (0 – 45) x* 10^{20} *H–atoms* cm^{-2}*; darker grey scales indicate higher HI column densities. LMC* $I_{100\mu m}$ *contours are at 5, 10, 20, 40, 60, 100, 200, 400, 600 MJy/sr.*

Fig. 8.2 shows the LMC ratio $I_{100\mu m}/N_{HI}$. *Grey scales range from (0.1 – 5) x* 10^{-14}*; darker grey scales indicate higher ratios. Contours are at 0.5, 0.75, 1.0, 1.5, 2.0, 10.0 (MJy* sr^{-1}*)/(*10^{20} *H–atoms* cm^{-2}*).*

Fig. 8.3 overlays SMC $I_{100\mu m}$ *with* N_{HI}. N_{HI} *grey scales range from (0 – 110) x* 10^{20} *H–atoms* cm^{-2}*; darker grey scales indicate higher HI column densities. SMC* $I_{100\mu m}$ *contours are at 2, 5, 10, 20, 30, 40, 50 MJy/sr.*

Fig. 8.4 shows the SMC ratio $I_{100\mu m}/N_{HI}$. *Grey scales range from (0.1 – 0.7) x* 10^{-14}*; darker grey scales indicate higher ratios. Contours are at 0.05, 0.075, 0.1, 0.2, 0.3, 0.4, 0.5 (MJy* sr^{-1}*)/(*10^{20} *H–atoms* cm^{-2}*).*

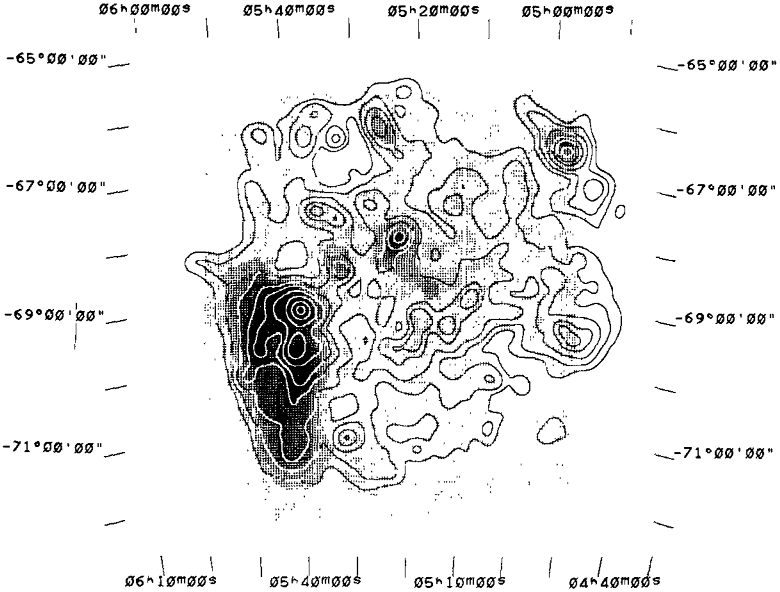

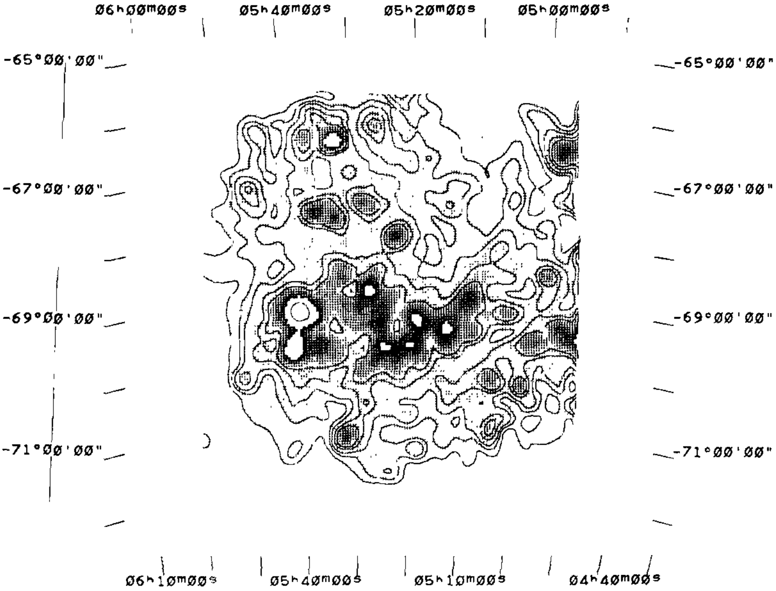

Fig. 8.1. LMC $I_{100\mu m}$ contour map and N_{HI} grey scale map.
Fig. 8.2. LMC $I_{100\mu m}/N_{HI}$ map.

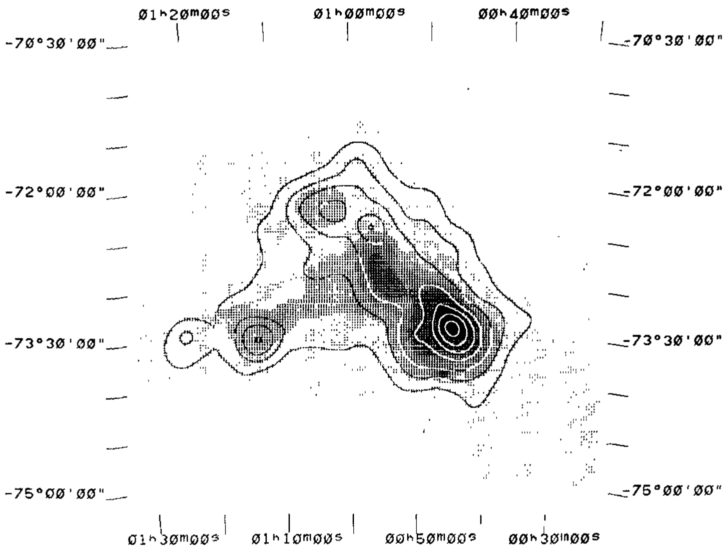

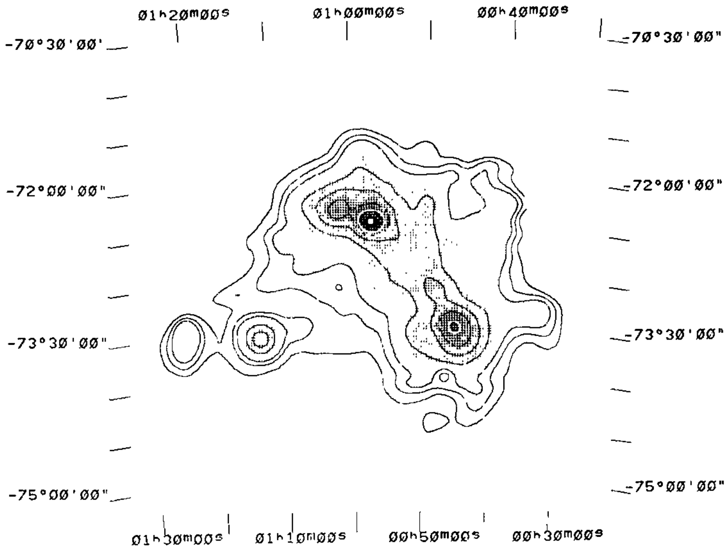

Fig. 8.3. SMC $I_{100\mu m}$ contour map and N_{HI} grey scale map.
Fig. 8.4. SMC $I_{100\mu m}/N_{HI}$ map.

Fig. 9.1. LMC $I_{12\mu m}$ - N_{HI}.

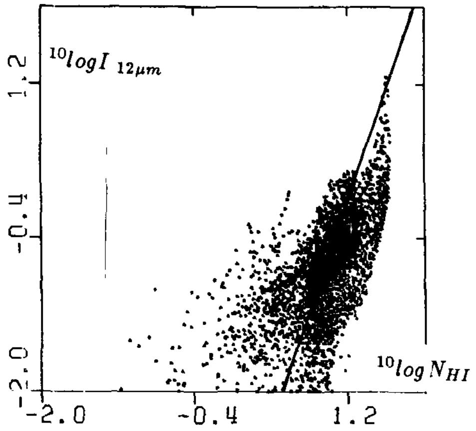

Fig. 9.2. LMC $I_{25\mu m}$ - N_{HI}.

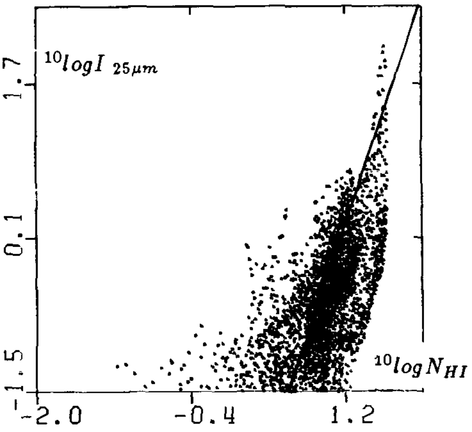

Fig. 9.3. LMC $I_{60\mu m}$ - N_{HI}.

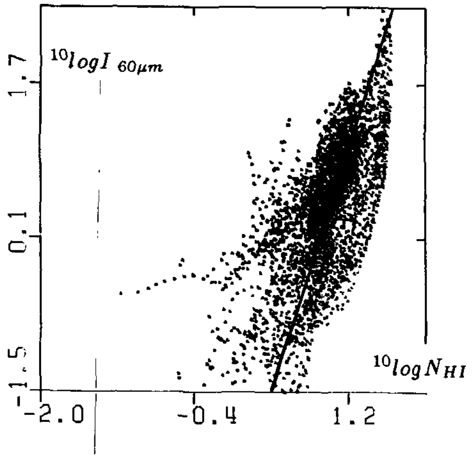

Fig. 9.4. LMC $I_{100\mu m}$ - N_{HI}.

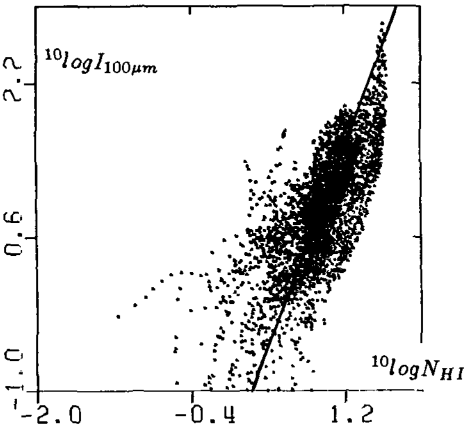

Figure 9. *LMC 6′ pixel-to-pixel scatter diagrams for $^{10}log I_{\nu;IR}$ $-^{10} log N_{HI}$ (with $I_{\nu;IR}$ in MJy/sr and N_{HI} in 10^{20} H-atoms cm^{-2}). The fitted lines, which show the relation between the infrared and HI emission are discussed in the text.*

Fig. 10.1. SMC $I_{12\mu m}$ - N_{HI}.

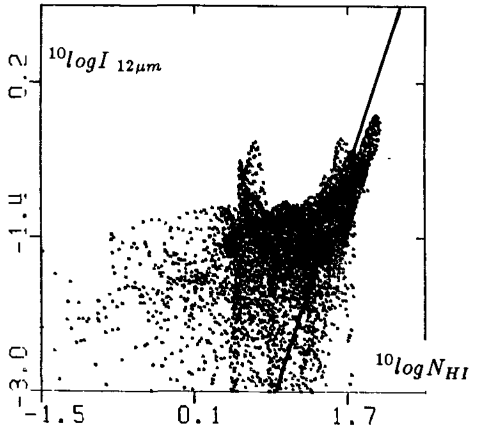

Fig. 10.2. SMC $I_{25\mu m}$ - N_{HI}.

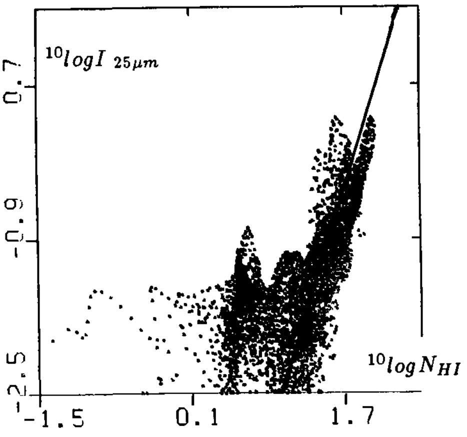

Fig. 10.3. SMC $I_{60\mu m}$ - N_{HI}.

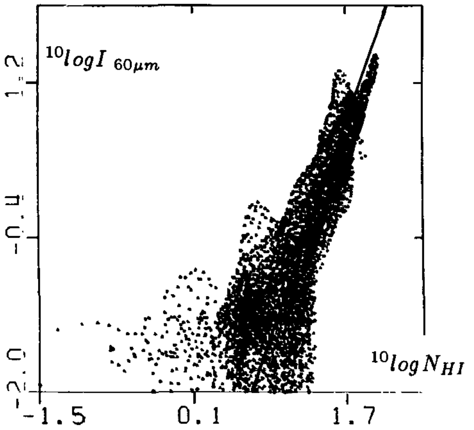

Fig. 10.4. SMC $I_{100\mu m}$ - N_{HI}.

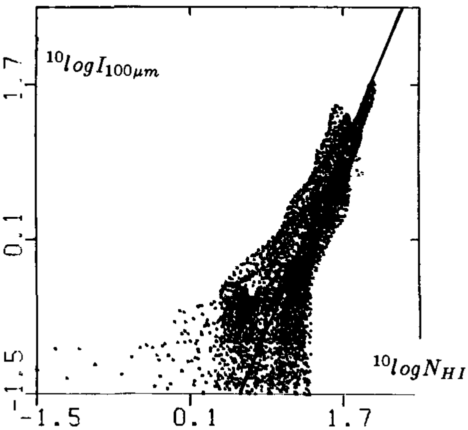

Figure 10. *SMC 3′ pixel-to-pixel scatter diagrams for $^{10}logI_{\nu;IR}$ $-^{10}logN_{HI}$ (with $I_{\nu;IR}$ in MJy/sr and N_{HI} in 10^{20} H-atoms cm^{-2}). The fitted lines, which show the relation between the infrared and HI emission are discussed in the text. The large scatter at 12 and 25 μm at low infrared intensities are due to noise effects and are not considered in the fit.*

The integrated Clouds' 100 μm flux densities and HI masses result in ratios $I_{100\mu m}/N_{HI} \approx 0.9$ MJy sr^{-1}/10^{20} H-atoms cm^{-2} for the LMC and 0.06 for the SMC. To compare the IRAS 100 μm AO maps with the HI maps, we obtained ratio maps $I_{100\mu m}/N_{HI}$ (Fig. 8.2 and 8.4). A comparison of the low-level diffuse infrared and HI emission ($N_{HI} < 10^{21}$ H-atoms cm^{-2}) gives ratios of 0.9 ± 0.5 in the LMC and 0.08 ± 0.05 MJy sr^{-1}/10^{20} H-atoms cm^{-2} in the SMC. For the LMC–Bar we find ratios of 2 – 4 and for 30 Doradus $I_{100\mu m}/N_{HI} > 15$, the maximum in the LMC. The SMC–Bar has ratios of 0.15 – 0.30, peaking just above 0.7 in the HII region N 66. The peak in the SW–Bar has $I_{100\mu m}/N_{HI} \approx 0.5$. We see that the infrared–to–HI ratio varies even at low infrared and HI intensity levels. The average ratio is 6 – 20 times higher in the LMC than in the SMC; this ratio difference increases with infrared intensity. It is a result of the SMC's relatively weak infrared emission, together with the high HI content. At low levels the LMC ratio is about 1.5 times higher than the Galactic ratio derived in Chapter IV. A difference of 10 % in T_d can account for this factor.

In Fig. 9 (LMC) and Fig. 10 (SMC) we show pixel–to–pixel scatter diagrams of the four IRAS infrared bands with the HI column densities. A summary of the fitted power–law relations, $I_\nu = \alpha_\nu \, HI^{\beta_\nu}$, is given in Table 11. The fits are also shown in the figures; they are not very accurate due to the large scatter for individual pixels, especially at low intensity levels. But they show that infrared emission increases much faster than the HI column densities ($2 < \beta_\nu < 3$). The SMC exponents β_ν are 0.5 lower than the LMC exponents in all four bands. For the SMC α_ν is 10 times lower at 60 and 100 μm. The variations in absolute values α_ν for the different bands is real, but the reality of the differences in β_ν cannot be validated due to the large scatter in the diagrams, and it probably reflects the fitting uncertainties. Similar results were found for the 60 and 100 μm bands for the Galactic foreground towards the Clouds (Chapter IV).

Explanations for ratio variations in the Galactic foreground are discussed in Chapter IV. Several causes can be: variations in dust temperature, possible optical depth effect in the HI or variations in the dust–to–gas ratio. We refer to Chapter IV for a more detailed discussion. In the Clouds we have a larger temperature range than in the Galactic foreground, allowing for larger infrared intensity variations. This discussion again shows that $I_{100\mu m}/N_{HI}$ should *not* be used as a global characteristic of galaxies. Variations of this ratio for different areas in galaxies could give rise to large errors.

Figure 11. *Relation between dust and HI column densities (at 15′ resolution). See pages 229 – 230.*

Fig. 11.1 shows the LMC dust mass density overlayed on the HI column density map. Dust mass contours are at 5, 10, 20, 40, 70, 100, 130, 160, 190 x 10^6 *$M_\odot$/sr.* N_{HI} *grey scales range from 0 – 45 x* 10^{20} *H–atoms cm*$^{-2}$*; darker grey scales indicate higher HI column densities.*

Fig. 11.2 shows the LMC dust–to–atomic gas mass ratio. Grey scales range from 0 – 2 x 10^{-3}*; darker grey scales indicate higher ratios; the top grey scales are in 30 Doradus and N55. Contours are at 2, 4, 6, 8, 10, 15 x* 10^{-4}*.*

Fig. 11.3 shows the SMC dust mass density overlayed on the HI column density. Dust mass contours are at 2, 5, 10, 15, 20, 25, 30, 40 x 10^6 *$M_\odot$/sr.* N_{HI} *grey scales range from 0 – 110 x* 10^{20} *H–atoms cm*$^{-2}$*; darker grey scales indicate higher HI column densities.*

Fig. 11.4 shows the SMC dust–to–atomic gas mass ratio. Grey scales range from 0 – 1.2 x 10^{-4}*; darker grey scales indicate higher ratios; the top grey scales are in N 76 and SW–Bar. Contourvalues are at 2, 4, 6, 8, 10 x* 10^{-5}*.*

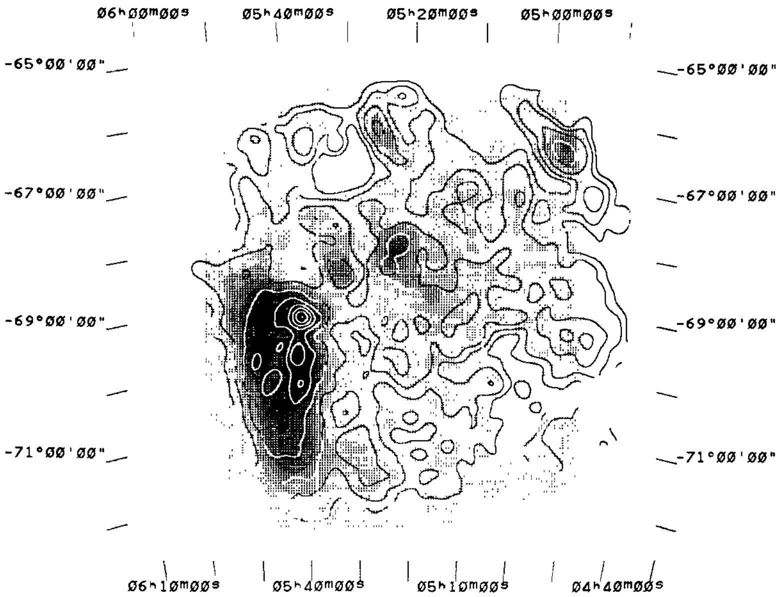

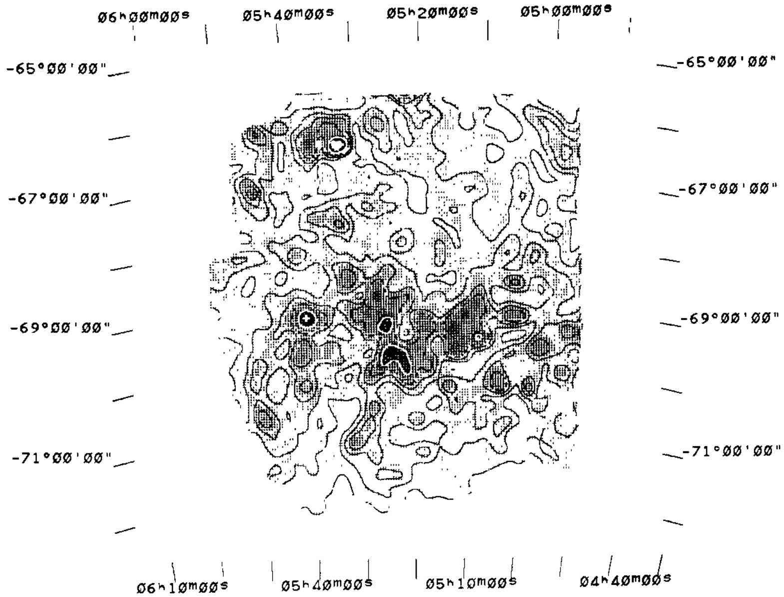

Fig. 11.1. LMC M_d contour map and N_{HI} grey scale map.
Fig. 11.2. LMC dust–to–gas mass ratio map M_d/M_{HI}.

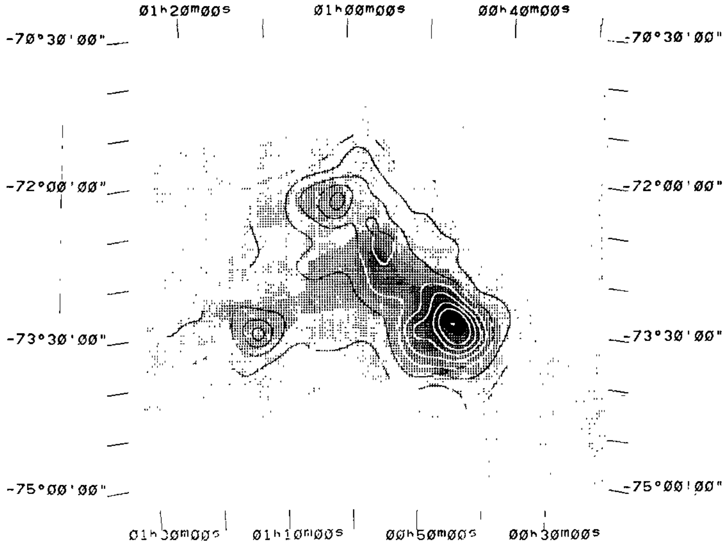

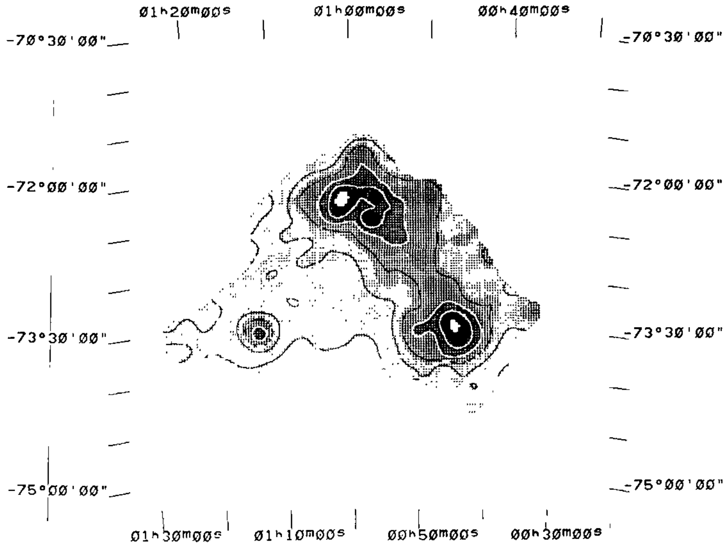

Fig. 11.3. SMC M_d contour map and N_{HI} grey scale map.

Fig. 11.4. SMC dust–to–gas mass ratio M_d/M_{HI}.

4.2. Dust and atomic hydrogen column densities

The infrared optical depths, calculated as $\tau_\nu = I_\nu / B_\nu(T_{60-100\mu m})$ are small and peak at 0.3 x 10^{-3} in the LMC (30 Doradus region) and at 0.4 x 10^{-4} in the SMC (SW-Bar). Hydrogen column densities might be underestimated if the optical depth for HI is not small; this may affect the peaks of the N_{HI} distribution (*e.g.* the Greater 30 Doradus Region). Generally, we will assume optically thin HI emission from the Clouds.

A comparison of HI column densities with line-of-sight dust column densities is shown in Fig. 11; overlays of HI and dust are given together with the dimensionless M_d/M_{HI} mass ratio maps. Locally there are variations in the derived dust-to-gas ratio (Fig. 11.2 and 11.4). M_d/M_{HI} is higher in HII regions (infrared emission peaks), while the diffuse infrared emission has a low ratio. In the figures the dust-to-gas ratio correlates with line-of-sight temperatures and infrared emission, but less than $I_{100\mu m}/N_{HI}$. In the LMC, peaks in the dust-to-gas ratio occur at 30 Doradus of 2.1 x 10^{-3}, and in N 55 of 2.5 x 10^{-3}. In the SMC peaks occur at N 76 (1.5 x 10^{-4}), the SW-Bar (1.5 x 10^{-4}) and N 83/84 (0.8 x 10^{-4}). Rather than a different gas-to-dust ratio, this result may indicate the presence of significant amounts of molecular gas in these locations. Fig. 12 shows the relation between T_d and M_d with N_{HI} in pixel-to-pixel scatter diagrams. The temperatures are rather uncorrelated with N_{HI}; on average there is a small increase in T_d with N_{HI}. M_d is better correlated with N_{HI}, however clear diversions from the straight line occur, especially at high HI column densities. From these diagrams we derive values for M_d/M_{HI} of 1/1800 (LMC) and 1/23000 (SMC), with a 40 % spread; Fig. 12 also shows these derived linear relations with their error bars. Correcting for the line-of-sight decomposition in temperature and the contribution by cold dust will give ratios 2 – 3 times higher. A complete discussion about the gas-to-dust ratio, related to other observations, will be given in the next chapter. Here we only note that in particular the increase of M_d/M_{HI} with increasing N_{HI} at $N_{HI} > 4$ x 10^{20} H-atoms cm^{-2} may indicate the presence of (unseen) molecular gas.

Table 11. *Relations of infrared and dust with HI.*[a)]

		LMC			*SMC*	
Data	α_ν	β_ν	*Fig.*	α_ν	β_ν	*Fig.*
$I_{12\mu m}$	*0.00025*	*2.8*	*9.1*	*0.000039*	*2.3*	*10.1*
$I_{25\mu m}$	*0.00017*	*3.1*	*9.2*	*0.0000060*	*2.8*	*10.2*
$I_{60\mu m}$	*0.0036*	*2.9*	*9.3*	*0.00033*	*2.5*	*10.3*
$I_{100\mu m}$	*0.017*	*2.7*	*9.4*	*0.0017*	*2.2*	*10.4*
$I_{60\mu m}/I_{100\mu m}$	*0.2 - 1.0*	—	—	*0.3 - 1.0*	—	—
T_d *(K)*	*23 - 43*	—	*12.1*	*28 - 43*	—	*12.3*
M_{HI}/M_d	*1800*	—	*12.2*	*23000*	—	*12.4*

Note to Table 11:

a) The specific intensities I_ν *are in MJy/sr and the HI column densities are in* 10^{20} *H-atoms cm*$^{-2}$.

Fig. 12.1. LMC T_d - N_{HI}. *Fig. 12.3. SMC T_d - N_{HI}.*

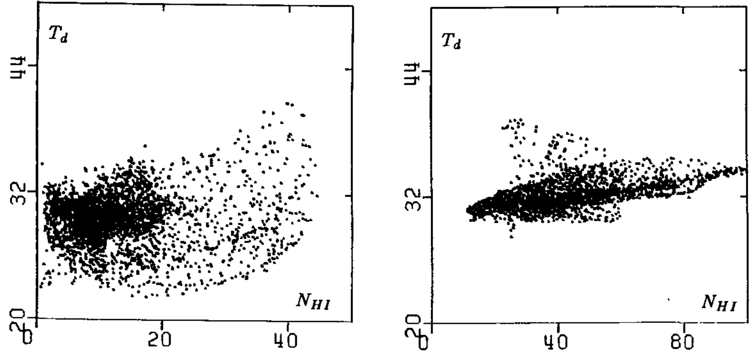

Fig. 12.2. LMC M_d - N_{HI}. *Fig. 12.4. SMC M_d - N_{HI}.*

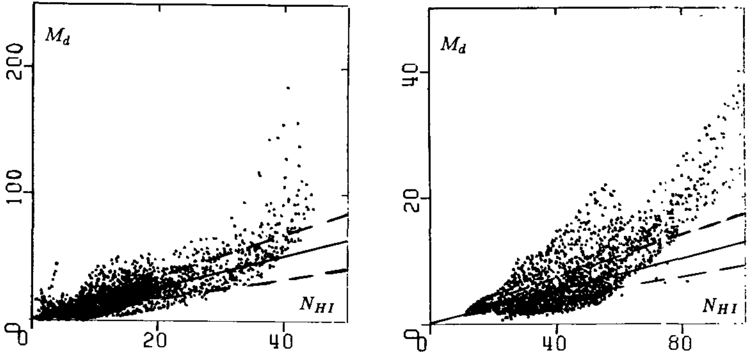

Figure 12. *Pixel-to-pixel scatter diagrams for both Clouds, showing the relation of T_d (K) and M_d (10^6 $M_\odot$/sr) with N_{HI} (10^{20} H-atoms cm^{-2}). LMC pixels are 6′, SMC pixels 3′ in size. In the dust-to-gas mass relation diagrams, the solid straight lines are fitted average dust-to-gas ratios, while the dashed ones are derived by using the global properties.*

5. Conclusions

As the Local Group spiral galaxies, the Magellanic Clouds contain 12 and 25 μm excess emission relative to the extrapolated cool dust emission. This excess is weak compared to that in the spiral galaxies, and the SMC excess is only half that of the LMC excess, which is similar to the excess emission in the giant irregular galaxy NGC 4449. The Clouds show low integrated $f_{12\mu m}/f_{25\mu m}$ ratios. The ratios $f_{12\mu m}/f_{25\mu m}$ and $f_{60\mu m}/f_{100\mu m}$ place the Clouds in the middle of the galaxy area in Helou's (1986) colour-colour diagram.

The nature of the mid–infrared emission in the Clouds is discussed. For both Clouds, very small grains (PAHs) heated to high non–equilibrium temperatures by single photon hits are the most likely explanation for the mid–infrared excess. In the SMC 25 % of the SMC mid–infrared emission might be caused by (proto) stellar objects. We created maps of the relative mid–infrared excess; these maps anti–correlate with infrared emission. We have derived 12 and 25 μm cirrus maps, by removing the large grain population, which show an anti–correlation with the ultraviolet radiation field. Detailed studies show that the excess and cirrus emission is less in HII regions. In the SMC, the Shapley Wing likewise shows little excess emission.

We have presented dust column density maps for the Magellanic Clouds. In the LMC the main complex of dust is the Greater 30 Doradus region. In the SMC no large dust mass concentration is present, and the bright HII region N 66 shows up only marginally; here high infrared intensities are caused by high dust temperatures. Mostly the effects of high dust content and high temperature combine to produce observed infrared radiation.

From the dust column density maps we have derived total dust masses for the cool (25 K) and warm (> 30 K) dust components in the Magellanic Clouds. We have estimated the amount of unobserved cold (< 20 K) dust in the Clouds using 1–mm observations of other galaxies and CO observations of the Clouds. The amount of hot dust, emitting at 12 and 25 μm is negligible compared to the mass of cool dust. We obtain dust masses of $M_{LMC} = (5.5 \pm 2) \text{ x } 10^5 \, M_\odot$ and $M_{SMC} = (2.4^{+2.2}_{-0.2}) \text{ x } 10^4 \, M_\odot$.

We discuss the relation between infrared 100 μm intensity and the neutral hydrogen column density for the Clouds. The ratio $I_{100\mu m}/N_{HI}$ varies strongly over the face of the Clouds. Scatter diagrams show that $I_\nu \propto N_{HI}^{\sim 2.5}$. Therefore $I_{100\mu m}/N_{HI}$ should not be used as a global characteristic of galaxies, nor should it be extrapolated over areas in a single galaxies. The dust column density map correlates well with the HI map. The dust–to–gas ratio varies over the face of the Clouds, but less strong as $I_{100\mu m}/N_{HI}$; its use is more justified.

References

Beichman, C.A., Wilson, R.W., Langer, W.D., Goldsmith, P.F.: 1988, IPAC preprint 36

Boulanger, F., Baud, B., van Albada, G.D.: 1985, ***Astron. Astrophys.*** **144**, L9

Boulanger, F., Beichman, C.A., Désert, F.X., Helou, G., Perault, M., Ryter, C.: 1988, *Astrophys. J.* in press

Chini, R., Kreysa, E., Mezger, P.G., Gemünd, H.–P.: 1984, ***Astron. Astrophys.*** **137**. 117

Cohen, R.S., Dame, T.M., Garay, G., Montani, J., Rubio, M., Thaddeus, P.: 1988, *Astrophys. J. (Letters)* in press

Conti, P.S.: 1987, in *"Starbursts and Galaxy Evolution"*, eds. T.X. Thuan, T. Montmerle, J. Tran Thanh Van, Editiones Frontières, Gif–sur–Yvette, 91

Cox, P., Krügel, E., Mezger, P.G.: 1986, ***Astron Astrophys.*** **155**, 380

Cox, P., Mezger, P.G.: 1988, in *"Comets to Cosmology"*, Lecture Notes on Physics **297**, ed. A. Lawrence, Springer Verlag, Berlin, 97

Draine, B.T., Anderson, N.: 1985, ***Astrophys. J.*** **292**, 494

Dufour R.J.: 1984, in ***"Structure and Evolution of the Magellanic Clouds"***, IAU Symp. 108, eds. S. van den Bergh, K.S. de Boer, Reidel Dordrecht, 353

Feast, M.W., Thackeray, A.D., Wesselink, A.J.: 1960, *Mon. Not. R. Astron. Soc.* **121**, 25

Gatley, I., Becklin, E.E., Hyland, A.R., Jones, T.J.: 1981, *Mon. Not. R. Astron. Soc.* **197**, 17P

Gatley, I., Hyland, A.R., Jones, T.J.: 1982, *Mon. Not. R. Astron. Soc.* **200**, 521

Habing, H.J.: 1988, *Astron. Astrophys.* in press

Helou, G.: 1986, *Astrophys. J. (Letters)*, **311**, L33

Henize, K.G.: 1956, *Astrophys. J. Suppl.* **2**, 315

Hildebrand, R.H.: 1983, *Quartly J. R. Astron. Soc.* **24**, 267

Hindman, J.V.: 1967, *Aust. J. Phys.* **20**, 147

Humphreys, R.M.: 1984, in *"Structure and Evolution of the Magellanic Clouds"*, IAU Symp. 108, eds. S. van den Bergh, K.S. de Boer, Reidel Dordrecht, 145

Hunter, D.A., Gillett, F.C., Gallagher III, J.S., Rice, W.L., Low, F.J.: 1986, *Astrophys. J.* **303**, 171

Israel, F.P.: 1984, in *"Stucture and Evolution of the Magellanic Clouds"*, IAU Symp. 108, eds. S. van den Bergh, K.S. de Boer, Reidel dordrecht, 319

Jones, T.J., Hyland, A.R., Straw, S., Harvey, P.M., Wilking, B.A., Joy, M., Gatley, I., Thomas, J.A.: 1986, *Mon. Not. R. Astron. Soc.* **219**, 603

Kennicutt, R.C., Hodge, P.W.: 1986, *Astrophys. J.* **306**, 130

Koornneef, J.: 1984, in *"Structure and Evolution of the Magellanic Clouds"*, IAU Symp. 108, eds. S. van den Bergh, K.S. de Boer, Reidel Dordrecht, 333

Lequeux, J.: 1984, in *"Structure and Evolution of the Magellanic Clouds"*, IAU Symp. 108, eds. S. van den Bergh, K.S. de Boer, Reidel Dordrecht, 67

Mathewson, D.S., Ford, V.L.: 1984, in *"Structure and Evolution of the Magellanic Clouds"*, IAU Symp. 108, eds. S. van den Bergh, K.S. de Boer, Reidel Dordrecht, 125

McGee, R.X., Milton, J.A.: 1966, *Aust. J. Phys.* **19**, 343

McGee, R.X., Newton, L.M.: 1981, *Proc. Astron. Soc. Aust.* **4**, 189

Mezger, P.G., Mathis, J.S., Panagia, N.: 1982, *Astron. Astrophys.* **105**, 372

Mezger, P.G.: 1985, in *"Birth and Infancy of Stars"*, eds. R. Lucas, A. Omont, R. Stora, North-Holland, Amsterdam, 31

Mihalas, D., Binney, J.: 1981, *"Galactic Astronomy"*, Freeman and Co., San Francisco, pp 138, 134, 554

Miller, G.E., Scalo, J.M.: 1978, *Astrophys. J. Suppl.* **41**, 513

de Muizon, M., Rouan, D.: 1985, *Astron. Astrophys.* **143**, 160

Puget, J.L., Léger, A., Boulanger, F.: 1985, *Astron Astrophys.* **142**, L19

Rice, W., Boulanger, F., Viallefond, F., Soifer, B.T., Freedman, W.,L.: 1988a, *Astrophys. J.* in prep.

Rice, W., Lonsdale, C.J., Soifer, B.T., Neugebauer, G., Kopan, E.L., Lloyd, L.A., de Jong, T., Habing, H.J.: 1988b, *"A Catalog of IRAS Observations of Large Optical Galaxies"*, in preparation

Rohlfs, K., Kreitschmann, J., Siegman, B.C. and Feitzinger, J.V.: 1984, *Astron. Astrophys.* **137**, 343

Rubio, M., Garay, G., Dame, T.M., Thaddeus, P.: 1987, in *"Molecular Clouds in the Milky Way and External Galaxies"*, in press

Scalo, J.M.: 1987, in *"Starbursts and Galaxy Evolution"*, eds. T.X. Thuan, T. Montmerle, J. Tran Thanh Van, Editiones Frontières, Gif-sur-Yvette, 445

Sellgren, K.: 1984, *Astrophys. J.* **277**, 623

de Vaucouleurs, G.: 1960, *Astrophys. J.* **131**, 574

de Vries, C.P.: 1986, Ph.D. Thesis, University of Leiden

Vuillemin, A.: 1988, *Astron. Astrophys. Suppl.* **72**, 249

Walterbos, R.A.M., Schwering, P.B.W.: 1987, *Astron. Astrophys.* **180**, 27

Werner, M.W., Becklin, E.E., Gatley, I., Ellis, M.J., Hyland, A.R., Robinson, G., Thomas, J.A.: 1978, *Mon. Not. R. Astron. Soc.* **184**, 365

Wood, P.R., Bessell, M.S., Whiteoak, J.B.: 1986, *Astrophys. J. (Letters)* **306**, L81

Chapter VII

DUST IN THE MAGELLANIC CLOUDS

1. Introduction

The Magellanic Clouds are the closest neighbour galaxies of the Milky Way. Their distances of 53 kpc (LMC) and 63 kpc (SMC) (Humphreys, 1984) imply for any (diffraction limited) instrument linear resolutions roughly ten times better than on the closest spiral galaxies M31 (690 kpc) and M33 (720 kpc), and 250 times better than on similar (dwarf) irregular galaxies in the Virgo cluster (15 Mpc). Detection limits for point sources are more than 100 times better than for all other galaxies. This makes the Clouds ideal objects to study their structure in detail and compare them with detailed studies in our Galaxy, and also to compare integrated properties with those of other galaxies.

In this chapter we discuss in Section 2 the infrared characteristics of the Magellanic Clouds, as derived in this thesis. This contains a summary of the foreground extinction, the Clouds' global infrared properties, a discussion of the strength of the radiation field in the Clouds, dust properties and a discussion about the gas–to–dust ratio. Section 3 gives relations between the infrared and dust properties derived on global scales and for local areas, and their implications for other galaxies. Because the Magellanic Clouds are part of the Local Group of galaxies, we compared the infrared properties with those of the larger Local Group spiral galaxies in Section 4 and also with other irregular and spiral galaxies, with emphasis on the degree to which the Magellanic Clouds are representative for these types of galaxies.

2. Infrared characteristics of the Magellanic Clouds

Before we discuss the Magellanic Clouds, we summarize the main characteristics of the Galactic foreground dust towards the Clouds.

2.1. Galactic foreground dust

Using HI observations, we showed that on scales of 15′ there is little variation in the foreground dust towards the SMC. The extinction caused by the foreground is $E_{B-V} = 0.08$ mag. This is twice that quoted by Koornneef (1984; and references therein), although Koornneef left open the possibility of large variations (0.01 – 0.07 mag). Thus, a large fraction of the observed reddening of SMC stars can be accounted for by foreground dust.

Towards the LMC, a significant variation in foreground reddening was found of 0.07 – 0.17, with an average of 0.10 mag. Towards this galaxy Koornneef (1984) gives a value of 0.07 ± 0.04. On average, our value is 40 % higher. Towards the LMC, the lowest reddening values are found for the Bar and the 30 Doradus region; the highest reddening values occur in the South region, where foreground filaments are observed by IRAS at infrared wavelengths.

The conversion from HI column densities to colour excess is done with the relation of Savage and Mathis (1979; and references therein). We showed that reddening values of McNamara and Feltz (1980) of 0.03 mag towards the LMC and 0.02 mag towards the SMC can only be obtained for values of N_{HI}/E_{B-V} 3 to 4 times larger than the value adopted by Savage and Mathis, which correponds to that of dense clouds such as the ρ Oph cloud. This value is unrealistically high and the interpretation of a larger foreground extinction is more likely. Visual and ultraviolet studies of the Clouds must be corrected for a higher and varying Galactic foreground. We do not exclude the possibility of more extreme foreground variations in E_{B-V} on smaller spatial scales ($< 30'$).

2.2. Global infrared properties

In Table 1 we summarize the global infrared properties as derived in this thesis. The two Clouds have similar infrared spectra, characteristic of warm dust with typical temperatures of 33 K; although the spectra differ somewhat between 25 and 60 μm. The SMC is 10 times weaker than the LMC at 60 and 100 μm and 20 times weaker at 12 and 25 μm. The infrared diameter of the LMC is 3 times larger than that of the SMC, and this can account for the most of the difference in far-infrared flux densities.

That the SMC has the same dust temperature as the LMC may look strange at first. The LMC is presently forming more stars per unit mass (Lequeux, 1984), and hence higher dust temperatures are expected. But for the SMC one must consider the effect that the stellar Bar occupies the whole galaxy with the exception of the Shapley Wing. The infrared observations show that the stars in the SMC-Bar are able to produce similar radiation fields as are found in the LMC. The Bar of the LMC only represents a fraction of the whole LMC. There we see an increase in dust temperature, against a cooler background; this shows the influence of the radiation field in areas with high stellar densities.

Table 1. *Integrated Magellanic Clouds infrared data.*

Quantity	Unit	LMC	SMC
Infrared area	$(^\circ)^2$	34.0	2.4
Foreground E_{B-V}	mag	0.07 - 0.17	0.08
$f_{12\mu m}$	Jy	4850	147
$f_{25\mu m}$	Jy	11300	385
$f_{60\mu m}$	Jy	103000	7170
$f_{100\mu m}$	Jy	208000	13900
$T_{12-25\mu m}$	K	240	240
$T_{25-60\mu m}$	K	73	63
T_d	K	33	33
ISRF (IR)	$J_\odot$	7	7
ISRF (UV)	$J_\odot$	1	3
ISRF Intrinsic	$J_\odot$	8	10
$L_{IR\ tot}$	$L_\odot$	9×10^8	8×10^7
L_{IR}/M_{gas}	$L_\odot/M_\odot$	1.3	0.12
M_d	$M_\odot$	5.5×10^5	2.4×10^4

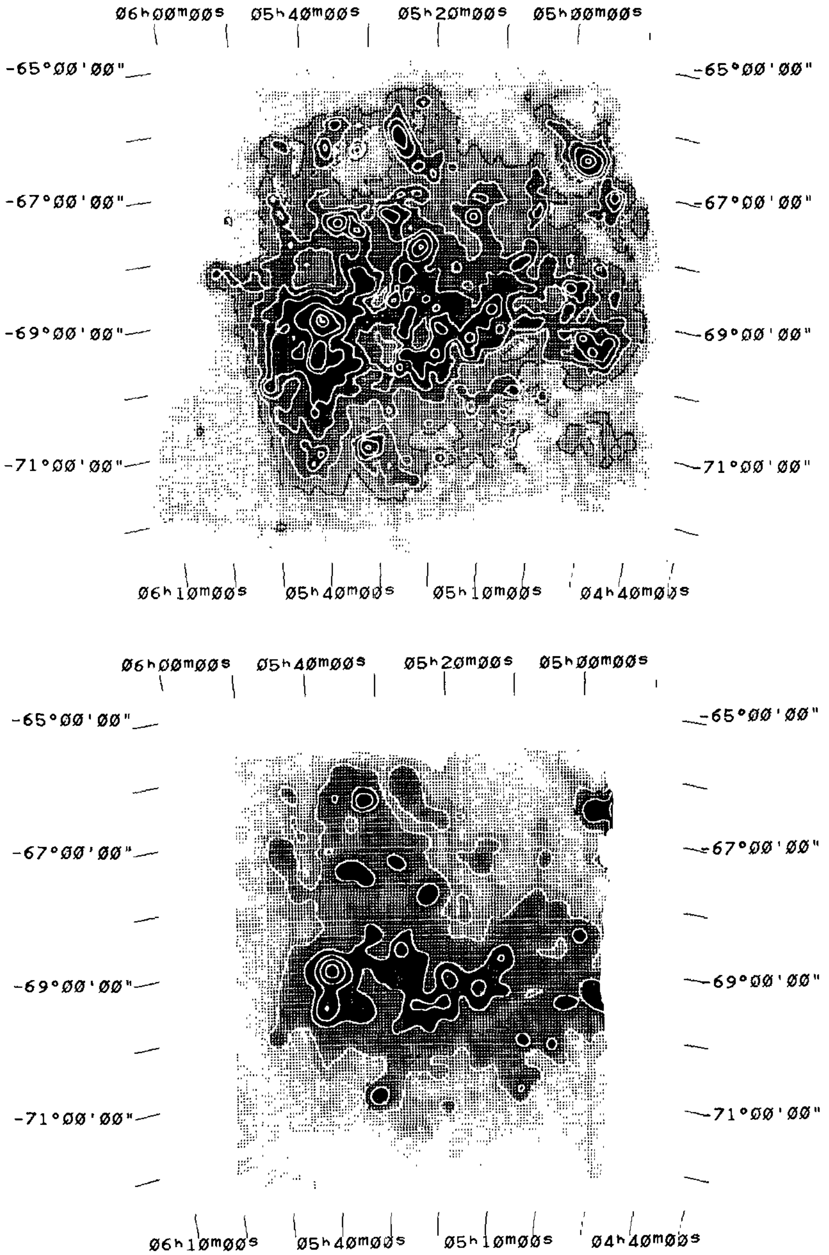

Figure 1. *Total infrared luminosity and luminosity–to–mass ratio for the LMC.*
Fig. 1.1 show the total infrared luminosity at a resolution of 8'. Grey scales range from 0 to 10^{13} $L_\odot/sr$, darker grey scales indicating higher luminosities. Contours are at 20, 50, 100, 200, 500, 1000, 5000, 10000 x 10^9 $L_\odot/sr$ (10^9 $L_\odot/sr$ = 0.36 $L_\odot/sr$).
Fig 1.2 shows the infrared luminosity–to–HI mass at a resolution of 15'. Grey scales range from 0 to 56 $L_\odot/M_\odot$, darker grey scales represent higher ratios. Contours are at 2, 5, 10, 20, 40 $L_\odot/M_\odot$.

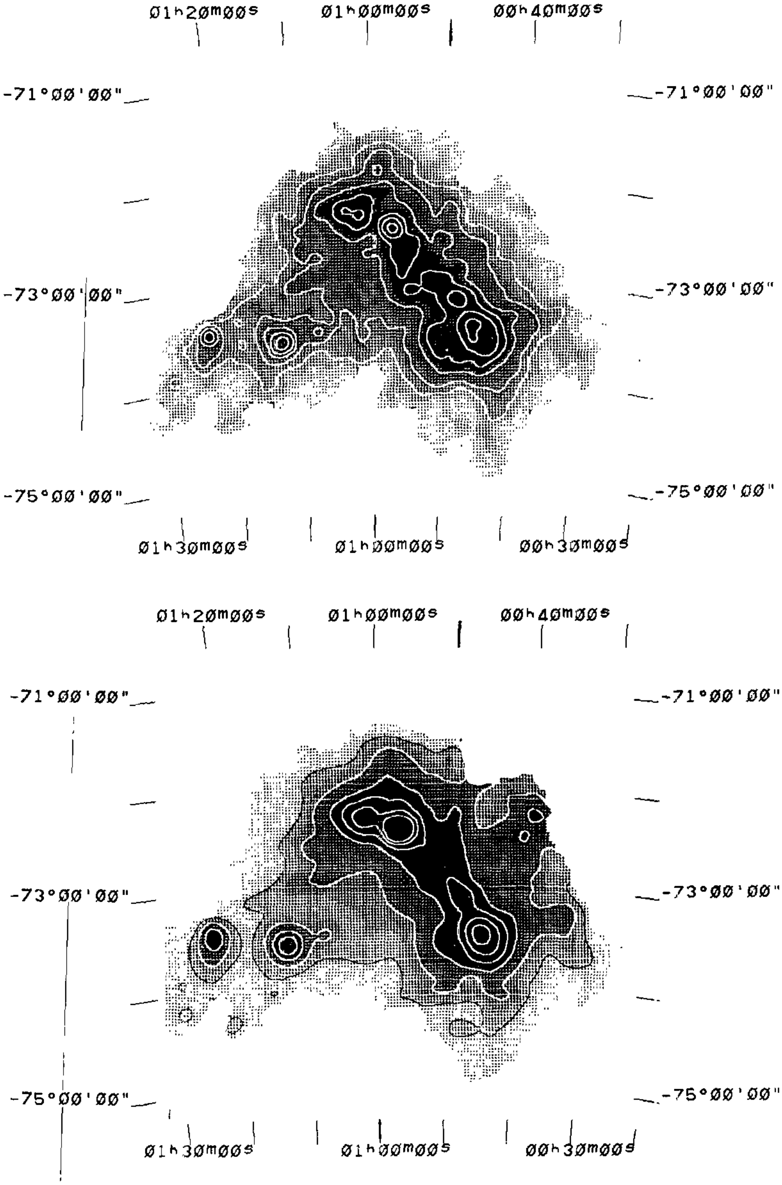

Figure 2. *Total infrared luminosity and luminosity–to–mass ratio for the SMC.*
Fig. 2.1 shows the total infrared luminosity at a resolution of 8'. Grey scales range from 0 to 5 x 10^{11} $L_\odot/sr$*, darker grey scales indicating higher luminosities. Contours are at 10, 20, 50, 100, 200, 400 x* 10^9 $L_\odot/sr$ *(*10^9 $L_\odot/sr = 0.25$ $L_\odot/sr$*).*
Fig 2.2 shows the infrared luminosity–to–HI mass at a resolution of 15'. Grey scales range from 0 to 1.7 $L_\odot/M_\odot$*, darker grey scales represent higher ratios. Contours are at 0.1, 0.2, 0.4, 0.6, 0.8, 1.0* $L_\odot/M_\odot$*.*

2.3. The radiation fields in the Magellanic Clouds

The intrinsic ultraviolet radiation fields in the Clouds are 8 (LMC) and 10 (SMC) times stronger than the Solar Neighbourhood radiation field (Chapter V). These fields are two times stronger than derived by Vangiomi–Flam *et al.* (1980), and show that their extinction corrections underestimate the emitted ultraviolet radiation. Therefore heating of dust is more efficient; it appears that 90 % (LMC) and 70 % (SMC) of the emitted ultraviolet emission is converted to infrared emission by dust. The higher fraction for the LMC is related to the higher dust content (see below). Because the average temperature of the dust is similar in the two galaxies, ultraviolet radiation is more efficiently absorbed by the higher dust content in the LMC, and in effect does not cause a significantly higher dust temperature in the SMC.

In Fig. 1 we show the distribution of infrared luminosity L_{IR} in the LMC, together with the luminosity–mass ratio map L_{IR}/M_{HI}; Fig. 2 shows the same for the SMC. In general the latter figures represent infrared activity per unit of HI mass. If all dust would emit at the same temperature, the luminosity–mass relation would be a scaled dust–to–gas ratio, and its distribution would show variations of the dust–to–gas ratio. If, on the other hand, we would assume a constant dust–to–gas ratio in the Clouds, L_{IR}/M_{HI} represents a temperature–to–mass ratio, indicating the strength of the radiation field. In general a combination of these two effects is expected. The infrared emission dominates the total luminosity of the galaxies while the HI mass contains a large fraction (10 – 30 %) of the total mass. The ratio L_{IR}/M_{HI} can be used as a luminosity–to–mass ratio for these galaxies.

2.4. Dust properties

Infrared emission at 60 and 100 μm is emitted by large dust grains (see Hildebrand, 1983). In Local Group spiral galaxies this type of dust is associated with atomic hydrogen (Cox *et al.*, 1988; Walterbos and Schwering, 1987; Rice *et al.*, 1988a). In spiral galaxies of the Virgo cluster, Leggett *et al.* (1986) have suggested dust to be associated with molecular gas and not with HI. Although H_2 and CO may be related in a different way in the Clouds than in the Galaxy, the absence of large amounts of carbon monoxide in the Clouds (Cohen *et al.*, 1988) and the relatively high atomic hydrogen content suggest a correlation with HI. As in general LMC maps of HI and CO correlate both with infrared emission, we cannot decide from these maps, which of these components is associated with the dust. In the SMC, little CO is observed (Rubio *et al.*, 1984), and this is also shows some evidence for a relation of dust with HI.

Polycyclic Aromatic Hydrocarbons are thought to be responsible for the mid–infrared (12 and 25 μm) emission. For the SMC we calculate that other constituents contribute at most 50 % of the mid–infrared emission, this may in fact be a large overestimate. Empirically (by allowing the emissivity exponent to vary) we find that about 25 % of the 25 μm emission should be related to the PAHs, and about 90 % of the 12 μm emission. The observed mid–infrared excess emission of the Clouds is much smaller than in the nearby spiral galaxies (M31, M33) and the Milky Way. As a consequence, the 60 μm emission of the Clouds contains a much smaller contribution by these small grains than in the case of the spirals. For the Galactic foreground we calculated a possible contribution of 40 % (Chapter IV). Using the Clouds global characteristics we find 60 μm PAH contributions of

17 % (LMC) and 8 % (SMC). The mass of *all* the dust is found to be $(5.5 \pm 2) \times 10^5$ $M_\odot$ for the LMC and $(2.4^{+2.2}_{-0.2}) \times 10^4$ $M_\odot$ for the SMC. An estimate for the fraction of cold (15 K) dust associated with molecular hydrogen is 20 % (LMC) resp. 30 % (SMC) of the total dust mass. From Table 1 we see that there appears to be no dust in the SMC with temperatures between 23 K (typical for Solar Neighbourhood dust) and 28 K; this results in the relatively large uncertainty. The mass of the hot (~ 300 K) dust that emits at 12 and 25 μm is only a few solar masses and is negligible compared to the cool dust mass.

2.5. The gas–to–dust ratio

Several authors have investigated the gas–to–dust ratios in the Magellanic Clouds. Instead of the total gas column density, the column density of atomic hydrogen is used and the ratio N_{HI}/E_{B-V} is derived. Neutral hydrogen column densities are taken from 21–cm radio line–radiation or 1216 Å Lyα absorption in line profiles, and visual extinction is obtained from measurements at B and V wavelengths, the Cepheid Period–Luminosity relationship or by galaxy counts. The ratios derived with these methods are compared with the average Galactic value (Bohlin *et al.* , 1978) of 5×10^{21} H–atoms cm^{-2} mag^{-1}. All of these studies show that the global gas–to–dust ratios in the Clouds are considerably larger than average Galactic values: approximately 4 (LMC; Koornneef, 1984) and 17 (SMC; Lequeux *et al.*, 1984) times. However, there is a large spread in gas–to–dust ratios derived from different observations. In Table 2 we summarize these observations.

Table 2. *Gas–to–dust ratios relative to the Galactic value.*

Object	Reference	$\frac{gas}{dust}$ $^{a)}$	Measurements
SMC	van den Bergh (1968)	> 10	HI 21–cm; Cepheid P–L relation.
	van Genderen (1969)	5 – 12	HI 21–cm; Cepheid P–L relation.
	Dachs (1970)	> 100	HI 21–cm; photometry. $^{b)}$
	Hodge (1974)	3	HI 21–cm; galaxy counts.
	MacGillivray (1975)	3	HI 21–cm; galaxy counts.
	Azzopardi and Vigneau (1977)	9 – 24	HI 21–cm; photometry.
	Lequeux *et al.* (1984)	17	HI Lyα; photometry.
	Bouchet *et al.* (1985)	8	HI Lyα; photometry.
	This chapter.	55^{+25}_{-40}	HI 21–cm, thermal dust maps.
LMC	van Genderen (1970)	4	HI 21–cm; photometry.
	Brunet (1975)	20	HI 21–cm; photometry. $^{b)}$
	Martin *et al.* (1976)	9	HI 21–cm; photometry. $^{b)}$
	Koornneef (1982)	4	HI Lyα; photometry.
	This chapter.	3^{+3}_{-1}	HI 21–cm, thermal dust maps.

Note to Table 2:

- a) $\frac{gas}{dust}$ *is the ratio of the gas–to–dust ratio of each Cloud divided by that of the Milky Way.*
- b) *These authors compare the extinction to the stars with the integrated line–of–sight HI emission; hence on average, half their values should be better.*

In Chapter VI we derived dust masses for the Clouds from infrared thermal emission. From these masses we find global gas–to–dust mass ratios, M_{HI}/M_d, for the Clouds of 980^{+560}_{-260} (LMC) and 20000^{+2000}_{-10000} (SMC). For the LMC the ratio is 3^{+3}_{-1} times higher than for the Galaxy and for the SMC 55^{+25}_{-40} times higher. We have assumed an average Galactic gas–to–dust ratio of 375^{+200}_{-100} by using the ratio of Chapter IV after correcting for the line–of–sight temperature decomposition (Chapter VI). Although this Galactic value is a few times higher than canonical values (Hildebrand, 1983), it was derived in a similar way as the dust mass of the Clouds and its use therefore greatly decreases the effect of systematical errors in the dust properties. We summarize different gas–to–dust ratios derived from various kinds of masses in Table 3.

We discuss our results in relation with the results of Lequeux *et al.* (1984) and Bouchet *et al.* (1985) for the SMC and Koornneef (1982) for the LMC, who all use direct line–of–sight measurements. From maps in Chapter VI we see variations in the gas–to–dust ratio over the face of each Cloud. For the LMC the derived global gas–to–dust ratio of 3 agrees very well with the average ratio of Koornneef (1982), while the errorbars are quite narrow. However, the average SMC ratio is 3 times larger than the value of Lequeux *et al.* (1984), and 6 times larger than the value derived by Bouchet *et al.* (1985). Our lower limit of 15, based on a possibly large amount of dust with temperatures of 23 – 28 K, is similar to their values. Note that to achieve this limit the lowest possible SMC gas–to–dust ratio was divided by the highest possible Galactic ratio.

Table 3. *Mass–ratios in the Magellanic Clouds.*

Quantity	LMC	SMC
Gas–to–dust ratios: [a]		
M_{HI}/M_d	980^{+560}_{-260}	20000^{+2000}_{-10000}
M_{gas}/M_d	1600^{+900}_{-400}	33000^{+3000}_{-16000}
M_{dyn}/M_d	11000^{+6000}_{-3000}	63000^{+5000}_{-30000}
M_{dyn}/M_{gas}	7	2
Ratio Cloud/Milky Way: [b]		
M_{HI}/M_d	3^{+3}_{-1}	55^{+25}_{-40}

Note to Table 3:

a) All mass ratios are dimensionless.

b) For the Milky Way we have used a gas–to–dust ratio of 375^{+200}_{-100}.

The agreement for the gas–to–(infrared) dust ratio and the gas–to–(E_{B-V}) ratio of the LMC has several implications. First of all, it confirms the high gas–to–dust ratio, and shows that dust is not locked up in very large grains with low visual reddening. The two completely independent methods give similar results and their connection is well understood. The third implication is that there are no large amounts of cold (15 K) dust in the LMC (about 20 % of the total dust mass), and that the dust mass is dominated by cool (25 K) dust. The strong average radiation field in the LMC has a destructive influence on molecular clouds, and heats their dust to higher average temperatures. Using the cool and cold components we extrapolate the observed IRAS integrated LMC 100 μm flux densities to 35 kJy at 300 μm (3 % by cold dust) and 1 kJy at 1–mm (8 % by cold dust).

Why then is the SMC gas–to–dust ratio that we derived so much higher than the value of Lequeux *et al.* (1984) and Bouchet *et al.* (1985) ? Let us assume that the value derived for the SMC dust mass is too small. We note that the calibration of the infrared maps are correct (Chapter V). To obtain agreement with Lequeux *et al.* (1984) three times more dust should be present. This can be achieved by adding cold (15 K) dust. The presence of such large amounts of cold dust can be confirmed directly from observations at sub–mm wavelengths and indirectly by measurements of molecular complexes. If we have three times more cold dust than cool dust, it will not influence the 100 μm flux density but the flux density at 300 μm would be $\sim$ 3400 Jy instead of 2600 Jy, and 120 Jy at 1 mm instead of 75 Jy without the cold dust. Lacking actual measurements we nevertheless believe that large amounts of cold dust in the SMC are improbable in view of the Milky Way's ratio of cold and cool dust (Cox and Mezger, 1988). The Clouds are young galaxies with low metallicities and a low molecular content, and we therefore, in fact, expect relatively less cold dust than in the Galaxy. The small amount of cold dust that can be added in the LMC is in agreement with this. A more likely possibility is more dust of about 25 K. The line–of–sight decomposition in the SMC shows only a small increase in dust mass because the lowest temperatures are 28 K. If there is 3 times more dust of 25 K, it is strange that there are no regions dominated by purely cool (25 K) dust. It is possible that such a dust component is mainly present in the line–of–sight. Mathewson *et al.* (1986) has observed stars in a long line–of–sight in the SMC SW–Bar; this line–of–sight is non–uniformly filled and observations of the farthest star in this region (*e.g.* HV 1369; van Genderen, 1981) do not show a large increase in E_{B-V}. But the contribution of more cool dust in the line–of–sight cannot be excluded. If this is the case, we may apply the LMC temperature decomposition (Chapter VI) on the SMC dust mass. An addition of a factor of three in 25 K dust would take up 40 % of the observed 100 μm flux density and dominate the prediction at 300 μm ($\sim$ 3600 Jy) and 1–mm ($\sim$ 110 Jy). The large contribution to the observed 100 μm flux densities would increase the average temperature of the cool/warm component from 33 K to 43 K. The changes that are needed in order to add enough cool (25 K) or cold (15 K) dust are too large to seem possible.

As a check, we have compared the SMC ratio with gas–to–dust ratios derived for other (dwarf) irregular galaxies. We used integrated data of Hunter *et al.* (1986) and Rice *et al.* (1988b) and found ratios for DDO 47 and DDO 50 even higher than the SMC gas–to–dust ratio based on integrated data. All irregulars have ratios $L_{100\mu m}/M_{HI}$ comparable to that of the SMC, and after temperature correction they have similar gas–to–dust ratios.

Hence the high gas–to–dust ratio in irregular galaxies compared to spirals is probably real. (See also the discussion in Section 4).

Let us consider the other possibility, that E_{B-V} derived by Lequeux *et al.* (1984) and by Bouchet *et al.* (1985) is too high, or that their Lyα profiles underestimate the HI column densities. To explore this possibility, we discuss the difficulties inherent in the determination of E_{B-V}. Observed HI column densities are on average 15 x 10^{20} H–atoms cm^{-2} for the LMC, 45 x 10^{20} H–atoms cm^{-2} for the SMC and only 5 x 10^{20} H–atoms cm^{-2} for the Galactic foreground; this shows that the SMC HI dominates the foreground emission. A variation of Galactic foreground on small spatial scales will produce larger errors and complicate the analysis of the gas–to–dust ratio. On large scales the SMC foreground is rather smooth (Chapter IV), but local variations cannot be excluded. (In the area of SN 1987A in the LMC, variations of 0.04 to 0.16 mag in foreground were found on a scale of 10$'$; Goudfrooij, priv. comm.). The foreground E_{B-V} derived towards the SMC in Chapter IV ($E_{B-V} = 0.08$ mag) is a factor of 2 higher than normally assumed for the foreground (Koornneef, 1984). This suggests that most of the observed extinction (E_{B-V} = 0.10 – 0.15) is associated with foreground material. The derived ratios N_{HI}/E_{B-V} are therefore closer to Galactic values than those taking into account the higher foreground. Towards the LMC the effect is less, as foreground reddening values differ only by 40 % and the internal LMC extinction is higher. A third possibility that complicates the analysis is spectral misclassification (*e.g.* binary stars), which leads to erroneous values of E_{B-V}.

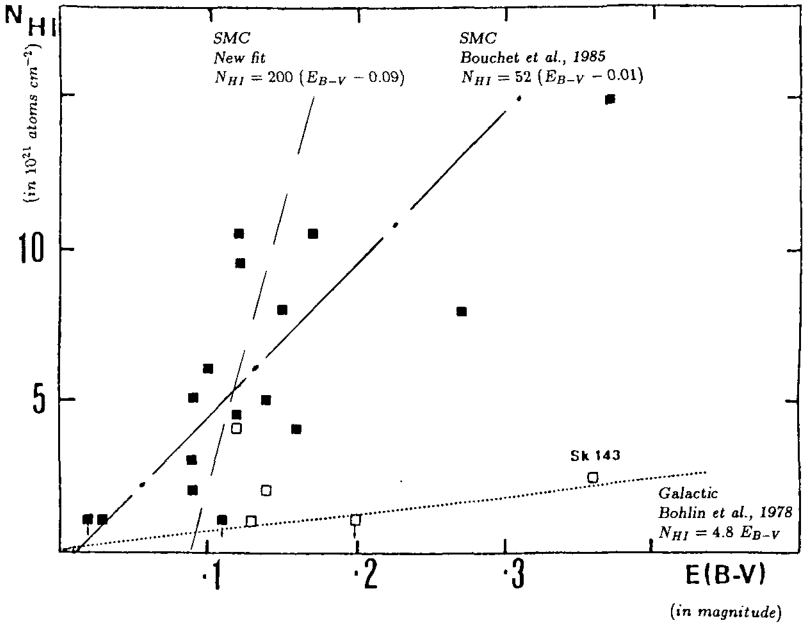

Figure 3. *Relation between N_{HI} and E_{B-V} for the SMC.*
The data are from Bouchet et al. (1985). The dotted line shows the Galactic gas–to–dust ratio, the dashed–dotted line shows the ratio derived by Bouchet et al. (1985) using the filled squares, except the two with the highest reddening. The dashed line give our refit of the data assuming large foreground variations for the two points with low reddening. See Bouchet et al. (1985) for more details.

We have re-evaluated the data of Bouchet *et al.* (1985). In their derivation the stars AV 214 and AV 398 were not included due to large reddening (> 0.27 mag) and the possibility of having H_2 in the line-of-sight. We also exclude these stars, which are located in the NE-Bar. In view of the large foreground we expect also relatively large errors for stars with $E_{B-V} < 0.05$ mag. In addition, we therefore ignore the two stars with exceptionally low reddening (Sk 94 and Sk 145). Foreground fluctuations at small scales are likely the cause of the extremely small or large observed reddenings. We then find a reasonably good correlation between the remaining data points, and a steep fit crossing the E_{B-V}-axis roughly at the foreground reddening of Chapter IV, but the uncertainties mentioned above also apply to these data points. We find a formal fit $N_{HI}/(E_{B-V} - 0.09) = 20 \times 10^{22}$ H-atoms cm^{-2}/mag, 40 times higher than the average Galactic gas-to-dust ratio. This value is in good agreement with the ratio M_{HI}/M_d, derived from the dust and HI masses. Because of the steep slope the actual value of N_{HI}/E_{B-V} has a high uncertainty. Fig. 3 shows the relations between N_{HI} and E_{B-V} derived from the data of Bouchet *et al.* (1985).

Only a few tens of supergiant stars have been studied, while the dust contents of the Clouds are low. To derive accurate values for E_{B-V}, lines-of-sight must be studied with relatively high dust contents, which therefore select lower gas-to-dust ratios, *e.g.* by using stars that are farther away than the average distance, or with extra foreground dust. This might result in biased extinction values, and hence in gas-to-dust ratios which are too small.

There is another problem. Is N_{HI}/E_{B-V} the same gas-to-dust ratio as M_{HI}/M_d ? If this is the case, we determine similar quantities. The relation between these quantities can be found from

$$A_V = R\ E_{B-V} = 1.086\ \tau_V = 1.086\ \pi a^2\ Q_V^{ext}\ N_d; \tag{1}$$

hence there is a linear relation between the two:

$$N_{HI}/E_{B-V} = R/(1.086\ \pi a^2\ Q_V^{ext})\ (\frac{4}{3}\pi a^3\ \rho_d/m_{HI})\ (M_{HI}/M_d) \tag{2}$$

(here m_{HI} represents the mass of a hydrogen atom, a and ρ_d resp. the average radius and density of grains; Q_V^{ext} is the visual extinction efficiency factor; R is the ratio of total to selective extinction). Therefore, if average values of R, a, ρ_d or Q_V^{ext} are not the same in the Clouds as in the Galaxy, a different relation between the two measures of the gas-to-dust ratio exist.

Differences in the ultraviolet part of the extinction curve of the SMC, the LMC and the Galaxy show that the dust particle size distribution of the SMC has a steeper rise for small grains than the LMC and the Galaxy. Hence a might be smaller. It also suggests $R \approx 2$. Isserstedt (1976, 1980) has observed that $R = 2$ in the SMC; later Stift (1984) found a value for R in the SMC considerably larger than the Galactic value of 3.1. Bouchet *et al.* (1985) have derived a value of $R = 2.7 \pm 0.2$ in the SMC, very near the Galactic value. These differences clearly show the uncertainties involved in determinations of R. To explain the difference in gas-to-dust determined from E_{B-V} and from infrared emission purely by dust property differences, the factor R *a* ρ_d/Q_V^{ext} must be 3 – 6 times smaller in the SMC than in the Milky Way. There are not enough data available to further discuss this possibility. The observed agreement for the LMC and the Galaxy may indicate that at least there this factor is not that large.

To summarize the gas–to–dust ratio, we have shown that the LMC ratio derived from infrared measurements, agrees with that based on recent measurements using E_{B-V}. For the SMC a discrepancy between M_{HI}/M_d and N_{HI}/E_{B-V} exists of a factor 3 – 6. This can be explained in several ways. First of all, large amounts of dust with temperatures between 23 and 28 K could be present, in lines–of–sight with large amounts of dust with higher temperatures. Second, the connection between E_{B-V} and M_d does not have to be similar to that in the Galaxy. Thirdly, the Galactic foreground is probably more important than commonly assumed in the analysis of reddening values. We have shown that the last option is the most probable one. We have re–analysed the data of Bouchet *et al.* (1985) and found that a good agreement can be obtained between their data and our gas–to–dust ratio by using the higher Galactic foreground reddening. From now on we will use gas–to–dust ratios (relative to the Galactic value) of 3 in the LMC and 50 in the SMC.

In the SMC ~70 % of the ultraviolet emission is absorbed by dust. In the LMC this fraction is ~90 %. These fractions seem to be related to the amount of dust in these objects. Relative to HI, the LMC contains 15 times more dust. It is obvious that ultraviolet photons will have more difficulty leaving the LMC than the SMC. If we assume the same thickness for the Clouds, their diameters of 7.8 kpc (LMC) and 2.6 kpc (SMC) indicate a factor of 9 in volume. The dust density is 2.5 times higher in the LMC than in the SMC, but it only accounts for a relatively small increase in ultraviolet absorption.

Why is there an underabundance of dust in the Magellanic Clouds ? The Clouds are young irregular galaxies, with high relative gas contents (see *e.g.* Israel, 1984). In the SMC 30 % of the total mass consists of HI, in the LMC 10 %, while the Milky Way Galaxy only contains 1 % of its mass in the form of atomic hydrogen. If similar equilibrium conditions would occur in the Clouds as in the Milky Way, large amounts of H_2 might be expected. On the other hand, the large amount of HI could also exclude large molecular gas abundances as H_2 would never have formed from HI. Formation of H_2 is done on grain surfaces. The lack of grains will then produce a lower abundance of H_2. CO is shielded from the interstellar radiation field by grains, which protect CO against dissociation. CO observations of the LMC (Cohen *et al.*, 1988) reveal a molecular underabundance. In the SMC this underabundance is even more extreme.

From the work of Koornneef (1982) and Bouchet *et al.* (1985) it seems that the dust–to–gas ratio is directly proportional to the metallicity. From Dufour (1984) we know that the abundance of oxygen is 2 times less in the LMC compared to the Solar Neighbourhood, and in the SMC it is 5 times less. For carbon the underabundance is 4 times in the LMC and 30 times in the SMC, compared to the Solar Neighbourhood. Hence the observed gas–to–dust ratios in the LMC and in the SMC go approximately linear with the abundance of carbon and roughly squared with the abundance of oxygen.

3. The relation between global and local characteristics

Studies of distant galaxies are hampered by low linear resolution. Distant objects are therefore seen as point sources, or marginally resolved; this is especially true for data of the IRAS satellite which had resolutions larger than $1' \times 5'$. In our Galaxy, the opposite is true: local phenomena can be studied but we cannot see the forest for the trees. The Magellanic Clouds offer a unique oppertunity to study both, galactic structure in detail as well as global properties.

There are two possibilities to achieve spatial resolutions. Firstly, there is spatial resolution in the sky plane (by high instrumental resolutions). Secondly, we can do some kind of modelling to resolve lines–of–sight. The following basic quantities, important in infrared analysis, are influenced by resolution effects.

Temperatures will be biased towards the highest values in the observing beam; thus properties derived from it will be biased (dust masses will be underestimated, extrapolated luminosities will be overestimated). In Chapter VI we have used a method to decompose lines–of–sight in galaxies into various temperature components.

From the Clouds' integrated data we can predict dust masses of other galaxies. The integrated data give rise to a dust temperature T_d, and a dust mass M_d. We assume that cool and warm dust are both present, with temperatures of above $\sim$ 23 K. From the LMC data we find that spatially resolving the galaxy to about 120 pc increases the mass by a factor of 1.4, while the line–of–sight temperature decomposition increases the mass by another factor of 2. If the coolest dust present has a temperature not much lower than T_d we have the SMC case. Then the decomposition will increase the dust mass by only 20 %.

The mass of cold (15 K) dust in the Clouds can be extrapolated to other irregular galaxies. From the mass of cool ($\sim$23 K) dust based on integrated data (M_d above) this cold dust mass can be found accurately as $(0.6 \pm 0.3) \times M_d$.

Helou's (1986) colour–colour diagram shows a relation between IRAS data $f_{12\mu m}/f_{25\mu m}$ and $f_{60\mu m}/f_{100\mu m}$ for integrated data of galaxies. The integrated flux densities of the Clouds also follow the curve for these galaxies. In Chapter V we showed that the Clouds' ratio maps also show the same relation. Individual areas of the Clouds show the same characteristics as the integrated data of all galaxies. Hence for other galaxies we expect the same to be true: individual areas must occupy a part of the relation in the diagram.

4. The Magellanic Clouds compared to other galaxies

4.1. Local Group spiral galaxies

The Local Group consists of about thirty galaxies, of which the largest spirals are the Milky Way Galaxy, M31 and M33. Integrated infrared data for these galaxies has been taken from Cox *et al.* (1986), Cox and Mezger (1988), Walterbos and Schwering (1987) and Rice *et al.* (1988a). For comparison reasons we have added a few well known spiral galaxies: IC342, M51, M81 and M101 (Rice *et al.*, 1988b). Although the sample is small, we try to find systematic similarities and differences between the Clouds and these spiral type galaxies from the infrared data.

We show the relation between the independent colours $f_{12\mu m}/f_{25\mu m}$ and $f_{60\mu m}/f_{100\mu m}$ for these galaxies in Fig. 4. The Magellanic Clouds are added as well as some other irregulars (see Section 4.2). The spirals are all at the lower right end of the diagram. Note the two very different positions of the Milky Way in the diagram (MWG1 is based on pre-IRAS data, MWG2 on post-IRAS data). The point marked X corresponds to infrared colours of cirrus dust; the point marked Y to infrared colours of dust in strong radiation fields. We see that the Clouds are to the left of the spirals, indicating stronger radiation fields. Together with the higher $f_{60\mu m}/f_{100\mu m}$, $f_{12\mu m}/f_{25\mu m}$ is lower in the Clouds than in the Local Group spirals. Except for MWG2 and NGC 1569, the galaxies are in the area of integrated galaxy colours of Helou (1986).

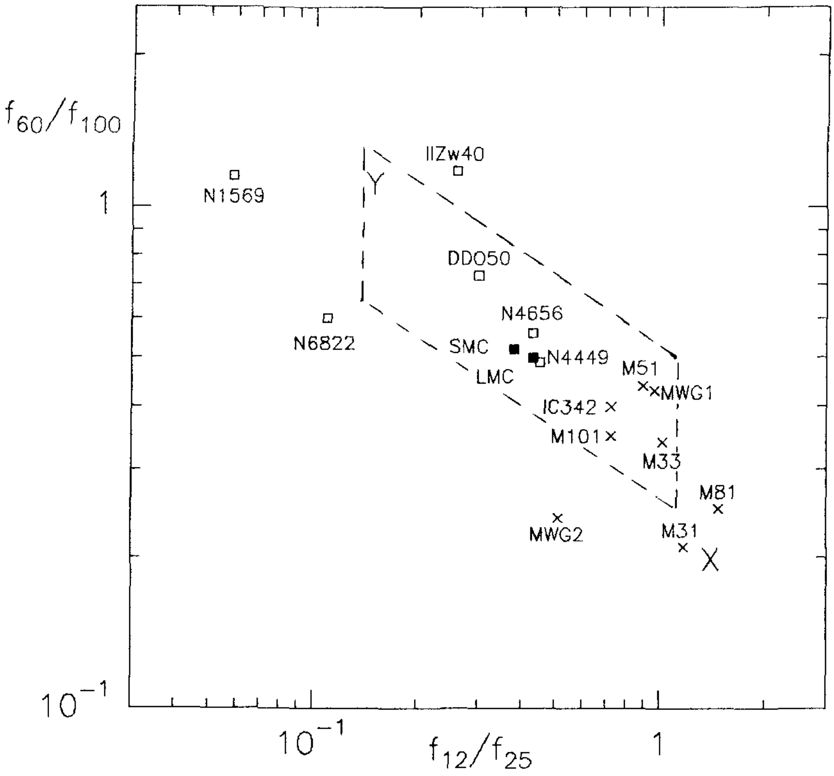

Figure 4. *IRAS infrared colour–colour diagram.*
The flux densities used for the colours are in Jy. Spirals are indicated by crosses while irregulars are indicated by open squares, the Clouds by filled squares. The points X and Y have infrared colours of cirrus dust and dust present in strong radiation fields resp. The galaxy names are used as labels. The galaxy area of Helou (1986) is indicated by the dashed area. Note that only galaxies with good infrared flux densities in four bands are shown.

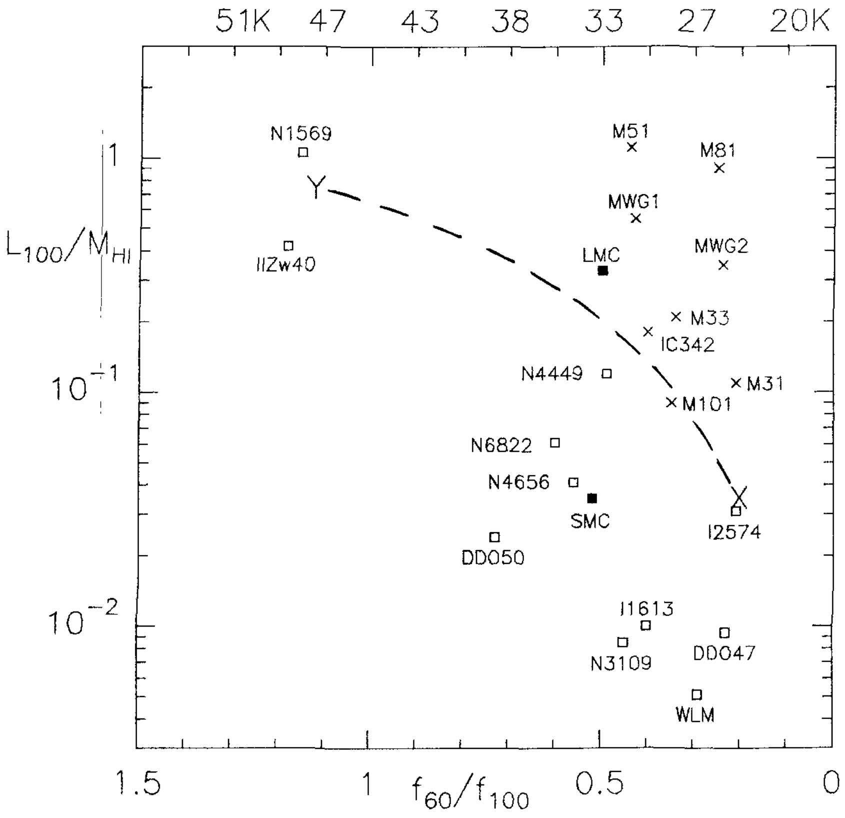

Figure 5. *Relation $L_{100\mu m}/M_{HI}$ with $f_{60\mu m}/f_{100\mu m}$.*
We used $L_{100\mu m}/L_\odot$ and $M_{HI}/M_\odot$ and the IRAS flux densities in Jy. Points X and Y are the same as in Fig. 4 (arbitrary scaled). Spirals are shown by crosses, irregulars by squares and the Clouds by filled squares. The galaxy names are used as labels. Lines parallel to the dashed line give the behaviour of galaxies with constant dust-to-gas ratio with temperature. Together with the band ratios, the dust temperature derived from this ratio are given above the diagram for $\epsilon_\nu \propto \nu^{1.5}$.

The integrated infrared properties of the Clouds are remarkebly different from those of the spirals. Spectral differences are expressed in their band ratios as shown in Fig. 4. Although $f_{25\mu m}/f_{60\mu m}$ are very similar ($\sim$ 0.1) for these galaxies (only M31 and MWG2 are different with $\sim$ 0.25), clear differences occur between 12 and 25 μm and between 60 and 100 μm. These spectral differences must be interpreted as follows. The small grains (PAH) cirrus emission in the spirals is larger than in the Clouds, which is probably related to the higher metallicity in these galaxies. Hence the contribution of PAHs at the 60 μm emission is also larger than in the Clouds, and physical dust temperatures are smaller than predicted from the ratio $f_{60\mu m}/f_{100\mu m}$. For the Clouds the contribution of PAHs at 60 μm is 17 % (LMC) resp. 8 % (SMC); in M31 it is probably higher (Walterbos and Schwering, 1987). Dust temperatures in the Clouds are higher than in the spirals. In Chapter VI we listed the infrared luminosities of the Local Group galaxies; their values correlate with the size of the objects and are therefore not clearly related to the galaxy type.

The Clouds have low dust abundances, hence smaller optical depths at ultraviolet wavelengths. These young galaxies, especially the LMC, are presently in a phase of star formation. Their ultraviolet radiation field is stronger than the average Galactic field. Combining these effects, the average dust grain can be heated to higher temperatures than in the spirals. The smaller size of the Clouds will make it easier for the field to heat all dust present.

The lower dust temperature of the spiral galaxies will make mass estimates easier for the cool (25 K) component. However the spirals contain larger amounts of cold (15 K) dust. Data presented by Cox and Mezger (1988) suggests a similar gas–to–dust ratio for the molecular and atomic components.

From the diagram of L_{IR}/L_B versus $f_{100\mu m}/f_{60\mu m}$ of Caspers (1987), we compare the Clouds with M31 and M33. Again both spirals are shown to be cooler than the Magellanic Clouds. But, L_{IR}/L_B of the Clouds and M33 are very similar, while that of M31 is about 7 times smaller. This can be accounted for by the activity of the Clouds and M33 compared to M31.

The relation between the gas–to–dust ratio in the Clouds and the spiral galaxies is shown in Fig. 5. We show $L_{100\mu m}/M_{HI}$ as a function of $f_{60\mu m}/f_{100\mu m}$. Lines parallel to the dashed line indicate a constant gas–to–dust ratios over the range of f_{60}/f_{100}. Vertical displacements at a single ratio f_{60}/f_{100}, represent differences in dust–to–gas ratio. Most spirals are above the line, showing high dust–to–gas ratios. From the figure we see that the dust–to–gas ratio of the LMC is somewhat lower than that of average spirals. The differences between the LMC and the Milky Way (a ratio of 3), and between the SMC and the Milky Way (a ratio of 30) agree with the differences in gas–to–dust ratio derived in Section 2. The diagram of Fig. 5 provides a simple but powerful tool for estimating relative dust–to–gas ratios in galaxies. It predicts dust–to–gas ratios in M31 and M33 two times less than in the Milky Way and in M51 and M81 about 2 times higher. For M101 and IC342 the ratios are somewhat lower than for the LMC. These dust–to–gas ratios agree at least qualitatively with the oxygen abundance determinations for the Clouds and some spiral galaxies (*cf.* Pagel and Edmunds, 1981). M31 does not fit in this picture, its weak infrared emission compared to M_{HI} and compared to L_B (see above) combined with the low dust temperature, are the main reasons for the low derived dust–to–gas ratio of this early type spiral. If a large fraction of the 60 μm emission of this galaxy is related to very small grains, the average grain temperature will be smaller and the galaxy moves to the right in the diagram.

4.2. Irregular galaxies

The Clouds are irregular galaxies. In addition to the data of spirals, Fig. 4 also shows data of some (dwarf) irregular galaxies. These data are from Hunter *et al.* (1986), Rice *et al.* (1988b) and Israel (1988). The HII/blue compact galaxy II Zw 40, NGC 1569 and NGC 6822 are located close to point Y, reflecting their present high star formation activity. NGC 1569 and 6822 have similar ratios $f_{60\mu m}/f_{100\mu m}$ as those of the other irregular galaxies, but the large discrepancy for $f_{12\mu m}/f_{25\mu m}$ causes the very different positions. The weakness at 12 μm for these galaxies, related to a low content of small grains, can account for their location. The other irregulars, DDO 50, NGC 4449, NGC 4656 are at the same position in the diagram as the Clouds. Their ratio $f_{25\mu m}/f_{60\mu m}$ are also very similar. All irregular and Magellanic type galaxies in the list of Rice *et al.* (1988b) have been used. Only those with good flux densities in all four IRAS bands have been plotted. Of the other five, three have similar $f_{60\mu m}/f_{100\mu m}$ ratios. This makes the difference between the Clouds and the spirals even more intriguing. All irregular galaxies show similar colour differences with the spirals.

The positional differences between the irregulars and the Clouds must be interpreted in terms of stellar activity and small grain content. More active galaxies are to the upper-left of the diagram. Because irregulars are more active than spirals, they are to the left of spirals. We have only a limited sample of galaxies, which should make us careful in extrapolating results to a complete sample of galaxies. We have observed the brightest irregulars, and so selected the closest and most active systems. The same is true for the spirals, except their larger size will make them easier visible.

Because of their position among the irregular galaxies, the Magellanic Clouds are representative of the sample of irregulars, and can be used to derive properties in these galaxies. The agreement is especially good for the ratio f_{60}/f_{100}. Differences in f_{12}/f_{25} must be explained by differences in the small grain contents. Especially the temperature distribution in the Clouds can be used to perform the line–of–sight decomposition to find total dust masses.

Caspers (1987) showed a diagram of L_{IR}/L_B versus $f_{100\mu m}/f_{60\mu m}$ for a sample of nearby dwarf irregular galaxies and a sample of blue compact galaxies. In the diagram he added our Magellanic Cloud data, together with some other well known galaxies. We restict ourselves to a comparison with the dwarf irregulars. The SMC is just in the middle of the sample. Its diameter of 2.6 kpc makes it a typical dwarf irregular galaxy. The LMC is larger (7.8 kpc diameter), and has a high ratio L_{IR}/L_B compared to the average value for the dwarf sample; some higher values occur (*e.g.* NGC 1569). The dust temperature of both Clouds is well within the range of the dwarf sample. The effect of removal of dust in galaxies on the diagram is explained by the Caspers. Because L_{IR} is directly proportional to the dust mass it will go down. Due to the lower number of absorbers, L_B goes up. With the same radiation field and less absorbers, the average number of photons impacting on each dust particle is larger and the equilibrium temperature will be higher. The effect is that galaxies move in the diagram to the lower–right. A similar scenario for a burst of star formation can be set up; it will lead to galaxy movements to the upper–right.

In Fig. 5 we show the relation between $L_{100\mu m}/M_{HI}$ and $f_{60\mu m}/f_{100\mu m}$ for the irregular galaxies and the Clouds, together with the spirals. Again we note the difference between NGC 1569 and II Zw 40 with the other irregulars (*cf.* the irregular galaxy NGC 6822).

The position of the SMC is in the middle of the sample of irregulars, showing that the dust content of the SMC is in agreement with that of the other irregulars. The relatively high positions of the LMC and NGC 4449 is the result of their higher dust–to–gas ratios. We see that the SMC is a good representitive of the sample of irregulars, but the LMC is an extreme case. The oxygen abundance of the LMC, the SMC, NGC 4449, NGC 6822 and II Zw 40 (Chiosi and Matteucci, 1984) are qualitatively in agreement with the positions of these galaxies in the diagram. From the figure we see that the galaxies with higher abundances (LMC, NGC 4449) have the highest dust–to–gas ratios.

Acknowledgements

I want to thank Drs. A. van Genderen and P. Goudfrooij for useful discussions.

References

Azzopardi, M., Vigneau, J.: 1977, *Astron. Astrophys.* **56**, 151

van den Bergh, S.: 1968, *J. R. Astron. Soc. Canada* **62**, 145

Bohlin, R.C., Savage, B.D., Drake, J.F.: 1978, *Astrophys. J.* **224**, 132

Bouchet, P., Lequeux, J., Maurice, E., Prévot, L., Prévot–Burnichon, M.–L.: 1985, *Astron. Astrophys.* **149**, 330

Brunet, J.P.: 1975, *Astron. Astrophys.* **43**, 345

Caspers, H.C.M.: 1987, in *"Starbursts and Galaxy Evolution"*, eds. T.X. Thuan, T. Montmerle, J. Tran Thanh Van, Editiones Frontières Gif–sur–Yvette, 173

Chiosi, C., Matteucci, F.: 1984, in *"Formation and Evolution of Galaxies and Large Structures in the Universe"*, eds. J. Audouze, J. Tran Thanh Van, Reidel Dordrecht, 401

Cohen, R.S., Dame, T.M., Garay, G., Montani, J., Rubio, M., Thaddeus, P.: 1988, *Astrophys. J. (Letters)* in press

Cox P., Krügel, E., Mezger, P.G.: 1986, *Astron. Astrophys.* **155**, 380

Cox, P., Mezger, P.G.: 1988, in *"Comets to Cosmology"*, Lecture Notes on Physics **297**, Springer Berlin, 97

Dachs, J.: 1970, *Astron. Astrophys.* **9**, 95

Dufour R.J.: 1984, in *"Structure and Evolution of the Magellanic Clouds"*, IAU Symp. 108, eds. S. van den Bergh, K.S. de Boer, Reidel Dordrecht, 353

van Genderen, A.M.: 1969, *Bull. Astron. Inst. Neth. Suppl.* **3**, 299

van Genderen, A.M.: 1970, *Astron. Astrophys.* **7**, 49

van Genderen, A.M.: 1981, *Astron. Astrophys.* **101**, 289

Helou, G.: 1986, *Astrophys. J. (Letters)* **311**, L33

Hildebrand, R.H.: 1983, *Quartly J. R. Astron. Soc.* **24**, 267

Hodge, P.W.: 1974, *Astrophys. J.* **192**, 21

Humphreys, R.M.: 1984, in *"Structure and Evolution of the Magellanic Clouds"*, IAU Symp. 108, eds. S. van den Bergh, K.S. de Boer, Reidel Dordrecht, 145

Hunter, D.A., Gillett, F.C., Gallagher III, J.S., Rice, W.L., Low, F.J.: 1986, *Astrophys. J.*, **303**, 171

Israel, F.P.: 1984, in *"Stucture and Evolution of the Magellanic Clouds"*, IAU Symp. 108, eds. S. van den Bergh, K.S. de Boer, Reidel dordrecht, 319

Israel, F.P.: 1988, *Astron. Astrophys.* **194**, 24

Isserstedt, J.: 1976, *Astron. Astrophys.* **47**, 463

Isserstedt, J.: 1980, *Astron. Astrophys.* **83**, 322

Koornneef, J.: 1982, *Astron. Astrophys.* **107**, 247

Koornneef, J.: 1984, in *"Structure and Evolution of the Magellanic Clouds"*, IAU Symp. 108, eds. S. van den Bergh, K.S. de Boer, Reidel Dordrecht, 333

Leggett, S.K., Brand, P.W.J.L., Mountain, C.M.: 1988, *Mon. Not. R. Astron. Soc.* in press.

Lequeux, J.: 1984, in *"Structure and Evolution of the Magellanic Clouds"*, IAU Symp. 108, eds. S. van den Bergh, K.S. de Boer, Reidel Dordrecht, 67

Lequeux, J., Maurice, E., Prévot, L., Prévot–Burnichon, M.–L., Rocca–Volmerange, B.: 1984, in *"Structure and Evolution of the Magellanic Clouds"*, IAU Symp. 108, eds. S. van den Bergh, K.S. de Boer, Reidel Dordrecht, 405

MacGillivray, H.T.: 1975, *Mon. Not. R. Astron. Soc.* **170**, 241

Martin, N., Prévot, L., Rebeirot, E., Rousseau, J.: 1976, *Astron. Astrophys.* **51**, 31

Mathewson, D.S., Ford, V.L., Visvanathan, N.: 1986, *Astrophys. J.* **301**, 664

McNamara, D.H., Feltz, K.A.: 1980, *Publ. Astron. Soc. Pac.* **92**, 587

Pagel, B.E.J., Edmunds, M.G.: 1981, *Ann. Rev. Astron. Astrophys.* **19**, 77

Rice, W., Boulanger, F., Viallefond, F., Soifer, B.T., Freedman, W.L.: 1988a, in preparation

Rice, W., Lonsdale, C.J., Soifer, B.T., Neugebauer, G., Kopan, E.L., Lloyd, L.A., de Jong, T., Habing, H.J.: 1988b, *"A Catalog of IRAS Observations of Large Optical Galaxies"*, IPAC preprint No. 0032

Rubio, M., Cohen, R., Montani, J.: 1984, in *"Structure and Evolution of the Magellanic Clouds"*, IAU Symp. 108, eds. S. van den Bergh, K.S. de Boer, Reidel Dordrecht, 399

Savage, B.D., Mathis, J.S.: 1979, *Ann. Rev. Astron. Astrophys.* **17**, 73

Stift, M.J.: 1984, in *"Stucture and Evolution of the Magellanic Clouds"*, IAU Symp. 108, eds. S. van den Bergh, K.S. de Boer, Reidel Dordrecht, 229

Vangiomi–Flam, E., Lequeux, J., Maucherat–Joubert, M., Rocca–Volmerange, B.: 1980, *Astron. Astrophys.* **90**, 73

Walterbos, R.A.M., Schwering, P.B.W.: 1987, *Astron. Astrophys.* **180**, 27

Appendix

ON THE INTERPRETATION OF IRAS INFRARED OBSERVATIONS

1. Introduction

For the interpretation of IRAS infrared data it is important to understand the nature of the infrared emission. This appendix gives an overview of the basic physical principles, astronomical ideas and objects that are responsible for the infrared radiation emitted by galaxies, as well as equations, tables and figures of use in obtaining physically relevant parameters from the observed infrared data.

Interpretation of the infrared observations by IRAS is complicated by the fact that the wavelength bands were not infinitely small and by the fact that we are dealing with various physical dust components in the line–of–sight. Other important considerations are resolutions of the different wavelength bands (which, for comparison reasons, should be identical) and calibration and noise effects.

Physically relevant parameters that can be derived from the infrared data are described in this appendix, these are dust temperature T_d, infrared luminosity L_{IR}, dust column densities N_d, dust masses M_d and dust–to–gas ratios M_d/M_{HI}.

2. Mechanisms and origin of infrared radiation

2.1. Mechanisms of infrared radiation

Line, band and continuum emission contribute to observed infrared radiation. Line emission is detected in ground based observations with high spectral resolution (*e.g.* Continuous Variable Filter, CVF; Cooled Grating Spectrometer, CGS). In the near–infrared (NIR: 1 μm $< \lambda <$ 10 μm) line emission has been found from various atoms (*e.g.* H: Brα, Pfα), ions (*e.g.* Ar III, S IV) and molecules (*e.g.* H_2) (Harwit, 1982: general discussion; Watson, 1982: Orion nebula; Smith, 1982: galaxies; Lacy, 1982: HII regions; Israel and Koornneef, 1987: H_2 in Magellanic Cloud HII regions). Very small grains may be responsible for 12 and 25 μm continuum radiation (Draine and Anderson, 1985). They are proposed to be Polycyclic Aromatic Hydrocarbons (PAHs), which also show line emission in the near–infrared (Léger and Puget, 1984); their existence explains some near–infrared emission features (Sellgren *et al.*, 1983). Line emission in the mid–infrared wavelength range (MIR: 10 μm $< \lambda <$ 30 μm) is seen in IRAS Low Resolution Spectrometer observations (IRAS LRS, 1986). Spectral features are observed at infrared wavelengths, in emission and in absorption: *e.g.* the silicate features at 9.7 and 18 μm, and various other features for $\lambda <$ 10 μm (Willner, 1982). Line emission in the far–infrared (FIR: 30 μm $< \lambda <$ 250 μm) was proposed by Pottasch (1986) and by Leene and Pottasch (1986) for various planetary nebulae (*e.g.* S III, S IV, O III, O IV, Ne II and N III lines). They showed that these lines may contribute a large fraction of the observed IRAS flux densities.

In general, continuum infrared emission is split in thermal and non–thermal contributions. The non–thermal processes are Inverse Compton radiation and Synchrotron emission. The latter of these, which decreases rapidly with increasing wavelength, plays a role in those SNRs that have a flat radio spectrum, like Taurus A (Crab nebula; Marsden *et al.*, 1984). Hildebrand *et al.* (1977) and Jones and Stern (1975) have shown that these emission processes cannot be main contributors to far–infrared emission of galaxies. Thermal emission processes are free–bound emission and free–free (Brehmstrahlung); these were discussed by Waters (1986) in his interpretation of the infrared excess of four Be stars with circumstellar discs. Blackbody emission from stars (the Rayleigh–Jeans tail of the Planck function) is seen in nearby stars. For example a G2V star, such as the Sun, with a temperature of 5800 K, has its maximum energy emission of the Planck curve νB_ν at 0.6 μm; at infrared wavelengths still 50 % of the maximum energy is left at 1.25 μm (J–band) but only 0.2 % at 10 μm (N–band). The most important emission mechanism is the modified blackbody emission of dust heated by an external heating source. This heating process is photo–heating (near ELD HII regions and in the general interstellar radiation field, ISRF; to which contribute the young and old stellar population) or shock–heating (possibly near supernova remnants or shell structures; see Braun, 1985; Dwek, 1988).

2.2. Origin and sources of infrared radiation

The principal heating sources of dust in the Galactic disk have been discussed by Cox *et al.* (1986) using pre–IRAS infrared observations. They propose the following dust components:

(1) Cold dust ($< T_C > \approx 14$ K) associated with quiescent molecular clouds (H_2), heated by the general ISRF, or at the outmost edges of galaxies.

(2) Cool dust ($T_C \approx 15 - 25$ K) associated with atomic hydrogen (HI), heated by the general ISRF. In our Galaxy components (1) and (2) contain a luminosity of 5.7 x 10^9 $L_\odot$.

(3) Warm dust ($T_C \approx 30 - 40$ K) associated with ionized gas in extended low density HII regions (ELD; $n_e \gtrsim 10^2$ cm^{-3}) and heated by O–stars; and with molecular gas in dense ($2n_{H_2} \approx 10^3$ cm^{-3}) shells surrounding B–stars. Its total luminosity in our Galaxy is ~ 7.6 x 10^9 $L_\odot$.

(4) Hot dust ($T_C \approx 250 - 500$ K) to which contribute in equal fractions very small grains (VSG; radius $a \gtrsim 0.5$ nm) in the form of PAHs heated by the ISRF, associated with the diffuse interstellar (HI) gas; and normal grains ($a \gtrsim 0.1$ μm) heated by M–giants with heavy mass outflow (observationally known as OH/IR stars).

A renewed discussion of the infrared emission of the Galaxy based on IRAS data is given by Cox and Mezger (1988); they derived new luminosities somewhat different from the ones of Cox *et al.* (1986).

3. IRAS in–band intensities, specific intensities and colour corrections

The in–band intensity of IRAS wavelength band i, is the integration over the band of specific intensity convolved with the relative system response $R_{i,\nu}$ (IRAS, 1985a; see Table

II.C.5 therein). In fact, the IRAS satellite measured in the i^{th} band:

$$I_i = \int_0^\infty d\nu \; R_{i,\nu} \; I_\nu \qquad i = 12,\ 25,\ 60,\ 100\ \mu\text{m band.} \tag{3.1}$$

Specific intensities I_{ν_i} are reconstructed from in-band intensities I_i by using bandwidth correction factors $I_{\nu_i} = I_i/\Delta\nu_i$. Because the IRAS photometric bands are rather wide compared to the wavelength ($\Delta\lambda/\lambda \approx 0.3 - 0.6$) these factors depend on the intrinsic source spectrum. The IRAS flux densities in the catalogues and the specific intensities in the maps (IRAS, 1985a) assume a $f_\nu = f_{\nu_i}(\nu/\nu_i)^{-1}$ intrinsic spectrum of the source or map pixel respectively; we call these $f_{\nu_i}^{quoted}$. The bandwidth correction factors for band i with nominal frequency ν_i are found from

$$\Delta\nu_i = \int_0^\infty d\nu \; R_{i,\nu} \; (\nu/\nu_i)^{-1}. \tag{3.2}$$

These factors — given in Table 1 — are roughly correct for dust associated with HII regions, but not for *e.g.* stellar objects (which follow the Rayleigh–Jeans tail of the Planck function in the infrared; see Chapters II and III). To find the actual specific intensities the quoted values must be corrected for the intrinsic source spectrum:

$$f_{\nu_i}^{actual} = f_{\nu_i}^{quoted}/K_i. \tag{3.3}$$

These division factors K_i for a range of spectral powers are given in Table 2.A, and for modified blackbody spectra in Table 2.B. Their curves are displayed in Fig. 1. If the intrinsic source spectrum is unknown, the observed, quoted band ratios of adjacent bands (f_{ν_i}/f_{ν_j}, assuming $f_\nu \propto \nu^{-1}$) can be used to correct each band, using Table 2. This procedure converts the actual bandwidths to

$$\Delta\nu_i = \int_0^\infty d\nu \; R_{i,\nu} \; (f_\nu/f_{\nu_i}), \tag{3.4}$$

with f_ν the true source spectrum, or map pixel spectrum normalized to its value on the nominal frequency of the band.

There are two ways in which theoretical infrared spectra can be related to IRAS observations: (i) A theoretical model spectrum can be used to predict the IRAS in–band intensities by numerically integrating the model's calculated specific intensities convolved with the relative system response. In this case no colour correction is needed; (ii) Obtaining colour corrected (*i.e.* true) specific intensities at the nominal band centres and relating these to the predicted model's specific intensities. The second method is more direct. A general set of colour correction tables can be found in Leene (1987).

Table 1. *IRAS wavelength band characteristics.* [a]

Quantity		Unit	12 μm	25 μm	60 μm	100 μm
Nominal band centre:	ν_i	10^{12} Hz	25	12	5	3
	$\bar{\nu}_i$	cm^{-1}	833	400	167	100
$\nu f_\nu / \Delta\nu f_\nu$			1.85	2.32	1.94	3.00
Bandwidth:	$\Delta\lambda$	μm	7.0	11.15	32.5	31.5
($f_\nu \propto \nu^{-1}$)	$\Delta\nu$	10^{12} Hz	13.48	5.16	2.58	1.00
Zero–magnitudes:	f_ν	Jy	28.3	6.73	1.19	0.43
($f_\nu \propto \nu^{-1}$)	F_λ	10^{-20} Watt cm^{-2} μm^{-1}	5890	323	9.91	1.29
Zero–magnitudes:	f_ν^E	10^{-15} Watt m^{-2}	4120	360	32.2	4.06
(10000 K)	f_ν^W	10^{-15} Watt m^{-2}	5130	448	40.0	4.86

Notes to Table 1:

a) *The values for f_ν^E for a 10000 K blackbody are derived from colour correction with values quoted in IRAS (1985a). The numbers quoted by Waters f_ν^W use an interpolation over the infrared band.*

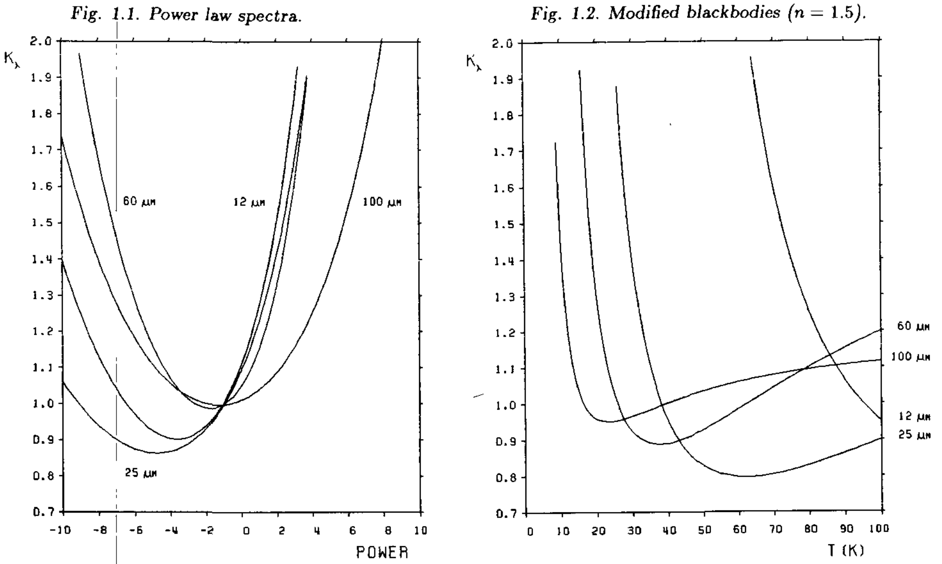
Fig. 1.1. Power law spectra.

Fig. 1.2. Modified blackbodies ($n = 1.5$).

Figure 1. *Colour correction factors for the four IRAS bands, for power–law spectra ($f_\nu \propto \nu^n$, with $-10 < n < +10$) and for modified blackbodies ($\nu^{1.5} B_\nu(T_d)$, with $0\ K < T_d < 100\ K$). The correct flux densities are obtained from $f_\nu^{correct} = f_\nu^{quoted} / K_\nu$.*

Table 2.A. Table for colour corrections of intrinsic power law spectra.

Intrinsic Spectral Power	Colour-correction factors				Band ratios before correction		
	K 12µm	K 25µm	K 60µm	K 100µm	12µm / 25µm	25µm / 60µm	60µm / 100µm
-10.00	1.40	1.06	2.33	1.74	0.00086	0.000072	0.0081
-9.50	1.32	1.03	2.14	1.64	0.0012	0.00012	0.0102
-9.00	1.25	0.99	1.97	1.55	0.0017	0.00019	0.0128
-8.50	1.19	0.96	1.82	1.47	0.0024	0.00031	0.0161
-8.00	1.13	0.94	1.68	1.40	0.0034	0.00051	0.0202
-7.50	1.08	0.92	1.56	1.33	0.0048	0.00083	0.0254
-7.00	1.04	0.90	1.46	1.28	0.0068	0.0013	0.0320
-6.50	1.00	0.89	1.37	1.23	0.0096	0.0022	0.0403
-6.00	0.97	0.87	1.29	1.18	0.0136	0.0035	0.0509
-5.50	0.94	0.87	1.22	1.14	0.0192	0.0058	0.0643
-5.00	0.93	0.86	1.16	1.11	0.0273	0.0093	0.0814
-4.75	0.92	0.86	1.13	1.09	0.0325	0.0119	0.0917
-4.50	0.91	0.86	1.11	1.08	0.0388	0.0151	0.1033
-4.25	0.91	0.87	1.09	1.07	0.0463	0.0192	0.1164
-4.00	0.90	0.87	1.07	1.06	0.0553	0.0245	0.1313
-3.75	0.90	0.87	1.05	1.04	0.0660	0.0311	0.1483
-3.50	0.90	0.88	1.04	1.04	0.0789	0.0395	0.1675
-3.25	0.90	0.88	1.02	1.03	0.0943	0.0501	0.1894
-3.00	0.91	0.89	1.01	1.02	0.1128	0.0636	0.2144
-2.75	0.91	0.90	1.00	1.01	0.1350	0.0807	0.2429
-2.50	0.92	0.91	1.00	1.01	0.1616	0.1022	0.2755
-2.25	0.93	0.92	0.99	1.00	0.1937	0.1294	0.3128
-2.00	0.94	0.93	0.99	1.00	0.2322	0.1638	0.3556
-1.75	0.95	0.95	0.99	1.00	0.2786	0.2071	0.4047
-1.50	0.97	0.96	0.99	1.00	0.3344	0.2616	0.4612
-1.25	0.98	0.98	0.99	1.00	0.4018	0.3302	0.5262
-1.00	1.00	1.00	1.00	1.00	0.4830	0.4163	0.6013
-0.75	1.03	1.02	1.01	1.00	0.5809	0.5244	0.6881
-0.50	1.05	1.04	1.02	1.00	0.6993	0.6599	0.7886
-0.25	1.08	1.07	1.03	1.00	0.8422	0.8295	0.9053
0.00	1.11	1.09	1.05	1.01	1.0151	1.0415	1.0408
0.25	1.14	1.12	1.07	1.02	1.2241	1.3060	1.1987
0.50	1.18	1.16	1.09	1.02	1.4771	1.6357	1.3830
0.75	1.22	1.19	1.12	1.03	1.7835	2.0459	1.5984
1.00	1.27	1.23	1.15	1.04	2.1546	2.5557	1.8507
1.25	1.32	1.27	1.19	1.05	2.6043	3.1879	2.1468
1.50	1.38	1.31	1.23	1.06	3.1496	3.9710	2.4950
1.75	1.44	1.36	1.28	1.07	3.8109	4.9392	2.9052
2.00	1.50	1.41	1.33	1.09	4.6133	6.1343	3.3894
2.25	1.57	1.47	1.38	1.10	5.5869	7.6070	3.9620
2.50	1.65	1.53	1.45	1.12	6.7688	9.4186	4.6404
2.75	1.74	1.59	1.52	1.14	8.2037	11.6435	5.4458
3.00	1.83	1.66	1.60	1.16	9.9463	14.3711	6.4035
3.25	1.93	1.74	1.69	1.18	12.0628	17.7093	7.5445
3.50	2.04	1.82	1.79	1.20	14.6336	21.7879	8.9064
3.75	2.16	1.91	1.90	1.23	17.7569	26.7625	10.5347
4.00	2.29	2.00	2.03	1.25	21.5515	32.8197	12.4850
4.25	2.44	2.11	2.17	1.28	26.1620	40.1826	14.8248
4.50	2.59	2.22	2.32	1.31	31.7642	49.1178	17.6367
4.75	2.76	2.34	2.49	1.34	38.5712	59.9433	21.0215
5.00	2.94	2.46	2.69	1.38	46.8424	73.0373	25.1023
5.50	3.36	2.75	3.15	1.45	69.1037	107.9152	35.9899
6.00	3.85	3.09	3.72	1.54	101.9646	158.4548	51.9641
6.50	4.44	3.48	4.46	1.63	150.4606	231.2460	75.5360
7.00	5.13	3.94	5.38	1.74	222.0073	335.4805	110.5091
7.50	5.96	4.47	6.57	1.86	327.5203	483.9165	162.6651
8.00	6.94	5.10	8.09	2.00	483.0603	694.1909	240.8210
8.50	8.11	5.84	10.05	2.15	712.2471	990.5757	358.4705
9.00	9.51	6.70	12.58	2.33	1049.7983	1406.3796	536.3184
9.50	11.18	7.71	15.88	2.52	1546.7151	1987.1638	806.2209
10.00	13.17	8.90	20.20	2.74	2277.9041	2795.0579	1217.3076

Table 2.8. Table for colour corrections of modified blackbodies (n = 1.5).

Blackbody Temperature (K)	Colour-correction factors				Band ratios before correction		
	$K_{12\mu m}$	$K_{25\mu m}$	$K_{60\mu m}$	$K_{100\mu m}$	$\frac{12\mu m}{25\mu m}$	$\frac{25\mu m}{60\mu m}$	$\frac{60\mu m}{100\mu m}$
5.00	----	----	----	12.10	----	----	.77E-05
7.50	----	----	48.68	2.55	----	----	0.00053
10.00	----	230.41	9.24	1.46	----	.34E-11	0.0043
12.50	----	41.76	3.79	1.15	----	.12E-08	0.0152
15.00	----	14.16	2.24	1.03	----	.62E-07	0.0361
17.50	----	6.80	1.61	0.98	----	.10E-05	0.0680
20.00	----	4.04	1.29	0.96	----	.82E-05	0.1111
22.50	579.18	2.75	1.12	0.95	.53E-08	.47E-04	0.1652
25.00	221.65	2.07	1.02	0.95	.43E-07	0.00015	0.2296
27.50	102.41	1.66	0.96	0.96	.24E-06	0.00044	0.3036
30.00	54.42	1.40	0.92	0.97	.10E-05	0.0011	0.3862
32.50	32.18	1.22	0.90	0.97	.33E-05	0.0023	0.4766
35.00	20.68	1.10	0.89	0.98	.94E-05	0.0043	0.5738
37.50	14.19	1.02	0.89	0.99	.23E-04	0.0076	0.6769
40.00	10.27	0.95	0.89	1.00	.50E-04	0.0124	0.7849
42.50	7.77	0.91	0.90	1.01	.99E-04	0.0192	0.8970
45.00	6.09	0.87	0.90	1.02	0.00018	0.0284	1.0123
47.50	4.91	0.85	0.92	1.03	0.00032	0.0403	1.1300
50.00	4.07	0.83	0.93	1.03	0.00051	0.0552	1.2496
52.50	3.44	0.81	0.94	1.04	0.00080	0.0736	1.3703
55.00	2.97	0.81	0.95	1.05	0.0012	0.0957	1.4915
57.50	2.60	0.80	0.97	1.05	0.0017	0.1217	1.6129
60.00	2.31	0.80	0.98	1.06	0.0024	0.1519	1.7339
65.00	1.89	0.80	1.01	1.07	0.0044	0.2253	1.9734
70.00	1.60	0.80	1.04	1.08	0.0073	0.3168	2.2077
75.00	1.40	0.82	1.07	1.09	0.0114	0.4266	2.4351
80.00	1.25	0.83	1.10	1.09	0.0169	0.5543	2.6546
85.00	1.14	0.85	1.13	1.10	0.0240	0.6991	2.8654
90.00	1.06	0.86	1.15	1.11	0.0328	0.8601	3.0672
95.00	1.00	0.88	1.18	1.11	0.0435	1.0360	3.2600
100.00	0.95	0.90	1.20	1.12	0.0561	1.2253	3.4438
105.00	0.91	0.92	1.22	1.12	0.0709	1.4266	3.6188
110.00	0.88	0.94	1.24	1.12	0.0879	1.6383	3.7852
115.00	0.86	0.96	1.26	1.13	0.1073	1.8590	3.9435
125.00	0.83	1.00	1.30	1.13	0.1530	2.3217	4.2371
150.00	0.81	1.09	1.37	1.15	0.3104	3.5463	4.8546
175.00	0.83	1.16	1.42	1.15	0.5282	4.7788	5.3404
200.00	0.86	1.23	1.47	1.16	0.7999	5.9524	5.7288
225.00	0.91	1.29	1.50	1.16	1.1157	7.0371	6.0446
250.00	0.96	1.34	1.53	1.17	1.4641	8.0240	6.3056
275.00	1.01	1.38	1.55	1.17	1.8345	8.9148	6.5244
300.00	1.06	1.41	1.57	1.17	2.2173	9.7163	6.7101
325.00	1.11	1.44	1.59	1.18	2.6048	10.4373	6.8696
350.00	1.15	1.47	1.60	1.18	2.9907	11.0866	7.0079
375.00	1.19	1.49	1.62	1.18	3.3705	11.6727	7.1290
400.00	1.23	1.51	1.63	1.18	3.7409	12.2030	7.2357
425.00	1.27	1.53	1.64	1.18	4.0997	12.6845	7.3305
450.00	1.30	1.55	1.65	1.18	4.4453	13.1228	7.4153
475.00	1.34	1.56	1.65	1.18	4.7771	13.5232	7.4915
500.00	1.37	1.58	1.66	1.19	5.0946	13.8900	7.5603
600.00	1.47	1.62	1.68	1.19	6.2246	15.0906	7.7800
700.00	1.55	1.65	1.70	1.19	7.1529	15.9825	7.9384
1000.00	1.69	1.70	1.73	1.19	9.0818	17.6522	8.2260
1500.00	1.81	1.74	1.75	1.20	10.7965	19.0000	8.4516
2000.00	1.87	1.76	1.76	1.20	11.7141	19.6871	8.5650
3000.00	1.93	1.78	1.77	1.20	12.6642	20.3816	8.6786
4000.00	1.96	1.79	1.77	1.20	13.1494	20.7312	8.7355
5000.00	1.98	1.80	1.78	1.20	13.4432	20.9417	8.7697
10000.00	2.01	1.81	1.78	1.20	14.0358	21.3640	8.8381
20000.00	2.03	1.82	1.79	1.20	14.3342	21.5759	8.8723

There are various uncertainties, related to the subjects in this section. The first are calibration uncertainties; these are at least 10 %. The accuracy of the bandwidth and the colour correction are uncertain. A comparison of Waters *et al.* (1987) with IRAS (1985a) for 10^4 K stars, see blackbody in Table 1, gives indications for an uncertainty of 20 – 30 % in the zero–magnitude flux density, solely on the basis of interpolations over the bands. For dust emission this uncertainty is less than for the steep spectra of stars.

The calibration of SMC and LMC IRAS Additional Observations is discussed in Chapters II and III; a discussion of convolved data is given in Chapter V.

4. Dust properties and radiative transfer theory

4.1. Dust properties

In principle, dust grains are formed in the cool (1000 K) and dense (10^{19} particles m^{-3}) outer layers of late type giant stars (Hasegawa, 1984; Dyson and Williams, 1980). The interstellar medium has a density which is too low to produce dust grains of 10^{10} atoms (with radii a of 0.1 μm); dust grains are removed from the stellar enveloppe by stellar winds and they evolve and grow in the interstellar medium (Greenberg, 1984). They are disrupted by photo– or shock–dissociation (see Seab and Shull, 1984; Dwek, 1988; Heiles, 1988). Mass, size, shape and chemical composition differ for all grains and dust properties are therefore only average properties of an ensemble. Mathis *et al.* (1977) have derived a grain size distribution for normal grains, from the ultraviolet extinction curve of $n(a) \propto a^{-3.5}$ with $a_{min} = 0.01$ μm and $a_{max} = 0.25$ μm (the MRN grain size distribution). Other models have been proposed by various people (*e.g.* Draine and Anderson, 1985), which increase the number of smaller grains relatively to the number of larger "normal" grains. These grains have radii as small as 0.3 nm and can be regarded as large molecules (Polycyclic Aromatic Hydrocarbons or PAHs; Puget *et al.*, 1985).

We give an estimate for the infrared spectrum of very small grains. From Draine and Anderson (1985) we find the infrared spectrum for modified MRN grain models. We derived the spectrum for grains with 0.3 nm $< a <$ 3 nm, in a Solar Neighbourhood radiation field from the difference between the curves labeled with a_{min} = 3 Å, and a_{min} = 30 Å. The relative spectral shape of the small grains is 1, 3, 4.5, 0 at 12, 25, 60 and 100 μm.

Grains interact in three ways with radiation: by emission, absorption and scattering. For infrared wavelengths (IR) only the first two are important. What happens to a single grain with radius a when it is hit by a visual (V) or ultraviolet (UV) photon with energy $h\nu_{ph}$ is described as follows. By absorbing the photon, the grain increases its energy and heats up from the initial temperature T_0 to T_1, depending on the heat capacity per volume $C_V(T)$, via

$$h\nu_{ph} = \frac{4}{3}\pi a^3 \int_{T_0}^{T_1} dT\ C_V(T). \tag{4.1}$$

Due to this increase in temperature, the emission is increased from $B_\nu(T_0)$ to $B_\nu(T_1)$. If the photon energy is very high compared to the heat capacity the increase in temperature may be so high that the grain sublimates. Especially small grains ($a <$ 1 nm), that are responsible for the mid-infrared excess emission, have strong temperature fluctuations due to single photon encounters (see Draine and Anderson, 1985; Puget *et al.* 1985). The larger grains are not warmed up much by single photon encounters and are assumed to be in equilibrium: $W_{UV,\ in} = W_{IR,\ out}$. The density of the radiation field influences the minimum grain radius a_{min}. A discussion of these very small grains in the Magellanic Clouds is given in Chapter VI.

For wavelengths (UV) comparable to grain radii a the absorption cross-section σ_ν^{abs} is nearly equal to the geometrical cross-section $\sigma^{geom} \equiv \pi a^2$, and by Babinet's principle the scattering cross-section σ_ν^{scat} is also nearly equal to σ^{geom}; thus $\sigma_\nu^{tot} = \sigma_\nu^{abs} + \sigma_\nu^{scat} \approx 2\,\sigma^{geom}$ ($\lambda = c/\nu \approx a$). At $\lambda = 0.2$ μm a resonance occurs with $\sigma_\nu^{tot} \approx 3\,\sigma^{geom}$ (the 2200 Å bump). For $\lambda >> a$ (IR) $\sigma_\nu^{scat} \rightarrow 0$ and $\sigma_\nu^{tot} = \sigma_\nu^{abs}$. The extinction is the total amount of radiation lost from a specific beam from a certain direction (absorption and scattering) minus that scattered back in the beam.

The absorption efficiency of the grains Q_ν^{abs} is defined as the ratio of the effective absorption cross-section σ_ν^{abs} of the grains at frequency ν and the geometrical cross-section $\sigma^{geom} \equiv \pi a^2$, *i.e.*

$$Q_\nu^{abs} = \frac{\sigma_\nu}{\pi a^2}. \tag{4.2}$$

$Q^{ext} \equiv Q^{abs} + Q^{scat}$ with $Q^{scat} = 0$ at infrared wavelengths and by Kirchhoff's law $Q_\nu^{abs} = Q_\nu$, the emission efficiency. Using these definitions, the optical depth τ_ν at this frequency over a spatial range R is written as

$$\tau_\nu = \int_R dr\ \alpha_\nu = \int_R dr\ n_d\ \pi a^2\ Q_\nu = \int_R dr\ \rho_d\ \kappa_\nu \tag{4.3}$$

and the relation between the mass absorption coefficient (opacity) κ_ν and the absorption efficiency coefficient Q_ν becomes

$$\kappa_\nu = \frac{n_d}{\rho_d}\ \pi a^2\ Q_\nu = \frac{3}{4a\rho_d}\ Q_\nu. \tag{4.4}$$

The transmission t_ν is written as $t_\nu = e^{-\tau_\nu}$; this gives the amount of radiation that passes through a region. In these equations, $\alpha_\nu = n_d\sigma_\nu = \rho_d\kappa_\nu$ is the absorption coefficient, n_d is the number density of the grains (depends on the object; for the interstellar medium: $n_d\ \rho_d/n_{HI}\ \rho_{HI} \approx 0.005 - 0.01$), a the average grain radius (0.1 μm) and ρ_d the density of the grain material ($\sim$ 3 g cm^{-3}) and $Q_{100\mu m} = 1/644$ (Hildebrand, 1983).

Now we describe the mass absorption coefficient κ_ν (cm^2/ g) that we have used. Table 3 gives a summary of emissivity exponents n, in $j_\nu \propto \nu^{+n}$, as derived for a range of objects. Another quantity that is used often to describe the mass absorption coefficient is σ_ν^H (the absorption of dust per H-atom). The two are related as follows:

$$\sigma_\nu^H \equiv \frac{\tau_\nu}{N_H} = \frac{1}{X(H)}\frac{M_d}{M_g}\ M_H\ \kappa_\nu \qquad \mathrm{cm^2/H-atom}, \tag{4.5}$$

where $M_d = n_d m_d$ is the dust mass density and $M_g = (n_H + 2\ n_{H_2}) m_H / X(H)$ is the gas density and $X(H)$ the fractional mass abundance of hydrogen ($X_\odot(H) \approx 0.7$) (see *e.g.* Mezger *et al.*, 1982).

From Table 3 we find that cool objects (integrated emission of galaxies) have $n = 2$ and the warmer $n = 1$ (Chini *et al.*, 1984a; 1984b). Of course fits for cold objects are primarily based on low frequency points and fits for warm objects on high frequency points. Draine and Lee (1984) showed possible variations of Q_{abs}/a with temperature. Because we want a temperature independent factor we have adopted a mass absorption coefficient

$$\kappa_\nu\ (\mathrm{cm}^2\ \mathrm{g}^{-1}) = \kappa_{100\ \mu\mathrm{m}}\ (\lambda/100\mu\mathrm{m})^{-n} = \kappa_{100\mu\mathrm{m}}\ (\nu/3 \ \mathrm{x}\ 10^{12}\mathrm{Hz})^{+n} \tag{4.6}$$

with $n = 1.5 \pm 0.5$ for $50\ \mu\mathrm{m} < \lambda < 150\ \mu\mathrm{m}$ and $\kappa_{100\mu m} = 40\ \mathrm{cm}^2/\mathrm{g}$, probably correct within a factor of two. Use of this exponent n gives the lowest error in the derived temperatures. The factor $\kappa_{100\mu m}$ was derived for $n = 1.5$ in the same way as described in Hildebrand (1983).

We compared values for dust temperature T_d and dust mass M_d from the absorption coefficient of Hildebrand (1983) with our mass absorption coefficient. Our temperatures and masses are both lower than Hildebrand's by 0.9. There are small variations with T_d, decreasing M_d for increasing T_d (see Sections 5 and 7).

Here we list some uncertainties that are involved in dust properties, size distribution and chemical composition. The 1983 Chicago assumptions and most other data given in Table 3 are based on galactic values (mainly bright HII regions). It is unknown if these values are also valid for all type of dust grains in all kinds of galaxies, like *e.g.* the Magellanic Clouds. It is known that there are differences in extinction curves between the Clouds and the Galaxy (Nandy, 1984), differences in chemical abundances (C, N, O), differences in molecular content (CO). The small 2200 Å bump in the Clouds is described to the absence of graphite in the Clouds, which corresponds to the lower C abundance; indicating that most grains in the Clouds are based on silicate cores. The steep UV rise of the extinction curve suggests a steeper grains size distrubution for small radii in the Clouds. The recent discovery of the absence of the silicate feature in some Magellanic Cloud HII region, (Roche *et al.*, 1987) makes this last statement less secure.

4.2. Radiative transfer

As described in Section 2 most of the infrared emission is starlight, re-emitted by dust grains. Infalling ultraviolet and visual light heat up dust particles and these particles radiate like blackbody emitters of equilibrium temperature T_d (K) via the Planck intensity function

$$B_\nu(T) = \frac{2h\nu^3}{c^2} \frac{1}{e^{h\nu/kT_d} - 1}. \tag{4.7}$$

The volume emission coefficient j_ν is written as

$$j_\nu = n_d\ \pi a^2\ Q_\nu\ B_\nu(T_d) = \rho_d\ \kappa_\nu\ B_\nu(T_d) = \alpha_\nu\ B_\nu(T_d) \tag{4.8}$$

Table 3. Literature emissivity exponents n.

Reference	Year	Wavelength range (µm)	n	Temperature of dust (K)	Comments (object, model, fit)
Greenberg	1978	—→ oo	2	--	Asymptotic limit of Qabs for lambda —→ oo; applies to mm region of spectrum; must be used with caution towards shorter wavelengths (even at 300µm).
Mezger et al.	1982	40 -1000	1.0-2.3	--	Model MRN; comparison of computed and observed absorption cross-sections per H-atom. Monotomically decreasing power n with increasing wavelength (n = 1 at 60µm).
Willner	1982	20 - 300	1.3	--	See Pipher et al. (1978), Herter et al. (1979), Thronson and Harper (1979), Erickson and Tokanunga (1980).
		> 300	(>)2.0	--	See Keene (1981), Gezari (1982), Righini et al. (1976).
Pipher et al.	1978	150 - 500	1.0	85	Fit KAO observations of KL-nebula. For lambda>150µm Tau=Taup (lambda/lamp)**(-n); with Taup=0.2 and Tau is gray below 150µm. For lambda> 20µm the relation gives good results near the spectral peak at 40µm, but fails above 250µm.
Herter et al.	1979	45 - 250	1.25	30	Fit KAO observations of W49, W51. Model: spherical or slab. Amorphous silicate dust. Fit: lamp=100µm and Taup= 0.12 (W51 slab), (W49 slab), 2-5 (W49 spherical).
Thronson and Harper	1979	10 - 350	1	30 - 50	W3, W51: 10 compact infrared sources. At 150µm the fitted curve with n=1 is above measured flux (optically thin).
Erickson and Takanuga	1980	29 - 155	0.0	70	W51-IRS2 (BB of 69K).
		350 -1250	1.3	70	W51-IRS2 (two points): Taup=8.3, nup=118/cm: opt. thin.
		29 - 155	2.8	52	W49-NW: best fit Taup=3.2; nup=118/cm; n=2.8.
Keene	1981	500 -1000	2	13 - 16	9 Globules with KAO and IRTF.
Gezari	1982	100 -1000	2	19 - 33	NGC 6334 / I (North).
Righini et al.	1976	350 -3000	> 1.2	50	DR-21; NRAO (3mm), MKO (350µm).
		350 -3000	> 1.5	--	Sgr-B2; NRAO (3mm), MKO (350µm).
Hildebrand	1983	50 - 250	1	--	See Schwartz (1982), Erickson et al. (1981).
		> 250	2	--	n = 1 at 100µm; to >= 2 at 1000µm. K (cm2/gram) = 10 (lambda/lamp)**(-n), with lamp=250µm. 1983 Chicago Assumptions.
Erickson et al.	1981	27 - 95	2.3-2.9	87	KAO spectrum (Res:6/cm) of Kleinmann-Low nebula in Orion. Broad absorption with maximum depth 5% at 42µm. Model: absorption layer of silicate-water-ice grains Tau = Taup (nu/nup)**n with Taup=5.2-6.6; nup=170/cm.
Schwartz	1982	1000 -3300	2.2-2.6	15 - 65	NGC 2264, 6334N, S140; silicate core grains with thin ice mantles. n decreases with T, but does not drop below 2.
Draine and Lee	1984	40 - 120	1.8±0.2	--	MRN + modified dielectic functions. Qabs/a depends on Temp. (their Fig. 11): 10 < T < 100K, 0.001 < <Qabs>/a(µm) < 0.1 and proportional to T-square.
Cox et al.	1986	40 - 120	1.8±0.3	--	From Draine and Lee (1984); K(100µm)=0.5 cm2/gram ISM.

Table 3, continued (2).

Reference	Year	Wavelength range (µm)	n	Temperature of dust (K)	Comments (object, model, fit)
Chini et al.	1984a				No points between 100 and 1000µm; only IRAS and 1000µm points.
		60 -1000	1.5±0.2	37 - 50	HII region and 4 reflection nebulae (average n).
		10 - 100	(1)	> 70	3 Dust clouds (warm part of spectrum).
		100 -1000	(2)	20 - 23	3 Dust clouds (cold part of spectrum).
		100 -1000	(2)	(20)	2 Galaxies; flux density upper limits at 1000µm.
		100 -1000	(2)?	16 - 20	3 Unidentified objects: IR spectra like normal spiral galaxies; at 10-25µm other T component.
Chini et al.	1984b				Fitting errors in n of 0.1 and in T of 2 K.
		60 -1000	1.3±0.3	55 - 60	2 HII regions: good fits.
		60 -1000	1.2±0.3	25 - 60	7 Warm dust clouds: good + poor fits.
		100 -1000	2	18 - 20	6 Galaxies; only M51 fitted; 5 adopted n=2. No well defined fit for these five.
Werner et al.	1976	20 100	1	70	Central 5' of Orion nebula (1' resolution KAO).
Scoville and Kwan	1976	30 -1000	1.5	68	KL-nebula; contains model calculations for molecular clouds. Tau(70µm)=1.
Campbell et al.	1976	50 -1000	1	375	KAO,MLO,Hale observations of IRC+10216. Adopted K(100µm)=50cm2/gram.
Gatley et al.	1977	30 - 150	1	50 - 80	KAO observations of the Galactic centre.
Erickson et al.	1977a	20 -1000	1	70 - 95	Fit KAO observations of KL-nebula. Taup=0.21; nup=185/cm.
Erickson et al.	1977b	50 - 250	1.5	32	KAO spectrum (Res:5/cm, 1.4'Gauss) of Sgr-B2 core. (uniform slab of dust filling the beam). Broad maximum at 120µm. Taup=1.6; nup= 100µm. Featureless: opt. thick or smooth spectrum.
Hildebrand et al.	1977	88 -1100	2.0±0.5	25 - 35	8 galaxies observed with MLO, CTIO, MKO. Opt. thin: Tau(390µm)=0.15.
Tokunaga et al.	1978	29 - 155	1	60 - 70	KAO observations of Sharpless 140 IR. Tau(80µm)=0.5-1.5: not opt. thin at emission peak at 80µm.
Harvey et al.	1978a	35 - 175	0.7-1.0	63	KAO observations of S140-IR. Tau(100µm)=0.3, k(100µm)>50cm2/gram.
Harvey et al.	1978b	35 - 175	1	250	KAO observations of Eta-Carinae. Tau(53µm)=0.12, Tau(100µm)=0.08.
Moseley	1980	37 - 108	1.0-2.0	100	13 Planetary nebulae (KAO + Yerkes photometers).
Day	1976				Two synthetic magnesium silicates; amorphous materials.
		100 - 300	1.25	77 -393	Na2SiO3
		100 - 300	1.5	77 -393	Na4SiO4
Hasegawa and Koike	1983	40 - 100	0.8-3.0	--	Laboratory experiments of synthetic materials. Far infrared peak structures. See their Table 1. Power n depends on used minerals.

Note to Table 3:
Values of n or T in brackets are adopted.
Abbreviations used are:
KAO : NASA's G.P. Kuiper Airborne Observatory (0.91 m).
MLO : Mount Lemmon Observatory (1.5 m).
MKO : Mauna Kea Observatory (2.2 m).
IRTF: NASA's Infrared Telescope Facility.
CTIO: Cerro Tololo Inter-American Observatory (4.0 m).

which is added in the (differential) radiative transfer equation along the line–of–sight l

$$dI_\nu = j_\nu dl - \alpha_\nu I_\nu dl. \tag{4.9}$$

The first term on the right hand side is responsible for emission and the second term for absorption of infrared radiation. The formal solution of the radiative transfer equation between τ_0 and τ_ν gives for the intensity (radiance)

$$I_\nu(\tau_\nu) = I_\nu(\tau_0)e^{-\tau_\nu} + \int\limits_{\tau_0}^{\tau_\nu} dt'_\nu \; S_\nu(t'_\nu) \; e^{-(\tau_\nu - t'_\nu)} \tag{4.10}$$

with $S_\nu \equiv j_\nu/\alpha_\nu = B_\nu$ the source function (by Kirchhoff's law). If S_ν is independent of τ_ν and a single temperature T is present, this equation reduces to $I_\nu = S_\nu(1 - e^{-\tau_\nu})$. In the opaque case ($\tau_\nu >> 1$) the emission is optically thick: $I_\nu \approx S_\nu$; in the transparant case ($\tau_\nu << 1$) the emission is optically thin: $I_\nu \approx \tau_\nu S_\nu$.

If the infrared background of the source is set to zero, the boundary condition $I_\nu(\tau_0) \equiv 0$ holds. Far–infrared radiation is optically thin (typically $\tau_{100\mu m} \approx 0.01$, see Fazio, 1978; Hildebrand *et al.*, 1977), hence we expand the exponential function to zero order

$$I_\nu(\tau_\nu) \approx \int\limits_0^{\tau_\nu} dt'_\nu \; S_\nu(t'_\nu) = \int\limits_0^{L} dl \; \rho_d \; \kappa_\nu \; B_\nu(T_l). \tag{4.11}$$

The flux density of radiation from an object at distance D is found from integrating j_ν over the whole volume V of the source and over all possible solid angles Ω. Assuming isotropic radiation from an homogeneous object the measured flux (or irradiance) density becomes

$$f_\nu = \frac{1}{4\pi D^2} \int_\Omega d\Omega \int_V dV \; \rho_d \; \kappa_\nu \; B_\nu(T_d) = \frac{M_d \; \kappa_\nu \; B_\nu(T_d)}{D^2}. \tag{4.12}$$

If the objects subtends a solid angle element $\Delta\Omega$ perpendicular to the line–of–sight l, the average intensity is recontructed over this solid angle $I_\nu = f_\nu/\Delta\Omega$. The detectors of the IRAS satellite measure in fact the flux in the band. The bandwidth correction has been explained in Section 3 and intensities have been obtained by dividing the solid angle subtended by each detector $\Delta\Omega_{det}$ on the sky (see IRAS, 1985a; Table IV.A.1 therein).

With κ_ν from Section 4.1, I_ν has the following form, which we call modified blackbodies:

$$I_\nu \;=\; \kappa_\nu \; B_\nu(T) \;=\; \kappa_0 \; c^{-n} \; \nu^{+n} \; B_\nu(T) \qquad \text{with} \quad \kappa_\nu \;=\; \kappa_0 \; (c/\nu)^{-n}. \tag{4.13}$$

These functions have their maximum emission where $x \equiv \frac{h\nu}{kT}$ obeys $x = (3+n)(1 - e^{-x})$. Numerical evaluation of this equation gives the relation between λ(T) and T(K) (see Table 4).

Table 4. *Peak values and integration constants of modified blackbodies.*

n	λ (m) T(K)	σ_n (kg s^{-1} K^{-4})
0.0 a)	5099	5.67×10^{-8}
0.5	4256	8.93×10^{-7}
1.0	3670	1.51×10^{-5}
1.5	3235	2.72×10^{-4}
2.0	2898	5.15×10^{-3}
2.5	2627	1.02×10^{-1}
3.0	2404	2.13×10^{-0}

Note to Table 4:

a) *For $n = 0.0$ we get the well known equation $\pi F = \sigma T^4$, with σ the Stefan–Boltzman constant.*

Integration of the modified blackbody functions leads to

$$\int_0^\infty d\nu \; I_\nu \; = \kappa_0 \; (\sigma_n/\pi) \; T^{4+n}, \tag{4.14}$$

where the σ_n are modified Stefan–Boltzman constants (see Table 4). Note that for $n = 0$ we get the Stefan–Boltzman constant. These functions are used in Chapters IV, V and VI.

5. Dust temperature from infrared observations

In radio astronomy brightness temperature is a well known term T_b. It defines the temperature of a blackbody that gives rise to the measured intensity at the observed wavelength in the Rayleigh–Jeans approximation, *i.e.*

$$I_\nu = 2 \; \lambda^{-2} \; kT_b. \tag{5.1}$$

In fact, for a single source this equation gives different temperatures at different radio wavelengths, as the emission process is synchrotron radiation or Brehmstralung. In the infrared wavelength regime, we want to determine real physical temperatures. We assume that only continuum emission is present.

As pointed out in Section 2 dust particles are heated to temperatures at which they radiate at infrared wavelengths. Not all dust particles have the same temperature, some are embedded in and heated by HII regions, others are in more quiescent galactic regions and heated by the more diluted interstellar radiation field (ISRF). Along each line–of–sight

l, and in integrated flux densities of objects, we see the contribution of various temperature components with mass density ρ_l merged together,

$$I_\nu = \int_l dl\ \rho_l\ \kappa_\nu\ B_\nu(T_l) = \int_T dT\ \rho_T\ \kappa_\nu\ B_\nu(T). \tag{5.2}$$

These integrands, which are modified blackbody functions have their maxima at λ (μm) T(K) $\approx$ 5100 $\frac{3}{3+n}$, for $\kappa_\nu \propto \nu^{+n}$. To obtain dust temperatures we assume that colour corrected specific intensities have been obtained (see Section 3) and that a single line-of-sight temperature T_d applies (hence $\rho_T = P_d\ \delta(T - T_d)$; with P_d the total dust mass in the line-of-sight). Then Equation (5.2) reduces to

$$I_\nu = P_d\ \kappa_\nu\ B_\nu(T_d). \tag{5.3}$$

Colour-temperatures are defined by relating the ratio of two spectral points to a blackbody. Our modified blackbodies give us "modified colour temperatures" which are the physical temperature of dust for the assumed emissivity. Using two specific intensity values, with similar resolution, at different frequency points ν_1 and ν_2 (from the IRAS 12, 25, 60 and 100 μm bands), and assuming the same amount of dust P_d emitting at ν_1 and ν_2, the ratio I_{ν_1}/I_{ν_2} gives us a recursive relation for T_d from

$$\frac{I_{\nu_1}}{I_{\nu_2}} = \frac{f_{\nu_1}/\Delta\Omega}{f_{\nu_2}/\Delta\Omega} = \frac{\kappa_{\nu_1}}{\kappa_{\nu_2}}\ \frac{B_{\nu_1}(T_d)}{B_{\nu_2}(T_d)}. \tag{5.4}$$

If κ_ν depends on the dust temperature, itself its temperature dependence cancels in Equation (5.4). Note that similar resolutions must be used. The use of integrated flux densities works similar as the same factor $\Delta\Omega$ occurs in numerator and denominator. For cool (20 – 50 K) galactic dust usually the 60 and 100 μm points are used; and this formula reduces T_d to a direct equation

$$T_d = \frac{h(\nu_1 - \nu_2)}{k\ \ln((\frac{\nu_1}{\nu_2})^{3+n}\ (\frac{I_{\nu_2}}{I_{\nu_1}}) + C_T)}, \tag{5.5}$$

with a temperature dependent correction factor of

$$C_T = (1 - (\frac{\nu_1}{\nu_2})^{3+n}\ (\frac{I_{\nu_2}}{I_{\nu_1}}))\ e^{-h\nu_2/kT_d}. \tag{5.6}$$

C_T gives the deviations of the true spectrum from the Wien regime of the blackbody spectrum. Leaving out C_T, *i.e.* assuming that we are in the Wien regime ($h\nu_2 >> kT_d$), while using the 60 and 100 μm bands an error of less than 1 K for T_d < 45 K is introduced, well below the (10 %) errors in the IRAS data; the value of C_T decreases monotomically from 0.0 (T_d = 0 K) to – 0.33 (T_d = 45 K). At T_d = 80 K ($C_T = -0.46$)

Equation (5.5) underestimates the "true" dust temperature by 10 %, independent of n; the underestimation increases rapidly above this temperature. Iteration of Equations (5.5) and (5.6), may be used to find T_d with the requested accuracy. The relation between flux density ratios and T_d is given in Fig. 2 for $n = 0 - 3$. Fig. 2.1 gives the relation for the colour corrected flux densities, while Fig. 2.2 gives the relation for flux densities assuming $f_\nu \propto \nu^{-1}$. Table 5 gives the relation between T_d and $I_{60\mu m}/I_{100\mu m}$ for $n = 1.5$, and also the relation between Fig. 2.1 and 2.2. An uncertainty in n of $\Delta n = \pm 0.5$ results in a relative uncertainty in the temperature $\Delta T/T = 10$ %. Define $R \equiv \frac{I_{\nu_1}}{I_{\nu_2}}$; then we derive for the relative errors $\frac{\Delta T}{T} = 0.4\,\frac{\Delta R}{R}$. For 10 % relative errors in I_ν, the error in R is 14 %; and we get 4 % relative errors in T_d. For our temperature calculations in Chapters IV and V we have used tables of theoretical in-band intensity ratios.

The observed dust temperature gives us the possibility to separate dust components (2), (3) and (4) of Section 2. The energy of a single grain absorbed from the heating source per second is

$$W_a = \int_0^\infty d\nu\, 4\pi\, J_\nu\, \sigma_\nu^{abs}, \qquad \text{with} \qquad J_\nu \equiv \frac{1}{4\pi}\int d\Omega\, I_\nu; \tag{5.7}$$

with J_ν the average intensity of the radiation field I_ν. Comparing this value with the energy emitted per second by the radiation field (see Equation (4.14)),

$$W_e = \int_0^\infty d\nu\, 4\pi\, B_\nu(T_d)\, \sigma_\nu^{abs} \approx 4\pi\, \sigma_0^{abs} \sigma_n T^{4+n} \tag{5.8}$$

for various kinds of input radiation fields, gives equilibrium dust temperatures. Here $\sigma_\nu^{abs} = \sigma_0^{abs}(c/\nu)^{-n}$; a numerical integration of σ_ν^{abs}, as given by Mezger *et al.* (1982) may be used instead of the power-law. The (modified Stefan-Boltzman) constants σ_n, have been described in Section 4.2. Using the ISRF of Mathis *et al.* (1983) with

$$\int_{0.09\mu m}^{8\mu m} d\lambda\; 4\pi J_{\lambda,\odot} = 0.0217 \text{ erg cm}^{-2}\text{ s}^{-1} \tag{5.9}$$

gives an equilibrium teperature of 16 K, via

$$T^{4+n} \approx \frac{<\sigma_{vis}>}{<\sigma_{FIR}>} \int d\lambda\; 4\pi\; J_\lambda. \tag{5.10}$$

A comparison of the measured dust temperatures and the model radiation field temperatures yields estimates for the strength of the radiation field. Hence the equilibrium temperature serves as a selection criteria for the strength of the radiation field that heats the dust.

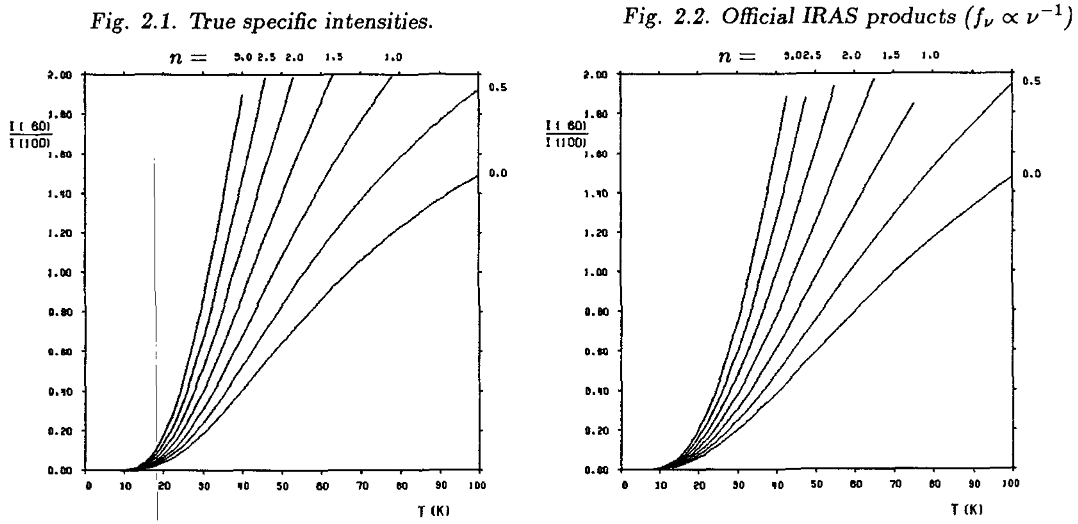

Fig. 2.1. True specific intensities.

Fig. 2.2. Official IRAS products ($f_\nu \propto \nu^{-1}$)

Figure 2. *Relation between dust temperature T_d (K) and $I_{60\mu m}/I_{100\mu m}$ (Jy–ratio) for emissivities with $n = 0 - 3$. The values of n label the curves.*

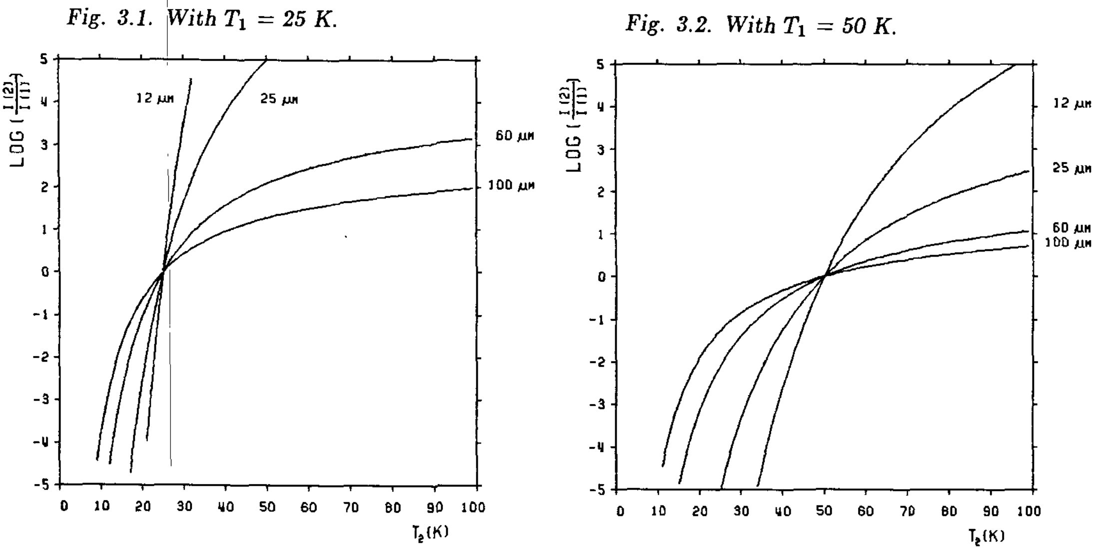

Fig. 3.1. With T_1 = 25 K.

Fig. 3.2. With T_1 = 50 K.

Figure 3. *Ratio of emitted intensities for equal amounts of dust at two temperatures, T_1 and T_2; T_1 is chosen fixed at 25 K (cool dust) and 50 K (warm dust) while T_2 varies from 0 to 100 K.*

Table 5. Relation between I_{60}/I_{100} and T_d for modified blackbodies ($n = 1.5$).

(1) T_d (K)	(2) I_{60}/I_{100} (in-band)	(3) I_{60}/I_{100} (Jy; $f_\nu \propto \nu^{-1}$)	(4) I_{60}/I_{100} (Jy)	(5) Ratio (column (4)/(3))	(6) $f_{100\,\mu m}$ (Jy)
5	0.000	0.000	0.000	----	----
10	0.011	0.004	0.001	0.16	----
15	0.093	0.036	0.017	0.47	0.01
20	0.287	0.111	0.082	0.74	0.09
25	0.593	0.230	0.214	0.93	0.36
30	0.997	0.386	0.404	1.05	0.95
35	1.481	0.574	0.633	1.10	1.94
40	2.025	0.784	0.883	1.13	3.34
45	2.612	1.012	1.139	1.13	5.14
50	3.224	1.249	1.392	1.11	7.30
55	3.848	1.491	1.635	1.10	9.78
60	4.472	1.733	1.865	1.08	12.5
65	5.090	1.973	2.080	1.05	15.5
70	5.694	2.207	2.281	1.03	18.8
75	6.280	2.434	2.466	1.01	22.1
80	6.845	2.653	2.638	0.99	25.7
85	7.389	2.864	2.796	0.98	29.4
90	7.909	3.065	2.942	0.96	33.2
95	8.405	3.258	3.078	0.95	37.1
100	8.879	3.441	3.203	0.93	41.1

Notes to Table 5:

a) The in-band intensity ratios (column 2) for T have been calculated by convolving the true spectrum with the IRAS responsivity function (IRAS, 1985a).
Use: Leiden AO-data and Co-added Survey data (see Schwering, 1986).

b) Column 3 has been calculated by dividing column 2 by the bandwidths and assuming an $f_\nu \propto \nu^{-1}$ intrinsic source spectrum.
Use: Official IRAS products like PSC, SSS, Skyflux images (IRAS, 1985a).

c) Column 4 gives the true ratio (after colour correction).

d) Column 5 gives the ratio of column (3) and column (4); this results in the colour correction factors of Table 2.B.

e) $f_{100\,\mu m}$ for 1 $M_\odot$ of dust at 53 kpc (LMC) is calculated. At 63 kpc (SMC) the flux densities are 0.71 times as much.

Fig. 3 shows the relative contribution of two dust temperature components T_1 and T_2, with different temperatures to the intensity in the line–of–sight. Fig. 3.1 uses a basic component T_1 of 25 K, the temperature of dust heated by the general interstellar radiation field; Fig. 3.2 uses a basic component T_1 of 50 K, typical HII regions dust temperatures. The component T_2 varies from 0 to 100 K.

Fig. 4 shows the line–of–sight temperature that is reconstructed with Equations (5.5) and (5.6), if there are two temperature components in the line–of–sight. The basic components are set to 15 K (dust associated with H_2), 25 K (dust associated with HI), and 50 and 75 K (HII region dust). The relative mass contribution is shown as labels to the curves. Although the calculated T_d (from $I_{60\mu m}/I_{100\mu m}$) depends on the emissivity exponent n the calculated T_d from T_1 and T_2 is independent of n. Because the infrared intensity goes as a high power $(4+n)$ of T_d, small fractions of hot dust give rise to high line–of–sight temperatures.

Fig. 4.1. With T_1 = 15 K.

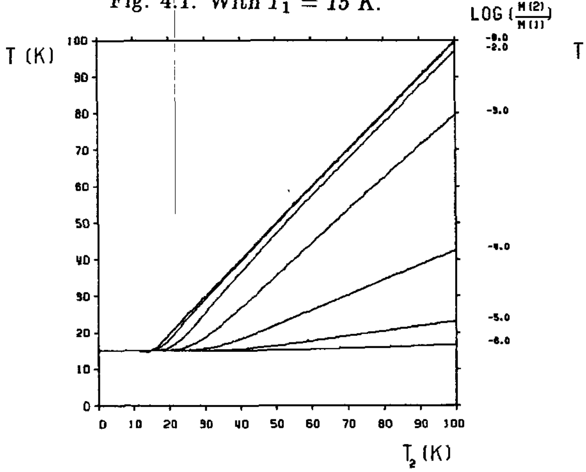

Fig. 4.2. With T_1 = 25 K.

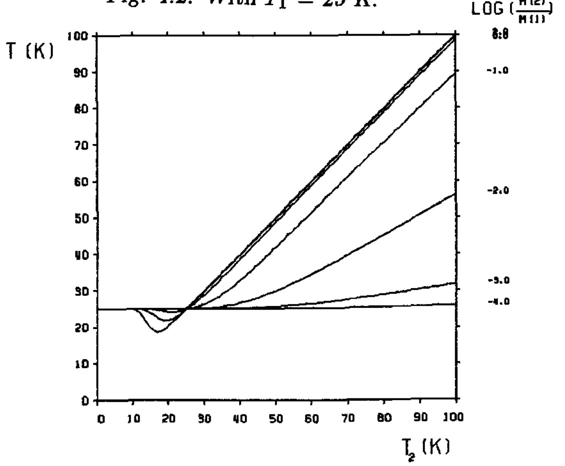

Fig. 4.3. With T_1 = 50 K.

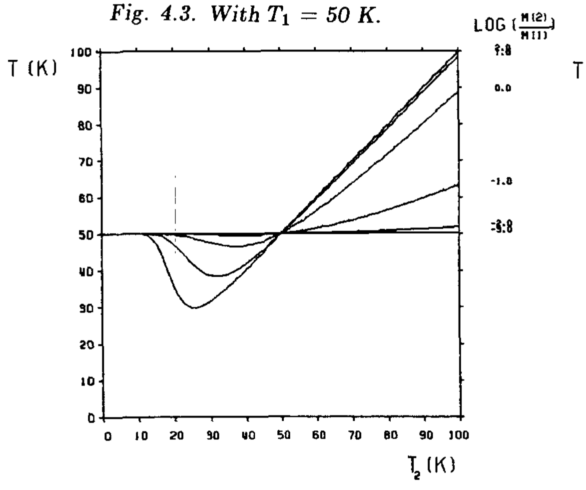

Fig. 4.4. With T_1 = 75 K.

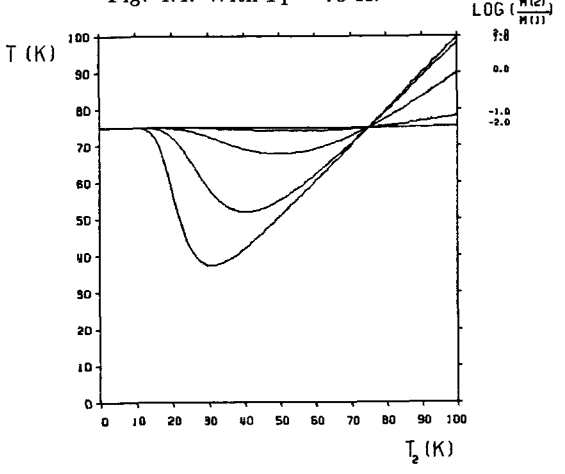

Figure 4. *Effect of reconstructing dust temperatures in a line–of–sight with two temperature components. The first component $M(T_1)$ is fixed at T_1 (15, 25, 50 and 75 K), an amount $M(T_2)$ of dust at T_2 is added; T is the derived line–of–sight temperature. T_2 varies from 0 to 100 K. The different curves are labeled according to the amount of dust at T_2 relative to the amount of dust at T_1.*

Temperature distributions are discussed in detail in Chapters IV (Galaxy) and V (Magellanic Clouds). In Chapter V we derive estimates for the radiation field in the Clouds. If the 60 μm and 100 μm, have partly different origins, *e.g.* part of the 60 μm emission comes from very small grains, only that fraction of the emission in the bands must be taken that is coming from the same emission mechanism; otherwise T_d is too high. The same is true if an extra 100 μm component is present; then T_d may be too low.

6. Far–infrared luminosity

A quantity that represents the total amount of infrared emission of objects is infrared luminosity L_{IR}. This quantity contains all the emitted infrared radiation and is an easy quantity to compare the infrared energy with *e.g.* visual energy. Galaxies emit a large part of their total infrared energy in the wavelength range covered by the IRAS 60 and 100 μm bands.

The infrared luminosity is calculated from the infrared flux using the known distance D to objects:

$$L_{IR} = 4\pi D^2 F_{IR}. \tag{6.1}$$

In the first papers after the IRAS mission (see de Jong *et al.*, 1984) the following quantity was used to estimate for the far–infrared flux:

$$F80 \equiv f_{80}\,\nu_{80} \qquad \text{where} \qquad f_{80} \equiv (f_{60} + f_{100})/2 \tag{6.2}$$

with f_{60} and f_{100} the observed IRAS flux densities at 60 and 100 μm respectively and ν_{80} the 80 μm frequency. Later another definition was given in *"Cataloged Galaxies and Quasars observed in the IRAS Survey"* (IRAS, 1985c) where the far–infrared parameter FIR is defined as:

$$FIR \equiv 1.26\ (f_{60}\Delta\nu_{60} + f_{100}\Delta\nu_{100}) \approx \int_{42.5\mu m}^{122.5\mu m} d\nu\ f_\nu \tag{6.3}$$

with $\Delta\nu_{60}$ and $\Delta\nu_{100}$ the IRAS 60 and 100 μm bandwidths (see Table 1). The factor 1.26 is used to fill the wavelength gap between these two IRAS bands. *FIR* is a good estimate for the flux that would have been measured within an ideal, square bandpass, 80 μm wide, centered at 82.5 μm. The emission of the thermal source is extremely well represented (within 1 %) for dust temperatures of 20 – 80 K and dust emissivity exponents ($n = 0,\ 1,\ 2$): the ranges of interest for galaxies. Irrespective of the detailed shape of the emission. *FIR* neglects emission at both shorter and longer wavelengths and therefore does not estimate the total far infrared emission very well.

The quantity *FIR* is compared to *F*80 as they resemble roughly the same thing. The relation is a function of the temperature of the dust (*i.e.* $\alpha \equiv f_{60\mu m}/f_{100\mu m}$), and $FIR/F80$ ranges from 0.67 for cool dust ($\alpha = 0$) and is monotomically increasing up to 1.73 at the other extreme ($\alpha = \infty$). FIR equals $F80$ for $\alpha = 0.45$, and for cool galactic dust with $\alpha \approx 0.2$ (Buat and Deharveng, 1987) the ratio is 0.85.

The total far-infrared emission (1 – 500 μm) TIR is found from FIR using the factors of Table 6.A. Figure 5.1 displays these values for $n = 0 - 3$. These bolometric correction factors extrapolate FIR over the whole infrared wavelength range using $I_{60\mu m}/I_{100\mu m}$ as a single temperature indication of the dust T_d and assuming the appropriate emissivity exponent n. The ratio TIR/FIR strongly depends on n and on T_d. The uncertainty in n (± 0.5) gives a relative uncertainty in TIR/FIR of 20 %.

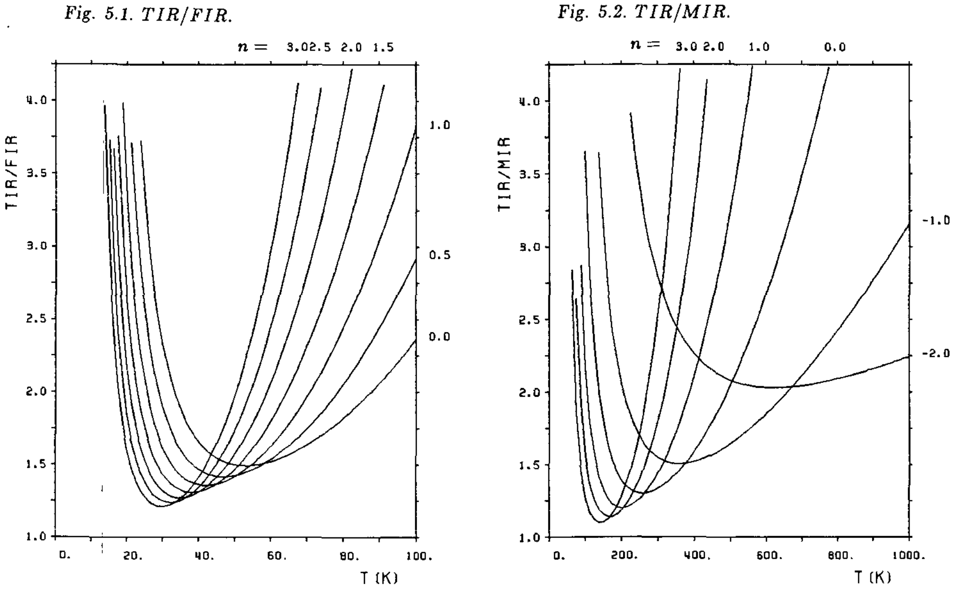
Fig. 5.1. TIR/FIR.

Fig. 5.2. TIR/MIR.

Figure 5. *Bolometric correction factors. For different emissivities, labeled n in the figure, correction factors are given at dust temperatures of 0 – 100 K, in order to integrate the observed far-infrared emission (FIR) and 0 – 1000 K to integrate the mid-infrared emission (MIR) over all wavelengths.*

The 12 and 25 μm emission as measured by IRAS are not fit very well with the 60/100 μm dust temperature. A two component model is better (one representing the 60 and 100 μm emission and the other the 12 and 25 μm emission), each extrapolated over the infrared wavelength range separately and added afterwards. Analog to FIR we define MIR that gives the amount of mid-infrared radiation (between 8 and 30 μm)

$$MIR \equiv 1.26\ (f_{12}\Delta\nu_{12} + f_{25}\Delta\nu_{25}) \approx \int_{8\mu m}^{30\mu m} d\nu\ f_\nu . \qquad (6.4)$$

Table 6.A. Bolometric correction factors for the cold 60 and 100 µm dust component: TIR / FIR (<10).

T(K)	n=0.0	n=0.5	n=1.0	n=1.5	n=2.0	n=2.5	n=3.0
10.0	-----	-----	-----	-----	-----	-----	-----
12.5	-----	-----	-----	-----	-----	7.604	5.741
15.0	-----	-----	8.831	6.394	4.802	3.732	2.995
17.5	9.673	6.777	4.949	3.760	2.965	2.421	2.038
20.0	6.035	4.391	3.336	2.640	2.168	1.842	1.611
22.5	4.276	3.216	2.529	2.072	1.761	1.545	1.394
25.0	3.303	2.558	2.074	1.750	1.531	1.382	1.280
27.5	2.712	2.157	1.796	1.556	1.397	1.292	1.225
30.0	2.328	1.897	1.618	1.437	1.320	1.248	1.210
32.5	2.068	1.723	1.503	1.364	1.281	1.237	1.225
35.0	1.885	1.604	1.429	1.325	1.270	1.252	1.265
37.5	1.755	1.523	1.385	1.309	1.280	1.287	1.327
40.0	1.662	1.470	1.362	1.313	1.308	1.342	1.411
42.5	1.595	1.437	1.356	1.332	1.353	1.414	1.517
45.0	1.549	1.420	1.365	1.365	1.412	1.504	1.644
47.5	1.518	1.416	1.385	1.410	1.485	1.611	1.795
50.0	1.500	1.423	1.416	1.467	1.572	1.737	1.971
52.5	1.493	1.440	1.456	1.534	1.673	1.881	2.175
55.0	1.495	1.464	1.505	1.612	1.789	2.046	2.407
57.5	1.504	1.496	1.563	1.701	1.919	2.232	2.672
60.0	1.519	1.535	1.628	1.801	2.064	2.442	2.973
62.5	1.541	1.580	1.702	1.911	2.226	2.676	3.312
65.0	1.568	1.631	1.783	2.033	2.405	2.937	3.694
67.5	1.599	1.688	1.872	2.167	2.601	3.227	4.122
70.0	1.635	1.750	1.969	2.312	2.817	3.547	4.602
72.5	1.676	1.818	2.074	2.470	3.053	3.902	5.138
75.0	1.720	1.891	2.187	2.641	3.311	4.292	5.736
77.5	1.768	1.969	2.308	2.825	3.591	4.721	6.399
80.0	1.820	2.053	2.438	3.024	3.896	5.192	7.136
82.5	1.876	2.143	2.577	3.237	4.226	5.708	7.952
85.0	1.934	2.237	2.724	3.466	4.583	6.272	8.855
87.5	1.997	2.337	2.881	3.712	4.970	6.888	9.852
90.0	2.063	2.443	3.048	3.974	5.387	7.560	-----
92.5	2.132	2.554	3.224	4.255	5.837	8.291	-----
95.0	2.204	2.671	3.410	4.553	6.320	9.087	-----
97.5	2.280	2.793	3.607	4.872	6.841	9.950	-----
100.0	2.359	2.922	3.815	5.210	7.399	-----	-----

Table 6.B. Bolometric correction factors for the warm 12 and 25 μm dust component: TIR / MIR (<10).

T(K)	n=-2.0	n=-1.0	n=0.0	n=1.0	n=2.0	n=3.0
25	-----	-----	-----	-----	-----	-----
50	-----	-----	-----	-----	-----	6.380
75	-----	-----	9.040	4.396	2.644	1.856
100	-----	8.247	3.656	2.169	1.559	1.274
125	-----	4.485	2.306	1.564	1.257	1.124
150	8.374	3.092	1.778	1.328	1.155	1.104
175	5.996	2.424	1.524	1.229	1.142	1.159
200	4.702	2.054	1.392	1.199	1.185	1.281
225	3.915	1.831	1.327	1.215	1.274	1.469
250	3.399	1.691	1.303	1.264	1.407	1.731
275	3.042	1.602	1.307	1.342	1.585	2.079
300	2.785	1.548	1.334	1.446	1.810	2.527
325	2.596	1.518	1.378	1.576	2.086	3.095
350	2.453	1.506	1.437	1.730	2.420	3.805
375	2.344	1.507	1.510	1.911	2.818	4.686
400	2.260	1.519	1.595	2.119	3.287	5.769
425	2.196	1.541	1.692	2.355	3.837	7.091
450	2.146	1.569	1.800	2.620	4.477	8.694
475	2.108	1.604	1.919	2.918	5.219	-----
500	2.079	1.645	2.049	3.250	6.072	-----
525	2.058	1.690	2.190	3.618	7.052	-----
550	2.044	1.740	2.342	4.024	8.170	-----
575	2.034	1.794	2.505	4.470	9.442	-----
600	2.029	1.852	2.679	4.961	-----	-----
625	2.028	1.913	2.865	5.497	-----	-----
650	2.030	1.977	3.062	6.082	-----	-----
675	2.035	2.044	3.271	6.719	-----	-----
700	2.043	2.115	3.492	7.410	-----	-----
725	2.052	2.188	3.726	8.160	-----	-----
750	2.063	2.264	3.972	8.970	-----	-----
775	2.076	2.343	4.232	9.843	-----	-----
800	2.090	2.424	4.504	-----	-----	-----
825	2.106	2.508	4.790	-----	-----	-----
850	2.122	2.594	5.090	-----	-----	-----
875	2.140	2.682	5.403	-----	-----	-----
900	2.159	2.773	5.731	-----	-----	-----
925	2.178	2.867	6.074	-----	-----	-----
950	2.198	2.962	6.431	-----	-----	-----
975	2.219	3.060	6.803	-----	-----	-----
1000	2.241	3.161	7.191	-----	-----	-----

The same factor of 1.26 is used, as this approximately fills the band gap. Extrapolating the 12 and 25 μm points using a blackbody spectrum (with T depending on the ratio $I_{12\mu m}/I_{25\mu m}$) gives us an estimate for the total flux in this component. Table 6.B and Figure 5.2 give these factors for values of n between -2 and $+3$ (note that the value $n = 1.5$ for the emissivity exponent is not valid for $\lambda < 50$ μm). When we do not take into account the emission of cold (15 K) dust in the very–far infrared ($\lambda > 250$ μm), the total infrared emission is the sum of the extrapolated FIR and MIR:

$$F_{IR} = (\frac{TIR}{FIR})\ FIR\ +\ (\frac{TIR}{MIR})\ MIR. \tag{6.5}$$

The Clouds integrated infrared luminosities are subjects of Chapter V. Detailed maps of the infrared luminosities are shown in Chapter VII.

7. Optical depth, dust column density and dust masses

For the ideal object with a homogeneous composition we are now in a situation where we can find integrated dust properties. Let us assume here that our object indeed fulfills this criterium.

In nearly all astronomical cases the optical depth determined from the spectra at wavelengths longer than 100 μm are found to be very much less than 1. Hence the observed flux densities sample with equal efficiency emission from all depths in the object. The optical depth for a homogeneous object is then found from

$$\tau_\nu = -\ln\,(1 - \frac{I_\nu}{B_\nu(T_d)}) \approx \frac{I_\nu}{B_\nu(T_d)} \qquad \text{for} \quad \tau_\nu << 1. \tag{7.1}$$

The characteristic that the emission is optically thin allows us to obtain dust masses from spatially integrated flux densities via (4.12)

$$M_d \ = \ \frac{f_\nu\ D^2}{\kappa_\nu\ B_\nu(T_d)}. \tag{7.2}$$

Here D is the distance to the object that emits the radiation. When using intensities instead of flux densities we cannot just invert Equation (5.3) because then we would get the mass of dust that radiates in a single line–of–sight. We assume isotropic radiation and we make use of the relation $I_\nu = f_\nu/\Delta\Omega$, where $\Delta\Omega$ is the solid angle of an area of which the mass has to be calculated (*e.g.* dust mass per beam). The equation for dust mass becomes

$$M_d \ = \ \frac{I_\nu\ D^2\ \Delta\Omega}{\kappa_\nu\ B_\nu(T_d)}. \tag{7.3}$$

Table 5 gives 100 μm flux densities that would be observed for sources of 1 $M_\odot$ at the distance of the LMC (53 kpc). If κ_ν depends on T_d, the exact relation $\kappa_\nu(T_d)$ affects the dust mass (see Draine and Lee, 1984; Dwek, 1988). The dust mass column density (when $\Delta\Omega$ is the solid angle of a 1 cm^2 column) is found from

$$\tilde{N}_d = \frac{M_d}{D^2\,\Delta\Omega} = \frac{I_\nu}{\kappa_\nu\, B_\nu(T_d)}. \tag{7.4}$$

This column density, as the optical depth, measures the whole line–of–sight and is therefore independent of distance. The above can be transformed in a dust particle column density by dividing by the mass of an average grain $m_d = 4/3\ \pi a^3\ \rho_d \approx 1.3 \times 10^{-17}$ kg (7.6 x 10^9 a.m.u.): $N_d = \tilde{N}_d/m_d$. In Chapter IV we use $N_d \equiv \tilde{N}_d/m_{HI}$, with m_{HI} the mass of a hydrogen atom (1.67 x 10^{-27} kg) to estimate the Galactic foreground dust column. Dust column densities in the Clouds are discussed in Chapter VI. In Chapter VII we discuss dust–to–gas ratios and luminosity–to–mass ratios for the Clouds.

The poor knowlegde of κ_ν at wavelengths below 30 μm makes the estimation of dust masses in that component very uncertain. The dust mass for this component is very small because of the high dust temperatures. Most of the dust in galaxies emits in the 60 and 100 μm range and hence the total dust mass is not influenced by mid–infrared emission.

8. Multiple dust components contributing to the infrared emission

A method for fitting an n–component model ($n \leq 3$) to the four bands of IRAS data was started at Leiden Observatory by Braun (1985). A description of this method is given by Walterbos and Schwering (1987). Another model to predict the far–infrared emission, is given by Buat and Deharveng (1987). Rowan–Robinson (1987) describes various models. These models assume fixed temperature components.

From inspection of the Magellanic Cloud infrared maps we noticed varying temperatures over the whole face of the Clouds. Modelling of those maps, similar to modelling done by Walterbos and Schwering (1987) on M31, did not give a result of the same quality.

In Chapter VI we have used another method to decompose temperature components in each line–of–sight. First of all, we calculated line–of–sight dust temperatures, as explained in Section 5. This also gives the dust column densities via Section 7. In the case that temperature variations are excluded both T_d and M_d are correct (*e.g.* if the line–of–sight is short). These column densities are assumed to be lower limits as the temperature is biased towards high infrared intensities; hence we obtain M_l. We have maps of T_d and M_d, based on line–of–sight data. We calculate the lowest temperature T_{low} and the highest temperature T_{high} for the object. We divide this range in temperature steps ΔT, and, starting at $T_i = T_{low}$, calculate for each $T_i = T_{i-1} + \Delta T$ in the range, the area covered by dust of this temperature. We then assume that in all lines–of–sight with $T_d > T_i$, also dust is present of temperature T_i, and take its mass surface density equal to the average of the observed density in the region with $T_d = T_i$. We correct infrared intensities for this component to conserve the total infrared flux, and continue up to $T_i = T_{high}$. The mass in each components is the sum of all lines–of–sight in each component. The mass in each line–of–sight is the sum of all components in that line–of–sight. The total dust mass is the sum of all components. This is an upper limit, as some lines–of–sight are dominated by the warmer dust, while others are thin; hence we obtain M_u. The best estimate for the dust mass is then set to $(M_l + M_u)/2$. The mass of the cold (15 K) dust component cannot be obtained from IRAS observations alone, but need additional observations at sub-mm wavelengths.

9. Summary

In this appendix we described the basic quantities that are of importance in interpreting far-infrared IRAS data. In relation to the data itself, some uncertainties are mentioned in Section 3 and we discussed the colour corrections, that have to be applied to the IRAS data, in detail. Colour correction tables and figures are included.

Dust characteristics are studied in Section 4. From a list of observed and theoretical spectra we have obtained an average emissivity in the far-infrared ($\lambda > 40\ \mu$m), using Q_ν of Hildebrand (1983) for the absolute scaling: κ_ν (cm^2 g^{-1}) $= 40\ (c/\nu)^{-1.5}$. Through our work we have used this dust absorption coefficient to derive dust temperatures and dust masses. At shorter wavelengths ($\lambda < 40\mu$m) we derived temperatures using $\kappa_\nu = constant$ (hence we obtained colour temperatures).

In Section 5 we have derived an equation to calculate dust temperatures, and we have discussed the relation of the temperature and the radiation field. A table with band ratios for different dust temperatures, based on different types of IRAS data, is given; figures are included. In Section 6 we obtained quantities to find the total infrared luminosity of objects. Tables and figures, giving the bolometric correction factors, are included. The dust mass calculation procedure is explained in Section 7 and Section 8 gives a new method to estimate dust masses in thick galaxies.

Acknowledgements

I wish to thank Mr. H. Greidanus for useful comments.

References

Braun, R.: 1985, Ph.D. Thesis, University of Leiden

Buat, V., Deharveng, J.M.: 1988, ***Astron. Astrophys.*** **195**, 60

Campbell, M.F., Elias, J.H., Gezari, D.Y., Harvey, P.M., Hoffmann, W.F., Hudson, H.S., Neugebauer, G., Soifer, B.T., Werner, M.W., Westbrook, W.E.: 1976, ***Astrophys. J.*** **208**, 396

Chini, R., Mezger, P.G., Kreysa, E., Gemünd, H.-P.: 1984a, ***Astron. Astrophys.*** **135**, L14

Chini, R., Kreysa, E., Mezger, P.G., Gemünd, H.-P.: 1984b, ***Astron. Astrophys.*** **137**, 117

Cox, P., Krügel, E., Mezger, P.G.: 1986, ***Astron. Astrophys.*** **155**, 380

Cox, P., Mezger, P.G.: 1988, in ***"Comets to Cosmology"***, Lecture Notes on Physics **297**, Springer Berlin, 97

Day, K.L.: 1976, ***Astrophys. J.*** **210**, 614

Draine, B.T., Lee, H.M.: 1984, ***Astrophys. J.*** **285**, 89

Draine, B.T., Anderson, N.: 1985, ***Astrophys. J.*** **292**, 494

Dwek, E.: 1988, ***Astrophys. J.*** in preparation

Dyson, J.E., Williams, D.A.: 1980, ***Physics of the Interstellar medium***, Wiley, New York, p62

Erickson, E.F., Tokunaga, A.T.: 1980, ***Astrophys. J.*** **238**, 596

Erickson, E.F., Strecker, D.W., Simpson, J.P., Goorvitch, D., Augason., G., Scargle, J.D., Caroff, L.J., Witteborn, F.C.: 1977, *Astophys. J.* **212**, 696

Erickson, E.F., Caroff, L.J., Simpson, J.P., Strecker, D.W., Goorvitch, D.: 1977, *Astrophys. J.* **216**, 404

Erickson, E.F., Knacke, R.F., Tokunaga, A.T., Haar, M.R.: 1981, *Astrophys. J.* **245**, 148

Fazio, G.G.: 1978, in *"Infrared Astronomy"*, eds. G. Setti, G.G. Fazio, Reidel Dordrecht, 25

Gatley, I., Becklin, E.E., Werner, M.W., Wynn-Williams, C.G.: 1977, *Astrophys. J.* **216**, 277

Gezari, D.Y.: 1982, *Astrophys. J. (Letters)* **259**, L29

Greenberg, J.M.: 1978, in *"Infrared Astronomy"*, eds. G. Setti, G.G. Fazio, Reidel Dordrecht, 51

Harvey, P.M., Campbell, M.F., Hoffmann, W.F.: 1978b, *Astrophys. J.* **219**, 891

Harvey, P.M., Hoffmann, W.F. Campbell, M.F.: 1978b, *Astron. Astrophys.* **70**, 165

Harwit, M.: 1982, in *"Galactic and Extragalactic Infrared Spectroscopy"*, eds. M.F. Kessler, J.P. Phillips, ESA, Paris, 143

Hasegawa, H.: 1984, in *"Workshop on Laboratory and Observational Infrared Spectra of Interstellar Dust"*, eds. R.D. Wolstencroft, J.M. Greenberg, Occas. Rep. R. Obs. Edinburgh **12**, 36

Hasegawa, H., Koike, C.: 1984, in *"Workshop on Laboratory and Observational Infrared Spectra of Interstellar Dust"*, eds. R.D. Wolstencroft, J.M. Greenberg, Occas. Rep. R. Obs. Edinburgh **12**, 137

Heiles, C., Reach, W.T., Koo, B.-C.: 1988, *Astrophys. J.* in press.

Herter, T., Duthie, J.G., Pipher, J.L., Savedoff, M.P.: 1979, *Astrophys. J.* **234**, 897

Hildebrand, R.H., Whitcomb, S.E., Winston, R., Stiening, R.F., Harper, D.A., Moseley, S.H.: 1977, *Astrophys. J.* **216**, 698

Hildebrand, R.H.: 1983, *Quartly J. R. Astron. Soc.* **24**, 267

IRAS: 1985a, IRAS Catalogs and Atlasses Explanatory Supplement, eds. C.A. Beichmann, G. Neugebauer, H.J. Habing, P.E. Clegg, T.J. Chester, JPL D-1855

IRAS: 1985b, IRAS Small Scale Structure Catalog, eds. G. Helou, D.W. Walker, JPL D-2988

IRAS: 1985c, Catalogued Galaxies and Quasars observed in the IRAS Survey, eds. C.J. Lonsdale, G. Helou, J.C. Good, W.L. Rice, JPL D-1932

IRAS: 1986b, *IRAS Atlas of low resolution spectra*, eds. F.M. Olnon, E. Raimond, Astron. Astrophys. Suppl. 65, 607 Quasars: JPL D-1932

Israel, F.P, Koornneef, J.: 1988, *Astron. Astrophys.* **190**, 21

Jones, T.W., Stern, W.A.: 1975, *Astrophys. J.* **197**, 297

Keene, J.: 1981, *Astrophys. J.* **245**, 115

Leene, A., Pottasch, S.R.: 1986, in *"Light on Dark Matter"*, ed. F.P. Israel, Reidel Dordrecht, 143

Léger, A., Puget, J.L.: 1984, *Astron. Astrophys.* **137**, L5

Marsden, P.L., Gillett, F.C., Jennings, R.E., Emerson, J.P., de Jong, T., Olnon, F.M.: 1984, *Astrophys. J. (Letters)* **278**, L29

Mathis, J.S., Rumpl, W., Nordsieck, K.H.: 1977, *Astrophys. J.* **217**, 425

Mathis, J.S., Mezger, P.G., Panagia, N.: 1983, *Astron. Astrophys.* **128**, 212

Mezger, P.G., Mathis, J.S., Panagia, N.: 1982, *Astron. Astrophys.* **105**, 372

Moseley, H.: 1980, *Astrophys. J.* **238**, 892

Nandy, K.: 1984, in *"Structure and Evolution of the Magellanic Clouds"*, IAU Symp. **108**, eds. S. van den Bergh, K.S. de Boer, Reidel Dordrecht, 341

Pipher, J.L., Duthie, J.G., Savedoff, M.P.: 1978, *Astrophys. J.* **219**, 494

Pottasch, S.R.: 1986, in *"Light on Dark Matter"*, ed. F.P. Israel, Reidel Dordrecht, 131

Puget, J.L., Léger, A., Boulanger, F.: 1985, *Astron. Astrophys.* **142**, L19

Righini, G., Simon, M., Joyce, R.R.: 1976, *Astrophys. J.* **207**, 119

Roche, P.F., Aitken, D.K., Smith, C.H.: 1987, *Mon. Not. R. Astron. Soc.*, in press

Rowan–Robinson, M.: 1987, in Star Formation in Galaxies , ed. C.J. Lonsdale Persson, NASA Conference Publication 2466, 133

Schwartz, P.R.: 1982, *Astrophys. J.* **252**, 589

Schwering, P.B.W.: 1986, Leiden Sterrewacht Internal Report

Scoville, N.Z., Kwan, J.: 1976, *Astrophys. J.* **206**, 718

Seab, G.M., Shull, J.M.: 1984, in *"Workshop on Laboratory and Observational Infrared Spectra of Interstellar Dust"*, eds. R.D. Wolstencroft, J.M. Greenberg, Occas. Rep. R. Obs. Edinburgh **12**, 26

Sellgren, K., Werner, M.W., Dinerstein, H.L.: 1983, *Astrophys. J. (Letters)* **271**, L13

Spitzer Jr., L.: 1978, *Physical Processes in the Interstellar medium*, Wiley, New York, p162

Thronson Jr., H.A., Harper, D.A.: 1979, *Astrophys. J.* **230**, 133

Tokunaga, A.T., Erickson, E.F., Caroff, L.J.: 1978, *Astrophys. J. (Letters)* **224**, L19

de Vries C.P.: 1986, Ph.D. Thesis, University of Leiden

Walterbos, R.A.M., Schwering, P.B.W.: 1987, *Astron. Astrophys.* **180**, 27

Waters, L.B.F.M.:1986, *Astron. Astrophys.* **162**, 121

Werner, M.W., Gatley, I., Harper, D.A., Becklin, E.E., Loewenstein, R.F., Telesco, C.M., Thronson, H.A.: 1976, *Astrophys. J.* **204**, 420

Watson, D.M.: 1982, in *"Galactic and Extragalactic Infrared Spectroscopy"*, eds. M.F. Kessler, J.P. Phillips, ESA, Paris, 193

Williams, D.A.: 1982, in *"Galactic and Extragalactic Infrared Spectroscopy"*, eds. M.F. Kessler, J.P. Phillips, ESA, Paris, 59

Willner, S.P.: 1982, in *"Galactic and Extragalactic Infrared Spectroscopy"*, eds. M.F. Kessler, J.P. Phillips, ESA, Paris, 37

Summary

This thesis presents the results of an extensive study of the infrared and dust properties of the Magellanic Clouds.

The space between stars is emptier than the best vacua produced in the laboratory. However, it still contains large amounts of gas and dust. The main form of gas is hydrogen. Dust (also called smoke) can be observed indirectly by its absorption of visual light of stars. This effect is more important at higher frequencies, resulting in the reddening of light. In most cases, infrared emission is not absorbed by dust.

The origin of infrared emission is dust. Dust grains consist of about 10^{10} atoms and have an average radius of 0.1 μm. Dust is formed in the outer layers of stars in their latest evolution phases, after which it is sent into interstellar space. Accumulations of dust can occur and molecular hydrogen can form on their surfaces. Dust grains are heated by the general interstellar radiation field or by closeby complexes of young stars. The temperature of the dust varies from $-260\,^\circ$C to $-200\,^\circ$C. This is warm enough to emit infrared emission with a maximum in the spectrum between 50 and 200 μm.

Together with M31 and M33 the Magellanic Clouds are the only two galaxies that could be resolved in substantial detail with the Infrared Astronomical Satellite (IRAS). Because of their closeness, details of order 10 times smaller than in the nearest spiral galaxy M31 and 50 times smaller than in comparable dwarf irregular galaxies can be seen. General morphological aspects of the infrared emission, relations between infrared emission and other wavelength data and properties of dust in the Magellanic Clouds are discussed. The infrared Galactic foreground in the direction of the Clouds is also discussed.

Chapter II describes the observations of the SMC obtained with the IRAS satellite. Maps are presented at wavelengths of 12, 25, 60 and 100 μm. From these maps a list of 219 discrete infrared sources is extracted. This source list is compared to known object lists (foreground stars, SMC stars, Hα nebulosities, clusters, supernova remnants, planetary nebula and dark clouds). There is a good correlation between HII regions and infrared emission from the SMC. In an Appendix a discussion of two fields at the SE and SW edges of the SMC is given. These areas contain 29 sources, which are also compared to other source lists.

Chapter III deals with IRAS infrared observations of the LMC. A similar presentation and discussion is given as for the SMC. A list of 1823 discrete sources is extracted, which is compared to similar source lists as in Chapter II. Seven fields at the North and West edges of the LMC are discussed in an Appendix. These fields contain another 68 sources, which are also compared to other source lists. As for the SMC, there is also a very good correlation of the infrared emission peaks with HII regions in the LMC.

Chapter IV contains a discussion of the Galactic infrared foreground emission. Until now most authors assume a constant Galactic foreground reddening towards the LMC of 0.07 magnitude. Foreground filaments disturb the image of this Cloud, and the IRAS data show significant variations in the foreground. The relation between the infrared foreground emission and the atomic hydrogen content is discussed and it is found to be non–linear. Infrared maps were corrected for temperature effects. These maps are compared to the atomic hydrogen emission. An estimate for the foreground infrared emission is derived, based on the average gas–to–dust ratio. The foreground towards the LMC varies from 0.07

to 0.17 magnitude, with an average of 0.10. The foreground towards 30 Doradus shows less extinction than towards other LMC regions. One of the implications is that studies of the LMC in the visual and ultraviolet wavelength regions should be corrected for a varying foreground. A more or less constant foreground of 0.08 magnitude towards the SMC is found.

Chapter V deals with the global properties of the Magellanic Clouds. Integrated infrared flux densities, infrared sizes, infrared luminosities and dust temperatures are derived. The infrared morphology is discussed, together with the temperature distribution. It turns out that the Greater 30 Doradus Region emits about 40 % of all infrared radiation. The density of the interstellar radiation field in the Clouds is derived. In some HII regions it is more than 10 times stronger than in the Galaxy, while the radiation fields at the edge of the Clouds are comparable to that in the Solar Neighbourhood. On average the fields are 7 times stronger than the Solar Neighbourhood field. A relation is found between infrared emission and the Hα supergiant shells in the LMC. Comparisons of the infrared maps are presented with ultraviolet data, Hα maps and with radio continuum observations. This shows the relation of the infrared emission with the radiation field in the Clouds. The spectral shape of the Clouds is similar to that of another irregular galaxy NGC 4449, but very different from that of M31. The SMC is 10 to 20 times weaker than the LMC in the infrared.

Chapter VI presents a discussion of the dust properties in the Magellanic Clouds. The mid–infrared (12 and 25 μm) emission is discussed in detail. This emission in the Clouds is less than that in the Local Group spiral galaxies. It is most likely that very small grains are responsible for this emission. Dust masses are derived for the combined warm ($\sim$ 50 K) and cool (25 K) dust components. The mass present in the cold (15 K) dust component is estimated to be between 1/3 and 1 times the mass of cool dust. Total dust masses of 550 000 solar masses for the LMC and 24 000 solar masses for the SMC are derived. Dust column density maps are presented for both Clouds. From a comparison of the infrared maps with atomic hydrogen maps, similar non–linear relations are found as for the Galactic foreground in Chapter IV.

Chapter VII contains a further discussion of the global properties of the Clouds, the relation of the Clouds with irregular galaxies and the relation of the Clouds with Local Group spiral galaxies. The infrared colours of the Clouds are similar to the colours of other irregular galaxies. There are some exceptions, NGC 6822 and NGC 1569 have much lower $f_{12\mu m}/f_{25\mu m}$ ratios than the Clouds, but their $f_{60\mu m}/f_{100\mu m}$ ratios are similar. The luminosity–to–mass ratio of the SMC is similar to that of other irregular galaxies. That ratio of the LMC is an order of magnitude higher, and is comparable to that of spiral galaxies such as IC 342, M101 and M33. Relative to the irregular galaxies, the gas–to–dust ratio in the LMC is low. Again NGC 1569 is an exceptional case. In the colour–colour diagrams, the Local Group spiral galaxies are clearly separated from the irregular galaxies, showing relatively cool dust emission in those galaxies. The LMC gas–to–dust ratio is probably not very different from that in M31 and M33. The gas–to–dust ratio in the Clouds is discussed. For the LMC a ratio 3 times higher than for the Milky Way is found; for the SMC the ratio is 50 times higher than for the Milky Way. The LMC value agrees well with that of other authors, based on photometric B and V measurements and Lyα absorption. The SMC value is, however, 3 to 6 times higher than those ratios. This difference is explained by Galactic foreground difficulties in photometric observations: high foreground extinction values from Chapter IV suggest large variations on small scales for individual stars. A new fit is made to the E_{B-V} and N_{HI} data, showing agreement with the dust mass based on infrared data. These findings also agree with the integrated ratio $L_{100\mu m}/M_{HI}$, which is about 30 times lower for the SMC than for the Galaxy.

In an Appendix, a description of the far-infrared radiative transfer theory is given. It also contains tables and figures for colour corrections, temperature calculations and bolometric corrections.

Resumen

En esta tesis se presentan los resultados de un extenso estudio de las propiedades del infrarrojo y del polvo de las Nubes de Magallanes.

El espacio existente entre las estrellas es más vacío que el mejor "vacuum" producido en el laboratorio. Pero, aún así, contiene grandes cantidades de gas y polvo. La principal forma de gas es el hidrógeno. El polvo puede ser observado indirectamente debido a su absorción de la luz visual de las estrellas. Este efecto es más importante a frecuencias más altas, resultando en un enrojecimiento de la luz. En la mayoría de los casos, la emisión infrarroja no es absorbida por el polvo.

El origen de la emisión infrarroja es el polvo. Las partículas de polvo consisten de, aproximadamente, 10^{10} átomos y tienen un radio promedio de 0.1 μm. El polvo se forma en las capas externas de las estrellas, en sus últimas fases de evolución, después de lo cual es enviado al espacio interestelar. Puede acumularse el polvo y formarse hidrógeno molecular en sus superficies. Las partículas de polvo son calentadas por el campo general de radiación interestelar o por complejos cercanos de estrellas jóvenes. La temperatura del polvo varía de $-260\,^\circ$C a $-200\,^\circ$C. Esta es lo suficientemente caliente para emitir radiación infrarroja con un máximo en el espectro entre 50 y 200 μm.

Junto con la M31 y la M33, las Nubes de Magallanes son las únicas dos galaxias que podrían ser resueltas en gran detalle con el Satélite Astronómico Infrarrojo (IRAS). Debido a su proximidad pueden ser vistos detalles del orden de 10 veces más pequeños que en la galaxia espiral más próxima, la M31, y 50 veces más pequeños que en galaxias enanas irregulares comparables. Se discuten aspectos morfológicos generales de la emisión infrarroja, relaciones entre emisión infrarroja y otros datos de longitud de onda, y las propiedades del polvo en las Nubes de Magallanes. Se trata el frente Galáctico infrarrojo en dirección a las Nubes.

En el capítulo II se describen las observaciones de la Nube Menor de Magallanes, obtenidas con el satélite IRAS. Los mapas se presentan en longitudes de onda de 12, 25, 60 y 100 μm. De estos mapas se extrajeron una lista de 219 fuentes discretas de infrarrojo. Esta lista de fuentes se compara a listas de objetos conocidos (estrellas de la Vía Láctea, estrellas de la Nube Menor, nebulosidades Hα, grupos de estrellas, remanentes de supernovas, nebulosa planetaria y nubes obscuras). Se muestra que hay una buena correlación entre las regiones HII y la emisión infrarroja desde la Nube Menor. En un apéndice de este capítulo se discuten dos zonas en los extremos SE y SO de la Nube Menor. Estas áreas contienen 29 fuentes que también se comparan a otras listas de fuentes.

El capítulo III versa sobre las observaciones en infrarrojo de la Nube Mayor de Magallanes, efectuadas con el IRAS. Se presenta una exposición y discusión similar sobre la Nube Menor. Se extrae una lista de 1823 fuentes discretas, la que se compara a las listas de fuentes similares al capítulo II. En un apéndice de este capítulo se discuten siete zonas en los extremos del Norte y Oeste de la Nube Mayor. Estas zonas contienen otras 68 fuentes, las cuales se comparan también a otras listas de fuentes. Se encuentra nuevamente una muy buena correlación de los puntos más altos de la emisión infrarroja y las regiones HII.

El capítulo IV contiene un análisis de la emisión del frente galáctico infrarrojo. Hasta ahora, la mayoría de los autores asume un constante enrojecimiento del frente galáctico

hacia la Nube Mayor de 0.07 magnitud. Filamentos del frente interfieren con la imagen de esta Nube y los datos obtenidos con el IRAS muestran fuertes variaciones en el frente. Se discute la relación entre la emisión infrarroja del frente y el contenido atómico del hidrógeno; se descubre que es no–lineal. Se corrigieron mapas infrarrojos para efectos de temperatura. Estos mapas se comparan con la emisión del hidrógeno atómico. Se deriva una estimación para el frente infrarrojo, basada en la proporción gas a polvo promedio. El frente hacia la Nube Mayor varía de 0.07 a 0.17 magnitud, con un promedio de 0.10. El frente hacia 30 Doradus muestra menos extinción que en otras regiones de la Nube Mayor. Una de las implicaciones al respecto es que estudios sobre la Nube Mayor, en las regiones de longitud de onda visual y ultravioleta, deberían ser corregidos por un frente variante. Hacia la Nube Menor se encuentra un frente de 0.08 magnitud.

El capítulo V trata de las propiedades globales de las Nubes de Magallanes. Se derivan densidades de flujo infrarrojo integrado, tamaños infrarrojos, luminosidades infrarrojas y temperaturas del polvo. Se discute la morfología infrarroja, junto con la distribución de la temperatura. Resulta que la región mayor del 30 Doradus, emite cerca del 40 % de toda la radiación infrarroja. Posteriormente se deriva la densidad de la zona de radiación interestelar en las Nubes. En algunas regiones HII es de 10 veces más potente que en la galaxia, mientras que las zonas de radiación en los extremos de las Nubes se comparan a aquellas en la proximidad solar. En promedio las zonas son 7 veces más potentes que la zona de proximidad solar. Se encuentra una relación entre la emisión infrarroja y los anillos super–gigantes Hα en la Nube Mayor. Se presentan comparaciones de los mapas infrarrojos con datos ultravioletas, con mapas Hα y con observaciones de radio continuo. Esto muestra la relación de la emisión infrarroja con la zona de radiación en las Nubes. La forma espectral de las Nubes es similar a la de otra galaxia irregular, la NGC 4449, pero muy diferente a la M31. En el infrarrojo, la Nube Menor es entre 10 y 20 veces más débil que la Nube Mayor.

En el capítulo VI se presenta un análisis de las propiedades del polvo en las Nubes de Magallanes. La emisión infrarroja–media (12 y 25 μm) se discute en detalle. En las Nubes esta emisión es menor que aquella en las galaxias espirales del Grupo Local. Lo más probable es que partículas muy pequeñas sean las responsables de esta emisión. Las masas de polvo se derivan para las componentes combinadas del polvo caliente (de –250 °C a –225 °C) y frío. La masa presente en la componente del polvo frío (–260 °C) se estima entre 1/3 y 1 veces la masa del polvo frío. Se derivan masas totales de polvo de 550 000 masas solares para la Nube Mayor y 24 000 masas solares para la Nube Menor. Se presentan, para ambas Nubes, mapas de densidad de columna del polvo. Al comparar los mapas infrarrojos con mapas de hidrógeno atómico, se encuentran relaciones no–lineales similares para el frente galáctico (ver capítulo IV).

El capítulo VII contiene un análisis más detenido de las propiedades globales de las Nubes, la relación de las Nubes con galaxias irregulares y la relación de las Nubes con las galaxias espirales del Grupo Local. Los colores infrarrojos de las Nubes son similares a los colores de otras galaxias irregulares. Hay algunas excepciones: la NGC 6822 y la NGC 1569 tienen proporciones de $f_{12\mu m}/f_{25\mu m}$ mucho más bajas que las Nubes, pero sus proporciones de $f_{60\mu m}/f_{100\mu m}$ son similares. La proporción luminosidad a masa de la Nube Menor es similar a la misma proporción para otras galaxias irregulares. La proporción de la Nube Mayor es un factor de 10 más alto y está entre varias galaxias espirales como la IC342, M101 y la M33. En relación a las galaxias irregulares, la proporción gas a polvo en la Nube Mayor es baja. Nuevamente, la NGC 1569 es un caso excepcional. En los diagramas color contra color, las galaxias espirales del Grupo Local están claramente separadas de las galaxias irregulares, mostrando una emisión de polvo relativamente frío en estas galaxias. La proporción gas a polvo de la Nube Mayor está probablemente no muy lejos de aquella en la M31 y M33. Mas aún, se discute la proporción gas a polvo en las Nubes. Para la Nube Mayor se encuentra una proporción de 3 veces más que el de la Vía Láctea; para la Nube Menor la proporción es 50 veces mayor que la de la Vía Láctea. El valor de la Nube Mayor concuerda bien con aquel de otros autores, basado en medidas fotométricas B y V y absorción Lyα. El valor de la Nube Menor es, sin embargo, de 3 a 6 veces más alto que aquellas proporciones. Esta diferencia se explica por las dificultades en las observaciones fotométricas a consecuencia del frente galáctico: altos valores de extinción del frente en el capítulo IV sugieren grandes variaciones en pequeñas escalas para estrellas individuales. Se ha hecho un nuevo ajuste de los datos E_{B-V} y N_{HI}, mostrando concordancia con la masa del polvo basada en datos infrarrojos. Estos descubrimientos también concuerdan con la proporción integrada de $L_{100\mu m}/M_{HI}$, la cual es alrededor de 30 veces menor para la Nube Menor que para la Galaxia.

En un apéndice se presenta una descripción de la teoría de transferencia de radiación infrarroja–lejana. También contiene tablas y figuras para la corrección de colores, cálculos de temperaturas y correcciones bolométricas.

Samenvatting

In dit proefschrift worden de resultaten van een uitgebreid onderzoek van de infrarood– en stofeigenschappen van de Magelhaense Wolken, ook wel Kaapse Wolken, besproken.

De ruimte tussen de sterren is leger dan het beste Aardse vacuum, maar bevat toch grote hoeveelheden gas en stof. Het gas bestaat voornamelijk uit waterstof. Het stof, ook wel rook genoemd, kunnen we indirect waarnemen omdat dit het licht van sterren verzwakt. Dit effect speelt een grotere rol voor het ultraviolette en blauwe licht dan voor het rode en infrarode licht, waardoor het licht verkleurt (het wordt roder: verroding). Meestal wordt het infrarode licht niet verzwakt en meet de astronoom dus alle infrarode straling die door een bron wordt uitgezonden.

De oorzaak van deze infrarode straling is ditzelfde stof. Stofdeeltjes bestaan uit circa 10 miljard atomen en hebben een gemiddelde straal van een tienduizendste millimeter. Stof wordt gevormd in de laatste evolutie–fasen van sterren. Daarna wordt het in het interstellaire medium verspreid, waar het zich kan ophopen en kan bijdragen aan de productie van waterstof–moleculen. In het interstellaire medium wordt het stof opgewarmd door het gezamelijke stralingsveld van alle sterren. Als het zich in een complex van jonge sterren bevindt zal het door deze sterren tot hogere temperaturen worden verhit. De temperatuur die zij hierbij krijgen varieert van −260 °C tot −200 °C. Dit is zo "warm" dat de stofdeeltjes infrarode straling gaan uitzenden met een maximale sterkte op golflenten tussen 50 en 200 micrometer (een twintigste tot een vijfde millimeter).

Samen met de Andromedanevel M31 en de Driehoeknevel M33, zijn de Magelhaense Wolken de enige melkwegstelsels die voldoende dichtbij staan om goed in detail te kunnen worden bestudeerd met de gegevens van de Infrarood Astronomische Satelliet (IRAS). Door hun nabijheid zijn tien maal kleinere details te zien dan in M31 en vijftig maal kleinere details dan in vergelijkbare onregelmatige sterrenstelsels. Er wordt een bespreking gegeven van de algemene morfologische aspecten van de infrarode emissie, de relaties tussen infrarode emissie en emissie bij andere golflengten, alsmede de eigenschappen van stof.

In hoofdstuk II worden IRAS waarnemingen van de Kleine Magelhaense Wolk gepresenteerd in de vorm van volledige–resolutie kaarten bij golflengten van 12, 25, 60 en 100 μm. Uit deze kaarten is een bronnenlijst met 219 discrete objecten samengesteld. Deze lijst is vergeleken met lijsten van andere objecten (voorgrond sterren, sterren in de Wolk, Hα emissienevels, clusters van sterren, supernova resten, planetaire nevels en donkere wolken). Er blijkt een goede correlatie te bestaan tussen de gebieden van geïoniseerde waterstof en gebieden van infrarode emissie in de Kleine Wolk. In een appendix worden twee velden aan de zuid–oost en zuid–west rand van de Kleine Wolk behandeld. Deze velden bevatten 29 infrarood–bronnen die eveneens zijn vergeleken met andere bronnenlijsten.

Hoofstuk III behandelt de IRAS waarnemingen van de Grote Magelhaense Wolk in een vergelijkbare presentatie als voor de Kleine Wolk. In totaal bevinden zich 1823 bronnen in de hiermee verkregen bronnenlijst. Deze lijst is vergeleken met identieke lijsten als voor de Kleine Wolk in hoofdstuk II. Zeven velden aan de noordelijke en westelijke rand van de Wolk zijn in een appendix behandeld. Deze velden bevatten nog eens 68 bronnen. Ook voor de Grote Wolk blijkt er een goede overeenkomst te bestaan tussen infrarode emissie en gebieden van geïoniseerde waterstof.

In hoofdstuk IV wordt de infrarode straling van de Galactische voorgrond behandeld. Tot nu toe werd er altijd aangenomen dat de voorgrond in de richting van de Grote Magelhaense Wolk een egale verroding veroorzaakt van 0.07 magnitude. In deze richting bevinden zich verschillende voorgrond filamenten, en IRAS kaarten laten significante variaties in stofdichtheden zien. De relatie tussen de infrarode straling en de emissie van atomaire waterstof blijkt niet lineair te zijn. De infrarood–kaarten zijn gecorrigeerd voor de stoftemperatuur en vergeleken met waterstof. Hieruit wordt de gemiddelde voorgrond gas–stof verhouding bepaald. In de richting van de Grote Wolk variëert de verroding van 0.07 tot 0.17 magnitude, met een gemiddelde van 0.10. De voorgrond van de 30 Doradusnevel vertoont minder verroding dan die van andere gebieden in de Grote Wolk. Een van de gevolgen is dat studies aan de Grote Wolk bij visuele of ultraviolette golflengten voor deze variërende voorgrond moeten worden gecorrigeerd. In de richting van de Kleine Wolk worden geen variaties gevonden en er wordt een verroding vastgesteld van 0.08 magnitude.

Hoofdstuk V behandelt de globale eigenschappen van de Magelhaense Wolken: geïntegreerde infrarood–helderheden, afmetingen van deze melkwegstelsels in het infrarood, lichtsterkten in het infrarood en stoftemperaturen zijn bepaald. Dit hoofdstuk bevat een uitgebreide behandeling van de infrarood–morfologie en de temperatuurverdeling. Het 30 Doradus gebied produceert 40 % van alle emissie in het infrarood. Het interstellaire stralingsveld in de Wolken is berekend en blijkt aan de randen overeen te komen met het Galactische stralingsveld in de Zonsomgeving. In HII gebieden is het ruim 10 maal zo sterk en gemiddeld is het 7 maal zo sterk in beide Wolken. Er is een relatie gevonden tussen infrarode emissie en Hα–schillen in de Grote Wolk. Vergelijkingen van de infrarood–kaarten met ultraviolette gegevens, Hα–kaarten en radiocontinuum–waarnemingen zijn gedaan. Deze laten zien dat de infrarood–emissie is gerelateerd aan zware jonge sterren. De vorm van het infrarode spectrum is voor beide Wolken hetzelfde; het spectrum lijkt op dat van het grote onregelmatige stelsel NGC 4449. Het laat warmer stof zien dan het spectrum van M31. Bij infrarode golflengten is de Kleine Magelhaense Wolk 10 tot 20 maal zwakker dan de Grote Wolk.

In hoofdstuk VI wordt een discussie van de eigenschappen van het stof in de Magelhaense Wolken gegeven. Er is minder 12 en 25 μm emissie in de Wolken dan in de spiraalnevels van de Lokale Groep. Zeer waarschijnlijk zijn zeer kleine stofdeeltjes verantwoordelijk voor deze emissie. Totale stofmassa's voor het warme (–225 °C), koele (–250 °C) en koude (–260 °C) stof zijn afgeleid. De totale stofmassa's zijn 550 000 zonsmassa's voor de Grote en 24 000 zonsmassa's voor de Kleine Magelhaense Wolk. Kaarten met stof–kolomdichtheden zijn gepresenteerd en vergeleken met atomair waterstof: er is een goede correlatie. Een vergelijkbare niet–lineaire relatie tussen infrarode emissie en atomaire waterstof–emissie is gevonden als voor de Galactische voorgrond (zoals bediscussieerd in hoofdstuk IV).

Hoofdstuk VII bevat een discussie van de globale eigenschappen van de Magelhaense Wolken, de relatie van de Wolken met andere onregelmatige melkwegstelsels en de relatie van de Wolken met Locale Groep–stelsels. De infrarode kleuren van de Wolken komen goed overeen met die van de andere onregelmatige stelsels. Uitzonderingen daarop zijn NGC 6822 en NGC 1569, die een veel lagere verhouding van de straling bij 12 en 25 μm hebben dan de Wolken; de 60 en 100 μm stralingsverhouding is niet opmerkelijk verschillend. De lichtkracht–massa verhouding van de Kleine Wolk stemt overeen met die van de andere onregelmatige stelsels; die van de Grote Wolk is een factor 10 hoger en valt tussen spiraalnevels als IC 342, M101 en M33. T.o.v de onregelmatige stelsels is de gas–stof verhouding in de Grote Wolk zeer laag. De kleuren van de Lokale Groep-spiraalstelsels zijn duidelijk verschillend van die van de onregelmatige stelsels. Dit laat zien dat zij koeler stof bevatten. De gas–stof verhouding in the Grote Wolk is bijna gelijk aan die in M33. De gas–stof verhouding in de Grote Wolk is bepaald op 3 maal, en die in de Kleine Wolk op 50 maal die in de melkweg. Deze waarde voor de Grote Wolk is ook door andere auteurs gevonden d.m.v. visuele en ultraviolette Lyα metingen. De waarde voor de Kleine Wolk is 3 tot 6 maal hoger dan gevonden met laatstgenoemde methode. De hogere voorgrond–verroding, die in hoofdstuk IV gevonden is, voorspelt voor individuele sterren op kleine schaal sterke voorgrond stof variaties. Een nieuwe vergelijking is gemaakt van de visuele en ultraviolette gegevens die laat zien dat deze methode ook een hogere gas–stof verhouding kan geven. De gevonden verhouding is in overeenstemming met de lichtkracht–massa verhoudingen gevonden m.b.v geïntegreerde waarden.

In een appendix wordt een beschrijving gegeven van het stralingstransport. Ook bevat de appendix tabellen en figuren voor kleurcorrecties, temperatuur bepalingen en bolometrische correcties van IRAS gegevens.

Curriculum Vitae

In juni 1978 behaalde ik het diploma Atheneum–B aan het Veurs College te Leidschendam. In september van dat jaar begon ik met de studie sterrenkunde aan de Rijksuniversiteit te Leiden. De eerste fase werd in april 1981 afgerond met het kandidaatsexamen A1 met hoofdvakken sterrenkunde en natuurkunde en bijvak wiskunde. Drie jaar later slaagde ik voor het doctoraal examen sterrenkunde met bijvak theoretische natuurkunde.

Tijdens de doctoraal fase volgde ik colleges van de hoogleraren Swarup, van de Hulst, van Schooneveld, Habing, Capel en Terwiel en van dr. van Leer. Gedurende een onderzoekje naar stationaire oplossingen van Burger's vergelijking d.m.v. impliciete tijdsafhankelijke differentieschemas, leerde dr. van Leer mij numeriek simuleren. Onder leiding van prof. W.B. Burton verrichte ik onderzoek aan de rotatiecurve van de melkweg m.b.v. 21–cm neutrale waterstof metingen van de Greenbank telescoop. Ik verhuisde voorgoed buiten de melkweg. Ik verwerkte en analyseerde, o.l.v. prof. W.W. Shane en dr. E. Brinks, 50–cm radiocontinuum metingen gemaakt met de Westerbork Synthese Radio Telescoop van het nabije melkwegstelsel, de Andromedanevel.

Het extragalactische werk werd voortgezet met het onderwerp van mijn proefschrift, de Magelhaense Wolken. Metingen gemaakt met de Infrarood Astronomische Satelliet zijn verwerkt, en de aanwezige informatie over de stofeigenschappen in deze naburige stelsels geanalyseerd. Het promotieonderzoek werd uitgevoerd tussen juni 1983 en augustus 1988, als wetenschappelijk assistent aan de Leidse universiteit. Voor mijn werk bezocht ik het IRAS grondcontrolestation in Chilton (U.K.), het Jet Propulsion Laboratory te Pasadena (U.S.A.) en de Europese Zuidelijke Sterrenwacht (ESO te Chile). Daarnaast bezocht ik IRAS software development workshops in Abingdon (U.K.), IPAC Pasadena (U.S.A.) en Groningen. Ik bezocht conferenties in zes plaatsen met een bijna evengroot aantal bijdragen: Nijmegen (1982), Groningen (1983), Toulouse (1984), Marseille (1985), Noordwijk (1985) en Les Arcs (1987).

Vanaf 1 december 1987 ben ik in dienst van het Fysisch en Electronisch Laboratorium van T.N.O. te 's–Gravenhage, waar ik aardse wolken bestudeer.

Nawoord

Velen hebben aan de totstandkoming van dit proefschrift bijgedragen. Aan de wetenschappelijke kant hebben interacties met stafleden, promovendi en studenten een positieve invloed op het resultaat gehad. De sfeer op de Leidse Sterrewacht komen die interacties zeer ten goede.

Conferentie bezoeken zijn mogelijk gemaakt door financiële steun van het Leids Kerkhoven–Bosscha Fonds. Een bezoek aan het Jet Propulsion Laboratory te Pasadena werd gefinancierd door de Stichting Ruimte Onderzoek Nederland. Samen met Arnaud Leene verbleef ik in de nederlandse IRAS residentie in La Cañada Flintridge, een suburb van L.A. Y en uno de mis viajes para observar el cielo austral encontré una estrella muy especial.

Zonder de IRAS satelliet zou dit werk niet mogelijk zijn geweest. De figuren zijn bekwaam afgedrukt door W. Brokaar, L. Zuyderduin en J. Ober. Er is gebruik gemaakt van verschillende tekstverwerkers, hierbij was de hulp en het advies van velen onmisbaar. Verscheidene programmeurs hielpen bij software problemen, schijfruimte gebrek en datachecks: K. Lugtenborg, K. Weerstra, T. Hoekema, D. Hogeweg, P. Alphenaar en A. Vos. Hedy heeft zich vakkundig bezig gehouden met veel zaken. De mooiste herineringen heb ik aan haar bijdrage in vele persoonlijke gesprekken.

Mijn ouders hebben mij de vrijheid gegeven om mijn eigen weg te volgen. Mimo siempre prepara rica comida. En los últimos tres años, Yoya ha enriquecido mi vida.